REPORT DOCUMENTATION PAGE

AFRL-SR-AR-TR-03-

0024

1. AGENCY USE ONLY *(Leave blank)*	2. REPORT DATE	3. REPORT TITLE AND DATES COVERED
		01 JUL 96 to 31 DEC 01 FINAL

4. TITLE AND SUBTITLE
ARPA MUR-95 Multidisciplinary Optical Switching Technology Center (MOST)

5. FUNDING NUMBERS
61103D
3484/RS

6. AUTHOR(S)
PROFESSOR BOWERS

7. PERFORMING ORGANIZATION NAME(S) AND ADDRESS(ES)
UNIVERSITY OF CALIFORNIA SANTA BARBARA
CHEADLE AHLL
SANTA BARBARA, CA 93106-2050

8. PERFORMING ORGANIZATION REPORT NUMBER

9. SPONSORING/MONITORING AGENCY NAME(S) AND ADDRESS(ES)
Department of the Air Force
Air Force Office of Scentific Research
801 N. Randolph St Rm 732
Arlington. VA 22203-1977

10. SPONSORING/MONITORING AGENCY REPORT NUMBER

F49620-96-1-0349

11. SUPPLEMENTARY NOTES

12a. DISTRIBUTION AVAILABILITY STATEMENT
Distribution Statement A. Approved for public release; distribution is unlimited.

12b. DISTRIBUTION CODE

13. ABSTRACT *(Maximum 200 words)*
This MURI grant was reviewed within the overall program in July of 1998 by government science and technology managers from DARPA, BMDO, and DDRandE as well as by the AFOSR program manager and found superlative in achieving stated goals and program objectives. Documentation of specific technical progress is retained with the grant funding records in the form of annual technical reports.
The MOST center successfully addressed the following aspects of optical switching technology within the MURI program:
 .3D Waveguide Lntercomnct Technolgies
 .40 0bps All-Optical Wavelength Conversion and Packet Routing
 .Optical Packet Schedulers and Optical Internet Protocol Routers
 . 4x4 Switches with integrated gain
 .Hybrid Polymer/Semiconductor Waveguide Devices
 .OEO Wavelength Converters and Crossbar Switches
 .Ultrafast optical communications with space-time multiplexers

20030305 101

14. SUBJECT TERMS

15. NUMBER OF PAGES

16. PRICE CODE

17. SECURITY CLASSIFICATION OF REPORT	18. SECURITY CLASSIFICATION OF THIS PAGE	19. SECURITY CLASSIFICATION OF ABSTRACT	20. LIMITATION OF ABSTRACT
Unclassified	Unclassified	Unclassified	UL

Standard Form 298 (Rev. 2-89) (EG)
Prescribed by ANSI Std. 239.18
Designed using Perform Pro, WHS/DIOR, Oct 94

MULTIDISCIPLINARY OPTICAL SWITCHING TECHNOLOGY CENTER (MOST)

FINAL REPORT

AUGUST 1, 1996 – DECEMBER 31, 2001

Program Managers:

Robert Leheny (DARPA)
Lt. Col. Gernot Pomrenke (AFOSR)

Director:

John E. Bowers
Electrical and Computer Engineering Department
University of California at Santa Barbara

TABLE OF CONTENTS

I. Overview

In the past 30 years, fiber optic communications and optical networks have progressed from a laboratory concept, to a multi-billion dollar telecommunications industry and recently on to form the backbone technology of the next generation Internet. The successful transmission of multiple wavelengths on a single fiber coupled with robust optical amplifiers and dispersion compensation has enabled transmission of high-speed signals over thousands of kilometers without converting the signal back to electronic form. Single wavelength transmission rates have increased from 50 Mbit/s 18 years ago to 40 Gigabits/sec (Gbps) in 2001. Commercial systems with 40-80 wavelengths operating at 10 Gbps per wavelength are being installed and systems capable of delivering 10 Gbps on each of 160 wavelengths have been commercially demonstrated. Ultra-high-Capacity transmission systems with greater than 10 Terabits/sec over a single fiber have been demonstrated in the laboratory (1 Tbps = 10^{12} bits/sec).

We have entered a new communications age that increasingly depends on the transmission and dissemination of Internet traffic. As the world moves to upgrade the existing communications network to accommodate this change, the exponentially increasing demand for packet-based traffic has outstripped traditional voice traffic as illustrated in Figure 1. The rapid deployment of DSL and cable modem technologies coupled with real-time applications like video streaming will mean that an additional 100 million homes will require Internet access via 100 Mbit/s to Gigabit Ethernet connections per home.
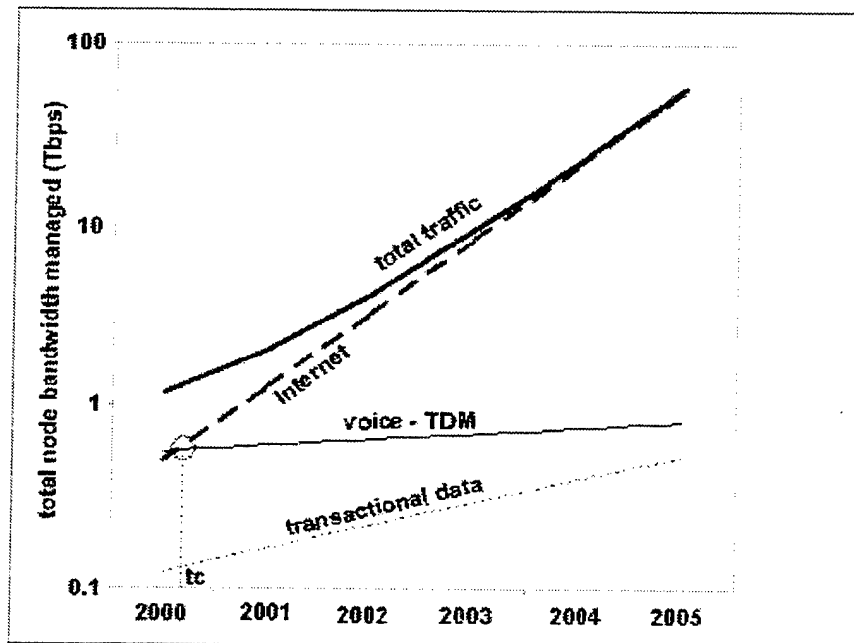

Figure 1. Voice vs. Internet traffic growth for Greenfield Networks.
[Source: "Greenfield Optical Switched Transport Networks: A Cost Analysis," C.R. Lima, M.Allen and B.Faer, Valiant Networks, Inc., NFOEC Technical Proceedings, pp. 1449-1457 (2001).]

A Roadmap to Next Generation Optical Networks

The current bandwidth explosion is placing demands on the network that moves beyond the transmission bandwidth and into the switching and routing capacity. It has become costly to switch and route the complete fiber transmission bandwidth using electronic technology alone, especially as wavelength counts exceed 40 and bit-rates climb to 10 Gbps and beyond. The next generation of fiber-optic networks will see a new partnership between optical switching and advance electronic technologies, where data is switched in the optical domain until it is necessary to interact with individual bits using electronics. Optical switching will undergo an evolution that mirrors advances in technology. The agility with which optical signals can be reconfigured has moved from static environment to a more dynamic optical circuit switched environment using reconfigurable photonic crossconnects (PXCs) and optical add/drop multiplexers (OADMs) as illustrated in the roadmap in Figure 2. Research today has moved to higher degrees of agility where signals are regenerated and converted to new wavelengths all-optically. Switching technologies go beyond circuits into switching bursts of data and optical packet switching.
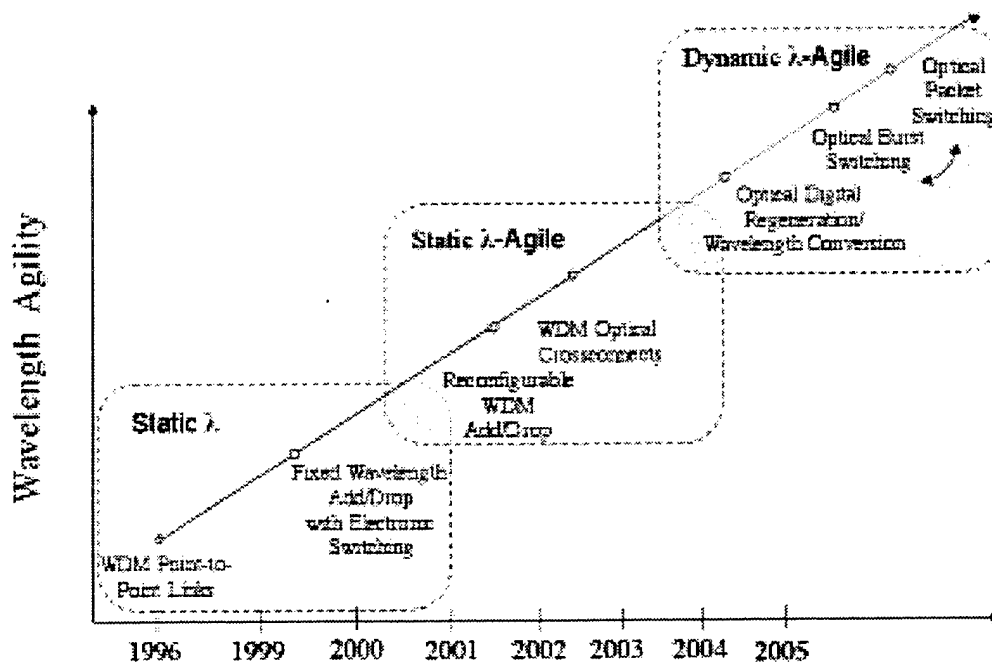

Figure 2. Evolutionary roadmap of optical networks.
[Source: D. J. Blumenthal, OIDA Workshop on Wavelength-Agile Photonic Systems, Rhode Island, October 18-19 (2001)]

3

MOST Multidisciplinary Research

The MOST Center at UCSB is a broad multidisciplinary research program sponsored by the DoD Multidisciplinary University Research Initiative (MURI) program. Over the 5-year lifetime of the center, a broad range of research topics related to optical switching, the underlying technologies and relevant network topics were supported and investigated. Photonic transmission and device researchers worked closely with protocol researchers and electrical integrated circuit designers. The high-performance requirements of optical switching systems and components required the close involvement of growth and processing specialists. The MOST Center and its research components over the Center lifetime is illustrated in Figure 3.
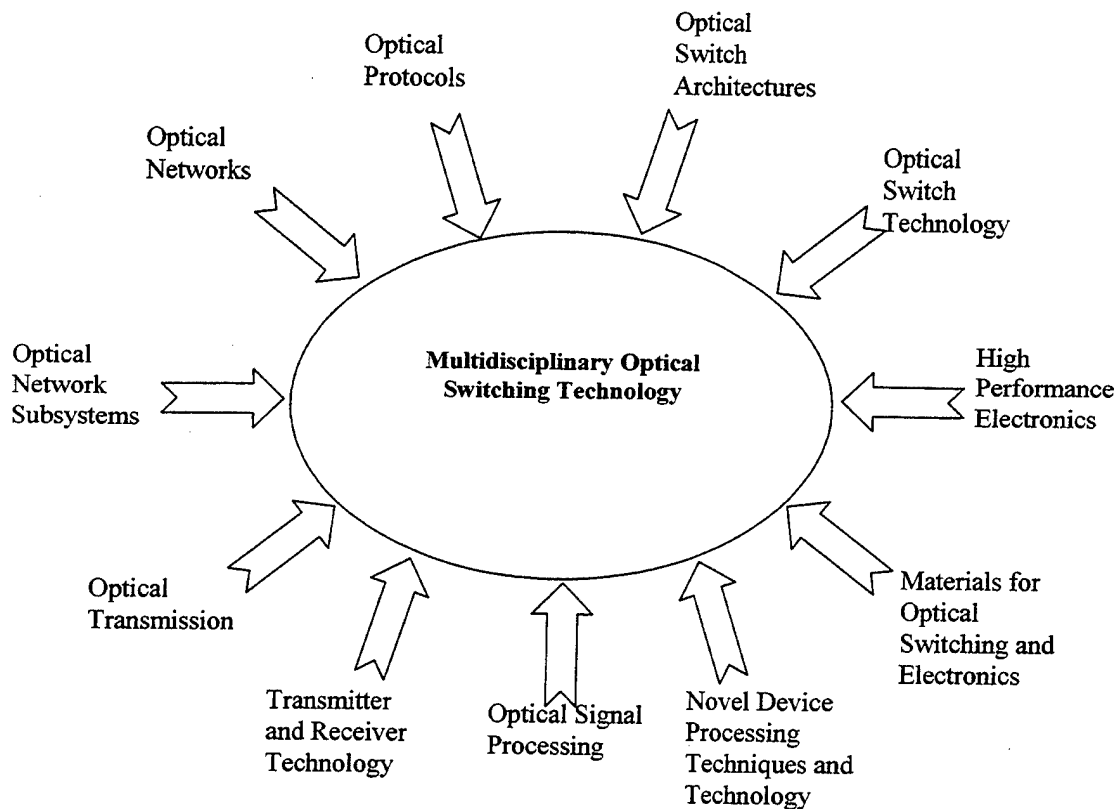

Figure 3. MOST Center multidisciplinary vision.

This publication represents the collective work of multiple faculty at UCSB and their students and collaborators over the 5 year period of the MURI award. We have assembled a representative collection of publications and MURI reviews as well as an overview of personnel supported, graduated students, facilities and technology transfer.

II. MOST Advisory Board

DARPA	Robert Leheny
	Bertram Hui (now at Intel)
AFOSR	Alain Craig (now at U. of Montana)
	Kent Miller
	Gernot Pomrenke
Rome Labs	Robert Payne
JPL	Larry Bergman
CIENA Corp.	Steve Chaddick
Rockwell	Derek Cheung
	K.C. Wang
Agilent	Waguih Ishak
Telcordia	P. Kaiser (now at Kaiser Consulting)
Alcatel	Adel Shamseldin
Cisco	Jacek Chrostowski
Caltrans	Ramez Gerges

MOST Faculty

Dan Blumenthal

John E. Bowers

Steve Butner

Larry Coldren

Nadir Dagli

Steve DenBaars

Yeshaiahu Fainman (UC San Diego)

Art Gossard

Michael Melliar-Smith

Luise Moser

Mark Rodwell

Manos Varvarigos

MOST Graduate Students

Jonathan Barton

Yi-Chen Chiu (now at National Sun Yat-sen University, Taiwan)

Hsu-Feng Chou

Jennifer Dolan

Greg Fish (now at Agility Communications)

Zachary Griffith (now postdoc at UCSB)

Mats Herolf (now at Ericsson)

Andrew Jackson (now at Cielo)

Volkan Kaman (now at Calient Networks)

Jonathan Lang (now at Calient Networks)

Bin Liu (now postdoc at UCSB)

Rajasekhar Pulella

Yae Okuno

Cem Ozturk

Maura Raburn

Lavanya Rau

Allen Shum (now at SPAWAR)

MOST Postdocs and Visitors

Patrick Abraham (now at Agility Communications)

Gabriella Bosco (now at Politecnico di Torino, Italy)

Adrian Keating (now at Calient Networks)

Boo-Gyoun Kim (Soongsil University, Korea)

Mads Lonstrup-Nielsen (now at Technical University of Denmark)

Bengt-Erik Olsson (now at Optillion)

Peter Ohlen (now at Optillion)

Joachim Piprek

Andrea Pozzi (now at Politecnico di Torino, Italy)

Giammarco Rossi (now at Agilent)

Lorene Samoska

Ali Shakouri (now at University of California, Santa Cruz)

MOST Staff

Mike Anzlowar

Vickie Edwards

Christina Loomis

Gerry Robinson

Diana Thurman

III. Group Summaries

3D Photonic Circuits and Active Devices for OTDM Systems

John E. Bowers

We have developed different elements of three-dimensional (3D) photonic circuits for sophisticated switching applications. Wafer bonding is the enabling technology that allows the fabrication of complex 3D photonic waveguide structures not realizable with any other approach. Figure 1 shows a schematic view of a wafer-bonded 3D photonic circuit. By vertical waveguide coupling across the fused interface, we achieve high coupling efficiency at short coupling lengths. By repeatedly etching waveguides and fusing additional planar layers, multilevel interconnects are fabricated. Several novel 3D routing waveguide devices have been created from InP/InGaAsP or GaAs/AlGaAs:
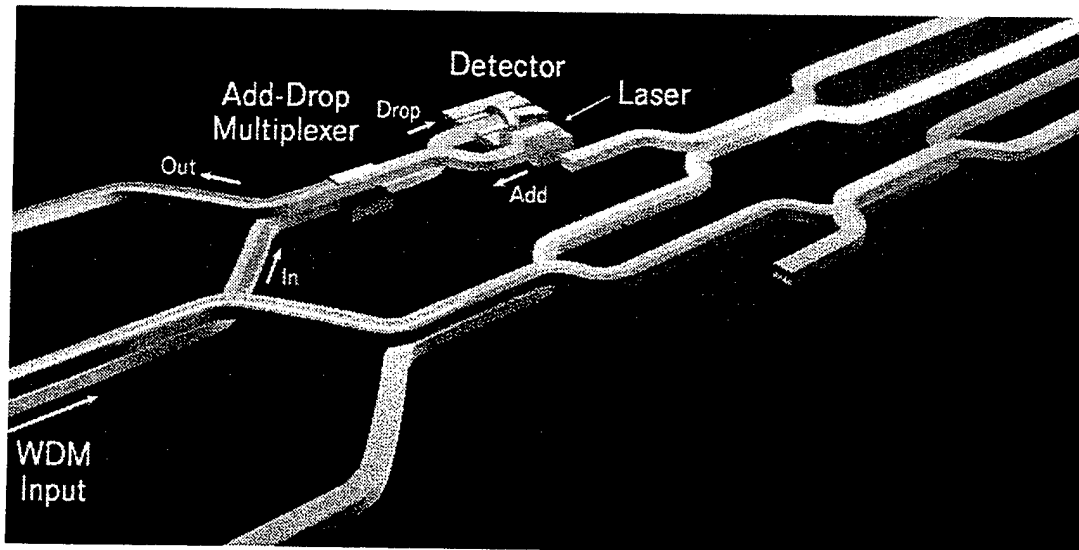
Fig. 1: Schematic view of a three-dimensional photonic circuit

(1) By anti-phase fusing two waveguide structures, the anisotropy of the linear electrooptic effect in zincblende crystals was used to produce an opposite index change in two coupled waveguides with only two contacts. A push-pull fused vertical coupler switch using this effect was realized and switched under 12 V reverse bias (Fig. 2).

(2) A 4-channel wavelength multiplexer/demultiplexer was also built by combining 3D vertical couplers. For this device 17 nm channel spacing with crosstalk less than 20 dB was achieved.

Fig. 2: Push-pull wafer-bonded vertical coupler switch. Top: design, bottom: performance.

Fig. 3: Three-layer wafer-bonded 1:8 beam splitter.

(3) A novel three-layer double-bonded InP-InGaAsP waveguide vertical coupler 1:8 beam splitter was demonstrated (Fig. 3). The strongly coupled waveguides allow a 583-micron device length, more than one hundred times shorter than that of the equivalent horizontal coupler. The device illustrates the use of multiple vertical layer optical interconnects for three-dimensional routing of optical signals.

9

(4) Multi-channel vertically coupled InP/InGaAsP optical add-drop multiplexers (OADMs) were fabricated for wavelength division multiplexing (WDM) applications (Fig. 4).
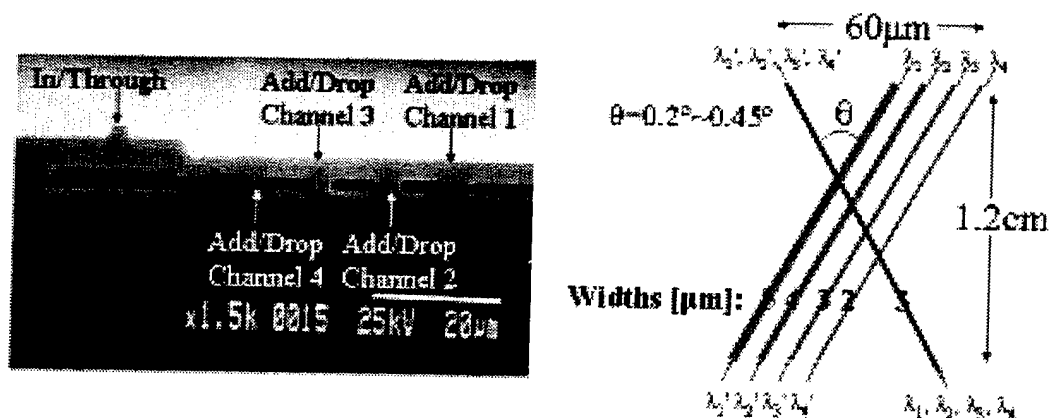

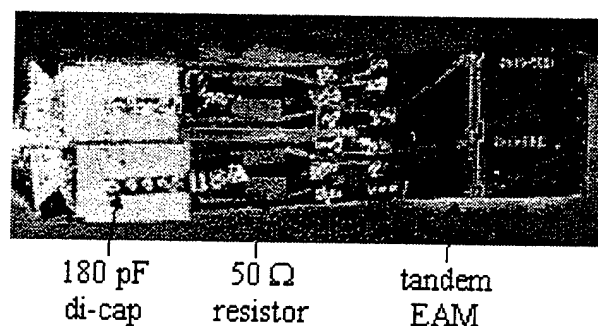
Fig. 4: InGaAsP/InP optical add-drop multiplexer.

Fig. 5: Integrated Tandem Electroabsorption Modulator.

Another field of our research was the development of low voltage, high extinction ratio and large bandwidth traveling wave electroabsorption modulators (TWEAMs) and their application in optical time division multiplexing (OTDM) systems. We demonstrated TWEAMs with 30 GHz bandwidth and 1.2 V switching voltage (Fig. 5). A four-channel 120 Gbit/s OTDM system was build that reduces the number of optical channels by increasing the base rate to 30 Gbit/s (Fig. 6). Integrated tandem modulators were used to (1) pulse shape and modulate data, and (2) demodulate and detect data. This experiment was conducted at 4 x 30 Gbit/s because that was the fastest electrical multiplexer that was available. The technology is certainly usable to achieve 160 Gbit/s and probably 320 Gbit/s. The integration of tandem devices is important to reduce the coupling loss, and to allow more complex processing than simple modulation or demultiplexing. In another experiment, simultaneous TDM drop and detect was demonstrated. A single device was used to drop one TDM channel and pass the other three channels. The absorption of the one channel generates a photocurrent that can be monitored to receive the incoming data.

10

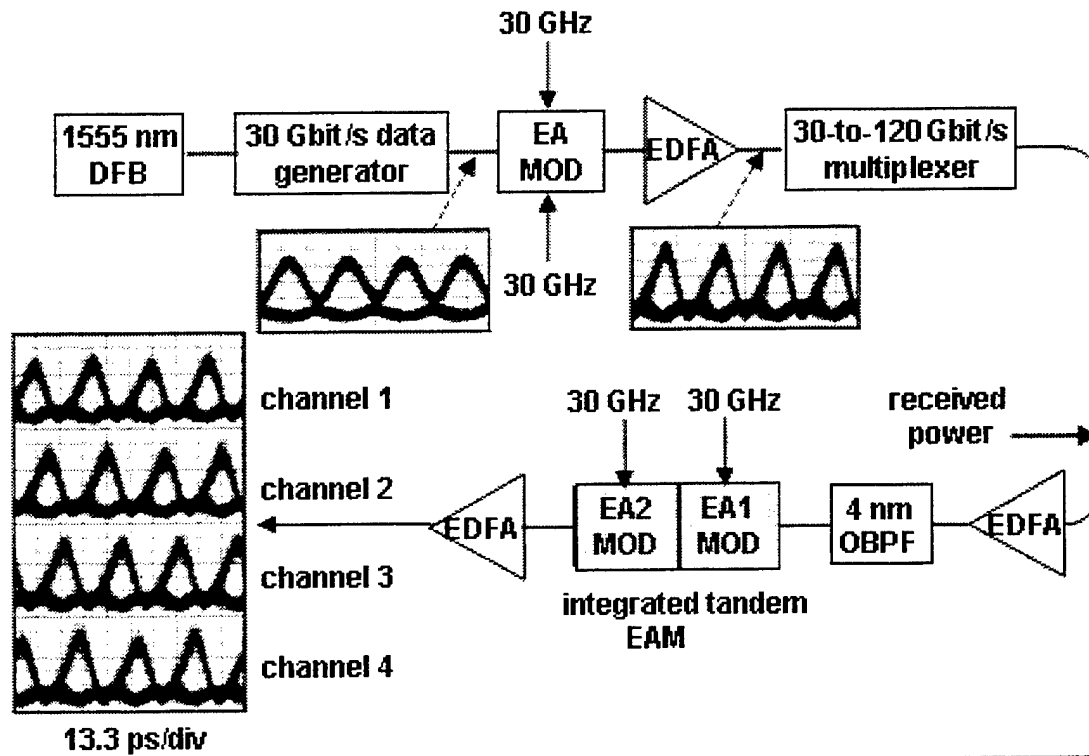This approach is much simpler than having a fast 1x2 switch followed by a fast photodetector.

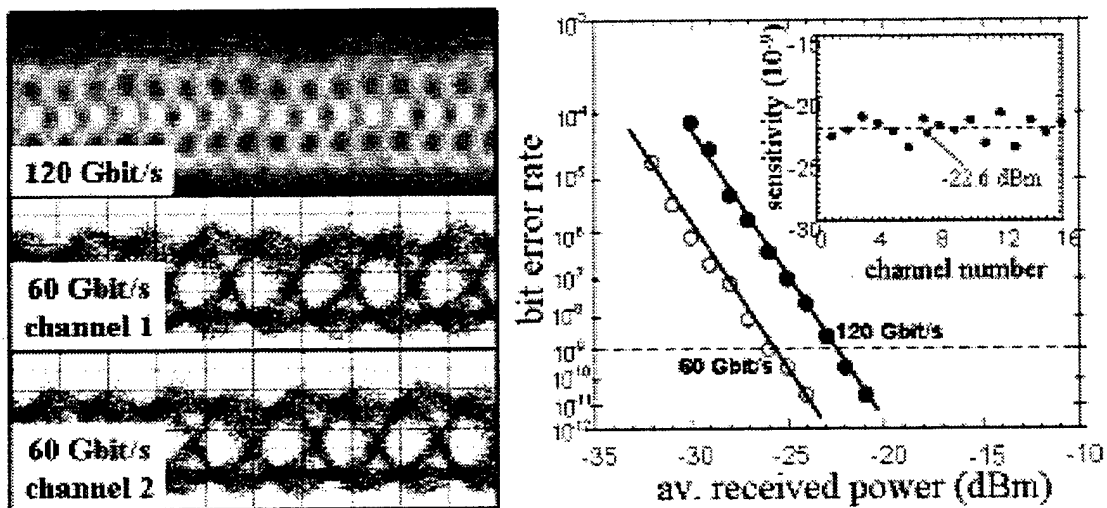Fig.6: 120 Gbit/s optical time division multiplexing system

Fig. 7: Left: Eye diagrams (13.3ps/div, limited by 40 GHz photodetector & 7.5 GHz scope trigger). Right: Bit error rate measurement.

Large-Scale Wavelength and Space Switching using Widely-Tunable Lasers

Larry A. Coldren

In this project the photonic IC technology previously developed at UCSB for widely tunable lasers was applied to two new efforts: an all-optical cross-bar switch, and an optoelectronic wavelength converter. The first effort resulted in 4 x 4 optical cross bar switches with approximately zero dB insertion loss and a 40 dB on/off and interchannel crosstalk level. This was all accomplished on a single chip of InP measuring less than 2mm on a side. These results represent the state of the art in such switches.

The crossbar switch fabric consisted of four input and four output waveguides, spaced by 250 microns, which intersected at right angles. At the intersection a pair of novel 1x2 suppressed modal interference (SMI) switches on the both the input and output guides connected a bypass semiconductor optical amplifier (SOA) that could be turned on simultaneously with the SMIs to provide switching from the bar to the cross state. These SOAs provided good isolation in the off (or bar) state and loss compensation in the on (or cross) state. SOAs and the inputs to and outputs from the chip compensated for fiber coupling losses.

In the latter years of this MOST project, this same photonic integration platform was used to form widely-tunable wavelength converters. In this case, an integrated O/E/O approach is taken using technology compatible with the formation of the Sampled-Grating DBR (SGDBR) lasers. It is proposed that these wavelength converters can then be integrated with compact wavelength routing elements, such as Arrayed-Waveguide (AWG) routers, to create a space switch. Additional wavelength converters may be desired at the output to convert the wavelength to some desired channel.

Modeling indicates that efficient, format-independent wavelength conversion, and therefore switching, can be accomplished up to data rates of 40Gb/s with devices occupying an area of about 1 mm^2. For low data rates (<10 Gb/s) direct modulation of the SGDBR is possible, and lossless conversion should be possible by directly wiring the photocurrent of a photodiode or APD to the gain region of an SGDBR which includes an integrated SOA post-amplifier. For higher frequencies, an integrated modulator is required, but this also generally requires some form of electronic amplification to obtain lossless operation. An integrated FET may suffice, but flip-chip bonding of the InP photonic chip to some electronic chip may be desired in this case. With such electronic interfaces, 2R and 3R regeneration functions may also be incorporated.

Initial experiments have provided SGDBR lasers with integrated SOAs and EAMs which function according to design. CW output powers exceeding 30 mW has been observed, and modulation bandwidths for both direct modulation of the gain section and external modulation of the integrated EAM have provided bandwidths > 5 GHz. Some of this work was done in collaboration with Agility Communications. Additional work on packaging and testing of these devices continues. Avalanche photodetectors have also be fabricated and tested in collaboration with Prof. J. C. Campbell of UT-Austin. Using his narrow avalanche region design, APDs with reasonable gain (> 10) with low excess noise factors (< 3) have been fabricated and measured. Masks have been designed to integrate detectors with the widely-tunable lasers, and further work is underway with additional support from industrial collaborators.
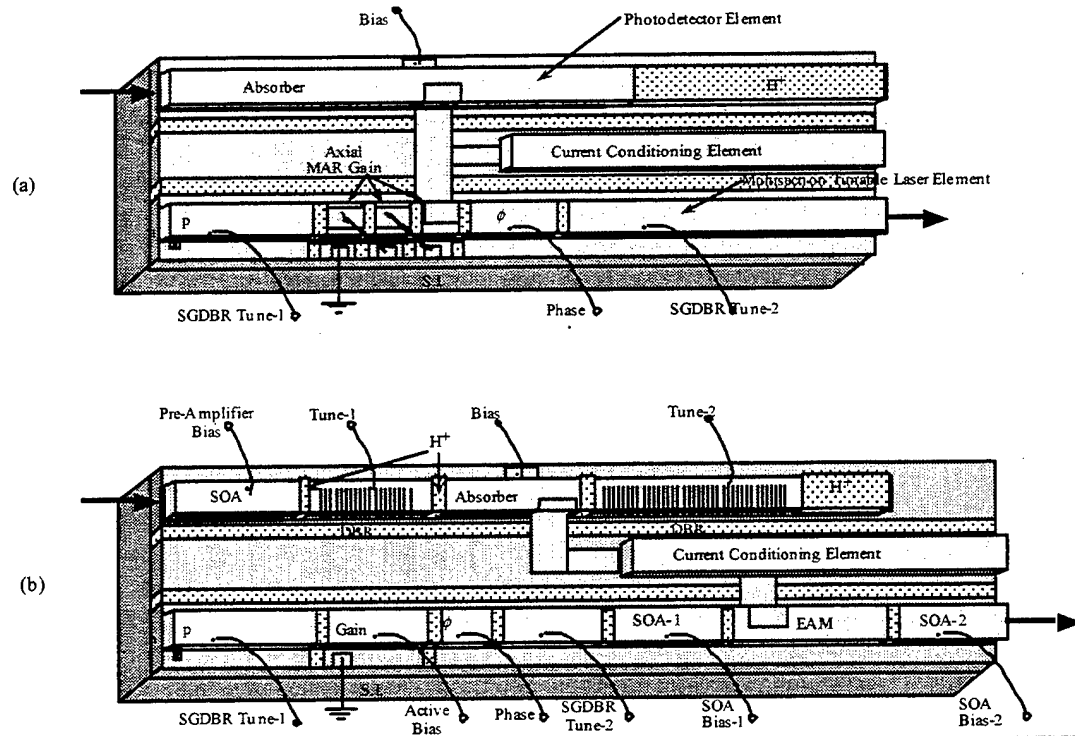
(a)

Bias — Photodetector Element

Absorber   H⁺

Axial MAR Gain   Current Conditioning Element

Multisection Tunable Laser Element

P   φ

SGDBR Tune-1   Phase   SGDBR Tune-2

(b)

Pre-Amplifier Bias   Tune-1   H⁺   Bias   Tune-2

SOA   Absorber   H⁺

DBR   DBR   Current Conditioning Element

p   Gain   φ   SOA-1   EAM   SOA-2

SGDBR Tune-1   Active Bias   Phase   SGDBR Tune-2   SOA Bias-1   SOA Bias-2

Fig. 1: Monolithic Wavelength Converter

A_1 DET   SGDBR λ_f

A_5 DET   SGDBR λ_k

A_n DET   SGDBR λ_q

Slab-Waveguide Beam-Expansion/ Interference Section

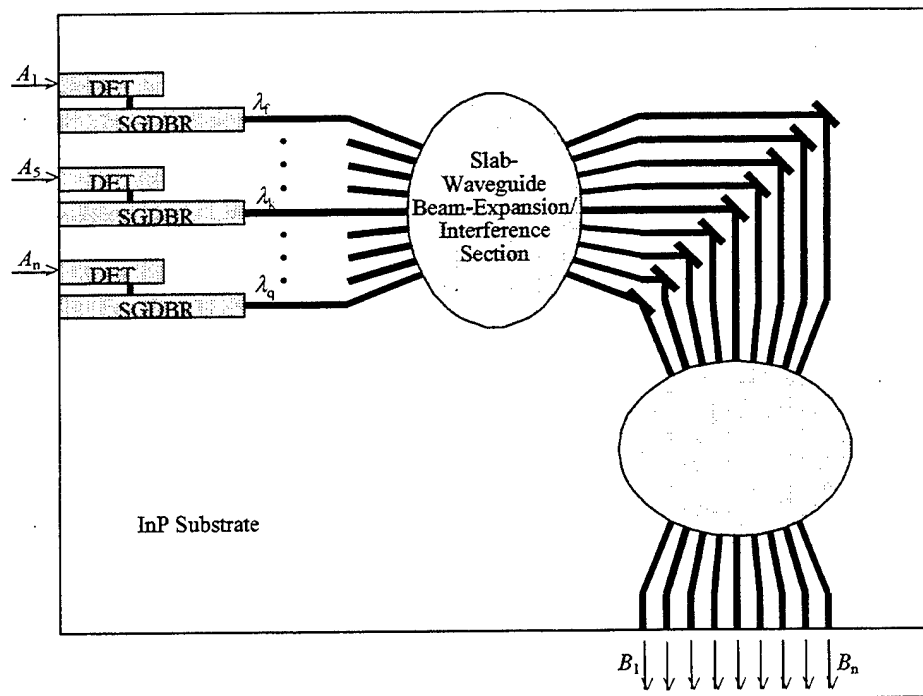InP Substrate

B_1 B_n

Fig. 2 Crossbar Space Switch

13

Compact, low-loss, electronically tunable filters based on hybrid integration of polymers and compound semiconductors

Nadir Dagli

Tunable filtering is a key technology for the successful implementation of WDM networks. It is difficult to satisfy all the requirements of tunable WDM filtering, such as low insertion loss, low cost, low crosstalk, wide and fast tunability using a single technology. In our work we utilize hybrid integration of polymers and compound semiconductors to realize WDM components with superior characteristics. Polymers are used for low propagation and fiber coupling loss. Compound semiconductors are used for high contrast gratings and electro optic properties needed for wide and fast tunability. We fabricated and characterized two types of filters using this technology.

The first one relies on the forward coupling between a polymer and a semiconductor waveguide. The single mode polymer waveguide is fabricated using polymers Benzocyclobutene (BCB), photo definable BCB (PDBCB) and Polymethylglutarimide (PMGI). A separately fabricated GaAs waveguide was glued on the polymer waveguide using one of the polymers as glue. Finally the growth substrate for the GaAs waveguide was removed by substrate etching, forming a coupled structure. GaAs and polymer waveguides have very different indices and index dispersion. Therefore, when coupled they act as a very asymmetrical coupler. Such asymmetrical couplers behave as narrow-band filters. In our approach input and output coupling to single mode fibers is done through the single mode polymer waveguide. This results in a band stop filter. Furthermore, fiber to fiber coupling loss can be low. In our experiments we observe less than 6 dB fiber to fiber insertion loss, which can be further improved by optimizing the mode shape of the polymer waveguide. By changing the electrical thickness (the product of the physical thickness and the index) of the GaAs waveguide coupling wavelength can be tuned. In our experiments we observe about 2 nm bandwidth with more than 15 dB suppression in a 3 mm long device. We were also able to tune the center wavelength by more than 50 nm by changing the thickness of the GaAs waveguide. We also observe fast electrical tuning in addition to tuning based on etching.

The second type filter based on the hybrid integration of polymers and compound semiconductors is very similar to the previous one. In this case a grating on the GaAs slab waveguide was introduced. Reflectivity of a grating in between two coupled dissimilar waveguides can be changed drastically by changing the electrical thickness of one of the waveguides. The reflectivity change is due to the modification of electrical field strength on the grating. In the transverse plane the field profile of dissimilar coupled waveguides is very similar to that of a Fabry Perot, hence is very wavelength sensitive. As a result by changing the electrical thickness of the GaAs waveguide as in the previous case, field strength on the grating can be modified strongly. This in turn modifies the reverse coupling coefficient of the grating. Hence the reflectivity of the grating can be turned on and off. Such a reflective device can work as an add/drop multiplexer when combined with two circulators at the input and output. We demonstrated turning a grating on and off this way by changing the thickness of the GaAs waveguide for a 3 mm long device. Fast electrical tuning should also be possible just like in the previous case.

The components demonstrated in this work have the potential of being the building blocks of compact, low-loss and fast tunable filters that can be utilized in optical networks.
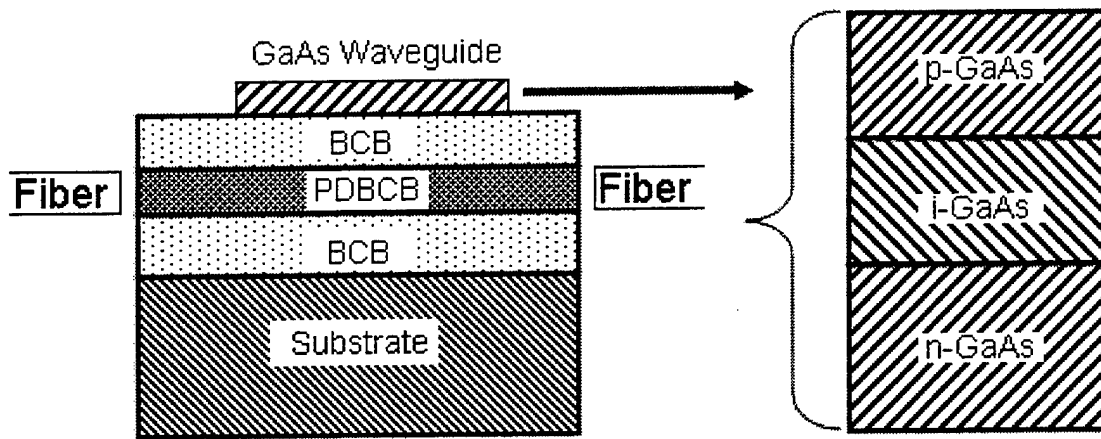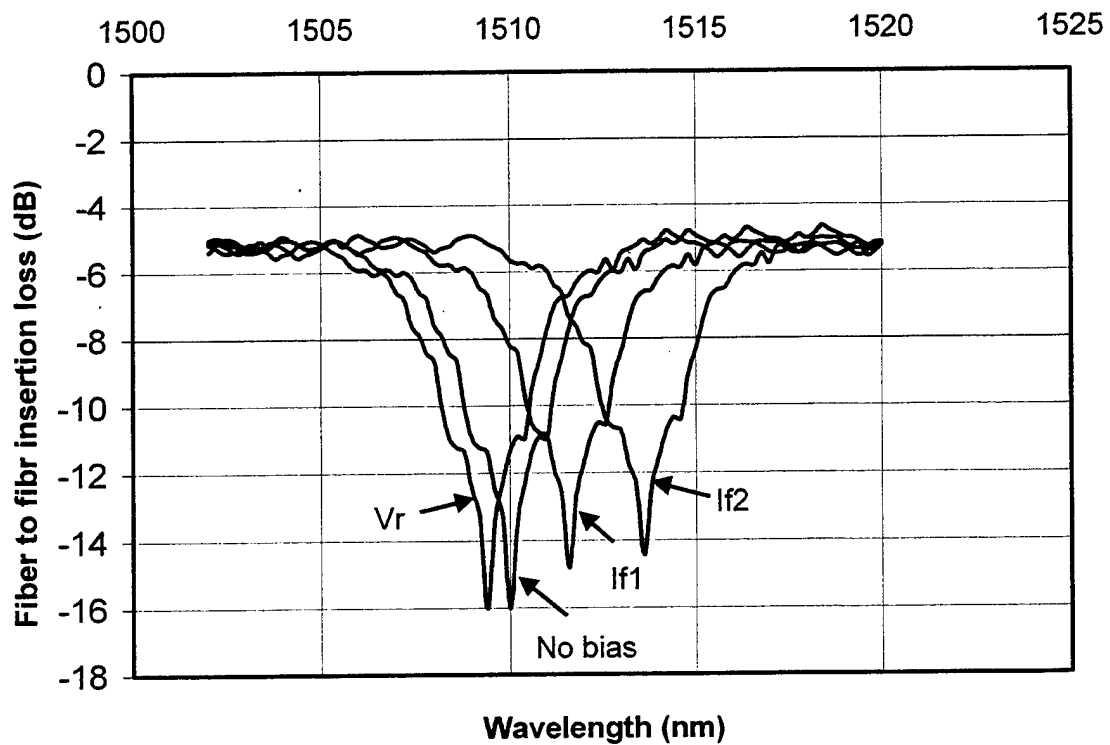
Fig. 1: Hybrid Waveguide Structure

Fig. 2: Transmission characteristics at different bias.

Optical Packet Switching, Label Swapping and Wavelength Conversion Technologies

Dan Blumenthal

All-optical label swapping is a promising approach to ultra-high packet-rate routing and forwarding directly in the optical layer. The overall network approach is to encapsulate packets with optical labels and process forwarding and routing functions independent of packet bit rate and format. We have experimentally demonstrated results various components and label swapping functions and demonstration of 40 Gbit/s optical label swapping. To allow operation at ultra-high bit rates we have demonstrated a new wavelength converter based on nonlinearities in an optical fiber that supports operation at 40 Gbit/s and beyond (possibly up to several hundred Gbit/s). In this scheme we utilize XPM in a dispersion shifted fiber imposed from the incoming data onto CW light, followed by conversion of the phase modulation to amplitude modulation using optical filtering. The incoming data is combined with a CW light signal and sent through an optical fiber where the data imposes a phase modulation onto the CW light via fiber XPM. This phase modulation generates optical sidebands on the CW signal, which are converted to amplitude modulation by suppressing the original CW carrier using an optical notch filter. A conventional band-pass filter to select one of the two sidebands then follows the notch filter. However, in principle it is sufficient to use a single band pass filter, e.g. a fiber Bragg-grating or fiber-loop mirror, provided that it can suppress the original CW carrier enough. This wavelength converter also erases 2.5 Gbps NRZ header data. In order to perform very high speed optical multiplexing and demultiplexing we collaborated with John Bowers group with respect to using electroabsorption modulators (EAMs).

We have also investigated optical switching architectures that utilize Wavelength Conversion (WC) that can be tuned at very high bit rates. We have demonstrated that the same rapidly tunable laser can be used as a rapidly tunable WC. Dynamic conversion of any wavelength to any wavelength using a single GCSR laser, where the output wavelength is set by rapidly changing the current in one of the laser sections was reported. Wavelength conversion in this case is achieved through the gain suppression of the lasing mode by the injected signal light. Among the most important advantages of this technique are the modulation format transparency, tunability of the converted signal wavelength, high conversion efficiency and extinction ratio and single element simplicity.

Optical label swapping and wavelength conversion switching technologies can be combined to realize the optical equivalent of an IP router. The Optical Internet Protocol Router (OIPR) project is aimed at investigating possible these approaches. When combining optical packet switching technologies into a single router, new issues arise with packet buffering and switch blocking. This year we collaborated with J. Lang and E. Varvarigos to investigate an all-optical packet wavelength scheduler/switch. The scheduler utilizes wavelength conversion and switching technology to collapse a large

number of programmable optical delays efficiently. Scalability of this approach depends on the ability to integrate many photonic devices on a single chip.
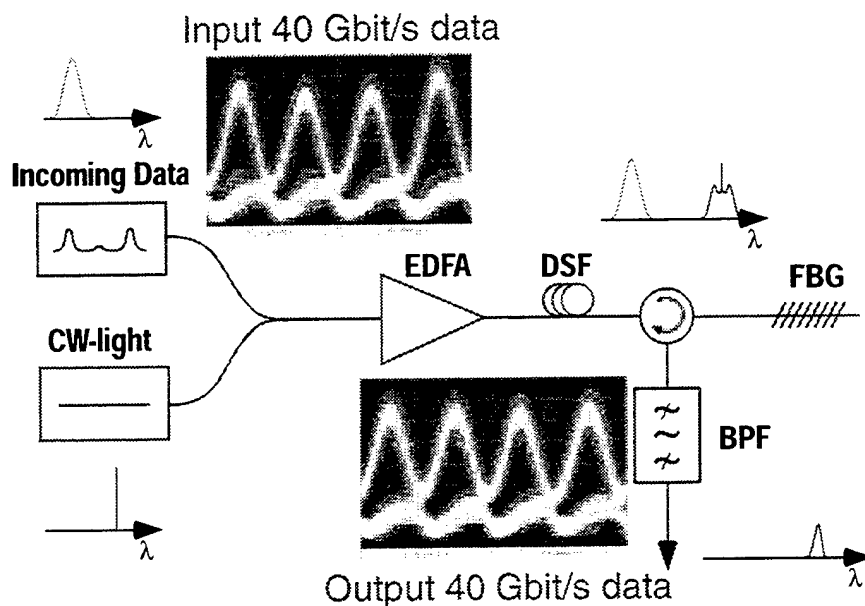
Figure 1. Experimental set-up of the ultra-fast all-optical wavelength converter

## Wavelength converter and optical packet routing technology

The main contribution in this project has been to develop a novel ultra high-speed all-optical wavelength converter, capable of operating at 40 Gbit/s and beyond [1]. The basic idea is to combine the incoming data with continuous wave (CW) light at the desired output wavelength and let them co propagate through an optical fiber with high power. The original data will impose a phase modulation via cross phase modulation (XPM) on the CW light according to the incoming data. A filter arrangement after the fiber is used to convert the phase modulation into amplitude modulation at the new wavelength. Figure 1 shows a typical set-up and eye patterns demonstrate wavelength conversion of 40 Gbit/s data. To better understand the physics of the wavelength converter, extensive research was performed, e.g. by analyzing the pulse response and bandwidth [2] as well as investigating noise limitations in the conversion process [3]. The wavelength conversion efficiency depends heavily on the derivative of the input signal and thus only return to zero (RZ) data can be converted. This effect allows the converter to be used in packet routing systems using all-optical label swapping (AOLS) [4]if the payload is coded using high-bit-rate RZ-data and the label is attached in the time domain to the payload and coded with non return to zero (NRZ) data. In this case the payload will be converted to the new wavelength while the label is not. A new label can then be inserted either by premodulating the CW light into the converter or simply by adding it after the wavelength converter. This feature was investigated in [5] at 10 Gbit/s but is certainly scalable to much higher bit-rates, as shown by simulations at 160 Gbit/s in [2].
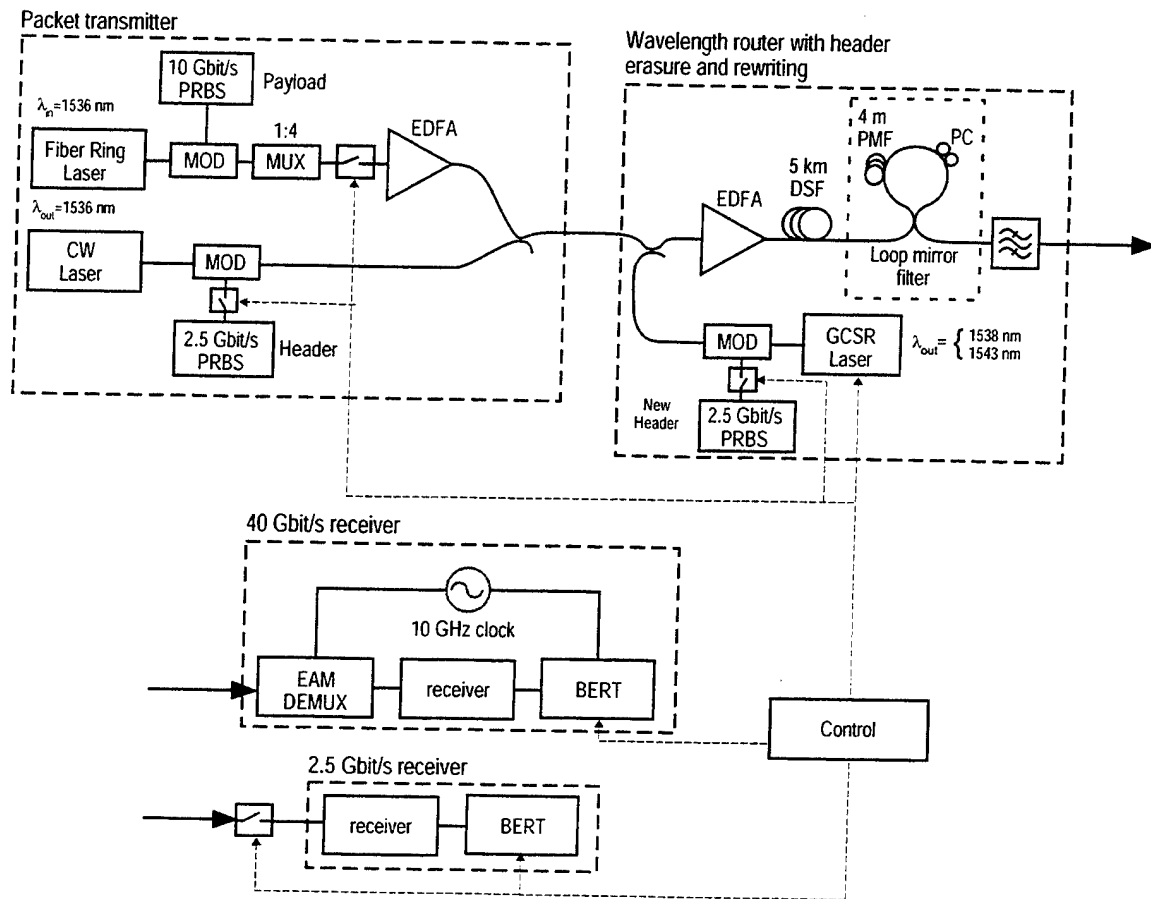
Figure 2. Experimental set-up of 40 Gbit/s packet routing and AOLS experiment.

To demonstrate AOLS at high bit rates an experiment was performed where packets of 40 Gbit/s data was routed to different wavelengths using a wavelength converter [6]. The 40 Gbit/s payload was in RZ format and an attached time domain label was encoded using NRZ at 2.5 Gbit/s. By using a fast tunable laser each packet can be routed to different wavelengths. The attached label is also replaced upon wavelength conversion by using the technique described above. Figure 2 shows the experimental set-up used in the routing experiment. Figure 3a shows the incoming packets to the node with the NRZ labels at lower power than the RZ payload to accomplish equal energy per data bit in header and payload. The lower trace shows the headers with the payload switched off. Figure 3b shows every other packet routed to 1538 nm and 1543 nm with new inserted labels. The eye patterns shown in Figure 3c and d were taken by zooming into the payload, before (1536 nm) and after wavelength converter (1543 nm). BER measurements were performed on both label and payload on incoming and outgoing packets and less than 4 dB penalty at a BER=10^{-9} was observed for all routed packets. The power penalty at a BER=10^{-9} for the replaced labels was less than 2.5 dB. For wavelength routing at 10 Gbit/s, the penalty was less than 1 dB for the payload, which indicates that a major part of the penalty is due to instabilities in the 40 Gbit/s data.

18
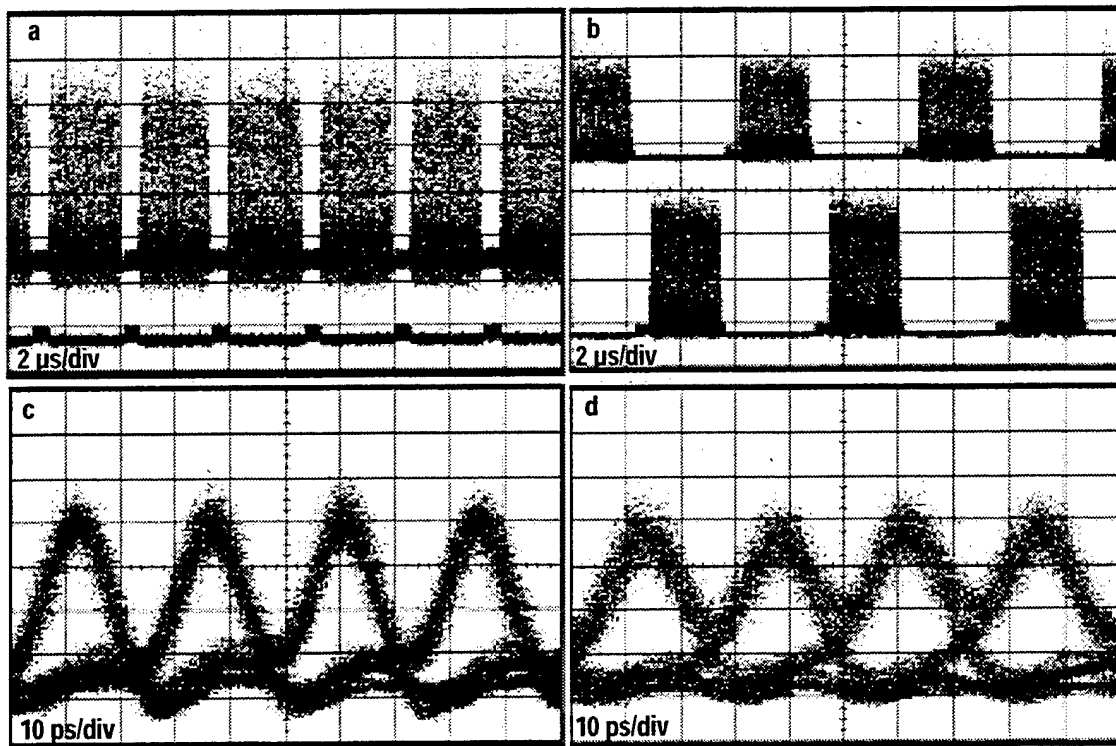
Figure 3. Packets (a) and 40 Gbit/s eye-patterns (c) before wavelength routing. Packets routed to 1538 nm and 1543 nm (b) and eye pattern of routed packet at 1543 nm (d).
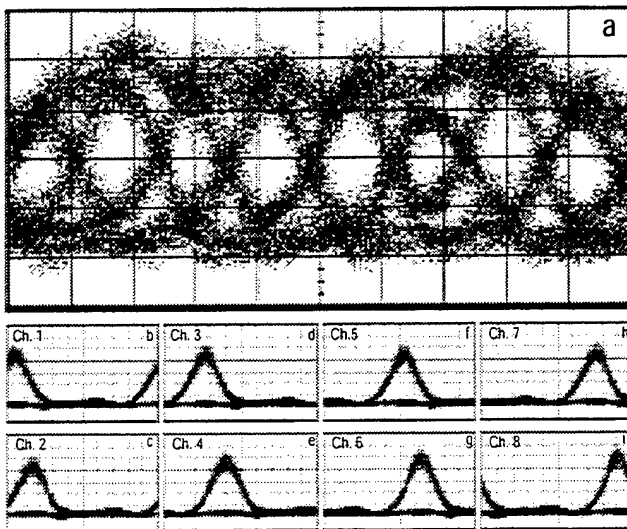

Figure 4. 80 Gbit/s eye pattern (a) and demultiplexed 10 Gbit/s channels (b-i).

The wavelength converter has also several other applications. Figure 4 shows the wavelength converter acting as an ultra fast demultiplexer where incoming 80 Gbit/s data

19

are demultiplexed down to 8 channels of 10 Gbit/s data [7,8]. Another application is multiplexing, where a number of wavelength channels can be multiplexed together into one optical time domain multiplexed (OTDM) channel [9]. Figure 5 shows the experimental set-up for this experiment and figure 6 shows bit-error rate measurements of the OTDM multiplexed data at the output.
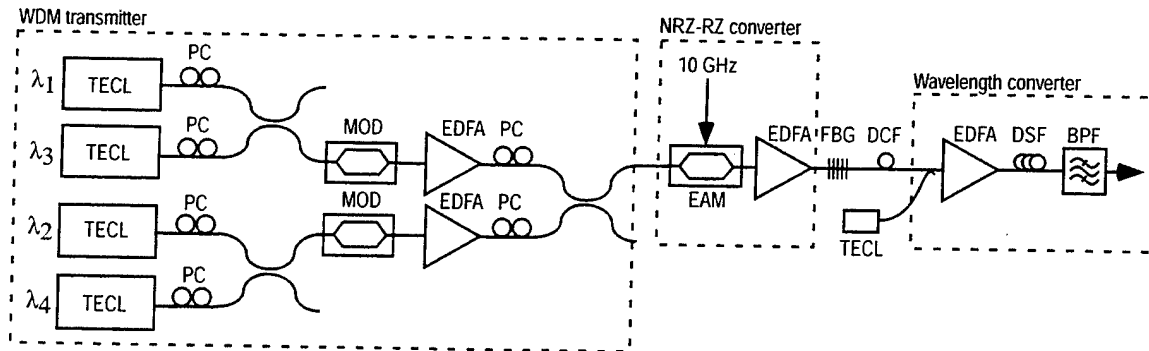
Figure 5. Experimental set-up for the multiplexer.
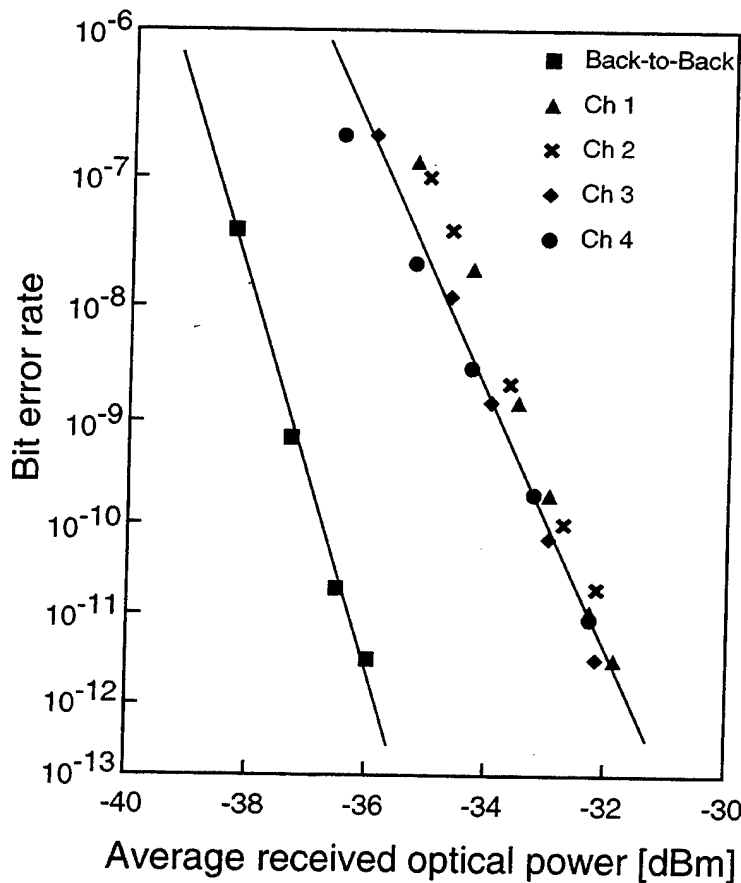
Figure 6. Bit-error rate measurements of one input 10 Gbit/s channel, baseline (B), and the four channels of the output 40 Gbit/s OTDM data stream.

Polarization mode dispersion

Polarization mode dispersion (PMD) is regarded as the most predominant obstacle for fiber optical transmission at ultra-high data rates, i.e. 40 Gbit/s and beyond. The impact from PMD varies with wavelength and over time, which makes it difficult to predict signal degradation in the system. In a packet network environment it is even more difficult since incoming packets to a node may have traveled different fibers and thus experienced different PMD. Traditionally the influence of PMD has been treated using statistics, i.e. the probability of certain signal degradation is calculated. However, in a network where decisions about possible signal degradation due to PMD have to be made in real time, statistics cannot be used. Instead we would like to measure some optical parameters and determine the signal degradation due to PMD in real time. One method investigated under the MOST program is to measure how the stokes vector of the data modulated light varies across the optical spectrum. From this data the pulse distortion due to PMD can be estimated. Figure 7 shows real and estimated pulse broadening for different PMD values. Another topic of interest is how sensitive different types of optical receivers are to PMD. Figure 8 shows a comparison of the Q-penalty introduced by PMD when using direct detection of 40 Gbit/s data and detection using a 40 to 10 Gbit/s optical demultiplexer with a subsequent 10 Gbit/s receiver. A seen from figure 8, the demultiplexer receiver performs significantly better in the presence of PMD than the non demultiplexed 40 Gbit/s receiver.
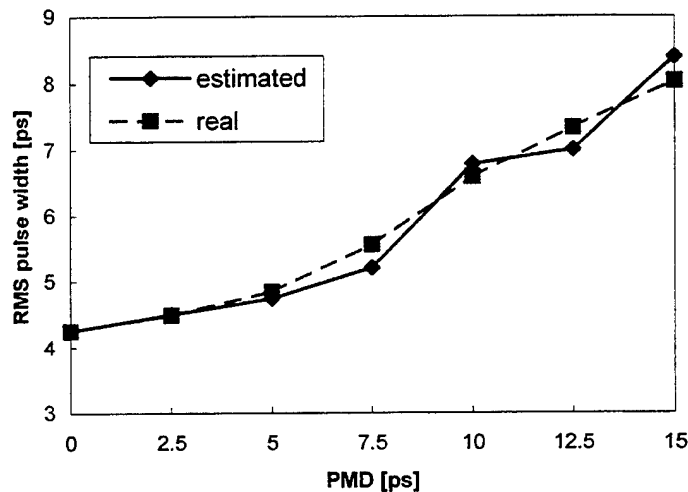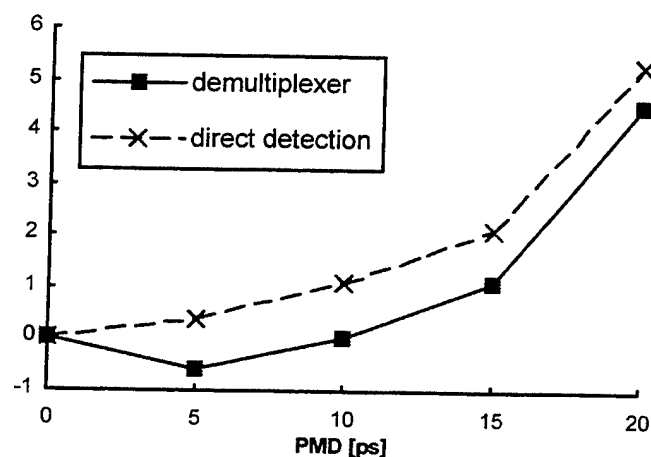

Figure 7. Real and estimated pulse widths for different values of PMD.

Figure 8. Q-penalty versus PMD for direct detection of 40 Gbit/s data and 40 Gbit/s optically demultiplexed to 10 Gbit/s with subsequent 10 Gbit/s detection.

[1] B. E. Olsson, P. Öhlén, L. Rau, and D. J. Blumenthal, "A simple and robust 40 Gbit/s waveength converter using fiber cross-phase modulation and optical filtering," Photon. Technol. Lett., vol. 12, pp. 846-848, July 2000.

[2] P. Öhlén, B. E. Olsson, and D. J. Blumenthal, "Wavelength dependence and power requirements of a wavelength converter based on XPM in a dispersion shifted optical fiber," Photon. Technol. Lett., vol 12. pp. 522-524, May 2000.

[3] L. Rau, B. E. Olsson M. Masanovic, and D. J. Blumenthal, "Noise in Fiber XPM Wavelength Converters due to Excitation of Random Higher Order Solitons," to be presented at Proc. European Conference on Optical Communication, Munich, Germany, vol. 3, pp. 93-94, 2000.

[4] D. J. Blumenthal, B. E. Olsson, G. Rossi, T. Dimmick, L. Rau, M. Masanovic, O. Lavrova, R. Doshi, O. Jerphagnon, J. E. Bowers, V. Kaman, L. A. Coldren, and J. Barton, "All-Optical Label Swapping Networks and Technologies," submitted to J. of Lightwave Technol.,invited paper, 2000.

[5] P. Öhlén, B. E. Olsson, and D. J. Blumenthal, "All-optical header erasure and penalty-free rewriting in a fiber-based high-speed wavelength converter," Photon. Technol. Lett., vol. 12, pp. 663-665, 2000.

[6] B. E. Olsson, P. Öhlén, L. Rau, G. Rossi, O. Jerphagnon, R. Doshi, D. S. Humphries, D. J. Blumenthal, V. Kaman, and J. E. Bowers, "Wavelength routing of 40 Gbit/s packets with 2.5 Gbit/s header erasure/rewriting using all-fibre wavelength converter," Electron. Lett., vol. 31, pp. 345-347, 2000.

[7] B. E. Olsson, and D. J. Blumenthal, "80 to 10 Gbit/s Demultiplexing using Fiber Cross-phase Modulation and Optical Filtering," IEEE/LEOS annual meeting, paper TuB 4, Puerto Rico, 2000.

[8] B. E. Olsson and D. J. Blumenthal, "All-optical demultiplexing using fiber cross phase modulation and optical filtering," submitted to Photon. Technol. Lett., 2000.

[9] B. E. Olsson, L. Rau, and D. J. Blumenthal, "WDM to TDM Multiplexing using an Ultrafast All Optical Wavelength Converter," submitted to Photon. Technol. Lett., 2000.

Ultrafast Optics for Optical Communications

Y. Fainman

Ultrashort pulse laser technology is commercially available today, producing high energy pulses of optical radiation in the femtosecond duration range. We are investigating methods of harnessing such ultrashort pulses to increase the speed, provide security and reliability in transmission, distribution and storage of information in communication and computing applications. To implement these features, real-time all-optical processing techniques for achieving information conversion between slower opto-electronic devices and the ultrafast pulse phenomena need to be constructed. This processing is performed primarily in the temporal frequency domain by spatially dispersing the frequency components in a spectral processing device (SPD) and performing operations on the spectrally decomposed wave (SDW). To fulfill our goal of real-time SDW processing, we utilize nonlinear wave mixing processes based on three- and four- wave mixing in a second order nonlinear crystal inside the SPD. The latter is achieved via cascaded second-order nonlinearities (CSN). The CSN arrangement consists of a frequency-up conversion process followed by a frequency-down conversion process satisfying the type-II non-collinear phase matching condition.

Our experiments are concerned with ultrafast information exchange between spatially parallel signals and higher bandwidth temporal signals. For the waveform synthesis experiment, we introduce two spatial information modulated waves carried by quasi-monochromatic light and a SDW of a ultrashort femtosecond pulse (see Fig. 1a). The four wave mixing process produces a SDW that is a product of three waveforms: a spatial Fourier Transform (FT) of the two spatial information carrying waves and the SDW (i.e., temporal FT) of a femtosecond laser pulse. The spatial-temporal information exchange (i.e., the generated SDW) results in a synthesized waveform that is a time-scaled version of the spatial image, performed on a single shot basis with femtosecond-rate response time due to the fast nonlinearity. We performed several experiments to demonstrate various synthesized waveforms. A spatial sequence of point sources, generated by a cylindrical lenslet array, was converted to an ultrafast pulse packet (see Fig. 1b). Modulating the individual point sources in the spatial domain resulted in an analogously modulated ultrafast waveform, with no evidence of crosstalk between the pulses. This functionality may be desired for an ultrahigh bandwidth optical communication application. When an adjustable slit was placed in the spatial channel, the ultrafast waveform resembled a square pulse (see Fig. 1c). The duration of the square pulse was adjusted in real time by varying the width of the slit. The synthesized waveforms were generated with a high conversion efficiency of 16%.
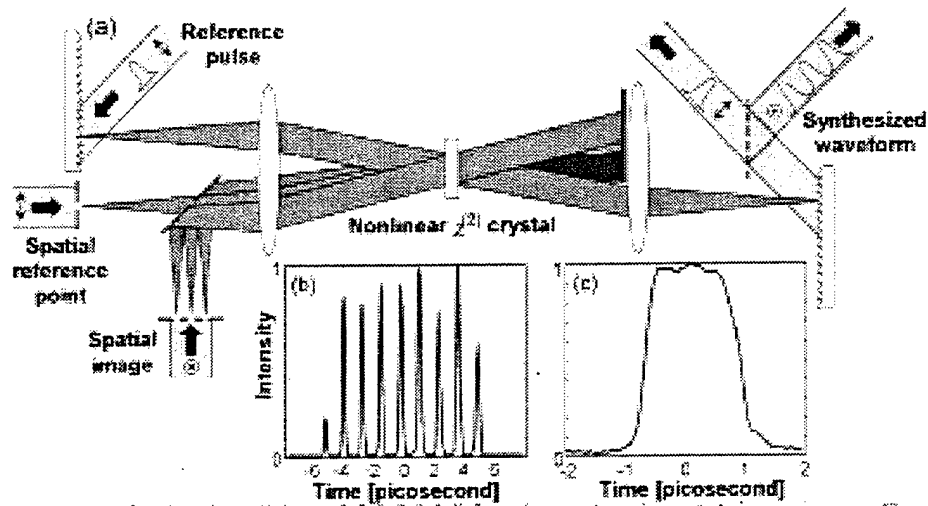
Fig.1. (a) Experimental setup of the real-time spatial-temporal wave-mixing processor. Generated ultrafast waveforms: (b) pulse packet from a spatial sequence of point sources and (c) square pulse from a slit.

The inverse time-to-space transformation for detection of femtosecond pulse sequences is achieved using nonlinear three-wave mixing in a $\chi(2)$ crystal. The two input waves are the SDW of a sequence of ultrashort pulses that need to be detected and a reference pulse. The nonlinear interaction between the two SDW's results in generating quasimonochromatic second harmonic wave. The frequency of the second harmonic fields is twice the center frequency of the incident fields. The generated second harmonic fields contain spatial frequencies determined by the time delay between the reference pulse and the pulses in the signal. Thus a 1-D spatial FT of the second harmonic field produces a 1-D spatial image equivalent to the temporal cross-correlation between the reference and the signal pulses. With short pulses, the spatial image has one-to-one correspondence with the signal pulse, implementing the desired time-to-space demultiplexing at femtosecond rates. The spatial image, formed by the generated second harmonic field, reveals spatially the information on the temporal signal waveform and can be detected using slower electronic detection devices.

For instantaneous time domain processing of ultrafast waveforms, three ultrafast waveforms are introduced to the SPD, giving rise to a fourth SDW by the CSN wave mixing process. The effective processing of the resultant ultrafast waveform depends on the configuration of the SPD, as it is possible to control the directions of the spatial dispersion, enabling new signal processing functionality. We demonstrated time reversal of ultrafast waveforms with our processor by both phase conjugation and spectral information inversion. The input complex amplitude ultrafast waveform consisted of a transform limited pulse followed by a positively chirped pulse. Depending on the time reversal configuration, the two pulses exchanged their location while the positively chirped pulse remains indeed positively chirped.

Relative to other spatial-temporal processing techniques, our nonlinear wave mixing approaches to spatio-temporal processing provide femtosecond rate processing due to the

25

fast bound electron nonlinearity and high efficiency on account of a relatively large $\chi(2)$ coefficient in bulk crystals. The spatial-temporal process that we have demonstrated generate output spatial and temporal waveforms that can be changed in real time. Since the technique realizes a general wave mixing process of temporal and spatial information-carrying waves, the setup may be converted to provide the convolution or correlation signal between spatial and temporal channels, with the output in either the temporal or the spatial domain. Thus, this spatial-temporal process can be considered a fundamental system for performing ultrafast signal processing on optical waveforms in the time and space domain. Currently, we investigate techniques for characterization of the spatial and temporal modes in the fiber optic channel, enabling real time monitoring and control of future optical network systems. We launch a signal wave into a few-mode optical fiber, where it excites several spatial modes, each propagating with corresponding group velocity. At the output of the fiber the signal wave is combined with the reference wave, and the total optical intensity is detected using a CCD camera. Using spatial Fourier domain filtering we decouple the interference portion of the total observed intensity from the background, and obtain background-free cross-correlation of the reference and signal waves. We perform this procedure for various relative time delays between the signal and the reference, and obtain spatio-temporal impulse response of the fiber (Fig.2).
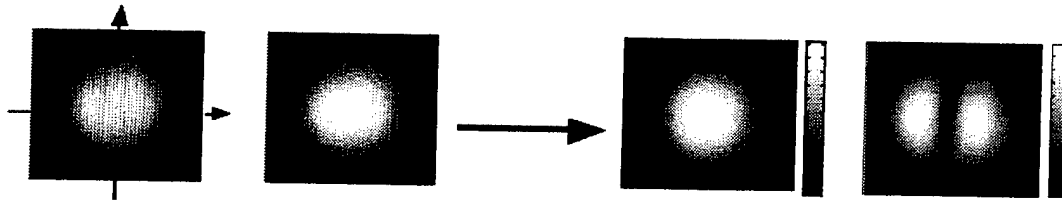

Fig. 2. Spatio-temporal modes of the fiber.

26

80 Gb/sec TDM based fiber ICs designs using InP DHBT technology

Mark J. W. Rodwell

Previously, SiGe and InP technologies were providing an f_t, $f_{max} \approx 90$ GHz and f_t, $f_{max} \approx 140$ GHz, respectively. Once established that data rates for fiber chipsets could be developed at greater than 10 Gb/sec using either of these technologies, a race began amongst telecommunication companies to be the first to bring 40 Gb/sec TDM based chipsets and equipment to the market. In looking at what will be needed from a device technology in terms of speed and scaling in order to take data rates to 80 Gb/sec and beyond, InP is years ahead of SiGe and will be the material system used for first generation results at 80 Gb/sec.

Amongst the components that compose a fiber IC chipset, the electro-optic (EO) modulator driver design provides a unique challenge in that it is a broadband amplifier (DC-70GHz bandwidth for 80 Gb/sec) that needs to produce 5 Volt drive into a 50 ohm load—I_{min} = 100 mA. It was our intent to design such a modulator driver into the aforementioned material systems with a conventional mesa structure for operation at 40 Gb/sec, and UCSB's transferred substrate TS-DHBT process for operation at 80Gb/sec—only the latter of which was completed. In addition to the modulator driver, we pursued other circuits that comprise a fiber IC chipset. Design and layout of a 2:1 multiplexer and Cherry-Hooper based limiting amplifier (LIA) were completed for operation at 100 Gb/sec in the TS-DHBT process. These circuits have not yet been fabricated.

Lastly, with continued processing difficulty and low circuit yield in the TS-HBT process, our device team has developed a conventional narrow mesa technology that utilizes the epitaxial engineering behind our transferred substrate devices. In making this technology feasible for circuits with hundreds of devices, we have retained our low loss dielectric, microstrip wiring environment to minimize parasitic loading.

I. Circuit design techniques

a. EO Modulator Driver

For the existing EO modulator drivers at 40 Gb/sec operation that are available commercially, a drive voltage for medium halt fiber applications is about 3.5 Volts into a 50 ohm load. If a conventional lumped design is used and back terminated with 50 ohms, we would need to switch (3.5 V)/(25 ohm) = 140 mA in the amplifier. We cannot simultaneously have devices large enough to pull this current, dissipate the heat generated by 140 mA in a small area, and have the bandwidth we need to satisfy our design goal—75 GHz for 80 Gb/sec.

The solution to all three of these problems is to use a distributed, traveling wave TWA topology. By distributing the amplifier into smaller cells and connecting them to a transmission line bus, we can superimpose the current contribution of each cell in order to meet our current needs. The parasitic input and output capacitances from the cells are absorbed by the transmission line, which shifts the characteristic impedance to:

$$Z_{TL, synthetic} = \sqrt{\frac{L_{TL}}{C_{TL} + C_{TWA, cell}}}$$

We choose Z_{TL} such that $Z_{TL,synthetic}$ = 50 Ω. By having the device capacitances part of the transmission line, our frequency limit is the Bragg cutoff frequency of the *synthetic* transmission line. This is a design variable we can manage:

$$f_{Bragg} = \frac{1}{\pi \sqrt{L_{TL} \cdot (C_{TL} + C_{TWA, Cell})}}$$

$$f_{Bragg} = \frac{1}{\pi \cdot Z_{TL, synthetic} \cdot (C_{TL} + C_{TWA, Cell})}$$

If the Bragg limit needs to be increased, we can reduce the capacitive contribution of each cell. For example, on the input line, the diffusion capacitance C_{BE} dominates. Reducing the current contribution of each cell, and then adding more cells will maintain the same output current and increase f_{Bragg}. At some point though the addition of more smaller cells will not contribute to the gain. The conductive losses from the TWA cells will accumulate because it looks like the transmission line is lossy. Evaluating the gain bandwidth product of the TWA with conductive losses yields an interesting result. The gain bandwidth product of a TWA is not $A_v f_t$—it becomes $A_v f_{max}$.

In this design, the number of cells (10 cells) and device sizes were picked in such a way as be able to drive large currents, and have f_{Bragg} = 75 GHz. By setting the Bragg frequency for only the bandwidth needed, we do not add any unnecessary loss by having more cells and this keeps the overall size of the circuit manageable, for an already large amplifier. The simulated performance of this amplifier showed an S(2,1) = 15.2 dB, f_{Bragg} = 114 GHz, with good input and output transmission line phase matching—S(1,1) and S(2,2) < -10 dB up to 70 GHz. The large signal eye diagram simulation at 80 Gb/sec is shown in Fig. 1.
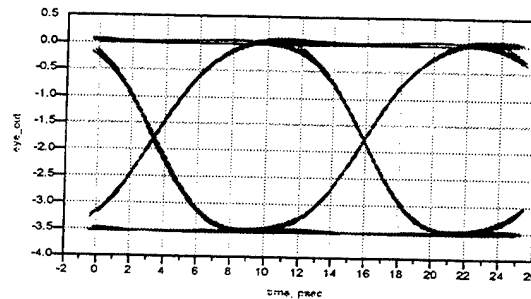

Fig. 1 Mod driver eye diagram—80Gb/sec, 3.5V out

b. 2:1 MUX

The 2:1 multiplexer employs traditional single level ECL gated logic with Master/Slave latch input data retiming and two stage differential buffering for output data restoration. In this 2:1 MUX design, the operating speed is limited by the ability to clock the retiming latches and serialize the two data streams at the selector circuit. Both the retiming latches and the selector are clocked at a *frequency* equal to the rate of the incoming data.

With this MUX design, the slowest part within it is the time of flight of the signal through the interconnects of the retiming latch. Minimizing the delay associated with this circuit and its interconnects is what will maximize the operating speed of the MUX—this is where we placed our efforts.

To do this optimization, we turned our attention to the static frequency divider—the digital benchmark circuit that tests the limit of a transistor technology. This circuit is an M/S latch whose output is fed-back to its input to make the output frequency half of that of the source clocking the circuit. Through careful design and tight layout, a maximum clocking frequency of 95 GHz was simulated. With this design and optimization complete, the footprint of the static frequency divider was configured back as an M/S latch and used for the input data retiming circuits and the selector in the MUX.
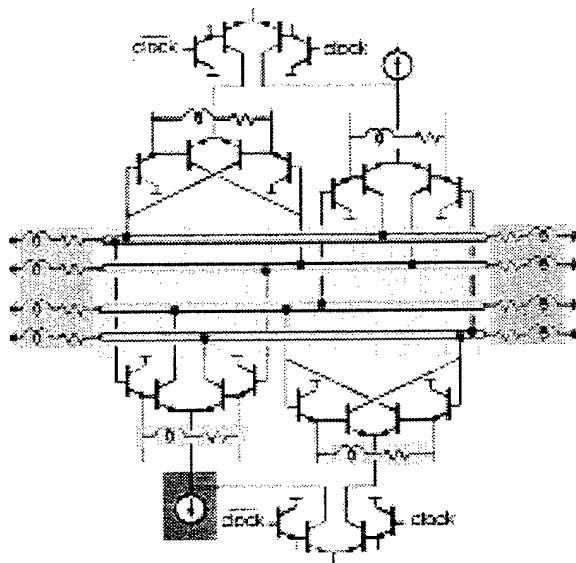

Fig. 2 Schematic of Static Frequency Divider

The layout of the 2:1 MUX contained 196 transistors. With layout parasitics included, an error free, open output eye diagram of 100 Gb/sec and 160 Gb/sec were simulated. This is quite close to the maximum clock frequency of the static frequency divider, thus validating the design approach taken. At output data rates higher than 160 Gb/sec, errors

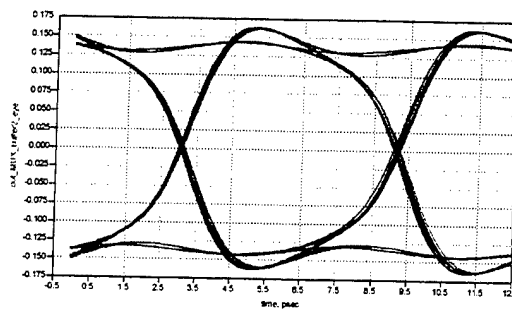began occurring due to the jitter on the data waveform at the selector input from the retiming circuits.
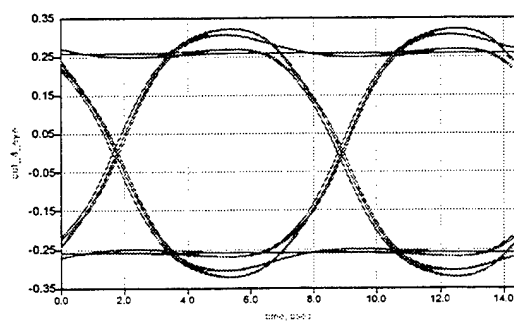

Fig. 3 2:1 MUX eye diagram—simulated at 160Gb/s

c. 4 stage Cherry-Hooper based limiting amplifier

The Cherry-Hooper amplifier through its use of *transconductance* to *transimpedance* transformation, provides excellent gain and graceful output voltage limiting for small and large signal inputs. A detailed analysis of the time constant delays of the circuit shows that the feedback resistance in the transimpedance level causes a very small amount of back loading on successive stages—allowing us to use many gain stages with a small penalty in circuit bandwidth. In addition, this characteristic makes the overall first order time constant of the circuit quite small. Unfortunately, the feedback does little to reduce the second order time constant. The step response of a circuit that has this small first order / large second order time constant is one that will be very fast, but will ring horribly.

The main design challenge then comes in trying to reduce the second order term, without losing speed due to increases in the first order term. By selective picking of the device geometry and careful distribution of the gain contributions of each cell, the gain bump was removed from frequency response and minimal ringing exhibited in the eye diagram. Designing with our transferred substrate DHBT devices, a four cell Cherry-Hooper LIA was designed. Simulated performance shows an S(2,1) = 43 dB, −3 dB bandwidth = 77 GHz, and an open eye diagram for V_{in} = 10 and 200 mV and V_{out} = 250 mV at 140 Gb/sec.

30
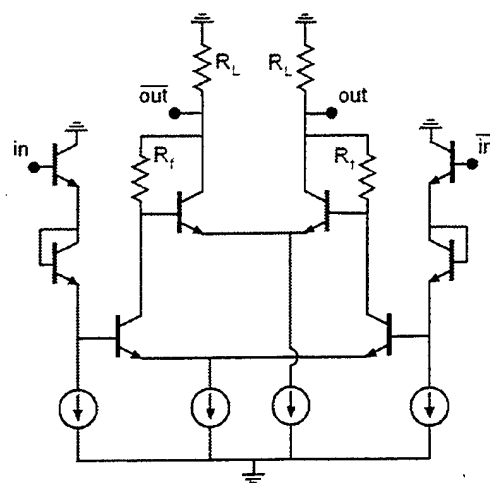
Fig. 4 Cherry-Hooper cell for 4 stage LIA

Fig. 5 LIA output eye diagram—simulated at
140 Gb/sec Vin = 10 mV, Vout = 250 mV
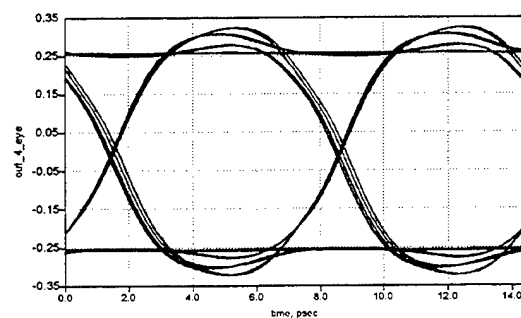
Fig. 6 LIA output eye diagram—simulated at
140 Gb/sec Vin = 200 mV, Vout = 250 mV

II. UCSB's InP Mesa DHBT process

We began the development of a traditional mesa HBT that could exploit the epitaxial engineering behind our TS-HBT devices, have narrow features to minimize C_{cb} parasitic loading, and reduce process complexity. With lithographic tools that can reliably produce submicron features at UCSB, our device team produced first generation mesa DHBTs with 0.5 um wide emitters W_E, and 0.5 um wide self-aligned base contacts W_B (Fig. 7). The f_t and f_{max} were > 140 GHz.
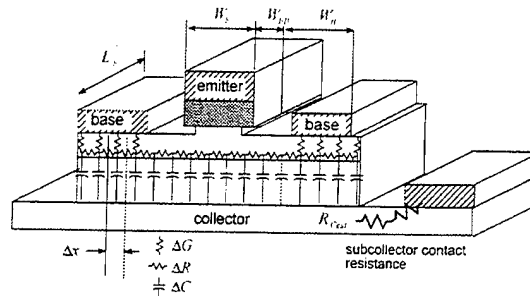

Fig. 7 Physical profile of Narrow Mesa DHBT

The initial device results from this process were very encouraging and efforts to make this technology support passive components, multi-level interconnects, and circuits were then pursued. Resistors are generated by evaporating NiCr of thickness to produce an $R_{sheet} = 40\ \Omega/$, and capacitors are realized by depositing SiN between M1 and M2. For the wiring environment, we spin over the top of the sample BCB (benzocyclobutene)—a low-loss, low ε_r dielectric that can be patterned for the microstrip wiring environment. Lastly, using a patterned top surface ground plane, we electroplate gold onto the BCB to complete the process. In special instances when we need to have transmission lines carry large currents, we can pattern the ground plane to support microstrip and coplanar waveguide.

Our first process run with the adopted circuit processing steps were very successful. The epitaxial layer structure was designed with an InP emitter, InGaAs base (400 A, 2e19·cm^{-3} Be doped), and InP collector (2000 A). All of the devices on the sample had 0.5 um wide emitters and lengths of 4, 6, and 10 um. The yield on the devices that had a base contact width ≥ 0.5 um was very good. Amongst the devices that had a 0.3 um base contact width, the yield was less than 50%

The maximum current density that could be supported before the device Kirk limit at V_{ce} = 0.7 V was $J_{kirk} = 2.25$ mA/um^2. The Rf performance of the better devices on the sample demonstrated a maximum $f_t = 205$ GHz, $f_{max} = 180$ GHz, at a $V_{ce} = 1.5$ V and J = 3 mA/um^2. In addition to devices, this maskset also had static frequency dividers (36 devices) and two stage Cherry-Hooper amplifiers (18 devices) on it with varying base contact widths to determine how narrow a contact we can reliably yield. Unfortunately, a

layout error was discovered on the static frequency dividers—they did not work. Amongst the Cherry-Hooper amplifiers, the yield was low because of a processing error during the electroplating step. For those that did work, the Rf performance was in good agreement with the simulated circuit. This circuit had an S(2,1) = 7 dB with a –3dB frequency at 35 GHz.

Lastly, test structures were fabricated for further characterization of the device yield with this process. Series and parallel diode test structures, and arrays of base-emitter and collector-base diodes (100 diodes in parallel) had good yield, the only failure mechanism showing an open circuit—a consequence of the same electroplating error. In addition to this success, our device team has recently yielded mesa DHBTs with a carbon doped, 300A, *graded base doping profile*, and 1500 A collector, that has generated an $f_t \approx 280$ **GHz and $f_{max} > 400$ GHz** at bias conditions of $V_{ce} = 2.0$ V and current density of 10 mA/um^2. This level of device performance makes the pursuit of fiber ICs at data rates of 160 Gb/sec a realizable quest.

III. Conclusion

Our efforts to design fiber ICs into UCSB's transferred substrate DHBT process showed simulated results that validated the pursuit of next generation fiber ICs at data rates of 80 Gb/sec and 160 Gb/sec. To decrease process difficultly and increase the yield of circuits with a device count in the hundreds, we have aggressively pursued a narrow mesa DHBT technology with speed comparable to our transferred substrate devices. Continued improvements in the epitaxial layer structure and scaling will then give us a traditional device with record speed, which is what is needed to make the circuits at 160 Gb/sec realizable.

Design and Evaluation of the Fibonacci Optical ATM Switch

P.M. Melliar-Smith, and Louise E. Moser

Electronic ATM switches are the bottleneck of an ATM network: ATM cells are not switched fast enough to match the transmission speed of the optical channels. It is expected that the gap between the electronic switching and optical transmission speeds will continue to increase as optical transmission technology matures. A solution to this problem is to implement ATM switches using optical technology. The major functions of an ATM switch are to route incoming cells to the appropriate output channels and to provide buffering for them, if necessary. The construction of a single monolithic fabric to interconnect large numbers of input and output channels may not be feasible due to physical and cost contraints. Consequently, the switching fabric of a high-performance ATM switch typically consists of a network of smaller switching elements, as shown in Fig. 1, with each small switching element having its own buffers, optical crossbar switch, and control unit, as shown in Fig. 2.
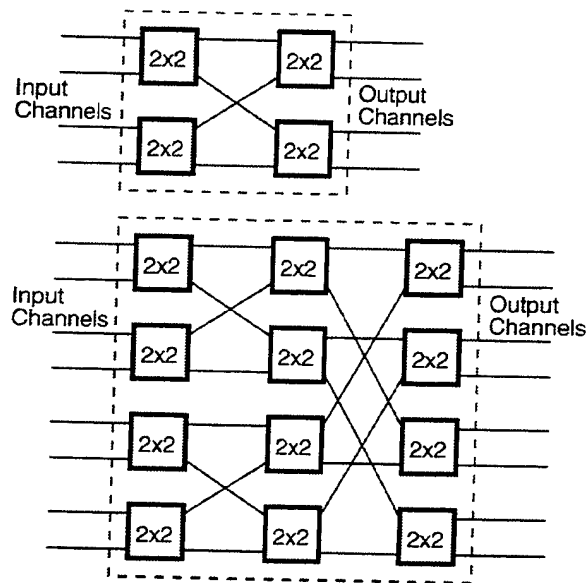

Fig. 1: Fig. 1. A 4-input and 4-output switch fabric with two stages of 2 x 2 switching elements and an 8-input and 8-output switch fabric with three stages of 2 x 2 switching elements.

Such an organization lends itself naturally to parallel processing of cells and parallel routing decisions. In optical switches, static buffering is not feasible and buffers are constructed by switching ATM cells into optical fibers that act as delay lines. The longer the fiber, the longer the delay and the greater the number of cells buffered in the fiber. By switching an ATM cell through a sequence of fiber delay lines, any required delay can be achieved. The difficulty of building an optical crossbar switch increases rapidly with the number of fibers. Consequently, it is important to minimize the number of fiber delay

lines while still achieving efficient operation of the switch. Although packet switch architectures using optical delay fibers as buffers have been proposed in the literature, as far as we can determine, studies on how to design an optical switch that addresses ATM-specific requirements while requiring few fibers and low processing complexity do not exist.
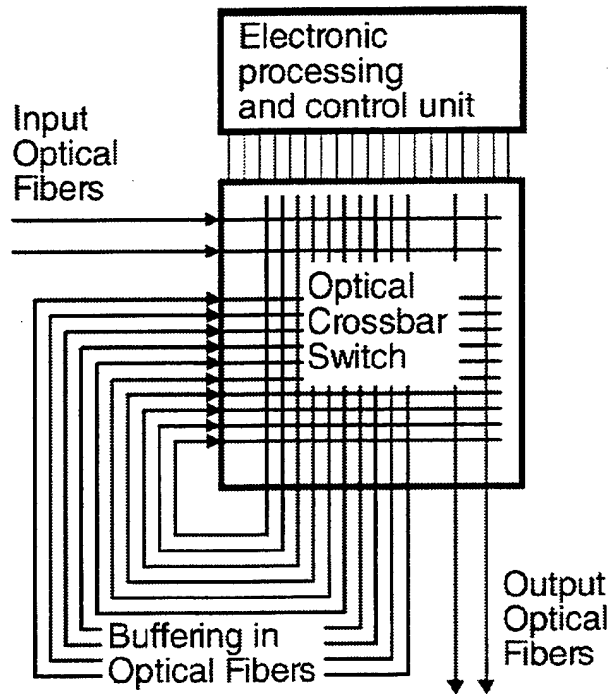
Fig. 2: A 2 x 2 optical switching element.

In this project, we developed the design of a novel optical ATM switch architecture [1]. Because of the remarkable properties of the Fibonacci numbers, the architecture is computationally efficient, requires few fibers, and yields low latency and cell loss rate across diverse time-correlated and heavily loaded traffic profiles. The buffer sets corresponding to an empirically lossless 2x2 ATM switch architecture under diverse traffic scenarios have been presented. The architecture exhibits the desirable characteristics that the cell loss rate decreases exponentially as the number of fibers increases, that the probability mass function for the sample latency decays rapidly, and that an exponential increase in the time correlation of traffic can be offset by a small increase in the number of fibers. Because of these salient characteristics, this architecture may play an integral role in future optical ATM networks.

[1] Allen Shum, P.M. Melliar-Smith, and Louise E. Moser, Design and Evaluation of the Fibonacci Optical ATM Switch, IEEE TRANSACTIONS ON COMPUTERS, VOL. 50, P. 466, MAY 2001

IV. MURI Success Stories

Optical Switching

# Calient Networks
Goleta, CA

John Bowers, Dan Blumenthal, *Founders*

The central focus of MOST was the development of optical switches. These switches utilized InP technology to make 4x4 nonblocking switch arrays. John Bowers and Dan Blumenthal started Calient Networks to commercialize optical switches for the telecommunications, test and military markets and hired a number of MOST graduates to develop optical switch technology (Olivier Jerphagnon, Jonathan Lang, Bin Liu, Adrian Keating).

A typical node in an fiber optic network typically has tens of fibers, and each fiber typically has tens of wavelengths. Hence the need is for nonblocking switches with large port counts, typically 100-1000. The 2D technology used in all N port crossbar optical switches up to the founding of Calient requires N^2 2x2 switches (Fig. 1). This is true for LiNbO3, InGaAsP, GaAs, and thermo-optic switches. This becomes prohibitively complicated and expensive for any switch with more than 32 ports. Calient developed a 3D technology (Fig. 2) that utilizes MEMS technology to solve this problem. In this case, only 2N switches are required. Hence a 256 port switch only requires 512 mirrors rather than the 65,536 switches required using 2D technology. This switch can switch data at 10 Gbit/s (Fig. 3), at 40 Gbit/s (Fig. 4), and should scale to 160 Gbit/s. This switch has been used to switch an aggregate of 10 Tbit/s without degradation. This technology promises to revolutionize the way wavelength division multiplexed optical networks are designed, deployed and the way bandwidth is managed within the core and metropolitan networks. A complete system containing redundant switches, network control software, input and output monitoring is shown in Fig. 5. Calient currently employs 95 people, and has sold systems to Japan Telecom, KDDI, Juniper Networks and Oki Networks.
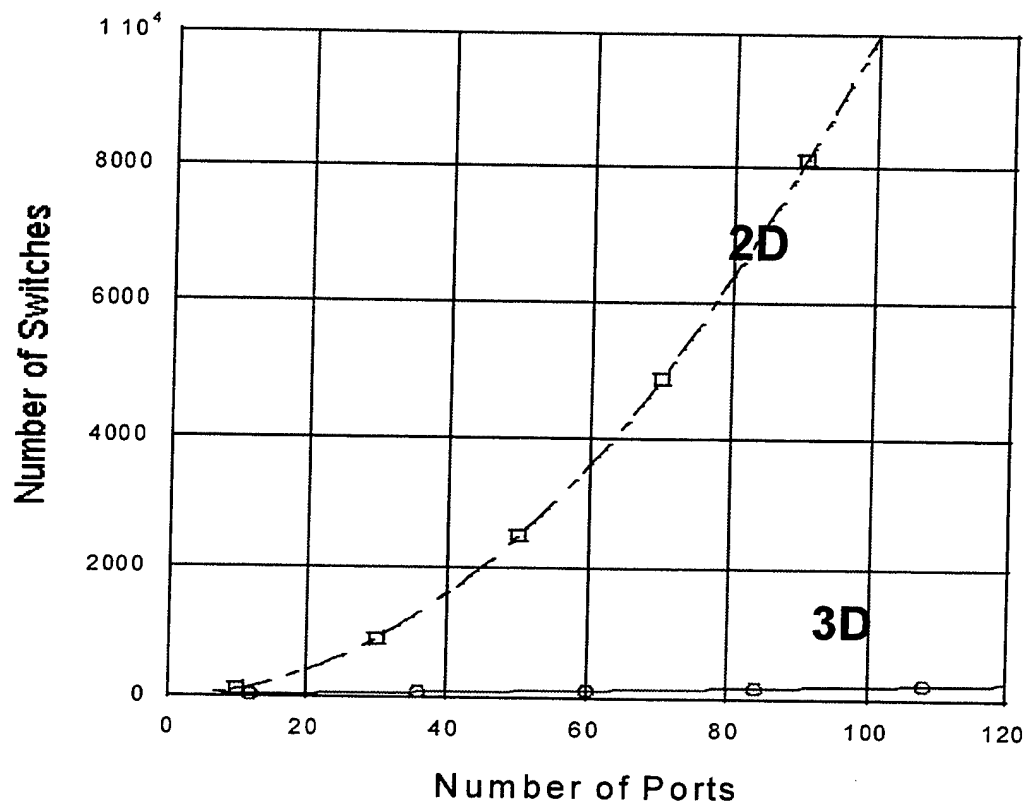
Figure 1 Comparison of 2D and 3D switch technologies.
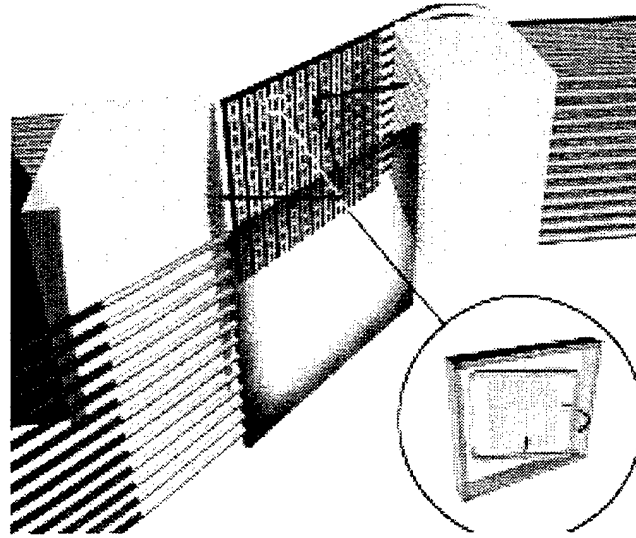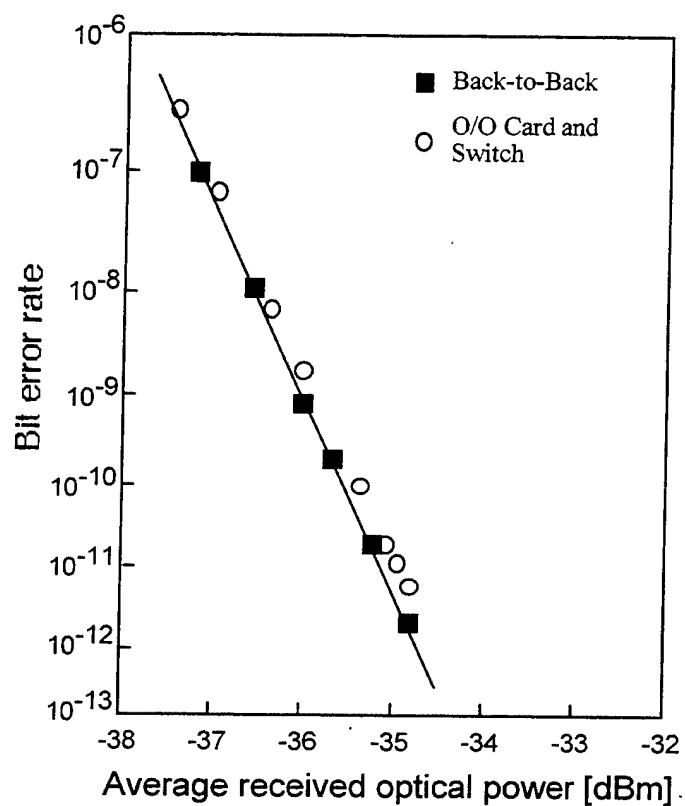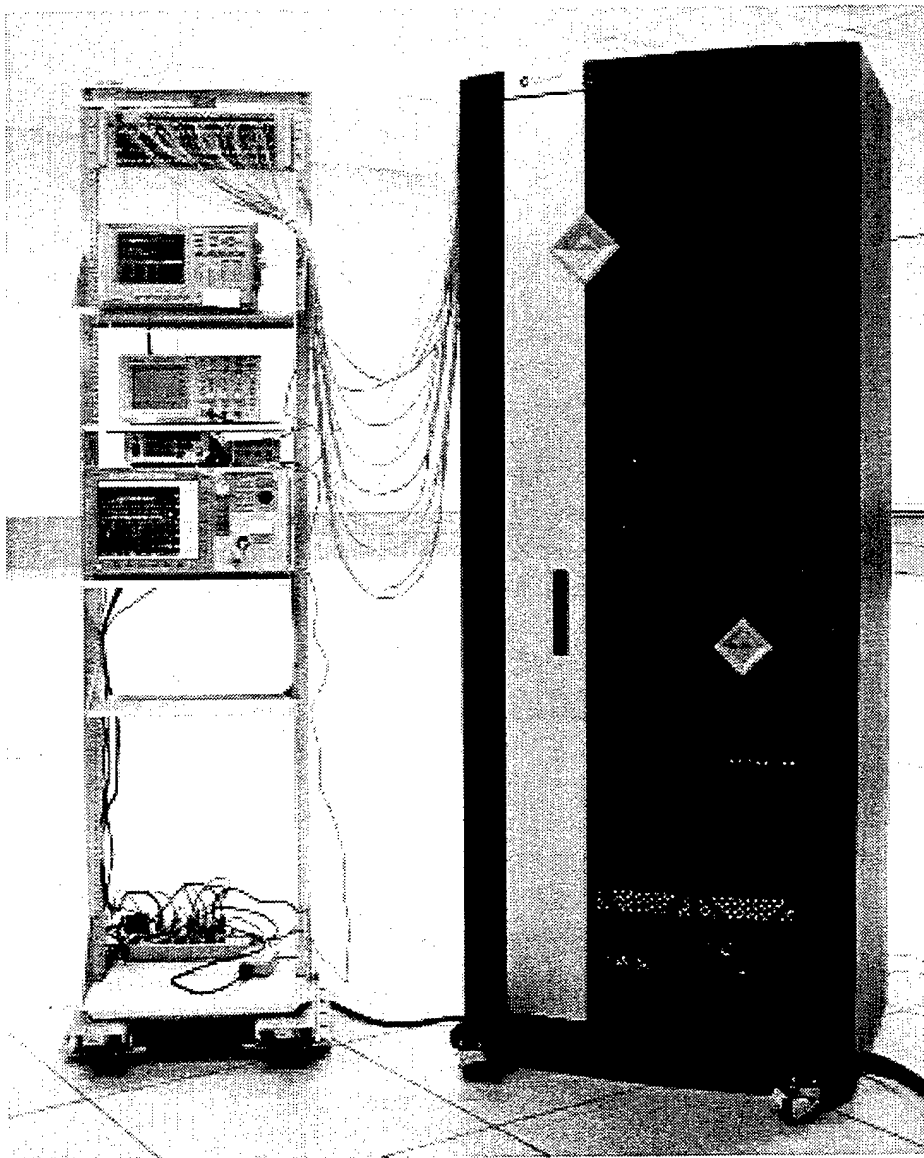
Figure 2 Schematic diagram of a 3D MEMS switch. The input and output fiber collimators are shown along with the two MEMS arrays.
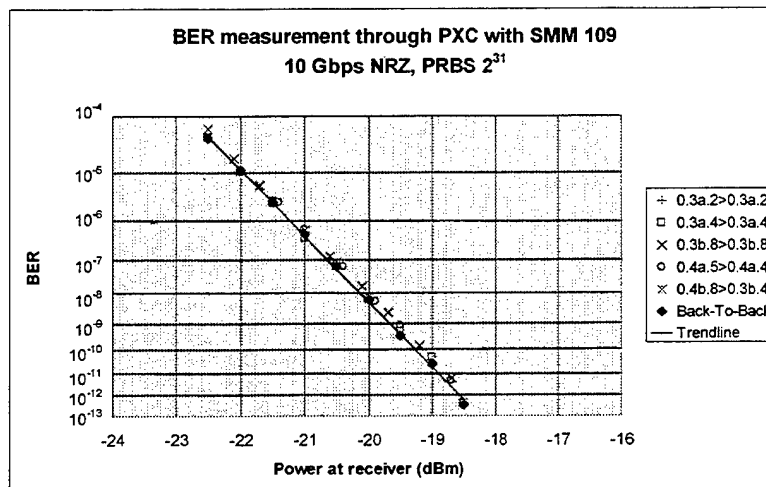
Figure 3 Performance of the switch at 40 Gbit/s.

Figure 4 Comparison of bit error rate in a 40 Gbit/s link with and without a 256 port 3D MEMS switch inserted.

Figure 5 Diamondwave 256: A 256 port photonic cross connect.

Tunable Lasers

## Agility Communications
Goleta, CA

Larry Coldren, Greg Fish, *Founders*

Researchers at the University of California, Santa Barbara have investigated the design, process and integration of semiconductor wavelength tunable lasers and their application to telecommunications and phased array radar systems. These lasers provide the capability to tune very narrow line-width emission over a large range of output wavelengths across THz of bandwidth. These advantages will have impact across a broad array of applications including sensors and bio-monitoring, phased array radar and communications networks. Military platforms that are sensitive to communications equipment weight, size and power dissipation will benefit from this technology. Applications to advance Internet optical communications in both the military and commercial sectors are foreseen.

Significant progress was made on high levels of integration based on indium phosphide integrated optic waveguide technology. Integration of tunable lasers with other critical functions like modulation, wavelength monitoring, optical amplification and all-optical wavelength conversion were demonstrated during the course of this work. Very high-speed wavelength switching over more than 50 wavelengths shows promise to adapt this technology to optical packet switched applications.

The basic - research results of this wavelength tuning technology has been commercialized at Agility Communications, a UCSB spin-out company that employs over 200 people in the States of California and Pennsylvania. A picture of the Sampled Grating Distributed Bragg Reflector (SGDBR) wavelength tunable structure, example tunable wavelength output and the Agility tunable laser product are shown in Figure 1.
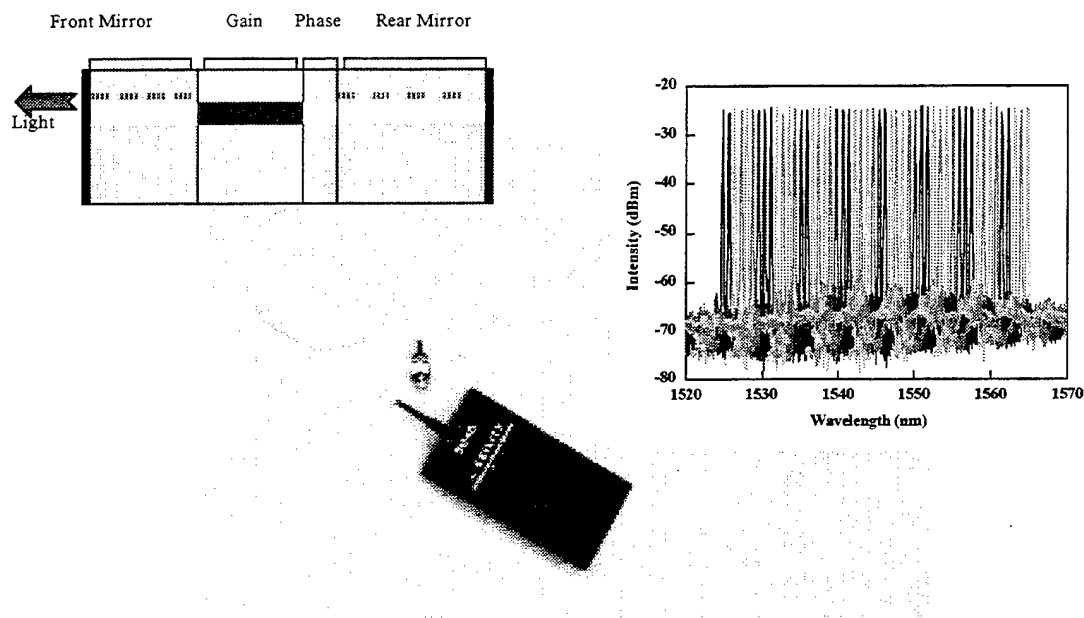
Figure 1. Phased Array Radar applications that can leverage advances in tunable laser integration technology.

V. MOST Publication List
(highlighted papers are attached)

Bowers Group

1. "Multidisciplinary Optical Switching Technology (MOST) Center," J. E. Bowers, N. Dagli, S. Butner, L. Coldren, M. Melliar-Smith, M. Rodwell, and A. Shakouri, Photonics Switching Conference, Tokyo, Japan (1996).

2. "1.55 μm lasers using separate strain compensation heterostructure," P. Abraham, A. L. Holmes, M. E. Heimbuch, G. A. Fish, S. P. DenBaars, J. E. Bowers, 8th biennial workshop on Organometallic Vapor Phase Epitaxy, Dana Point (CA), April 13-17 (1997).

3. "Substrate engineering of 1.55 μm lasers," P. Abraham, A. K. Black, N. Margalit, A. R. Hawkins, S. P. DenBaars, J. E. Bowers, International Conference on Indium Phosphide and Related Materials (IPRM '97), Cape Cod, MA, May 11-15 (1997).

4. "Wafer Fusion: Materials Issues and Device Results," K.A. Black, A. R. Hawkins, N. M. Margalit, D. I. Babic, A. L. Homes, Jr., and E.L. Hu, Journal of Selected Topics in Quantum Electronics, 3 (3), June (1997).

5. "Fused vertical directional couplers," B. Liu, A. Shakouri, and J. E. Bowers, LEOS Annual meeting, San Francisco, Nov. 10-13 (1997).

6. "Fused vertical couplers," B. Liu, A. Shakouri, P. Abraham, B. Kim, and J. E. Bowers, OFC '98, San Jose, CA, February 22-27, (1998).

7. "Ultra short fused optical switches," Ali Shakouri, Bin Liu, Patrick Abraham, Boo-Gyoun Kim, Andrew W. Jackson, Art Gossard, and John E. Bowers, Presented at Workshop on Compound Semiconductors and Devices (WOCSEMMAD'98), Monterey, CA, February 1998.

8. "Improved extinction ratio in ultra short directional couplers using asymmetric structures," Boo-Gyoun Kim, Ali Shakouri, Bin Liu, and John E. Bowers, Integrated Photonic Research Conference, Victoria, Canada, March 1998.

9. "Fused Vertical Couplers," B. Liu, A. Shakouri, P. Abraham, B.-G. Kim, A. W. Jackson and J. E. Bowers, *Applied Physics Letters,* 72(21), 2637-2638, May 25 (1998).

10. "Wafer fused optoelectronics for switching ," Ali Shakouri, Bin Liu, Patrick Abraham, and John E. Bowers, Invited Presentation, IEEE/LEOS Summer Topical Meeting on Broadband OpticalNetworks, Monterey, CA, July 1998.

11. "Improved Extinction Ratio in Ultra Short Directional Couplers Using Asymmetric Structures," B. Kim, A. Shakouri, B. Liu, and J. E. Bowers, Japanese *Journal of Applied Physics*, 37(8A), 930-932, August 1, (1998).

12. "Fused Vertical Coupler Switches," B. Liu, A. Shakouri, P. Abraham, and J.E. Bowers, *Electronics Letters*, 34(22), 2159-2161, October 29, (1998).

13. "Wafer-Fused Optoelectronics for Switching," A. Shakouri, B. Liu, B.G. Kim, P. Abraham, A. Jackson, A. Gossard, and J.E. Bowers, *IEEE Jour. Lightwave Tech.*, vol. 16, no. 12, pp. 2236-2242, Dec. (1998).

14. "Fused InP-GaAs vertical coupler filters", Bin Liu; Shakouri, A.; Abraham, P.; Chiu, Y.J.; Zhang, S.; Bowers, J.E. IEEE Photonics Technology Letters, vol.11, (no.1), IEEE, Jan. 1999. p.93-5.

15. "3D photonic integrated circuits for WDM applications," A. Shakouri, B. Liu, P. Abraham, and J. E. Bowers, invited paper, *SPIE Critical Reviews*, San Jose, CA, pp. 181-204, January 25-26 (1999).

16. "25-GHz Polarization-Insensitive Electroabsorption Modulators with Traveling-Wave Electrodes," Sheng Z. Zhang, Yi-Jen Chiu, Patrick Abraham, and John E. Bowers, IEEE Photonics Technology Letters, Volume 11, Number 2, p. 191, February 1999

17. "Fused III-V vertical coupler filter with reduced polarisation sensitivity", Liu, B.; Shakouri, A.; Abraham, P.; Chiu, Y.J.; Bowers, J.E. Electronics Letters, vol.35, (no.6), IEE, 18 March 1999. p.481-2.

18. "High-speed operation of travelling-wave electroabsorption modulator", V. Kaman, S.Z. Zhang, A.J. Keating, J.E. Bowers; Electronics Letters, vol.35, (no.12), IEE, 10 June 1999. p.993-5.

19. "30 Gbit/s operation of a traveling-wave electroabsorption modulator", S.Z. Zhang, V. Kaman, P. Abraham, Y.-J. Chiu, A. Keating, and J. E. Bowers, OFC'99 Technical Digest, paper ThT3.

20. "Push-pull fused vertical coupler switch", Liu, B.; Shakouri, A.; Abraham, P.; Bowers, J.E. IEEE Photonics Technology Letters, vol.11, (no.6), June 1999. p.662-4.

21. "Vertical Coupler With Separated Inputs and Outputs Fabricated Using Double-Sided Process," B. Liu, A. Shakouri, P. Abraham, and J.E. Bowers, Electronics Letters, 35(18), 1552-1554, September 2 (1999)

22. "A 100 kHz to 50 GHz traveling-wave amplifier IC module", V. Kaman, T. Reynolds, A. Petersen, J.E. Bowers; IEEE Microwave and Guided Wave Letters, 9(10), 416-418, October (1999).

23. "Characteristic equations for different ARROW structures", Bin Liu, Ali Shakouri and John E. Bowers, Optical and Quantum Electronics, vol. 31(12): pp. 1267-1276, December 1999.

24. "Wavelength routing of 40 Gbit/s packets with 2.5 Gbit/s header erasure/rewriting using all-fibre wavelength converter," Olsson, B.-E.; Ohlen, P.; Rau, L.; Rossi,

25. G.; Jerphagnon, O.; Doshi, R.; Humphries, D.S.; Blumenthal, D.J.; Kaman, V.; Bowers, J.E., Electronics Letters , Volume: 36 Issue: 4 , 17, Page(s): 345 -347, Feb. 2000.

26. "Wavelength multiplexers by cascading 3D vertical couplers", Bin Liu, Ali Shakouri, Patrick Abraham and John E. Bowers, Appl. Phys. Lett., vol. 76 (3), pp. 282-284 (Jan. 2000)

27. "3.7 ps pulse generation at ≥ 30 GHz by dual-drive electroabsorption modulators", V. Kaman, Y. J. Chiu, S. Z. Zhang and J. E. Bowers, *Electronics Letters*, vol. 36, pp. 1130-1132, 2000.

28. "120 Gbit/s OTDM system using electroabsorption transmitter and demultiplexer operating at 30 GHz", V. Kaman and J. E. Bowers, *Electronics Letters*, vol. 36, pp. 1477-1479, 2000.

29. "A compact 40 Gbit/s demultiplexing receiver based on integrated tandem electroabsorption modulators" V. Kaman, Y. J. Chiu, T. Liljeberg, S. Z. Zhang and J. E. Bowers,, *Electronics Letters*, , Volume: 36 Issue: 23 , 9 Nov. 2000 Page(s): 1943 -1944

30. "Simultaneous OTDM Demultiplexing and Detection using an Electroabsorption Modulator," Volkan Kaman, Adrian J. Keating, Sheng Z. Zhang and John E. Bowers, IEEE Photonics Technology Letters, Vol. 12, No. 6, p. 711, June 2000.

31. "Integrated tandem traveling-wave electroabsorption modulators for > 100 Gbit/s OTDM applications", V. Kaman, Y. J. Chiu, T. Liljeberg, S. Z. Zhang and J. E. Bowers, IEEE Photonics Technology Letters, Vol. 12, No. 11, pp. 1471-73 (2000).

32. "Integrated tandem electroabsorption modulators for high-speed OTDM applications," V. Kaman, Y. J. Chiu, T. Liljeberg, S. Z. Zhang and J. E. Bowers, *Microwave Photonics Conference 2000*, paper TU4, Sept. 11-13 2000.

33. "Electroabsorption modulator as a compact OTDM demultiplexing receiver", V. Kaman, A. J. Keating, S. Z. Zhang and J. E. Bowers, *ECOC 2000*, paper 9.4.6, Sept. 3-7 2000.

34. "Double-Bonded InP/InGaAsP Vertical Coupler 1:8 Beam Splitter," Maura Raburn, Bin Liu, John E. Bowers, and Patrick Abraham, IEEE Photonics Technology Letters, Vol. 12, NO. 12, pp. 1639-41, December 2000.

35. "All-optical label swapping networks and technologies," Blumenthal, D.J.; Olsson, B.-E.; Rossi, G.; Dimmick, T.E.; Rau, L.; Masanovic, M.; Lavrova, O.; Doshi, R.; Jerphagnon, O.; Bowers, J.E.; Kaman, V.; Coldren, L.A.; Barton, J. Lightwave Technology, Journal of , Volume: 18 Issue: 12 , Page(s): 2058 -2075, Dec. 2000.

36. "InP-InGaAsP wafer-bonded vertically coupled x-crossing multiple channel optical add-drop multiplexer," Raburn, M.; Bin Liu; Yae Okuno; Bowers, J.E., IEEE Photonics Technology Letters , Volume: 13 Issue: 6 , Page(s): 579 -581, June 2001.

Coldren Group

37. "Compact InGaAsP/InP 1 x 2 Optical Switch Based on Carrier Induced Suppression of Modal Interference," G.A. Fish, L.A. Coldren, and S.P. DenBaars, *Electron. Letts.* 33, (22) 1898-1900, (October 1997).

38. "Suppressed Modal Interference Switches with Integrated Curved Amplifiers for Scaleable Photonic Crossconnects," G.A. Fish, L.A. Coldren, and S.P. DenBaars, *IEEE Photon. Techn. Letts.* 10, (2) 230-232, (February 1998).

39. "InGaAsP/InP Suppressed Modal Interference Switches with Integrated Curved Amplifiers for Scaleable Photonic Crossconnects," G.A. Fish, L.A. Coldren, and S.P. DenBaars, *Optical Fiber Conference '98*, paper no. TuH4, San Jose, CA, 44, (February 22-27, 1998).

40. "Improved Compositional Uniformity of InGaAsP Grown by MOCVD Through Modification of the Susceptor Temperature Profile," G.A. Fish, B. Mason, S.P. DenBaars, and L.A. Coldren, *Journal of Crystal Growth,* vol. 186/1-2, 1-7, (March 1, 1998).

41. "InGaAsP/InP Scaleable, Photonic Crossconnects Using Optically Amplified Suppressed Modal Interferences Switch Arrays," G.A. Fish, L.A. Coldren, and S.P. DenBaars, *Integrated Photonics Research '98*, paper no. ITuE4, Victoria, Canada, 243-245, (March 29-April 1, 1998).

42. "Compact, 4 x 4 InGaAsP/InP Optical Crossconnect With a Scaleable Architecture," G.A. Fish, B. Mason, L.A. Coldren, and S.P. DenBaars, *Photon. Techn. Letts.,* 10, (9), 1256-1258, (September 1998).

43. "Compact 1.55μm Spot-Size Converters for Photonic Integrated Circuits," G.A. Fish, B. Mason, L.A. Coldren, and S.P. DenBaars, *Integrated Photonics Research '99*, paper no. RWD4 Santa Barbara, CA, 375-377, (July 19-21, 1999).

44. "Monolithic InP Optical Cross Connects: 4 x 4 and Beyond," G.A. Fish, B. Mason, L.A. Coldren, and S.P. DenBaars, *Photonics in Switching '99*, paper no. JWB2 Santa Barbara, CA, 339-341, (July 19-23, 1999).

45. "Optical Crossbar Switches on InP," G.A. Fish, B. Mason, S.P. DenBaars, and L.A. Coldren, *LEOS '99*, paper no. WC1, San Francisco, CA, 405-406 (November 8-11, 1999). INVITED TALK

46. "All-Optical Label Swapping Networks and Technologies," D.J. Blumenthal, B.-E. Olsson, G. Rossi, T.E. Dimmick, L. Rau, M. Masanovic, O. Lavrova, R. Doshi, O. Jerphagnon, J.E. Bowers, V. Kaman, L.A. Coldren, and J. Barton, *J. Lightwave Technol.*, 18, (12), 2058-2075, (December 2000).

47. "Tunable Lasers Using Sampled Grating DBRs," J. Barton, G. Fish, and L.A. Coldren, *LEOS Summer Topicals,* paper no. I 0004, Copper Mountain Resort, CO, 33-34 (July 30-August 1, 2001).

Dagli Group

48. "Substrate-Removed (SURE) Optical Waveguides in GaAs/AlGaAs Epitaxial Layers Embedded in Benzocyclobutene (BCB)," S. R. Sakamoto, C. Ozturk, Y. T. Byun, J. Ko and N. Dagli, Proceedings of Integrated Photonics Research Conference, Paper

49. "Polymer/Semiconductor Photonic Integrated Circuits," N. Dagli, S. R. Sakamoto, C. Ozturk and J. Ko, Paper 30, SPIE International Symposium on Optoelectronics'98, San Jose, CA, January 28-30, 1998. (Invited)

50. "Drive Voltage Reduction in Mach-Zehnder Electrooptic Modulators Using Systems Approach," Nadir Dagli, Integrated Photonics Research Conference, Paper ITuI4, Victoria, British Columbia, Canada, March 30 - April 3, 1998.

51. "Low Loss Substrate-Removed (SURE) Optical Waveguides in GaAs/AlGaAs Epitaxial Layers Embedded in Organic Polymers," S. R. Sakamoto, C. Ozturk, Y. T. Byun, J. Ko, N. Dagli, IEEE Photonics Technology Letters, vol. 10, No. 7, pp.985-987, July 1998.

52. "Integrated Polymer/Semiconductor Grating Reflector for WDM Applications," C. Ozturk, Y. T. Byun, S. R. Sakamoto and N. Dagli, IEEE/LEOS 1998 Annual Meeting, Paper ThA, Orlando, FL, December 1- 4, 1998.

53. "Low Loss Optical Waveguides and Polarization Splitters Utilizing Oxidized AlxGa1-xAs Layers," A. Bek, A. Aydinli, J. G. Champlain, R. Naone and N. Dagli, IEEE/LEOS 1998 Annual Meeting, Paper WCC, Orlando, FL, December1-4, 1998.

54. "Hybrid Integration of Polymers and Semiconductors," Nadir Dagli, (Invited Paper) CLEO/Pacific Rim'99, Seoul, Korea, August 30 - September 3 (1999).

55. "Coupled Polymer Waveguides and Substrate Removed GaAs Waveguides as Tunable Filters," Cem Ozturk and Nadir Dagli, Integrated Photonics Research Conference Proceedings, Paper IFD1-1, pp. 240-242, Quebec, Canada, July 12-15, 2000.

56. "Filtering characteristics of coupled polymer waveguides and substrate removed (SURE) GaAs waveguides," Cem Ozturk and Nadir Dagli, Optoelectronic Integrated Circuits, SPIE International Symposium on Optoelectronics '00, San Jose, CA, January 22-28, 2000.

Blumenthal Group

57. "Broadband Optically Preamplified Receiver Using an Interferometric Wavelength Converter," L. Rau, P. Ohlen, and D. J. Blumenthal, *OSA Topical Meeting on Photonics in Switching '99*, Paper PThD4-1, pp. 103-105 Santa Barbara, CA, July 21-23 (1999).

58. "Wavelength Routing of 40 Gbit/s Packets with 2.5 Gbit/s Header Erasure/Rewriting using an All-Fiber Wavelength Converter," B. E. Olsson, P. Ohlen, L. Rau, G. Rossi, O. Jerphagnon, R. Doshi, D. S. Humphries, V. Kaman, J. E. Bowers, and D. J. Blumenthal, *Proceeding of the 25th European Conference on Optical Communication (ECOC '99)* Nice, France, Postdeadline Paper PD3-4, pp. 50-51, September (1999)

59. "A Simple and robust High-Speed Wavelength Converter using Fiber Cross-Phase Modulation and Filtering," B. Olsson, P. Ohlen, L. Rau, and D. J. Blumenthal, *Technical Digest of the Optical Fiber Communication Conference (OFC '00)*, Baltimore, MD, Paper WE1-1, pp. 64-66, March 5-10, (2000).

60. "Generation of 10 GHz Pulse Packets From an Actively Mode-Locked Fiber Ring Laser," B. E. Olsson and D. J. Blumenthal, *Technical Digest of the Optical Fiber Communication Conference (OFC '00)*, Baltimore, MD, Paper ThL2-1, pp. 175-177, March 5-10, (2000).

61. "Optical SCM Data Extraction using a Fiber Loop Mirror for WDM Network Systems," G. Rossi, O. Jerphagnon, B. Olsson, and D. J. Blumenthal, *Technical Digest of the Optical Fiber Communication Conference (OFC '00)*, Baltimore, MD, Paper FD7-1, pp. 74-76, March 5-10, (2000)

62. "Wavelength Dependence and Power Requirements of a Wavelength Converter Based on XPM in a Dispersion-shifted Optical Fiber," P. Ohlen, B.E. Olsson, and D. J. Blumenthal, *IEEE, Photonic Technology Letters,* 12 (5), 522-524, May, 2000.

63. "All-optical Header Erasure and Penalty-free Rewriting in a Fiber-based high-speed Wavelength Converter," P. Ohlen, B. E. Olsson, and D. J. Blumenthal, *IEEE Photonic Technology Letters*, 12 (6), 663-665, June, 2000.

64. "A Simple and Robust 40 Gbit/s Wavelength Converter using Fiber Cross-Phase Modulation and Optical Filtering," B. E. Olsson, P. Ohlen, L. Rau, and D. J. Blumenthal, *IEEE Photonic Technology Letters*, 12 (7), 846-848S. Han, C.-H. Lee, B. Matinpour, J. Laskar, D. J. Blumenthal, *IEEE Microwave and Guided Wave Letters*, 10 (7), 282-284, July, 2000.

65. "Optical SCM Data Extraction using a Fiber Loop Mirror for WDM Network Systems," G. Rossi, O. Jerphagnon, B. E. Olsson, and D. J. Blumenthal, *IEEE Photonics Technology Letters*, 12 (7), 897-899, July, 2000.

66. "The λ-Scheduler: A Multiwavelength Scheduling Switch," J. P. Lang, E. Varvarigos, and D. J. Blumenthal, *IEEE Photonic Technology Letters*, 18 (8), 1049-1062, August, 2000.

67. "All-Optical Label Swapping Networks and Technologies," D. J. Blumenthal, B. E. Olsson, G. Rossi, T. Dimmick, L. Rau, M. Masanovic, O. A. Lavrova, R. Doshi, O. Jerphagnon, J. E. Bowers, V. Kaman, L A. Coldren, and J. Barton, *IEEE Journal of Lightwave Technology*, Special Issue on Optical Networks, 18 (12), pp. 2058-2075, December, 2000. (Invited Paper)

68. "Wavelength Multicasting Using an Ultra High-Speed All-Optical Wavelength Converter", L. Rau, B.E. Olsson, D.J. Blumenthal, *Technical Digest of the Optical Fiber Communication Conference (OFC '01)*, Anaheim, CA., WDD52-1 - WDD52-4, March 17-23, 2001.

69. "A Multiwavelength RZ Pulse Source Generator Using an Ultra High-Speed All-Wavelength Converter," L. Rau, B.E. Olsson, D.J. Blumenthal, *Photonics in Switching 2001*, Monterey, CA, Paper PThC4-2, June 13-15, (2001).

70. "A Rapid Tunable Wavelength Converter Using a GCSR Laser," O. A. Lavrova, L. Rau, D.J. Blumenthal, *Photonics in Switching 2001*, Monterey, CA, Paper PThC3-1, June 13-15, (2001).

71. "All-Optical Demultiplexing using Fiber Cross-Phase Modulation and Optical Filtering," B.E. Olsson and D.J. Blumenthal, *IEEE Photonics Technology Letters*, 13 (8), pp. 875-877, August, (2001).

72. "WDM to OTDM Multiplexing using an Ultra-fast All-Optical Wavelength Converter," B. E. Olsson, L. Rau, and D. J. Blumenthal, *IEEE Photonics Technology Letters*, 13 (9), September, 2001. (2001)

Fainman Group

73. D. Marom, D. Panasenko, P. C. Sun, Y. Fainman, "Femtosecond rate space-to-time conversion," J. Opt. Soc. Am.: B, 17, 1759-73, 2000

74. Y. Fainman, D. Marom, D. Panasenko, R. Rokitski, K. Oba, Y. Mazurenko, and P. C. Sun, "Optical conversion between space and time parallelism," presented at the *Optics in Computing 2000*, Quebec City, Canada, June 18-23, 2000, *SPIE Conference Proceedings*, Vol 4089, p. 1028, 2000 (Invited)

75. D.M. Marom, K.S. Kim, L.B. Milstein, Y. Fainman, "Hybrid pulse position Modulation/ultrashort light pulse code division multiple access for data networking,"" *Optics in Computing 2000*, Quebec City, Canada, June 18-23, 2000, *SPIE Conference Proceedings*, Vol 4089, pp. 479-484, 2000.

76. Y. Fainman, "Nonlinear mixing of femtosecond laser pulses for communication and informationprocessing," presented at the Laser Optics 2000, St.-Petersburg, Russia, June 2000 (Invited)

77. K. Oba, P. C. Sun, Y. T. Mazurenko, Y. Fainman, "Femtosecond optics for data storage and detection," presented at the SPIE's 45-th Annual Meeting, paper #4110-33, July 2000; Proceedings of the SPIE - The International Society for Optical Engineering, 2000, vol.4110:242-53. (Invited)

78. P. C. Sun, D. M. Marom, D. Panasenko, R. Rokitskii, P. C. Lin, Y. T. Mazurenko, and Y. Fainman, "Nonlinear space-time information processing," presented at the SPIE's 45-th Annual Meeting, paper #4113-01, July 2000; Proceedings of the SPIE - The International Society for Optical Engineering, 2000, vol.4113:1-12. (Keynote Address)

79. Y. Fainman,"Nonlinear femtosecond informationprocessing systems," presented at the 2000 OSA/ILS XVI Annual Meeting, Providence, Rhode Island, 2000 (Invited)

80. L. B. Milstein, Y. Fainman, D. Marom, K. Kim, "Optical CDMA for Internet Operation at Terabit Rates," presented at the 2000 Second Annual International Symposium on Advanced Radio Technologies, September 6-8, 2000 (Invited)

81. Y. Fainman, D. Marom, D. Panasenko, Y. Mazurenko, and P. C. Sun, "Superfast information processing with femtosecond laser pulses," to be presented at the International Optical Congress "Optics - XXI Century", St. Petersburg, October 16-20, 2000 (Invited)

82. Y. Fainman, "Ultrafast optics for communications and computing," presented at the the IEEE/LEOS 2000 Annual Meeting, November 13-16, 2000 IEEE Annual Meeting Conference Proceedings, Rio Grande, Puerto Rico, 13-16 Nov. 2000). Piscataway, NJ, USA: IEEE, 2000. p. 601-2 vol.2. (Invited)

83. R. Rokitski, P.-C. Sun, and Y. Fainman, "Study of spatial-temporal characteristics of optical fiber based on ultra-short pulse interferometry," OFC 2001 Technical Digest, Edited by: Sawchuk, A.A. Washington, DC, USA: Opt. Soc. America, p. WDD21-1-3 vol.3. (Optical Fiber Communication Conference, Anaheim, California, March 21, 2001).

84. D.Panasenko, P.-C. Sun, N.Alic and Y. Fainman, 'Ultrashort laser pulse diagnostics using the local spectrum function,' presented at Ultrafast electronics and optoelectronics OSA topical meeting, January 2001, paper UWA-5.

85. D. Marom, D. Panasenko, P. C. Sun, Y. Fainman, "Linear and Nonlinear Operation of a Time-to-Space Processor," J. Opt. Soc. Am.: A, 18, 448-458, 2001

86. W. Nakagawa, R. Tyan, P. C. Sun, Y. Fainman, "Ultrashort Optical Pulse Propagation in Periodic Diffractive Structures using Rigorous Coupled-Wave Analysis," J. Opt. Soc. Am.:A, 18, pp. 1072-1081, 2001

87. R. Rokitski, P. C. Sun, Y. Fainman, "Study of spatial-temporal characteristics of optical fiber based on ultrashort-pulse interferometry," Optics Letters, vol.26, 1125-7, 2001

88. K. Oba, P. C. Sun, Y. Mazurenko, Y. Fainman, " Optical data storage and detection with femtosecond laser pulses," Optical Memory & Neural Networks, vol.9, (no.4):287-300, 2001

89. D. Marom, D. Panasenko, P. C. Sun, Y. Mazurenko, Y. Fainman, "Real-Time Spatial-Temporal Signal Processing with Optical Nonlinearities," IEEE Journal of Selected Topics in Quantum Electronics, v. 7, No. 4, pp. 683-693, 2002

Wafer Fusion: Materials Issues and Device Results

A. Black, A. R. Hawkins, N. M. Margalit, D. I. Babić, A. L. Holmes, Jr.,
Y.-L. Chang, P. Abraham, J. E. Bowers, and E. L. Hu

Abstract—A large number of novel devices have been recently demonstrated using wafer fusion to integrate materials with different lattice constants. In many cases, devices created using this technique have shown dramatic improvements over those which maintain a single lattice constant. We present device results and characterizations of the fused interface between several groups of materials.

Index Terms—Detectors, optical fiber communication, semiconductor device bonding, semiconductor device fabrication, semiconductor heterojunctions, semiconductor lasers.

I. INTRODUCTION

IN EACH material system, nature has dictated a set of physical properties (i.e., mobility, optical absorption, thermal conductivity, and resistivity). For a given application, the optimal properties may not reside in a single material, but in a variety of disparate materials. To this end, high performance semiconductor-based electronic and optoelectronic device design can be greatly enhanced if we can freely integrate heterogeneous materials. An effective integration method has remained a challenge due to lattice constant mismatch between semiconductor systems. "Monolithic techniques" such as the epitaxial or pseudomorphic growth of mismatched materials can result in highly defective layers which degrade or inhibit device operation.

Recently, there has been exciting progress in the solution to the problem of matching disparate materials to optimize device performance: a process termed "wafer fusion". Fusion bonding is a special case of direct bonding in which chemical bonds are established directly between two materials at their hetero-interface in the absence of an intermediate layer. For fusion bonding to occur in semiconductors, two oxide-free (and contaminant-free) crystals are directly bonded and then annealed to yield a crystalline junction.

Fig. 1 shows the range of wafer applications that have been currently addressed. In many cases, record performances have been achieved as a result of using fusion to eliminate the limitations imposed by lattice matched epitaxy. Moving clockwise around the chart starting in the upper-left corner, bonding GaAs–AlAs mirrors to InGaAsP active regions solves the fundamental limits in InP–InGaAsP mirror reflectivities in vertical cavity lasers [1]. Deeper quantum wells with strong optical confinement can be achieved by using AlGaAs as the outer confining layer for in-plane InGaAsP lasers. The problem
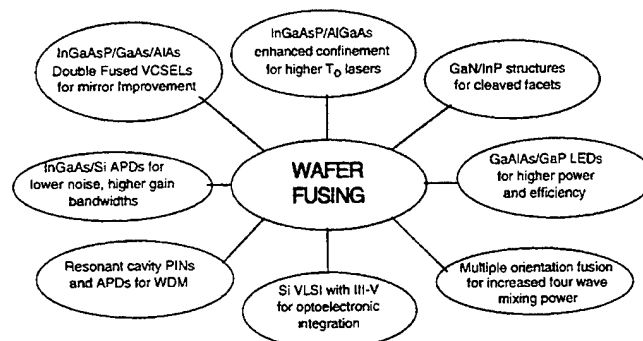
Fig. 1. Applications of fusing and bonding processes in optoelectronics and electronics.

of cleaving perpendicular facets in hexagonal crystals can be solved by fusing to a cubic crystal and removing most of the hexagonal crystal [2]. Hewlett Packard has used fusing in light-emitting diodes (LED's) to replace an absorptive substrate with a transparent substrate, and also to reduce the substrate thermal resistance [3]. Bellcore has used fusing to increase the four-wave mixing power in waveguides for wavelength-division multiplexing (WDM) applications [4]. Oki and other companies have wafer fused III–V sources and detectors to Si with the goal of optoelectronic-integrated circuits (OEIC) [5]. Several groups have used GaAs–AlAs mirrors to get sharper bandpass features in WDM detectors [6], [7]. Finally, improved silicon telecommunication APD's have been demonstrated by combining the ideal avalanche characteristics of silicon with the absorption characteristics of InGaAs to get higher gain bandwidth products, lower noise and reduced temperature sensitivity [8].

This paper will begin with a brief description of the fusion process in Section II. Section III will be a description of various device applications utilizing wafer fusion. The device results have thus far been dramatically successful, but point out critical issues that need to be explored. Section IV discusses some of these issues, as well as the electrical and optical characterization of wafer fused interfaces.

II. WAFER FUSING: PROCESS DESCRIPTION

The technique of fusion bonding consists of three steps: surface preparation, placement of the substrates into contact with each other, and an elevated temperature anneal while the substrates are maintained in contact under pressure. The surface preparation steps include removal of oxides and organic contaminants, as well as chemical activation of the surface for interfacial bonding. Bonding by Van der Waals forces occurs when two such clean and smooth macroscopic bodies are placed in contact, while chemical reactions and

re-crystallization takes place during the elevated temperature anneal [9].

There are a number of techniques used for surface preparation and placing substrates in intimate contact. Bonding may be classified as "wet" or "dry." In wet bonding, the samples are put together and pressure is applied on them while the samples are still immersed in an oxide removing or passivating chemical. In the dry-bonding technique, the oxides are removed using a suitable chemical, and the samples are placed in contact after the surfaces have been dried. Surface oxidation must be prevented when using the latter technique. In Si bonding, hydrofluoric acid is often used in this application since it leaves a hydrogen-terminated (hydrophobic) silicon surface [10]; HF is also known to leave an oxide-free InP surface [11]. Surface preparation may also be carried out in an environment with reduced oxygen partial pressure. In both wet and dry bonding, it is necessary to allow the chemicals adsorbed at the surface to escape before the bonding occurs. One way of achieving this is to etch "escape channels" into the substrate. This technique has been successfully used in a number of InP–GaAs fusion experiments [12], and in silicon direct bonding [13]. If the surface is not patterned, the trapped liquids and gases produce large scale bubbles (size $\sim$100 μm) [14], and a large density of microscopic voids or oxide islands (size $\sim$1 μm). After channel etching and cleaning, the surface preparation typically consists of sequential oxidation and oxide removal steps. The surface may be oxidized by oxygen plasma, UV-ozone oxidation [15], or wet chemical oxidation (hydrogen peroxide), while the oxide removal may be achieved using various acids and bases [16]–[18]. After the samples are placed into contact, they are subjected to an annealing step at an elevated temperature so that a crystalline junction is formed. The process of fusion bonding of GaAs and InP (or other Ga–In–As–P materials) is not fully understood, but is believed to rely on the proximity annealing [19] of InP with a GaAs cap. As phosphorus desorbs from the InP surface and fills the gaps in the fused junction, indium diffuses laterally and fills the voids, ultimately reacting with the phosphorus to form an InGaAsP alloy [20], [21]. Phosphorus and indium are the primary mobile species during fusion bonding of GaAs and InP [12]. The pressure maintained on the two wafers to be bonded helps to even out the surface nonuniformities.

The fusion anneal of GaAs–InP junctions is performed under pressure and elevated temperature in specially designed fixtures. The sample sizes used in experiments vary from less than 1 cm^2 to full 2$''$ wafers [22], [23]. The fusion pressure reported in the literature varies over a wide range, from relatively small pressures of 3 kPa [17], [18], 30 kPa [24], 100 kPa [25], to $\sim$3 MPa [12], [20], [22], [26]. The key factor in the effective application of the force on the samples is its uniformity. The fusion temperatures for GaAs–InP fusion range between 550 °C–650 °C, with peak temperatures usually held for less than 30 min. Higher pressures should result in the ability to carry out lower temperature fusing.

The most common substrate orientation used for fusion bonding is (001), but many other combinations have been explored [17]. In particular, the smooth surface morphology of epitaxially grown layers is critical for successful fusing. This
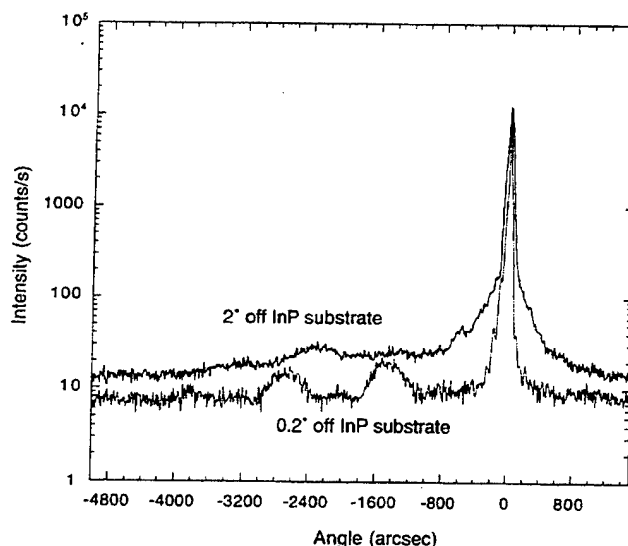

Fig. 2. X-ray diffraction spectra of two samples consisting of three compressively strained InGaAsP QW's with unstrained InGaAsP barriers. One sample is grown on a 2°-off (100) InP substrate whereas the other one is grown on a 0.2°-off substrate.

may in turn dictate growth on substrates slightly misoriented from (001). We have found this to be true in MOCVD growth of InP-based materials for fusing. The MOCVD growths employ trimethylindium (TMI), trimethylgallium (TMG), tertiarybutylarsine (TBA) and tertiarybutylphosphine (TBP), using growth temperatures ranging from 610 °C–650 °C, at either atmospheric pressure or 350 torr. More details about the growth conditions can be found in reference [19]. Teardrop-like hillock defects can result in the grown material, resulting from preferential nucleation on the screw dislocations emerging at the surface of the crystal. A misorientation of the crystal surface with respect to the exact (100) orientation creates monoatomic steps that are also preferential adsorption sites, making it possible for the growth to proceed without the formation of hillock defects. However, too high a misorientation can give rise to step bunching, also creating surface roughness. The optimum misorientation will produce smooth surface morphology; this depends on growth parameters that influence the diffusion length of the atomic species at the surface: temperature, growth rate and V–III ratio [27]. We chose a misorientation of 0.2°. Fig. 2 shows the X-ray diffraction spectra of two samples consisting of three compressively strained InGaAsP QW's with unstrained InGaAsP barriers. One sample is grown on a 2° off substrate whereas the other one is grown on a 0.2° off substrate. The comparison of the two spectra clearly show that the crystallographic quality of the 2°-off sample is not as good as that of the 0.2° sample. Moreover, the full-width at half-maximum (FWHM) of the photoluminescence (PL) peak of the 2°-off sample is larger (about double) than that of the 0.2° off sample. This results from the rougher surface of the former sample, with attendant thickness variations that increase the widths of the luminescence peaks.

The number of dangling bonds and quality of the fused interface directly influences the electrical characteristics [21]. In order to achieve a near-perfect crystal continuation, the

two substrates should be *enantiomorphic*.[1] Since zinc-blend crystals have S4 point-group symmetry, the two substrates (A and B) to be fused must be aligned in such a way that cleaved (011) planes of substrate A are perpendicular to cleaved (011) planes of substrate B. This substrate orientation is called "in-phase" bonding [18]. If the two (001) cleavage planes of the two substrates are kept parallel in the alignment, then we have "antiphase" bonding [18]. Recently, a form of a compliant substrate has been investigated using bonding of twisted thin GaAs epitaxial layers [17]. This compliant substrate promises to transcend the lattice matching requirement and enables growing epitaxial layers on top of nonlattice matched substrates.

III. DEVICE REALIZATIONS OF WAFER FUSION

A. Vertical-Cavity Lasers and Resonant Cavity Photodetectors

Wafer fusion has had an important impact in developing long wavelength surface normal devices, such as vertical-cavity lasers (VCL's) and resonant cavity photodetectors. VCL's are potentially important sources for fiber optic communications. They offer high modulation bandwidths at low-bias currents as well as ease in testing and packaging. Recent work in nonwafer-fused GaAs-based VCL's has shown record power conversion efficiency as well as record low-threshold currents (57% and 40 μA, respectively) [28], [29]. Lasers which emit at wavelengths between 850–980 nm do not match up well with the minima in dispersion and loss of standard optical fibers. To effectively use VCL's for fiber-optic communications, sources with wavelengths near 1.3 and 1.5 μm must be fabricated. This was initially found to be a difficult task since the lattice-matched InP–InGaAsP mirror materials had reflectivities and thermal conductivities too poor to achieve room temperature CW operation. Wafer fusion allows the integration of InP-based active regions with high reflectivity GaAs–AlAs based mirrors to achieve high performance operation.

Fig. 3 shows the theoretical reflectivity as a function of the number of mirror periods, for two types of epitaxial DBR mirrors available for long wavelength devices. The maximum reflectivity is limited by absorptive losses in the mirrors. The InP–InGaAsP-based mirrors, with lower differences in the indices of refraction, have a larger optical penetration depth and thus lower maximum reflectivity. High-performance operation of a VCL requires mirror reflectivities well above 99%. High-mirror reflectivities also reduce the necessary gain for lasing, which in turn permits higher temperature operation.

The first room temperature CW operation of any long-wavelength VCL over 980 nm, was demonstrated by Babic et al., using two wafer fused GaAs–Al(Ga)As mirrors along with an InP–InGaAsP 1.55 μm based active region [30]. The threshold and quantum efficiency of that laser was limited by optical scattering from the mesa sidewalls. A significant improvement in all characteristics can be achieved with the addition of an AlAs oxidation layer, which can be used to
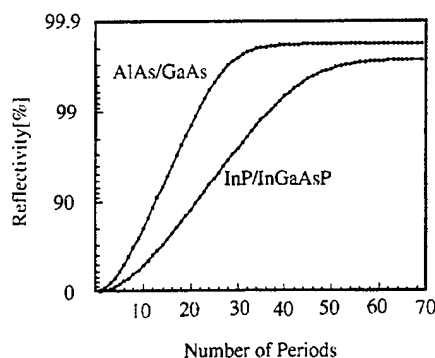

Fig. 3. Comparison of the reflectivity that can be achieved with different quarter-wave mirror stacks.
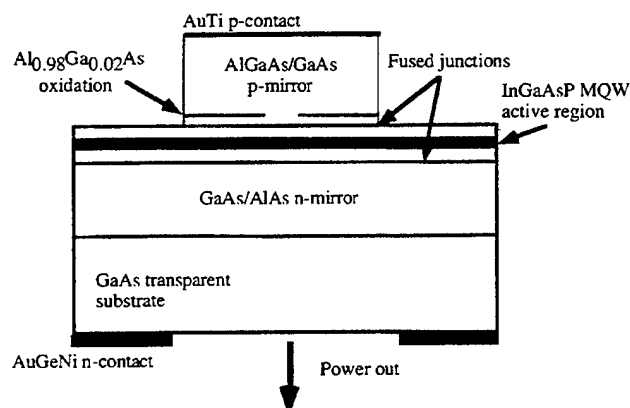

Fig. 4. Schematic structure of double-fused laterally oxidized 1.55-μm VCL operating to 64°C CW.

form a dielectric aperture to confine the current, and provide improved confinement of the optical mode, away from the rough-etched sidewalls of the VCL pillars [1]. This structure is shown in Fig. 4.

The addition of a dielectric aperture allowed CW operation up to 64 °C and pulsed operation up to 100 °C. Further device improvements should soon allow for CW operation up to the 85 °C necessary for commercial applications. These wafer-fused 1.55-μm VCL's have recently been used in transmission experiments, with data rates as high as 2.5 Gb/s over 200 km of optical fiber [31].

Any surface normal device that requires a high reflectivity DBR mirror along with an InP active region can take advantage of the wafer fusion of GaAs to InP. Resonant cavity photodetectors have a narrow absorption bandwidth which is determined by the finesse of the cavity in which the absorption layer is placed. High-reflectivity mirrors are needed to achieve a narrow absorption line. Such devices have been fabricated, yielding a record 94% quantum efficiency with a 14-nm absorption bandwidth [7].

B. Long-Wavelength, In-Plane Lasers

Wafer fusion has clearly been a critical factor in the realization of long-wavelength surface emitting lasers. The benefits of this process also extend to in-plane lasers operating at 1.55 μm. Long wavelength in-plane lasers behave quite differently from

---

[1] Enantiomorph: either of a pair of chemical compounds or crystal whose molecular structures have mirror image relationship to each other.
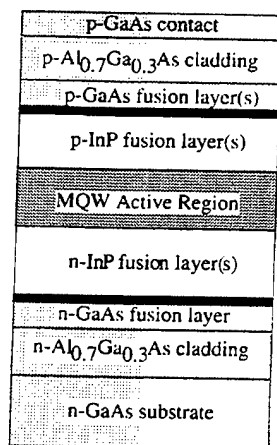
Fig. 5. Proposed structure for improved performance of 1.55-μm in-plane lasers.
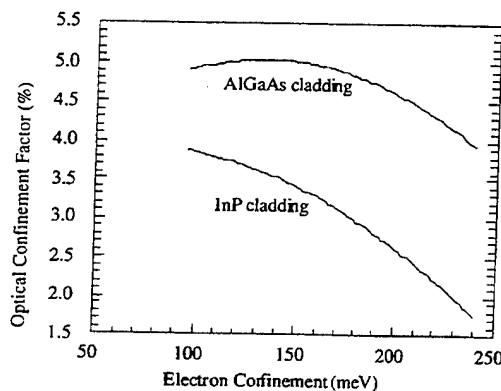

Fig. 6. Optical confinement comparison for a three quantum-well active region with InP and AlGaAs cladding layers.

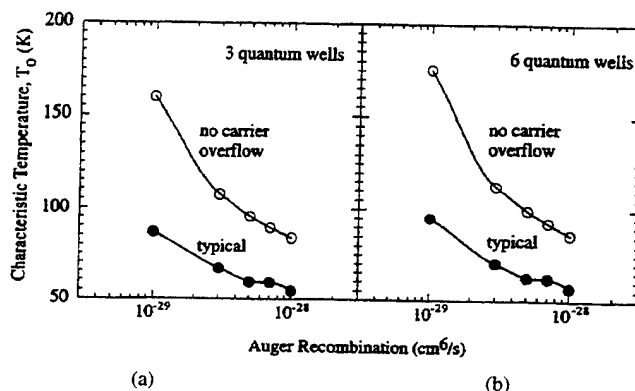Fig. 7. Comparison of T_0 when carrier overflow is present or eliminated by fusing for (a) three and (b) six quantum wells.

their 980-nm InGaAs–AlGaAs counterparts. The characteristic temperature, or T_o of 980-nm lasers is ≥ 200 K [32], [33] while the T_0 values for 1.55 μm lasers are in the range of 40–70 K [34], [35]. In addition, the 1.55-μm lasers cannot be modulated as quickly nor work at as high an operating temperature as the 980-nm lasers [32], [36]–[38]. In the last decade much effort has been expended to better understand this discrepancy. Historically, Auger nonradiative recombination has been designated as the principal cause of the poor temperature performance [39], but recent work highlights the role of poor electron confinement in the GaInAsP–InP material system [40]–[42]. We have carried out detailed theoretical modeling to analyze the relative magnitude of these effects. Our results suggest that, while Auger effects do indeed limit device performance, a two-fold increase in T_0 can be achieved through a reduction in the amount of carrier overflow [43]. This would also lead to an increase in the maximum operating temperature and mitigate the decrease in the slope efficiency of the laser.

Working with lattice-matched (to InP) 1.55-μm materials alone, the enhanced electron confinement can only be achieved with an ensuing severe reduction in the optical overlap of the lasing mode. Wafer fusion allows us to engineer increased electron confinement, without compromising optical confinement. We propose the improved in-plane laser structure shown in Fig. 5, where $Al_{0.7}Ga_{0.3}As$ forms the cladding layer, rather than the more conventional, lattice-matched InP or InAlAs material. With the lower index of refraction of the AlGaAs [44], the optical confinement of the laser can be kept high while the electron confinement is also increased. This is shown in Fig. 6 for a three quantum-well active region.

The theoretical improvement in high temperature performance is significant, as shown in Fig. 7. Here, we calculate the characteristic temperature as a function of the Auger coefficient. The elimination of carrier overflow by fusing to GaAlAs layers results in significantly higher T_0, even if the Auger coefficient is large. Performance comparable to GaAs may eventually be possible.

These wafer-fused in-plane lasers may be more sensitive to the fused interface than the wafer-fused VCL's discussed

earlier. In this case, the lasing mode will interact more heavily with the fused interface: contamination, doping spikes, dislocations, and other irregularities at this interface could provide additional scattering losses for the laser. The structure shown in Fig. 8 was used to assess the extent of those losses. The active region consists of four 55-Å GaInAsP quantum wells with a compressive strain of 0.7%. These quantum wells are separated by 10 nm barriers of lattice-matched GaInAsP with a bandgap of 1.25 μm; this composition of GaInAsP also serves as the waveguide material. The total waveguide thickness is 300 nm, with a 500-Å p-InP layer cap layer. This active region was grown by MOCVD under conditions similar to those discussed earlier. The cladding layer was grown by MBE and consisted of a 50 nm p-GaAs layer for fusion, a 1.5-μm $Al_{0.7}Ga_{0.3}As$ cladding layer, and a 1500 Å p+-GaAs contact layer. The fusion conditions were a pressure of approximately 2.5 MPa, a fusion temperature of 630 °C, and a fusion time of 30 min. For comparison purposes, a piece of the active region had 2 μm of p-InP regrown to make a laser structure with InP cladding. In addition, this structure was taken through the same temperature cycle as the fusion structure. These structures were processed into broad-area devices (50-μm stripes) using standard procedures.

Preliminary results for the structure indicate a higher threshold for the fused laser of approximately 1600 A/cm² while the reference structure is lower at 610 A/cm². In addition, the slope efficiency in the fusion case is smaller suggesting that high internal losses are the cause of the increase in threshold
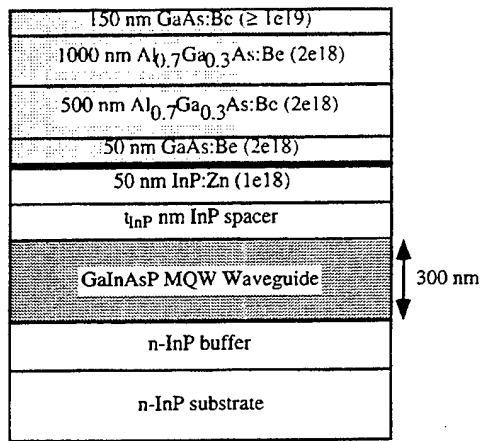
Fig. 8. Test structure for the effect of wafer fusion on 1.55-μm in-plane lasers.

Fig. 9. Structure of SHIP detector after fabrication. The InGaAs absorption layer is 0.7-μm thick and the Si multiplication layer is 0.6-μm thick.

current. For the reference case, the internal efficiency was 73% with internal losses of 20 cm^{-1}. Temperature dependent measurements were performed for both cases, resulting in $T_o = 59$ K for the reference structure, and $T_o = 29.1$ K for the fusion structure. From the reference structure's results, we believe that there are an additional 40 cm^{-1} of loss in the fusion structure which would be consistent with the lower T_o values. Work is currently underway to identify the cause of these additional losses. One encouraging result is that the quantum efficiency of the fused laser is constant at high temperatures, and does not show the high-temperature reduction common in InP lasers.

C. Avalanche Photodetectors

Wafer fusion has also had an impact in the field of avalanche photodetectors (APD's). APD's are designed to first convert absorbed light into an electrical signal, then amplify this signal through avalanche multiplication. To construct a fast, efficient APD one must choose materials with high optical absorption coefficients and high speed, low noise amplification characteristics. In the near infrared, important to optical communications, the obvious choice for an absorber is InGaAs. For avalanche multiplication, Si is the semiconductor of choice due to the large disparity in its electron and hole ionization coefficients, which leads to desired low-noise, high-speed amplification.

Efforts to integrate InGaAs with Si through epitaxial growth have resulted in hetero-interfaces with large numbers of threading dislocations due to the lattice mismatch between the semiconductors. These threading dislocations produce large dark currents in fabricated PIN photodetectors [45] and cause premature breakdown in these type of devices and prevent them from being biased to the voltages necessary for avalanche multiplication.

The silicon hetero-interface photodetector (SHIP) [46] has been created by wafer fusing a Si substrate to epitaxial InGaAs layers grown lattice matched to InP. The fusion is done in a H$_2$ atmosphere at a temperature of 650 °C, near the growth temperature of the InGaAs. SEM scans of the fused interface indicate that the lattice mismatch between the two materials
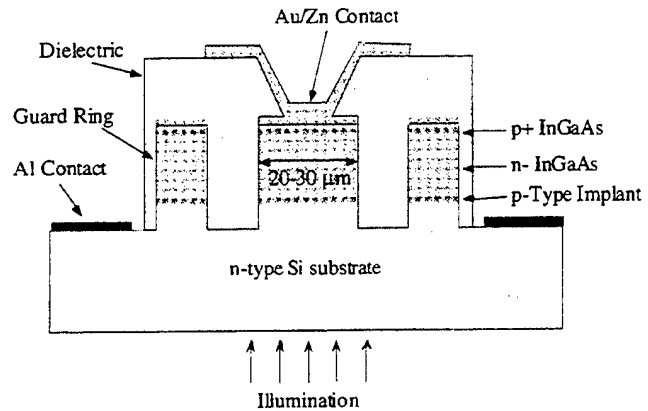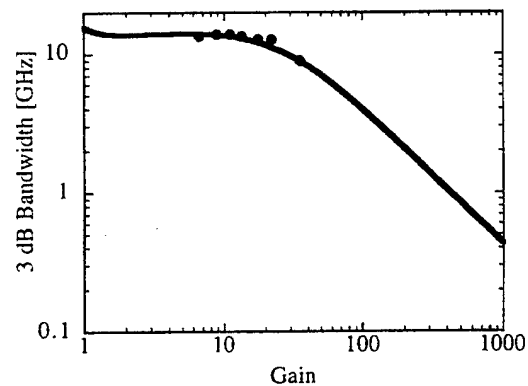

Fig. 10. Bandwidth versus gain for a SHIP detector modulated with a 1.3 μm laser. Points indicate experimental data, line represents theory.

is accommodated by edge dislocations that remain at the junction and do not propagate through either semiconductor. To determine the effects of this hetero-interface on optical loss and carrier transport, a careful study was done using a PIN structure with undoped Si and InGaAs fused together [47]. No loss in quantum efficiency was measured compared to InGaAs on InP PIN's of similar thicknesses. This indicates the InGaAs–Si fused interface causes no optical loss and does not act as a carrier transport barrier in the detectors.

SHIP APD's were designed with doping schemes similar to existing separate avalanche and multiplication region (SAM) APD's. The electric field was kept low in the absorbing InGaAs layer and high in the multiplication layer of the silicon. Photocurrent gains of over 100 have been measured for SHIP's with thick multiplication regions, and SHIP's with thinner regions have demonstrated the highest gain-bandwidth-product (315 GHz) for a near-infrared APD measured to date [8], more than double the achievable gain-bandwidth of InGaAs–InP APD's. Fig. 9 shows the structure of a SHIP APD and Fig. 10 shows its bandwidth as a function of photocurrent gain.

IV. THE WAFER FUSED INTERFACE

A. Introduction

The discussions of Section III have highlighted the power of the wafer fusion process in enabling device optimization

through integration of heterogeneous materials. Despite these successes in device fabrication, there remain improvements that can be made in the fused structures, and much is still not understood about the basic mechanism of fusing itself. More complete characterization will allow us to understand how electrically and optically transmissive we can make the fused interface, how wide a latitude in processing parameter space exists for reliable fusing, and what long term reliability issues exist for fused devices. In addition, we need to understand what limitations exist to fusing: can we integrate any sets of disparate materials? The sections below discuss some aspects of our initial characterization of the fusing process and the fused interface.

B. Electrical Characterization

The electrical characteristics of fused junctions have been made primarily through current versus voltage (I–V) measurements made across the fused junctions. Several parameters are known to influence the character of the junctions. The cleanliness of the surfaces before bonding, namely, trapping of contaminants at the junctions, will have an adverse effect on the conduction of carriers. In the absence of surface contamination, another parameter that can influence the electrical properties is the exact matching of the bonds at fused junctions. Since the main reason for GaAs–InP fusion bonding is to transcend the lattice matching requirement, exact bond-for-bond matching of [100] substrates is not possible to realize, but bonding off-axis cut substrates may help reduce the number of dangling bonds and dislocations.

The bonding of off-axis substrates has been investigated for GaInP on GaAs [48] and has revealed that small deviations from on-axis bonding result in dramatic increases in junction resistance. GaAs–InP bonding between different substrate orientations also results in reduced junction conductivity [27]. Since the surfaces of different III–V compound semiconductors have different oxidation properties and terminations, certain surface preparations and procedures may produce different results on different materials. A good example is that of [011] GaP–[001] InGaP in which there is a large difference in the V–J characteristics between in-phase and antiphase bonding [48] whereas for [001] GaAs on [001] InP, the difference is hardly noticeable [17].

The electrical characteristics of fused junctions critically depend on the presence of potential barriers arising from discontinuous energy-band lineups and interface charge. Theoretical considerations predict a staggered band lineup between strained GaAs–InP with the GaAs valence band several hundred millielectronvolts above that of InP [20]. However, no agreement between theoretical and experimental values of band offset has yet been reported. Potential barriers at fused junctions also originate from thin oxide layers or a high concentration of surface charge introduced by surface contamination before bonding. Oxygen has been found to be the major contaminant, in addition to high concentrations of carbon and hydrogen at the fused surface. The SIMS profile of a fused GaAs–InP epilayer shown in Fig. 11 does indeed reveal the presence of oxygen at the interface. This may
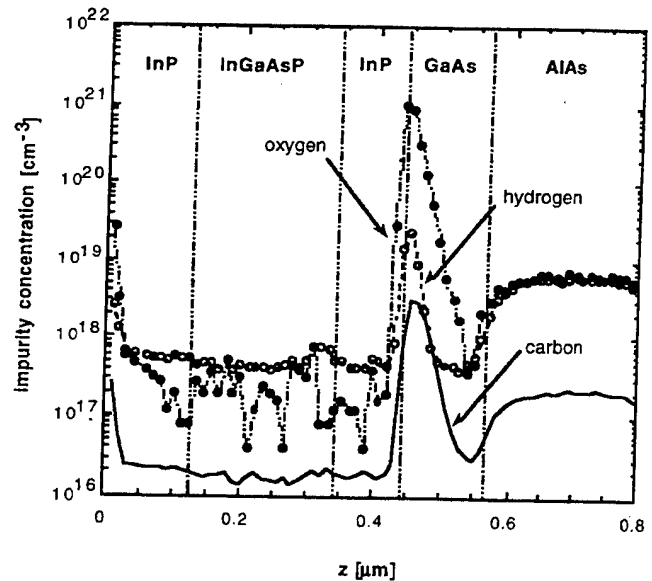

Fig. 11. SIMS profile of a fused GaAs–InP epilayer.

be a result of our sample preparation procedures, resulting in high O_2 incorporation at the surface. Although the oxide is nominally removed prior to sample transfer to the fusing fixture, a ~1-nm-thick native may nevertheless form before the onset of the fusing process itself. Surface oxide layers and charge affect both electron and hole flow, but because of the lower electron effective mass this has a greater impact on the holes. For this reason, n-n-junctions are expected to perform better than p-p-junctions. Furthermore, minority carrier recombination at the junction has not been investigated, to date. Most devices employ fused junctions in regions with only majority carrier flow. It is not yet clear to what extent the dopant species and its diffusion across the fused junction can improve the electrical characteristics.

C. Optical Characterization

In spite of evidence of organic contaminants, misfit dislocations, and higher than ideal voltage drops across the fused junctions, wafer fused technology has enabled the realization of high quality interfaces for optoelectronic design. In order to assess the extent over which the highly dislocated and contaminated interface impacts the optical quality of the surrounding material, multiple-quantum-well (MQW) photoluminescence (PL) studies were performed. The premise of such experiments is simple; the MQW structure acts as a depth resolved probe to compare the luminescence efficiency of the material in the interface region before and after fusion.

Lattice matched InGaAs and GaAs quantum wells of varying widths were therefore strategically grown on InP and GaAs substrates by MOCVD and MBE, respectively, to probe the optical quality of the epilayer region before and after wafer fusion; the structures are shown in Fig. 12. A reference quantum well was grown deep in each epilayer to facilitate accurate normalization, 4160 Å from the surface in the InP sample and 6200 Å from the surface in the GaAs sample. The location of these reference quantum wells should be far
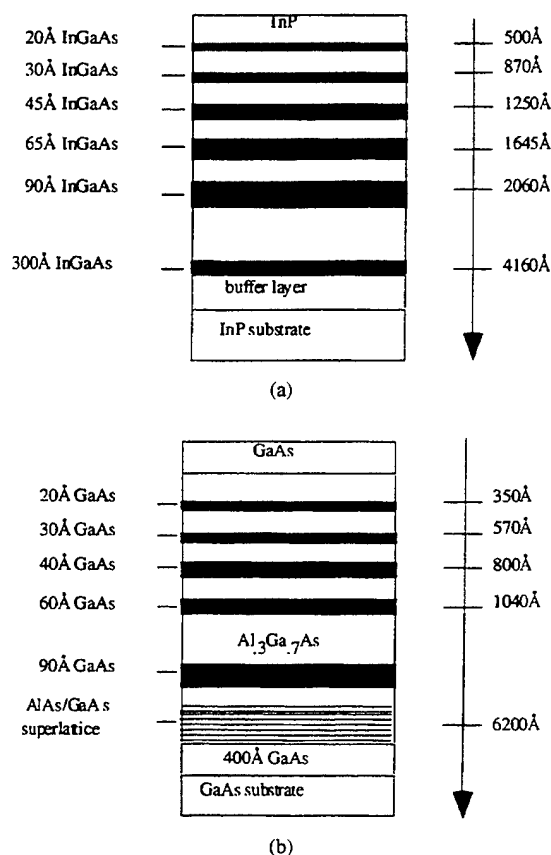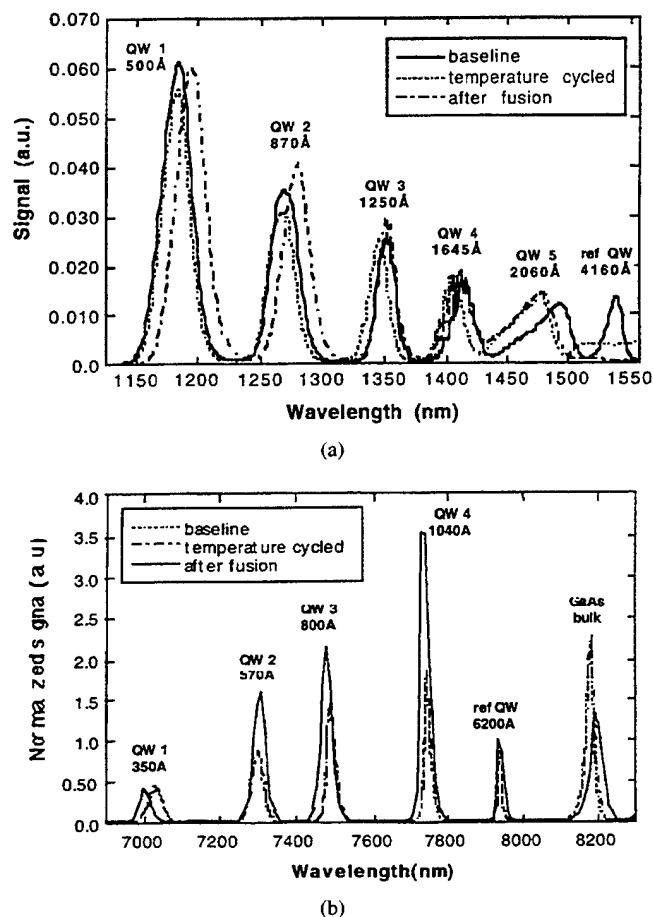
Fig. 12. MQW structures for PL studies.

Fig. 13. PL data, before and after fusing for (a) InGaAs MQW's and (b) GaAs MQW's.

Fig. 14. Wavelength shifts of InGaAs MQW's after fusing and after temperature cycling.

enough from the subsequently fused interface to ensure that their photoluminescence is not affected by the fusing process. The InP MQW sample was -fused to a 1000-Å-thick GaAs epilayer grown by MBE; the GaAs MQW sample was fused to a 3000-Å thick InP epilayer grown by MOCVD. PL data was taken at 10 K with a 514-nm Argon 5W laser at an optical power of 5 mW. Our current analysis employs three PL data sets: PL of the "as grown" material to provide a baseline, after fusion upon removal of the fused epilayer by wet etching, and finally after temperature cycling the MQW substrate under the fusing conditions as described in Section II to decouple the effects of the temperature cycling employed in the fusion process from the effects of fusion itself.

The resulting PL spectra are shown in Fig. 13. Fig. 13(a) shows the raw PL data taken on the InGaAs–InP MQW sample, including the baseline ("as grown"), the temperature cycled, and the fused spectra. The three spectra have not been normalized to a particular quantum well but are based on absolute measured luminescence based on the same laser power. We see no appreciable decrease in luminescence efficiency of the quantum wells as close as 500 Å from the fused interface. The same is true for the GaAs MQW structure as seen in Fig. 13(b). However, in this case, we have normalized to a reference peak at 7960 nm and demonstrated what appears to be an increase in the luminescence efficiency of all the quantum wells, venturing as close as 350 Å to the fused interface. We currently attribute this increase in luminescence intensity to the fused junction acting as a gettering source for

defects, a process much akin to the gettering of defects at any strained interface.

PL data on peak position, in addition to peak intensity, provides information on the subtle effects of strain and materials interaction. While there are no peak shifts, within measurement error, after the fusing or temperature-cycling process for the GaAs MQW samples, there are slight shifts in the InP-based samples. This is perhaps consistent with the presumed greater mobility of the In; while temperature cycling alone produces a blue shift in all quantum-well peaks, shown in Fig. 14,

the actual fusing process introduces a competing redshift increasing pronounced for those quantum wells closest to the fused interface. More work is required to fully decouple the effects of strain, strain relaxation, compositional intermixing, and defect passivation introduced through the fusing process. Nevertheless, these initial low temperature PL measurements provide an optimistic prognosis for the optical quality of the fused interface, and the material immediately adjacent to that interface.

V. CONCLUSION

Fusing frees the device designer from the constraints of lattice matched growth or critical thicknesses of strained layers. Although heteroepitaxy results in threading dislocations, fusing dissimilar lattice constant materials results in interfaces with edge dislocations instead of threading dislocations. The device results to date show dramatic improvements in telecommunication VCSEL's, in telecommunication APD's, and in visible LED's. Expansion of these techniques to II–VI and IV materials will be very interesting in the next few years. These techniques are ideal for optoelectronic integration and for new devices that have not yet been considered.

ACKNOWLEDGMENT

REFERENCES

[1] N. M. Margalit, D. I. Babic, K. Streubel, R. P. Mirin, R. L. Naone, J. E. Bowers, and E. L. Hu, "Submilliamp long-wavelength vertical cavity lasers," *Electron. Lett.*, vol. 32, no. 18, pp. 1675–1677, Aug. 29, 1996.

[2] R. K. Sink, S. Keller, B. P. Keller, D. I. Babic, A. L. Holmes, D. Kapolnek, S. P. DenBaars, J. E. Bowers, X. H. Wu, and J. S. Speck, "Cleaved facets in GaAn by wafer fusion of GaN to InP," *Appl. Phys. Lett.*, vol. 68, no. 15, pp. 2147–2149, Apr. 8, 1996.

[3] F. A. Kish, D. A. DeFevere, D. A. Vanderwater, G. R. Trott, R. J. Weiss, and J. S. Major, Jr., "High luminous flux semiconductor wafer-bonded AlGaInP/GaP large-area emitters," *Electron. Lett.*, vol. 30, no. 21, 1790–1972, 1994.

[4] S. J. B. Yoo, C. Caneau, R. Bhat, M. A. Koza, A. Rajhel, and N. Antoniades, "Wavelength conversion by difference frequency generation in AlGaAs waveguides with periodic domain inversion achieved by wafer bonding," *Appl. Phys. Lett.*, vol. 68, no. 19, pp. 2609–2611, 1996.

[5] H. Wada, T. Takamori, and T. Kamijoh, "Room-temperature photo-pumped operation of 1.58-μm vertical-cavity lasers fabricated on Si substrates using wafer bonding," *IEEE Photon. Technol. Lett.*, vol. 8, pp. 1426–1428, Nov. 1996.

[6] I.-H. Tan, E. L. Hu, and J. E. Bowers, "Modeling and performance of wafer-fused resonant-cavity enhanced photodetectors," *IEEE J. Quantum Electron.*, vol. 31, pp. 1863–1875, Oct. 1995.

[7] S. S. Murtaza, I.-H. Tan, R. V. Chelakara, M. R. Islam, A. Srinivasan, K. A. Anselm, J. E. Bowers, E. L. Hu, R. D. Dupuis, B. G. Streetman, and J. C. Campbell, "High-efficiency, dual-wavelength, wafer-fused resonant-cavity photodetector operating at long wavelengths," *IEEE Photon. Technol. Lett.*, vol. 7, pp. 679–681, June 1995.

[8] A. R. Hawkins, W. Wu, P. Abraham, K. Streubel, and J. E. Bowers, "High gain-bandwidth-product silicon heterointerface photodetector," *Appl. Phys. Lett.*, vol. 70, pp. 303–305, 1997.

[9] J. Haisma, G. A. C. M. Spierings, T. M. Micheielsen, and C. L. Adema, "Surface preparation and phenomenoligical aspects of direct bonding," *Philips J. Res.*, vol. 49, nos. 1/2, pp. 23–46, 1995.

[10] S. Bengtsson, "Semiconductor wafer bonding: A review of interfacial properties and applications," *J. Electron. Mater.*, vol. 21, no. 8, pp. 841–862, 1992.

[11] A. Knauer, D. Hirsch, R. Staske, and U. Zeimer, "Oxide-free etching of (100) InP surfaces," *Cryst. Res. Technol.*, vol. 24, no. 4, pp. 443–451, 1989.

[12] D. I. Babic, J. E. Bowers, E. L. Hu, L. Yang, and K. W. Carey, "Wafer fusion for surface-normal optoelectronic device applications," *Int. J. High Speed Circuits and Syst.*, to be published.

[13] H. Yamaguchi, S. Fujino, T. Hattori, and Y. Hamakawa, "Superjunction by wafer direct bonding," *Jpn. J. Appl. Phys.*, vol. 34, pt. 2, no. 2B, pp. L199–L202, 1995.

[14] S. J. Yun, K.-Y. Ahn, K.-S. Yi, and S.-W. Kang, "Studies on microvoids at the interface of direct bonded silicon wafers," *J. Electrochem. Soc.*, vol. 139, no. 8, pp. 2326–2330, 1992.

[15] Z. H. Lu, B. Bryskiewicz, J. McCaffrey, Z. Wasilewski, and M. J. Graham, "Ultraviolet-ozone oxidation of GaAs(100) and InP(100)," *J. Vac. Sci. Technol., B*, vol. 11, no. 6, pp. 2033–2037, 1993.

[16] Y.-H. Lo, R. Bhat, D. M. Hwang, M. A. Koza, and T. P. Lee, "Bonding by atomic rearrangement of InP/InGaAsP 1.5 μm wavelength lasers on GaAs substrates," *Appl. Phys. Lett.*, vol. 58, no. 18, pp. 1961–1963, 1991.

[17] F. E. Ejeckam, Y. H. Lo, S. Subramanian, H. Q. Hou, and B. E. Hammons, "Lattice engineering compliant substrate for defect-free heteroepitaxial growth," *Appl. Phys. Lett.*, vol. 70, pp. 1685–1687, 1997.

[18] H. Wada and T. Kamijoh, "Effects of heat treatment on bonding properties in InP-to-Si direct wafer bonding," *Jpn. J. Appl. Phys.*, vol. 33, pt. 1, no. 9A, pp. 4878–4879, 1994.

[19] R. E. Williams, *Gallium Arsenide Processing Techniques.* Dedham, MA: Artech House, 1984.

[20] R. J. Ram, J. J. Dudley, J. E. Bowers, L. Yang, K. Carey, S. J. Rosner, and K. Nauka, "GaAs to InP wafer fusion," *J. Appl. Phys.*, vol. 78, no. 6, pp. 4227–4237, 1995.

[21] Z.-L. Liau and D. E. Mull, "Wafer fusion: A novel technique for optoelectronic device fabrication and monolithic integration," *Appl. Phys. Lett.*, vol. 56, no. 8, pp. 737–739, 1990.

[22] J. J. Dudley, D. I. Babic, R. P. Mirin, L. Yang, B. I. Miller, R. J. Ram, T. E. Reynolds, E. L. Hu, and J. E. Bowers, "Low threshold, wafer fused long-wavelength vertical-cavity lasers," *Appl. Phys. Lett.*, vol. 64, no. 12, pp. 1463–1465, 1994.

[23] D. I. Babic, K. Streubel, R. P. Mirin, N. M. Margalit, J. E. Bowers, E. L. Hu, D. E. Mars, L. Yang, and K. Carey, "Room-temperature continuous-wave operation of 1.54 μm vertical-cavity lasers," *IEEE Photon. Technol. Lett.*, vol. 7, pp. 1225–1227, Nov. 1995.

[24] K. Mori, K. Tokutome, K. Nishi, and S. Sugou, "High-quality In-GaAs/InP multiquantum-well structures on Si fabricated by direct bonding," *Electron. Lett.*, vol. 30, no. 12, pp. 1008–1009, 1994.

[25] G. Patriarche, F. Jeannes, F. Glas, and J. L. Oudar, "TEM study of GaAs/InP heterostructures fabricated by wafer bonding," presented at the 9th Int. Conf. on Microscopy of Semiconducting Materials, Oxford, UK, 1995.

[26] H. Tanobe, F. Koyama, and K. Iga, "Etching and optical characteristics in GaAs/GaAlAs surface emitting laser fabrication using a novel spray etch," *Jpn. J. Appl. Phys.*, vol. 31, pp. 1597–1601, 1992.

[27] M. Nakamura, S. Katsura, N. Makino, E. Ikeda, K. Suga, and R. Hirano, "Effect of substrate misorientation on tear-drop-like hillocks defects densities in InP and GaInAsP grown by metalorganic chemical vapor deposition," *J. Cryst. Growth*, vol. 129, pp. 456–464, 1993.

[28] D. L. Huffaker, L. A. Graham, H. Deng, and D. G. Deppe, "Sub-40 μA continuous wave lasing in an oxidized vertical-cavity surface-emitting laser with dielectric mirrors," *IEEE Photon. Technol. Lett.*, vol. 8, pp. 974–976, 1996.

[29] B. Weigl, M. Grabherr, R. Jager, and K. J. Ebeling, "57% wallplug efficiency wide temperature range 840 nm wavelength oxide confined," in *Proc. 15th IEEE Int. Semiconduct. Laser Conf.*, vol. PDP2, 1996.

[30] D. I. Babic, K. Streubel, R. P. Mirin, N. M. Margalit, J. E. Bowers, E. L. Hu, D. E. Mars, L. Yang, and K. Carey, "Room-temperature continuous-wave operation of 1.54 μm vertical-cavity lasers," *IEEE Photon. Technol. Lett.*, vol. 7, pp. 1225–1227, 1995.

[31] S. Z. Zhang, N. M. Margalit, T. E. Reynolds, and J. E. Bowers, "1.54 μm vertical-cavity surface-emitting laser transmission at 2.5 Gb/s," *IEEE Photon. Technol. Lett.*, vol. 9, pp. 374–376, Mar. 1997.

[32] Y. K. Chen, M. C. Wu, W. S. Hobson, S. J. Pearton, A. M. Sergent, and M. A. Chin, "High-power 980-nm AlGaAs/InGaAs strained quantum-well laser grown by OMVPE," *IEEE Photon. Technol. Lett.*, vol. 3, pp. 406–408, 1991.

[33] P. L. Derry, H. E. Hager, K. C. Chiu, D. J. Booher, E. C. Miao, and C. S. Hong, "Low threshold current high-temperature operation of InGaAs/AlGaAs strained-quantum-well lasers," *IEEE Photon. Technol. Lett.*, vol. 4, pp. 1189–1191, 1992.

Fused vertical couplers

Bin Liu,[a)] Ali Shakouri, Patrick Abraham, Boo-Gyoun Kim, Andrew W. Jackson, and John E. Bowers

Department of Electrical and Computer Engineering, University of California, Santa Barbara, California 93106

A vertical directional coupler fabricated using wafer fusion is demonstrated with a very short coupling length of 62 μm. The optical propagation loss introduced by the fused layer is investigated. An excess loss of 1.1 dB/cm at 1.55 μm was measured for waveguides which incorporate a fused junction near the core region. Fused vertical couplers make it possible to realize three-dimensional waveguide structures and compact switching arrays and they solve some of the topology problems of large switch arrays. © *1998 American Institute of Physics.* [S0003-6951(98)02221-9]

Compact semiconductor optical waveguide switches are critical components in photonic integrated circuits for high-speed optical communication networks and optical information processing. A large-scale switching array requires low space consumption, so it is essential to minimize the length of each switch. Conventional directional couplers with laterally arranged waveguides[1] cannot achieve very short coupling lengths because of low modal overlap and because of technological limits to obtaining uniform and small gap layers. Vertical directional couplers, on the other hand, can offer a short coupling length which is even smaller than 100 μm.[2,3] The difficulty of separating the two vertical coupled waveguides into two distinct inputs and outputs limits the application of these couplers to large-scale switching arrays. In this letter, we demonstrate a fused vertical coupler (FVC) with a very short coupling length, which can solve this problem.

Wafer fusion is a powerful technique to fabricate structures that cannot be realized by conventional epitaxial growth and processing. In addition to the inherent advantage of combining material with different lattice constants,[4] wafer fusion can give an extra degree of freedom in the design and fabrication of three-dimensional (3D) photonic devices.[5] By displacing the input and output waveguides vertically in different planes, scaling of switch arrays to large sizes is easy to realize (Fig. 1). In order to switch a large number of input waveguides, it is essential to have compact, high extinction ratio fused vertical couplers. In the following, we will analyze theoretically and experimentally straight fused vertical couplers.

The structure of the FVC is shown in Fig. 2. The material was grown by metal–organic chemical-vapor deposition and consisted of a 0.5 μm InGaAsP ($\lambda = 1.3$ μm) guiding layer on an InP substrate, followed by a 0.1 μm InP cladding layer, a 20 nm InGaAsP ($\lambda = 1.15$ μm) etch-stop layer, and a 0.4 μm InP coupling layer. To fabricate the vertical coupler, two 8×10 mm^2 samples are cleaved from the grown wafer. In the first sample, the top 0.4 μm InP layer is removed. On the second sample, a ridge waveguide (WG) structure is fabricated using standard photolithography and selective wet

etching. The ridges have 3–6 μm width, 0.4 μm height, and they are separated by 125 μm. The two samples are then fused together at a temperature of 630 °C in a hydrogen atmosphere for 30 min. Figure 1 shows the stain etched scanning electron microscope (SEM) picture of a finished FVC. The fused interface is not visible, even after staining. This is an indication of the high quality of the fusion process. There is mass transport at the edge of the ridge. This is beneficial in obtaining a symmetric coupler and improves the sidewall flatness.

The near-field pattern at the output of the FVCs is recorded by an IR camera and is shown in Fig. 3. The light is the input from a 8 μm diam single-mode fiber. The total length of the FVC is 5.5 mm. It can be seen that by changing the input wavelength, the light is switched from the upper to the lower waveguide. Since the shapes of the two waveguide modes are very similar, one can obtain a high extinction ratio. Our measurement shows the extinction ratio is about 15 dB. This is particularly difficult to achieve in conventional high mesa vertical couplers.[2] BPM[6] simulations show that extinction ratios up to 20–35 dB are possible. Figure 4 shows the intensities of the upper and lower waveguides as a function of wavelength. From the oscillation period (about 11.5 nm), and considering material and waveguide disper-
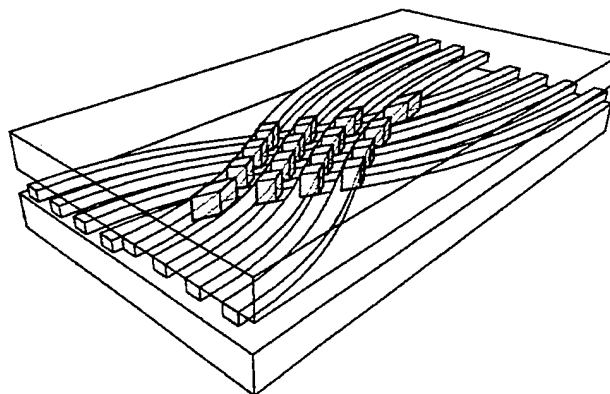

FIG. 1. 4×4 crossbar switch array based on vertical coupling between two substrates.

[a)]Electronic mail: liu@opto.ucsb.edu

[34] H. Temkin, D. Coblentz, R. A. Logan, J. P. van der Ziel, T. Tanbun-Ek, R. D. Yadvish, and A. M. Sergent, "High temperature characteristics of InGaAsP/InP laser structures," *Appl. Phys. Lett.*, vol. 62, pp. 2402–2404, 1993.

[35] P. J. A. Thijs, L. F. Tiemeijer, P. I. Kuindersma, J. J. M. Binsma, and T. Van Dongen, "High-performance 1.5 μm wavelength InGaAs-InGaAsP strained quantum well lasers and amplifiers," *IEEE J. Quantum Electron.*, vol. 27, p. 1426, 1991.

[36] H. Nobuhara, K. Tanaka, T. Yamamoto, T. Machida, T. Fujii, and K. Wakao, "High-temperature operation of InGaAs/InGaAsP compressive-strained QW lasers with low threshold currents," *IEEE Photon. Technol. Lett.*, vol. 5, pp. 961–963, 1993.

[37] P. A. Morton, T. Tanbun-Ek, R. A. Logan, N. Chand, K. W. Wecht, A. M. Sergent, and P. F. Sciortino, Jr., "Packaged 1.55 μm DFB laser with 25 GHz modulation bandwidth," *Electron. Lett.*, vol. 30, pp. 2044–2046, 1994.

[38] S. Weisser, E. C. Larkins, K. Czotscher, W. Benz, J. Daleiden, I. Esquivias, J. Fleissner, J. D. Ralston, B. Romero, R. E. Sah, A. Schonfelder, and J. Rosenzweig, "Damping-limited modulation bandwidths up to 40 GHz in undoped short-cavity In/sub 0.35/Ga/sub 0.65/As-GaAs multiple-quantum-well lasers," *IEEE Photon. Technol. Lett.*, vol. 8, pp. 608–610, 1996.

[39] N. K. Dutta, J. Lopata, D. L. Sivco, and A. Y. Cho, "Temperature dependence of threshold of strained quantum well lasers," *Appl. Phys. Lett.*, vol. 58, pp. 1125–1127, 1991.

[40] A. A. Bernussia, H. Temkin, D. L. Coblentz, and R. A. Logan, "Effect of barrier recombination on the high temperature performance of quaternary multiquantum well lasers," *Appl. Phys. Lett.*, vol. 66, no. 1, pp. 67–69, 1995.

[41] N. Tessler, V. Mikhaelashvili, R. Nagar, G. Eisenstein, A. G. Dentai, C. H. Joyner, and S. Chandrasekhar, "Temperature and output power dependence of carrier overflow and internal loss in InGaAs/InGaAsP multiple quantum well lasers," in *Pro. IEEE 14th Int. Semiconductor Laser Conf.*, Maui, HI, 1994, p. 67.

[42] V. Mikhaelashvili, N. Tessler, R. Nagar, G. Eisenstein, A. G. Dentai, S. Chandrasakhar, and C. H. Joyner, "Temperature dependent loss and overflow effects in quantum well lasers," *IEEE Photon. Technol. Lett.*, vol. 6, pp. 1293–1295, 1994.

[43] A. L. Holmes, "1.55 μ in-plane lasers using wafer fused cladding layers," ECE Tech. Rep. no. 9712, Univ. of California, Santa Barbara, 1997.

[44] M. A. Afromowitz, "Refractive index of Ga$_{1-x}$Al$_x$As," *Solid State Commun.*, vol. 15, p. 59, 1974.

[45] A. M. Joshi and R. Brown, "Monolithic InGaAs-on-silicon short wave infrared detector arrays," in *SPIE Photonics West '97, Conf. 2999*, San Jose, CA.

[46] A. R. Hawkins, T. E. Reynolds, D. R. England, D. I. Babic, M. J. Mondry, K. Streubel, and J. E. Bowers, "Silicon hetero-interface photodetector," *Appl. Phys. Lett.*, vol. 68, pp. 3692–3694, 1996.

[47] B. F. Levine, A. R. Hawkins, S. Hiu, B. J. Tseng, C. A. King, L. A. Gruezke, R. W. Johnson, D. R. Zoinowski, and J. E. Bowers, "20 Ghz high performance Si/InGaAs PIN photodetctor," *Appl. Phys. Lett.*, vol. 70, no. 18, pp. 2449–2451.

[48] F. A. Kish, D. A. Vanderwater, M. J. Peanasky, M. J. Ludowise, S. G. Hummel, and S. J. Rosner, "Low-resistance ohmic conduction across compound semiconductor wafer-bonded interfaces," *Appl. Phys. Lett.*, vol. 67, no. 14, pp. 2060–2062, 1995.

A. Black, photograph and biography not available at the time of publication.

A. R. Hawkins, photograph and biography not available at the time of publication.

N. M. Margalit, photograph and biography not available at the time of publication.

D. I. Babić, photograph and biography not available at the time of publication.

A. L. Holmes, Jr., photograph and biography not available at the time of publication.

Y.-L. Chang, photograph and biography not available at the time of publication.

P. Abraham, photograph and biography not available at the time of publication.

J. E. Bowers, for photograph and biography, see this issue, p. 738.

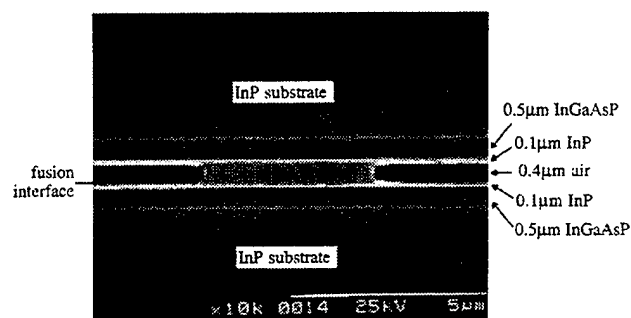**E. L. Hu**, photograph and biography not available at the time of publication.

FIG. 2. The stain etched SEM picture of a fused vertical coupler.

sions, the index difference between the even and odd modes can be calculated, which is 0.0124. The corresponding coupling length is 62 μm at 1.55 μm, which agrees well with the theoretical value of 58 μm, derived from 3D BPM calculations. One important advantage of this strong vertical coupling is the capability of attaining highly selective WDM add/drop multiplexers by making longer couplers with significant overcoupling. Figure 4 illustrates the possibility of a lossless combination or splitting of two signals separated by just 6 nm. The wavelength selectivity of a FVC can be enhanced by using strong asymmetry in the waveguide structure.

To investigate the optical propagation loss at 1.55 μm due to the fused interface, two single-mode ridge waveguides are fabricated. The first one has a 0.5 μm InGaAsP (1.3 μm quartenary) core region, a 0.2 μm InP slab layer, and a 0.6 μm InP ridge height. The second sample is identical to the first except for a fused interface in the middle of the InP slab
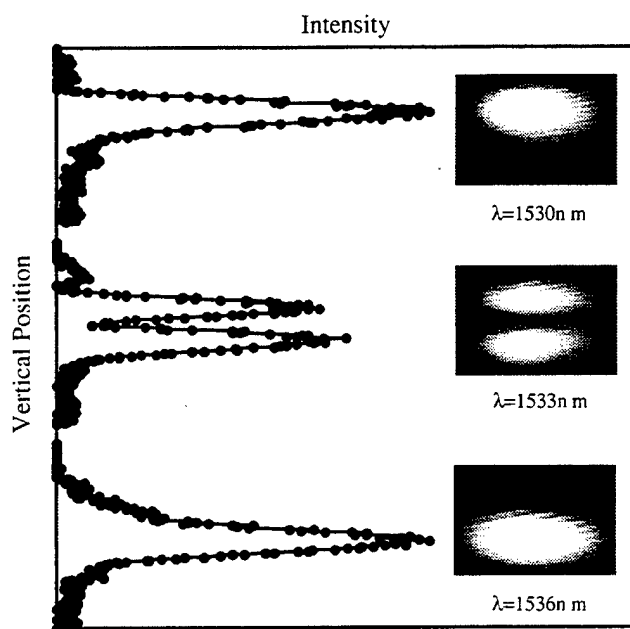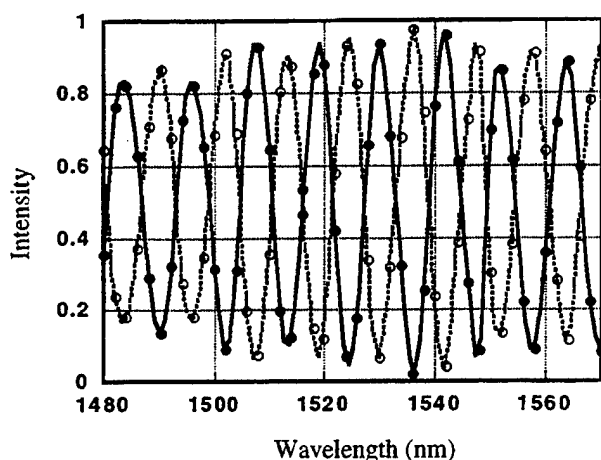

FIG. 3. Photograph of the near-field pattern at 1530, 1533, and 1536 nm. The width of the ridge is 3 μm, and the distance between the upper and the lower WGs is 1.1 μm. The left curve is the profile of the near field.

FIG. 4. Measured intensity of the upper (closed circle) and lower (open circle) waveguides as a function of wavelength.

layer, where the mode field is as high as 50% of the maximum. A Fabry–Perot resonance technique is used to measure the optical loss.[7] The second sample shows only 1.1 dB/cm excess loss due to the presence of the fused interface compared with the unfused single-mode waveguides. We believe it can be reduced further with the improvement of the fusion process.

The issue of uniformity for fused waveguides is very important for large-scale monolithic integration. For the present size of our fused wafer (8×10 mm^2), we found very good uniformity in terms of excess loss or coupling length. More than 90% of the waveguides can work well, even for the ones near the edge of the fused wafers. We have also checked the multimode behavior of the 150 μm width slab fused waveguides. They do not show any dark spots or dead regions.

In conclusion, a fused vertical coupler was demonstrated with a 62 μm coupling length. It is shown that 1.1 dB/cm excess optical loss is introduced due to the fusion process, which is even lower than the loss caused by doping. The fused vertical couplers and waveguides give us an added advantage of vertical dimension by separating the input and output waveguides to realize compact and scalable 3D directional coupler structures.

[1] J. E. Zucker, K. L. Jones, M. G. Young, B. I. Miller, and U. Koren, Appl. Phys. Lett. **55**, 2282 (1989).
[2] M. Kohtoku, S. Baba, S. Arai, and Y. Suematsu, IEEE Photonics Technol. Lett. **3**, 225 (1991).
[3] F. Dollinger, M. Borcke, G. Bohm, G. Trankle, and G. Weimann, Electron. Lett. **32**, 1509 (1996).
[4] A. Black, A. Hawkins, N. Margalit, D. Babic, A. Holmes, Jr., Y. L. Chang, P. Abraham, John E. Bowers, and E. L. Hu, IEEE J. Sel. Top. Quantum Electron. **3**, 943 (1997).
[5] S. Noda, N. Yamamoto, and A. Sasaki, Jpn. J. Appl. Phys., Part 2 **35**, L909 (1996).
[6] BeamProp, Version 2.0, Rsoft Inc., 1996.
[7] K. H. Park, M. W. Kim, Y. T. Byun, D. Woo, S. H. Kim, and S. S. Choi, J. Appl. Phys. **78**, 6318 (1995).

Improved Extinction Ratio in Ultra Short Directional Couplers Using Asymmetric Structures

Boo-Gyoun KIM[*], Ali SHAKOURI, Bin LIU and John E. BOWERS

Department of Electrical and Computer Engineering, University of California, Santa Barbara, CA 93106, U.S.A.

Various means of increasing the extinction ratio in ultra short directional couplers using slight asymmetry in the coupled waveguide structure are investigated. It is shown that couplers with 10–200 μm coupling length and with high extinction ratios larger than 30 dB can be achieved. Shorter asymmetric couplers have an extinction ratio that is more fabrication tolerant.

KEYWORDS: directional coupler, coupled mode theory, extinction ratio, asymmetric couplers, vertical couplers

1. Introduction

Directional couplers are critical components in photonic integrated circuits used in optical communication systems. The conventional directional couplers with laterally arranged waveguides can not achieve very short coupling lengths due to extreme sensitivity to fabrication variations and limitations to produce uniformly very narrow gap layers.[1] Vertical directional couplers, however, can obtain a short coupling length that is smaller than 100 μm.[2] The difficulty of separating the two vertically coupled waveguides into two distinct inputs and outputs limits the application of these devices.[3] Recently, a novel fused vertical coupler (FVC) with a very short coupling length of 62 μm was demonstrated, that can solve this problem.[4] To use FVC in large switching fabrics, it should have a low crosstalk. Ultra short directional couplers have an inherent limitation in their extinction ratio due to non-orthogonality of individual waveguide modes.[5] In this paper, we analyze various means to improve the extinction ratio using slight asymmetry in the structure. We also study the fabrication tolerance needed to maintain these improved characteristics. Since vertical coupling through the ridge structure defined by etch-stopping techniques is much less sensitive to the ridge waveguide width and sidewall smoothness than the planar waveguide couplers,[6] it is expected that these slight asymmetric structures can be better realized in fused vertical coupler configuration.

2. Model Used in the Analysis

Figure 1(a) shows the FVC with separated input and output waveguides. Since the two waveguides are brought together with an air gap except the interaction region, we could minimize unwanted couplings for the separation of the output of the FVC. The two-dimensional index profile of the FVC is reduced to one dimension using effective index method. The schematic diagram of one dimension index profile in the straight coupling region is shown in Fig. 1(b). The structure is composed of two waveguides A and B with effective indices n_a and n_b, and thicknesses d_a and d_b, separated by an inner cladding region, index n_{ci} and thickness t. The outer cladding regions have indices n_{ca} and n_{cb}. Since the two waveguides are strongly coupled ($t = 0.2-1$ μm separation), an improved coupled mode theory (ICMT) is used to model accurately the crosstalk. This theory takes into account explicitly the finite
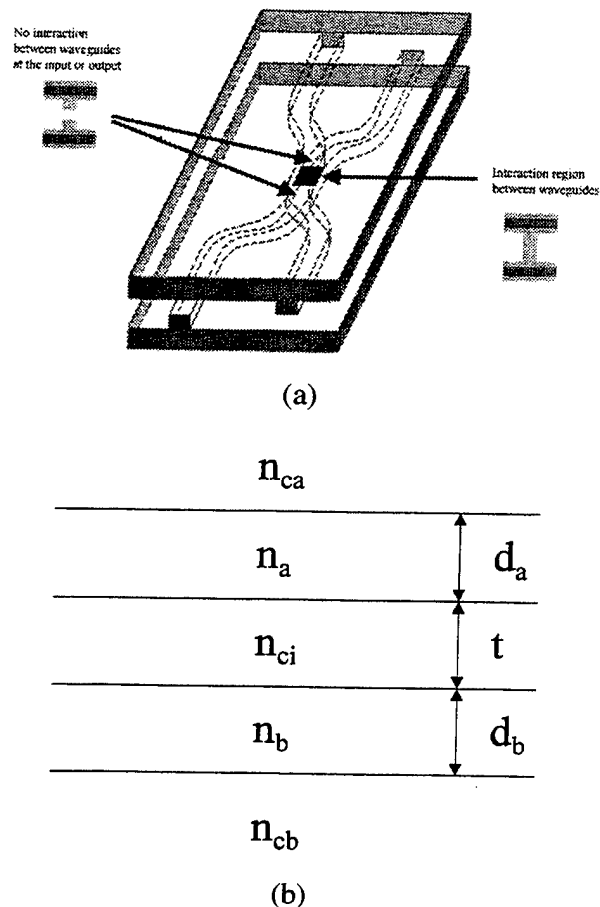

(a)

(b)

Fig. 1. (a) Fused vertical coupler with separated input and output waveguides. (b) Schematic diagram of one dimension index profile in the straight interaction region.

overlap integral between modes of individual waveguides.[7-9] Assuming that the power is incident into the waveguide A, without the loss of generality, the extinction ratio after a distance equal to the coupling length is defined as p_b/p_a where p_a and p_b are the guided mode powers in waveguides A and B respectively. The wavelength used in the calculation is 1.55 μm.

3. Results

Figures 2 and 3 show the extinction ratio and coupling length of TE and TM modes as a function of the refractive index of waveguide A using ICMT and also 2D finite difference beam propagation method (BPM). The parameter values used in the calculation are $n_b = 3.37$, $n_{ca} = n_{cb} = n_{ci} = 3.17$, $d_a = d_b = 0.5$ μm, and $t = 0.6$ μm. We can see that the data

*Present address: School of Electronic Engineering, Soongsil University, Seoul 156-743, Korea. E-mail address: bgkim@sunbee.soongsil.ac.kr
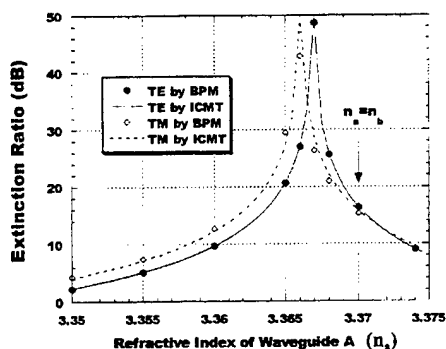
Fig. 2.   Extinction ratio for TE and TM modes as a function of the index of waveguide A calculated using ICMT and BPM.
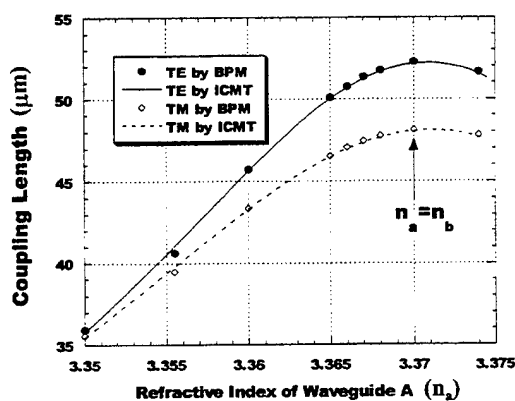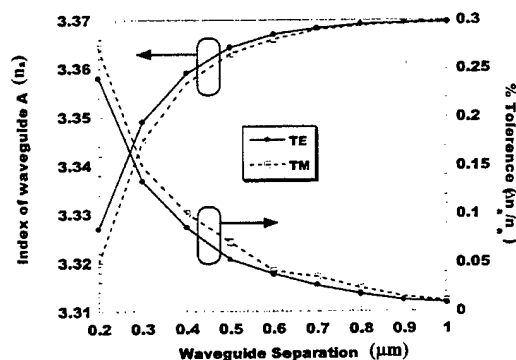

Fig. 4.   Index of waveguide A for maximum extinction ratio and tolerance to achieve larger than 30 dB extinction ratio as a function of waveguide separation.

Fig. 3.   Coupling length for TE and TM modes as a function of the index of waveguide A calculated using ICMT and BPM.
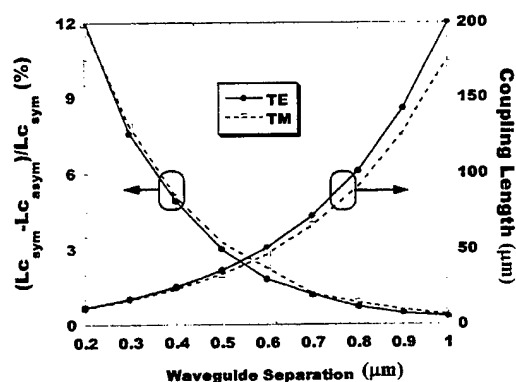

Fig. 5.   Coupling length of the asymmetric coupler for the different values of n_a corresponding to Fig. 4 and its percent difference with respect to the symmetric case as a function of waveguide separation.

calculated by ICMT agrees very well to that by BPM. The extinction ratio larger than 50 dB for TE (TM) mode occurs at $n_a = 3.367$ ($n_a = 3.366$) and the coupling length in this case is 51 μm (47 μm). The extinction ratio and the coupling length in the symmetric case for TE (TM) mode are 16.4 dB (15.7 dB) and 52 μm (48 μm) respectively. We can see that the extinction ratio is increased considerably at the expense of having less than 100% power tranfer to the waveguide B by slight detuning of the two waveguide eigenmodes as Chuang showed in ref. 10. The coupling length is not significantly affected by making the waveguides asymmetric.

Figure 4 shows the optimum asymmetry in the index of waveguide A (n_a) for TE and TM modes as a function of waveguide separation with the parameters used in Figs. 2 and 3. It also displays the percent tolerance ($\Delta n_a / n_a$) to obtain an extinction ratio larger than 30 dB. One can see that the optimum value of n_a for TE mode is larger than that of TM mode, while the percent tolerance of TM mode is larger than that of TE mode. When the waveguides are separated by 0.6 μm, the asymmetry defined by $n_b - n_a$ required to achieve the highest extinction ratio for TE (TM) mode is 0.003 (0.004). Having index of waveguide A within ± 0.019 % (± 0.021 %) of the optimum value for TE (TM) mode, one can achieve the extinction ratio larger than 30 dB. As the separation between the two waveguides decreases, more asymmetry is needed

but the tolerance to obtain an extinction ratio larger than 30 dB increases to 0.24 % (0.27%). This means that the peak in extinction ratio in Fig. 2 becomes broader as the coupling length decreases. This facilitates the fabrication of passive ultra short asymmetric couplers or setting the voltage or current in active components.

Figure 5 shows the coupling length of the optimum asymmetric coupler for the different values of n_a corresponding to Fig. 4 and its percent difference with respect to the the symmetric case as a function of waveguide separation. The coupling length decreases and the percent difference increases as the separation decreases. One can see that, as expected, the coupling length of TM mode is shorter than that of TE mode. By making the waveguides very close to each other (< 0.4 μm) one can achieve ultra short coupling lengths less than 30 μm and at the same time maintain the extinction ratio larger than 30 dB.

In the case of symmetric couplers, even though the coupling lengths are comparable to those of asymmetric ones (see Fig. 5), the extinction ratios are severely deteriorated to less than 15 dB when the separation between the two waveguides is less than 0.55 μm (see Fig. 6).

To confirm that the effect of the asymmetry on the extinction ratio comes from the slight difference in the shapes of the two waveguide eigenmodes, the extinction ratio and coupling length of TE and TM modes as a function of the width
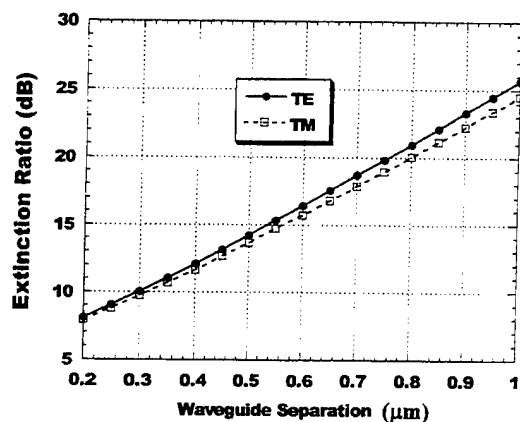
Fig. 6.   Extinction ratio for TE and TM modes for the symmetric coupler as a function of waveguide separation.
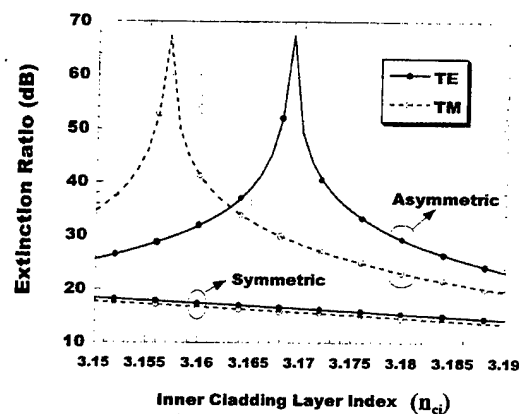

Fig. 7.   Extinction ratio for TE and TM modes for the asymmetric and symmetric structures as a function of refractive index of inner cladding layer.

of waveguide A rather than its refractive index are calculated with the parameter values $n_a = n_b = 3.37, n_{ca} = n_{cb} = n_{ci} = 3.17$, $d_b = 0.5$ μm, and $t = 0.6\,\mu$m. An extinction ratio larger than 42 dB for TE (TM) mode occurs at $d_a = 0.486\,\mu$m (0.484 μm) while the extinction ratio in the symmetric case was around 16 dB. The effect of inner cladding layer on the characteristics of the coupler is also studied. Figure 7 shows the extinction ratio of TE and TM modes as a function of the refractive index of inner cladding layer for the symmetric and asymmetric structures. The parameter values used in the calculation are $n_b = 3.37, n_{ca} = n_{cb} = 3.17, d_a = d_b = 0.5\ \mu$m, $t = 0.6\ \mu$m, $n_a = 3.367$ for the asymmetric structure and $n_a = 3.37$ for the symmetric one. The extinction ratio for the symmetric structure does not change much as a function of the refractive index of the inner cladding layer. It increases slightly as the inner cladding layer index decreases due to smaller overlap integral between two individual waveguide modes. For the asymmetric structure, the extinction ratio changes considerably (> 40dB) as a function of the inner cladding layer index. The highest extinction ratio occurs at $n_{ci} = 3.169$ for TE mode and at $n_{ci} = 3.157$ for TM mode. A slight asymmetry can equalize the overlap integral of one of the waveguide modes with the symmetric and antisymmetric supermodes of the coupler and thus increase the extinction ratio.[5]

4.   Conclusions

We have shown that one can achieve ultra short vertical directional couplers (coupling length 10–200 μm) while main-

taining a high extinction ratio larger than 30 dB with slight asymmetry in the coupled waveguide structure. Shorter asymmetric couplers have an extinction ratio that is more fabrication tolerant. Also, we confirmed that the high extinction ratio of asymmetric stuctures comes from the slight difference in the shapes of the two waveguide eigenmodes by changing the refractive index of inner cladding layer and the width of one of the waveguides.

Acknowledgment

1) J. E. Zucker, K. L. Jones, M. G. Young, B. I. Miller and U. Koren: Appl. Phys. Lett. 55 (1989) 2280.
2) F. Dollinger, M. Borcke, G. Bohm, G. Trankle and G. Weimann: Electron. Lett. 32 (1996) 1509.
3) S. Baba, K. Shimomura and S. Arai: IEEE Photon. Technol. Lett. 4 (1992) 486.
4) B. Liu, A. Shakouri, P. Abraham, B.-G. Kim, A. W. Jackson and J. E. Bowers: Appl. Phys. Lett. 72 (1998) 2637.
5) K.-L. Chen and S. Wang: Appl. Phys. Lett. 44 (1984) 166.
6) A.Shakouri, B. Liu, , B.-G. Kim, P. Abraham, A. Jackson, A. Gossard and J. E. Bowers: submitted to J. Lightwave Technol.
7) A. Hardy and W. Streifer: J. Lightwave Technol. 3 (1985) 1135.
8) S.-L. Chuang: J. Lightwave Technol. 5 (1987) 5.
9) H. A. Haus, W.P. Huang, S.Kawakami and N. A. Whitaker: J. Lightwave Technol. 5 (1987) 16.
10) S.-L. Chuang: IEEE J. Quantum Electron. 23 (1987) 499.

Experimental results and discussion: The wavelength-tunable device consists of two iron-based programmable magnets, 5.6cm long and 0.26cm in diameter, and a 3.8cm long fibre Bragg grating. We chose a magnetic material with a low coercivity (H_c) value of 85 for ease of programmability with low fields. The magnets and grating were packaged inside a stainless steel tube and inserted inside a solenoid. The solenoid is ~10cm long with 5000 turns and produces a field of ~100Oe with a current of ~140mA.
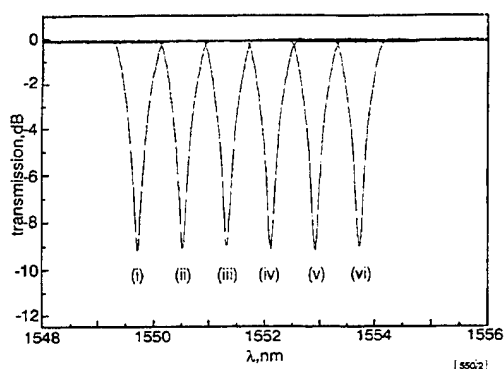
Fig. 2 *Superimposed transmission spectra showing various wavelength shifts*

(i) 0nm
(ii) 0.8nm
(iii) 1.6nm
(iv) 2.4nm
(v) 3.2nm
(vi) 4.0nm
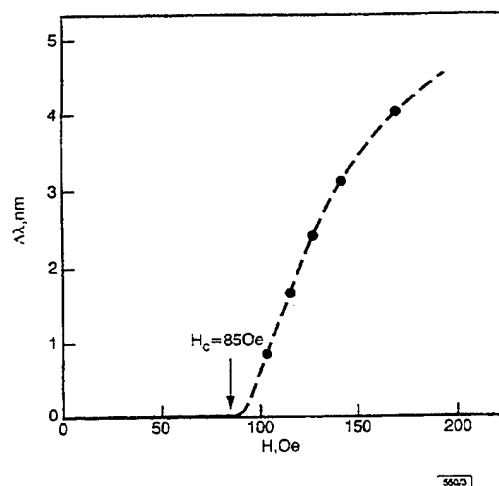
Fig. 3 *Wavelength shift against applied field*

When the magnitude of the pulse current in the solenoid is altered, the magnetisations in the two magnets change, thus affecting the magnetic force and hence, the latched fibre grating wavelength. Fig. 2 shows actual data of the programmably altered and latched wavelength shifts induced. The transmission spectrum of a Bragg grating with initial wavelength at 1549.7nm, on activation of the device with applied magnetic fields of 105, 118, 127, 138, and 168Oe. is reproducibly shifted by 0.8, 1.6, 2.4, 3.2 and 4.0nm, respectively. These wavelength shifts approximately correspond to a one-, two-, three-, four- and five-channel shift, respectively, in a 100GHz channel spacing DWDM communications system. The extent of wavelength shift changes with the magnetic field strength (Fig. 3), although nonlinearly, reflecting the magnetisation loop shape. The wavelength shift occurs relatively quickly, in the time frame of the order of milliseconds.

To demonstrate the capability of our technique, we built a similar device with increased magnet dimensions and magnetic field intensity for maximum wavelength tunability. Fig. 4 shows an example of a broad-range wavelength shift induced in a fibre Bragg grating. The wavelength shift in this case was ~15.7nm

(from 1560.7 to 1576.4nm) with a pulsed field of 230Oe. This shift would correspond to about a 39-channel shift in a 50GHz DWDM system.
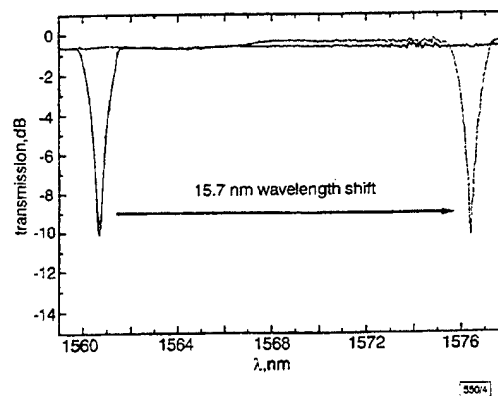
Fig. 4 *Transmission spectrum of fibre Bragg grating showing large shift of 15.7nm*

Conclusion: Broad-range strain-tuning of fibre Bragg gratings using latchable magnetic force has been demonstrated. The attractive magnetic force between the poles of two programmable and latchable magnets controllably shifts the wavelength of a Bragg grating by more than 15nm. The key advantages of this technique are that the strain tuning is latchable, a high magnitude of wavelength shift is possible, and the tuning speed is high. These novel tunable fibre gratings can find use in a variety of optical networking applications such as programmable add/drop multiplexing in DWDM communication systems.

S. Jin, R.P. Espindola, H. Mavoori, T.A. Strasser and J.J. DeMarco (*Bell Laboratories, Lucent Technologies, 700 Mountain Avenue, Murray Hill, N 07974, USA*)

References

1 QUETEL, L., RIVOALLAN, L., DELEVAQUE, E., POIGNANT, H., MONERIE, M., and GEORGES, T.: 'Programmable fiber grating based wavelength demultiplexer'. 1996 Optical Fiber Commun. Conf., Tech. Dig. Series. San Jose, CA. 1996. Vol. 2, Paper WF6, pp. 120-121

2 KIM, S.Y., LEE, S.B., KWON, S.W., CHOI, S.S., and JEONG, J.: 'Channel-switching active add/drop multiplexer with tunable gratings', *Electron. Lett.*, 1998, **34**, pp. 104-105

3 CRUZ, J.L., DIEZ, A., ANDRES, M.V., SEGURA, A., ORTEGA, B., and DONG, L.: 'Fibre Bragg gratings tuned and chirped using magnetic fields', *Electron. Lett.*, 1997, **33**, pp. 235-236

4 KRAUSS, J.D.: 'Electromagnetics' (McGraw-Hill, New York, 1984), 3rd edn., Chap. 6

Fused vertical coupler switches

B. Liu, A. Shakier, P. Abraham and J.E. Bowers

Electrical switching of fused vertical couplers (FVCs) is demonstrated. For a 3.5mm long coupler, complete switching is observed at 3V reverse bias. This low voltage is attributed to excess current induced internal heating and the thermo-optic effect. By changing the electrode design and reducing the excess current, a 6.9mm long FVC with 12V switching voltage is demonstrated.

Vertical directional couplers [1 – 4] are attractive candidates for realising photonic switches and narrowband filters because of their very short coupling length and the feasibility of integration with other optoelectronic devices. However in conventional vertical couplers, the two input or output waveguides are so close together that direct coupling of individual waveguides with fibres is very difficult. This has limited the practical applications of vertical couplers in fibre optic systems. We recently proposed a novel fused vertical coupler [5] based on a wafer fusion technique. By displacing the input and output waveguides vertically in different planes, separation of two strongly coupled waveguides and a scalable switch array can be easily realised. A passive fused vertical coupler (FVC) with a very short coupling length of 62µm has been demonstrated. In this Letter, we report the electrical performance of a *pin* straight fused vertical coupler.
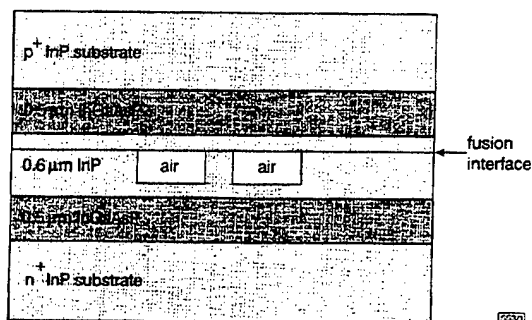

Fig. 1 *Schematic drawing of fused vertical coupler*

Ridge waveguide in centre is 'protected' during fusion process by large slab regions on the two sides

The schematic structure of the FVC is shown in Fig. 1. Two wafers are grown using MOCVD. One was on an *n*⁻ InP substrate and the other on a *p*⁺ substrate. These samples had a 0.5µm InGaAsP (λ_x = 1.3µm) guiding layer, followed by a 0.1µm InP cladding layer, a 20nm InGaAsP (λ_x = 1.15µm) etch stop layer and finally a 0.4µm InP coupling layer. All layers were undoped. Device fabrication starts by cleaving two ~10 × 12mm² samples from the grown wafers. In one sample the top 0.4 µm InP layer is removed. On another sample, a ridge waveguide structure along the [110] direction is fabricated using standard photolithography and selective wet etching techniques. To support the narrow, 2–5µm wide, 0.4µm high ridges during the fusion process, 10µm wide InP layers were etched on both sides of the ridges as shown in Fig. 1. The adjacent ridge waveguides are separated by 125µm. The two samples are then fused together at a temperature of 630°C in a hydrogen atmosphere for 30min. After fusion, the sample was thinned to 200µm using an HCl etchant. 300nm of gold was then deposited on both sides for applying the bias voltage.
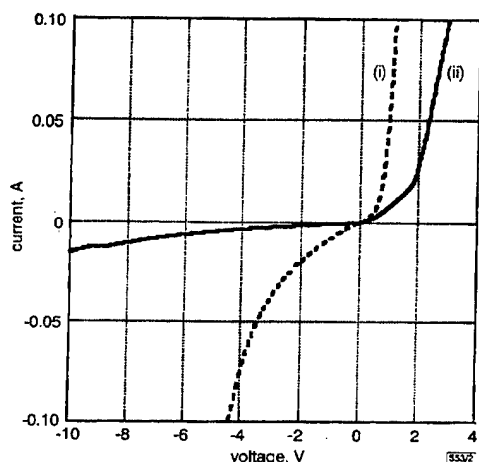

Fig. 2 *I-V curves of pin-FVC with broad and narrow ohmic contacts*

(i) broad Ohmic contact
(ii) narrow Ohmic contact

Fig. 2(i) shows the measured I-V curves of the FVCs. The sample size is 3.5 × 4.5mm² Since 80% of the area of two samples are fused together, and only 3% of this area is the actual ridge waveguide, there is a large leakage current that can be reduced by etching mesas and depositing metal only on the FVC ridge regions. When the wafer fusion technique is used to fabricate VCSELs and detectors [6], those devices are relatively small and uniformity of the fused material is not so critical for individual device operation. To make long waveguide couplers and switches, on the other hand, good uniformity of the fusion interface is required. We used electroluminescence images of the FVC to study the fusion uniformity under current flow. The near field pattern at the output facet of the coupler is observed by an IR camera with a ×80 objective lens. Fig. 3 shows the luminescence image of the fused area at 200mA forward current. The image area is 64µm wide. Luminescence from the two quartanery layers can be clearly distinguished. There are no dark areas and the intensity is very uniform along the fused interface.
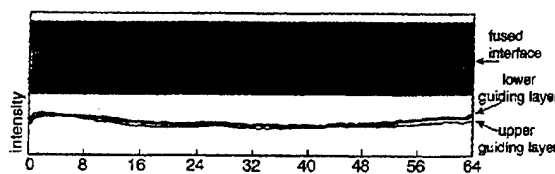

Fig. 3 *Electroluminescence image of 64µm wide fused area under 200mA current and intensity distribution of upper and lower guiding layers*

Fig. 4 *Measured intensity of upper and lower waveguides against reverse bias for broad area Ohmic contact FVC*

● upper waveguide
○ lower waveguide

To characterise the FVCs, a tunable laser is used to launch light at the input of the coupler through an 8µm diameter singlemode fibre. The near field images at the output of a 3.5mm long FVC for three reverse biases 0, 1.8 and 3V are shown in Fig. 4, along with the normalised intensities of the upper and lower waveguides. The linear electro-optic effect at 3V is too small to explain the switching. We believe that the thermo-optic effect plays a major role in this device because of the high leakage current which contributes to internal heating of this structure. To confirm this, we changed the stage temperature, and switching is observed when 30°C temperature change. To reduce the leakage current, we fabricated another FVC. In this case, one of the InP substrates is removed and the electrodes are evaporated on the exact ridge area through narrow windows of an SiN insulation layer. The I-V curve of a 7mm × 3µm FVC with this modification is shown in Fig. 2(ii). As can be seen in Fig. 5, a 12V reverse bias is needed to achieve switching. The insert pictures show the near fields at different biases.

In conclusion, the switching of fused vertical couplers has been demonstrated. For bulk InGaAsP materials, a 12V reverse bias is needed to realise the switching for a 6.9mm long device. Using quantum well structures, the switching voltage can be further reduced. The wafer fusion technique can be used to fabricate vertical couplers and 3D photonic integrated circuits without requiring complicated regrowths.
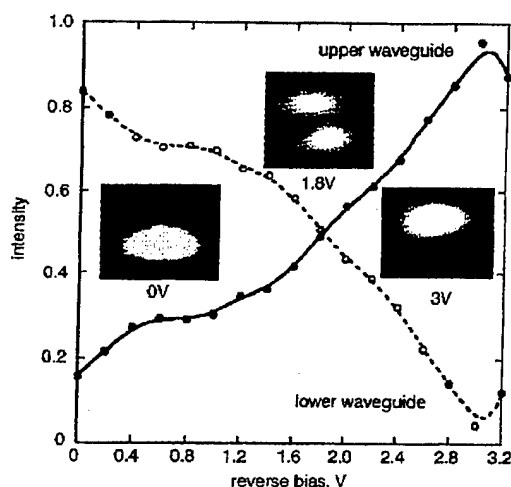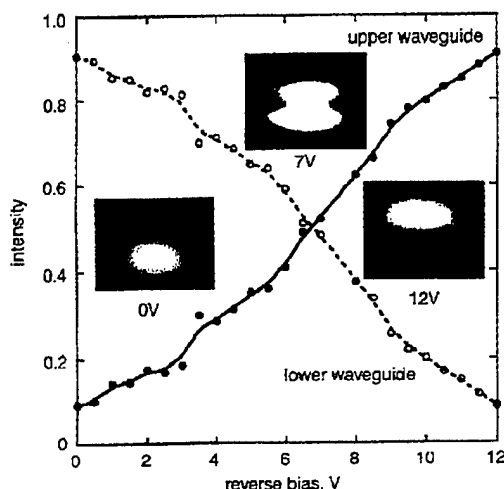

Fig. 5 *Measured intensity of upper and lower waveguides against reverse bias for narrow area Ohmic contact FVC*

● upper waveguide
○ lower waveguide

B. Liu, A. Shakier, P. Abraham and J.E. Bowers (*Department of Electrical and Computer Engineering, University of California, Santa Barbara, CA 93106, USA*)

E-mail: liu@opto.ucsb.edu

A. Shakier: Permanent address: Jack Baskin School of Engineering, University of California, Santa Cruz, CA 95064, USA

References

1   KOHTOKU, M., BABA, S., ARAI, S., and SUEMATSU, Y.: 'Switching operation in a GaInAs-InP MQW integrated-twin-guide (ITG) optical switch', *IEEE Photonics Technol. Lett.*, 1991, **3**, (3), pp. 225–226

2   DOLLINGER, F., BORCKE, M., BOHM, G., TRANKLE, G., and WEIMANN, G.: 'Ultrashort low-loss optical multiquantum-well GaAs/GaAlAs vertical directional coupler switch', *Electron. Lett.*, 1996, **32**, (16), pp. 1509–1510

3   ALFERNESS, R.C., BUHL, L.L., KOREN, U., YOUNG, M.G., KOCH, T.L., BURRUS, C.A., and RAYBON, G.: 'Broadly tunable InGaAsP/InP buried rib waveguide vertical coupler filter', *Appl. Phys. Lett.*, 1992, **60**, (8), pp. 980–982

4   CHI WU, ROLLAND, C., PUETZ, N., BRUCE, R., CHIK, K.D., and XU, J.M.: 'A vertically coupled InGaAsP/InP directional coupler filter of ultranarrow bandwidth', *IEEE Photonics Technol. Lett.*, 1991, **3**, (6), pp. 519–521

5   BIN LIU, AH SHAKOURI, ABRAHAM, P., KIM, B.G., JACKSON, A.W., and BOWERS, J.E.: 'Fused vertical couplers', *Appl. Phys. Lett.*, 1998, **72**, (21), pp. 2637–2638

6   BLACK, A., HAWKINS, A.R., MARGALIT, N.M., BABIC, D.I., HOLMES, A.L., Jr., CHANG, Y.L., ABRAHAM, P., BOWERS, J.E., and HU, E.L.: 'Wafer fusion: Materials issues and devices results', *IEEE J. Sel. Topics Quantum Electron.*, 1997, **3**, (3), pp. 943–951

Highly sensitive and compact cross-correlator for measurement of picosecond pulse transmission characteristics at 1550nm using two-photon absorption in Si avalanche photodiode

K. Kikuchi, F. Futami and K. Katoh

A highly sensitive and compact cross-correlator in which an Si avalanche photodiode (APD) is used as a two-photon absorber is described, which was developed for the measurement of picosecond pulse transmission characteristics at 1550nm. A 10GHz, 1.7ps pulse under test is generated from an external-cavity modelocked semiconductor laser, and is transmitted through an 80km long dispersion-shifted fibre. A 200fs sampling pulse is obtained from the pulse under test by pulse compression. An Si APD is used as a two-photon absorber for the cross-correlation measurement of the transmitted pulse waveform. The asymmetric pulse-waveform distortion stemming from the dispersion slope is clearly detected by the system.

Introduction: In future ultra-high-speed optical fibre communication systems employing optical time-division multiplexing (OTDM), picosecond or sub-picosecond optical pulses will be transmitted through an optical fibre [1]. Hence, there have been strong demands for compact, sensitive and low-cost systems for measuring the transmission characteristics of such ultra-short optical pulses.

Intensity autocorrelators have been most widely used to estimate the pulsewidth by assuming that the pulse waveform has a Gaussian or $sech^2$ profile. However, a pulse transmitted through an optical fibre may be asymmetrically distorted due to the dispersion slope and/or the Kerr nonlinearity of the fibre, and it is very difficult to evaluate such distorted pulse waveforms using intensity autocorrelators. On the other hand, optical sampling systems can more precisely determine the pulse waveform. However, in such systems, we have to prepare two sets of optical pulse sources in which the repetition rates are highly synchronised [2, 3]. One pulse source generates the optical pulse under test, and the other generates the sampling pulse, the width of which should be much shorter than that of the pulse under test.

In this Letter, we propose an alternative approach to picosecond pulse waveform measurement, which is more compact, more sensitive, and much easier to handle than conventional methods. The proposed system has three features that distinguish it from the others. First, a 10GHz, 1.7ps pulse under test is generated from an external-cavity modelocked semiconductor laser, which ensures much more stable operation against environmental effects than modelocked fibre lasers. Secondly, a 200fs sampling pulse is obtained from the picosecond pulse under test by pulse compression. By taking the cross-correlation between the two kinds of pulse, we can diagnose the pulse waveform under test. Thirdly, we introduce an Si avalanche photodiode (APD) as a two-photon absorption (TPA) receiver into the system. The combination of a nonlinear optical crystal and a highly sensitive photodetector used in conventional autocorrelators and optical sampling systems can be replaced by an Si APD, and hence the system construction is greatly simplified. In addition, an Si APD can greatly improve the sensitivity of the cross-correlator because the avalanche process amplifies the TPA-induced photocurrent [3, 4].

The 10GHz, 1.7ps optical pulse is transmitted through an 80km long dispersion-shifted fibre (DSF), and the asymmetric distortion of the pulse waveform stemming from the dispersion slope $\beta^{(3)}$ of the DSF is clearly detected by the cross-correlator we have developed.

Experimental setup: Fig. 1 shows the experimental setup for the cross-correlator used to measure the waveform of 1550nm picosecond optical pulses transmitted through a fibre.

An external-cavity modelocked semiconductor laser with a saturable absorption section was used as a picosecond pulse source [5]. When sinusoidally modulating the reverse bias voltage applied to the absorption section at the cavity resonance frequency around 10GHz, we could lock the repetition rate at the modulation frequency. The phase-noise measurement for the generated pulses showed that the timing jitter was suppressed to < 0.5ps. The pulsewidth (FWHM) measured from the intensity autocorrelation

Wafer-Fused Optoelectronics for Switching

Ali Shakouri, Bin Liu, Boo-Gyoun Kim, Patrick Abraham, Andrew W. Jackson,
Arthur C. Gossard, *Senior Member, IEEE,* and John E. Bowers, *Fellow, IEEE*

Abstract— Wafer fusion technique for realization of compact waveguide switches and three-dimensional (3-D) photonic integrated circuits is investigated theoretically and experimentally. Calculations based on beam propagation method show that very short vertical directional couplers with coupling lengths from 40 to 220 μm and high extinction ratios from 20 to 32 dB can be realized. These extinction ratios can be further improved using a slight asymmetry in waveguide structure. The optical loss at the fused interface is investigated. Comparison of the transmission loss in InGaAsP-based ridge-loaded waveguide structures with and without a fused layer near the core region, reveals an excess loss of 1.1 dB/cm at 1.55 μm wavelength. Fused straight vertical directional couplers have been fabricated and characterized. Waveguides separated by 0.6 μm gap layer exhibit a coupling length of 62 μm and a switching voltage of about 2.2 V. Implications for GaAs-based fused couplers for 850 nm applications will also be discussed.

Index Terms—Integrated optoelectronics, optical couplers, optical switches, optical waveguide components, wafer bonding.

I. INTRODUCTION

MAJOR requirements for optical packet switching elements are scalability, low-loss, and low crosstalk. In addition, these structures should be compatible for coupling with fiber ribbon cables and should incorporate integrated optical amplifiers to compensate for losses associated with fiber loop memories. We are investigating here the use of wafer fusion to give an extra degree of freedom in the fabrication of coupled waveguide structures. The technique of wafer fusion has been used to combine materials of very different lattice constants which could not be grown by heteroepitaxy [1]. This technique can also be used to combine planar waveguides fabricated on two different substrates into a three dimensional structure in which there is vertical coupling between arrays of single mode waveguides through the fused regions (Fig. 1) [2]. In addition, application of a bias at fused areas will allow a change of gain or index for switching purposes. Because of the differences between fused vertical couplers and conventional planar couplers [3]–[6], we have studied theoretically the coupling length and extinction ratio using three-dimensional (3-D) beam propagation method [7]. In order to gain insight into fundamental limitations in the performance of these *strongly* coupled structures, we have also used improved coupled mode

theories where the nonorthogonality of the modes of individual waveguides is taken into account explicitly. From a fabrication point of view, realization of vertical couplers requires a detailed optical characterization of the loss and uniformity of the fused interface. In the following, after discussion of various design issues for fused vertical couplers, their fabrication and characterization are described.

II. BEAM PROGAGATION METHOD ANALYSIS

In order to calculate the coupling length and the extinction ratio in these two-dimensional (2-D)-fused waveguide structures a 3-D finite difference beam propagation program is used. The fused vertical coupler (FVC) is shown in Fig. 2. A single-mode ridge-loaded waveguide structure based on InP substrate, with 0.5 μm InGaAsP ($\lambda_{gap} = 1.3$ μm) core region, 0.1 μm cladding and 0.1 μm ridge height, is vertically coupled through a fused gap layer to an identical waveguide. The gap layer thickness is varied from 0.1 to 0.6 micron with its index ranging from InP to InGaAsP ($\lambda_{gap} = 1.4$ μm).

Fig. 3(a) displays the coupling length for different parameters of the gap layer. As expected, increasing the gap layer index reduces the coupling length. In a coupled-mode picture, this can be explained by an increase in the overlap integral of the two modes of adjacent waveguides. On the other hand, the dependence of the coupling length on the gap layer thickness shows a mixed behavior. When the gap region has small indexes close to InP layer, increasing its thickness will decouple the two waveguides and thus increases the coupling length. However, when the index of the gap layer is large (close to 1.3 μm quartenary), the mode amplitude in this region is not anymore exponentially decaying, but sinusoidal. So a thicker gap layer will increase the overlap integral between modes of adjacent waveguides and thus reduces the coupling length. When the gap layer thickness is more than 0.3–0.4 μm, an analysis based on the supermodes of three coupled waveguide is more appropriate, but the appearance of undesirable modes in the gap layer will deteriorate the performance of the directional coupler.

In order to quantify the effect of higher order modes, power transfer between two waveguides was analyzed. The eigenmode of one of the uncoupled waveguides was taken for the input field, and power transfer to the other waveguide as a function of propagation distance was monitored by the beam propagation method (BPM) simulation. Fig. 3(b) displays the extinction ratio defined as the ratio of mode powers in the two waveguides after a coupling length. When the gap layer is thick and its index is high, the coupler has poor extinction ratios from 5 to 10 dB. In this case BPM simulation reveals 3–4
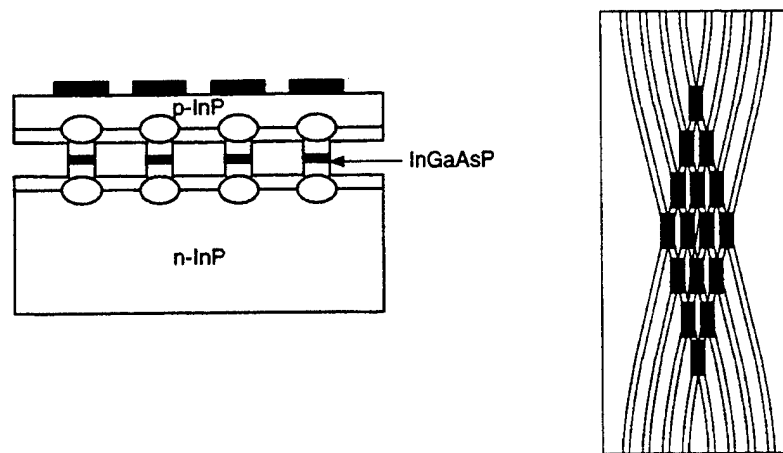
Fig. 1. InP crossbar switch based on coupling between independent arrays of waveguides on each substrate.

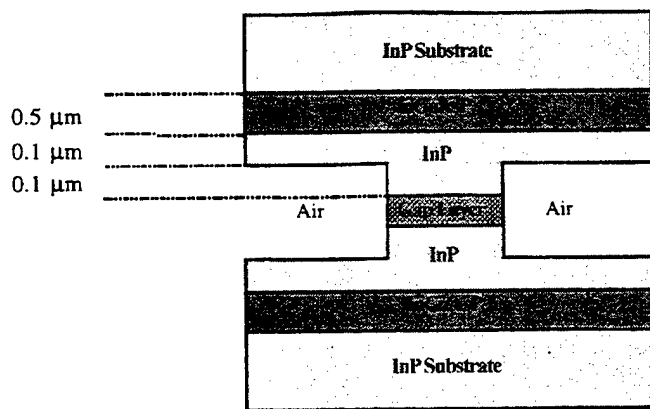Fig. 2. The coupling region between two fused waveguides, and the parameters used for BPM simulations ($\lambda = 1.55$ μm, n(InP) $= 3.17$, n(InGaAsP) $= 3.37$).

Fig. 3. (a) The coupling length and (b) the extinction ratio as a function of gap layer index for different thicknesses of the gap layer.

supermodes in the coupling region. In addition to the expected symmetric and antisymmetric eigenmodes, there are modes of the gap layer and some leaky modes. But for a wide range of parameters (gap thickness from 0.2 to 0.6 μm, and gap index from 3.2 to 3.4), extinction ratios from 20 to 32 dB can be achieved. From Fig. 3(a) we see that this corresponds to coupling lengths of the order from 40 to 220 μm. Since the two waveguides are very close, it is almost impossible to excite only of the them and to measure the extinction ratio experimentally. In practice, the two ridge structures will be separated by curved regions and on/off ratio is limited by unwanted couplings at regions where the waveguides join together. The above analysis, however, shows the inherent limitation in extinction ratios.

In these symmetric ultra short couplers, the main problem to achieve low extinction ratio is nonorthogonality of the modes of individual waveguides [8], [9]. Using a slight asymmetry, one can improve extinction ratios to arbitrary small values. To see this, lets consider the one dimensional index profile of the coupling region of FVC in Fig. 2 with 0.2 μm InP gap layer. Fig. 4 shows calculations based on improved coupled mode theories, where corrections due to overlap integrals are incorporated [8]. BPM simulations agree very well with these results. When the gap layer thickness is 0.2 μm, the asymmetry
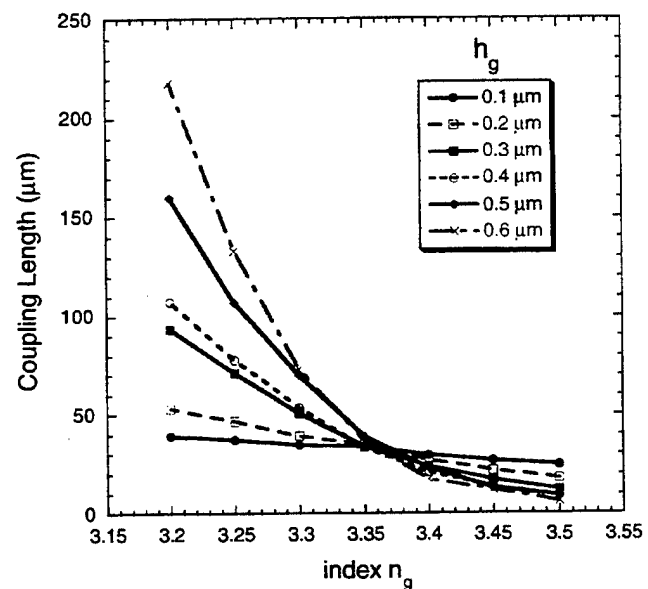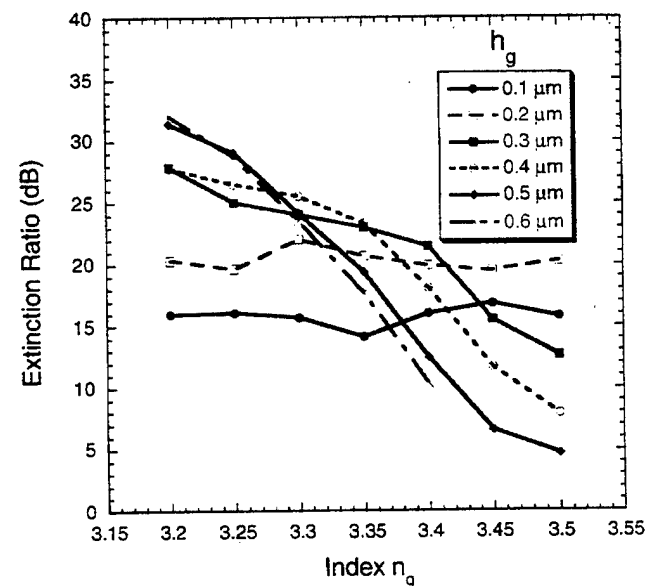
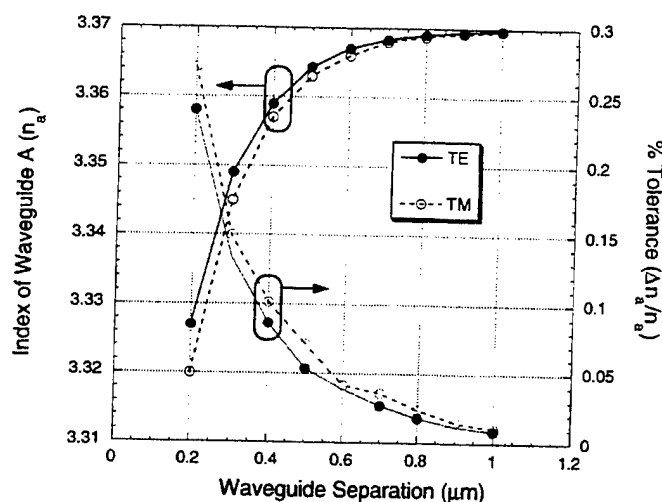Fig. 4. Index of waveguide A for maximum extinction ratio and tolerance on that to achieve >30 dB extinction ratio as a function of waveguide separation.
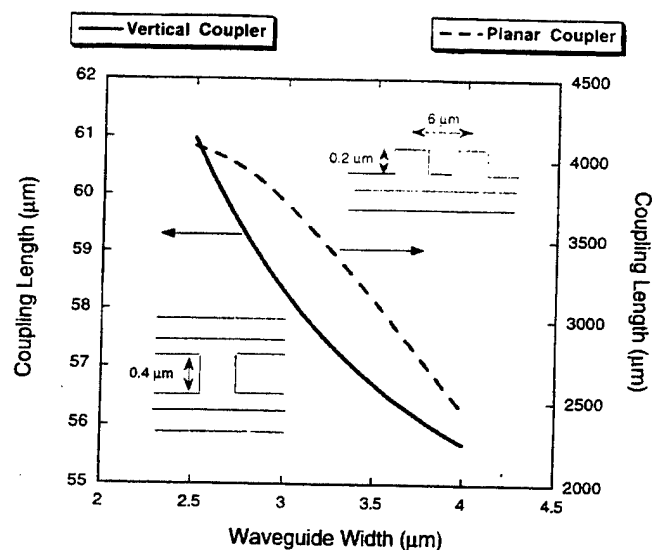

Fig. 5. Coupling length for the vertical coupler and conventional planar coupler as a function of waveguide width.

Fig. 6. Different steps of fabrication process for single-mode waveguide structure with a fused interface near core region.

in core waveguide index required to achieve the highest extinction ratio for TE (TM) mode is 0.003 (0.004). Having the core index within ±0.019 (±0.021%) of the optimum value for TE (TM) mode, one can achieve the extinction ratio larger than 30 dB (Fig. 4). As the separation between the two waveguides decreases, more asymmetry is needed but the tolerance to obtain an extinction ratio larger than 30 dB increases. This facilitates fabrication of passive asymmetric couplers or setting the voltage or current in active components. An intuitive picture is that a slight asymmetry can equalize the overlap integral of the single waveguide mode with the symmetric and antisymmetric supermodes of the coupler and thus increase the extinction ratio.

Vertical coupling through the ridge structure whose height is defined by etch-stopping techniques is much less sensitive to the ridge waveguide width and sidewall smoothness than the planar waveguide couplers. In fact, the difficulty in making reproducibly and uniformly very narrow gap (<1 μm) couplers

have mitigated their development for ultra short switching devices. Fig. 5 shows the coupling length as a function of waveguide width for the case of a conventional ridge-loaded structure with 0.5 μm InGaAsP ($\lambda_{gap} = 1.3$ μm) core layer, 0.1 μm InP slab layer and 0.2 μm InP ridge. The center of the two waveguides are separated by 6 μm. It can be seen that a change of 1 μm in waveguide width will change the coupling length by 30–40%. When the same waveguides are coupled vertically, the coupling length is about two orders of magnitude smaller and at the same time less sensitive to waveguide width variation (4–5% change in coupling length for one micron change in waveguide width).

Another requirement for optical switches is polarization insensitivity. The fused vertical coupler shown in Fig. 2 has coupling length for TM polarized light at 1.55 μm wavelength which is 7–13% shorter than the TE one (for gap layer thicknesses between 0.1–0.6 μm). However, it is possible to make the switch polarization insensitive using the difference in materials dispersion, e.g., by combining GaAs and InP waveguides [10].

III. OPTICAL LOSS AT THE FUSED INTERFACE

The single mode waveguide structure was based on MOCVD grown material with 0.5 μm InGaAsP ($\lambda_{gap} = 1.3$ μm) guiding layer, 0.24 μm cladding layer which includes two 0.1 μm InP layers and two 0.02 μm InGaAsP ($\lambda_{gap} = 1.15$ μm) etching stop layers, and finally 0.6 μm InP ridge layer. For the purpose of comparison, we use the same wafer and single mode waveguide geometry with and without a fused interface near the core region. The control waveguide has 3 μm wide and 0.6 μm high ridges defined

Fig. 7. The stain-etched SEM picture of the single-mode waveguide structure with fused interface.

Fig. 8. The stain-etched SEM picture of a fused vertical coupler.

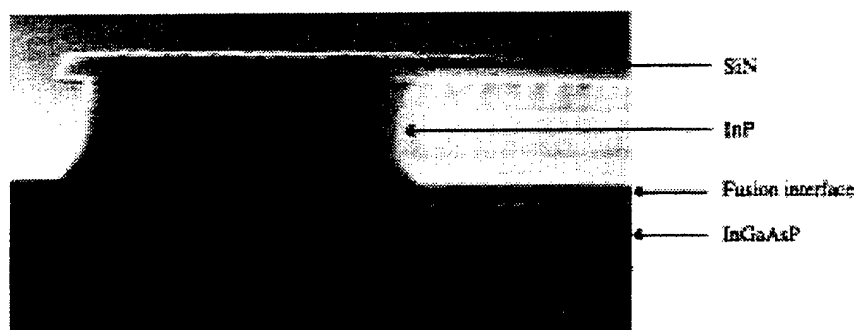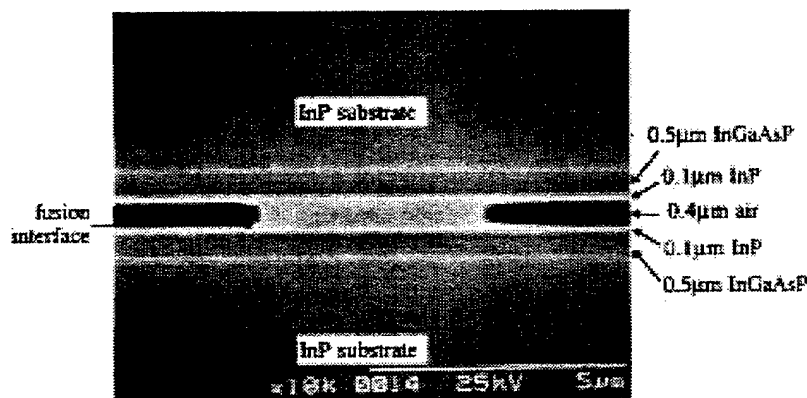using wet-etching techniques. To fabricate the single mode fused waveguide, two 1×0.8 cm^2 samples are cut from the MOCVD grown wafer. First, the 0.6 μm InP layer and 0.1 μm cladding layer of one sample are removed using selective wet-etching (Fig. 6); then 10 μm wide, 0.6 μm deep channels with 160 μm spacing are opened in a second sample. The two samples are then fused at 630 °C in a hydrogen atmosphere for 30 min. Subsequently, InP substrate and 0.5 μm guiding layer of the top wafer is removed and 3 μm wide ridge waveguides are fabricated using wet etching. Fig. 7 shows a stain-etched SEM picture of finished device. The fused interface can not be seen in this picture. This is an indication of the high quality of the fused interface. The presence of the channels prior to fusion is crucial. Without these channels, we could see microscopic voids at the fused junction and many of the fabricated waveguides did not show clear eigenmodes.

Fabry–Perot resonance technique was used to measure the optical propagation loss [2]. The optical loss of the unfused waveguide is about 2.4 dB/cm, while the fused structure showed a loss of 3.5 dB/cm at 1.55 μm. Since the geometry and materials are identical, the 1.1 dB/cm excess loss should be attributed to the fused interface. BPM calculations indicate that the field strength at the center of the fused interface is 49% of the maximum field. The issue of waveguide uniformity for large scale monolithic integration is very important. The size of our fused wafers is about 1×0.8 cm^2. After thinning and cleaving, the size of the sample for measurement is about 6×6 mm^2. The yield of the fused waveguides is more than 90% which is almost same as unfused sample. The existence of channels in fused sample provides 150 μm wide multimode
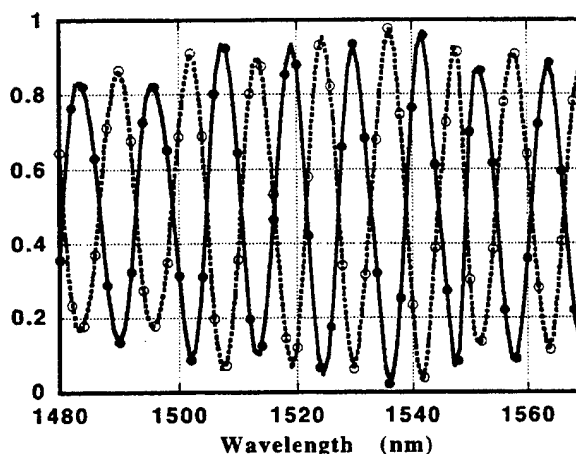
Fig. 9. Measured intensity of the upper and lower waveguides as a function of wavelength.

slab waveguides that contain a fused interface. We did not notice any "dark" spot in these multimode structures.

We have also investigated mass transport at the fused interface by comparing samples with different effective fused areas. In conventional fused structures, after fabrication of narrow channels on one of the wafers prior to fusion, typically over 90% of the surface of the samples is in contact during the fusion process. We studied samples where the fusion was only over the surface on the top of waveguides (3–6 μm thickness, separated by 125 μm, and about 1 cm long). In this case only 4% of the surface of the two wafers is in contact during fusion. We did not notice any substantial degradation or nonuniformity in the ridge waveguide structure.
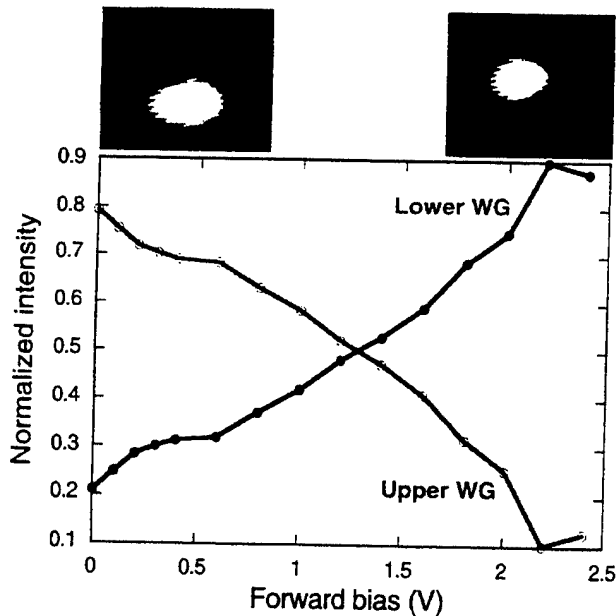
Fig. 10.   Measured bias dependence of the output light intensity in upper and lower waveguides for a 3.5 mm fused vertical switch. The top pictures are photographs of the near field pattern at the output of the coupler at 0 and 2.2 V.

Fig. 11.   Asymmetric fused vertical coupler.

(a)

(b)
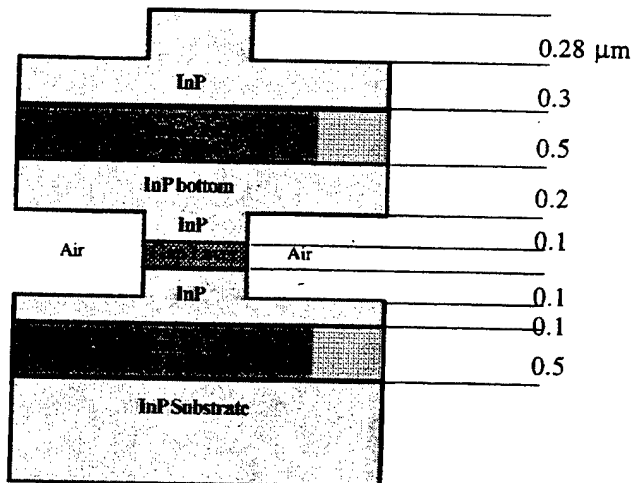
Fig. 12.   (a) The coupling length and (b) the extinction ratio as a function of gap layer index for different thicknesses of the gap layer, for asymmetric fused vertical coupler.

IV. FUSED VERTICAL DIRECTIONAL COUPLER AND SWITCH

The structure of the coupler is identical to that in Fig. 2, with 0.2 μm thick InP gap layer. The material was grown by MOCVD and consisted of a 0.5 μm InGaAsP ($\lambda_{gap} = 1.3\ \mu$m) guiding layer on InP substrate, followed by 0.1 μm InP cladding layer, 20 nm InGaAsP ($\lambda_{gap} = 1.15\ \mu$m) etch stop layer and 0.4 μm InP coupling layer. To fabricate the vertical coupler, two 8 × 10 mm^2 samples are cleaved from the grown wafer. In the first sample the top 0.4 μm InP layer is removed. On the second sample, a ridge waveguide structure is fabricated using standard photolithography and selective wet etching. The ridges have 3–6 μm width, 0.4 μm height and they are separated by 125 μm. The two samples are then fused together at a temperature of 630°C in a hydrogen atmosphere for 30 min. Fig. 8 shows the stain-etched SEM picture of a

finished fused vertical coupler (FVC). The fused interface is not visible, even after staining. There is mass transport at the edge of the ridge. This is beneficial to get a symmetric coupler and improves the side wall flatness.

The near field pattern at the output of FVC's, 4.5 mm long, is recorded by an IR camera. The light is input from a 8 μm diameter single mode 1.55 μm fiber. It can be seen that by changing the input wavelength, light is switched from the upper to the lower waveguide. Fig. 9 shows the intensities of the upper and lower waveguides as a function of wavelength. Our measurements show that the extinction ratio can be >15 dB. This is particularly difficult to achieve in conventional high mesa vertical couplers [3]–[6]. From the oscillation

Fig. 13. SEM pictures of the separated top and bottom waveguides for an asymmetric fused vertical coupler. The bottom picture is a photograph of the near field pattern at the output of the coupler where the two waveguides are separated by 250 μm.

period (about 12 nm) and considering material and waveguide dispersions, the index difference between the even and odd modes can be calculated which is 0.0121. The corresponding coupling length is 62 μm at 1.55 μm, that agrees very well with 58 μ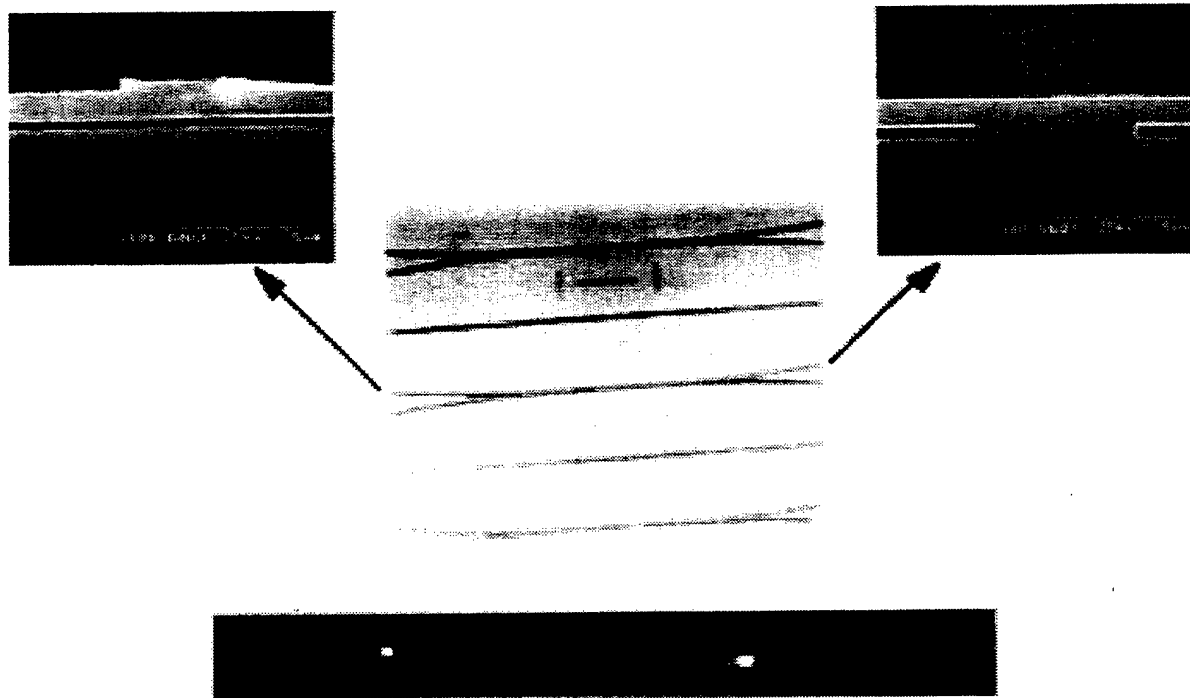m result from BPM simulations. Finally a PIN FVC was fabricated and characterized. The structure was identical to the one in Fig. 8, the only difference is that the top InP substrate is p-doped and the bottom wafer n-doped. It can be seen in Fig. 10 that with a bias of 2.2 V the light is switched from the top to the bottom waveguide. Electro-optic effect at such a small bias is not enough to explain the switching. We believe that thermo-optic effect plays a major role in this device because of the high leakage current and local heating of the coupler [11].

V. ASYMMETRIC FUSED VERTICAL DIRECTIONAL COUPLER

In order to fabricate multilevel 3-D photonic integrated circuits, an asymmetric fused structure is needed (see Fig. 11). By repeating the fusion process, one can obtain multiple layers of waveguide interconnects. For fabrication, first, a set of ridge waveguides on a InP wafer are defined using the usual wet- and dry-etching techniques. Subsequently, a wafer is bonded on top of the waveguides. After removing the substrate of this top wafer using selective etching, a second set of waveguides is fabricated. These top waveguides are coupled vertically to the waveguides beneath them in areas where the two structures are connected by wafer fusion. The issue of alignment in the coupling regions is facilitated using infrared photolithography. Even though the top and bottom waveguides are very dissimilar, by matching the modes effective indexes, one can theoretically achieve coupling lengths of the order of 60 μm with 25 dB extinction ratio [see Fig. 12(a) and (b)].

Fig. 13 displays the SEM cross section of the bottom and top waveguides along with the near field infrared image at the output of an InGaAsP asymmetric coupler where the two waveguides are separated by 250 μm.

VI. PROSPECTS FOR GaAs FUSION

Wafer fusion technique can also be used to fabricate vertical couplers in other materials. To investigate the optical loss due to fusion process in AlGaAs, a single mode waveguide structure similar to the one in Fig. 7 was fabricated. The reference structure was based on GaAs substrate, with 2.5 μm $Al_{0.4}Ga_{0.6}As$ bottom cladding layer, 0.2 μm $Al_{0.15}Ga_{0.85}As$ core region, 0.3 μm $Al_{0.4}Ga_{0.6}As$ slab layer and 0.6 μm $Al_{0.4}Ga_{0.6}As$ ridge. The waveguides were 3 μm wide and they exhibited a loss of about 5 dB/cm. This high loss was due to the poor quality of the sidewalls. SEM pictures revealed a roughness on the order of one micron. Single mode waveguides with a fused interface in the middle of the slab layer (i.e., 0.15 μm away from the core region), had an excess loss of about 3 dB/cm at 1.55 μm wavelength.

It will be difficult to achieve ultra short coupling lengths with fused vertical couplers at shorter wavelengths (e.g., 850 nm). If the single mode AlGaAs waveguide structure described above has only 0.1 μm ridge height and is coupled vertically to an identical waveguide, the coupling length at 850 nm is over 500 μm. The same structure at 1.55 μm wavelength will have a coupling length of about 5 μm.

VII. SUMMARY AND CONCLUSION

In conclusion, wafer fusion technique for fabrication of vertical couplers and switches is described. Very short directional couplers with a coupling length from 40 to 220 μm

and high extinction ratios from 20 to 32 dB can be realized. These extinction ratios can be further increased using a slight asymmetry in waveguide structure. It is shown that 1.1 dB/cm excess optical loss is introduced due to fusion process in InP based waveguides at 1.55 μm wavelength. Fused straight vertical directional couplers separated by 0.6 μm gap layer exhibit a coupling length of 62 μm and a low switching voltage of about 2.2 V. These fused waveguides give us the added advantage of vertical dimension by separating the input and output waveguides to realize compact and scalable 3-D photonic integrated circuits.

REFERENCES

[1] A. Black, A. R. Hawkins, N. M. Margalit, D. I. Babic, A. L. Holmes, Y. L. Chang, P. Abraham, J. E. Bowers, and E. L. Hu, "Wafer fusion: Materials issues and device results," *IEEE J. Select. Topics Quantum Electron.*, vol. 3, pp. 943–951, June 1997.

[2] B. Liu, A. Shakouri, P. Abraham, B. G. Kim, A. W. Jackson, and J. E. Bowers, "Fused vertical couplers," *Appl. Phys. Lett.*, vol. 72, pp. 2637–2638, May 1998.

[3] J. E. Zucker, K. L. Jones, M. G. Young, B. I. Miller, and U. Koren, "Compact directional coupler switches using quantum well electrorefraction," *Appl. Phys. Lett.*, vol. 55, pp. 2280–2282, Nov. 1989.

[4] M. Kohtoku, S. Baba, S. Arai, and Y. Suematsu, "Switching operation in a GaInAs-InP MQW integrated twin guide (ITG) optical switch," *IEEE Photon. Technol. Lett.*, vol. 3, pp. 225–226, Mar. 1991.

[5] F. Dollinger, M. Borcke, G. Bohm, G. Trankle, and G. Weimann, "Ultrashort low-loss optical multiquantum well GaAs/GaAlAs vertical directional coupler switch," *Electro. Lett.*, vol. 32, pp. 1509–1510, Aug. 1996.

[6] S. Noda, N. Yamamoto, and A. Sasaki, "New realization method for three-dimensional photonic crystal in optical wavelength region ," *Japanese J. Appl. Phys.*, vol. 35, pp. L909–L912, July 1996.

[7] BeamProp, Version 2.0, Rsoft Inc. 1996.

[8] B. G. Kim, A. Shakouri, B. Liu, and J. E. Bowers, "Improved extinction ratio in ultra short directional couplers using asymmetric structures," in *Proc. Integr. Photon. Res. Conf.*, Vancouver, B.C., Canada, Apr. 1998.

[9] S. L. Chuang, "Application of the strongly coupled-mode theory to integrated optical devices," *IEEE J. Quantum Electron.*, vol. 23, pp. 499–509, May 1987.

[10] B. Liu, A. Shakouri, P. Abraham, Y. J. Chiu, S. Zhang, and J. E. Bowers, "InP/GaAs fused vertical coupler filter," *IEEE Photon. Technol. Lett.*, to be published.

[11] B. Liu, A. Shakouri, P. Abraham, and J. E. Bowers, "Fused vertical coupler switches," *Electron. Lett.*, to be published.

Ali Shakouri received the undergraduate degrees from University of Paris, France, and Ecole Nationale Superieure des Telecommunications de Paris, France. He received the Ph.D. degree from the California Institute of Technology, Pasadena, in 1989, 1990, and 1995, respectively. His dissertation was on electron transport in quantum well infrared photodetectors.

He is currently an Assistant Professor at the University of California at Santa Cruz. His research interests are in wafer-fused optoelectronics, fiber-optic telecommunication systems, and integrated cooling of electronic components.

Bin Liu received the B.S. degree from Zhejiang University, China, in 1990 and the M.S. degree from Shanghai Institute of Optics and Fine Mechanics, Chinese Academy of Sciences, China, in 1995. He is currently pursuing the Ph.D. degree at the University of California at Santa Barbara.

His research includes the simulation and fabrication of wafer-fused semiconductor waveguide, coupler, filter, and switch.

Boo-Gyoun Kim was born in Taejon, Korea. He received the B.S. degree in electronic engineering from Seoul National University, Seoul, Korea, in 1979 and the M.S. degree in electronic engineering from KAIST, Seoul, in 1981. He received the Ph.D. degree in electrical engineering from the University of Southern California at Los Angeles, in 1989.

He joined the Department of Electronic Engineering at Soongsil University in 1981 and is an Associate Professor in the School of Electronic Engineering at Soongsil University. During the summer of 1993, he was a Visiting Researcher of IBM Almaden Research Center, San Jose, CA. During the 1997 academic year, he was a Visiting Associate Professor in the Department of Electrical and Computer Engineering at the University of California at Santa Barbara. His main research interests are in the areas of optical communication devices and systems.

Patrick Abraham received the M.S. and Ph.D. degrees in material science from the University C. Bernard Lyon 1, France, in 1984 and 1987, respectively.

He was a researcher at Centre National de la Recherche Scientifique (CNRS), France, and worked until 1988 at the Laboratoire de Physico-Chimie Minerale, France. He is currently a research engineer at the University of California at Santa Barbara, where his research interests include MOCVD growth, compliant substrates, and wafer bonding.

Andrew W. Jackson, photograph and biography not available at the time of publication.

Arthur C. Gossard (SM'88) received the B.A. degree in physics (summa cum laude) in 1956 from Harvard University, Cambridge, MA, and the Ph.D. degree in physics from University of California at Berkeley, in 1960.

From 1960 to 1987, he was a Member of Technical Staff at AT&T Bell Laboratories and since 1987 he has been Professor of Materials and Electrical and Computer Engineering at University of California at Santa Barbara. His research involves the growth of artificially structured materials by molecular beam epitaxy. His special interests are the growth of quantum wells and superlattices and their application to high- performance electrical and optical devices.

Dr. Gossard is a Fellow of the American Physical Society. He received the Distinguished Technical Staff Member Award from AT&T Bell Laboratories in 1983, the Oliver E. Buckley Condensed Matter Physics Prize from the American Physical Society in 1984, and the Leigh Page Prize Lecturer from Yale University Physics Department in 1986. He was elected to Membership of the National Academy of Engineering in 1987.

John E. Bowers (S'78–M'81–SM'85–F'93) received the M.S. and Ph.D. degrees from Stanford University, Palo Alto, CA.

He is Director of the Multidisciplinary Optical Switching Technology Center (MOST), and a Professor in the Department of Electrical and Computer Engineering at the University of California at Santa Barbara (UCSB). He is a member of the Heterogeneous Optoelectronics Technology Center and the NSF Center on Quantized Electronic Structures. His research interests are in the development of novel optoelectronic devices for the next generation of optical networks. His research interests include novel ways of growing quantum wires and dots using MBE and MOCVD, techniques to fuse dissimilar materials together for new devices and improved performance, the design of quantum-well structures for high-speed light generation and detection, and the design of high-speed time-division multiplexed systems and devices. He has worked for AT&T Bell Laboratories and Honeywell before joining UCSB in 1987.

Dr. Bowers is a fellow of American Physical Society and a recipient of the IEEE LEOS William Steifer Award. He is a recipient of Sigma Xi's Thomas F. Andrew prize and the NSF Presidential young Investigator Award and NSF graduate fellowship.

Fused InP–GaAs Vertical Coupler Filters

Bin Liu, Ali Shakouri, P. Abraham, Y. J. Chiu, S. Zhang, and John E. Bowers, *Fellow, IEEE*

Abstract— A novel vertical coupler filter based on fused In-GaAsP–InP and AlGaAs–GaAs waveguide structures is proposed and demonstrated. The large material dispersion difference between InGaAsP and AlGaAs around 1.55 μm and similar waveguide geometries are used to realize a less sensitive polarization and narrow-band filter with two separated inputs and outputs and more than −40-dB sidelobe suppression should be possible.

Index Terms— Integrated optoelectronics, optical directional couplers, optical waveguide filters, wafer bonding.

INTEGRATED compact and narrow-band optical filters are key components for dense wavelength division multiplexing (DWDM) systems as add/drop multiplexers and demultiplexers. To date, many types of add/drop filters have been proposed and realized including diffraction gratings, arrayed-waveguide gratings, Mach–Zehnder interferometers and directional couplers. Compared to other structures, asymmetric directional coupler filters [1]–[3] using two dissimilar waveguide on III–V semiconductors are promising because of the precise control of waveguide thickness and indexes during crystal growth and monolithic integration with other devices such as optical amplifiers, photodectors, modulators, and lasers. There are, however, several obstacles to using these vertical coupler structures in system applications. The characteristics are strongly polarization dependent, launching the light into and coupling light out of two very close waveguide are very difficult and the coupling efficiency for two dissimilar waveguide geometries can be very different. In this letter, a novel vertical coupler filter (VCF) based on wafer fusion technology is proposed and demonstrated. This combines two different material systems: AlGaAs–GaAs with a low material dispersion at 1.55 μm and InGaAsP with a very high material dispersion. With a proper design, a narrow-band and polarization independence filter with two separated inputs and outputs can be easily realized, which solves all of the above problems.

It is well known that the response bandwidth of the asymmetrical directional coupler is inversely proportional to both the device length and the difference of mode dispersion in the two waveguide $\sigma = (dn_1/d\lambda) - (dn_2/d\lambda)$, where n_1 and n_2 are effective indices of the two waveguide eigenmodes. To minimize the device length and reduce the sidelobes, the filter bandwidth can only be narrowed by increasing σ. The modal dispersion depends on two factors. The first one is waveguide dispersion that depends on waveguide geometry;

the other one is the material dispersion. Vertical coupler filters realized up to now use mainly waveguide dispersion difference [1]–[3]. A narrow bandwidth requires one of the waveguide to have a very small index difference between the core and the cladding, and a large core size, while the other one should have a large index difference and a small core size. To keep the single-mode operation and a high coupling efficiency with fibers, the waveguide core size can not be too large or too small, and this limits the bandwidth of the filter. On the other hand, the difference in effective indices between TE and TM modes for a waveguide with a large index difference and small core is much more than the TE and TM difference of another waveguide with small index difference and large core size. Consequently, these devices have a strong polarization dependence. Generally the polarization dependent wavelength shift is more than 30 nm [4], [5] and that is a disadvantage in fiber optic communication systems. A birefringence compensation technique [5] has been used to solve this problem. But this needs a complicated structure design and a critical material growth. Since the polarization dependence and different coupling efficiency come from the strong asymmetry of two waveguide geometries, these problems can be solved if the two waveguide have similar structures. For these waveguide with almost identical waveguide dispersions, a large material dispersion difference between two waveguide is needed to realize a narrow-band polarization independent filter. It is known that a material has strong dispersion when the operation wavelength is near the band gap. So InGaAsP material can have much higher dispersion than AlGaAs material around 1.55 and 1.3 μm. For example, the material dispersion of InGaAsP ($\lambda g = 1.45 \mu$m) at 1.55 μm is −0.48/μm [6], which is almost one order of magnitude higher than that of $Al_{0.1}Ga_{0.9}As$, −0.059/μm [7]. Such a large dispersion difference is very difficult to obtain if one only uses different waveguide geometries. Unfortunately, because of the large lattice mismatch, good quality InP can not be grown on GaAs substrate or vise versa. Recently, a new technique called wafer fusion [8] or wafer bonding [9] has been developed that combines two materials with a large lattice mismatch. Wafer fusion can also be used to fabricate three-dimensional (3-D) photonic devices. For conventional vertical coupler filters, the difficulty of separating the two waveguide limits its application to WDM systems. Using wafer fusion, the two close inputs and two outputs can be easily separated in different planes [10], [11]. Fig. 1(a) is the schematic drawing of a fused InGaAsP–InP–AlGaAs–GaAs vertical coupler filter with separated inputs and outputs.

The detailed structure of the proposed fused vertical coupler filter is illustrated in Fig. 1(b). The upper InGaAsP–InP waveguide consists of a 0.4-μm InGaAsP ($\lambda g = 1.45 \mu$m) guiding
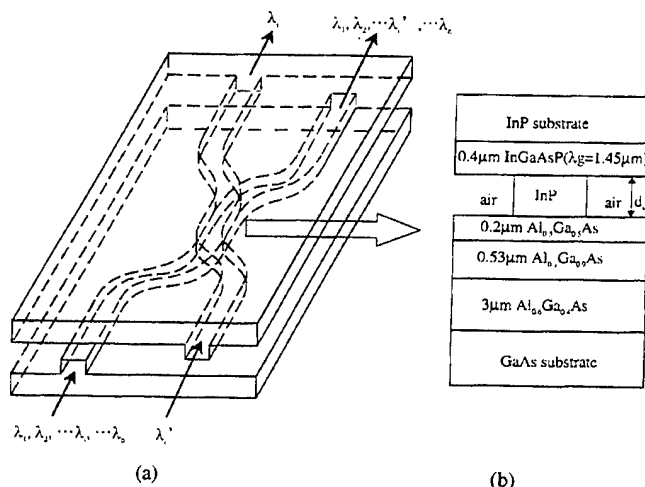
Fig. 1. (a) The proposed fused vertical coupler with separated inputs and outputs for add/drop applications. (b) The detailed structure of fused In-GaAsP–InP and AlGaAs–GaAs filter.
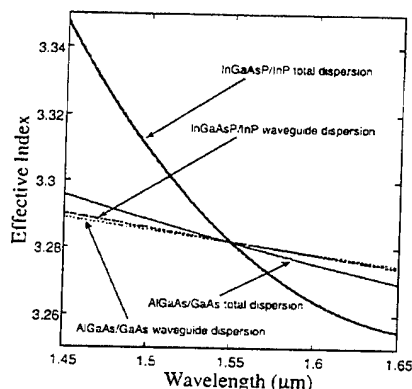

Fig. 2. The calculated waveguide dispersions and total dispersions of In-GaAsP–InP and AlGaAs–GaAs waveguide.

Fig. 3. The calculated effective index for TE and TM modes. The In-GaAsP–InP waveguide has 0.4-μm quaternary ($\lambda_g = 1.37$ μm) core and 0.1-μm InP cladding layer. The AlGaAs–GaAs waveguide is similar as before except the core thickness is 0.46 μm.
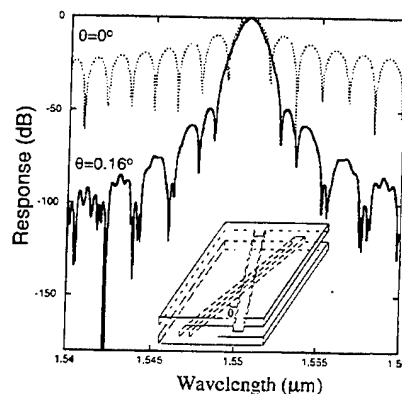
Fig. 4. The response of an X-crossing fused vertical coupler filter with $\theta = 0°$ and 0.16°. $d_s = 1.2$ μm. The insert is the schematic drawing of X-crossing fused vertical coupler filter.

layer and an InP cladding layer. The lower AlGaAs–GaAs waveguide includes a 0.53 μm Al$_{0.1}$Ga$_{0.9}$As core and a 0.2 μm Al$_{0.5}$Ga$_{0.5}$As cladding layer. Those two waveguide are phase matched at 1.55 μm. Fig. 2 shows waveguide and total dispersions of 3 μm wide upper InGaAsP–InP and lower AlGaAs–GaAs waveguide calculated by a transfer matrix method with effective index approximation. The index data are taken from [6] and [7]. The waveguide dispersions of the two waveguide are very small and almost identical, so the material dispersion dominates in our vertical coupler filter. In the current structure, because of similar waveguide structures, there is only 8-nm polarization dependent wavelength shift which is much less than the value of more than 30 nm in the conventional vertical coupler filter. It is easy to realize polarization independent vertical coupler filters by replacing 1.45-μm quaternary with 1.37-μm quaternary. This is shown in Fig. 3. Since the material dispersion of 1.37-mm quaternary is a little lower than that of 1.45-μm quaternary, a small bandwidth will be sacrificed in this structure.

Using a 3-D beam propagation method (BPM), the performance of fused filters is simulated. When the separations of two waveguide $d_s = 1.2$, 1.6, and 2 μm, the corresponding coupling lengths (100% power transfer) are 1, 4.5 mm, and

2 cm and the bandwidths are 4, 0.8, and 0.2 nm at the coupling length. As we expected, the central wavelength is independent of the separation distance of two waveguides and the bandwidth is inversely proportional to the coupler length. Because of uniform coupling, there is a −9-dB sidelobe, which is too high for practical application. By using an X-crossing structure [12], the sidelobe can be suppressed to more than −40 dB, which satisfies the requirement of most WDM systems. Fig. 4 shows the calculated response of an X-crossing fused vertical coupler with a crossing angle $\theta = 0.16°$ using coupled mode theory. One should note that the fabrication of an X-crossing vertical coupler filter structure with separated inputs and outputs is very easy with the use of wafer fusion technology.

We have fabricated a fused straight ($\theta = 0°$) vertical coupler filter based on MBE grown GaAs and MOCVD grown InP waveguide. The structure is shown in Fig. 1(b) and the separation of the two waveguides is 1.2 μm, which corresponds to 1-mm coupling length. A 3 mm long device has been measured. Fig. 5 shows the measured response. The 3-dB bandwidth is 1.2 nm, which agrees very well with theoretical value of 1.3 nm. The measured coupling efficiency (the optical power from the output waveguide divided by the sum of the optical power from both the

Fig. 5. The measured response of a 5-μm-wide fused vertical coupler.

difference between InGaAsP–InP and AlGaAs–GaAs waveguide, this kind of fused filters will be very promising in WDM systems. Furthermore, these fused waveguide structures can be used to realize tunable wavelength lasers and wavelength selective detectors.

output and input waveguide) of the current device is about 50%. The polarization dependent wavelength shift is only 5 nm. Theoretical calculations predict a 7-nm shift, and as shown in Fig. 3, this polarization dependence can be eliminated with proper design. To optimize the design of fused InP–GaAs coupler, one should take into account material losses. The bandgap of InGaAsP guiding layer is closer than GaAs–AlGaAs material to the operation wavelength at 1.55 μm. One thus expects larger band-to-band absorption in InGaAsP waveguides. However in doped materials, free carrier absorption increases and dominates when the wavelength is farther from the bandgap. We have measured 4–6-dB/cm optical propagation loss for both InP–InGaAsP and GaAs–AlGaAs waveguides at 1.55 μm. We did not notice substantial increase in loss for the lower bandgap material InGaAsP. The fusion process adds 1–3-dB/cm loss [10].

In conclusion, a novel fused vertical coupler filter has been demonstrated. Due to its inherent polarization-independence and narrowband that comes from a large material dispersion

REFERENCES

[1] R. C. Alferness and R. V. Schmidt, "Tunable optical wavelength directional coupler filter," *Appl. Phys. Lett.*, vol. 33, no. 2, pp. 161–163, 1978.

[2] C. Wu, C. Rolland, N. Puetz, R. Bruce, K. D. Chik, and J. M. Xu, "A vertically coupled InGaAsP/InP directional coupler filter of ultranarrowbandwidth," *IEEE Photon. Technol. Lett.*, vol. 3, pp. 519–521, June 1991.
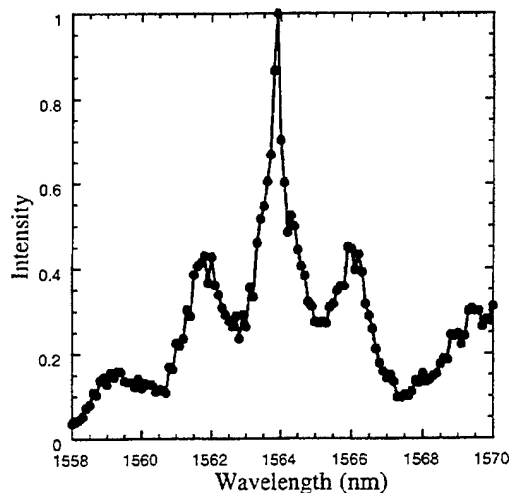
[3] R. C. Alferness, L. L. Buhl, U. Koren, M. G. Young, T. L. Koch, C. A. Burrus, and G. Raybon, "Broadly tunable InGaAsP/InP buried rib waveguide vertical coupler filter," *Appl. Phys. Lett.*, vol. 60, pp. 980–982, 1992.

[4] C. Wu, C. Rolland, F. Shepherd, C. Larocque, N. Puetz, K. D. Chik, and J. M. Xu, "InGaAsP/InP vertical directional coupler filter with optimally designed wavelength tunability," *IEEE Photon. Technol. Lett.*, vol. 4, pp. 457–459, Apr. 1993.

[5] R. J. Deri, M. A. Emanuel, F. G. Patterson, S. P. Dijaili, and L. T. Naguyen, "Polarization-insensitive wavelength filters by birefringence compensation of vertical couplers," *Appl. Phys. Lett.*, vol. 68, no. 8, pp. 1037–1039, 1996.

[6] "Properties of indium phosphide," emis DATAREVIEWS SERIES, no. 6. London, U.K.: INSPEC, 1991, pp. 422–427.

[7] "Properties of aluminum gallium arsenide," S. Adachi, Ed., emis DATAREVIEWS SERIES, no. 7. London, U.K.: INSPEC, 1993, pp. 126–140.

[8] A. Black, A. R. Hawkins, N. M. Margalit, D. I. Babic, A. L. Holmes, Jr., Y. L. Chang, P. Abraham, J. E. Bowers, and E. L. Hu, "Wafer fusion: Materials issues and devices results," *IEEE J. Select. Topics Quantum Electron.*, vol. 3, pp. 937–951, June 1997.

[9] Z. H. Zhu, F. E. Ejeckam, Y. Qian, J. Zhang, G. L. Christensen, and Y. H. Lo, "Wafer bonding technology and its application in optoelectronic devices and material," *IEEE J. Select. Topics Quantum Electron.*, vol. 3, pp. 927–936, June 1997.

[10] B. Liu, A. Shakouri, P. Abraham, B. G. Kim, A. W. Jackson, and J. E. Bowers, "Fused vertical couplers," *Appl. Phys. Lett.*, vol. 72, no. 21, pp. 2637–2638, 1998.

[11] A. Shakouri, B. Liu, B. G. Kim, P. Abraham, A. W. Jackson, A. Gossard, and J. E. Bowers, "Wafer fused optoelectronics for switching," *J. Lightwave Technol.*, to be published.

[12] S. T. Chu, W. Pan, S. Sato, B. Little, and Y. Kokubum, "Reduction of filter sidelobe level by an X-crossing vertical coupler ARROW filter," *IEEE Photon. Technol. Lett.*, vol. 10, pp. 391–393, Mar. 1998.

25-GHz Polarization-Insensitive Electroabsorption Modulators with Traveling-Wave Electrodes

Sheng Z. Zhang, Yi-Jen Chiu, Patrick Abraham, and John E. Bowers, *Fellow, IEEE*

Abstract— Electroabsorption modulators with traveling-wave electrodes have been designed and fabricated using MOCVD grown InGaAsP–InGaAsP quantum wells. A modulation bandwidth of 25 GHz is achieved for a 2-μm-wide 300-μm-long device. Driving voltage of 1.20 V is achieved for an extinction ratio of 20 dB for operation at 1.55 μm.

Index Terms—Electroabsorption, optical fiber communication, optical modulation, quantum-confined Stark effect, quantum-well devices, traveling-wave devices.

I. INTRODUCTION

ELECTROABSORPTION (EA) modulators are very attractive devices for optical fiber communications because of their very low driving voltage, very high modulation efficiency and integratibility with lasers [1]. However, conventional EA modulators are lumped-electrode devices, whose speeds are limited by the total parasitics of the devices, which restricts the devices to very short length for high-speed operation [2]–[4]. One way to overcome the parasitic limitation is by integrating passive waveguides with a short absorption section [2]–[3]. However, this kind of device with short active regions has lower extinction ratio and requires relatively higher driving voltage. On the other hand, a traveling wave electrode structure can overcome the *RC* limitation and allows for longer devices for the same speed requirement, which potentially lowers the required driving voltage, increases the extinction ratio and the optical saturation power [5]–[7].

In this letter, we demonstrate 1.55-μm traveling-wave EA modulators (TEAM) fabricated with MOCVD grown InGaAsP–InGaAsP quantum wells. We also examine the effect of load termination on the high-speed performance.

II. DESIGN AND FABRICATION

A coplanar waveguide (CPW) electrode structure is designed for both the microwave feed line region and the optical waveguide region [7]–[8]. Fig. 1 shows the SEM picture of a 300-μm-long device. The feed line is 500 μm long on each side of the optical waveguide. The ridge is formed by CH$_4$/H$_2$/Ar reactive ion etch (RIE) followed by a HCl:H$_3$PO$_4$ wet etch to reduce RIE damage. PMGI is used to passivate the sidewalls and to reduce the capacitance due to the p-electrode on the
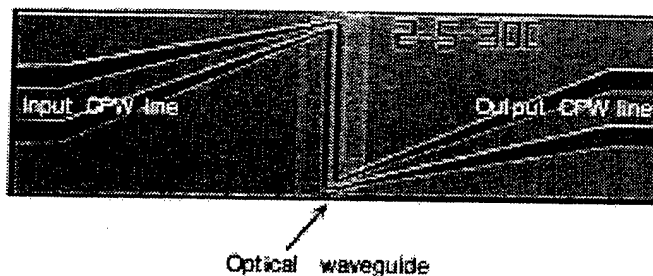
Fig. 1. SEM picture of the top view of a 300-μm traveling-wave EA modulator.
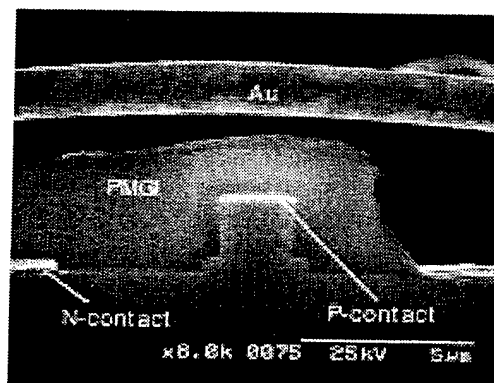
Fig. 2. SEM facet view of a cleaved modulator with a ridge width of 2 μm.

optical waveguide. As shown in the figure, PMGI bridges are formed on both ends of the optical waveguide to connect grounds from different sides of the optical waveguide.

The material structure consists of 0.5-μm n$^+$-InP bottom contact layer, 0.3-μm n-InP cladding layer, ten strain-compensated InGaAsP quantum well (10.4 nm, 0.37% tensile strain) and InGaAsP barrier (7.6 nm, 0.5% compressive strain), 1.5-μm p-InP cladding layer and 0.1-μm p$^+$-InGaAs top contact layer on the semi-insulating InP substrate. The material has a room temperature photoluminescence (PL) peak at 1495 nm. Fig. 2 shows the SEM facet view of a cleaved device with a width of 2 μm.

III. EXPERIMENTAL RESULTS

A lens pair is used to couple light from fiber to the waveguide and vice versa. High-frequency measurements are performed with an HP Lightwave Component Network Analyzer. Two Cascade probes are used for the microwave connection and one of the probes is terminated with a 50-Ω load.

Fig. 3. Fiber-to-fiber transmission versus reverse bias voltage for several wavelengths and for TE and TM polarization states. Solid: TE polarization, Dashed: TM polarization.
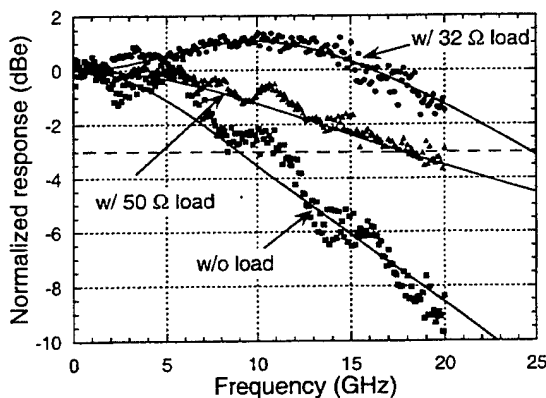
Fig. 4. Measured and simulated EO responses (in dBe) for a 2-μm wide 300-μm-long traveling-wave modulator. Curves: Theory. Dots: Measurement.

Fig. 3 shows the fiber-to-fiber transmission. versus reverse bias voltage for several wavelengths and for TE and TM polarization states. The device shows little dependence on the polarization, which is a result of proper bandgap engineering. The 2-μm-wide 300-μm-long device has driving voltages of 1.20 and 1.28 V for 20 dB extinction ratio for TE and TM modes respectively at wavelength of 1.55 μm. A fiber-to-fiber insertion loss of 13.6 dB is achieved at 1.57 μm for TM polarization without antireflection coating.

An equivalent circuit model is used to simulate the electrical to optical response performance [8]. Three different cases are compared: 1) no termination, 2) with 50-Ω termination, and 3) with 32-Ω termination. The calculated EO responses are shown as lines in Fig. 4.

The frequency responses at three different terminations are measured and shown as dots in Fig. 4. The 32-Ω termination is achieved by wire bonding a thin-film resistor to the device. With a 50-Ω termination, a bandwidth of 18 GHz is obtained, yielding a bandwidth to driving voltage (0.8 V for 10-dB extinction) ratio of 22.5 GHz/V. The bandwidth reduces to 10.7 GHz when there is no termination. The reason for this large bandwidth reduction is the large reflection from the unterminated port. The capacitance and the series resistance of the device deduced from the electrical S_{11} measurement are 0.40 pF and 4.6 Ω, which infers RC limited bandwidths of 7.3
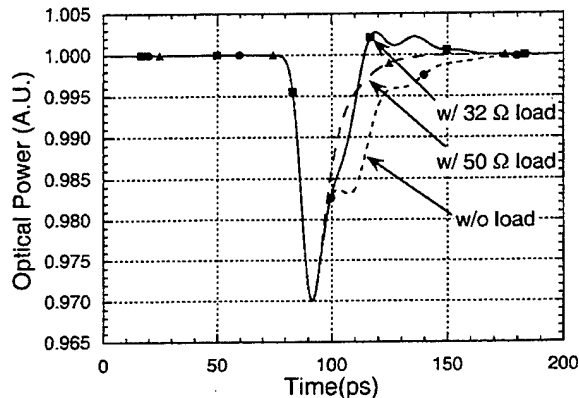
Fig. 5. Simulated optical output under the modulation of a Gaussian pulse.

and 13.4 GHz for cases with and without a 50-Ω termination. The larger bandwidth for the TEAM than that for the lumped device confirms that traveling-wave electrode structure can overcome the RC limitation.

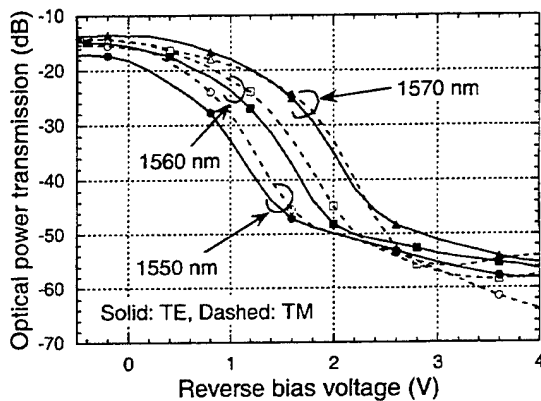The bandwidth for the case with a 32-Ω termination increases to about 24.5 GHz, yielding a bandwidth to driving voltage (0.8 V for 10-dB extinction) ratio of 30.6 GHz/V.

IV. DISCUSSION

The key feature on the response curve with 32-Ω termination is the resonance peak, which is mainly caused by the microwave reflections at the load and the source ends and at the interfaces between the optical waveguide and the feed lines. Because of the negative reflection at the load, the response at some frequencies is enhanced. This can be seen in Fig. 5, which shows the simulated optical signal output under small signal modulation. Here, a Gaussian-shaped pulse with $T_{\mathrm{FWHM}} = 10\ \sqrt{\ln 2}$ ps and an amplitude of 0.07 V is used as the modulation signal that superimposes on a dc bias level of 1.2 V. Without any load termination, the output optical pulse profile shows multiple reflection structures that come from the interfaces between the optical waveguide and the feed line, and between the feed lines and the source/load. These reflections have the same sign as the output signal because both the source and the load have higher impedance than the waveguide (characteristic impedance $\sim$25 Ω) and the feed line (characteristic impedance $\sim$42 Ω). The reflections become much weaker when a 50-Ω termination is used. The reflection changes the sign when the load impedance is reduced to 32 Ω and cancels the reflection at the connections between the optical waveguide and the feed lines. This cancellation in reflection causes a frequency response enhancement at high frequencies. This is another proof that the device is operating in a traveling-wave mode. The inductance due to the ribbon is about 0.07 nH and is not the main reason for this resonance as verified by simulation. The use of a 32-Ω load will increase the required drive voltage, which is about 1.2 times that required for a load of 50 Ω. This could be overcome by the longer device length than that of conventional EA modulators.

To separate the microwave propagation loss from the impedance-mismatch induced reflection loss, the microwave transmission (S_{21}) for devices with lengths of 300, 400,

500, and 600 μm was measured. It is found that at 20 GHz, the 600-μm devices have about 2.0-dB extra loss than 300-μm devices. This suggests that for the 300-μm device, the propagation loss at 20 GHz is about 2.0 dB, while the sum of the reflection loss and the other excess loss is about 1.0 dB since the total microwave loss is 3.0 dB. Consequently, to improve the device bandwidth, we need to reduce the propagation loss and increase the waveguide characteristic impedance to reduce the reflection loss.

The improvement in bandwidth with terminating the transmission line is larger for longer devices, as expected for a traveling-wave modulator. However, the propagation loss (about 0.67 dB/100 μm at 20 GHz) is the dominant factor that limits the bandwidth in longer devices.

Long distance digital transmission has been demonstrated at 10 and 30 Gb/s with the 300-μm traveling-wave modulator and will be presented in the future.

V. CONCLUSION

We have demonstrated traveling-wave electroabsorption modulators using the InGaAsP–InGaAsP–InP material system. For a 300-μm-long device, a modulation bandwidth of 25 GHz is achieved. The devices show little dependence on the polarization state. Driving voltages of 1.20 and 1.28 V are achieved for an extinction ratio of 20 dB for TE and TM modes. A resonance effect is observed for devices terminated with 32-Ω loads. This resonance effect is the result of microwave reflections at the source and the load ends. These results show that with good design, traveling-wave EA modulators can overcome the *RC* limitation and obtain higher speed, lower driving voltage and larger extinction ratio for optical fiber communication applications.

REFERENCES

[1] F. Devaux and A. Carenco, "Optical processing with electroabsorption modulators," in *OFC'98 Tech. Dig.*, 1998, pp. 285–287, paper ThH3.
[2] F. Devaux, S. Chelles, A. Ougazzaden, A. Mircea, and J. C. Harmand, "Electroabsorption modulators for high-bit-rate optical communications: A comparison of strained InGaAs/InAlAs and InGaAsP/InGaAsP MQW," *Semiconduct. Sci. Technol.*, vol. 10, pp. 887–901, 1995.
[3] T. Ido, S. Tanaka, M. Suzuki, M. Koizumi, H. Sano, and H. Inoue, "Ultra-high-speed multiple-quantum-well electro-absorption optical modulators with integrated waveguides," *J. Lightwave Technol.*, vol. 14, pp. 2026–2034, 1996.
[4] K. Wakita, K. Yoshino, I. Kotaka, S. Kondo, and Y. Noguchi, "High-speed, high efficiency modulator with polarization insensitive and very low chirp," *Electron. Lett.*, vol. 31, pp. 2041–2042, 1995.
[5] K. Kawano, M. Kohtoku, M. Ueki, T. Ito, S. Kondoh, Y. Noguchi, and Y. Hasumi, "Polarization-insensitive travelling-wave electrode electroabsorption (TW-EA) modulator with bandwidth over 50 GHz and driving voltage less than 2 V," *Electron. Lett.*, vol. 33, pp. 1580–1581, 1997.
[6] H. Liao, X. Mei, K. Loi, and C. Tu, "Microwave structures for traveling-wave MQW electro-absorption modulators for wide band 1.3 μm photonic links," *Proc. SPIE*, vol. 3006, pp. 291–300, 1997.
[7] S. Zhang, Y. Chiu, P Abraham, and J. Bowers, "Polarization-insensitive multiple-quantum-well traveling-wave electroabsorption modulators with 18 GHz bandwidth and 1.2 V driving voltage at 1.55 μm," in *Int. Topical Meeting Microwave Photonics (MWP'98)*, Princeton, NJ, Oct., 1998, pp. 33–36, paper MC2.
[8] K. Giboney, M. Rodwell, and J. Bowers, "Traveling-wave photodetector theory," *IEEE Trans. Microwave Theory Tech.*, vol. 45, pp. 1310–1319, 1997.

Summary: We have proposed a novel scheme for in-line optical regeneration in RZ transmission systems. The scheme is based on the principle of black box RZ/soliton conversion, synchronous modulation and filtering, followed by reverse soliton/RZ conversion. Potential applications range from SMF-based terrestrial systems to dispersion-managed soliton systems for global-distance transmission.

P. Brindel, B. Dany, O. Leclerc and E. Desurvire (*Alcatel-CIT, Corporate Research Centre, Route de Nozay, 91460 Marcoussis, France*)

E-mail: Patrick.Brindel@alcatel.fr

References

1   CHIARONI. D., LAVIGNE. B., JOURDAN. , HAMON. L., JANZ. C., and RENAUD. M.: 'New 10Gbit/s 3R NRZ optical regenerative interface based on semiconductor optical amplifiers for all-optical networks'. ECOC'97, 1997, Vol. 5-PDP, pp. 41–44
2   NAKAZAWA. M., YAMADA. E., KUBOTA. H., and SUSUKI. K.: '10Gbit/s soliton data transmission over one million kilometres', *Electron. Lett.*, 1991, **27**, (14), pp. 1270–1271
3   LUCEK. J.K., and SMITH. K.: 'All-optical signal regenerator'. *Opt. Lett.*, 1993, **18**, (15), pp. 1226–1228
4   BIGO. S., LECLERC. O., BRINDEL. P., VENDROME. G., DESURVIRE. E., DOUSSIERE. P., and DUCELLIER. T.: 'All-optical regenerator for 20Gbit/s transoceanic transmission', *Electron. Lett.*, 1997. **33**, (11), pp. 975–976

Fused III-V vertical coupler filter with reduced polarisation sensitivity

B. Liu, A. Shakouri, P. Abraham, Y.J. Chiu and J.E. Bowers

A novel fused InGaAsP/InP-AlGaAs/GaAs vertical coupler filter is demonstrated. By using the large material dispersion between InGaAsP and AlGaAs and similar waveguide geometries, a 3.6nm bandwidth and 5nm polarisation dependent wavelength shift using a 1.1mm long fused vertical coupler has been achieved.

Introduction: Dense wavelength division multiplexing (DWDM) requires narrowband optical filters and add/drop channel multiplexer/demultiplexers. Asymmetrical vertical directional coupler filters [1 – 4] using two dissimilar waveguides on III-V semiconductors are promising because of their inherent on- chip integration with other optoelectronic devices and ease of fabrication. In conventional vertical coupler filters, both waveguides are fabricated using the same material system, InGaAsP/InP [2 – 4] or AlGaAs/GaAs. A narrow bandwidth requires a strong waveguide dispersion difference between two waveguides. This is usually achieved using dissimilar waveguide geometries. One of the waveguides is narrow with high index contrast. And the other wide with low index contrast. There are several obstacles to the use those vertical coupler filters, including a strong polarisation dependence (the centre wavelength shift for TE and TM modes is > 60nm), a large difference in coupling efficiency between the two dissimilar waveguides, and the difficulty of launching the light into and coupling light out of two very close waveguides. Since the polarisation dependence and different coupling efficiency come from the strong asymmetry of two waveguide geometries, these problems can be solved if the two waveguides have similar structures and indices, but they have a large material dispersion difference.

In this Letter, we report a novel vertical coupler filter (VCF) based on wafer fusion technology [5, 6], which combines two different material systems: InGaAsP/InP and AlGaAs/GaAs. By utilising the large material dispersion difference between InGaAsP

and AlGaAs around 1.55µm wavelength to realise narrowband filters using similar waveguide geometry which ensures that both waveguides have almost identical waveguide dispersions (same birefringence), it is possible to considerably reduce the polarisation sensitivity of the vertical coupler filter. Furthermore, wafer fusion can facilitate the separation of the waveguides at the input and at the output [7, 8].

b
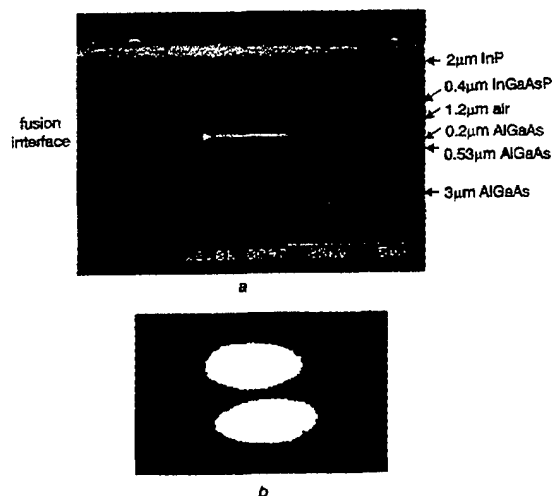
Fig. 1 *SEM photograph of fused InGaAsP/InP-AlGaAs/GaAs vertical coupler filter and near field of fused coupler filter*

a SEM photograph
b Near field

Fabrication: The structure of the fused vertical coupler filter is shown in Fig. 1. The upper InGaAsP/InP waveguide consists of a 0.4µm InGaAsP (λ_{gap} = 1.45µm) guiding layer and a 1.2µm InP cladding layer, which was grown on an InP substrate by metal organic chemical vapour deposition (MOCVD). The lower AlGaAs/GaAs waveguide, grown on a GaAs substrate by MBE, includes a 3µm $Al_{0.6}Ga_{0.4}As$ isolation layer, 0.53µm $Al_{0.1}Ga_{0.9}As$ core layer, 0.2µm $Al_{0.5}Ga_{0.5}As$ cladding layer and 200nm GaAs cap layer that serves to protect the AlGaAs layer from oxidation. The two waveguides are phase matched around 1.55µm. 3D BPM calculations predict a 1mm coupling length. To fabricate the fused vertical coupler filter, rib waveguides with a ridge height of 1.2µm and 3–6µm widths on an InP sample are formed using selective wet etching. After the standard cleaning procedure, the InP sample with rib waveguides and the GaAs sample are fused together at a temperature of 630°C in a hydrogen atmosphere for 50min. Subsequently the InP substrate is removed by HCl etching. Fig. 1 shows the SEM photograph of the finished device.
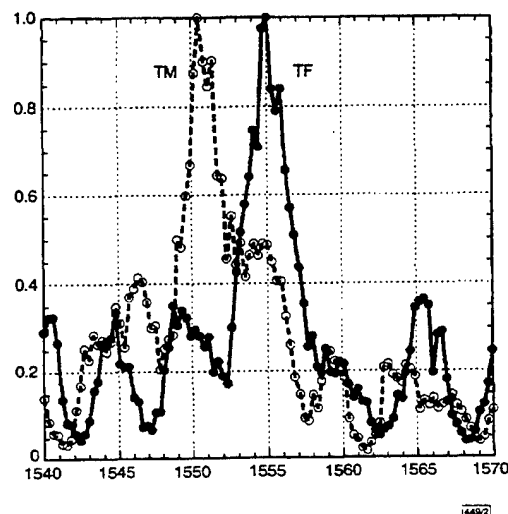
Fig. 2 *Measured response of 3µm wide fused vertical coupler filter for TE and TM modes*

Results and discussions: The optical transmission of fused vertical coupler filters is measured with polarised light from a tunable semiconductor laser that is coupled to the filters via a singlemode lensed fibre. The light at the output of the filters is coupled to another singlemode lensed fibre connected to a detector. Fig. 1*b* shows the near field image with a ×80 objective at the output of the fused vertical coupler filter. The mode profiles of the two waveguides are very similar, which is important for realising polarisation independence and similar coupling efficiency. Fig. 2 shows the transmission data for TE and TM polarised light for a 3μm wide 1.1mm long fused filter. The 3dB bandwidths of the TE and TM modes are 3.6 and 3.3nm, which closely agree with the theoretical values of 3.8 and 3.5nm. The polarisation dependent wavelength shift is only 5nm. Theoretical calculations predict a 7nm shift and this polarisation dependence can be eliminated by a slight modification to the design by replacing the 1.45μm InGaAsP with 1.37μm InGaAsP. Since the material dispersion is increased when the wavelength is near the bandgap, the 3dB bandwidth is narrower for shorter wavelength. Fig. 3 shows the dependence of bandwidth on wavelength, which is agreement with the theoretical calculations.
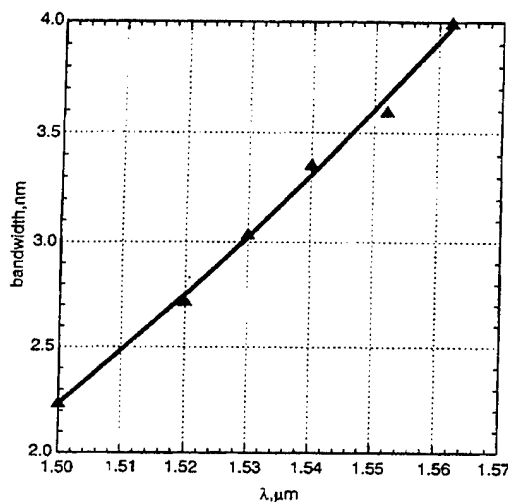
Fig. 3 *Wavelength dependence of filter bandwidth*

Summary: A novel fused InGaAsP/InP-AlGaAs/GaAs vertical coupler filter with reduced polarisation dependence has been fabricated and characterised. The large material dispersion difference between InGaAsP and AlGaAs was used to achieve narrowband filters. A polarisation dependent wavelength shift of 5nm has been achieved. The corresponding wavelength shift in conventional vertical coupler filters is > 60nm. With an improved design, polarisation-independent and narrowband fused vertical coupler filters can be realised. These filters are promising components for future WDM systems.

B. Liu, P. Abraham, Y.J. Chiu and J.E. Bowers (*Department of Electrical and Computer Engineering, University of California, Santa Barbara, CA 93106, USA*)

E-mail: liu@opto.ucsb.edu

A. Shakouri (*Jack Baskin School of Engineering, University of California, Santa Cruz, CA 95064, USA*)

References

1 ALFERNESS, R.C., and SCHMIDT, R.V.: 'Tunable optical wavelength directional coupler filter', *Appl. Phys. Lett.*, 1978, **33**, (2), pp. 161–163

2 CHI WU., ROLLAND. C., PUETZ. N., BRUCE. R., CHIK. K.D., and XU. J.M.: 'A vertically coupled InGaAsP/InP directional coupler filter of ultranarrow bandwidth', *IEEE Photonics Technol. Lett.*, 1991, **3**, (6), pp. 519–521

3 ALFERNESS. R.C., BUHL. L.L., KOREN. U., YOUNG. M.G., KOCH. T.L., BURRUS. C.A., and RAYBON. G.: 'Broadly tunable InGaAsP/InP buried rib waveguide vertical coupler filter', *Appl. Phys. Lett.*, 1992, **60**, pp. 980–982

4 CHI WU., ROLLAND. C., SHEPHERD. F., LAROCQUE. C., PUETZ. N., CHIK. K.D., and XU. J.M.: 'InGaAsP/InP vertical directional coupler filter with optimally designed wavelength tunability', *IEEE Photonics Technol. Lett.*, 1993, **4**, (4), pp. 457–459

5 BLACK. A., HAWKINS. A.R., MARGALIT. N.M., BABIC. D.I., HOLMES. A.L., Jr., CHANG. Y.L., ABRAHAM. P., BOWERS. J.E., and HU. E.L.: 'Wafer fusion: Materials issues and devices results', *IEEE J. Sel. Topics Quantum Electron.*, 1997, **3**, (3), pp. 943–951

6 ZHU. Z.H., EJECKAM. F.E., QIAN. Y., ZHANG. J., CHRISTENSEN. G.L., and LO. Y.H.: 'Wafer bonding technology and its application in optoelectronic devices and material', *IEEE J. Sel. Topics Quantum Electron.*, 1997, **3**, (3), pp. 927–936

7 LIU. B., SHAKOURI. A., ABRAHAM. P., KIM. B.G., JACKSON. A.W., and BOWERS. J.E.: 'Fused vertical couplers', *Appl. Phys. Lett.*, 1998, **72**, (21), pp. 2637–2638

8 SHAKOURI. A., LIU. B., KIM. B.G., ABRAHAM. P., JACKSON. A.W., GOSSARD. A., and BOWERS. J.E.: 'Wafer fused optoelectronics for switching', to be published in *J. Lightwave Technol.*, 16, (12), pp. 2236–2242

Increased speed of semiconductor optical amplifier wavelength converter at multiple channels using Fabry-Perot and microelectromechanical filters

D. Mahgerefteh, P.S. Cho and P. Tayebati

A Fabry-Perot optical discriminator is used to reduce the pattern dependence of a semiconductor optical amplifier wavelength converter at 10Gbit/s. In conjunction with a voltage tunable microelectromechanical bandpass filter, this allows a reduction of conversion penalty for multiple wavelength channels.

Semiconductor optical amplifier based all-optical wavelength converters are being considered for used in reconfigurable nodes of future WDM systems because of their compactness, high-speed operation and low power requirements [1]. To be cascadable, semiconductor optical amplifiers (SOAs) have to have a modulation bandwidth that exceeds the bit rate of operation. In addition the wavelength converter should be able to convert an incoming data to one of many wavelength channels as specified by a circuit control signal.

High-speed operation can be obtained by using long semiconductor optical amplifiers, high currents, and high optical powers. Bit rates as high as 40Gbit/s have been demonstrated in SOAs [2]. It was recently demonstrated that a fibre Bragg grating optical discriminator placed after the converter can also increase the dynamic bandwidth and therefore the bit rate of operation of an SOA wavelength converter [3]. As described in [3] the discriminator converts the phase modulation that accompanies the converted signal to amplitude modulation to sharpen the transition edges between the 1 and 0 bits. This requires that the wavelength of the converted data match the transmission edge of the fibre grating such that the converted spectrum lies in the linear transmission region of the grating, making it difficult to tune to different channels.

Here we use a Fabry-Perot filter with a free-spectral range of 100GHz (ITU standard) as the optical discriminator. Hence the relative spectral position of the signal and Fabry-Perot transmission spectrum remains fixed as the wavelength of the converted data is changed from one channel on the ITU grid to the other. In addition we use a voltage tunable microelectromechanical filter for channel selection [4].

Fig. 1 shows a schematic diagram of the conversion experiment. 10Gbit/s NRZ data and a CW signal are launched into an SOA in a co-propagating configuration. The SOA is a fibre-pigtailed amplifier with an unsaturated gain of 26dB at 200mA. The bias of the SOA was 145mA. The optical power of the data and CW

optical amplifier (SOA). The phase conjugated signal is produced by four-wave mixing. The wavelength shift in the SOA-OPC is −10nm. The converted signal is filtered out in two stages of 3nm filter and amplified by an EDFA. The measured conversion efficiency is −20.5dB [4]. In this system, it is assumed that the condition $\beta_2^{(1)} z_1 = \beta_2^{(2)} z_2$ is satisfied, where the amounts of total dispersion in both sections are the same. The lengths of the transmission fibres in each section are $z_1 = 51.0$km and $z_2 = 53.5$km. The dispersion values are $\beta_2^{(1)} = -21.5$ps^2/km (at 1550.5nm) and $\beta_2^{(2)} = -20.5$ps^2/km (at 1540.5nm). The input powers P_{in} at the position indicated in Fig. 1b are set to be equal. The signal is detected with a 50GHz pin photodetector. The electrical signal is mixed down with the LO, demodulated, and directed to the BER tester.
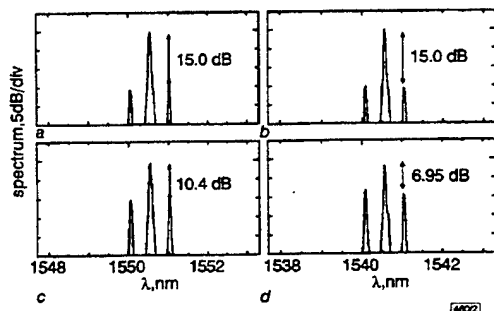

Fig. 2 *Measured optical spectra at midway OPC and at output, when input power P_{in} is 5dBm, and measured optical spectra at midway OPC and at output, when input power P_{in} is 15dBm*

a Midway OPC, $P_{in} = 5$dBm
b Output, $P_{in} = 5$dBm
c Midway OPC, $P_{in} = 15$dBM
d Output, $P_{in} = 15$dBm

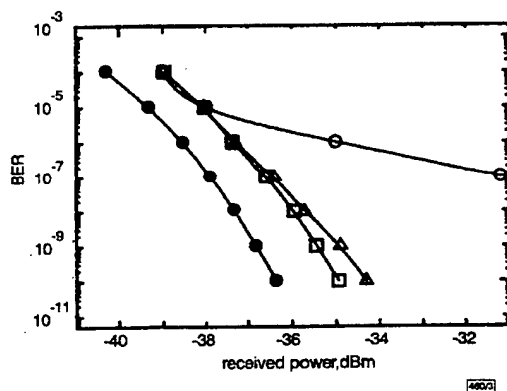**Fig. 3** *Measured BER against received optical power*

☐ Pin = 5dBm
△ Pin = 10dBm
○ Pin = 15dBm
● back-to-back
$z_1 = 51$km (at 1550.5nm), $z_2 = 53.5$km (at 1540.5nm)

Fig. 2a and b, respectively, show the spectra at the midway OPC and at the output of the system when the input power $P_{in} = 5$dBm. The nonlinear length L_{NL}, as defined by $1/\gamma P_{av}$, is calculated to be 306km. In this case, the transmission lengths z_1 and z_2 are much shorter than L_{NL}. No change in the optical spectrum is observed at both positions. Fig. 2c shows the optical spectrum at the midway OPC when $P_{in} = 15$dBm. In this case, L_{NL} is 30.6km and the transmission lengths z_1 and z_2 are longer than L_{NL}. The modulation depth, which can be observed by the power ratio of the sideband to the carrier light, becomes higher after the propagation compared with the case of $P_{in} = 5$dBm. This is because of the modulational instability [5, 6], which is induced by the small modulation of the 60GHz millimetre-wave data signal. Four-wave mixing in the anomalous dispersion regime along with SPM causes modulational instability. In an ideal OPC system, the modulational instability that occurs in the first section can be compensated for in the second section. In a practical OPC system,

however, the power change is not symmetric with respect to the OPC position, which results in distorted optical spectra. The degree of imperfect compensation becomes larger as the input power increases. Fig. 2d shows the output spectra when P_{in} is 15dBm. The distorted spectrum caused by the modulational instability is also observed despite the use of the midway OPC. Compared with the case in which the midway OPC is not inserted, where the power of the sideband is only −5.65dB below the carrier, the distortion caused by GVD and SPM is partially compensated for by the midway OPC. The measured BERs are plotted in Fig. 3. No error floor is observed when the input power is <5.0dBm. With increasing input power, the error floor is clearly observed. The error floor is produced by the asymmetric power change. A comparison of L_{NL} with the transmission lengths z_1 and z_2 shows that the OPC must be inserted at the position where the transmission length is much less than the nonlinear length.

Conclusion: We have observed the limitation of the midway OPC system applied for 60GHz SCM optical DSB signal transmission. The BER degradation was caused by the asymmetry of the power change in the sections of fibre on either side of the OPC. These results indicate that the transmission length before and after the OPC must be much less than the nonlinear length.

H. Sotobayashi and K. Kitayama (*Communications Research Laboratory, Ministry of Posts and Telecommunications, Lightwave Network Section, Photonic Technology Division, 4-2-1, Nukui-Kita, Koganei, Tokyo 184-8795, Japan*)

E-mail: soba@crl.go.jp

K. Kitayama: Now with Osaka University, Department of Electronics and Information Systems, Graduate School of Engineering, Osaka, Japan

References

1 WATANABE, S., NAITO, T., and CHIKAMA, T.: 'Compensation of chromatic dispersion in a single-mode fiber by optical phase conjugation', *IEEE Photonics Technol. Lett.*, 1993, **5**, pp. 92-95
2 MESLENER, G.J.: 'Chromatic dispersion induced distortion of modulated monochromatic light employing direct detection', *IEEE J. Quantum Electron.*, 1984, **QE-20**, pp. 1208–1216
3 MARTI, J., and RAMOS, F.: 'Compensation for dispersion-induced nonlinear distortion in subcarrier systems using optical-phase conjugation', *Electron. Lett.*, 1997, **33**, pp. 792–794
4 KITAYAMA, K., and SOTOBAYASHI, H.: 'Fading-free fiber-optic transport of 600Hz-optical DSB signal by using in-line phase conjugator'. Optical Fiber Communication Conf. (OFC '99), San Diego, February 1999, Paper WD4
5 HASEGAWA, A., and BRINKMAN, W.F.: 'Tunable coherent IR and FIR sources utilizing modulational instability', *IEEE J. Quantum Electron.*, 1980, **QE-16**, (7), pp. 694–697
6 HASEGAWA, A.: 'Generation of a train of soliton pulses by induced modulational instability in optical fibers', *Opt. Lett.*, 1984, **9**, (7), pp. 288–290

High-speed operation of travelling-wave electroabsorption modulator

V. Kaman, S.Z. Zhang, A.J. Keating and J.E. Bowers

The authors describe the high-speed operation of an electroabsorption modulator with travelling-wave electrodes. The modulator exhibited good performance over a broad bandwidth in 10 and 30Gbit/s transmission experiments. The polarisation-insensitive electroabsorption modulator required a low switching voltage of ~ 1.6V$_{p-p}$.

Introduction: The speed of optical fibre telecommunication systems based on electrical time division multiplexing has increased rapidly over the last decade enabling 40Gbit/s throughput for a single carrier [1, 2]. Electroabsorption (EA) modulators with very low driving voltage, high modulation efficiency, polarisation insensitivity

and integrability with lasers [3 - 6], make them very attractive devices for optical communications systems. The bandwidth of EA modulators based on a lumped-electrode structure is limited by the total capacitance; short lengths result in high bandwidths while longer devices exhibit better extinction ratios, necessitating a tradeoff between bandwidth and extinction ratio. Recently, it has been shown that longer devices with potentially lower drive voltages and increased extinction ratio can be achieved using a travelling-wave electrode structure that overcomes the RC limitation [7, 8].

We have recently demonstrated a polarisation-insensitive travelling-wave EA modulator operating at 1.55μm, with a bandwidth of 25GHz and a 20dB extinction ratio (DC) voltage of 1.20 and 1.28V for the TE and TM modes, respectively [9]. In this Letter, we report on the 10 and 30Gbit/s operation of this modulator.

Modulator characteristics: The travelling-wave EA modulator used in this experiment is similar to the device described in [9]. The device was designed to be polarisation-insensitive over a range of wavelengths. The fibre-to-fibre insertion loss was 16dB at 1542nm. A drive voltage of 2V was required for a maximum extinction ratio (DC) of 30dB. The 25GHz bandwidth was achieved by terminating the travelling-wave electrode in a low resistance using a thin-film resistor.
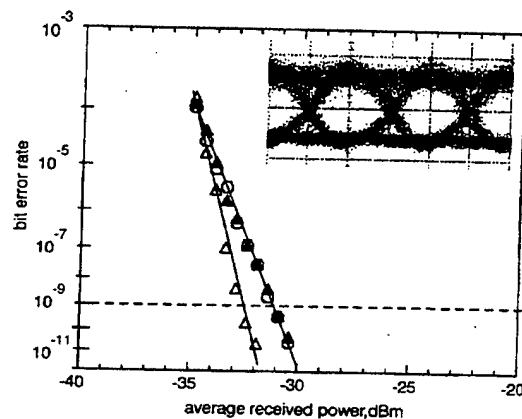
Fig. 1 *Bit error rate curves for 10Gbit/s transmission*

Inset: Received eye diagram after 150km transmission (H: 50ps/div, V: 80mV/div)
▲ back-to-back, TM mode
○ back-to-back, TE mode
△ 150km DSF transmission

10Gbit/s transmission: Transmission experiments using the travelling-wave EA modulator at 10Gbit/s were carried out (2^31-1 pattern length) with commercially available components. A drive voltage of ~ 1.6V_pp was applied to the EA modulator by high-speed probes. A DFB laser operating at 1542nm followed by a polarisation controller was used as the light source into the EA modulator. Two lens pairs were used to couple the light into and out of the modulator. The output signal from the EA modulator was amplified by an erbium-doped fibre amplifier (EDFA) before it was launched into 150km of dispersion-shifted fibre (DSF) with a mean dispersion parameter of –0.93ps/(nm-km). The α parameter of the modulator was +1.2 at the operating bias of –1.1V. Fig. 1 shows the bit error rate (BER) performance of the EA modulator for back-to-back and > 150km of DSF. In the back-to-back measurements, error-free operation and a sensitivity of –31.2dBm were achieved for both the TM and the TE polarisations without changing the operating conditions of the modulator. This indicates that the polarisation dependence of the EA modulator is very low. An improved sensitivity of –32.8dBm was achieved after 150km DSF transmission due to the interplay between the positive chirp of the modulator and the slightly negative dispersion of the fibre. The inset in Fig. 1 shows the received eye diagram after transmission over 150km of DSF fibre. The long pattern length used in this transmission indicates the good low-frequency characteristics for this modulator.

30Gbit/s transmission: To explore the higher-speed characteristics of the EA modulator, transmission experiments at 30Gbit/s were carried out using the setup shown in Fig. 2. The 30Gbit/s NRZ electrical signal was generated by multiplexing four 7.5Gbit/s (2^7-1 pattern length) data streams delayed by 10 bits from each other using a 4:1 multiplexer (MUX) [10]. The pattern length was limited by the receiver electronics; however, excellent low frequency performance of the EA modulator was confirmed with the 10Gbit/s transmission experiment described earlier. At the receiver, an EDFA was used as an optical preamplifier into the packaged receiver with a 30GHz bandwidth [11]. Broadband electrical amplifiers followed the optical receiver and the signal was fed into a 30Gbit/s 1:4 demultiplexer (DMUX) and a clock recovery circuit (CRC) [10].
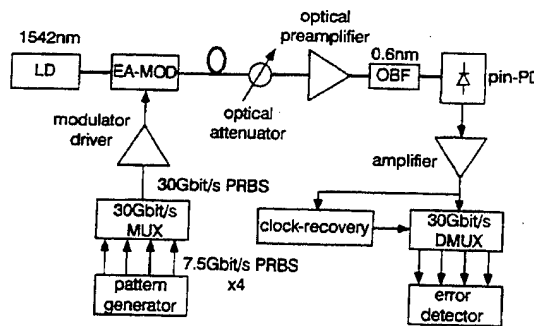
Fig. 2 *Schematic diagram of 30Gbit/s setup*
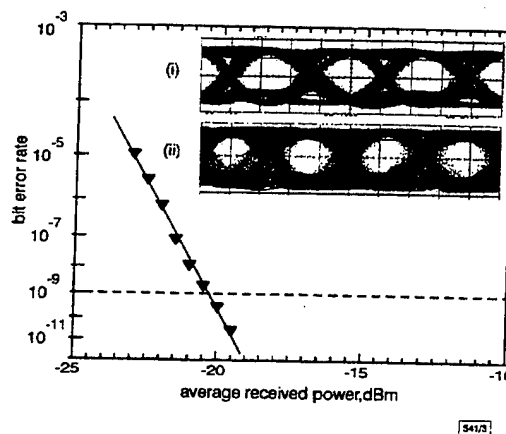
Fig. 3 *Bit error rate for back-to-back 30Gbit/s transmission*

Inset: (H: 13ps/div, V: 100mV/div)
(i) 30Gbit/s output signal from 4:1 MUX
(ii) received back-to-back 30Gbit/s signal

Fig. 3 shows the BER performance of the travelling-wave EA modulator for back-to-back transmission at 30Gbit/s. Error-free operation and an optical sensitivity of –20.2dBm were achieved for the best demultiplexed channel. The inset in Fig. 3 shows (a) the 30Gbit/s output of the 4:1 MUX and (b) the received 30Gbit/s signal after back-to-back transmission. The slight eye closure on every other channel, we believe, is due to an on-chip clock-phase alignment problem in the electrical MUX. Improvement in the 30Gbit/s optical sensitivity should be possible by improving the receiver and the fibre coupling into and out of the EA modulator.

Summary: We have successfully demonstrated 10 and 30Gbit/s operation of a travelling-wave EA modulator. These experiments confirmed a broad bandwidth and a low switching voltage for these modulators. Our results indicate that travelling-wave EA modulators, with their low driving voltage and polarisation-insensitivity, are strong candidates for future high-speed optical communication systems.

V. Kaman, S.Z. Zhang, A.J. Keating and J.E. Bowers (*Department of Electrical and Computer Engineering, University of California, Santa Barbara, CA 93106, USA*)

E-mail: kaman@opto.ucsb.edu

References

1 BOGNER, W., GOTTWALD, E., SCHOPFLIN, A., and WEISKE, C.-J.: '40 Gbit/s unrepeatered optical transmission over 148 km by electrical time division multiplexing and demultiplexing', *Electron. Lett.*, 1997, 33, pp. 2136–2137

2 HAGIMOTO, K., YONEYAMA, M., SANO, A., HIRANO, A., KATAOKA, T., OTSUJI, T., SATO, K., and NOGUCHI, K.: 'Limitations and challenges of single-carrier full 40-Gbit/s repeater system based on optical equalization and new circuit design'. OFC '97 Tech. Dig., 1997, Paper ThC1, pp. 242–243

3 YOSHINO, K., WAKITA, K., KOTAKA, I., KONDO, S., NOGUCHI, Y., KUWANO, S., TAKACHIO, N., OTSUJI, T., IMAI, Y., and ENOKI, T.: '40 Gbit/s operation of InGaAs/InAlAs MQW electroabsorption modulator module with very low driving-voltage'. Proc. ECOC '96 Tech. Dig., 1996, pp. 203–206

4 TAKEUCHI, H., TSUZUKI, K., SATO, K., YAMAMOTO, M., ITAYA, Y., SANO, A., YONEYAMA, M., and OTSUJI, T.: 'NRZ operation at 40Gb/s of a compact module containing an MQW electroabsorption modulator integrated with a DFB laser', *IEEE Photonics Technol. Lett.*, 1997, 9, pp. 572–574

5 IDO, T., TANAKA, S., and INOUE, H.: 'MQW electroabsorption modulators for 40-Gbit/s TDM systems'. OFC '97 Tech. Dig., 1997, Paper WG5, pp. 140–141

6 DEVAUX, F., BORDES, P., OUGAZZADEN, A., CARRE, M., and HUET, F.: 'Experimental optimisation of MQW electroabsorption modulators with up to 40GHz bandwidths', *Electron. Lett.*, 1994, 30, pp. 1347–1348

7 KAWANO, K., KOHTOKU, M., UEKI, M., ITO, T., KONDOH, S., NOGUCHI, Y., and HASUMI, Y.: 'Polarisation-insensitive travelling-wave electrode electroabsorption (TW-EA) modulator with bandwidth over 50GHz and driving voltage less than 2V', *Electron. Lett.*, 1997, 33, pp. 1580–1581

8 JAGER, D., STOHR, A., and HEINZELMANN, R.: 'Advanced microwave photonic devices for analog optical links'. 1998 Int. Topical Meeting on Microwave Photonics (MWP'98), 1998, Paper TuC1, pp. 153–156

9 ZHANG, S., CHIU, Y., ABRAHAM, P., and BOWERS, J.: '25GHz polarization-insensitive electroabsorption modulators with traveling-wave electrodes', *IEEE Photonics Technol. Lett.*, 1999, 11, pp. 191–193

10 RUNGE, K., ZAMPARDI, P.J., PIERSON, R.L., THOMAS, P.B., BECCUE, S.M., YU, R., and WANG, K.C.: 'High speed AlGaAs/GaAs HBT circuits for up to 40Gb/s optical communication'. IEEE GaAs Symp., 1997, pp. 211–214

11 PETERSEN, A.K., REYNOLDS, T., NAGARAJAN, R., WEY, Y.-G., BOWERS, J.E., and RODWELL, M.: '3MHz – 30GHz traveling-wave optical front-end receiver'. OFC '95 Tech. Dig., 1995, Paper WM4, pp. 157–158

Increased input power dynamic range of Mach-Zehnder wavelength converter using a semiconductor optical amplifier power equaliser with 8dBm output saturation power

J.-Y. Emery, B. Lavigne, C. Porcheron, C. Janz,
F. Dorgeuille, F. Pommereau, F. Gaborit, I. Guillemot-
Neubauer and M. Renaud

A two-section semiconductor optical amplifier is proposed and investigated for use as a power equaliser, providing a 3dB output saturation power of 8 ± 1dBm. Using the device to control the input power of a Mach-Zehnder wavelength converter, an increase in the input power dynamic range of the converter from 2.5 to > 20dB is demonstrated at 10Gbit/s.

Introduction: Semiconductor optical amplifiers (SOAs) are promising devices for optical system applications such as amplification,

switching and wavelength conversion. Recently, a power equalisation function has been identified as important in order to increase the low input power dynamic range of optical wavelength converters based on interferometric structures [1 – 3]. Single SOA devices can provide power equalisation, but the usable output power is limited because of the dependence of the output saturation power on the driving current. As a consequence, the input power dynamic range of the equaliser is also limited. By cascading two optical amplifiers the capability of increasing the output power saturation of the power equaliser has been demonstrated [2, 4]. In such a device, the input signal power is controlled by the first amplifier while the second amplifier maintains a sufficient gain and a high output saturation power. By cascading an SOA and an Er-doped fibre amplifier, the input power dynamic range of an interferometric wavelength converter has previously been increased from 3 to 28dB [1]. Recently, 5 dBm output saturation power has been demonstrated in a two-section SOA based on a multiquantum well structure [4].

In this Letter, we report an optical power equaliser based on a two-section SOA which provides 8dBm output saturation power. 10Gbit/s experiments with NRZ signal have been carried out using the two-section SOA to control the input power of a Mach-Zehnder interferometer (MZI) wavelength converter. Control of the bias current in the first section enables us to increase the input power dynamic range of the MZI from 2dB to > 20dB with a sensitivity penalty of < 1dB.
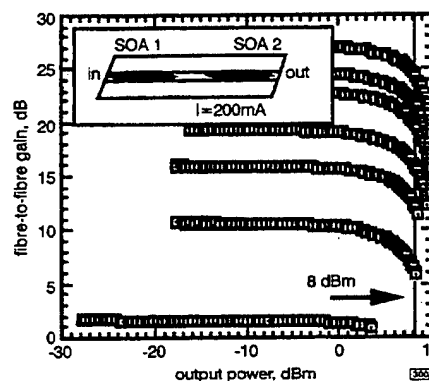
Fig. 1 *Fibre-to-fibre gain against output power measured at 1.55μm for different bias currents in first section of SOA power equaliser*

Inset: schematic diagram of two section SOA with passive waveguide in between
From top to bottom: Bias current = 200, 100, 80, 60, 50, 40, 30mA

Device principle and design: The power equaliser is based on a two-section SOA (inset Fig. 1). In such a device, the bias current of the first section allows us to control the optical power entering into the second section. In the second section, a high current is maintained in order to provide a sufficient gain and a high output power. To accept a high input signal power, the input SOA has to work in a near-transparent regime. In this regime the noise figure increases rapidly, leading to a reduction in the output optical signal-to-noise ratio. The noise figure can be limited by either decreasing the cavity length of the SOA or by decreasing the optical confinement factor of the active layer. The device shown in Fig. 1 is realised by a combination of these two approaches. The polarisation-insensitive SOA structure is based on a low-tensile strained bulk separate confinement heterostructure [5] with an active layer thickness of 0.12μm, giving an optical confinement factor of ~0.25. The active buried ridge stripe is 800μm in total length including 150μm long tapered sections at both ends. A double core taper consisting of the tapered active region and an underlying passive waveguide enables us to couple the two SOAs. The passive section, in between the two SOAs, provides electrical insulation of the electrodes and an attenuation function. This attenuation due to propagation losses (5–7dB) limits the gain saturation of the second amplifier by the amplified spontaneous emission emitted from the first SOA (and reciprocally). The overall device length is 2.4mm including passive waveguides at each end which provide typical full beam divergences of 13° × 15° [6].

Push–Pull Fused Vertical Coupler Switch

Bin Liu, Ali Shakouri, Patrick Abraham, and John E. Bowers, *Fellow, IEEE*

Abstract—A single-electrode push–pull fused vertical coupler (FVC) switch using macroscopic crystal inversion symmetry is demonstrated. The anisotropic linear electrooptic effect in a zinc-blende crystal is used to achieve optical switching under 12-V reverse bias for a 6.9-mm-long FVC whose two guiding layers have different crystal symmetries. No switching is observed for the identical structure in which the two guiding layers have the same crystal symmetry.

Index Terms—Electrooptic effects, optical directional couplers, optical switches, water bonding.

Fig. 1. SEM pictures and the crystal orientations of (a) antiphase FVC and (b) in-phase FVC.

VERTICAL directional couplers [1]–[3] are very attractive candidates to make optical waveguide switches and narrowband filters because of their very short coupling length and the feasibility of integration with other optoelectronic devices. Generally, switching is achieved by introducing a phase mismatch $(\Delta\beta)$ between two waveguides through the electrooptic effect. In a push–pull operation, the introduction of positive and negative phase shifts in the two waveguides of the coupler reduces the driving voltage and chirping for switching. It is well known that the linear electrooptic effect is anisotropic [4], [5] in zinc-blende crystal structures. When the applied electric field is perpendicular to the (001) surface, it gives a positive index change $+\Delta n$ for the TE-polarized light propagating along [110] direction and a negative index change $-\Delta n$ for the light propagating along the [1$\bar{1}$0] direction. In conventional epitaxial vertical couplers, the upper and lower waveguides have the same crystal orientation [see Fig. 1(b)]. Consequently push–pull operation requires the signs of the electric fields in the upper and lower waveguides to be opposite. This requires presence of a third electrode between waveguides and application of positive and negative biases to the upper and lower waveguides. The fabrication is difficult in conventional vertical couplers. Since the electrooptic effect is anisotropic, if one of the waveguides in the vertical couplers is along the [110] orientation and the other one along the [1$\bar{1}$0] orientation [see Fig. 1(a)], then under an applied bias, the index changes in two waveguides have different signs. This simplifies the electrode fabrication and only requires one electrode for push–pull operation. In this letter, a vertical coupler
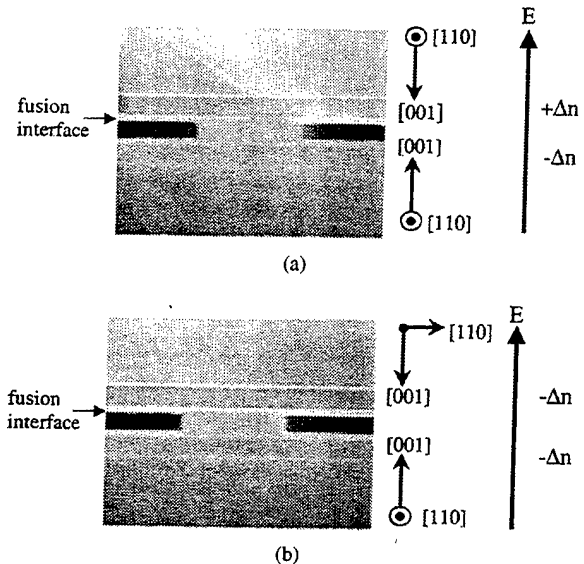
switch with macroscopic inversion symmetry is demonstrated that uses the wafer fusion technique.

Wafer fusion [6], [7] is a powerful technique to fabricate optoelectronic devices that cannot be realized using conventional epitaxial growth and processing. In addition to the inherent advantage of combining two materials with a large lattice mismatch, wafer fusion has another unique feature to integrate two wafers with various crystallographic orientations. For (001) InP and GaAs wafers, there are two ways to orient the samples before fusion. One is in-phase fusion [8], which is shown in Fig. 1(b), where the [110] axis of the top wafer is perpendicular to the [110] axis of the bottom wafer. This structure is equivalent to that grown by heteroepitaxy. The other one is antiphase fusion which is shown in Fig. 1(a), where the [110] axes of two wafers are parallel. This structure cannot be realized using epitaxial growth techniques. Macroscopically, the lattice structure of antiphase fused material has inversion symmetry at the fusion interface. It is obvious that the push–pull vertical coupler switch requires antiphase fusion so that the applied vertical electrical field induces opposite index change in the two waveguides. Since some of the electrical and optical properties of crystals, as well as their processing characteristics depend on the crystal orientation, wafer fusion gives an extra degree of freedom to fabricate new types of devices. For example, Yoo [9] has used wafer fusion to change the crystal orientation periodically to realize quasi-phase-matched second-harmonic generation (SHG).

B. Liu, P. Abraham, and J. E. Bowers are with the Department of Electrical and Computer Engineering, University of California at Santa Barbara, Santa Barbara, CA 93106 USA.

A. Shakouri is with the Department of Electrical and Computer Engineering, University of California at Santa Barbara, Santa Barbara, CA 93106 USA. He is also with the Jack Baskin School of Engineering, University of California at Santa Cruz, Santa Cruz, CA 95064 USA.
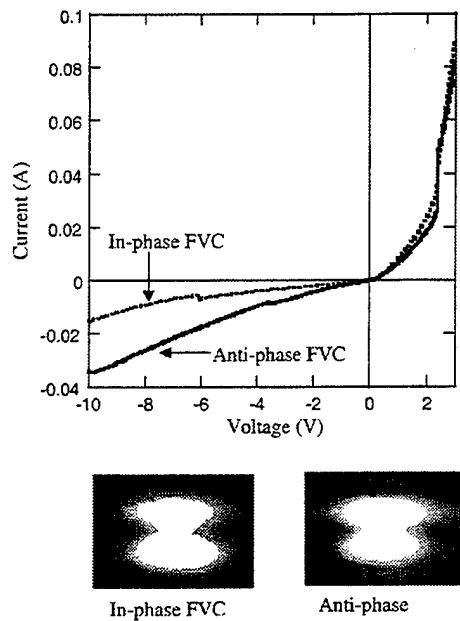
Fig. 2. *I–V* curves of in-phase and anti-phase FVC's and the electroluminescence images under 80-mA forward current.

(a)

(b)

Fig. 3. The light intensity at·the output of upper (solid line) and lower (dash line) waveguides of (a) antiphase, (b) in-phase FVC's as a function of wavelength.

In this letter, we study two kinds of FVC's fabricated using in-phase and antiphase fusion. The schematic structure of the devices is shown in Fig. 1, which uses the technology reported in [10] and [11]. Two wafers were grown using metal–organic chemical vapor deposition (MOCVD). For the first wafer, on n+ (001) InP substrate, a 0.5-μm InGaAsP ($\lambda_g = 1.3$ μm) guiding layer, followed by 0.1-μm InP cladding layer, 20-nm InGaAsP ($\lambda_g = 1.15$ μm) etch stop layer and 0.4-μm InP coupling layer were grown. All layers were undoped. The second wafer was grown on p+ (001) InP substrate. It consists of 0.2-μm p+ InGaAs layer, followed by 2 μm p (5×10^{17}/cm^3) InP layer and the same intrinsic InGaAsP and InP layers as the first wafer. The last 190 nm of the bottom 2-μm InP layer was undoped to avoid Zn diffusion to the quaternary layer during the end of the growth and wafer fusion. The 0.2-μm p+ InGaAs layer was used as an etch stop layer to remove the substrate. The device fabrication starts by cleaving two approximately 8×12 mm^2 samples from each of the grown wafers. The top 0.4-μm InP layer of p+ samples is removed. On n+ samples, a ridge waveguide structure with 2–3-μm width along the [110] direction is formed using standard photolithography and selective wet etching techniques. The [110] direction was chosen since HCl etchant produces straight side walls in this direction. The n+ and p+ samples are then fused together at a temperature of 630 °C in a hydrogen atmosphere for 50 min. In one case (fused sample A), the p+ sample was oriented so that its [110] direction was parallel to the waveguides on n+ substrate (i.e., antiphase fusion). For fused sample B, the orientation of the p+ sample was chosen to get the in-phase fusion. After fusion, p+ InP substrates for both samples are removed using HCl etching. Standard ohmic contacts were formed on both sides of the wafers to be able to apply a bias. Fig. 1 shows the stain etched scanning electron microscope (SEM) pictures for both antiphase (A) and in-phase (B) FVC's.
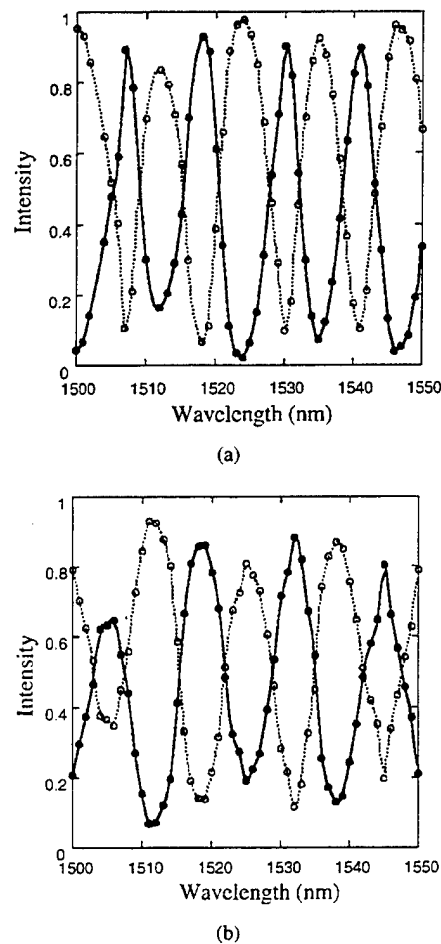
Fig. 2 shows the current versus voltage (*I–V*) curves of the samples A and B. The device size is about 7 mm × 3 μm. There is a small forward voltage drop of 1 V at the fusion interface. The leakage current of sample A at reverse biases is a little higher than that of sample B. Under forward bias, the luminescence images of anti- and in-phase fused devices are found to be similar as it can be seen in Fig. 2.

To characterize FVC's, a tunable laser source is used to input TE-polarized light through a lensed single-mode fiber (SMF). The image at the output of coupler facet is recorded with an IR camera with an 80× objective. The samples are mounted to a temperature stabilized stage. First, the passive switching of the two FVC structures was characterized by changing the input wavelength. In response, the effective coupling length changes and the output light switches between upper and lower waveguides (Fig. 3). The oscillation period is a function of the coupling strength between two waveguides and the total length of the couplers. The difference in the measured oscillation period of sample A (11 nm) and sample B (13 nm) matches very well with the different length of the couplers (sample A: 6.9 mm long, sample B: 5.9 mm long). This shows that samples A and B have the same coupling length. Because of the variation in amplitude, the half period looks different at different wavelength (the "eye"

(a)

(b)
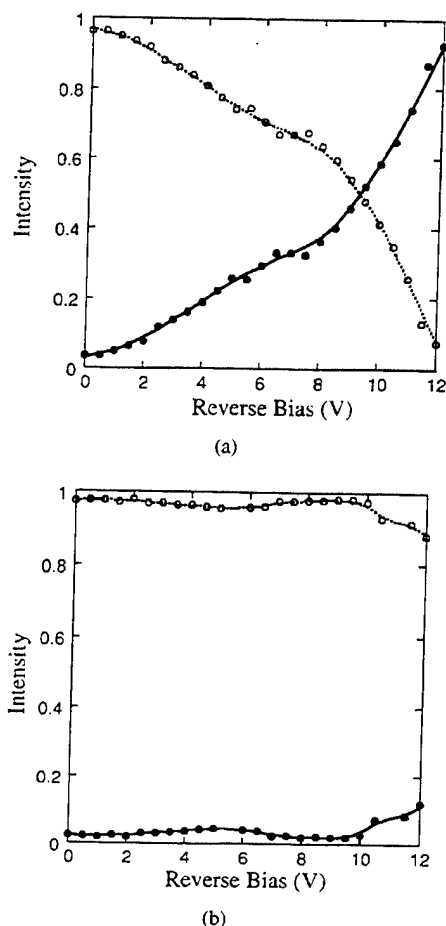
Fig. 4. The light intensity at the output of upper (solid line) and lower (dashed line) waveguides of (a) antiphase and (b) in-phase FVC's as a function of reverse bias voltage.

is big or small), but the actual oscillation period measured from a distance between consecutive minimums is within our experimental resolution (±1 nm). Then a reverse bias is applied to both samples. The normalized intensities at the output of upper and lower waveguides as a function of bias voltage are shown in Fig. 4(a) (sample A) and (b) (sample B). The antiphase FVC switches at a bias of 12 V while no switching is observed for in-phase fused sample B.

It is known that the mechanisms of index change in p-i-n structures include the linear electrooptic (LEO) effect, the quadratic electrooptic (QEO) effect and the free-carrier effect due to the modulation of the depletion layer. In the current structure, because of a thick 1.6-μm intrinsic layer and because the operation wavelength is far away from the

bandgap, the QEO and free-carrier effects are very weak. Furthermore, QEO and free-carrier effects should be the same for both samples, because they are independent of the crystal orientation. Therefore, the LEO effect dominates in current FVC structures. The switching in sample A is because of the push–pull configuration which comes from the inverted crystal orientation. In sample B, the index change in top and bottom waveguides is the same, so the switching requires a much higher voltage.

In conclusion, a push–pull fused vertical coupler switch with crystal inversion symmetry has been demonstrated. Switching under 12-V reverse bias is observed for antiphase FVC's while there is no switching for in-phase FVC's. The wafer fusion technique simplifies the complicate electrode configuration in conventional push–pull type couplers. Additionally, other novel devices can be realized using different crystal structures integrated together.

REFERENCES

[1] M. Kohtoku, S. Baba, S. Arai, and Y. Suematsu, "Switching operation in a GaInAs-InP MQW integrated-twin-guide (ITG) optical switch," *IEEE Photon. Technol. Lett.*, vol. 3, pp. 225–227, Mar. 1991.
[2] F. Dollinger, M. Borcke, G. Bohm, G. Trankle, and G. Weimann, "Ultrashort low-loss optical multiquantum-well GaAs/GaAlAs vertical directional coupler switch," *Electron. Lett.*, vol. 32, pp. 1509–1510, 1996.
[3] R. C. Alferness, L. L. Buhl, U. Koren, M. G. Young, T. L. Koch, C. A. Burrus, and G. Raybon, "Broadly tunable InGaAsP/InP buried rib waveguide vertical coupler filter," *Appl. Phys. Lett.*, vol. 60, pp. 980–982, 1992.
[4] H. G. Bach, J. Krauser, H. P. Nolting, R. A. Logan, and F. K. Reinhart, "Electro-optical light modulation in InGaAsP/InP double heterostructure diodes," *Appl. Phys. Lett.*, vol. 42, no. 8, pp. 692–694, Apr. 1983.
[5] A. Yariv, *Quantum Electronics*, 2nd ed. New York: Wiley, 1975, ch. 14.
[6] A. Black, A. R. Hawkins, N. M. Margalit, D. I. Babic, A. L. Holmes Jr., Y. L. Chang, P. Abraham, J. E. Bowers, and E. L. Hu, "Wafer fusion: Materials issues and devices results," *IEEE J. Select. Topics Quantum Electron.*, vol. 3, pp. 937–951, June 1997.
[7] Z. H. Zhu, F. E. Ejeckam, Y. Qian, J. Zhang, G. L. Christensen, and Y. H. Lo, "Wafer bonding technology and its application in optoelectronic devices and material," *IEEE J. Select. Topics Quantum Electron.*, vol. 3, pp. 927–936, June 1997.
[8] Y. Okuno, K. Uomi, M. Aoki, T. Taniwatari, M. Suzuki, and M. Kondow, "Anti-phase direct bonding and its application to the fabrication of InP-based 1.55 μm wavelength lasers on GaAs substrates," *Appl. Phys. Lett.*, vol. 66, no. 4, pp. 451–453, 1995.
[9] S. J. B. Yoo, R. Bhat, C. Caneau, and M. A. Koza, "Quasiphase-matched second-harmonic generation in AlGaAs waveguides with periodic domain inversion achieved by wafer-bonding," *Appl. Phys. Lett.*, vol. 66, pp. 3410–3412, June 1995.
[10] B. Liu, A. Shakouri, P. Abraham, B. G. Kim, A. W. Jackson, and J. E. Bowers, "Fused vertical couplers," *Appl. Phys. Lett.*, vol. 72, no. 21, pp. 2637–2638, 1998.
[11] A. Shakouri, B. Liu, B. G. Kim, P. Abraham, A. W. Jackson, A. Gossard, and J. E. Bowers, "Wafer fused optoelectronics for switching," *J. Lightwave Technol.*, vol. 16, pp. 2236–2242, Dec. 1998.

As with our earlier devices, the structures are ridge-guided optical waveguide rings formed in GaAlAs/GaAs double quantum well material. The ridge width is 2μm and the cavity lengths are 7.35 and 7mm. When the laser is at threshold, the cavity losses are compensated for by the gain and an optimum value of $k_2 = 0.5\%$ is found. The rings are placed one within another, lightly coupled by a directional coupler section (Fig. 2). The outer one is coupled via a multimode interference (MMI) coupler to a straight output waveguide. The MMI coupler is 6μm wide and 370μm long, and has been designed for a −3dB split ($k_1 = \sqrt{0.5}$). The directional coupler between the two resonant rings has a minimum waveguide separation of 4μm to give a much smaller coupling ratio; the design has been simulated by BPM, which gives $k_2 = 0.03$. The output waveguide is tilted at 5° to the cleaved sides of the substrate to reduce reflections back into the resonator. Separate contacts are made to the inner ring and to the outer ring.
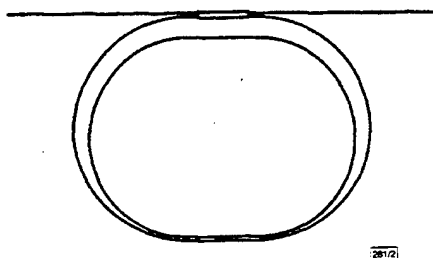

Fig. 2 *Layout of double-ring laser; inner and outer ring directionally coupled (weakly); MMI coupling to output waveguide*
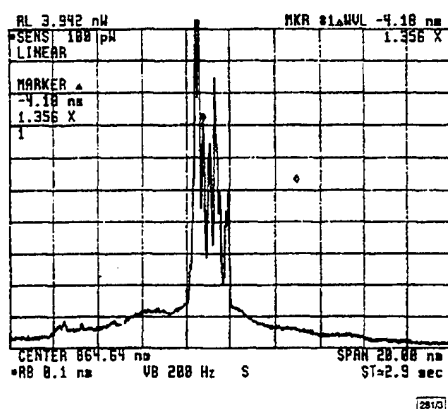
Fig. 3 *Double ring laser – output spectrum with $I_{ext} = 900mA$ and $I_{int} = 0$*
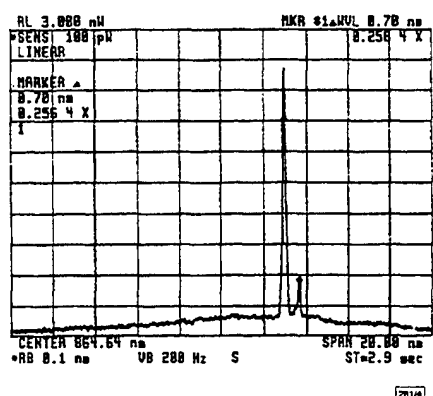
Fig. 4 *Double ring laser – output spectrum with $I_{ext} = 900mA$ and $I_{int} = 900mA$*

The devices have been tested by biasing the outer ring above threshold and observing how the biasing of the inner ring affects the output of the device. With a forward current of 900mA applied to the outer ring (1.5 times threshold), a multimode spectral output was observed, as in Fig. 3. By applying a forward bias

to the inner ring and increasing the drive current by degrees, the multiple lasing resonances of the outer ring are gradually suppresses and are replaced with wider-spaced resonances, the frequency spacing of which corresponds to the free spectral range (FSR) of the two-ring resonant structure, as shown in Fig. 3 for an inner-ring drive current of 900mA. Two lasing modes are apparent here; the measured frequency separation of ~0.7nm is near to the calculated FSR of the double ring resonator of 0.64nm. The centre frequency of the spectrum has moved to a longer wavelength. We think this is because the inner, lower loss, ring cavity has a gain peak at a longer wavelength, due to a lower carrier density at threshold altering the refractive index.

The filter theory used to describe the coupled ring resonant circuit is linear, excluding saturation, and is of limited value when applied to the lasing structure, but confirms the experimental behaviour. The need for a small coupling ratio has been emphasised by numerical simulation based on the model of Lang and Kobayashi [4]. Dynamic behaviour ranging from self-pulsation to coherence collapse was found for a master-slave in-line semiconductor laser system [5], for which dynamically stable operation was only obtained with a coupling ratio < 1%. In that analysis the lasers were coupled through an isolator, although subsequent calculations on a similar system but omitting the isolator generated similar results. We plan to extend that dynamic analysis to the present case, to obtain a realistic model of the double-ring laser. Further designs of double-ring resonator are being fabricated, to be used either as passive transmission filters or as lasers. Operation outside the regimes of stability should be possible, where we hope to observe self-pulsation and coherence collapse.

M. Sorel, S. Gluck and P.J.R. Laybourn (*Department of Electronics and Electrical Engineering, University of Glasgow, Glasgow, G12 8QQ, United Kingdom*)

References

1 KRAUSS, T., DE LA RUE, R.M., GONTIJO, I., LAYBOURN, P.J.R., and ROBERTS, J.S.: 'Strip-loaded semiconductor ring lasers employing multi-mode interference couplers', *Appl. Phys. Lett.*, 1994, 64, (21), pp. 2788–2790

2 WISS, R.Q.: 'Double-tuned circuits' in VALLEY, G.E., and WALLMAN, H. (Eds.): 'Vacuum tube amplifiers' (McGraw-Hill, New York, 1948)

3 HOHIMER, J.P., VAWTER, G.A., CRAFT, D.C., and HADLEY, G.R.: 'Interferometric ring diode lasers', *Appl. Phys. Lett.*, 1992, 61, (12), pp. 1375–1377

4 LANG, R., and KOBAYASHI, K.: 'External optical feedback effects on semiconductor injection laser properties', *IEEE J. Quantum Electron.*, 1980, 16, (3), pp. 347–355

5 ANNOVAZZI-LODI, V., SCIRE, A., SOREL, M., and DONATI, S.: 'Dynamic behavior and locking of a semiconductor laser subjected to external locking', *IEEE J. Quantum Electron.*, 1998, 34, (12), pp. 2350–2357

Vertical coupler with separated inputs and outputs fabricated using double-sided process

B. Liu, A. Shakouri, P. Abraham and J.E. Bowers

A novel vertical coupler used as a wavelength multiplexer with separated input and output waveguides is demonstrated. The wafer fusion technique enables both frontside and backside processing of the thin epitaxial films. A vertical coupler with a 4mm interaction region demonstrates 20nm wavelength spacing.

Introduction: Directional waveguide couplers are fundamental components in photonic integrated circuits used in optical communications systems. They can be used as optical switches, splitters, modulators and narrowband filters [1 – 4]. Conventional directional couplers are planar where the two waveguides are horizontally (laterally) arranged. One disadvantage of the planar design is

that the spacing between two coupled waveguides is limited by the fabrication techniques. This results in long coupling lengths (around several millimetres) [1 – 3]. Vertical directional couplers, on the other hand, have a very short coupling length that is even smaller than 100μm [5], because the spacing between two vertically stacked waveguides can be reduced to < 0.5μm, and this can be precisely controlled by the material growth. However, the two input or output waveguides in vertical couplers are so close (< 1μm) together that the direct coupling of individual waveguides to fibres is very difficult. This has limited the practical applications of vertical couplers in fibre-optic systems. To solve this problem, recently a novel fused vertical coupler [6, 7] based on the wafer fusion technique [8] has been proposed where the two strongly coupled waveguides are fabricated on two different substrates and separated laterally.
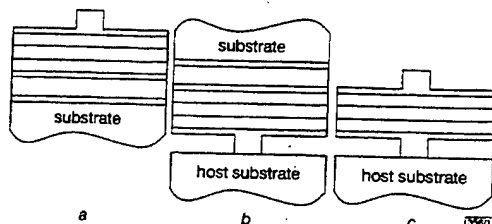
Fig. 1 *Coupler fabrication steps*

a Conventional processed epitaxial layer structure
b Epitaxial structure is inverted and bonded to another host substrate
c After removing original substrate, exposed backside of epitaxial structure is processed
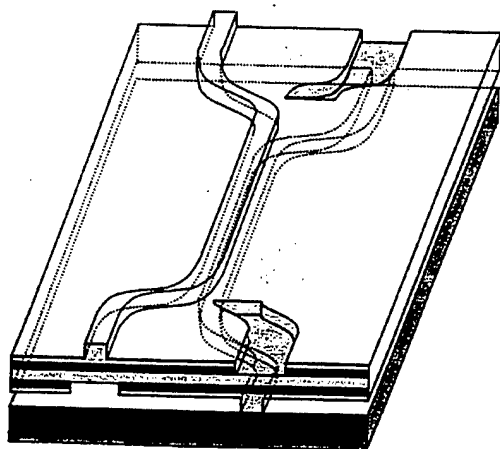
Fig. 2 *Schematic diagram of vertical coupler with separated inputs and outputs*
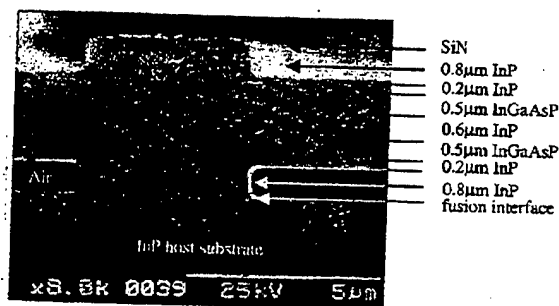
Fig. 3 *SEM picture of vertical coupler fused to InP substrate*

In this Letter, we demonstrate a vertical coupler with separated input and output waveguides fabricated using both frontside and backside processing of the same substrate. Using wafer fusion, a conventionally processed epitaxial layer structure (Fig. 1a) is inverted and bonded to a new host substrate (Fig. 1b). After removing the top substrate and leaving only the thin epitaxial film bonded to the host material, the exposed backside of the epitaxial

structure can then be processed as well (Fig. 1c). This technique enables the fabrication of 3D photonic integrated circuits.

Experiments: The schematic drawing in Fig. 2 shows a vertical coupler with separated inputs and outputs, where the two waveguides are coupled vertically and separated horizontally in different planes. The device fabrication begins with a metal-organic chemical vapour deposition (MOCVD)-grown structure (Fig. 3), which includes a 0.8μm InP frontside ridge layer, a 15nm InGaAsP (bandgap 1.1μm) etching stop layer, a 0.2μm InP cap layer, a 0.5μm InGaAsP (bandgap 1.3μm) frontside guiding layer, a 0.6μm InP coupling layer, the same backside guiding, cap, etch stop and ridge layers, and finally a 0.2μm InGaAs for substrate removal on InP substrate. First, the 3μm width frontside ridge waveguides are formed by reactive ion etching (RIE) and chemical wet etching. The frontside guiding layer above the backside waveguide structure in non-coupling areas is removed by further wet etching. The waveguide sample is then inverted and fused to a bare InP substrate under pressure for 40min at 630°C. After removing the top substrate and InGaAs etch stop layer, the backside waveguides are fabricated and the unnecessary guiding layer above the frontside waveguide structure is removed as before. The waveguide alignment is facilitated using infrared photolithography.
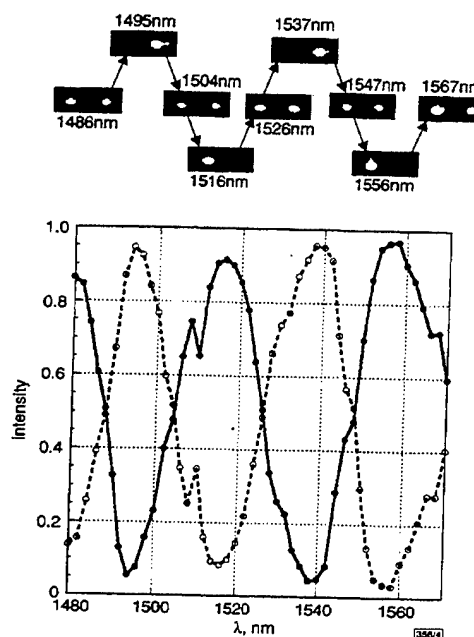
Fig. 4 *Light output intensity against wavelength*

- -○- - right waveguide
—●— left waveguide
Near field images at outputs are also shown

Fig. 3 shows the SEM picture of the coupling region. In our former fused vertical couplers [6], the fused interface was between the two guiding layers. This introduced an excess optical loss due to imperfections at the non-epitaxial interface. To separate the input and output waveguides, it was necessary to align the two wafers with submicrometre resolution during the wafer fusion process. In our current work, the fused interface is not important since it is far away from the guiding layer. Also, no alignment is necessary during the fusion process.

Results and discussions: To characterise the device performance, light from a tunable laser was coupled to an input waveguide by a singlemode fibre. The light at the output was collected by another singlemode fibre which was connected to a detector. Fig. 4 shows the measured output light intensity as a function of wavelength. The near field images at the output were recorded by an IR camera with a lens and they are shown in Fig. 4. The total device length is 8mm, the coupler length is 4mm and the separation between two waveguides is 20μm. As we expected, the output

intensity is a periodic function of wavelength and the oscillation period is ~40nm. This means that the device can be used as a wavelength multiplexer/demultiplexer for 20nm wavelength spacing. This small wavelength spacing is very difficult to achieve in a conventional horizontally arranged coupler because of the weak wavelength dependence of the coupling coefficient [9]. By cascading several strongly coupled vertical couplers together, multi-channel multiplexers with several-nanometre spacing can be realised.

It is worth noting that in the processing of both sides by the wafer fusion technique only one epi-wafer is needed and another host wafer can be of any material, such as Si, glass, etc. This will reduce the cost and give more flexibility for the fabrication of 3D photonic integrated circuits.

Conclusion: We have successfully realised a vertical coupler with separated input and output waveguides by using wafer fusion technology. This device can be used as a wavelength multiplexer in fibre-optic systems. 20nm channel spacing has been achieved for a vertical coupler with 4mm coupling region. Wafer fusion technology enables both frontside and backside processing of thin epitaxial films and is an important tool for realising novel devices and 3D photonic integrated circuits.

B. Liu, P. Abraham and J.E. Bowers (*Department of Electrical and Computer Engineering, University of California, Santa Barbara, CA 93106, USA*)

E-mail: liu@opto.ucsb.edu

A. Shakouri (*Jack Baskin School of Engineering, University of California, Santa Cruz, CA 95064, USA*)

References

1   HAMAMOTO, K., ANAN, T., KOMATSU, K., SUGIMOTO, M., and MITO, I.: 'First 8*8 semiconductor optical matrix switches using GaAs/AlGaAs electro-optic guided-wave directional couplers', *Electron. Lett.*, 1992, **28**, pp. 441–443

2   MILIOU, A.N., SRIVASTAVA, R., and RAMASWAMY, R.V.: 'A 1.3μm directional coupler polarization splitter by ion exchange', *J. Lightwave Technol.*, 1993, **11**, pp. 220–225

3   KHAN, M.N., YANG, W., and GOPINATH, A.: 'Directional coupler electro-optic modulator in AlGaAs/GaAs with low voltage-length product', *Appl. Phys. Lett.*, 1993, **62**, pp. 2033–2035

4   ALFERNESS, R.C., BUHL, L.L., KOREN, U., MILLER, B.I., YOUNG, M.G., KOCH, T.L., BURRUS, C.A., and RAYBON, G.: 'Broadly tunable InGaAsP/InP buried rib waveguide vertical coupler filter', *Appl. Phys. Lett.*, 1992, **60**, pp. 980–982

5   DOLLINGER, F., BORCKE, M.V., BOHM, G., TRANKLE, G., and WEIMANN, G.: 'Ultrashort low-loss optical multiquantum-well GaAs/GaAlAs vertical directional coupler switch', *Electron. Lett.*, 1996, **32**, pp. 1509–1510

6   BIN, L., SHAKOURI, A., ABRAHAM, P., BOO-GYOUN, K., JACKSON, A.W., and BOWERS, J.E.: 'Fused vertical couplers', *Appl. Phys. Lett.*, 1998, **72**, pp. 2637–2638

7   SHAKOURI, A., BIN, L., BOO-GYOUN, K., ABRAHAM, P., JACKSON, A.W., and GOSSARD, A.C.: 'Wafer-fused optoelectronics for switching', *J. Lightwave Technol.*, 1998, **16**, pp. 2236–2242

8   LIAU, Z.L., and MULL, D.E.: 'Wafer fusion: a novel technique for optoelectronic device fabrication and monolithic integration', *Appl. Phys. Lett.*, 1990, **56**, pp. 737–739

9   ROTTMANN, F., NEYER, A., MEVENKAMP, W., and VOGES, E.: 'Integrated-optic wavelength multiplexers on lithium niobate based on two-mode interference', *J. Lightwave Technol.*, 1988, **LT-6**, pp. 946–952

Compact optoelectronic oscillator with ultra-low phase noise performance

Yu Ji, X.S. Yao and L. Maleki

A compact optoelectronic oscillator (OEO) is presented which is using constructed using a DFB laser, a semiconductor Mach-Zehnder modulator, and a dielectric resonator based RF filter. The achieved phase noise is ~50dBc/Hz at 10Hz and ~130dBc/Hz at 10kHz from a 10GHz oscillation frequency, a performance comparable to that of an OEO constructed with a diode-pumped YAG laser and an LiNbO₃ modulator.

Introduction: Optoelectronic oscillators (OEOs) have the capability of achieving ultra-low phase noise for both microwave and optical communications [1]. The oscillation in an OEO is produced via a feedback loop which includes a modulator, an optical fibre delay element, and a photodetector. However, the previously demonstrated OEOs were constructed with expensive and bulky diode-pumped YAG lasers, LiNbO₃ modulators, and cavity RF filters. For communications, radar, and space applications, compact and low cost OEOs are preferred. We report in this Letter a compact and high performance OEOs constructed with an integrated module consisting of a DFB laser and a semiconductor modulator, and a dielectric resonator based RF filter. The experimental results demonstrate that low cost semiconductor lasers and modulators, together with low cost dielectric resonators, can be used to construct optoelectronic oscillators.
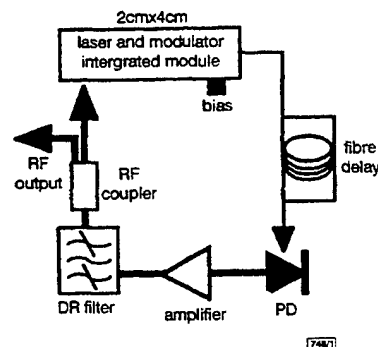
Fig. 1 *Configuration of compact OEO*

Configuration of compact OEO: The configuration of the compact 10GHz OEO is shown in Fig. 1. We used a DFB laser integrated with a semiconductor Mach-Zehnder modulator. The measured RIN (relative intensity noise) of the laser output is −110dBc/Hz at 10Hz and −135dBc/Hz at 10kHz, which sets a limit on the phase noise of the OEO.

The key to the low phase noise performance of an OEO is the long optical fibre loop delay. The highest spectral purity signals with the OEO are achieved with the longest fibre length [1]. Because the OEO is essentially a multimode device, with its mode spacing inversely proportional to the length of the fibre, achieving ultra-low phase noise requires a filter with narrow enough bandwidth to select a mode for operation at a single frequency. Although a multi-loop scheme can be used for singlemode selection [2], it increases the complexity and size of the OEO. In this Letter, we use an ultra-narrow-bandwidth filter constructed with a dielectric resonator (DR) for singlemode selection.

Dielectric-resonator-loaded high-Q narrowband filters can be designed to occupy a total volume only ~5% of that of a waveguide filter with an equivalent performance and their Q at room temperature can be as high as 10^4. In addition, the temperature coefficient of the filter is exceptionally low, down to ±1 ppm/°C at room temperature [3]. We designed and fabricated such a filter by placing an 8.7mm × 4mm high dielectric constant ($\varepsilon_r = 30$) ceramic cylindrical disc at the centre of an aluminium cavity with a size three times that of the DR disc. Using a design tool based on the finite element method, we found that the TE$_{5,1,δ}$ mode has a frequency of 10GHz, and more than 90% of the energy can be confined in the disc. To obtain optimum mode matching, a tiny wire loop probe was used for both mode excitation and coupling.

A 100-kHz to 50-GHz Traveling-Wave Amplifier IC Module

Volkan Kaman, *Student Member, IEEE*, Tom Reynolds, Anders Petersen, and John E. Bowers, *Fellow, IEEE*

Abstract— Broad-band microwave packaging of a traveling-wave amplifier with an on-chip bandwidth of 2–50 GHz is described. Techniques to reduce overall insertion losses and to extend the low-frequency cutoff of the amplifier while maintaining gain-flatness are discussed. The packaged amplifier modules exhibit excellent performance from 100 kHz to 50 GHz. They are demonstrated as modulator drivers and receiver amplifiers in a 30-Gbit/s digital optical communication system.

Index Terms—Coplanar waveguides, MMIC amplifiers, optical communication, packaging, traveling-wave amplifiers.

I. INTRODUCTION

THE SPEED of optical fiber telecommunication systems based on electrical time division multiplexing has increased rapidly over the last decade. Systems operating at 10 Gbit/s are beginning to be deployed while the expected next generation of 40 Gbit/s-per-wavelength optical communication systems has already been demonstrated in various laboratory experiments [1], [2]. Baseband amplifiers used as modulator drivers, preamplifiers, and postamplifiers are key components for such high-speed systems. A linear response with little magnitude variation and a constant group delay over a broad bandwidth is essential for low bit error rates with long pattern lengths. Amplifiers with these characteristics have been demonstrated in various integrated circuit (IC) technologies (see for example [3]–[5]). The packaging of high-speed IC's is a real challenge since the overall package parasitics (the transmission line, discontinuities, wire bonds and lumped elements used in the module) become significant at high frequencies and can severely limit the performance of the broadband IC being packaged. Some very impressive high-speed modules have been demonstrated for in-house IC's either by optimizing the module for the given IC [6]–[8] or by designing the IC according to the known package parasitics [9], [10].

In this letter, we present the packaging of a commercially available traveling-wave amplifier that has an on-chip band-width of 2–50 GHz [11]. We describe packaging techniques on reducing the overall insertion losses as well as the design of the drain bias circuitry to extend the low-frequency cutoff of the amplifier down to 100 kHz while maintaining gain-flatness over a broad bandwidth. The packaged modules were used as modulator drivers and receiver amplifiers in a 30-Gbit/s optical transmission system [12].

II. AMPLIFIER PACKAGING

A. *IC Characteristics*

The frequency response for on-wafer measurements and other characteristics for the commercial amplifier are given in [11]. Bonding pads are provided to allow the amplifier to operate at frequencies lower than 2 GHz and to supply the drain and gate biases by means of external circuit components. However, since the output of the amplifier is directly connected to the drain bias pad, any parasitic coupling in the drain bias circuitry reflects as resonances and frequency response deterioration. In addition to these constraints, the input and the output of the amplifier need to be externally AC-coupled without introducing excess insertion loss.

B. *Package Design*

A coplanar waveguide (CPW) transmission line was chosen for the ease of providing a low-inductance ground between the chip and the surface ground of the substrate. A quartz substrate was used to minimize CPW radiation and skin losses since it has a low dielectric constant ($\varepsilon_r = 3.92$). In order to suppress cavity resonances and microstrip modes, the quartz substrate was suspended over an air gap with a microwave absorber. The 3350-μm-long identical substrates used at the input and the output of the amplifier were designed to have minimum insertion and return losses. Fig. 1 shows a photograph of the packaged IC.

An important package parasitic comes from the wire bond connection between the chip and the CPW transmission line, which introduces inductance for both the signal and the ground connections. It was shown in [9] that this parasitic could be reduced by designing the IC according to the outer bonding wire inductance. However, this technique is not possible for the packaging of a commercial IC; therefore, an optimization of this interconnection is required. We observed experimentally that gold ribbon with a width of 75 μm has less inductance than the conventionally used wire bonds. The bonding pads of the IC were aligned with the top surface of

Fig. 1. Photograph of the packaged amplifier IC.

the substrate to minimize the length and the inductance of the ribbon. The length of the ribbons was approximately 150 μm long with an estimated inductance of less than 1 nH/mm.

The AC-coupling of the input and the output of the amplifier are conventionally achieved by mounting a surface mount dielectric (SMD) capacitor across a gap on the signal line. However, since broad-band (100 kHz to 50 GHz) SMD's are commercially unavailable, a parallel combination of a 180-pF dielectric capacitor (di-cap) and a 33-nF SMD was chosen [Fig. 2(a)]. In order to simulate the input and output substrates simultaneously, a pair of the capacitor combination was epoxied on a 7-mm-long CPW line. Frequency response measurements showed that there was about 2.4-dB extra insertion loss due to the two gaps and the capacitor combinations at 40 GHz. In order to eliminate the discontinuities on the CPW, the module was designed such that the capacitors would be placed directly under the K-connector launch [Fig. 2(b)]. This new design improved the insertion loss by 1 dB at 40 GHz and allowed for slightly shorter CPW lines.

A similar parallel configuration of capacitors was connected to the low-frequency extensions of the amplifier. The parasitics of the capacitors or the gold ribbon were not seen to be significant on the frequency response of the amplifier. However, at frequencies below 2 GHz, a gain rise was caused due to the increase in the drain termination resistor value from 50 to 65 Ω ([11, Fig. 1]). This is overcome in the drain bias circuitry as will be described in the following section.

III. DRAIN BIAS CIRCUIT DESIGN

The challenge of the drain bias circuit design was to use commercial components (with limited bandwidth and uncertain parasitics) while also incorporating an external resistor to reduce the low-frequency gain; it was essential that the whole circuit looked like an open from the output pad up to 50 GHz. This design turned out to be the most crucial aspect of the package since any coupling of the parasitics resulted
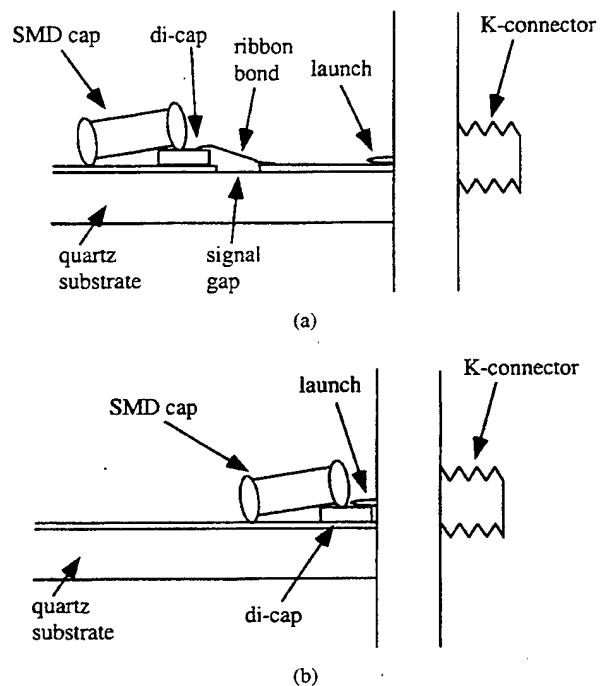
Fig. 2. Illustrative diagrams of different AC-coupling schemes: (a) capacitor combination mounted on the signal line next to a gap. Ribbon bonds are used to connect the capacitor and the signal line over the gap and (b) capacitor combination mounted under the K-connector launch, thereby eliminating the gap (signal line discontinuity) and the ribbon bonds.

in huge resonances in the frequency response of the module. The circuit schematic that gave a consistent flat response for a broad bandwidth is shown in Fig. 3. The inductor/resistor combination L1/R1 through L4 ensures gain-flatness from 100 kHz to 2 GHz. It is significant to mention that the components were chosen by simulation to minimize any resonance between a pure inductor and the preceding parasitic capacitance. In order to minimize the coupling between the ribbon inductance (L6) and its preceding parasitic capacitance (which resonates strongly in the gigahertz range), an inductor
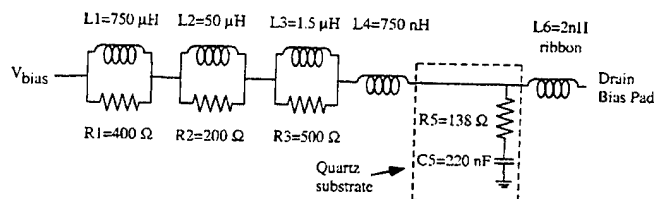
Fig. 3. The drain bias circuitry used for biasing the amplifier. R5 is the low-frequency gain reduction thin-film resistor patterned on a quartz substrate.
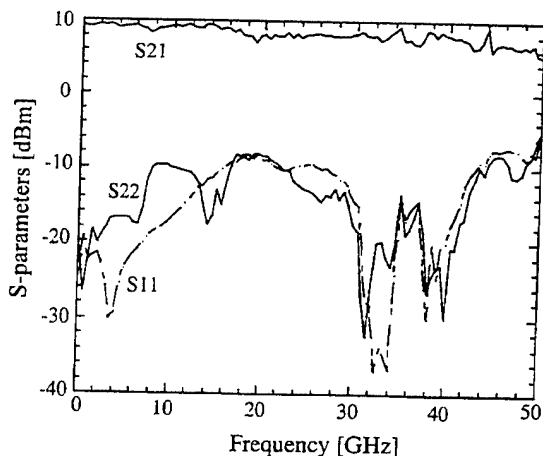
Fig. 4. Measured insertion and return losses of the amplifier module.

(a)

(b)
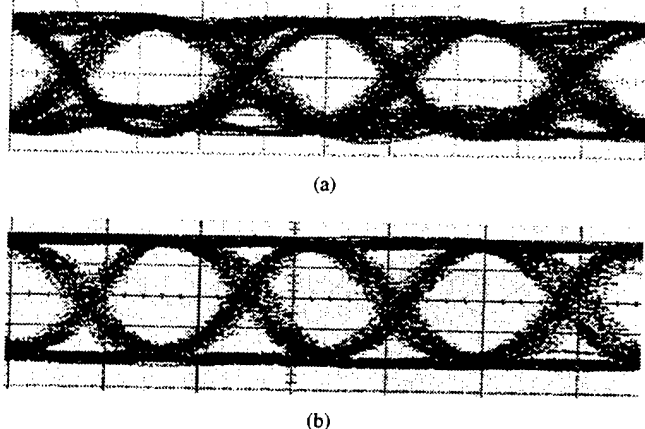
Fig. 5. The 30-Gbit/s transmission performance of three cascaded amplifier modules: (a) 30-Gbit/s NRZ input (H: 13 ps/div, V: 100 mV/div) and (b) 30-Gbit/s output from the amplifiers (H: 20 ps/div, V: 750 mV/div).

with a high self-resonating frequency and a thin-film resistor with minimal parasitics and a small bonding pad were used. The purpose of the R5 thin-film resistor was to reduce the low-frequency gain described in the preceding section. The ribbon length of 2.5 mm was very critical for the high-frequency (>2 GHz) response of the module. It was chosen to be long enough to act as a broadband high-frequency inductor, but short enough to shift the resonance due to the preceding parasitic capacitance out of the operational bandwidth.

IV. PERFORMANCE OF PACKAGED AMPLIFIER

Fig. 4 shows the measured gain and return losses for the module. The gain is at an average of 8.5 dB with a gain-flatness within ±1.5 dB from 100 kHz to 50 GHz. The

packaged amplifier's response is in good agreement with the chip performance with the exception of a resonance at 45 GHz and a deterioration of the return losses. The resonance around 45 GHz is due to the bandwidth limit of the K-connectors used, which will be improved by using V-connectors. We also believe that the return loss will be improved once broad-band capacitors for ac-coupling are available. The amplifier modules were used as modulator drivers and receiver postamplifiers in a 30-Gbit/s NRZ transmission experiment [12]. Fig. 5(a) shows the 30-Gbit/s input and (b) the 3 V_{p-p} output of three cascaded amplifier modules. No significant degradation of the eye is observed. Bit error rate measurements confirmed this with error free operation for input signals above −22 dBm.

V. CONCLUSION

In summary, we presented the microwave packaging of a commercially available traveling-wave amplifier with an on-chip bandwidth of 2–50 GHz. By using techniques to reduce excess insertion loss and a careful design of the drain bias circuitry, a bandwidth of 100 kHz to 50 GHz was achieved. These amplifier modules are suitable for high bit-rate transmission systems, which was successfully demonstrated in a 30-Gbit/s transmission experiment.

REFERENCES

[1] K. Hagimoto, M. Yoneyama, A. Sano, A. Hirano, T. Kataoka, T. Otsuji, K. Sato, and K. Noguchi, "Limitations and challenges of single-carrier full 40-Gbit/s repeater system based on optical equalization and new circuit design." in OFC'97 Tech. Dig., paper ThC1, pp. 242–243, 1997.

[2] W. Bogner, E. Gottwald, A. Schopflin, and C.-J. Weiske, "40 Gbit/s unrepeatered optical transmission over 148 km by electrical time division multiplexing and demultiplexing," Electron. Lett., vol. 33, pp. 2136–2137, 1997.

[3] S. Kimura, Y. Imai, S. Yamaguchi, and K. Onodera, "0–56 GHz GaAs MESFET gate-line-division distributed baseband amplifier IC with 3D transmission lines," Electron. Lett., vol. 33, pp. 93–95, 1997.

[4] Z. Lao, A. Thiede, U. Nowotny, H. Lienhart, V. Hurm, M. Schlechtweg, J. Hornung, W. Bronner, K. Kohler, A. Hulsmann, B. Raynor, and T. Jakobus, "40-Gb/s high-power modulator driver IC for lightwave communication systems," IEEE J. Solid-State Circuits, vol. 33, pp. 1520–1526, 1998.

[5] C. J. Madden, R. L. Van Tuyl, M. V. Le, and L. D. Nguyen, "A 17 dB gain, 0.1–70 GHz InP HEMT amplifier IC," in Proc. IEEE Int. Solid-State Circuits Conf. (ISSCC'94), 1994, pp. 178–179.

[6] A. K. Petersen, R. Yu, K. Runge, J. E. Bowers, and K. C. Wang, "Microwave packages for 30 Gbit/s analog and digital circuits," in Proc. Electrical Performance of Electronic Packaging (EPEP'95), 1995, pp. 152–154.

[7] R. Yu, S. Beccue, P. J. Zampardi, R. L. Pierson, A. Petersen, K. C. Wang, and J. E. Bowers, "A packaged broad-band monolithic variable gain amplifier implemented in AlGaAs/GaAs HBT technology," IEEE J. Solid-State Circuits, vol. 31, pp. 1380–1387, 1996.

[8] Y. Imai, T. Otsuji, E. Sano, and Y. Umeda, "40-Gb/s IC and packaging technologies for future lightwave communications," Proc. SPIE, vol. 3038, pp. 186–197, 1997.

[9] R. Ohhira, Y. Amamiya, T. Niwa, N. Nagano, T. Takeuchi, C. Kurioka, T. Chuzenji, and K. Fukuchi, "A high-sensitivity 40-Gbit/s optical receiver using packaged GaAs HBT-IC's," in OFC'98 Tech. Dig., paper WI4, pp. 155–156, 1998.

[10] H.-M. Rein and M. Moller, "Design considerations for very-high-speed Si-bipolar IC's operating up to 50 Gb/s," IEEE J. Solid-State Circuits, vol. 31, pp. 1076–1090, 1996.

[11] Hewlett Packard Co., "2–50 GHz distributed amplifier technical data," Communication Components Designer's Catalog, pp. 6-40–6-46, 1997.

[12] V. Kaman, S. Z. Zhang, A. J. Keating, and J. E. Bowers, "High-speed operation of traveling-wave electroabsorption modulator," Electron. Lett., vol. 35, pp. 993–995, 1999.

Characteristic equations for different ARROW structures

BIN LIU, ALI SHAKOURI* AND JOHN E. BOWERS
*Department of Electrical and Computer Engineering, University of California, Santa Barbara, CA 93106,
USA (E-mail: liu@opto.ucsb.edu)*
**Permanent address: Jack Baskin School of Engineering, University of California, Santa Cruz, CA 95064,
USA*

Abstract. Based on radiation modes and phase relations in different ARROW structures, the characteristic equations are presented that can avoid root searching in the complex plane and find the effective index, loss and field profile easily. This simple model gives an accurate intuitive picture for low loss leaky modes and it can be used to design and optimize the low loss ARROW devices of practical interest.

1. Introduction

Antiresonant reflecting optical waveguides (ARROW) (Duguay *et al.* 1986) have attracted a great deal of interest during the past several years. Instead of total internal reflection in conventional waveguides, ARROWs use antiresonant reflection as the guiding mechanism. This gives ARROW some remarkable features that are used in many applications, such as remote couplers (Gehler *et al.* 1994), filters (Chu *et al.* 1996), and polarization splitters (Trutschel 1995). In order to design ARROW devices, the knowledge of the characteristics of ARROW modes is important. An approximate expression for the propagation constant and loss have been given by Baba *et al.* (1998) and Baba and Kokubun (1992). The equivalent transmission line (Jiang *et al.* 1989) and the transverse resonance method (Huang *et al.* 1992) have also been used to investigate the dispersion and loss. A rigorous numerical method is based on a well known transfer matrix method (Chilwell and Hodgkinson 1984; Kubica *et al.* 1990). Because of the leaky property of ARROW modes, the solutions must be found in the complex plane. The root searching in the complex plane could be time consuming and tedious, especially for optimization of multiple layer structures. In this paper, we will give a set of simple characteristic equations for ARROW structures. The root searching for the new equations needs to be carried only on the real axis and

the error is negligible for low loss ARROW modes of practical interest (loss smaller than a few dB/cm). In section 2, characteristic equations of different ARROW structures are presented, which are based on radiation modes and the phase relation in ARROW devices. Section 3 examines the modal characteristics such as effective index, loss and mode profiles in most of the ARROW structures proposed up to now.

The results from our equations and the exact model are then compared. Furthermore, a new ARROW filter, which combines a conventional InP/InGaAsP waveguide and an AlGaAs/GaAs ARROW, is proposed and simulated in Section 4.

2. Characteristic equations

We consider a planar multilayer waveguide as shown in Fig. 1. The general solution of the wave equation in each layer is well known:

$$E_{y,j} = A_j \exp(k_j(x - x_j)) + B_j \exp(-k_j(x - x_j)) \tag{1}$$

where $k_j = \sqrt{\beta^2 - k_0^2 n_j^2}$, A_j and B_j are the complex field coefficients, k_0 is the free space wavenumber, $\beta = k_0 n_{\text{eff}}$ is the propagation constant, n_{eff} is the effective index and x_j is the position of layer j. By imposing the continuity of the field and its derivative for each interface, it is easy to find:
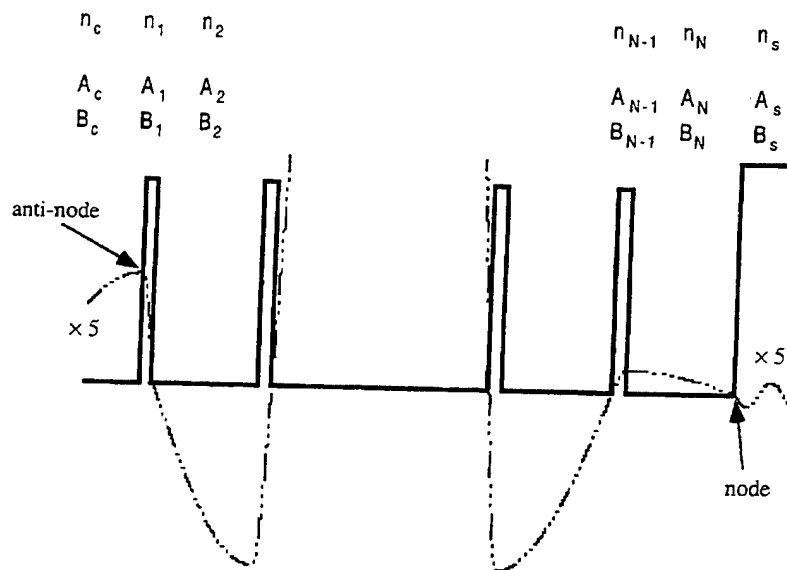
Fig. 1. Schematic diagrams of a planar ARROW structure and the field profile (dash line).

$$\begin{bmatrix} A_{j+1} \\ B_{j+1} \end{bmatrix} = T_j \begin{bmatrix} A_j \\ B_j \end{bmatrix}$$

where

$$T_j = \frac{1}{2} \begin{bmatrix} \left(1 + \zeta_j \frac{k_j}{k_{j+1}}\right) \exp(k_j d_j) & \left(1 - \zeta_j \frac{k_j}{k_{j+1}}\right) \exp(-k_j d_j) \\ \left(1 - \zeta_j \frac{k_j}{k_{j+1}}\right) \exp(k_j d_j) & \left(1 + \zeta_j \frac{k_j}{k_{j+1}}\right) \exp(-k_j d_j) \end{bmatrix}$$

d_j is the thickness of jth layer and

$$\zeta_j = \begin{cases} 1, & \text{TE} \\ n_{j+1}^2/n_j^2, & \text{TM} \end{cases}$$

So we can relate field coefficients in the cover (A_c and B_c) with the coefficients in the substrate (A_s and B_s):

$$\begin{bmatrix} A_s \\ B_s \end{bmatrix} = T \begin{bmatrix} A_c \\ B_c \end{bmatrix} \tag{2}$$

$$T = T_N \cdots T_1 T_c = \begin{bmatrix} t_{11} & t_{12} \\ t_{21} & t_{22} \end{bmatrix}$$

For the guiding modes, the fields should be evanescent in the cap and the substrate layers, so $A_c = 0$ and $B_s = 0$ that results in the characteristic equation:

$$t_{11}(\beta) = 0 \tag{3}$$

For ARROW modes, since they are leaky, a characteristic equation $t_{11}(\beta) = 0$ can be found by assuming outgoing waves in the cover and substrate layers, with correct sign of k_c and k_s chosen (Chilwell and Hodgkinson 1984). The root β resides in the complex plane, so the root searching for structures with many layers and for optimization purposes could be time consuming and tedious. In the following, based on physical arguments, we will introduce a different characteristic equation for the radiation modes, that gives the ARROW mode effective indices on the real axis.

Radiation modes require both incoming and outgoing components to form standing waves in the substrate layer for one sided radiation modes, or in both cover and substrate layers for two sided radiation modes.

Equation (1) holds for radiation modes as well. Since the number of unknown variables is larger than the number of boundary conditions, a characteristic equation cannot be established. A simple relation between A_s (A_c) and B_s (B_c) will allow us to get a characteristic equation for the case of low loss ARROW modes. When the interference layers in ARROW waveguides satisfy the antiresonant condition, the reflectivity is very close to unity and the phase shift in each layer is 90°. This assures that the field at the outermost interface is a node or an anti-node. i.e., $A_s = \pm B_s$ or $A_c = \pm B_c$ for one sided radiation modes and $A_s = \pm B_s$, $A_c = \pm B_c$ for two sided radiation modes from Equation (1). The sign depends on the index of outermost two layers.

Now, let us look at each case separately.

(a) *One sided ARROW modes*: In one sided ARROW, the field in one side (cover) is evanescent $B_c = 0$ and in another side (substrate) is standing wave (actually the amplitude of the 'mode' is increased with the distance because of its lossy nature (Peierls 1979), i.e. $n_{\mathrm{eff}} > n_c$ and $n_{\mathrm{eff}} < n_s$. When the substrate index is larger than that of the last layer, $n_s > n_N$ (the right side of Fig. 1), the field in the outmost interface is a node, $A_s = -B_s$. From Equation (1) we get the characteristic equation:

$$t_{11} + t_{21} = 0 \tag{4}$$

When the index of substrate is smaller than that of the last film layer $n_s < n_N$, the field in the outmost interface is a anti-node (the left side of Fig. 1), $A_s = B_s$. So

$$t_{11} - t_{21} = 0 \tag{5}$$

(b) *Two sided ARROW modes*: In two sided ARROW, the field in both sides are standing waves, i.e. $n_{\mathrm{eff}} < n_c$ and $n_{\mathrm{eff}} < n_s$. There are three cases:
- $n_s > n_N$ and $n_c > n_1$. In this case, $A_s = -B_s$ and $A_c = -B_c$, so

$$t_{11} - t_{12} + t_{21} - t_{22} = 0 \tag{6}$$

- $n_s > n_N$ and $n_c < n_1$ (Fig. 1) or $n_s < n_N$ and $n_c > n_1$, $A_s = -B_s$ and $A_c = B_c$ or $A_s = B_s$ and $A_c = -B_c$, so

$$t_{11} + t_{12} + t_{21} + t_{22} = 0 \tag{7}$$

- $n_s < n_N$ and $n_c < n_1$, $A_s = B_s$ and $A_c = B_c$, so

$$t_{11} + t_{12} - t_{21} + t_{22} = 0 \tag{8}$$

Equations (3)–(8) are the characteristic equations for all kinds of ARROW structures. For all of these the effective index for guided (Equation (3)) and leaky modes (Equations (4)–(8)) for lossless materials can be found on the real axis. After finding the mode's effective index, it is simple to get its profile if we choose the correct A_c and B_c. Based on the first order perturbation theory, the loss of leaky modes can be found: $\alpha = 4.34 k_0$ $\mathrm{Im}\left[t_{11}(n_{\mathrm{eff}})/t'_{11}(n_{\mathrm{eff}})\right] \mathrm{dB}/\mu\mathrm{m}$, where Im is the imaginary part, $t'_{11}(n_{\mathrm{eff}})$ is the differential with respect to n_{eff}.

3. Examples

In order to check the accuracy of our characteristic equations for different ARROW structures, we have compared the calculations with the exact model (Chilwell and Hodgkinson 1984; Kubica et al. 1990). Figs. 2(a)–(d) show the calculated effective index, loss and error as a function of the first interference layer thickness d_1 of an ARROW-A structure using our method and the exact model (Chilwell and Hodgkinson 1984; Kubica et al. 1990). Although this model is based on antiresonant condition, our computation shows that
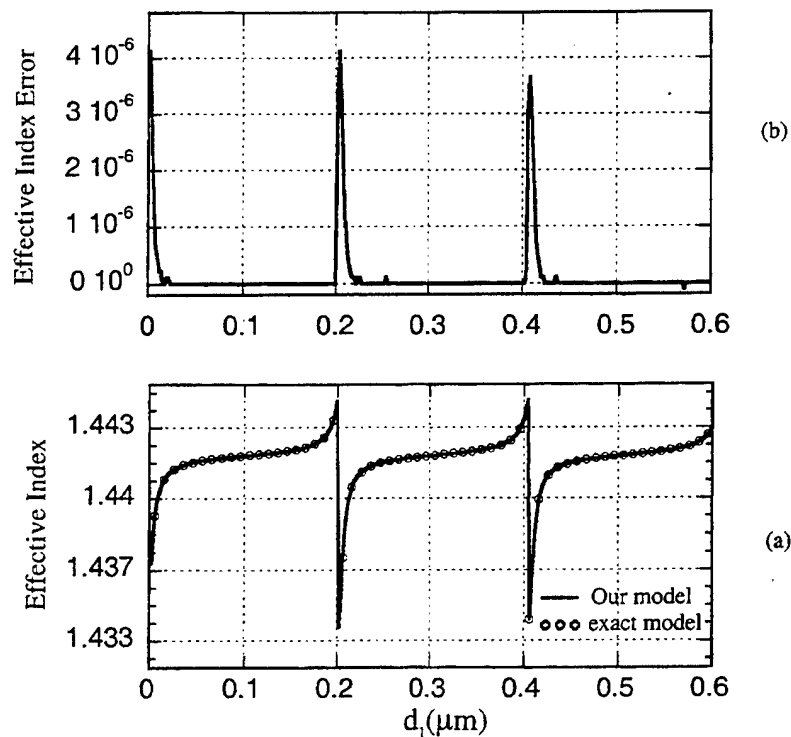
Fig. 2a,b
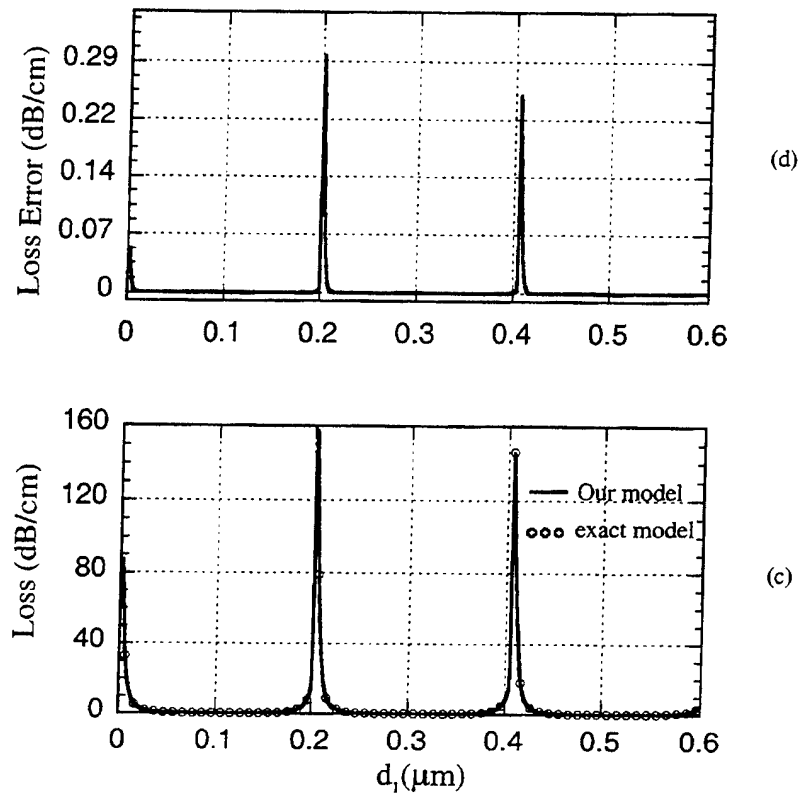
Fig. 2. The calculated effective index (a) and loss (c) of TE_0 mode of ARROW-A structure as a function of the thickness of the first antiresonant layer. (b) and (d) are the errors in our model comparing to the exact calculations.

antiresonance is not critical. Even when the thickness d_1 is far away from antiresonant condition, the current model matches the exact calculations very well (see Fig. 2). For example, when d_1 is around the resonant point where loss is the highest, the error between our method and the exact model is still smaller than 0.2% for TE1 mode. Table 1 displays the effective index and loss for several ARROW waveguides including ARROW-B (Baba and Kokubun 1992), two sided ARROWs and ARROW couplers (Chen and Huang 1996). We can see that for low loss ARROW modes, which are of main interest in practical applications, the approximate model with real roots in identical to the exact complex analysis.

4. InP/InGaAsP–AlGaAs/GaAs ARROW filter

In this section, we propose and design an ARROW filter (Fig. 3) which is based on two different waveguides: a conventional InGaAsP/InP waveguide

Table 1. Comparison of the effective index and loss between our model and exact model

Structure[a]	Characteristic equation	Mode	Effective index (this study)	Loss (dB/cm) (this study)	Effective index (exact)	Loss (dB/cm) (exact)
One sided ARROW-A	$t_{11} + t_{21} = 0$	TE1	1.4417085	0.25	1.4417085	0.25
		TE2	1.41798	270	1.4176	407
One sided ARROW-B	$t_{11} + t_{21} = 0$	TE1	1.5382528	0.11	1.5382527	0.11
		TE2	1.5336896	95	1.5336856	98
Two sided ARROW 1	$t_{11} - t_{12} + t_{21} - t_{22} = 0$	TE1	1.4578523	0.11	1.4578523	0.11
		TE2	1.4518589	76	1.4518454	98
Two sided ARROW 2	$t_{11} + t_{12} - t_{21} - t_{22} = 0$	TE1	3.1540497	0.53	3.1540497	0.53
		TE2	3.1393856	103	3.1393856	113
Two sided ARROW 3	$t_{11} + t_{12} + t_{21} + t_{22} = 0$	TE1	1.4578558	0.06	1.4578558	0.06
		TE2	1.4518726	49	1.4518551	58
ARROW Coupler	$t_{11} - t_{21} = 0$	Even	3.1541037	0.12	3.1541037	0.12
		Odd	3.1539980	0.14	3.1539980	0.14

[a] The structures (index, thickness (from the cap to substrate layers) and wavelength) of calculated ARROWs are listed below:

1. ARROW-A: $n = 1/1.45/3.5/1.45/3.5$; $d = \infty/4/0.1019/2.0985/\infty/\mu m$; $\lambda = 1.3\,\mu m$ (Jiang et al. 1989; Kubica et al. 1990; Huang et al. 1992).

2. ARROW-B: $n = 1/1.54/1.46/1.54/3.85$; $d = \infty/4/0.3/2/\infty/\mu m$; $\lambda = 0.633\,\mu m$ (Baba and Kokubun 1992).

3. Two sided ARROW 1: $n = 3.8/1.46/2.3/1.46/2.3/1.46/3.8$; $d = \infty/2/0.088/4/0.088/2/\infty/\mu m$; $\lambda = 0.633\,\mu m$.

4. Two sided ARROW 2: $n = 3.16/3.55/3.16/3.55/3.16/3.55/3.16/3.55/3.16$; $d = \infty/0.237/2/0.237/4/0.237/2/0.237/\infty/\mu m$; $\lambda = 1.55\,\mu m$.

5. Two sided ARROW 3: $n = 1.46/2.3/1.46/2.3/1.46/2.3/1.46/3.5$; $d = \infty/0.089/2/0.089/4/0.089/2/\infty/\mu m$; $\lambda = 0.6328\,\mu m$.

6. ARROW coupler: $n/1/3.16/3.55/3.16/3.55/3.16/3.55/3.16/3.55/3.16/3.55/3.16$; $d/\infty/2/0.237/4/0.237/2/0.237/4/0.237/2/0.237/\infty/$; $\lambda = 1.55\,\mu m$ (Chen and Huang 1996).

and an AlGaAs/GaAs ARROW waveguide. Since ARROW has a very small waveguide dispersion (Duguay et al. 1986; Chu et al. 1996) and AlGaAs has a low material dispersion compared to a high material dispersion of InGaAsP around 1.55 µm, this structure can realize a narrowband filter. Another advantage of this structure is that ARROW's large mode allows efficient coupling with fibers. In order to make such a filter, the large lattice mismatch between InP and GaAs can be overcome with the use of wafer fusion technology (Liu et al. 1999).

To optimize the design of this ARROW, first we use the approximation equations in Baba et al. (1988) to get the initial d_1 (0.382 µm) and d_2 (2.204 µm), then use an iteration technique to find the optimal d_1 (0.406 µm) and d_2 (2.21 µm) for minimum loss. Since there is no root searching in the complex plane, the calculating time is reduced and the calculated value is the same as the rigorous model. For example, when $\lambda = 1.55\,\mu m$, $d_1 = 0.406\,\mu m$, $d_2 = 2.21\,\mu m$, starting with an initial effective index 3.24 and an initial searching step 0.00001, our model takes 18 s to
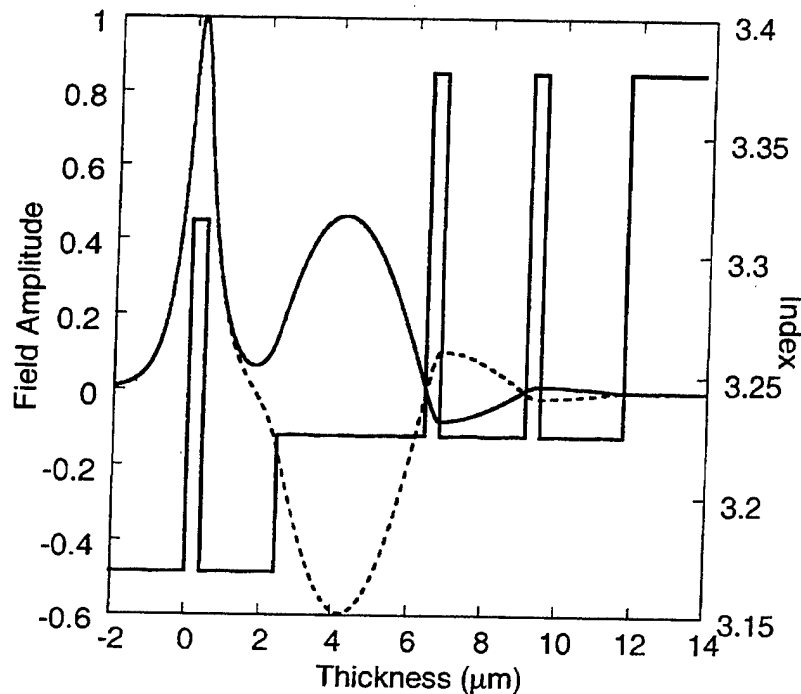
Fig. 3. The structure of InGaAsP/InP–AlGaAs/GaAs ARROW filter and the profiles of even and odd modes. The detailed structure is (from left to right): InP/In$_{0.81}$Ga$_{0.19}$As$_{0.4}$P$_{0.6}$ (0.403 μm)/InP (2 μm)/Al$_{0.4}$Ga$_{0.6}$As (4 μm)/GaAs (d_1)/Al$_{0.4}$Ga$_{0.6}$As (d_2)/GaAs (d_1)/Al$_{0.4}$Ga$_{0.6}$As (d_2)/GaAs.

find the root with $<$ le $-$ 10 error, while the rigorous model takes 31 s on a PC (Pentium II, 266 MHz). The thickness of InGaAsP/InP waveguide is chosen to be 0.403 μm in order to satisfy the phase matching around 1.55 μm. The important characteristics of the filter are the dispersion curves of the two waveguides. Figs. 4 and 5 show the effective index and the loss of the separated waveguides and the even and odd supermodes of the coupled structure. As we expect from the design, the effective indices of two separated waveguides are the same at the phase matching point at 1.549 μm. Without coupling, the conventional InGaAsP/InP waveguide has no loss (neglecting the loss introduced by the material and process), and the AlGaAs/GaAs ARROW has a small loss, which increases slightly with the wavelength. When the two waveguides are coupled, the losses of even and odd modes of the coupler are the same at the phase matching condition. The field profiles of even and odd modes are also calculated and they are shown in Fig. 3. All these calculations match very well the rigorous model.
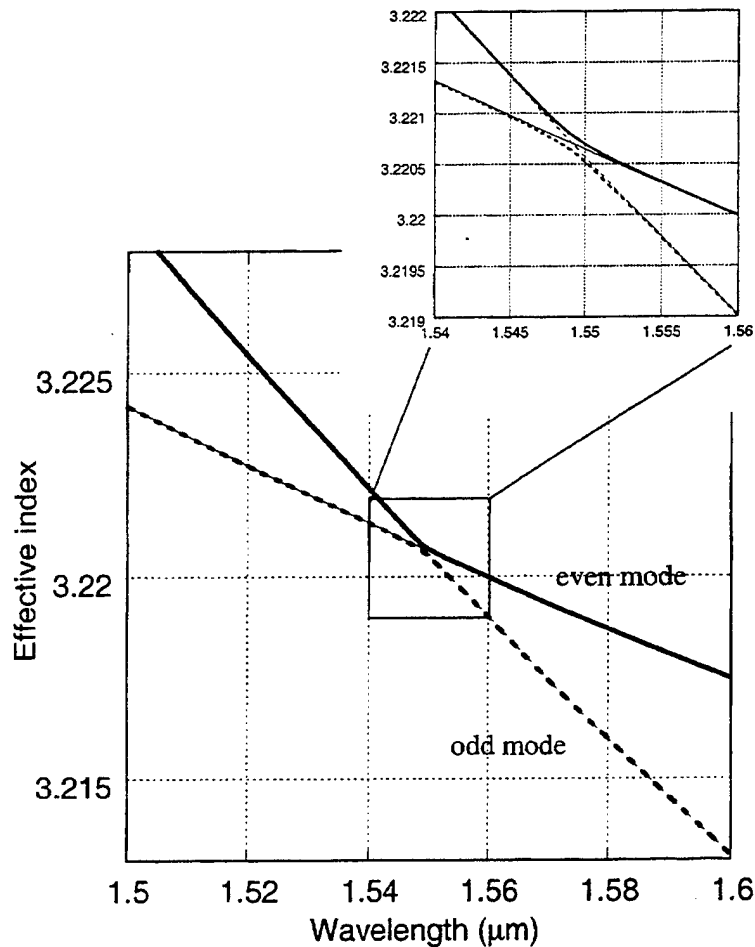
Fig. 4. The dispersion for the modes of the individual waveguides and the supermodes of the coupler filter. The calculations include the material dispersion.

5. Conclusion

In this paper, a set of simple and versatile characteristic equations is given for different ARROW structures. This method gives the precise effective index, loss and mode profile for low loss ARROW modes of practical interest (i.e. when their loss is smaller than a few dB/cm). This enables root searching in the real domain. The physical argument is simply based on the property of antiresonance and small loss, which means that the reflectivity at the outer-most boundaries is near 1, and a phase relation existing for the field at the outermost layers. The use of these characteristic equations is demonstrated for different ARROW waveguides, couples and filter. This simple physical
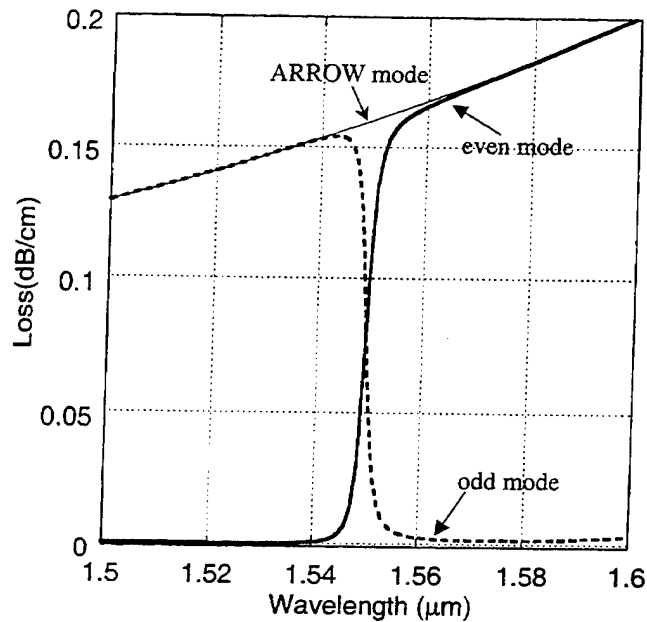
Fig. 5. The loss of even and odd supermodes of InGaAsP/InP–AlGaAs/GaAs ARROW filters. The top thin line is the loss of the separated AlGaAs/GaAs ARROW.

argument gives an accurate intuitive picture for loss leaky modes and it can be used to design and optimize ARROW devices.

References

Baba, T. and Y. Kokubun. *IEEE J. Quantum Electron.* **28** 1689, 1992.
Baba, T., Y. Kokubun, T. Sakakia and K. Iga. *J. Lightwave Technol.* **6** 1440, 1988.
Chen, Y.H. and Y.T. Huang. *J. Lightwave Technol.* **14** 1507, 1996.
Chilwell, J. and I. Hodgkinson. *J. Opt. Soc. Am. A* **1** 742, 1984.
Chu, S.T., M. Miura and Y. Kokubun. *IEEE Photon. Technol. Lett.* **8** 1492, 1996.
Duguay, M.A., Y. Kokubum and T.L. Koch. *Appl. Phys. Lett.* **49** 13, 1986.
Gehler, J., A. Brauer and W. Karthe. *Electron. Lett.* **30** 218, 1994.
Huang, W.P., R.M. Shubair, A. Nathan and Y.L. Chow. *J. Lightwave Technol.* **10** 1015, 1992.
Jiang, W., J. Chrostowski and M. Fontaine. *Opt. Commun.* **72** 180, 1989.
Kubica, J., D. Uttamchandani and B. Culshaw. *Opt. Commun.* **78** 133, 1990.
Liu, B., A. Shakouri, P. Abraham, Y. Chiu, S. Zhang and J.E. Bowers. *IEEE Photon. Technol. Lett.* **11** 93, 1999.
Peierls, R. *Surprises in theoretical physics*, Princeton University Press, Princeton, NJ, 1979.
Trutschel, U., F. Ouellete, V. Delisle, M.A. Duguay, G. Fogarty and F. Legerer. *J. Lightwave Technol.* **13** 239, 1995.

Conclusion: We have confirmed that the temperature-coefficient of the average dispersion of a ZDF transmission line is 100 times smaller than that of a conventional DSF. Temperature-independent 80Gbit/s OTDM transmission using the 168km ZDF transmission line has been successfully demonstrated. No penalty was observed for the ZDF transmission line over a temperature range of 50°C without adaptive dispersion equalisation while the penalty for 151km DSF transmission was 4.1dB.

Acknowledgment: The authors would like to thank M. Kawachi and K. Sato of NTT Network Innovation Laboratories and O. Mitomi of NTT Photonics Laboratories for their continuous encouragement.

K. Yonenaga, A. Hirano, S. Kuwahara, Y. Miyamoto, H. Toba and K. Sato (*NTT Network Innovation Laboratories, 1-1 Hikarinooka. Yokosuka-shi, Kanagawa-ken, 239-0847, Japan*)

E-mail: yonenaga@exa.onlab.ntt.co.jp

H. Miyazawa (*NTT Photonics Laboratories, 3-1 Morinosato Wakamiya. Atsugi-shi, Kanagawa-ken, 243-0198, Japan*)

References

1 HAGIMOTO, K., YONEYAMA, M., SANO, A., HIRANO, A., KATAOKA, T., OTSUJI, T., SATO, K., and NOGUCHI, K.: 'Limitations and challenges of single-carrier full 40Gbit/s repeater system based on optical equalization and new circuit design'. Tech. Dig. OFC '97, Dallas, 1997, Paper ThC1, pp. 242–243

2 KIM, K.S., and LINES, M.E.: 'Temperature dependence of chromatic dispersion in dispersion-shifted fibers: Experiment and analysis', *J. Appl. Phys.*, 1993, 73, (5), pp. 2069–2074

3 KUWAHARA, S., SANO, A., YONENAGA, K., MIYAMOTO, Y., and TOBA, H.: 'Simple zero dispersion detection technique using alternating chirp signal in automatic dispersion equalisation systems', *Electron. Lett.*, 1998, 34, (20), pp. 1956–1958

4 SANO, A., KUWAHARA, S., and MIYAMOTO, Y.: 'Adaptive dispersion equalization of 8-ps pulses in 400-km transmission line by monitoring relative phase shift between spacing-fixed WDM signals'. Tech. Dig. OFC '99, San Diego, 1999, Paper WJ4, pp. 165–167

5 MUKASA, K., AKASAKA, Y., SUZUKI, Y., and KAMIYA, T.: 'Novel network fiber to manage dispersion at 1.55µm with combination of 1.3µm zero dispersion single mode fiber'. Tech. Dig. ECOC '97, Edinburgh, 1997, Vol. 1, pp. 127–130

6 MIYAMOTO, Y., YONENAGA, K., HIRANO, A., SHIMIZU, N., YONEYAMA, M., KATARA, H., NOGUCHI, K., and TSUZUKI, K.: '1.04-Tbit/s DWDM transmission experiment based on alternate-polarization 80-Gbit/s OTDM signals'. Tech. Dig. ECOC '98, Madrid, 1998, Post-Deadline Papers, pp. 53–57

7 YONENAGA, K., and MIYAMOTO, Y.: 'Dispersion-managed high-capacity WDM systems using zero-dispersion-flattened transmission line'. Paper FD4, Tech. Dig. OFC '99, 1999, (San Diego), pp. 71–73

8 OTSUJI, T., YONEYAMA, M., IMAI, Y., ENOKI, T., and UMEDA, Y.: '64 Gbit/s 2:1 multiplexer IC using InAlAs/InGaAs/InP HEMTs', *Electron. Lett.*, 1997, 33, (17), pp. 1488–1489

9 NOGUCHI, K., MITOMI, O., and MIYAZAWA, H.: 'Low-voltage and broadband Ti:LiNbO₃ modulators operating in the millimeter wavelength region'. Tech. Dig. OFC '96, San Jose, 1996, Paper ThB2, pp. 205–206

10 SATO, K., HIRANO, A., ASOBE, M., and ISHII, H.: 'Chirp-compensated 40 GHz semiconductor modelocked lasers integrated with chirped grating', *Electron. Lett.*, 1998, 34, (20), pp. 1944–1946

Wavelength routing of 40Gbit/s packets with 2.5Gbit/s header erasure/rewriting using all-fibre wavelength converter

B.-E. Olsson, P. Öhlén, L. Rau, G. Rossi, O. Jerphagnon, R. Doshi, D.S. Humphries, D.J. Blumenthal, V. Kaman and J.E. Bowers

40Gbit/s packet wavelength routing and 2.5Gbit/s header replacement is demonstrated using an ultra-high-speed wavelength converter. Burst-mode bit error rate measurements are performed on both the header and payload before and after wavelength routing, with < 4dB penalty in the payload and < 2.5dB penalty in the header.

Introduction: The exponential growth in Internet traffic is forcing next generation IP data networks to a scale far beyond present performances. Optical packet switching technologies may be required to deliver low-latency packet forwarding and routing at terabit wire rates and should support header erasure and rewriting. The latter is important for all-optical label swapping (AOLS) [1] and new simpler IP routing protocols such as multi-protocol label switching (MPLS) [2]. Initial experiments on AOLS with packet rate wavelength conversion [3] and optical packet switching [4] have been reported as well as basic routing experiments at 100Gbit/s using all-optical header processing [5]. However, demonstrations of wavelength routing with bit error rate (BER) measurements and header replacement have been limited to bit rates at 10 Gbit/s or below, mainly due to speed limitations in the wavelength converter technology. In this Letter we report the wavelength routing of packets with 40Gbit/s return-to-zero (RZ) payloads and replacement of 2.5 Gbit/s time domain non-return-to-zero (NRZ) headers. Every other packet is routed to two different wavelengths while simultaneously erasing the old header and rewriting a new one on the new wavelength. A novel wavelength converter (WC) [6] plays a key role in the header replacement process by wavelength converting the payload while simultaneously erasing and rewriting the header. Burst-mode BER measurements were performed on packets for the payload before and after wavelength conversion, and on the original and the replaced header. The possible switching speed and packet length in this architecture are determined by the tunable laser in the wavelength converter, presently ~5ns. The WC is based on cross-phase modulation (XPM) in an optical fibre, which has the potential for operating at ultra-high bit rates. When the incoming data are combined with a continuous wave (CW) signal and sent through an optical fibre, the data impose a phase modulation on the CW light through XPM. This phase modulation generates optical sidebands in the CW signal, which can be converted to amplitude modulation by suppressing the original CW carrier using an optical notch filter. In this Letter, a loop mirror filter (LMF) was used which consisted of a short piece of birefringent fibre in a Sagnac interferometer. Such a filter is tunable, polarisation independent, and has repetitive notches, which enables conversion to different equally spaced wavelengths to be achieved without any further adjustment. The transfer function of the WC is nonlinear, thus if the amplitude of the input signal is low, a very small portion is converted to the new wavelength. This phenomenon is used to remove the header of the packet since the header peak power can be substantially lower than the RZ payload while still keeping the same energy per bit in the header and the payload.

Experimental results: Fig. 1 shows the experimental setup. The packet generator consisted of an actively modelocked fibre ring laser generating 10ps pulses with a time-bandwidth product (TBP) of 0.45 at 1536nm followed by an LiNbO₃ modulator encoding 10Gbit/s PRBS data with a word length of $2^{31}-1$. The 10Gbit/s data were injected into a passive 10 to 40Gbit/s multiplexer consisting of polarisation maintaining (PM) fibre with 75 and 150ps delays. An acousto-optical modulator (AOM) gated out a 2.5µs payload that was combined with a 2.5Gbit/s (PRBS 27–1) 500ns long header. The header was aligned in front of the payload with a 100ns guard band determined by the 100ns rise time in the AOM, and a 100ns guard band was inserted between each packet, giving a total packet length of 3.2µs. The packets were injected into the WC which consisted of an erbium-doped fibre amplifier

(EDFA) with an average output power of +18dBm followed by 5km dispersion-shifted fibre (DSF) with a zero-dispersion wavelength of 1542nm. A grating coupled sampled rear reflector (GCSR) laser [7] that could be tuned to either 1538 or 1543nm within 5ns determined the new wavelength. The GCSR laser was also used to encode the new 2.5Gbit/s header before entering the WC. After the DSF, an LMF, consisting of a loop mirror with 4m of PM fibre and a polarisation controller to allow adjustment of the filter wavelength, was used to suppress the original CW light. The separation between the notches was 1 nm (given by the length of the PM fibre) and the suppression was better than 27dB. A second filter was used to select one of the two sidebands and to suppress the original data. The use of only one sideband retained the pulse width and TBP from the input pulse. The 40Gbit/s receiver consisted of a 40 to 10Gbit/s demultiplexer followed by a 10Gbit/s preamplified receiver. The demultiplexer was based on an electroabsorption modulator (EAM), driven with a 30ps electrical pulse to achieve a 15ps switching window. The 2.5Gbit/s header receiver consisted of an AOM to remove the payload, which otherwise would dominate the measured optical average power, followed by an optically preamplified receiver. The BER measurements were made on both the payload and header, and gated to select the appropriate time interval.
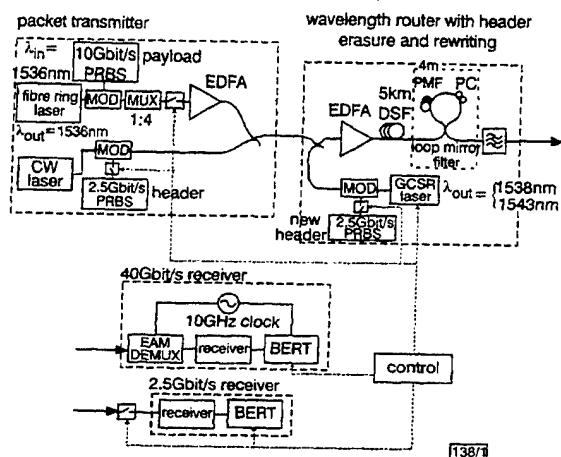
Fig. 1 *Experimental setup*

MOD: LiNbO₃ modulator; MUX: passive 10 to 40 Gbit/s multiplexer; PC: polarisation controller; EAM DEMUX: demultiplexer using electroabsorption modulator; BERT: bit error rate test set
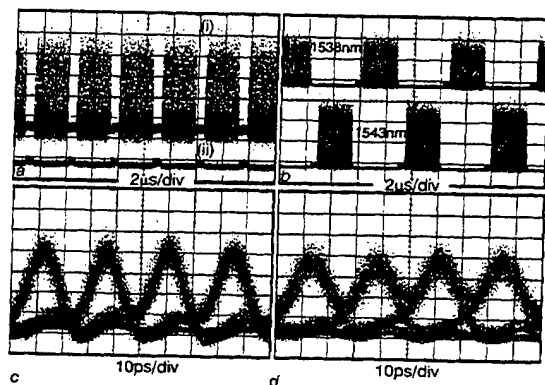
Fig. 2 *Packets and eye-patterns before and after wavelength routing*

a Packets before wavelength routing
(i) 40Gbit/s RZ payload and 2.5Gbit/s NRZ header
(ii) headers without payload
b 40Gbit/s eye-patterns before wavelength routing
c Packets routed to 1538 and 1543nm
d Eye pattern of routed packet at 1543nm

Fig. 2*a* shows the input packets consisting of the 40Gbit/s RZ payload and the 2.5Gbit/s NRZ header with ~10dB less peak power. The lower trace shows the headers without the payload.

Fig. 2*b* shows every other packet routed to 1538 and 1543nm with new inserted headers. The eye patterns of Fig. 2*c* and *d* were taken zooming into the payload, before (1536nm) and after the WC (1543nm). BER measurements were performed on both the header and payload on incoming and outgoing packets. The BER detector was gated and error measurements could only be performed on ~80% of all bits in the packets due to the number of bits required to synchronise the BER detector. Fig. 3*a* shows the BER for all four 10Gbit/s TDM channels in the 40Gbit/s payload for the input packets at 1536 nm and the output packets at 1543 and 1538nm. All channels at both output wavelengths have < 4dB penalty compared with the input packets, and this penalty is believed to be due to non-optimal filtering in the wavelength converter and to polarisation instabilities in the input 40Gbit/s data.
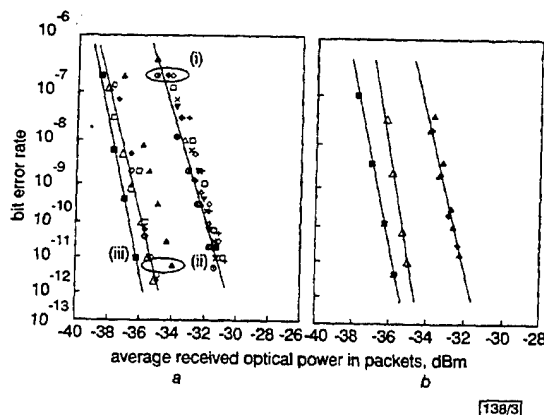
Fig. 3 *Bit error rate measurements*

a Bit error rate measurements for 40Gbit/s before and after wavelength routing

■ 10Gbit/s data	◇ channel 2, 1538nm
△ 10Gbit/s packet	▼ channel 3, 1538nm
▲ channel 1, 1536nm	✕ channel 4, 1538nm
◆ channel 2, 1536nm	⊙ channel 1, 1543nm
☐ channel 3, 1536nm	✢ channel 2, 1543nm
○ channel 4, 1536nm	⊠ channel 3, 1543nm
△ channel 1, 1538nm	+ channel 4, 1543nm

(i) 40Gbit/s wavelength conversion
(ii) 40Gbit/s input packets
(iii) 10Gbit/s baseline
b Bit error rate measurements for 2.5Gbit/s baseline, original header and replaced headers

■ baseline CW	▲ header 1538nm
△ original header	◆ header 1543nm

At 10Gbit/s wavelength conversion the penalty was < 1dB which indicates that a major part of the penalty is due to instabilities in the 40Gbit/s data. Fig. 3*b* shows BER measurements of the old and replaced headers. The old header is completely removed in the wavelength converter and a new header could be successfully inserted, with no crosstalk penalty from the old header. However, a receiver penalty of 2.5dB was measured, probably due to distortion from the sharp notches of the LMF. In a filter with a flatter stop band, e.g. a fibre Bragg grating, this distortion would probably be avoided.

B.-E. Olsson, P. Öhlén, L. Rau, G. Rossi, O. Jerphagnon, R. Doshi, D.S. Humphries and D.J. Blumenthal (*Optical Communications and Photonic Networks Group, University of California, Department of Electrical and Computer Engineering, Santa Barbara, CA 93106, USA*)

V. Kaman and J.E. Bowers (*Ultrafast Optoelectronics Research Group, University of California, Department of Electrical and Computer Engineering, Santa Barbara, CA 93106, USA*)

P. Öhlén: On leave from Royal Institute of Technology, Sweden

G. Rossi: On leave from University of Pavia, Italy

References

1 BLUMENTHAL, D.J., et al.: 'All-optical label swapping with wavelength conversion for WDM-IP networks with subcarrier multiplexed addressing', *IEEE Photonics Technol. Lett.*, 2000, **11**, pp. 1497–1499

2 VISWANATHAN, A., et al.: 'Evolution of multiprotocol label switching', *IEEE Commun. Mag.*, 1998, **36**, pp. 165–173

3 CARENA, A., et al.: 'OPERA: An optical packet experimental routing architecture with label swapping capability', *J. Lightwave. Technol.*, 1998, **LT-16**, pp. 2135–2145

4 CHIARONI, D., et al.: 'Physical and logical validation of a network based on all-optical packet switching systems'. *J. Lightwave. Technol.*, 1998, **LT-16**, pp. 2255–2264

5 TOLIVER, P., et al.: 'Routing of 100Gb/s word in a pocket-switched optical networking demonstration (POND) node', *J. Lightwave. Technol.*, 1998, **LT-16**, pp. 2169–2180

6 OLLSON, B.E., et al.: 'A simple and robust high-speed wavelength converter using fiber cross-phase modulation and filtering'. Proc. Opt. Fiber Comm. Conf., 2000, Baltimore, USA, Paper WE1

7 RIGOLE, P.-J., et al.: '114-nm wavelength tuning range of a vertical grating assisted codirectional coupler laser with a super structure grating distributed Bragg reflector', *IEEE Photonics Technol. Lett.*, 1995, **7**, pp. 697–699

Characterisation of single stage, dual-pumped Raman fibre amplifiers for different gain fibre lengths

F. Koch, S.V. Chernikov, S.A.E. Lewis and J.R. Taylor

The power dependent gain length of dispersion shifted fibre Raman amplifiers has been characterised. The noise performance has also been investigated.

Broadband silica fibre Raman amplifiers (FRAs) are particularly attractive for ultra-broadband applications in telecommunications. Raman amplifiers can operate throughout the low loss window of optical fibres from 1.1 to 1.7μm compared with conventional erbium doped amplifiers which are deployed in the 1.55μm region. Raman amplification offers the advantages of greatly extended bandwidth and distributed amplification [1] with the installed fibre as the gain medium. Here we report the characterisation of the pump power requirements and spontaneous noise performance of a dual wavelength pumped Raman amplifier for a wide range of gain fibre lengths covering the range applicable to discrete or distributed amplification.

The amplifier was constructed from sections of dispersion shifted fibre of different lengths spliced together, with optical circulators employed to multiplex and demultiplex the pump and signal. The single stage amplifier was counter-pumped [2] using fibre Raman lasers operating at fundamental wavelengths of 1423 and 1455nm. This configuration allows broadband amplification in the 1.5μm region [3, 4]. For each amplifier length, the pump power was adjusted to achieve a peak gain of 15dB. At lower pump power levels the trends shown in the gain and noise figures were similar to those at 15 dB which are exclusively reported in this Letter.

A CW diode laser tunable from 1500 to 1580nm at a power of –20dBm was used as the signal source. The measurements were carried out with a computer-automated system controlling the tunable laser and optical spectrum analyser using the spectral division method. For each amplifier length the pump power was adjusted to equalise the gain peaks to 15dB. The pump power was calibrated using a broadband thermal detector with an accuracy of 6%, with the error in this measurement arising primarily from the calibration of the power meter and an additional small systematic error dependent on the repeatability of the splice to the circulator. Unlike the erbium amplifier the spontaneous noise figure does not depend sensitively on the pump power.

Fig. 1 shows the required pump powers for the 1423 and 1455nm pumps to achieve a 15dB gain at the two gain peaks around 1523 and 1555nm, respectively. The short wavelength pump is operated at a higher power due to the inter-pump Raman

interaction which causes a progressive power transfer from the short to the long wavelength pump as these signals propagate along the length of the amplifier. The overall required pump power decreases with the amplifier length as the effective nonlinear interaction length grows, while the differential pump power increases as a result of the inter-pump interaction. Around an amplifier length of ~23km the amplifier starts to become very weakly pumped at the input and the pump power at 1423nm has to be increased to maintain the desired gain. In the case of an unsaturated amplifier the maximum gain is limited by the direct loss at the signal wavelength and the effective length given by the loss at the pump wavelength [5]. From the minimum required pump power from Fig. 1 it can be estimated that the pump power is used most efficiently for the 1423nm pump when the amplifier length is less than ~23km. This length is slightly longer than the effective nonlinear length for a single wavelength pumped amplifier as a result of the inter-pump Raman interaction.
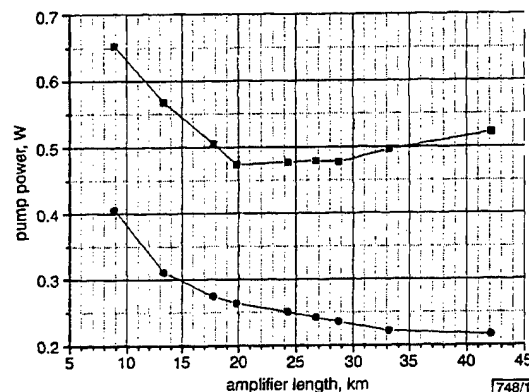
Fig. 1 *Required pump power for 15dB maximum gain*

—■— 1423nm
—●— 1455nm
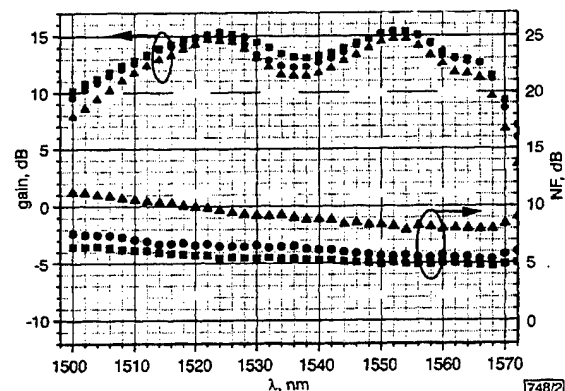
Fig. 2 *Noise figure and gain for different amplifier lengths*

■ 9km
● 19km
▲ 46km

Fig. 2 shows the representative gain and noise figure spectra for three different lengths for peak gains of 15dB. All the measurements include the loss of the splices and circulator coupling losses which add to the noise figure. The variations in the gain shape are mainly due to slight variations in the pump peak wavelength and spectral width with different pump powers. Some gain narrowing occurs for longer fibre lengths because the gross gain is higher to compensate for the increased loss, but the main contribution is due to the pump variations. This has been confirmed by numerical simulation [3]. The variation in noise figure for three representative wavelengths is shown against amplifier length in Fig. 3. As expected, the noise figure increases with length as the fibre becomes less strongly pumped at the amplifier input and, for

A wavelength multiplexer using cascaded three-dimensional vertical couplers

Bin Liu,[a] Ali Shakouri,[b] P. Abraham, and John E. Bowers
Department of Electrical and Computer Engineering University of California, Santa Barbara, California 93106

A four-channel wavelength multiplexer/demultiplexer for sparse wavelength division multiplexing was demonstrated using cascaded three-dimensional (3D) vertical couplers. 17 nm channel spacing with crosstalk less than 15 dB was achieved. Strong coupled vertical couplers were fabricated using wafer bonding to invert a conventionally processed epitaxial layer and bond to a new host substrate. This technology makes the fabrication of 3D photonic integrated circuits and the realization of multilevel optical interconnects possible. © *2000 American Institute of Physics.*
[S0003-6951(00)03303-9]

Increasing integration density is a key factor to reduce cost and improve performance in optoelectronic circuits. In conventional wafer processing, only one side of epitaxial films are used to fabricate photonic integrated circuits. If both sides of the epitaxial layers can be processed, three-dimensional (3D) structures can be fabricated and the integration density can be considerably increased. Since epitaxial layers, by themselves, are too thin to handle and process directly they must be transferred and bonded to other host substrates. For optoelectronic device applications, the bonded interface must be both electronically and optically transparent to make multilevel electrical and optical interconnects possible. The requirement for optical transparency means that the conventional bonding techniques such as flip-chip solder bonding are not suitable for photonic integration. Wafer bonding,[1,2] on the other hand, provides an interface with low electrical and optical loss.[3–5] In this letter, we demonstrate a wavelength multiplexer by cascading strong coupled 3D vertical couplers using wafer bonding technique and double-sided processing.

Wavelength multiplexers and demultiplexers (MUX/DEMUX) are the essential components in wavelength division multiplexing (WDM) networks. Although multiplexers based on directional couplers have been studied for a long time, they are applicable only to the case where the channel spacing is quite large (e.g., 980 and 1550 nm or 1300 and 1550 nm).[6] This is because of the weak wavelength dependence of the coupling coefficient in horizontally arranged directional couplers. Otherwise a very long device length is required. Compared to horizontal couplers, vertical couplers offer much stronger coupling since the thickness of the guiding layer and the space between two waveguides can be very small and precisely determined by the epitaxial growth.[4,7] The multichannel multiplexers with narrow channel spacing can be achieved by cascading several strongly coupled vertical couplers. However, separating the two input and output waveguides in conventional vertically coupled twin waveguide structures is difficult. This limits practical applications, and makes the cascading of several vertical couplers impos-

sible. This problem is solved using double-sided epitaxial layer processing by wafer bonding in this letter.

The schematic drawing in Fig. 1(a) shows a four-channel multiplexer, which cascades two stages of 3D vertical couplers with different lengths. As can be seen in Fig. 1(b), the two waveguides of the 3D vertical couplers are coupled vertically and separated horizontally in different planes. This separation makes the cascading of vertical couplers possible. The operation principle of a multiplexer by cascading verti-
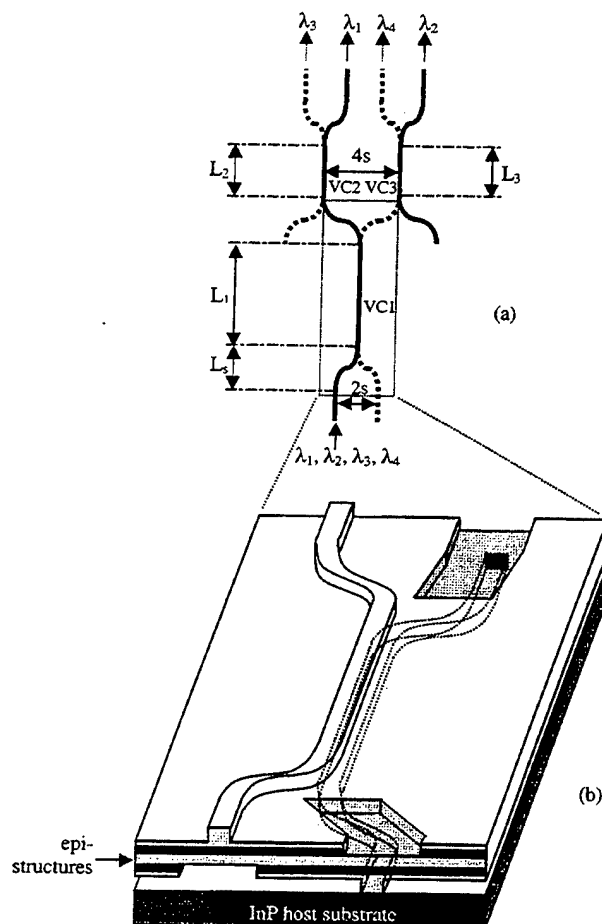
FIG. 1. (a) Schematic drawing of a four-channel MUX/DEMUX. Solid lines are the top waveguides and the dashed lines are the bottom ones, and (b) 3D vertical coupler with horizontally separated input and output waveguides.

[a]Electronic mail: liu@opto.ucsb.edu
[b]Also at: Jack Baskin School of Engineering, University of California, Santa Cruz, CA 95064.
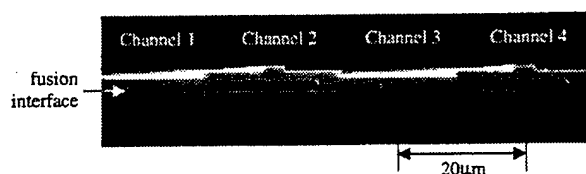
FIG. 2. The SEM picture of the output facet of a four-channel MUX/DEMUX.

cal couplers is the same as that of two-mode-interference (TMI) based multiplexers.[8,9] The output intensity of each stage is a periodic function of the optical frequency. The period is inversely proportional to the coupler length. Vertical coupler 1 (VC1) is twice as long as that of VC2 in the second stage, so the wavelength oscillation period (channel spacing) of VC1 is half that of VC2. VC3 has nearly the same wavelength period as VC2, but the peaks in the output should be shifted by a quarter period to match the channels. This can be achieved by a small adjustment to the length of VC3. In our design, after considering the coupling in the s-bend regions using a 3D beam propagation analysis, the parameters are chosen: $L_1 = 5$ mm, $L_2 = 2.397$ mm, $L_3 = 2.37$ mm for the vertical couplers and $s = 10 \mu$m, $L_s = 500 \mu$m for s-bends.

The epitaxial structure is grown using metal organic chemical vapor deposition (MOCVD). It includes a 0.8 μm InP frontside ridge layer, a 15 nm InGaAsP (band gap 1.1 μm) etch stop layer, a 0.1 μm InP cap layer, a 0.5 μm InGaAsP (band gap 1.3 μm) frontside guiding layer, a 0.6 μm InP coupling layer, the same backside guiding, cap, etch stop, and ridge layers, and finally a 0.2 μm InGaAs layer used to remove the InP substrate. First, the 3 μm width frontside ridge waveguides are formed by reactive ion etching (RIE) and chemical wet etching. The frontside guiding layer above the backside waveguides in noncoupling areas is removed by another step of photolithography and wet etching. The waveguide sample is then inverted and bonded to a bare InP host substrate under pressure for 50 min at 630 °C in H_2 atmosphere. After removing the original InP substrate and InGaAs etch stop layer, the alignment windows are opened by photolithography and wet etching to expose alignment marks, then the other side waveguides are fabricated and the unneeded guiding layers are removed as before. Figure 2 shows a scanning electron microscope (SEM) picture of the output facet of a four-channel device. The device length is

FIG. 4. Four-channel multiplexer transmission spectra.

about 1.4 cm after cleaving both facets. The transferred and bonded thin epitaxial film is robust and it is processed using the same techniques as other planar photonic integrated circuits.

To characterize the device performance, light from a tunable laser was coupled to an input waveguide by a single mode fiber. The light at the output was collected by another single mode fiber that was connected to a detector. The near field images were recorded by an infrared (IR) camera with a 20× lens. Figure 3 shows the near field images at different wavelengths: 1508, 1524, 1543, and 1561 nm, which are the peak response of the four channels. The corresponding output light intensity as a function of wavelength for the four channels is shown in Fig. 4. The free spectral range is about 68 nm, as can be seen in the response of channel 2. The channel spacing is 17 nm for a four-channel multiplexer. The measured adjacent channel crosstalk ranges from −13 dB to −20 dB. This can be further improved by fine tuning the second stage of vertical couplers to overcome fabrication imperfections. The channel spacing can be reduced by increasing the device length or the wavelength dependence of the coupling coefficient. Figure 5 shows the transmission spectrum of a 2-channel MUX/DEMUX with an 8 mm interaction length. The channel spacing is about 11 nm.

In conclusion, a four-channel wavelength multiplexer

FIG. 3. Near field images of a four-channel multiplexer at different wavelengths.
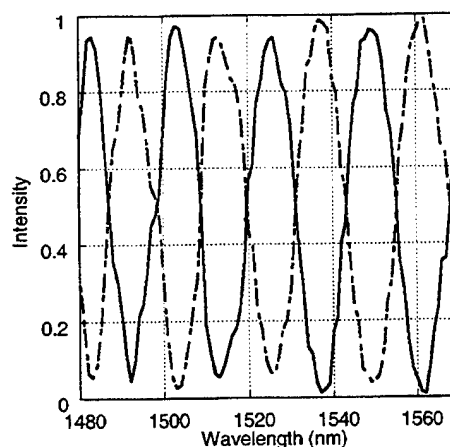
FIG. 5. The transmission spectrum for a two-channel MUX/DEMUX with an 8 mm interaction length.

using cascaded 3D vertical couplers has been successfully demonstrated. 17 nm channel spacing with crosstalk less than 13 dB–20 dB is achieved. By cascading additional stages of vertical couplers, a multichannel MUX/DEMUX can be realized. Using wafer bonding, a conventionally processed epitaxial layer can be inverted and bonded to a new host substrate. The backside of the epitaxial films can then be processed as well. This kind of double-sided processing makes the fabrication of 3D photonic integrated circuits possible and increases the integration density.

[1] Z. L. Liau and D. E. Mull, Appl. Phys. Lett. **56**, 737 (1990).

[2] Y. H. Lo, R. Bhat, D. M. Hwang, M. A. Koza, and T. P. Lee, Appl. Phys. Lett. **58**, 1961 (1991).

[3] Z. H. Zhu, F. E. Ejeckam, Y. Qian, Z. Jizhi, Z. Zhenjun, G. L. Christenson, and Y. H. Lo, IEEE J. Sel. Top. Quantum Electron. **3**, 927 (1997).

[4] L. Bin, A. Shakouri, P. Abraham, K. Boo-Gyoun, A. W. Jackson, and J. E. Bowers, Appl. Phys. Lett. **72**, 2637 (1998).

[5] A. Shakouri, L. Bin, P. Abraham, and J. E. Bowers, Crit. Rev. Opt. Sci. Technol. , **CR-71**, 181 (1999).

[6] H. C. Cheng and R. V. Ramaswamy, IEEE Photonics Technol. Lett. **2**, 637 (1990).

[7] F. Dollinger, M. V. Borcke, G. Bohm, G. Trankle, and G. Weimann, Electron. Lett. **32**, 1509 (1996).

[8] Y. Chung, J. C. Yi, S. H. Kim, and S. S. Choi, J. Lightwave Technol. **7**, 766 (1989).

[9] J. P. Lin, R. Hsiao, and S. Thaniyavarn, Electron. Lett. **25**, 1608 (1989).
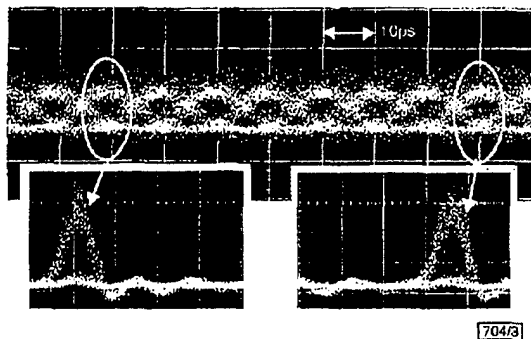
Fig. 3 *Eye diagram of 100Gbit/s signal (photodiode bandwidth 50GHz)*

Insets: Eye diagrams showing clear and open eyes of two demultiplexed 10Gbit/s signals
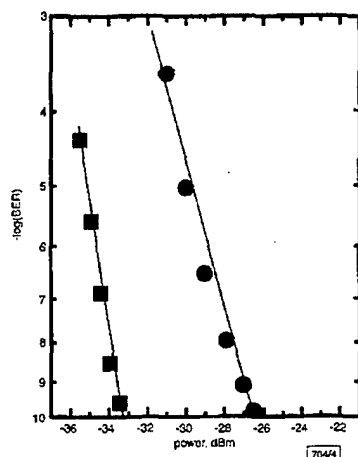
Fig. 4 *Measured BER of 100Gbit/s wavelength converted signal against received power at input to optical preamplifier*

$PRBS = 2^{31}-1$
◆ back-to-back
● BER of converted signal

Eye diagrams of the 100Gbit/s signal as recorded with a 500Hz bandwidth photodiode are shown in Fig. 3. There is not sufficient resolution to resolve the 100Gbit/s eye diagram. However, the 100Gbit/s signal was subsequently demultiplexed into ten signal streams of 10Gbit/s [9] and the eye diagrams of these demultiplexed signals show clear and open eyes. The eye diagrams of the second and ninth demultiplexed signals are shown as an example in the lower left and right inset of Fig. 3. The BER of the converted 100Gbit/s signal, as shown in Fig. 4, was measured after demultiplexing back to 10Gbit/s and feeding this signal to an optically preamplified *pin* receiver. Thus, the received power was measured for 10Gbit/s. The penalty is due to format conversion (~2dB), extinction ratio degradation (~0.5dB), the pattern dependence of long words (~3dB) and signal-to-noise ratio degradation. All ten demultiplexed signals gave a BER within 1dB around the depicted curve. The polarisation sensitivity against the input signal was below 2dB.

Conclusions: We have performed the first 100Gbit/s wavelength conversion experiment exploiting cross-phase modulation in an SOA. A novel compact and fully packaged SOA delayed-interference wavelength converter was employed to perform the experiments. BER measurements show that these are the best SOA based wavelength conversion results ever obtained at 100Gbit/s.

J. Leuthold, C.H. Joyner, B. Mikkelsen, G. Raybon, J.L. Pleumeekers, B.I. Miller, K. Dreyer and C.A. Burrus (*Bell Labs, Lucent Technologies, Holmdel, NJ 07733, USA*)

References

1 DANIELSEN, S.L., *et al.*: 'Bit error rate assessment of 40Gbit/s all-optical polarisation independent wavelength converter', *Electron. Lett.*, 1996, **32**, (18), pp. 1688–1690
2 ELLIS, A.D., *et al.*: 'Error free 100Gbit/s wavelength conversion using grating assisted cross-gain modulation in 2mm long semiconductor amplifier', *Electron. Lett.*, 1998, **34**, (20), pp. 1955–1956
3 PERINO, J.S., *et al.*: 'Fibre transmission of 10Gbit/s signals following wavelength conversion using a travelling-wave semiconductor optical amplifier', *Electron. Lett.*, 1994, **30**, (3), pp. 256–258
4 MIKKELSEN, B., *et al.*: 'All-optical wavelength converter scheme for high speed RZ signal formats', *Electron. Lett.*, 1997, **33**, (25), pp. 2137–2139
5 LEUTHOLD, J., *et al.*: 'Compact and fully packaged wavelength converter with integrated delay loop for 40Gbit/s RZ signals'. Proc. Opt. Fiber Comm. Conf. (OFC'2000), Baltimore, USA, 2000. Postdeadline Paper PD-17
6 STUBKJAER, K.E., *et al.*: 'Optical wavelength converters'. Proc. Europ. Conf. Opt. Comm. ECOC'94, Firenze, Italy, 1994, Vol. 2, pp. 635–642
7 UENO, Y., *et al.*: '3.8THz wavelength conversion of picosecond pulses using a semiconductor delayed-interference signal-wavelength converter (DISC)', *Photonics Technol. Lett.*, 1998, **10**, (3), pp. 346–348
8 LEUTHOLD, J., *et al.*: 'Spatial mode filters realized with multimode interference couplers', *Opt. Lett.*, 1996, **21**, pp. 836–839
9 RAYBON, G., *et al.*: '100Gbit/s single-channel transmission over 200km truewave and 160km conventional fiber with electroabsorption modulator source and demultiplexer'. Proc. Europ. Conf. Opt. Comm., ECOC'99, Nice, France, 1999, pp. 1192–1193

3.7ps pulse generation at ≥ 30GHz by dual-drive electroabsorption modulator

V. Kaman, Yi-Jen Chiu, S.Z. Zhang and J.E. Bowers

The authors describe optical short pulse generation at frequencies ≥ 30GHz by a dual-drive scheme of a high-saturation power travelling-wave electroabsorption modulator. Sub-4ps almost-transform-limited pulses are achieved with > 20dB dynamic extinction ratio and low polarisation sensitivity.

Introduction: Optical fibre transmission based on single channel optical time division multiplexing (OTDM) has recently attracted a lot of attention as a means of upgrading future TDM systems [1, 2]. Sinusoidally driven electroabsorption (EA) modulators play a key role in OTDM systems as optical short pulse generators and optical demultiplexers. Owing to advances in high-speed electrical TDM, it is inevitable that next-generation OTDM systems will operate at a base rate of 40Gbit/s with optical multiplexing to 160Gbit/s or more [3]. Therefore, it is important to investigate the high-frequency switching performance of EA modulators. Owing to its nonlinear attenuation characteristic, a highly reverse biased EA modulator with an applied sinusoidal RF signal is capable of producing switching windows with duty ratios as small as 7.2% [4]. However, since the optical loss depends strongly on the insertion loss and the duty ratio of the pulses, the average optical output power and consequently the signal-to-noise ratio (SNR), especially at high frequencies, can be very low. Therefore, an EA modulator with a high-saturation input power is required [5]. Another limiting factor at high-frequency operation is the available RF power as well as the response of the modulator, which can result in broader pulses with degraded extinction ratios than is theoretically predicted [6].

In this Letter, we demonstrate ≥ 30GHz pulse generation of a high-saturation power travelling-wave EA modulator. A novel dual-drive scheme is employed to effectively double the RF drive and to achieve < 15% duty ratios, which we believe is the smallest duty ratios ever reported for these frequencies using a single EA modulator.

Experimental setup: The travelling-wave EA modulator, fabricated using MOCVD grown InGaAsP-InGaAsP quantum wells, is similar to the device used in the previously demonstrated 30Gbit/s data modulation experiment [7]. The fibre-to-fibre insertion loss at 1555nm was 10.8dB while the maximum extinction ratio was 36.4 and 40.3dB at a reverse bias of −6V for the TE and TM polarisations, respectively. It is important to mention that the optical input power was +7.5dBm, which demonstrates the high saturation power characteristic of this 2μm wide, 300μm long modulator. The 3dBe bandwidth of the device was 26GHz.
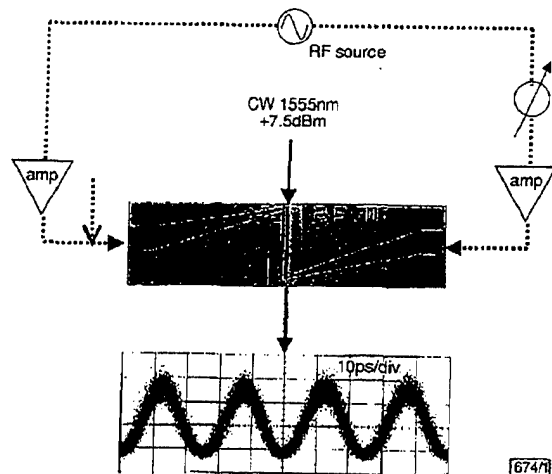
Fig. 1 *Experimental setup for dual-drive scheme of EA modulator*

– – – – electrical path
———— optical path
Optical output is a typical 40GHz waveform
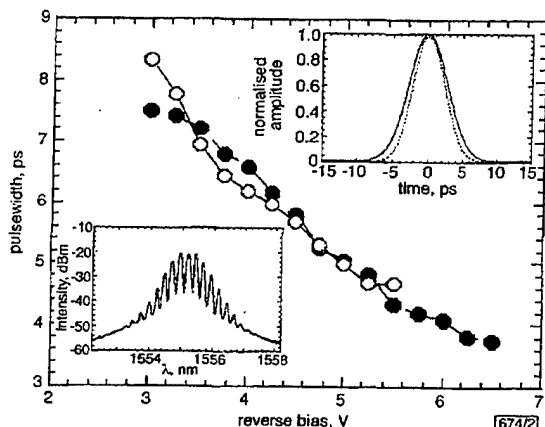
Fig. 2 *Pulsewidth against reverse bias for 30GHz modulation*

○   single drive
●   dual drive
Upper inset: autocorrelation traces of pulses
– – – · single drive
– – – – dual drive
Lower inset: optical spectrum for dual-drive modulation

Fig. 1 shows the device operation for the dual-drive scheme. Two RF signals, synchronised by an electrical delay line, were fed into the two electrodes of the modulator while a single reverse bias was applied. Since AC-coupled amplifiers effectively terminated both electrodes, heating effects were reduced and external temperature cooling was not employed. The optical output of the modulator was then amplified by an optical amplifier, which was followed by a 1.9nm optical bandpass filter. The output pulses were then measured on a second-harmonic generation autocorrelator and an optical spectrum analyser. The width of the obtained pulses was deconvolved assuming a Gaussian pulse shape as inferred from the optical spectrum measurements. It is very important to note that the following criteria were used for the these measurements: (i) the average optical output power was higher

than −25dBm in order to ensure a high SNR, and (ii) the dynamic extinction ratio was estimated to be > 20dB.
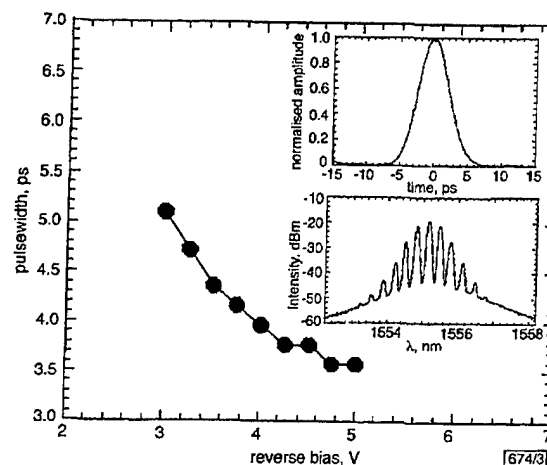
Fig. 3 *Pulsewidth against reverse bias for 40GHz dual-drive modulation*

Upper inset: autocorrelation trace of pulse
Lower inset: optical spectrum

High-frequency operation: Fig. 2 shows the obtained pulsewidths as a function of reverse bias at 30GHz. The RF amplifiers generated $7V_{pp}$ into a 50Ω load. Using only a single drive (the other electrode was terminated in 50Ω), a minimum pulsewidth of 4.7ps was achieved at a reverse bias of −5.5V. Under the dual-drive modulation, an almost-transform-limited pulsewidth of 3.7ps was obtained with a low polarisation sensitivity of 0.3ps. This result corresponds to a duty ratio of ~11% at 30GHz. Further pulse compression was not observed when the EA modulator was followed by dispersion-compensating fibre. The inset in Fig. 2 shows the autocorrelation trace of the pulses achieved for single and dual modulation. The optical spectrum obtained for the dual-drive operation is also shown as an inset in Fig. 2. The bandwidth was 0.84nm, resulting in a time-bandwidth product of 0.39. It is important to mention that shorter pulsewidths were obtained at higher reverse biases at the expense of a degraded SNR and dynamic extinction ratio.

The EA modulator was also driven with 40GHz $7V_{pp}$ dual RF signals. Fig. 3 shows the pulsewidths obtained as a function of reverse bias. A minimum pulsewidth of 3.6ps with an optical bandwidth of 0.83nm was achieved at −5V (insets to Fig. 3), which corresponds to a duty ratio of 14.4%. These results indicate that 160 to 40Gbit/s optical demultiplexing should be feasible with an optical power penalty of < 1dB [8].

Summary: We have successfully demonstrated optical short pulse generation at frequencies ≥ 30GHz using a dual-drive scheme in a travelling-wave EA modulator. Sub-4ps pulses were obtained with low polarisation sensitivity (0.3ps), high dynamic extinction ratio (> 20dB), high optical input power (+7.5dBm) and high average optical output power (> −25dBm).

V. Kaman, Yi-Jen Chiu, S.Z. Zhang and J.E. Bowers (*Department of Electrical and Computer Engineering, University of California, Santa Barbara, Santa Barbara, CA 93106, USA*)

E-mail: kaman@opto.ucsb.edu

S.Z. Zhang: Currently at Zaffire, Inc., San Jose, CA 95134, USA

References

1 MIKKELSEN, B., RAYBON, G., ESSIAMBRE, R.-J., DREYER, K., SU, Y., NELSON, L.E., JOHNSON, J.E., SHTENGEL, G., BOND, A., MOODIE, D.G., and ELLIS, A.D.: '160Gbit/s single-channel transmission over 300km nonzero-dispersion fiber with semiconductor based transmitter and demultiplexer'. ECOC '99, 1999, Paper PD2-3

2 ELLIS, A.D., LUCEK, J.K., PITCHER, D., MOODIE, D.G., and COTTER, D.: 'Full 10 × 10Gbit/s OTDM data generation and demultiplexing using electroabsorption modulators', Electron. Lett., 1998, 34, pp. 1766-1767

3 ELLIS, A.D., MANNING, R.J., PHILLIPS, I.D., and NESSET, D.: '1.6ps pulse generation at 40GHz in phaselocked ring laser incorporating highly nonlinear fibre for application to 160Gbit/s OTDM networks', Electron. Lett., 1999, 35, pp. 645-646

4 OSHIBA, S., NAKAMURA, K., and HORIKAWA, H.: 'Low-drive-voltage MQW electroabsorption modulator for optical short-pulse generation', IEEE J. Quantum Electron., 1998, 34, pp. 277-281

5 SUZUKI, M., TANAKA, H., EDAGAWA, N., UTAKA, K., and MATSUSHIMA, Y.: 'Transform-limited optical pulse generation up to 20GHz repetition rate by a sinusoidally driven InGaAsP electroabsorption modulator', J. Lightwave Technol., 1993, 11, pp. 468-473

6 TAKEUCHI, H., TSUZUKI, K., SATO, K., MATSUMOTO, S., YAMAMOTO, M., and ITAYA, Y.: 'High-speed electroabsorption modulator integrated with DFB laser with bandwidth over 30GHz and its pulse generation'. MWP '96 Tech. Dig., 1996, pp. 301-304

7 KAMAN, V., ZHANG, S.Z., KEATING, A.J., and BOWERS, J.E.: 'High-speed operation of travelling-wave electroabsorption modulator', Electron. Lett., 1999, 35, pp. 993-995

8 MOODIE, D.G., CANNARD, P.J., DANN, A.J., MARCENAC, D.D., FORD, C.W., REED, J., MOORE, R.T., LUCEK, J.K., and ELLIS, A.D.: 'Low polarisation sensitivity electroabsorption modulators for 160Gbit/s networks', Electron. Lett., 1997, 33, pp. 2068-2070

Interferometric crosstalk reduction by phase scrambling in WDM integrated cross-connects

E. Tangdiongga, R. Jonker, H. de Waardt and G.D. Khoe

Interferometric crosstalk mitigation in a four-channel 2.5Gbit/s InP-based 2 × 2 cross-connect using phase scrambling is reported. Bit error rate performance is improved from a large power penalty indicated by a floor at 10^{-8} to a penalty of < 1dB.

Introduction: A phase scrambling (PS) technique has been investigated as a means for mitigating the detrimental effects of interferometric noise in optical links [1]. This type of noise may occur in integrated wavelength-selective devices such as InP-based optical cross-connects (OXCs). Owing to the compact size of a few millimetres and the switching speed of a few nanoseconds, the InP-based OXC is very attractive for packet switching applications. As a disadvantage, InP-based OXCs still show moderate crosstalk levels [2], although considerable improvements have been achieved recently [3]. A theoretical study of PS for a single-channel point-to-point transmission has been published in [4]. In this Letter, we report for the first time the application of the PS technique to a multi-channel 2 × 2 InP-based OXC in order to improve its performance. Without the PS, a 2.5Gbit/s bitrate transmission showed poor performance due to interferometric crosstalk and bit error rate (BER) floors occured at 10^{-8}. By using the PS, error-free transmission with a penalty of < 0.5dB is obtained. This result demonstrates clearly the potential of the PS technique in WDM networks employing OXCs for which the crosstalk performance does not yet fully comply with the stringent telecom requirements.

Experimental setup: A four-channel integrated InP-based OXC was placed in the experimental setup (Fig. 1). Four DFB lasers provided CW sources at wavelengths of 1551.0, 1554.2, 1557.4 and 1560.6nm. Pseudorandom nonreturn-to-zero (NRZ) data of a sequence length of $2^{31} - 1$ was encoded at a bit rate of 2.5Gbit/s using an external modulator to generate optical signals with narrow spectra. The four channels were subsequently scrambled in phase by the phase scrambler section to broaden their spectra, and

amplified by an EDFA before being split to create two paths for feeding both input ports of the OXC. To obtain two uncorrelated input signals, we inserted a delay fibre in one arm before the input. The delay fibre was chosen to be much longer than the coherence length of each laser source. Two polarisation controllers were used to maximise the detrimental effects of interferometric beating noise. The combination of the power splitter and polarisation controllers created a worst-case condition in the setup: wavelength and polarisation alignment. The experimental results represent, therefore, the worst-case crosstalk performance that may occur in WDM networks. To couple the signals into and out of the OXC, we adopted the same technique as [5]. After travelling through the single-phase array OXC, the channels were amplified to compensate for fibre-to-fibre losses. The BER evaluation for each channel was performed by an optical demultiplexer (bandwidth 90GHz) for channel selection and a variable attenuator before the receiver for input power adjustment. The receiver consisted of an InGaAs *pin* photodiode followed by a variable gain electrical amplifier to boost the photocurrent. The electrical bandwidth of the receiver circuit is 1.8GHz, which is sufficient to detect 2.5Gbit/s signals without significant signal distortion. The phase scrambler section was realised by using a phase modulator driven by a noise signal. The noise signal was made by mixing a 200MHz band-limited white noise source with an RF signal. The obtained noise signal caused a phase deviation of the value π and it was centred at the RF frequency of 2.5GHz. The spectrum of the 2.5Gbit/s signal due to the PS is shown in Fig. 2. Compared to the original spectrum, there is a phase scrambler induced spectral broadening of 75pm (measured at −20dB). This spectral broadening will cause an additional penalty of < 1dB after 200km standard fibre due to chromatic dispersion [4].

Fig. 1 *Experimental setup*

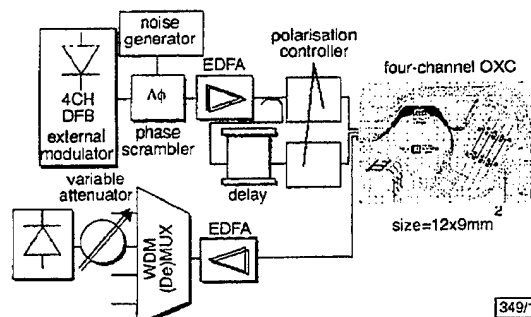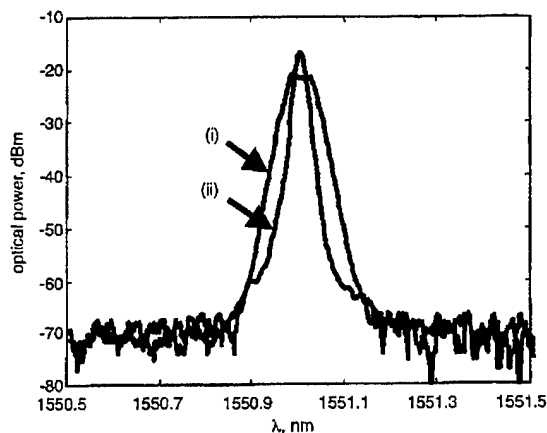Fig. 2 *Signal spectrum*

(i) due to phase scrambling
(ii) original spectrum

Results: The penalties due to interferometric crosstalk in the OXC were measured by taking input powers corresponding to a BER value of 10^{-9}. As a reference, the BER of a scheme without crosstalk (only one input port being used) was used. Measurement of the statical transmission properties of the OXC showed that the

was achieved at room temperature. No penalty was observed after transmission over 10km of standard singlemode fibre.
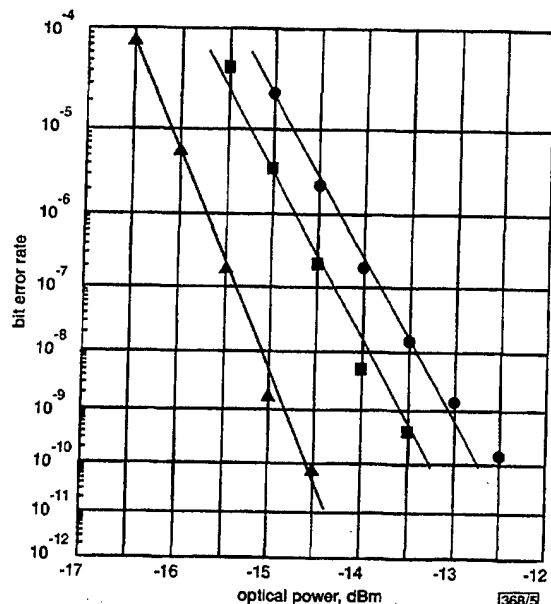
Fig. 5 *BER measurement*

▲ back to back at room temperature
■ back to back at *T* = 65°C
● over 4km of singlemode fibre at *T* = 65°C

To investigate the effects of temperature, transmission experiments at a transmitter case temperature of 65°C were performed. Fig. 5 shows the measured bit error rate performance at room temperature, and at 65°C for a back-to-back configuration and over 4km of singlemode fibre, respectively. The increase in temperature results in a power penalty of ~1.2dB, while transmission over 4km of standard singlemode fibre at 650°C yields another penalty of ~0.5dB. The 1dB difference in sensitivity at room temperature compared to Fig. 4 is due to the use of a different receiver module with a reduced fibre-to-chip coupling efficiency in this transmission experiment.

Conclusions: We have presented a 10Gbit/s transmission system using an uncooled MQW ridge waveguide laser as a transmitter. We achieved a sensitivity of −13.0dBm at a transmitter case temperature of 65°C over 4km of standard singlemode fibre. Using standard T046 packages for the transmitter and receiver offers low cost potential, which is essential for future high-speed datacommunications applications.

5 June 2000

A. Ebberg (*Fachhochschule Westkueste, Rungholtstrasse 9, D-25746 Heide, Germany*)

E-mail: ebberg@fh-westkueste.de

F. Auracher and B. Borchert (*Infineon Technologies AG, Otto Hahn Ring 6, D-81730 Munich, Germany*)

References

1 FEISTE, U., LUDWIG, R., DIETRICH, E., DIEZ, S., EHRKE, H.J., RAZIC, Dz., and WEBER, H.G.: '40Gbit/s transmission over 434km standard fibre using polarisation independent mid-span spectral inversion', *Electron. Lett.*, 1998, 34, (21), pp. 2044–2045

2 MOLLER, M., REIN, H.-M., FELDER, A., and MEISTER, T.-F.: '60Gbit/s time-division multiplexer in SiGe-bipolar technology with special regard to mounting and measuring technique', *Electron. Lett.*, 1997, 33, pp. 679–680

3 OptoSpeed SA, Mezzovico, Switzerland http://www.optospeed.ch

4 EBBERG, A., BAUKNECHT, R., BITTNER, M., GRUMM, M., and BITTER, M.: 'A high performance optical receiver module for 10Gbit/s applications with low cost potential', *Electron. Lett.*, 2000, 36, (8), pp. 741–742

120Gbit/s OTDM system using electroabsorption transmitter and demultiplexer operating at 30GHz

V. Kaman and J.E. Bowers

The authors describe a 120 Gbit/s (4 × 30Gbit/s) OTDM system in which the transmitter and the receiver are based on electroabsorption modulators operating at 30GHz. Error-free operation with an average 120Gbit/s sensitivity of −22.6dBm is achieved.

Introduction: Sinusoidally driven electroabsorption (EA) modulators have recently attracted much attention in high-speed optical time division multiplexed (OTDM) systems as optical short pulse generators and optical demultiplexers [1, 2]. An 80Gbit/s OTDM data stream (with 10Gbit/s base rate) was realised by short pulses generated from EA modulators without using any nonlinear pulse compression [1]. Conversely, a 160Gbit/s optically multiplexed data stream was demultiplexed to 10Gbit/s using two concatenated EA modulators [2]. Owing to advances in high-speed electrical TDM, it is inevitable that next generation OTDM systems will operate at a base rate of 40Gbit/s, with optical multiplexing to 160Gbit/s or more [3, 4]. The increase of the base rate and the consequent reduction in the number of optical channels should allow for more robust and stable high-speed OTDM systems [5].

Recently, we demonstrated sub-4ps pulse generation using a single EA modulator at modulation frequencies ≥ 30GHz [6] as well as integrated tandem EA modulators for > 100Gbit/s optical demultiplexing [7]. In this Letter, we demonstrate a 120Gbit/s (4 × 30Gbit/s) OTDM system based on 30GHz modulation of these devices. We believe that this is the first demonstration of the feasibility of using EA modulators in conjunction with high-speed (> 20Gbit/s) electrical multiplexing and demultiplexing for > 100Gbit/s OTDM systems.
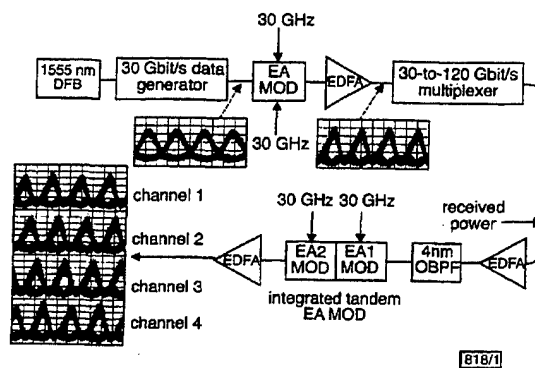
Fig. 1 *Experimental setup for 120Gbit/s OTDM system*
Eye diagrams - 13.3ps/div

Experimental setup and results: The experimental setup for the 120Gbit/s OTDM system is shown in Fig. 1. The base rate of 30Gbit/s was generated by electrically multiplexing two 7.5Gbit/s channels with pattern lengths of 2^{31}−1, followed by optical multiplexing to 30Gbit/s. The 30Gbit/s optical signal of 2dBm was then coupled into the dual-drive EA modulator [6], which has a maximum extinction ratio of 40.3dB and a bandwidth of 26GHz. The modulator was reverse biased at −6V and driven by two 30GHz RF amplifiers ($7V_{pp}$) which were synchronised to the 30Gbit/s data stream by electrical delay lines. Transform-limited 4ps pulses were generated and external compression was not employed after the modulator. The 30Gbit/s signal was then passively multiplexed

(with 200 bits of delay between channels) to generate the 120Gbit/s OTDM data stream. Both time and polarisation multiplexing were employed at the last stage of the multiplexer to minimise coherent interference between adjacent channels. Fig. 2 shows the two 60Gbit/s optical channels measured using a 30GHz photodiode.
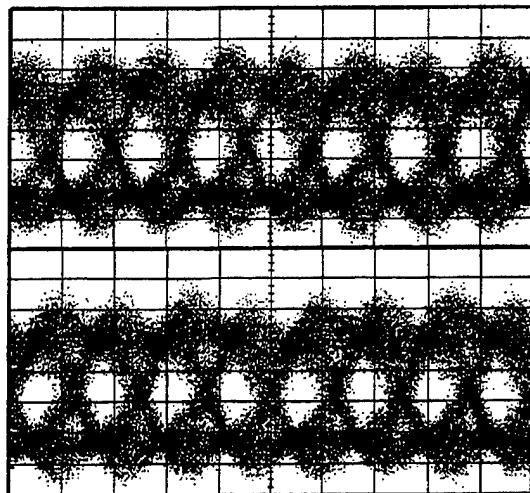
Fig. 2 *Two 60Gbit/s channels measured with 30GHz photodiode*

13.3ps/div
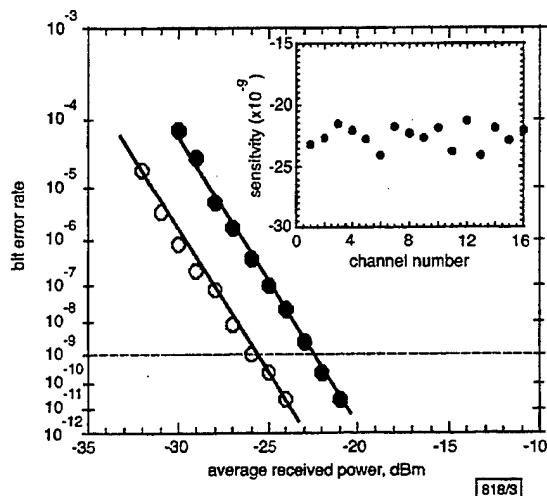
Fig. 3 *BER measurements*

● 120Gbit/s
○ 60Gbit/s
Inset: Receiver sensitivity at 10^{-9} for all 16 channels

In the receiver, the 120Gbit/s data stream was optically preamplified and fed into the optical demultiplexer which consisted of integrated tandem EA modulators [7]. The two modulators (EA1 and EA2) are 300µm and 400µm long, respectively, and are separated by a 20µm long optical waveguide region. H^+ ion-implantation was used between the modulators to reduce electrical crosstalk and capacitance. The insertion loss of the device was 14.2dB while the maximum extinction ratio was ~50dB. Both modulators were driven by 30GHz RF signals and a switching window of 5 to 6ps was achieved over a wide range of reverse biases. The output in Fig. 1 shows the four demultiplexed 30Gbit/s optical channels. A polarisation sensitivity of −2dB was observed which had a minimal impact on the 30Gbit/s eye opening. The received 30Gbit/s eye diagrams also indicate that further high-speed electrical demultiplexing is feasible. It should also be noted that a similar dual-drive EA modulator used in the transmitter could have been employed as the optical demultiplexer.

To simplify bit error rate (BER) measurements, EA2 was only driven by a 7.5GHz RF signal and the 120Gbit/s data stream was directly demultiplexed to 7.5Gbit/s. Fig. 3 shows the 120Gbit/s and 60Gbit/s BER measurements for an arbitrarily selected channel. Error-free operation with a 120Gbit/s receiver sensitivity of −22.2dBm was achieved. The inset to Fig. 3 shows the sensitivities of all 16 channels for a BER of 10^{-9} (mean of −22.6dBm) while Fig. 4 shows all the demultiplexed channels.
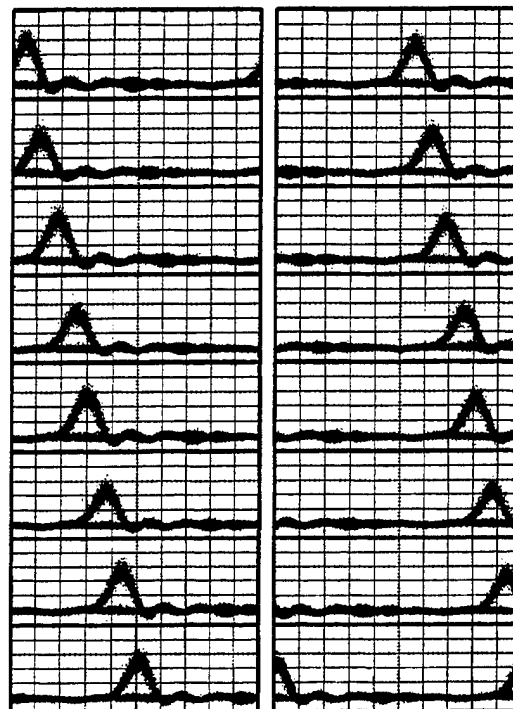
Fig. 4 *Eye diagrams for all 16 demultiplexed channels*

13.3ps/div

Summary: We have successfully demonstrated a four-channel 120Gbit/s OTDM system that reduces the number of optical channels by increasing the base rate to 30Gbit/s. This is achieved by employing electroabsorption modulators operating at 30GHz for pulse generation and optical demultiplexing. Further operation at a base rate of 40Gbit/s for an aggregate data rate of 160Gbit/s should be feasible with these devices.

V. Kaman and J.E. Bowers (*Department of Electrical and Computer Engineering, University of California, Santa Barbara, CA 93106, USA*)

E-mail: kaman@opto.ucsb.edu

References

1 MARCENAC, D.D., ELLIS, A.D., and MOODIE, D.G.: '80Gbit/s OTDM using electroabsorption modulators', *Electron. Lett.*, 1998, **34**, pp. 101–103

2 MIKKELSEN, B., RAYBON, G., ESSIAMBRE, R.-J., DREYER, K., SU, Y., NELSON, L.E., JOHNSON, J.E., SHTENGEL, G., BOND, A., MOODIE, D.G., and ELLIS, A.D.: '160Gbit/s single channel transmission over 300km nonzero-dispersion fiber with semiconductor based transmitter and demultiplexer'. ECOC '99, 1999, Paper PD2-3

3 BOGNER, W., GOTTWALD, E., SCHOPFLIN, A., and WEISKE, C.J.: '40Gbit/s unrepeatered optical transmission over 148km by electrical time division multiplexing and demultiplexing', *Electron. Lett.*, 1997, 33, pp. 2136–2137

4 HAGIMOTO, K., YONEYAMA, M., SANO, A., HIRANO, A., KATAOKA, T., OTSUJI, T., SATO, K., and NOGUCHI, K.: 'Limitations and challenges of single-carrier full 40Gbit/s repeater system based on optical equalization and new circuit design'. OFC'97 Tech. Dig., 1997, pp. 242–243

5 ELLIS, A.D., MANNING, R.J., PHILLIPS, I.D., and NESSET, D.: '1.6ps pulse generation at 40GHz in phaselocked ring laser incorporating highly ·nonlinear fibre for application to 160Gbit/s OTDM networks', Electron. Lett., 1999, 35, pp. 645–646

6 KAMAN, V., CHIU, Y.J., ZHANG, S.Z., and BOWERS, J.E.: '3.7ps pulse generation at ≥ 30GHz by dual-drive electroabsorption modulator', Electron. Lett., 2000, 36, (13), pp. 1130–1132

7 KAMAN, V., CHIU, Y.J., LILJEBERG, T., ZHANG, S.Z., and BOWERS, J.E.: 'Integrated tandem traveling-wave electroabsorption modulators for > 100Gbit/s OTDM applications', accepted for publication in IEEE Photonics Technol. Lett., 2000

8 × 40Gbit/s transmission over 640km of large-effective-area nonzero-dispersion shifted fibre with an input power tolerance greater than 7dB

H. Murai, H.T. Yamada, A.R. Pratt and Y. Ozeki

40Gbit/s transmission is reported over 640km of large-effective-area nonzero dispersion shifted fibre for eight wavelength division multiplexed channels with a channel spacing of 100GHz and an input power tolerance greater than 7dB.

Introduction: Reducing nonlinear effects in high-speed, dense wavelength division multiplexing (DWDM) transmission systems has become increasingly more important as bit rates evolve to keep pace with bandwidth demand. Whereas the dispersion of the transmission fibre can be compensated for using standard dispersion compensating techniques [1], fibre nonlinearity increases proportionally with bit rate and represents the ultimate limit to system performance. Large-effective-area nonzero-dispersion shifted (NZDS) fibre has an increased light-carrying cross-section and can potentially support higher input powers, while at the same time suppressing four wave mixing (FWM), cross-phase modulation (XPM) and pulse distortion due to self-phase modulation (SPM) [2]. Reducing the fibre nonlinearity facilitates linear-like transmission at higher bit rates. This improves the transmission characteristics since the fibre dispersion can be almost completely compensated using the appropriate length of dispersion compensating fibre (DCF). In this Letter we demonstrate for the first time the feasibility of transmitting a 40Gbit/s return-to-zero (RZ) signal over eight 80km spans of large-effective-area nonzero-dispersion shifted fibre. Eight multiplexed wavelength channels, with a channel spacing of 100GHz, have been successfully transmitted, error free, over a total transmission distance of 640km with an input power tolerance greater than 7dB.
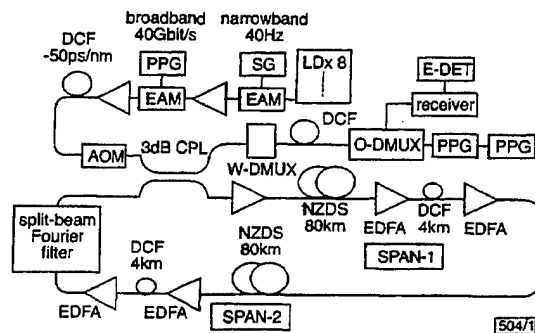
Fig. 1 *Recirculating loop experiment*

Experiment: Fig. 1 shows the experimental setup. Eight 100GHz-spaced wavelength channels, ranging from 1547.0nm to 1552.6nm, were combined and modulated using two high-speed InGaAsP-

based multiple quantum well electroabsorption (EA) modulators [3, 4], to generate a 40Gbit/s optical pulse stream. Data encoding at 40 GBit/s, with a $2^{15} - 1$ pseudorandom binary sequence (PRBS) was performed using the second EA modulator. Four 10Gbit/s signals, each encoded with $2^{15} - 1$ PRBS, were electrically multiplexed to generate the $3.0V_{pp}$ 40Gbit/s modulation signal. The 40Gbit/s RZ signal was amplified and the wavelength channels decorrelated using 0.75km of DCF (–50ps/nm), which also introduced pre-chirp prior to transmission. The recirculating loop experiment consisted of two amplifier spans, comprising 80km of NZDS fibre with an effective area of 75μm² and an average dispersion of 3.8ps/nm/km (at 1549nm). An additional amplifier was included in each span to prevent signal-to-noise ratio (SNR) degradation and to maintain a power level of ~–5dBm before launching into the dispersion compensating fibre (DCF). 4km of DCF, with a typical average dispersion of –80ps/nm/km, was inserted at the end of each span. The wavelength corresponding to zero average dispersion was set to 1549.1nm. After transmission, each wavelength channel was demultiplexed using a tunable optical bandpass filter with a 3dB bandwidth of ~60GHz (0.5nm). A length of DCF was also adjusted outside the loop to individually compensate the accumulated dispersion at each wavelength. The transmission of the individual channels was evaluated by optically demultiplexing the 40Gbit/s data stream to 10Gbit/s using two 20Gbit/s EA modulators. An electronic phase-locked loop (PLL) clock recovery setup was used to drive the EA modulators and act as a trigger for the bit error rate (BER) measurements.
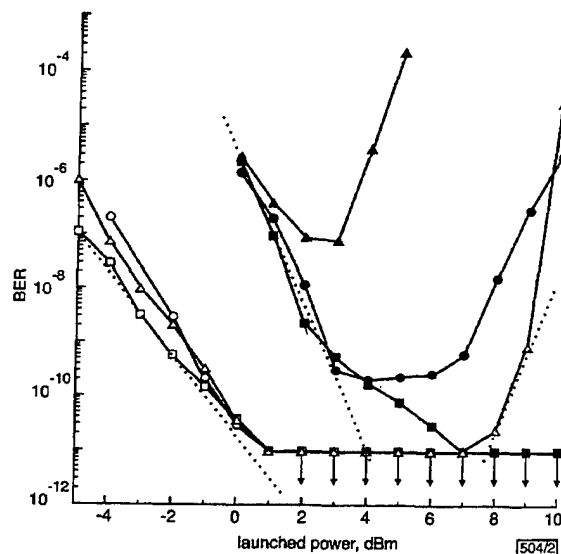
Fig. 2 *Single-channel, 40Gbit/s transmission*

Wavelength	
□ 1549.4nm (640km)	■ 1549.5nm (1120km)
△ 1552.6nm (640km)	▲ 1552.6nm (1120km)
○ 1547.0nm (640km)	● 1547.0nm (1120km)

Results and discussions: Fig. 2 shows the BER characteristics for single-channel 40Gbit/s RZ transmission at three wavelengths of 1547.0nm, 1549.4nm and 1552.6nm. The results clearly demonstrate that error-free transmission (corresponding to a BER < 10⁻⁹) was achieved after a total transmission distance of 1120km (equivalent to fourteen 80km spans of NZDS fibre) for all but the longest wavelength channel. Owing to the relatively large dispersion slope of the NZDS fibre (~0.1ps/nm²/km), the accumulated dispersion was largest at 1552.6nm, and the transmission at this wavelength was limited by nonlinear effects. The launch power per channel was also varied to determine the input power tolerance afforded by the large-effective-area fibre. Close to the zero-dispersion wavelength, the eye patterns showed clear openings over an input range of 10dBm, indicating that nonlinear effects did not limit the transmission. At a transmission distance of 640km, error-free transmission was achieved at all three wavelengths with a similar input power tolerance of 10dB. It is worth noting that the EA

In conclusion, in this Letter a new learning algorithm for pattern classification has been developed. The authors have shown that the performances of the proposed approach are better than those obtained using well known pattern classification techniques. It is worth noting that the choice of the neural model has been motivated by the fact that, differently from other neural architectures, CNNs make feasible the implementation of VLSI devices for real-time vision [6]. Therefore, this Letter introduces the possibility of implementing neural devices for efficient pattern classification.

G. Grassi (*Dipartimento di Ingegneria dell'Innovazione, Università di Lecce, 73100 Lecce, Italy*)

E-mail: giuseppe.grassi@unile.it

E. Di Sciascio (*Dipartimento di Elettrotecnica ed Elettronica, Politecnico di Bari, 70125 Bari, Italy*)

References

1 GRASSI, G.: 'A new approach to design cellular neural networks for associative memories', *IEEE Trans.*, 1997, **CAS-44**, (9), pp. 835–838

2 GRASSI, G.: 'On the design of discrete-time cellular neural networks with circulant matrices', *Int. J. Circuit Theory Appl.*, 2000, **28**, pp. 193–202

3 BRUCOLI, M., CARNIMEO, L., and GRASSI, G.: 'Associative memory design using discrete-time second-order neural networks with local interconnections', *IEEE Trans.*, 1997, **CAS-44**, (2), pp. 153–158

4 GONZALES, R.C., and WOODS, R.E.: 'Digital image processing' (Addison Wesley, 1992)

5 RU, Y., SHE, A., and HUANG, T.S.: 'A modified Fourier descriptor for shape matching in MARS', *in* 'Image databases and multimedia search', Series on Software Engineering and Knowledge Engineering (World Scientific Publishing House, Singapore, 1998), pp. 165–180

6 RODRIGUEZ-VAZQUEZ, A., and ROSKA, T.: 'Special issue on bio-inspired processors and cellular neural networks for vision', *IEEE Trans.*, 1999, **CAS-46**, (2), pp. 225–334

Compact 40 Gbit/s demultiplexing receiver based on integrated tandem electroabsorption modulators

V. Kaman, Y.-J. Chiu, T. Liljeberg, S.Z. Zhang and J.E. Bowers

A compact 40 Gbit/s demultiplexing receiver based on integrated tandem electroabsorption modulators is described. Error-free operation and a receiver sensitivity of –27 dBm are achieved, while the feasibility of this device as an 80 Gbit/s demultiplexing receiver is reported.

Introduction: High-speed demultiplexing is one of the key features in high bit rate time-division-multiplexed transmission systems. Demultiplexing based on high-speed integrated circuit technology has been demonstrated at 60 Gbit/s [1]; however, it has been limited to 40 Gbit/s in fibre transmission experiments [2, 3]. Conversely, optical demultiplexing using a sinusoidally-driven electroabsorption (EA) modulator has emerged as an alternative approach to electrical demultiplexing [4], with demonstrations at 80 Gbit/s [5] and 160 Gbit/s [6]. The major drawback with this technique is the high insertion (coupling) losses in EA modulators, which requires the demultiplexed optical channel to be externally amplified before detection using a receiver. There are two consequences to this: (i) each channel to be demultiplexed requires an optical amplifier and a receiver, which increases the cost and the complexity of the receiver node, and (ii) environmentally induced timing asynchronisation between the demultiplexer and the clock-recovery unit can lead to possible signal-to-noise ratio (SNR) deterioration. Therefore, it is desirable to integrate the demultiplexer and the photodetector, which not only allows for a compact

receiver, but also provides efficient coupling without the need for additional optical components.

In this Letter, we demonstrate a compact 40 Gbit/s demultiplexing receiver based on integrated tandem EA modulators. The feasibility of this device for 80 to 20 Gbit/s demultiplexing and photodetection is also presented.
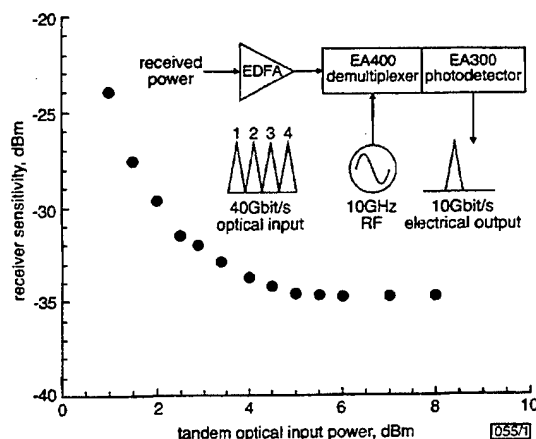
Fig. 1 *Single-channel 10 Gbit/s performance of demultiplexing receiver for BER of 10^{-9} as function of optical input power*

Inset: Schematic diagram of device operation (EA – electroabsorption modulator)

Device characteristics: The tandem EA modulators (300 and 400 µm long) are based on a travelling-wave electrode structure with ten periods of strain-compensated InGaAsP quantum wells fabricated by metal-organic chemical vapour deposition (MOCVD) on semi-insulating InP substrate [7]. The 400 µm-long device (the optical demultiplexer) achieved a maximum extinction of 38 dB at –6 V while the 300 µm-long device was used as a reverse biased photodetector with a responsivity of 0.5 A/W. The two modulators were separated by a 20 µm-long optical waveguide defined by H⁺ ion implantation, which also extended 50 µm into each modulator to reduce capacitance and microwave crosstalk. The measured impedance and the microwave crosstalk were 50 kΩ and < –30 dB, respectively, while the optical insertion loss of the ion-implanted region was estimated to be 2.3 dB. Both modulators were terminated in thin-film resistors and dielectric capacitors, which reduced heating effects and allowed for long-term operation of the tandem without any external temperature cooling. The 400 µm-long device had a modulation bandwidth of 16 GHz while the 300 µm device had a photodetection bandwidth of 18 GHz, which is suitable for 20 Gbit/s detection applications.
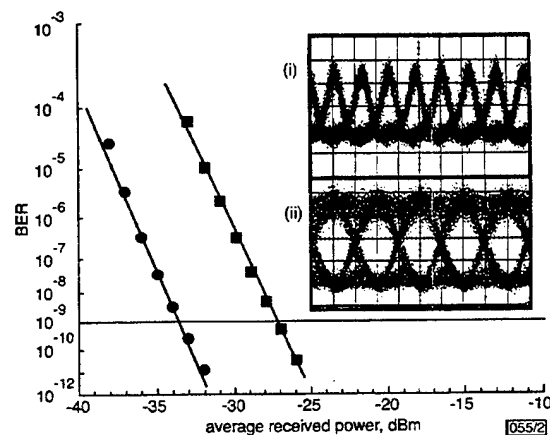
Fig. 2 *BER curves*

9.2 dBm optical input power to tandem device
● 10 Gbit/s single channel
□ 40 Gbit/s data stream
Inset: (i) 40 Gbit/s optical input (20 ps/div)
(ii) 10 Gbit/s demultiplexed and received channel (50 ps/div)

Results: The operation of the tandem EA modulators as a demultiplexing receiver is shown as an inset to Fig. 1. The 40Gbit/s optical time-division multiplexed (OTDM) data stream was realised by passively multiplexing with 1m-long fibre delay lines of 10Gbit/s data-encoded ($2^7 - 1$ pattern length) 8ps pulses, which were generated by a harmonically driven EA modulator at 1555nm. The 40Gbit/s data stream was then optically preamplified before it was coupled into the tandem receiver. The 400µm EA modulator was reverse biased at –4.8V and driven by a 6V$_{pp}$ 10GHz RF signal to generate a 14ps switching window, which was synchronised to the desired optical channel by an electrical delay line. The demultiplexed optical channel was then detected by the 300µm device biased at –8V.

Single-channel 10Gbit/s bit error rate (BER) measurements were performed in order to determine the photodetection performance of the tandem device. Fig. 1 shows the average received power (at the input of the optical preamplifier) required for a BER of 10^{-9} as a function of the optical input power into the tandem. Degradation in receiver sensitivity is observed for low input powers owing to the low SNR at the photodetector while no power penalty is acquired at high input powers. It is important to mention that a 2dB optical power penalty was observed for a pattern length of $2^{31} - 1$, which was determined to be due to electrical reflections from the RF termination of the 300µm photodetector device. Fig. 2 shows the BER measurements at 10 and 40Gbit/s. Error-free operation was achieved for 40Gbit/s operation with a receiver sensitivity of –27dBm. The insets to Fig. 2 show the 40Gbit/s optical input data stream and the received 10Gbit/s channel.
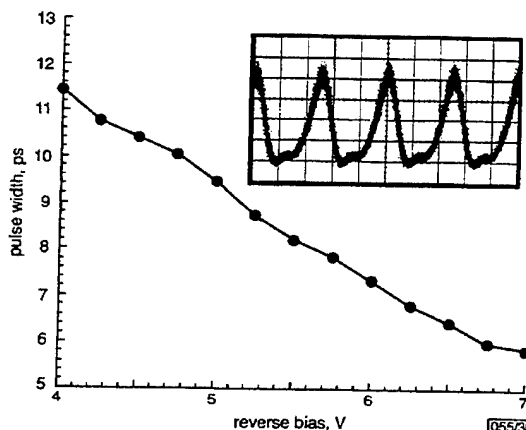
Fig. 3 *Pulse width as function of reverse bias at 20GHz modulation for 400µm EA modulator*

Inset: Oscilloscope trace of pulses measured using 40GHz photodetector (20ps/div)

To investigate the possibility for 80Gbit/s operation, the 400µm demultiplexing modulator was driven with a 6.4V$_{pp}$ 20GHz RF signal and a CW input at 1555nm. The output pulses were then measured on a second harmonic generation autocorrelator and deconvolved assuming a Gaussian pulse shape as inferred from the optical spectrum measurements. Fig. 3 shows the pulse widths (FWHM) obtained as a function of reverse bias while the dynamic extinction ratio was estimated to be > 20dB. Pulse widths as short as 6ps were achieved, which indicates that penalty-free demultiplexing of 80Gbit/s data stream is possible [5, 8].

Summary: We have successfully demonstrated error-free 40Gbit/s operation of a compact demultiplexing receiver based on integrated tandem EA modulators. Our results indicate that these devices can be used as efficient receivers at bit rates up to 80Gbit/s.

4 September 2000

V. Kaman, Y.-J. Chiu, T. Liljeberg, S.Z. Zhang and J.E. Bowers
(*Department of Electrical and Computer Engineering, University of California, Santa Barbara, Santa Barbara, CA 93106, USA*)

E-mail: kaman@opto.ucsb.edu

S.Z. Zhang: Now at Zaffire, Inc., San Jose, CA 95134, USA

References

1   FELDER, A., MOLLER, M., WURZER, M., REST, M., MEISTER, T.F., and REIN, H.-M.: '60Gbit/s regenerating demultiplexer in SiGe bipolar technology', *Electron. Lett.*, 1997, **33**, pp. 1984–1986

2   BOGNER, W., GOTTWALD, E., SCHOPFLIN, A., and WEISKE, C.J.: '40Gbit/s unrepeatered optical transmission over 148km by electrical time division multiplexing and demultiplexing', *Electron. Lett.*, 1997, **33**, pp. 2136–2137

3   HAGIMOTO, K., YONEYAMA, M., SANO, A., HIRANO, A., KATAOKA, T., OTSUJI, T., SATO, K., and NOGUCHI, K.: 'Limitations and challenges of single-carrier full 40-Gbit/s repeater system based on optical equalization and new circuit design'. OFC '97 Tech. Dig., 1997, pp. 242–243

4   SUZUKI, M., TANAKA, H., and MATSUSHIMA, Y.: '10Gbit/s optical demultiplexing and switching by sinusoidally driven InGaAsP electroabsorption modulators', *Electron. Lett.*, 1992, **28**, pp. 934–935

5   MARCENAC, D.D., ELLIS, A.D., and MOODIE, D.G.: '80Gbit/s OTDM using electroabsorption modulators', *Electron. Lett.*, 1998, **34**, pp. 101–103

6   MIKKELSEN, B., RAYBON, G., ESSIAMBRE, R.J., DREYER, K., SU, Y., NELSON, L.E., JOHNSON, J.E., SHTENGEL, G., BOND, A., MOODIE, D.G., and ELLIS, A.D.: '160Gbit/s single-channel transmission over 300km nonzero-dispersion fibre with semiconductor based transmitter and demultiplexer'. ECOC '99, 1999, Paper PD2-3

7   ZHANG, S.Z., CHIU, Y.J., ABRAHAM, P., and BOWERS, J.E.: '25GHz polarization-insensitive electroabsorption modulators with traveling-wave electrodes', *IEEE Photonics Technol. Lett.*, 1999, **11**, pp. 191–193

8   MOODIE, D.G., ELLIS, A.D., THURLOW, A.R., HARLOW, M.J., LEALMAN, I.F., PERRIN, S.D., RIVERS, L.J., and ROBERTSON, M.J.: 'Multiquantum well electroabsorption modulators for 80Gbit/s OTDM systems', *Electron. Lett.*, 1995, **31**, pp. 1370–1371

Demonstration of high robustness to SNR impairment in 20Gbit/s long-haul transmission using 1.5µm saturable absorber

O. Leclerc, G. Aubin, P. Brindel, J. Mangeney, H. Choumane, S. Barré and J.-L. Oudar

Improved robustness to signal-to-noise ratio impairment is shown for the first time at 20Gbit/s in an RZ transmission loop using a 1.5µm heavy-ion-irradiated quantum well saturable absorber. Error-free transmission is achieved over 7800km.

Introduction: Passive optical regeneration using saturable absorbers can contribute to increased bit-rate or error free distance in signal-to-noise ratio (SNR)-limited transmission systems [1, 2]. We recently showed the efficiency of a multi-quantum well (MQW) saturable absorber (SA) in a 10Gbit/s RZ long-haul transmission [3]. In this Letter we report the ability of such an ultra-fast passive device to reduce amplified spontaneous emission (ASE) accumulation at 20Gbit/s in a 1.55µm loop experiment, yielding both increased transmission distances and improved system robustness.

Saturable absorber characteristics: The vertical cavity structure of the MQW semiconductor saturable absorber is that detailed in [3]. The device is used in reflection mode and is polarisation-insensitive thanks to the normal incidence of the input light-wave. Under low repetition rate of short pulses, it was shown to exhibit an on/off contrast ratio of 10:0 and a reflectivity of 40% with a saturation energy < 2pJ. Irradiated by 11MeV Ni$^+$ ions, with an irradiation dose of 1×10^{11} cm^{-2}, it yields a response time of 10ps [4 – 6].

The discrimination properties of the SA have been analysed at higher frequency using purposely degraded 20GHz RZ signals

Simultaneous OTDM Demultiplexing and Detection Using an Electroabsorption Modulator

Volkan Kaman, *Student Member, IEEE*, Adrian J. Keating, *Member, IEEE*, Sheng Z. Zhang, *Member, IEEE*, and John E. Bowers, *Fellow, IEEE*

Abstract—A traveling-wave electroabsorption modulator is used to simultaneously demultiplex and electrically detect a single 10-Gb/s channel from a 20-Gb/s optical time-division multiplexed data stream while transmitting the other channel in an optically transparent manner. A bit-error-rate penalty of 0.5 dB and an error floor were observed for the dropped channel due to residual absorption of the other channel. Error-free operation was achieved for the transparent channel.

Index Terms—Demultiplexing, electroabsorption, optical fiber communication, optical switches, photodetectors, traveling wave devices.

I. INTRODUCTION

ELECTROABSORPTION (EA) modulators are suited to optical time-division-multiplexing (OTDM) network applications as their nonlinear transfer function permits narrow optical switching windows with large extinction ratios. Recently, there have been several demonstrations of key processing features required in OTDM systems, such as optical short pulse generation [1], optical demultiplexing [2], [3], optical regeneration [4], [5] and drop and insert multiplexing [6] using EA modulators. The ability to drop a single channel from a high-speed OTDM data stream is significant at a network node since optical demultiplexing is performed while still transmitting the other channels in an optically transparent manner for further processing. This has the advantage of optical power conservation in contrast to standard optical demultiplexing (for example, using an EA modulator) in which the other channels are suppressed [2]. It is also desirable to perform the demultiplexing (or channel drop) and optical-to-electrical (O/E) conversion simultaneously using a single device in order to reduce the cost and complexity of the node. EA modulators are ideal for this application since they can be used as optical switches and photodetectors due to their absorptive characteristic.

In consideration of the use of an EA modulator in OTDM drop and detect applications, several crosstalk issues need to be

addressed. The electrical extinction ratio (defined as the ratio between the responsivity at high reverse bias and zero bias) has to be high enough to prevent absorption of the undropped channels that would interfere with the dropped channel. If a new channel is to be inserted in the available bit slot after a channel is dropped, it is also important to have a high optical extinction ratio to prevent interference between the dropped channel and the channel to be inserted.

To date, only the ability of an EA modulator to drop a channel without detection has been demonstrated [6]. In this paper, we demonstrate for the first time the use of an EA modulator to simultaneously demultiplex and detect the desired channel from an OTDM data stream while transmitting the other channel in an optically transparent manner.

II. PRINCIPLE OF OPERATION

The EA modulator used for the OTDM drop and detect application is a 2.5-μm-wide 300-μm-long device with traveling-wave electrodes as described in reference [7]. The 3-dB bandwidth was about 10 GHz when operated as a modulator at a reverse bias of −3 V and as a photodetector at −6 V (the traveling-wave electrode is terminated in 50 Ω). The maximum static optical and electrical extinction ratios are 40 dB and 28 dB, respectively, while the fiber-to-fiber insertion loss is 10 dB.

Fig. 1 shows the operation principle of the EA modulator for simultaneous drop and detection. The traveling-wave modulator is a four-port device; the optical input and output are shown as port 1 and 3, respectively. The EA modulator is biased at a high reverse bias and a 10-GHz driving signal is applied to port 2 using a high power amplifier. When the RF drive signal swings negative, the EA modulator is in the high absorption state and any optical signal passing through the modulator is absorbed and converted to photocurrent. On the other hand, when the RF signal swings positive, the EA modulator switches to high optical transparency with low absorption. Port 4 functions as the 10-Gb/s optical pulse detector. The output at this port consists of photogenerated carriers (if data "1" is present) as well as the attenuated 10-GHz driving RF signal. This signal is rejected from the data using a 6.4-GHz low-pass filter (with 60-dB attenuation at 10 GHz) and reflected back into the modulator synchronized with the original drive using an electrical phase shifter. The low-pass filter also converts the return-to-zero (RZ) data into nonreturn-to-zero (NRZ) format for bit-error-rate (BER) measurements. The alignment of the optical bits to the electrical drive signal is performed using an optical delay line. It is significant to mention that when the EA modulator operates as a

Fig. 1. Operation of the OTDM drop and detect experiment. Ports 1 and 3 are the optical input and output, respectively. Electrical RF drive is applied to port 2 while port 4 acts as the 10-Gb/s pulse detector.

Fig. 2. Set-up for the 20-Gb/s OTDM drop and detect experiment (PC-polarization controller).

Fig. 3. Eye diagrams. (a) The 20-Gb/s OTDM data stream input to the EA modulator at port 1. (b) Optical transparency gating of the EA modulator aligned to channel 2. (c) The 10-Gb/s channel 2 transmitted in an optically transparent manner at port 3. (d) Simultaneously demultiplexed and O/E converted 10-Gb/s channel 1 at port 4.

photodetector, the output impedance of the high-power RF amplifier at port 2 acts as the termination. Since our drive amplifier had a low-frequency cutoff of about 10 MHz, this limited our experiment to a pseudorandom bit stream of $2^7 - 1$.

III. EXPERIMENTAL SET-UP AND RESULTS

The experimental setup for the 20-Gb/s OTDM simultaneous channel drop and detect is shown in Fig. 2. An EA modulator harmonically driven at 10 GHz was used to generate 11-ps pulses at 1555 nm. The 10-Gb/s data was encoded onto the 10-GHz pulse train by a LiNbO$_3$ modulator. The 10-Gb/s RZ data was then passively multiplexed (with 20 bits of delay between channels) to generate a 20-Gb/s OTDM data stream [Fig. 3(a)]. The 20-Gb/s signal of about 5 dBm was coupled into the drop and detect EA modulator using an optical preamplifier followed by a 0.6-nm bandwidth optical filter. A polarization controller was used at the input of the modulator for best operation. Fig. 3(b) shows the optical gating performed by the modulator at a bias of −5 V with the 10-GHz drive signal (10 V$_{pp}$) aligned to channel 2 for optical transparency. Fig. 3(c) shows the optical output at port 3, where channel 2 is transmitted, while channel 1 has been completely removed. The optically transparent channel 2 was then amplified before being detected at a commercial 10-Gb/s receiver. The simultaneously dropped and detected 10-Gb/s NRZ converted channel 1 is

shown in Fig. 3(d). Sufficient eye opening is achieved with most of the noise due to the residual absorption of channel 2.

Fig. 4 shows the BER measurements at 10 and 20 Gb/s, where the average received power was determined at the input of the optical preamplifier to the EA modulator for all measurements. Single-channel 10-Gb/s BER measurements were performed in order to determine the photodetection performance of the EA modulator by blocking one of the arms of the optical multiplexer. The reference line is when port 2 was terminated in 50 Ω and port 4 was as illustrated in Fig. 1 (the modulator was biased at −5 V). A receiver sensitivity of −31 dBm for a BER of 10^{-9} and a slight error floor is observed. It was determined that the error floor was due to the high-frequency limitations of the EA modulator at this bias; at a bias of −6 V, error-free operation and an improved sensitivity of −34 dBm was achieved (not shown). Next, the 50-Ω termination at port 2 was replaced by the driving amplifier with the RF signal applied to the EA modulator at a bias of −5 V. A negative penalty of 1 dB and error-free operation is observed. This improvement at −5 V is simply due to the higher reverse bias obtained from the negative swing of the
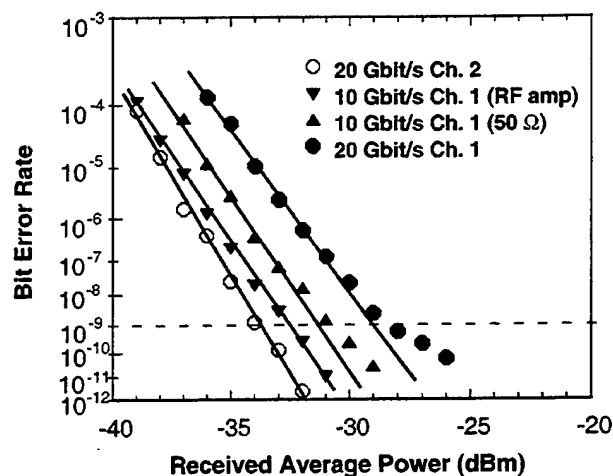
Fig. 4. BER curves for 10-Gb/s (triangles) and 20-Gb/s (circles) demultiplexing. The filled and open symbols correspond to the detected channel 1 and transparent channel 2, respectively.

10-GHz signal during the time period of the 10 Gb/s channel. However, it should also be mentioned that eye diagram deterioration was observed due to the high noise figure and imperfect output impedance of the driving amplifier.

20-Gb/s BER measurements were then performed with the EA modulator operated as a simultaneous demultiplexer and O/E converter at a bias of -5 V. The optically transparent channel 2 operated error-free with a 20-Gb/s sensitivity of -33.5 dBm and a 10-Gb/s sensitivity (when channel 1 was blocked) of -36.5 dBm (not shown). This result indicates the good optical extinction of the modulator as verified in the eye diagram [Fig. 3(c)]. On the other hand, the simultaneously dropped and detected channel 1 exhibited a 20-Gb/s sensitivity of -28.5 dBm and an error floor. From the single-channel 10-Gb/s sensitivity of -32 dBm, one can expect a 20-Gb/s sensitivity of -29 dBm for the same channel if there is no penalty. However, our measurements indicate that there is a power penalty of 0.5 dB and an error floor, which we attribute to the crosstalk from the residual absorption of channel 2. We believe that this penalty can be reduced with an EA modulator with sufficient bandwidth when operated as a photodetector at lower reverse biases. This would not only decrease the residual absorption, but also allow for a longer optical transparency

window and a shorter detection window, which would be ideal for simultaneous demultiplexing and detection of a single channel from a four-channel 40-Gb/s OTDM data stream.

IV. CONCLUSION

In summary, we have demonstrated that a single component, the traveling-wave EA modulator, can be used to simultaneously demultiplex and detect a single channel from a bit-interleaved data stream, leaving the other channel unaffected. An error floor was incurred for the dropped channel due to residual absorption of the error-free transparent channel. We believe that this technique has the potential to realize a compact, high-speed full demultiplexing receiver (optical-serial to electrical-parallel conversion) by integrating a series of EA modulators on a single chip.

REFERENCES

[1] M. Suzuki, H. Tanaka, K. Utaka, N. Edagawa, and Y. Matsushima, "Transform-limited 14-ps optical pulse generation with 15-GHz repetition rate by InGaAsP electroabsorption modulator," *Electron. Lett.*, vol. 28, pp. 1007–1008, 1992.
[2] M. Suzuki, H. Tanaka, and Y. Matsushima, "10 Gb/s optical demultiplexing and switching by sinusoidally driven InGaAsP electroabsorption modulators," *Electron. Lett.*, vol. 28, pp. 934–935, 1992.
[3] I. D. Phillips, A. Gloag, D. G. Moodie, N. J. Doran, I. Bennion, and A. D. Ellis, "Simultaneous two-channel OTDM demultiplexing using a single electroabsorption modulator in a novel bi-directional configuration," *Electron. Lett.*, vol. 33, pp. 1811–1812, 1997.
[4] T. Miyazaki, N. Edagawa, M. Suzuki, and S. Yamamoto, "Novel optical-regenerator using electroabsorption modulator," in *OFC'99 Tech. Dig.*, 1999, pp. 350–352.
[5] Y. Kisaka, A. Hirano, M. Yoneyama, and N. Shimizu, "Simple 2R repeater based on EA modulator directly driven by uni-travelling-carrier photodiode," *Electron. Lett.*, vol. 35, pp. 1016–1017, 1999.
[6] I. D. Phillips, A. Gloag, D. G. Moodie, N. J. Doran, I. Bennion, and A. D. Ellis, "Drop and insert multiplexing with simultaneous clock recovery using an electroabsorption modulator," *IEEE Photon. Technol. Lett.*, vol. 10, pp. 291–293, 1998.
[7] S. Z. Zhang, Y. Chiu, P. Abraham, and J. E. Bowers, "25-GHz polarization-insensitive electroabsorption modulators with traveling-wave electrodes," *IEEE Photon. Technol. Lett.*, vol. 11, pp. 191–193, 1999.

Integrated Tandem Traveling-Wave Electroabsorption Modulators for >100 Gbit/s OTDM Applications

Volkan Kaman, *Student Member, IEEE*, Yi-Jen Chiu, *Member, IEEE*, Thomas Liljeberg, *Student Member, IEEE*, Sheng Z. Zhang, *Member, IEEE*, and John E. Bowers, *Fellow, IEEE*

Abstract—Integrated tandem traveling-wave electroabsorption modulators are demonstrated as high-speed optical short pulse generators and demultiplexers for >100 Gbit/s optical time-division-multiplexed systems. The tandem significantly increases the extinction ratio and further compresses the optical pulses in comparison to a single modulator. An extinction ratio of ~ 50 dB is achieved while optical pulses of 4–6 ps width at 30–40 GHz are generated.

Index Terms—Demultiplexing, electroabsorption, optical fiber communication, optical switches, traveling wave devices.

Fig. 1. Photograph of the integrated tandem traveling-wave EA modulators (dashed areas are the ion-implanted regions).

I. INTRODUCTION

OPTICAL fiber transmission based on single channel optical time-division multiplexing (OTDM) has recently attracted a lot of attention as a means of upgrading future TDM systems [1]–[3]. Due to advances in high-speed electrical TDM, it is inevitable that next generation OTDM systems will operate at a base rate of 40 Gbit/s with optical multiplexing to 160 Gbit/s or more [4]. For high-speed OTDM systems, sinusoidally driven electroabsorption (EA) modulators have become key devices as optical short pulse generators and optical demultiplexers. An 80 Gbit/s OTDM data stream (with 10 Gbit/s base rate) was realized by short pulses generated from EA modulators without using any nonlinear pulse compression, which is the highest aggregate data rate achieved using this technique to date [5]. On the other hand, a 160 Gbit/s optically multiplexed data stream was demultiplexed to 10 Gbit/s using only EA modulators [1].

Single EA modulators are usually limited to ~ 20 dB dynamic extinction ratio, which is sufficient for demultiplexing purposes, but can lead to incoherent interference between multiplexed adjacent pulses in OTDM transmitters [2]. Therefore, a fiber-coupled pair of separate modulators was used for pulse generation in [5] and for demultiplexing in [1]. This configuration not only effectively doubles the dynamic extinction ratio, but also reduces the switching window. However, it is desirable to integrate the tandem on a single chip in order to eliminate the external optical amplifier, which compensates for the coupling losses between the modulators [6], [7]. This results in a com-

pact and cost-effective transmitter (or demultiplexer) as well as an environmentally robust module.
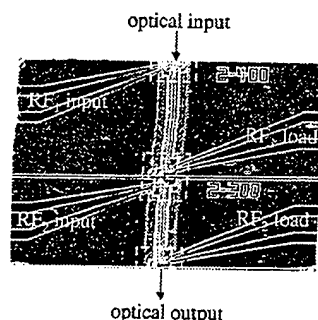
In this letter, we investigate the optical short pulse generation and demultiplexing capability of integrated tandem traveling-wave EA modulators at repetition frequencies of 30 GHz and 40 GHz for >100 Gbit/s OTDM systems. This is also the first demonstration of optical pulse generation using traveling-wave EA modulators, which were previously demonstrated in a 30 Gbit/s data modulation experiment [8].

II. DEVICE CHARACTERISTICS

The EA modulators used for the OTDM application were based on a traveling-wave electrode structure fabricated with MOCVD grown ten periods of strain-compensated InGaAsP quantum wells on semi-insulating InP substrate [9]. Traveling-wave EA modulators have the advantage of overcoming the RC limitation (in comparison to lumped EA modulators) resulting in longer devices with higher bandwidths and increased extinction ratios. The 2-μm wide, 300-μm and 400-μm long EA modulators were cleaved as a tandem (Fig. 1). The 20-μm long optical waveguide between the two modulators was defined by H^+ ion implantation and the measured impedance was 50 kΩ. The ion implantation also extended 50 μm into each modulator in order to reduce capacitance and microwave crosstalk (<-30 dB); however, the absorption region for each modulator was shortened by 100 μm. Both modulators were terminated in a thin-film resistor and a dielectric capacitor, which reduced heating effects and allowed for long-term operation of the tandem without any external temperature cooling.

Fig. 2 shows the transmission characteristics of the tandem as a function of reverse bias. An optical input power of 7 dBm was applied at 1555 nm. The insertion loss of the tandem was 14.1 dB and 15.3 dB for the TE and TM polarizations, respectively. Each device was individually characterized by keeping

Fig. 2. Fiber-to-fiber transmission versus reverse bias voltage for the integrated tandem EA modulators. Solid: TE polarization. Dashed: TM polarization.

Fig. 3. Pulsewidth as a function of reverse bias at 30 GHz modulation for the individual devices. Circle symbols: 300-μm device; Square symbols: 400-μm device. Inset: Autocorrelation trace of the 5.6 ps pulse generated by the 400-μm device at a reverse bias of −4.5 V.

the other modulator at zero bias. The 400-μm device achieved a maximum extinction of 38 dB at −6 V while 26 dB of extinction was observed for the 300-μm device. The difference in the maximum extinction ratios is due to the shorter absorption region of the 300-μm device. It should also be noted that at high reverse biases, a saturation of absorption due to the quantum well excitonic peak is observed for both devices. Even though it is desirable to apply a high reverse bias in order to generate short switching windows using sinusoidal modulation, the absorption saturation will deteriorate the extinction ratio and generate significant wings [10]. These wings are detrimental for OTDM applications since the resulting incoherent interference in the transmitter and the crosstalk in the receiver will significantly degrade system performance. On the other hand, the tandem configuration shows an improved extinction ratio of ∼50 dB while the absorption saturation is well suppressed in comparison to single device operation. A 14-dB reduction in the total expected extinction is observed, which is attributed to higher-order mode coupling.

III. EXPERIMENTAL RESULTS AND DISCUSSION

The optical switching capability of the tandem was first characterized at 30 GHz. Both modulators were driven with $7V_{pp}$ sinusoidal RF signals, which were synchronized by an electrical delay line. The widths of the optical pulses were measured using a second harmonic generation autocorrelator and deconvolved assuming a gaussian pulse shape as inferred from the optical spectrum measurements. It is important to mention that the following criteria were used for these measurements: 1) the average optical output power was higher than −25 dBm in order to ensure a high signal-to-noise ratio (SNR), and 2) the dynamic extinction ratio was estimated to be >20 dB. The pulsewidths obtained from the individual devices by keeping the other device at zero bias are shown in Fig. 3. At a reverse bias of −4.5 V, a minimum pulsewidth of 6.5 ps and 5.6 ps were obtained for the 300- and 400-μm devices, respectively. Even though shorter pulses were achieved at higher reverse biases, degradation in the dynamic extinction ratio was observed due to the absorption saturation as discussed in the preceding section.
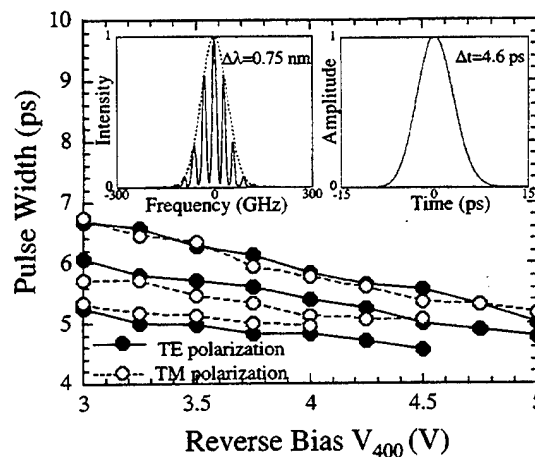
Fig. 4. Pulsewidth as a function of 400-μm reverse bias and for several 300-μm biases (top-to-bottom) at 30 GHz modulation. Closed symbols: TE polarization (top-to-bottom: −3.5 V, −4 V, −4.5 V); Open symbols: TM polarization (top-to-bottom: −3 V, −3.5 V, −4 V). Left inset: Optical spectrum; Right inset: Autocorrelation trace of the 4.6 ps pulse.

Fig. 4 shows the obtained pulsewidths as a function of reverse biases for the tandem configuration. A minimum pulsewidth of 4.6 ps (inset to Fig. 4) with a fiber-coupled output power of −24.2 dBm was achieved while an average of 5–6 ps pulses were observed over a wide range of reverse biases and polarization states. This switching window is well suited for >100 Gbit/s optical demultiplexing applications [2]. The inset to Fig. 4 also shows the optical spectrum of the modulated tandem of EA modulators, which has a gaussian shape of 0.75 nm. The time-bandwidth product of 0.43 suggests that the pulses were slightly chirped. When the tandem was followed by dispersion-compensating fiber (DCF) with a dispersion of about −6 ps/nm, the pulses were linearly compressed to a transform-limited pulsewidth of 4.2 ps (Fig. 5). This pulsewidth suggests that the tandem is suitable as an optical pulse source for simultaneous polarization- and TDM systems in excess of 100 Gbit/s.

The optical switching response of the tandem EA modulators was also performed at 40 GHz with RF drives of $7V_{pp}$. The frequency response of the devices was estimated to be ∼4 dB lower
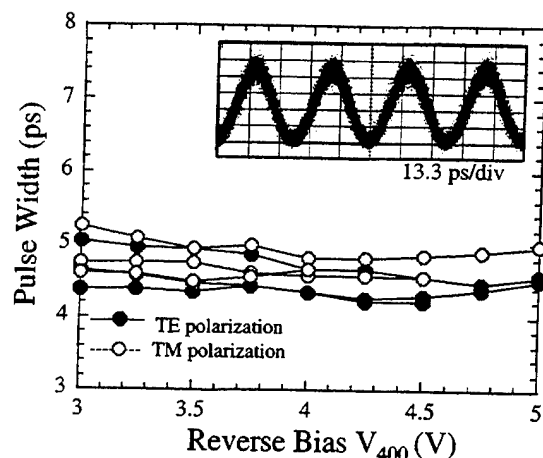
Fig. 5. Pulsewidth as a function of 400-μm reverse bias and for several 300-μm biases (top-to-bottom) at 30 GHz modulation (tandem device followed by dispersion-compensating fiber). Closed symbols: TE polarization (top-to-bottom: -3.5 V, -4 V, -4.5 V); Open symbols: TM polarization (top-to-bottom: -3 V, -3.5 V, -4 V). Inset: Oscilloscope trace of the 30 GHz pulses (13.3 ps/div).
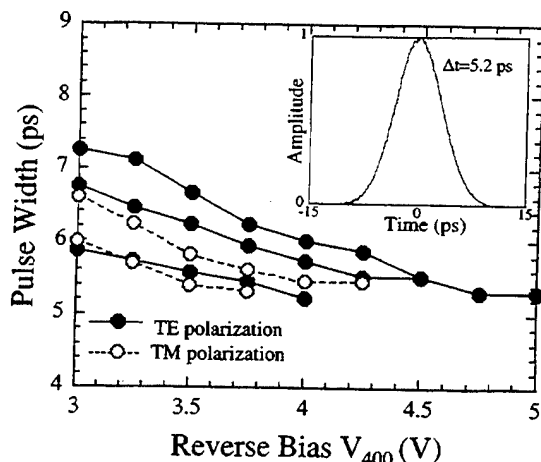
Fig. 6. Pulsewidth as a function of 400-μm reverse bias and for several 300-μm biases (top-to-bottom) at 40 GHz modulation. Closed symbols: TE polarization (top-to-bottom: -3 V, -3.5 V, -4 V); Open symbols: TM polarization (top-to-bottom: -3 V, -3.5 V). Inset: Autocorrelation trace of the 5.2 ps pulse.

at 40 GHz (in comparison to the 30 GHz response), which resulted in a compromise between pulsewidth, dynamic extinction ratio and average optical output power. A minimum op-

tical pulsewidth of 5.2 ps with an optical bandwidth of 0.59 nm was achieved (Fig. 5). These results should improve when the tandem is driven with higher power RF amplifiers at 40 GHz and enable low-penalty optical demultiplexing of 160 Gbit/s OTDM data stream to 40 Gbit/s [2].

IV. CONCLUSION

In summary, we have successfully demonstrated integrated tandem traveling-wave EA modulators for >100 Gbit/s OTDM applications. Optical pulses of 4 to 6 ps width were obtained with high extinction ratio, high optical input power, and high average optical output power. These devices are a viable technology for optical demultiplexing of bit rates up to 160 Gbit/s.

REFERENCES

[1] B. Mikkelsen et al., "160 Gbit/s single-channel transmission over 300 km nonzero-dispersion fiber with semiconductor based transmitter and demultiplexer," in Proc. ECOC, vol. PD2-3, 1999.
[2] A. D. Ellis et al., "Full 10 × 10 Gbit/s OTDM data generation and demultiplexing using electroabsorption modulators," Electron. Lett., vol. 34, pp. 1766–1767, 1998.
[3] S. Kawanishi et al., "120 Gbit/s OTDM system prototype," in Proc. ECOC, 1998, pp. 43–45.
[4] A. D. Ellis, R. J. Manning, I. D. Phillips, and D. Nesset, "1.6 ps pulse generation at 40 GHz in phaselocked ring laser incorporating highly nonlinear fiber for application to 160 Gbit/s OTDM networks," Electron. Lett., vol. 35, pp. 645–646, 1999.
[5] D. D. Marcenac, A. D. Ellis, and D. G. Moodie, "80 Gbit/s OTDM using electroabsorption modulators," Electron. Lett., vol. 34, pp. 101–103, 1998.
[6] H. Tanaka, S. Takagi, M. Suzuki, and Y. Matsushima, "Optical short pulse generation by double optical gate operation of tandem connected electroabsorption modulators driven by sinusoidal voltages," Electron. Lett., vol. 29, pp. 1449–1451, 1993.
[7] F. Devaux et al., "Tandem of modulators for high on/off pulse generation (−55 dB)," Electron. Lett., vol. 33, pp. 1491–1492, 1997.
[8] V. Kaman, S. Z. Zhang, A. J. Keating, and J. E. Bowers, "High-speed operation of travelling-wave electroabsorption modulator," Electron. Lett., vol. 35, pp. 993–995, 1999.
[9] S. Z. Zhang, Y. J. Chiu, P. Abraham, and J. E. Bowers, "25 GHz polarization-insensitive electroabsorption modulators with traveling-wave electrodes," IEEE Photon. Technol. Lett., vol. 11, pp. 191–193, 1999.
[10] S. Oshiba, K. Nakamura, and H. Horikawa, "Low-drive-voltage MQW electroabsorption modulator for optical short-pulse generation," IEEE J. Quantum Electron., vol. 34, pp. 277–281, 1998.

Double-Bonded InP–InGaAsP Vertical Coupler 1:8 Beam Splitter

Maura Raburn, Bin Liu, Patrick Abraham, and John E. Bowers

Abstract—A novel three-layer double-bonded InP–InGaAsP waveguide vertical coupler 1:8 beam splitter is demonstrated. The strongly coupled waveguides allow a 583-μm device length, more than 100 times shorter than that of the equivalent horizontal coupler. The device illustrates the use of multiple vertical-layer optical interconnects for three-dimensional routing of optical signals.

Index Terms—Beam splitting, optical directional couplers, semiconductor waveguides, wafer bonding, waveguide couplers.

I. INTRODUCTION

THE PHOTONIC integrated circuit (IC) industry has yet to witness the rapid developments made in the electronic IC industry for several reasons, one of which is the confinement of photonic circuits to two dimensions. The complexity of two-dimensional photonic ICs is limited by the substrate size and the difficulty in connecting large numbers of input and output fibers or electrical connections. By making the leap to multilayer interconnects, more compact devices can be obtained. Fewer connections between chips are required and some devices can be made smaller than their in-plane counterparts. The need to combine different materials on a single chip can be addressed as well. Three-dimensional routing of signals will thus be necessary for significantly more compact and powerful photonic ICs. However, there have been relatively few optical devices in the literature that have been developed specifically for the realization of three-dimensional photonic ICs.

Vertical directional couplers allow for very compact and fast three-dimensional optical switching devices, with coupling lengths less than 40 μm [1], [2]. Unfortunately, traditional vertical couplers have the drawbacks that the inputs and outputs are difficult to separate, and the materials are restricted by growth parameters. Wafer bonding overcomes these limitations by allowing separated input and output waveguides and the joining of materials of different lattice constants and crystallographic orientations. Using bonded vertical couplers, a large number of photonic IC planar layers of various compositions are possible, and with the right fabrication conditions, the current six to seven layers for typical electronic ICs may eventually be surpassed [3]–[5]. We describe in this letter the use of three-layer photonic interconnects to make a compact semiconductor 1:8 beam splitter.

II. DEVICE FABRICATION AND STRUCTURE

Cascaded 3-dB vertical couplers incorporating three layers (two InP-to-InP bondings) were fabricated. Three wafers were grown using metal–organic chemical vapor deposition (MOCVD). Due to the inversion resulting from the bonding, the order in which the wafers were processed is the opposite of the top-to-bottom order of the layers of the resulting bonded device. For the first (bottom layer) wafer, on a (001) InP substrate, a 0.5-μm InGaAsP ($\lambda_g = 1.3$ μm) guiding layer, followed by a 0.1-μm InP cladding layer were grown. All layers were undoped. The second (middle layer) wafer was grown on a (001) InP substrate as well. It consisted of a 0.2-μm InGaAs etch stop layer, followed by a 0.1-μm InP cladding layer, a 0.5-μm InGaAsP ($\lambda_g = 1.3$ μm) guiding layer, and a 0.5-μm InP support layer. For the third (top layer) wafer, on another (001) InP substrate, a 0.2-μm InGaAs etch stop layer, followed by a 0.9-μm InP cladding layer, a 0.5-μm InGaAsP ($\lambda_g = 1.3$ μm) guiding layer, and a 0.5-μm InP support layer were grown.

The device fabrication begins with the cleaving of the first wafer into a 1.3 × 1.5-cm sample, deposition of SiN, and standard photolithography with the corresponding removal of SiN to define the position of the bottom-layer waveguides. The waveguides were then etched using CH_4–H_2–Ar reactive ion etching, the SiN was removed, and the sample was bonded at 630 °C in a hydrogen atmosphere for 50 minutes to a blank sample of the second wafer cleaved to the same size. The substrate of the second wafer was removed in HCl and the InGaAs etch stop layer was removed in H_2SO_4–H_2O_2. After substrate removal, the processing for the second and third layers is identical to that of the first except that alignment marks were uncovered using infrared photolithography and wet etching with HCl and H_2SO_4–H_2O_2 after the SiN deposition. Lastly, the sample is cleaved into devices approximately 2 mm long including input and output waveguides to allow flexibility in the position of the cleave.

The waveguides were 3 and 4 μm wide. Support regions were placed 10 μm away from all waveguides to ensure that the structure did not deform. Unwanted coupling from the waveguides to the InGaAsP–InP support regions on adjacent layers will take place if the waveguides on one layer are allowed to be close to the InGaAsP of the other layer. The InP cladding region and InGaAsP guiding regions were hence removed from within 10 μm of waveguides on adjacent layers to prevent unwanted coupling.

M. Raburn and J. E. Bowers are with the Electrical and Computer Engineering Department, University of California, Santa Barbara, CA 93106 USA (e-mail: maura@opto.ucsb.edu).

B. Liu is with Calient Networks, Goleta, CA 93117 USA.

P. Abraham is with Agility Communications, Inc., Goleta, CA 93117 USA.
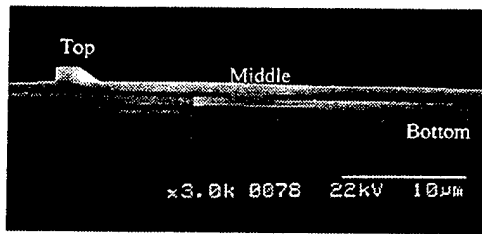
Fig. 1. SEM of output waveguides. From left to right, top, middle, and bottom waveguides are shown. Bonded region below top waveguide is for support.

Fig. 1 shows a SEM of the cleaved side of the device. To prevent a coupling asymmetry due to the lack of a 0.5-μm InP support layer above it, the top layer waveguide (1.4 μm high) was made taller than the bottom and middle layer waveguides (0.6 μm high).

III. DEVICE DESIGN

The principle of operation of the 1 : 8 beam splitter is one of two-mode interference. That is, the coupling of light is due to the overlap of the evanescent fields of the two waveguides such that after a given length, light entering one waveguide will couple half of its power to the other waveguide if the propagation constants of both individual waveguides are similar. Using the three-dimensional finite-difference beam propagation method (BPM [6]), the performance was simulated for various materials, coupling lengths, s-bend lengths, and waveguide heights. 1.3-μm InGaAsP ($n = 3.37$) was chosen as the waveguide layer rather than InGaAsP of a larger index of refraction because lower index waveguide layers result in shorter coupling lengths; this can be explained in a coupled-mode picture as an increase in the overlap integral of the two modes of adjacent waveguides [7]. The choices of waveguide height and separation were also influenced by the high index of the waveguide layer. For the structure described earlier, thinner waveguide layers, by providing less modal confinement, will also increase the overlap integral between modes of adjacent waveguides and will thus reduce the coupling length [7]; less separation between waveguides will also provide shorter couplers. With the material and waveguide heights used above, the 3-dB coupling lengths for the three stages of the 1 : 8 splitter are 37 μm, 39 μm, and 47 μm, respectively. The total device length, not including the straight input and output waveguides appended for ease of cleaving, is 583 μm.

By contrast, a beam splitter made from horizontal couplers using the same material and waveguide heights and widths as in layer 1, and with 1 μm separation between waveguides would have a 3-dB coupling length of 4.73 cm for a single stage consisting of straight waveguides only. Using s-bends long enough to allow the same output waveguide spacing as the bonded splitter, the total device length would be approximately 14 cm. Although a smaller waveguide separation would allow a shorter coupling length, the difficulty in making reproducible and uniform narrow-gap (<1 μm) horizontal couplers have hindered their development for ultra-short splitting and switching devices [7]. Thus, vertical couplers offer a great advantage in terms of device compactness.
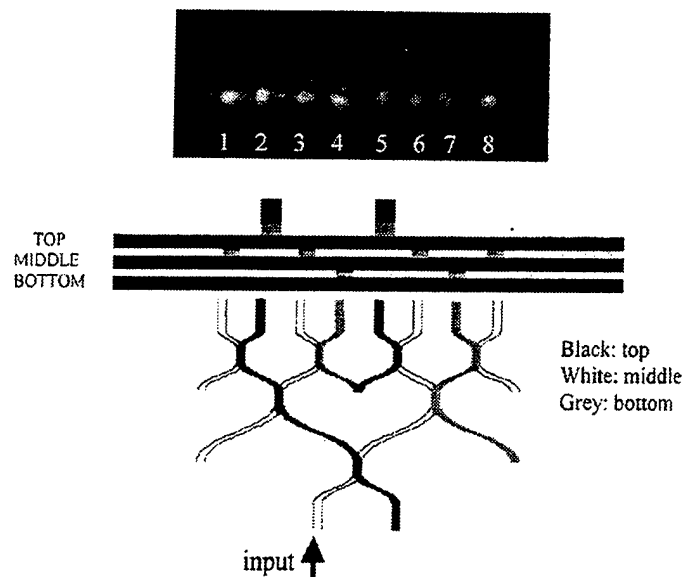
Fig. 2. Device output at $\lambda = 1483$ nm as captured by IR camera, and corresponding waveguide layout.
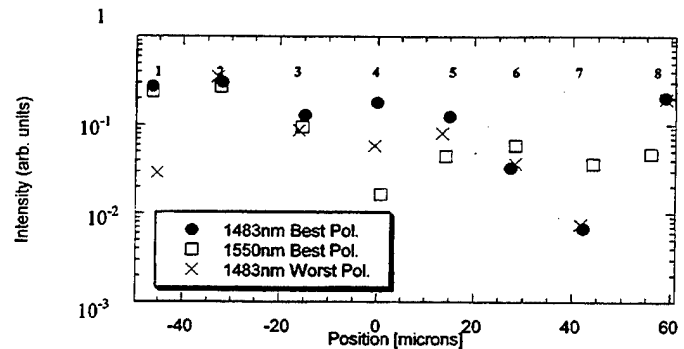
Fig. 3. Peaks of line scan of device output at 1483 and 1550 nm for best polarization and at 1483 nm for worst polarization.

IV. RESULTS

The device output at $\lambda = 1483$ nm as captured by an infrared (IR) camera and the corresponding waveguide positions are shown in Fig. 2. Light from a tunable semiconductor laser is coupled to the waveguides via a single-mode lensed fiber. The output beams have slight height differences corresponding to the waveguide heights. They are separated by 15 μm for ease of coupling to the output fiber.

To measure the polarization and wavelength sensitivity of the device, the output of the device was coupled to a single-mode lensed fiber connected to a detector. The output fiber was mounted on a computer-controlled adjustable xyz stage, and was scanned across the output waveguides at different polarizations and wavelengths. As shown in Fig. 3, although the splitter can operate at different wavelengths and polarizations, the ratios of light intensity coupled to the various output waveguides changes somewhat. The unevenness in splitting is thought to arise from the less-than-ideal alignment obtained with a standard mask aligner, as the alignment tolerance was simulated to be approximately 0.25 μm. It is believed that more uniform splitting could be obtained through the use of a stepper mask aligner. The wavelength dependence could be lessened by

Another direction to be investigated is the transformation of the three-layer beam splitter into a demultiplexer through a change to the lengths of the coupling regions. This would be achieved by utilizing the wavelength dependence of the coupling. Couplers on each successive stage can be chosen to have lengths such that every other channel is split to a different output waveguide, as shown in Fig. 4.

V. CONCLUSION

A novel three-layer bonded vertical coupler 1 : 8 beam splitter is demonstrated. To our knowledge, this is the first three-layer three-dimensional waveguide beam splitter. A device length of 583 μm, two orders of magnitude smaller than the length of an equivalent horizontal coupler splitter, is obtained. This illustrates the powerful potential of the use of wafer bonding to fabricate three-dimensional photonic integrated circuits.

Fig. 4. Proposed demultiplexer with structure similar to that of beam splitter except for the coupler lengths.

designing even shorter couplers, for which the s-bends provide all of the coupling. The polarization dependence is a function of the structure and material parameters as well; the device could be made polarization-independent through a modification of waveguide design [8].

A Fabry–Perot resonance technique was used to measure the waveguide optical loss [9]. Straight waveguide regions were cleaved off of the sample and tested to give 1 dB of loss per 583-μm 1 : 8 splitter length. Total s-bend losses were calculated using BPM [6] to be 0.9 dB.

Future considerations include an optimization of the waveguide s-bends through use of the conformal transformation method [10]. The default s-bend shape provided by the BPM simulation program [6] was composed of two circular arcs. This design does not provide a minimum s-bend loss; a further reduction could be obtained through a conformal transformation analysis.

REFERENCES

[1] A. Shakouri, B. Liu, P. Abraham, and J. E. Bowers, "3-D photonic integrated circuits for WDM applications," in *SPIE Critical Reviews*, San Jose, CA, Jan. 25–26, 1999, invited paper, pp. 181–204.

[2] M. Kohtoku, S. Baba, S. Arai, and Y. Suematsu, "Switching operation in a GaInAs–InP MQW integrated-twin-guide (ITG) optical switch," *IEEE Photon. Technol. Lett.*, vol. 3, pp. 225–227, Mar. 1991.

[3] B. Liu, A. Shakouri, P. Abraham, Y. J. Chiu, and J. E. Bowers, "Push–pull fused vertical coupler switches," *IEEE Photon. Technol. Lett.*, vol. 11, pp. 662–664, June 1999.

[4] A. Black, A. R. Hawkins, N. M. Margalit, D. I. Babic, A. L. Holmes Jr., Y. L. Chang, P. Abraham, J. E. Bowers, and E. L. Hu, "Wafer fusion: Materials issues and device results," *IEEE J. Select. Topics Quantum Electron.*, vol. 3, pp. 937–951, June 1997.

[5] Z. H. Zhu, F. E. Ejeckam, Y. Qian, J. Zjamg, G. L. Christensen, and Y. H. Lo, "Wafer bonding technology and its application in optoelectronic devices and material," *IEEE J. Select. Topics Quantum Electron.*, vol. 3, pp. 927–936, June 1997.

[6] "BeamProp, Version 2.0," Rsoft, Inc., 1999.

[7] A. Shakouri, B. Liu, B. G. Kim, P. Abraham, A. Jackson, A. Gossard, and J. E. Bowers, "Wafer-fused optoelectronics for switching," *J. Lightwave Technol.*, vol. 16, pp. 2236–2242, Dec. 1998.

[8] B. Liu, A. Shakouri, P. Abraham, Y. J. Chiu, and J. E. Bowers, "Fused III–V vertical coupler filter with reduced polarization sensitivity," *Electron. Lett.*, vol. 35, no. 18, pp. 481–482, Mar. 1999.

[9] K. H. Park, M. W. Kim, Y. T. Byun, D. Woo, S. H. Kim, and S. S. Choi, "Nondestructive propagation loss and facet reflectance measurements of GaAs/AlGaAs strip-loaded waveguides," *J. Appl. Phys.*, vol. 78, no. 10, pp. 6318–6320, Nov. 1995.

[10] M. Heiblum and J. H. Harris, "Analysis of curved optical waveguides by conformal transformation," *IEEE J. Quantum Electron.*, vol. QE-11, Feb. 1975.

InP–InGaAsP Wafer-Bonded Vertically Coupled X-Crossing Multiple Channel Optical Add–Drop Multiplexer

Maura Raburn, Bin Liu, Yae Okuno, and John E. Bowers, *Fellow, IEEE*

Abstract—A vertically coupled InP–InGaAsP crossed waveguide optical add–drop multiplexer has been realized through the use of wafer bonding. Designed for signals in the 1550-nm range, this novel device requires only a single epitaxial growth and illustrates the use of vertical optical interconnects for the three-dimensional routing of optical signals. To our knowledge, it is also one of the first optical vertically coupled devices with no horizontally coupled counterpart.

Index Terms—Optical directional couplers, optical filters, semiconductor waveguides, wafer bonding, waveguide couplers, wavelength-division multiplexing (WDM).
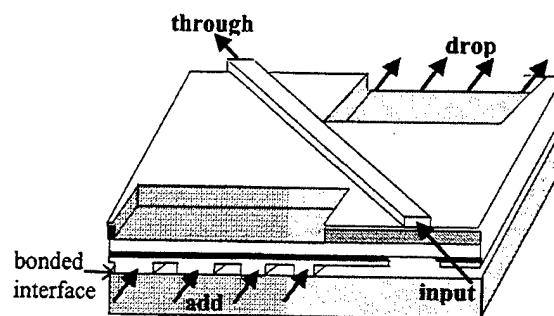
Fig. 1. Layout of the OADM.

I. INTRODUCTION

OPTICAL add–drop multiplexers (OADMs) are key channel routing components in wavelength-division-multiplexed (WDM) systems. OADM implementation methods include fiber or polymer gratings with circulators [1], arrayed waveguides [2], and cascaded unbalanced Mach–Zehnder structures [3]. InP–InGaAsP OADMs [4] are of particular interest because monolithic integration of other optoelectronic devices onto the same chip is possible. Vertical coupling enables the creation of simpler, shorter devices than equivalent horizontally coupled structures, and also allows laterally separated inputs and outputs for ease of coupling to fibers when wafer bonding is employed [5].

In this letter, a simple multichannel OADM is proposed and demonstrated. The device consists of straight waveguides that cross to form Xs. One "in/through" top waveguide is vertically coupled to, and crossed at an angle of 0.3° with, four parallel "add–drop" bottom waveguides (Fig. 1). Only one growth was required for the structure because waveguides were etched on both surfaces of the epitaxial material. The OADM operation is based on coherent coupling of light between the top waveguide and a bottom waveguide, which will only take place when their effective refractive indices are nearly identical. The different widths of the four add–drop waveguides thus correspond to different channels, as the effective indices are functions of both wavelength and waveguide width.

II. DEVICE FABRICATION AND STRUCTURE

Vertically coupled waveguides that cross to form long, narrow Xs were fabricated. One wafer was grown using metal–organic chemical vapor deposition (MOCVD). On a (001) InP substrate, a 0.2-μm InGaAs etch stop, 0.8-μm InP layer, 15-nm InGaAsP etch stop, 0.2-μm InP cladding layer, 1-μm InGaAsP ($\lambda_g = 1.066$ μm) guiding layer, 1.5-μm InP cladding and support layer, 0.22-μm InGaAsP ($\lambda_g = 1.359$ μm) guiding layer, 0.4-μm InP cladding layer, 15-nm InGaAsP etch stop, and 0.8-μm InP layer were grown.

The bottom waveguides were fabricated first because the bonding and substrate removal steps in effect reverse the epitaxial growth order. The device fabrication began with the deposition of SiN, standard photolithography, and CF$_4$ plasma etching to form a SiN etch mask. Wet etching of the top 0.8-μm InP layer (HCl:H$_2$O=2:1) defined the position of the bottom layer waveguides. Another set of SiN, photolithography, and wet etching steps (HCl:H$_2$O=2:1, H$_2$SO$_4$:H$_2$O$_2$:H$_2$O=1:1:10) removed the etch stop layer, the 0.4-μm InP layer and the 0.22-μm bottom guiding layer in certain regions (Fig. 1). These layers will induce unwanted coupling of light from the top waveguide to the slab mode of the bottom waveguide guiding layer if allowed to remain. After thorough cleaning, the sample was bonded at 630 °C in a nitrogen atmosphere for 50 min to a new, blank InP wafer cleaved to the same size. The substrate and the 0.2-μm etch stop layer of the grown wafer were removed via wet etching. The backside of the new InP wafer was then polished to aide in the subsequent infrared (IR) photolithography, which defined the top layer waveguides while alignment with the bottom-level pattern was maintained. Processing of the top waveguides was the same as that for the bottom except CH$_4$–H$_2$–Ar reactive ion etching was used instead of wet etching. Lastly, the sample was cleaved.
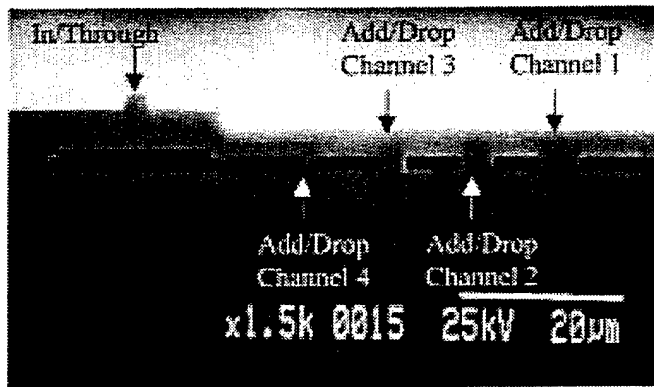
Fig. 2. SEM of sample resulting from cleaving of output facet, including in/through waveguide and four add–drop waveguides.

Fig. 3. Output of OADM as captured with IR camera and 80× microscope objective lens.

III. DEVICE DESIGN

The finished OADMs were 60 μm wide and 1.2 cm long. Each device has one top in/through waveguide of width 3 μm and four parallel bottom add–drop waveguides of width 2, 3, 4, and 5 μm, separated laterally by 10 μm for coupling into lensed fibers (Fig. 2). Since growth variations cause changes in the fraction of light coupled, crossing angles between the top waveguide and the four bottom waveguides ranging from 0.2° to 0.45° were used. The x-crossing arrangement allowed by the bonding also provides lateral separation of the top waveguide from the four bottom waveguides. Support regions were placed 10 μm away from all waveguides to ensure that neither deformation of the structure nor unwanted coupling to the supports would occur.

If the difference between the propagation constants of two crossed waveguides is very small, after a given length, light entering one waveguide will couple completely to the other waveguide. Dissimilar indexes and dimensions for the top and bottom waveguides were chosen because the difference in material and waveguide dispersion allows complete coupling over a much narrower wavelength range than with identical coupled waveguides. Away from the center wavelength, the coupling will be very small due to the phase mismatch. The x-crossing geometry reduces coherent coupling of sidelobes as well [4].

The effective index and transfer matrix methods [6], [7] were used to calculate the effective refractive indexes at different wavelengths, material compositions, and waveguide widths. The material compositions were altered slightly from the previous single channel OADM design [4] because it was found that [8] while the formerly used Henry et al. approach [9] gave a satisfactory relationship between bandgap and index of refraction of InGaAsP for smaller bandgaps (1.3–1.55 μm), the expression derived by Weber [10] provided a better approximation for higher bandgaps (~1.1 μm).

This four-channel OADM does not have a horizontally coupled equivalent, as the waveguides cannot be rearranged or bent in such a manner that they yield an in-plane device with the same capabilities without excessive losses or crosstalk. The dissimilarity between the top and bottom waveguides further complicates any approach to reduce the number of dimensions. Thus, this device illustrates the wonderful flexibility in layout afforded by wafer bonding to form vertically coupled structures.
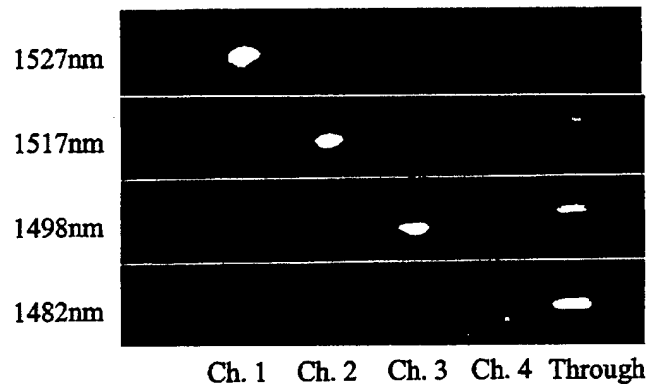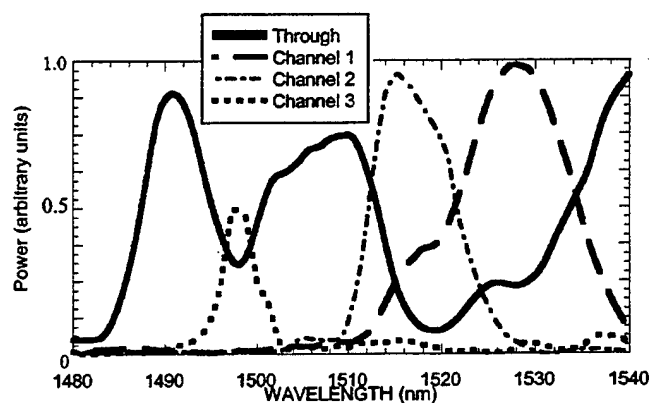
Fig. 4. Smoothed (wavelength averaged) wavelength scan of OADM.

IV. RESULTS

A tunable semiconductor laser with a polarization controller was used to investigate the behavior of the devices. The bandgaps of the InGaAsP regions of the actual growth ($\lambda_g = 1.066$ μm, $\lambda_g = 1.359$ μm) deviated slightly from that of the desired growth ($\lambda_g = 1.068$ μm, $\lambda_g = 1.370$ μm) needed for room temperature operation. This offset necessitated the heating of the sample to 104.3 °C to shift the indices of the material to allow coupling within the range of the tunable laser. The temperature-induced shift in the center wavelengths of the drop channels was 0.39 nm/°C.

The center wavelength of the device has a strong dependence on the InGaAsP bandgaps due to the large dispersion difference between the top and bottom waveguides. Increasing the bandgap wavelength of the top waveguide InGaAsP by 1 nm decreases the center wavelength of the device by 4.1 nm; the ratio of wavelength shifts for the bottom InGaAsP is 2.5:1. The growth variation of InGaAsP bandgaps was 10 nm.

The near-field output is shown in Fig. 3 at the peak wavelength of each channel. The four channels lie at 1482, 1498, 1517, and 1527 nm. Fig. 4 shows a wavelength scan of the OADM throughput and the first three channels. Unfortunately, the fourth channel was damaged before the data for Fig. 4 was taken. The high temperature required for operation of the device aggravated air drafts around the lensed fibers, resulting in noise despite attempts to shield the setup; smoothed data is hence plotted.
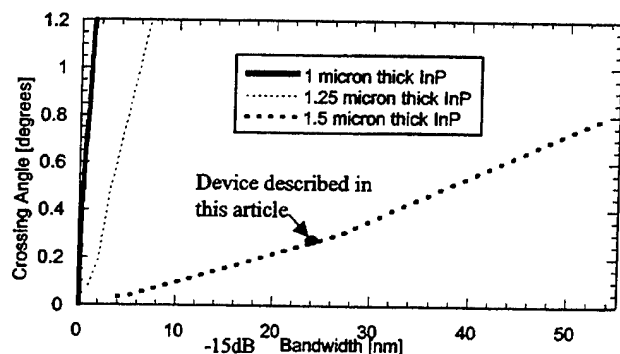
Fig. 5. Theoretical OADM bandwidth as determined by crossing angle, thickness of InP between the two InGaAsP guiding layers.

The four bottom waveguide widths were chosen such that the four channels would be close in wavelength yet suffer low crosstalk. Though due to the undesirable growth, this was not the case for channels 1 and 2, the crosstalk between channels 2 and 3 is less than −17 dB. Adjusting the waveguide widths for 20-nm channel spacing would give a maximum crosstalk of −15 dB for all channels. This wide channel spacing indicates suitability for datacom rather than telecom operation. The bandwidth can be reduced by decreasing the crossing angle, decreasing the thickness of InP between the InGaAsP guiding layers (Fig. 5), or using guiding materials with more different dispersion characteristics (e.g., InP–InGaAsP bonded to AlGaAs–GaAs).

82% of channel 1, 93% of channel 2, and 65% of channel 3 are dropped. Simulations predict that the maximum intensities of all channels can be made equal by using slightly different crossing angles between the in/through waveguide and each add–drop waveguide. The percentage of power dropped can be increased through fine-tuning the crossing angles as well.

Another property matching theoretical predictions is stronger coupling for TE polarizations. TE and TM coupling wavelengths were found to differ by 200 nm. TM-oriented light resulted in a drop channel intensity 11 dB less than that for TE light. The polarization sensitivity results from the strong waveguide geometry asymmetry; large material dispersion differences rather than waveguide dispersion differences (e.g., InP–InGaAsP bonded to AlGaAs–GaAs) would allow TE and TM coupling at the same wavelength. An OADM with waveguide parameters adjusted for TM coupling can be cascaded after the OADM described here for polarization-independent coupling as well.

The fiber-to-fiber device loss was 11.3 dB. The in/through waveguide loss was 7.7 dB/cm using a Fabry–Perot resonance technique [11].

V. CONCLUSION

A novel InP–InGaAsP vertical coupler OADM is demonstrated. Though the layout is simple, the device cannot be reduced to two dimensions. This illustrates the powerful potential of wafer bonding to fabricate three-dimensional photonic integrated circuits.

REFERENCES

[1] H. Mavoori, S. Jin, R. P. Espindola, and T. A. Strasser, "Enhanced thermal and magnetic actuations for broad-range tuning of fiber Bragg grating-based reconfigurable add-drop devices," Opt. Lett., vol. 24, pp. 714–716, 1999.

[2] C. R. Doerr, L. W. Stulz, J. Gates, M. Cappuzzo, E. Laskowski, L. Gomez, A. Paunescu, A. White, and C. Narayanan, "Arrayed waveguide lens wavelength add–drop in silica," IEEE Photon. Technol. Lett., vol. 11, pp. 557–559, May 1999.

[3] B. J. Offrein, G. L. Bona, F. Horst, W. M. Salemink, R. Beyeler, and R. Germann, "Wavelength tunable optical add-after-drop filter with flat passband for WDM networks," IEEE Photon. Technol. Lett., vol. 11, pp. 239–241, Feb. 1999.

[4] B. Liu, A. Shakouri, P. Abraham, and J. E. Bowers, "Optical add/drop multiplexers based on X-crossing vertical coupler filters," IEEE Photon. Technol. Lett., vol. 12, pp. 410–412, Apr. 2000.

[5] M. Raburn, B. Liu, P. Abraham, and J. E. Bowers, "Double fused InP–InGaAsP vertical coupler beam splitter," IEEE Photon. Technol. Lett., vol. 12, pp. 1639–1641, Dec. 2000.

[6] L. Coldren and S. Corzine, Diode Lasers and Photonic Integrated Circuits. New York: Wiley, 1995.

[7] J. Chilwell and I. Hodgkinson, "Thin-films field-transfer matrix theory of planar multilayer waveguides and reflection from prism-loaded waveguides," J. Opt. Soc. Amer. A, vol. 1, pp. 742–753, 1984.

[8] B. Broberg and S. Lindgren, "Refractive index of $In_{1-x}Ga_xAs_yP_{1-y}$ layers and InP in the transparent wavelength region," J. Appl. Phys., vol. 55, pp. 3376–3381, 1984.

[9] C. H. Henry, L. F. Johnson, R. A. Logan, and D. P. Clarke, "Determination of the refractive index of InGaAsP epitaxial layers by mode line luminescence spectroscopy," IEEE J. Quantum Electron., vol. QE-21, pp. 1887–1892, 1985.

[10] J. P. Weber, "Optimization of the carrier-induced effective index change in InGaAsP waveguides—Application to tunable Bragg filters," IEEE J. Quantum. Electron., vol. 30, pp. 1801–1816, 1994.

[11] K. H. Park, M. W. Kim, Y. T. Byun, D. Woo, S. H. Kim, and S. S. Choi, "Nondestructive propagation loss and facet reflectance measurements of GaAs/AlGaAs strip-loaded waveguides," J. Appl. Phys., vol. 78, no. 10, pp. 6318–6320, Nov. 1995.

Wavelength Dependence and Power Requirements of a Wavelength Converter Based on XPM in a Dispersion-Shifted Optical Fiber

Peter Öhlén, Bengt-Erik Olsson, and Daniel J. Blumenthal, *Member, IEEE*

Abstract—A 40-Gb/s wavelength converter based on cross-phase modulation in a dispersion-shifted fiber has been investigated through pulse measurements and simulation. The most important parameter is the dispersive walkoff, which makes the required input power wavelength dependent and determines the optical bandwidth. Simulations show the feasability of the 160-Gb/s operation by using 2-ps pulses and a highly nonlinear dispersion-shifted fiber.

Index Terms—Cross-phase modulation, nonlinear fiber optics, optical fiber communication, optical networks, wavelength converters.

Fig. 1. Experimental setup of the XPM wavelength converter. Er-FRL: fiber ring laser; TECL: tunable external cavity laser; MOD: Mach–Zehnder modulator; EDFA: erbium-doped fiber amplifier; PC: polarization controller; PMF: polarization maintaining fiber; DSF: dispersion shifted fiber.

I. INTRODUCTION

ALL-OPTICAL wavelength conversion can play an important role in future ultrahigh-speed networks using wavelength-division multiplexing (WDM). The wavelength channels will probably be switched by optical add/drop multiplexers, optical crossconnects, and possibly optical packet switching techniques. Wavelength converters will greatly increase the flexibility in such networks and can be used as a basic switching element in, e.g., an optical crossconnect or an optical packet router [1].

Ultrahigh-speed wavelength conversion of return-to-zero (RZ) data has previously been demonstrated using four-wave mixing (FWM) in fiber [2] and semiconductor optical amplifiers [3] and by use of cross-phase modulation (XPM) in the nonlinear optical loop mirror [4]. Schemes using XPM and soliton formation [5] or XPM and polarization discrimination [6] have previously been proposed. We have recently demonstrated a different XPM-based scheme to wavelength convert 40-Gb/s RZ data [7].

The basic idea of this scheme is to utilize XPM in a dispersion shifted fiber. Continuous-wave (CW) light is launched into the fiber along with the data pulses. The pulses will impose a phase modulation that generates sidebands on the CW light. After suppression of the original CW wavelength, and filtering out one
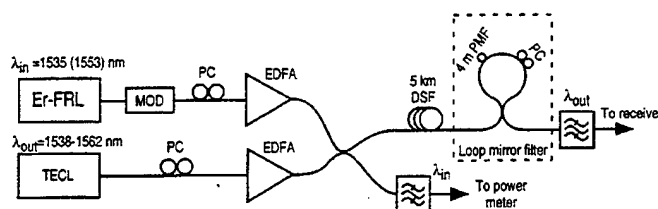
of the generated sidebands, the wavelength-converted data remain at the output. Here we report on pulse measurements in the wavelength converter in order to assess its fundamental operating characteristics at 40 Gb/s, as well as simulations using a highly nonlinear fiber and shorter pulses aiming at 160 Gb/s. For a wavelength converter, both the maximum data rate as well as the conversion wavelength span are important. When RZ data are used, it is important that the output pulsewidth is retained as well as having a stable operating point of the wavelength converter. When the wavelength changes, the optimum operating point will change, and the input power would have to be controlled to compensate for this. Together, these two effects will determine the optical bandwidth and the maximum bit rate of the wavelength converter.

II. EXPERIMENT

Fig. 1 shows the experimental setup where 8-ps pulses with a repetition rate of 10 GHz were generated from an actively mode-locked erbium-doped fiber ring laser, suitable for 40-Gb/s data. The pulses were gated with a Mach–Zehnder modulator to increase the available optical peak power, combined with CW light from a tunable external-cavity laser, and sent through 5 km of dispersion-shifted fiber with a zero-dispersion wavelength of 1542 nm. The pulse power was monitored at one port of the combiner. After the fiber, a loop-mirror filter (LMF) was used to notch out the original CW light, and a 0.4-nm bandpass filter was used to select one of the two generated sidebands. The loop-mirror filter has a sinusoidal filter function with repetitive notches, separated by 1 nm, and 27-dB suppression in the notches. An optically preamplified receiver with a 0.6-nm noise-suppression filter and a sampling oscilloscope was used to measure the pulse characteristics.

In the first experiment, pulses at 1535 nm were converted to longer wavelengths, and the CW light was varied from

Fig. 2. Measured transfer functions for the wavelength converter using 8-ps input pulses and 5-km dispersion-shifted fiber.

Fig. 3. Required input power to reach the maximum of the transfer function. Input pulses at (a) 1535 and (b) 1553 nm.

1538 to 1558 nm. Depending on which sideband is chosen, the behavior is somewhat different. For the left sideband, the output pulsewidth of 12 ps is essentially transform limited over this wavelength range and given by the optical filter bandwidth. The right sideband shows the same behavior up to 1550 nm where the pulsewidth starts to increase, due to asymmetric spectral broadening due to SPM. In terms of optical power, the measured input–output transfer function has a nonlinear shape shown in Fig. 2 for three different wavelengths. When the wavelength separation between the pump and the CW light increases, the input pulse power required for maximum output power increases due to dispersive walkoff between the input pulses and the CW light. The input pulse power is then distributed over a time slice of the CW light, which corresponds to this walkoff. The maximum of the transfer function is chosen as the operating point. It should be noted that the wavelength converter can be used with input powers below the maximum of the transfer function, but this is a good reference point for the measurements and would also to some extent absorb variations in the input power. As shown in Fig. 3(a), the required input power for maximum output power increases when the wavelength is changed from 1538 nm to the zero-dispersion wavelength, where it decreases until the walkoff is zero around 1549 nm. At this point, the required power starts increasing very rapidly, due to higher dispersion. This behavior can be explained from simple theory. If pulse dispersion and loss are neglected, the frequency shift of the CW light for Gaussian pulses can be described by $\Delta f \sim P_{in}L[\exp(-(t-\beta)^2) - \exp(-t^2)]/\beta$, where P_{in} is the input power and L the fiber length. The walkoff time β and the time t are normalized to the $1/e$ half-width of the input pulse. In this equation, an increased β requires an increased power to get the same frequency shift. This increase in power for constant frequency shift is shown together with the measured data in Fig. 3(a) after fitting the power required for zero walkoff. In a second experiment, we show conversion of pulses at 1553 nm to shorter wavelengths. Fig. 3(b) shows that the required input power has a similar shape as for upconversion. However, this turns out to be more difficult because the pump is located in the anomalous dispersion regime, where the spectral broadening is much more significant than in the normal dispersion regime,
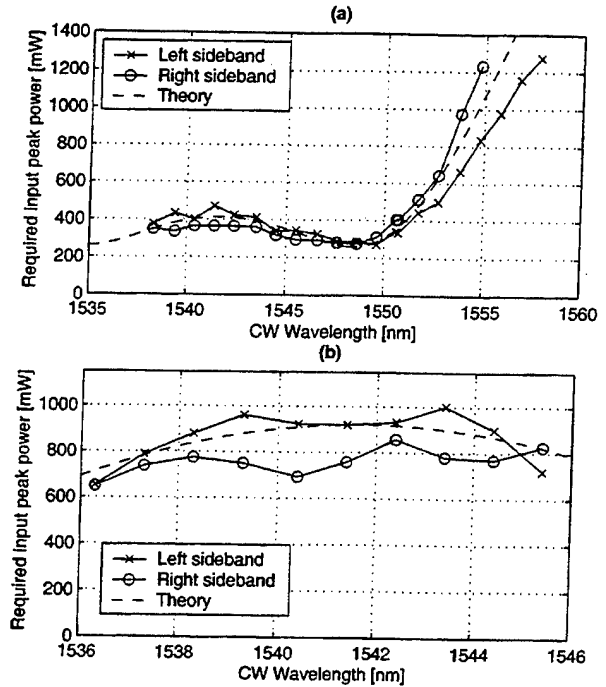
and higher order solitons will be generated. When the separation between the two wavelengths gets smaller, the spectrally broadened input pulses will interfere with the CW light, which generates interferometric noise in the output pulses. This effect starts to be significant at 1537 nm for input pulses at 1535 nm and at 1547 nm for input pulses at 1553 nm.

III. SIMULATION

The wavelength converter used in the experiment was simulated using the nonlinear Schrödinger equation and 8-ps unchirped Gaussian pulses. For the 5-km normal dispersion shifted fiber (DSF), the zero-dispersion wavelength was 1542 nm, the dispersion slope was 0.086 ps/nm²/km, the nonlinear refractive index $n_2 = 2.8 \cdot 10^{-20}$ m²/W, the effective area 60 μm², and the loss 0.4 dB/km. The simulated pulsewidths for the left sideband vary between 12 and 13.5 ps for wavelengths between 1538 and 1555 nm, and the right sideband has similar pulsewidths until 1550 nm where the pulsewidth starts increasing, which is the same behavior as seen in the experiment. The required input power to reach the maximum of the transmission function is shown in Fig. 4 and has a good agreement to the measurements in Fig. 3. By using a highly nonlinear fiber [10], it is possible to decrease the required pulse power, or to use a shorter fiber, where the dispersive walkoff would be less significant. Fig. 4 also shows results for simulations with a 350-m-long highly nonlinear fiber with $n_2 = 5.2 \cdot 10^{-20}$ m²/W and an effective area of 10.7 μm², with the same loss and dispersion characteristics as the 5-km DSF. It can be seen that the difference between the left and right sideband is negligible and that the required input power only changes slightly, due to less dispersive walkoff. For this case, the simulated pulsewidths change only slightly between
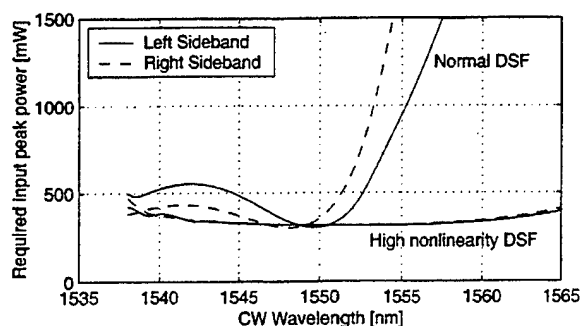
Fig. 4.   Simulation of the wavelength converter using 8-ps input pulses at 1535 nm with 5-km normal DSF and 350-m highly nonlinear DSF.

Fig. 6.   Required input peak power to reach the maximum of the transfer function using 2-ps input pulses at 1535 nm using 350- and 35-m highly nonlinear dispersion-shifted fiber.
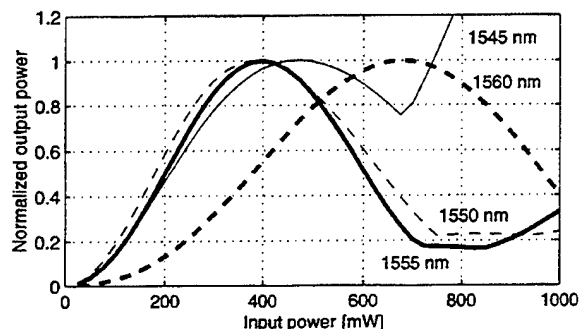
Fig. 5.   Simulation of the transfer function for 2-ps input pulses at 1535 nm using a highly nonlinear DSF, aiming at 160 Gb/s.

12.1 and 12.5 ps for both sidebands. It would also be possible to use a 5-km-long highly nonlinear DSF, leading to the same behavior as the normal DSF, only that the required optical power would be decreased by a factor of ten.

Due to the fast response time of the fiber nonlinearity, it should be possible to use this wavelength converter at even higher speeds. To show this, a wavelength converter with 350-m highly nonlinear DSF was simulated with 2-ps input pulses, aiming at 160 Gb/s. The spacing of the LMF notches was 5 nm, and the bandpass filter has a 3-dB bandwidth of 1.8 nm. Fig. 5 shows the transfer function for four different wavelengths for 2-ps input pulses, using the left sideband. The rise in output power for the 1545-nm transfer function at 700-mW input peak power is due to the spectral broadening of the pump, which causes interferometric crosstalk on the new wavelength. Fig. 6 shows the required input peak power to reach the maximum of the transmission function with 350- and 35-m highly nonlinear DSF. The general behavior is similar to the 40-Gb/s case with standard DSF, where the required input power for the right sideband starts increasing before the left sideband for the long fiber. Also, the pulsewidth of the right sideband increases after 1550 nm, whereas the left sideband shows pulsewidths between 2.2 and 2.4 ps in the wavelength range 1544–1560 nm. For the 35-m fiber, the wavelength dependence is much smaller, but the required input powers are higher.

IV. CONCLUSION

We have investigated the wavelength dependence of a fiber-based 40-Gb/s wavelength converter and experimentally demonstrated a wavelength conversion span of 14 nm with a
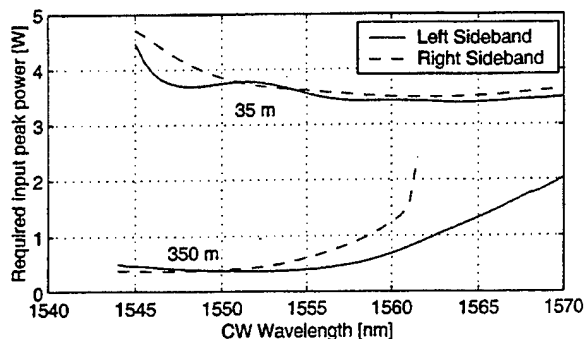
2-dB variation in the input power required for maximum output. In this range, the output pulsewidth was 12 ps. Simulations can reproduce the experimental results, and they show a substantial improvement if a highly nonlinear DSF could be used [10]. For this fiber, the power and pulse-width changes are very small over a wavelength range of over 20 nm, due to a much lower dispersive walkoff. This type of wavelength converter has a polarization dependence originating from the underlying XPM process. However, it can probably be made polarization independent by use of polarization scrambling in the dispersion shifted fiber [8] or circularly birefringent fiber [9]. Simulations with 2-ps pulses show that the scheme is probably scalable to even higher bit rates.

REFERENCES

[1] B.-E. Olsson, P. Öhlén, L. Rau, G. Rossi, O. Jerphagnon, R. Doshi, D. S. Humphries, D. J. Blumenthal, V. Kaman, and J. E. Bowers, "Wavelength routing of 40 Gbit/s packets with 2.5 Gbit/s header erasure/rewriting using an all-fiber wavelength converter," in *Proc. ECOC'99*, Nice, France, postdeadline paper.

[2] K. Inoue and H. Toba, "Wavelength conversion experiment using fiber four-wave mixing," *IEEE Photon. Technol. Lett.*, vol. 4, pp. 69–72, 1992.

[3] S. Murata, A. Tomita, J. Shimizu, and A. Suzuki, "THz optical-frequency conversion of 1 Gb/s-signals using highly nondegenerate four-wave mixing in an InGaAsP semiconductor laser," *IEEE Photon. Tech. Lett.*, vol. 3, pp. 1021–1023, 1991.

[4] K. A. Rauschenbach, K. L. Hall, J. C. Livas, and G. Raybon, "All-optical pulse width and wavelength conversion at 10 Gb/s using a nonlinear optical loop mirror," *IEEE Photon. Technol. Lett.*, vol. 6, pp. 1130–1132, 1994.

[5] D. Schadt and B. Jaskorzynska, "Generation of short pulses from CW light by influence of crossphase modulation (CPM) in optical fibres," *Electron. Lett.*, vol. 23, pp. 1090–1091, 1987.

[6] D. M. Patrick and A. D. Ellis, "10 GHz pulse train derived from a CW DFB laser using crossphase modulation in an optical fiber," *Electron. Lett.*, vol. 29, pp. 1391–1399, 1993.

[7] B.-E. Olsson, P. Öhlén, L. Rau, and D. J. Blumenthal, "A simple and robust high-speed wavelength converter using fiber cross-phase modulation and filtering," in *Proc. Optical Fiber Communications Conf. (OFC'2000)*, Baltimore, MD, 2000, paper WE1.

[8] B.-E. Olsson and P. A. Andrekson, "Polarization independent all-optical AND-gate using randomly birefringent fiber in a nonlinear optical loop mirror," in *Proc. Optical Fiber Communications Conf. (OFC'98)*, vol. 2, 1998, pp. 375–376.

[9] Y. Liang, J. W. Lou, J. K. Andersen, J. C. Stocker, O. Boyraz, and M. N. Islam, "Polarization-insensitive nonlinear optical loop mirror demultiplexing with twisted fiber," *Opt. Lett.*, vol. 24, pp. 726–728, 1999.

[10] M. Onishi, T. Okuno, T. Kashiwada, S. Ishikawa, N. Akasaka, and M. Nishimura, "Highly nonlinear dispersion-shifted fibers and their application to broadband wavelength converter," *Opt. Fiber Technol.*, vol. 4, pp. 204–214, 1998.

All-Optical Header Erasure and Penalty-Free Rewriting in a Fiber-Based High-Speed Wavelength Converter

Peter Öhlén, Bengt-Erik Olsson, and Daniel J. Blumenthal

Abstract—All-optical erasure and rewriting of 2.5–Gb/s nonreturn-to-zero (NRZ) data from high-speed return-to-zero (RZ) data has been demonstrated using a fiber-based wavelength converter. Such a wavelength converter will block the low frequencies of the NRZ data while converting the RZ pulses. This approach uses the frequency discriminating feature of the wavelength converter, and does not require active control. Penalty-free rewriting of new NRZ data was then performed.

Index Terms—Cross-phase modulation, nonlinear fiber optics, optical fiber communication, optical networks, optical packet switching, wavelength converters.

Fig. 1. Experimental setup of the XPM wavelength converter. Er-FRL: Fiber ring laser; TECL: Tunable External Cavity Laser; MOD: Mach–Zehnder modulator; EDFA: Erbium-doped fiber amplifier; PC: Polarization controller; PMF: Polarization maintaining fiber; DSF: Dispersion shifted fiber.

I. INTRODUCTION

TODAY wavelength-division multiplexing (WDM) is well established and has been able to support the increasing demand for transmission capacity. While the performance of present systems continues to improve, optical packet-switching technologies may be required to deliver low-latency packet routing and forwarding at terabit wire rates. The technologies that are being developed should also support header erasure/rewriting in order to enable next-generation IP routing approaches like all-optical label swapping (AOLS) [1]–[3] and new simpler IP routing protocols such as multiprotocol label switching (MPLS) [4] to simplify route lookup and optical implementation.

In all-optical packet switching, the header can be encoded at a lower bit rate and inserted in front of the payload [1], [5], or encoded on a subcarrier at the same wavelength, but outside the data frequency band [3]. At each node, the header is processed and replaced using relatively low-speed electronics, while the high-speed payload remains in the optical domain and is transmitted through the node. A new header is generated electronically and multiplexed with the payload to form the outgoing packet.

In an optical switching node, a tunable wavelength converter combined with a wavelength-selective element, can be used as
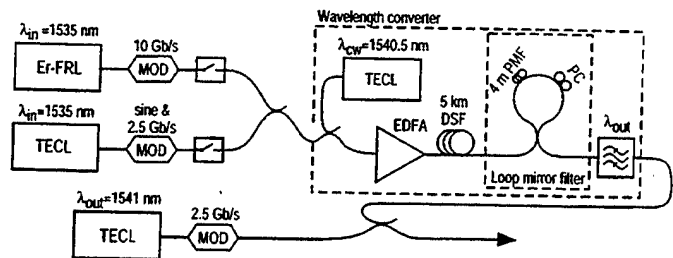
a switching element. Here we describe how a wavelength converter based on cross-phase modulation in an optical fiber [6] can be used to passively remove a low-bit-rate nonreturn-to-zero (NRZ) header from a high-speed return-to-zero (RZ) payload. In the wavelength converter, the input data is combined with a local continuous-wave (CW) signal and launched into a dispersion-shifted fiber. The input data will impose a phase modulation on the CW light, which can be turned into an amplitude modulation by filtering out one of the generated sidebands. Such a wavelength converter has a nonlinear transfer function than can be used to suppress a header to some extent, but it also has a differentiating nature which is the main mechanism employed to remove low-frequency data used in a header. A new header can then be inserted by premodulating the local CW source in the wavelength converter [5]. If the CW source is not very stable small changes in wavelength will cause power fluctuations in the output. Here we use a separate source for the new data to overcome this problem.

II. EXPERIMENT

In the first experiment, the wavelength converter was characterized with a sinusoidal input. Fig. 1 shows the experimental setup where 8-ps pulses with a repetition rate of 10 GHz were generated from an actively mode-locked erbium-doped fiber ring laser, and modulated with 10-Gb/s PRBS data. (This pulsewidth is suitable for optically multiplexing the 10-Gb/s data to 40 Gb/s.) A tunable external cavity laser was externally modulated with a sine signal ranging from 1 to 20 GHz. These two sources were gated with acoustooptic modulators and combined to form data and sine packets as shown in Fig. 2(a). In the wavelength converter, the input signal is combined with a local continuous-wave (CW) souce, and amplified before

Fig. 2. Generated packets with a 10 GHz sine and 10-Gb/s RZ data before (a) and after (b) the wavelength converter. Packets with 2.5-Gb/s NRZ data and 10-Gb/s RZ data before (c) and after (d) the wavelength converter. It can clearly be seen how the RZ data is converted, while the lower frequency part is suppressed.

Fig. 3. Frequency dependence of the wavelength converter for a sine signal when the input sine peak power was adjusted to the input pulse power and half the input pulse power. Output powers are normalized to the output pulse peak power, and half the output pulse peak power, respectively.

entering a 5-km dispersion-shifted fiber (DSF). The local CW light is spectrally broadened by cross-phase modulation from the input signal, and will have two sidebands at the output of the DSF. A loop-mirror filter which has a sinusoidal transfer function (in the frequency domain) with repetitive notches [6] is used to remove the original CW light. Then a bandpass filter selects one of the remaining two sidebands with the wavelength converted data. (This process can be seen in Fig. 4.) Fig. 2(a) shows data packets together with 10-GHz sine packets at the input, where the peak amplitudes were adjusted to the same value. The extinction ratio of the sine signal is lower because we used the linear regime of the Mach–Zehnder transfer function. In the generation of the optical sidebands on the CW signal, the input pulse power causes a phase modulation on the CW light, and the instantaneous optical frequency deviation of the CW light is given by the derivative of the optical phase. Thus the instantaneous frequency deviation will depend on the derivative of the input pulse power, which is turned into amplitude modulation after filtering. Due to this differentiating nature, the rise and fall times determine the conversion efficiency, which means that the wavelength converter will block low signal frequencies. In Fig. 2(b), it can clearly be seen how the RZ data is converted and the 10-GHz sine is suppressed. Fig. 3 shows the output peak power, normalized to the output pulse peak power. When the frequency of the sine is decreased, the output power drops quickly to levels below −20 dB at 1.24 GHz. Fig. 3 also shows the suppression when the input sine signal was adjusted to half the RZ data amplitude, where the suppression is initially higher, but drops slower. Due to the nonlinear behavior of the wavelength converter, the output will generally not be a sine, but the peak power is still a good measure of the suppression. For pulses, the pulsewidth, and not the bit rate, will determine the conversion efficiency. It should be noted that NRZ data cannot be converted, as only the edges of a signal are converted. In a sequence of consecutive ONE's, only the first ONE would generate an output signal. However, there would still be some output that could cause crosstalk when a new header is inserted, even though the old
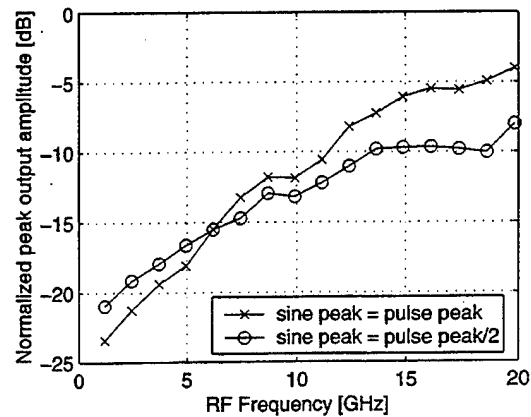
Fig. 4. Optical spectra for the 10-Gb/s RZ and the 2.5-Gb/s NRZ, at the wavelength converter input, after the dispersion-shifted fiber, and after the wavelength converter.

header data has been corrupted. Fig. 2(c) and (d) shows the situation for packets of 2.5-Gb/s NRZ and 10-Gb/s RZ, before (c) and after (d) the wavelength converter. On the oscilloscope, the remainder of the 2.5-Gb/s NRZ data was totally hidden in the detector noise. By averaging the signal, the suppression was estimated to around −23 dB, which agrees with the sine measurements.
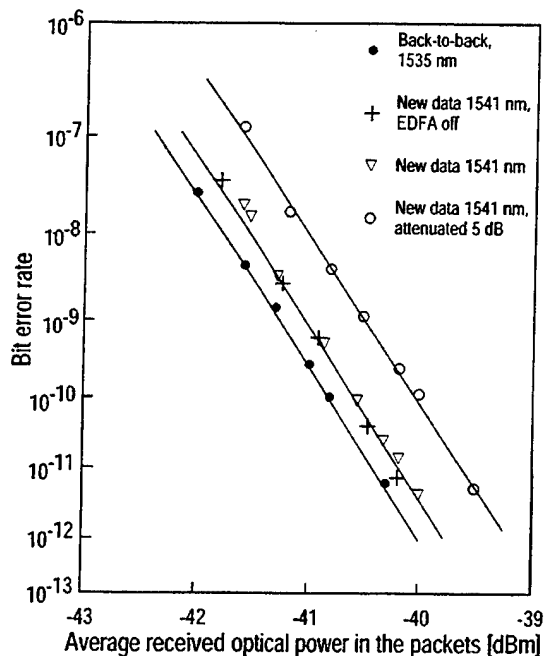
Fig. 5. BER measurements: (●) the original 2.5-Gb/s NRZ data at 1535 nm; (+) new 2.5-Gb/s NRZ data at 1541 nm with EDFA in the wavelength converter turned off; (▽) new 2.5-Gb/s NRZ data with the wavelength converter turned on; and (○) new 2.5-Gb/s NRZ data attenuated 5 dB, otherwise as ▽.

In the second experiment, the 10-Gb/s RZ data and the 2.5-Gb/s NRZ data were switched manually, to measure the optical spectra, and to measure the penalty for rewriting new 2.5-Gb/s data where the original data was erased. At the input to the wavelength converter, the average power of the NRZ and the RZ data were equal. Fig. 4 shows the optical spectra as measured with an optical spectrum analyzer at the input to the wavelength converter, after the DSF, and after the wavelength converter. It can clearly be seen how the RZ data significantly broadens the CW source in the WLC, whereas no broadening can be noticed in the diagrams for the 2.5-Gb/s data.

Then the bit-error rate (BER) was measured for the original and rewritten header data using continuous $2^{31} - 1$ pseudo-random data. Fig. 5 shows the back-to-back measurements for the original transmitter at 1535 nm (●) as well as for the new transmitter at 1541 nm with the EDFA in the wavelength converter turned off (+). The small difference in sensitivity of 0.2 dB could be due to minor differences in the transmitters and the wavelength. The average power of the new data was adjusted to the same average power as the converted RZ data. The bit-error rate when the wavelength converter is turned on (▽) shows no penalty compared to the case with the amplifier turned off. The new data is offset by 0.5 nm, which means that the crosstalk will not be interferometric. With a suppression of around -20 dB, one should not see a penalty and the experimental result is expected. When the power of the new data is attenuated by 5 dB (○), keeping everything

else constant, a penalty of 1 dB can be seen, which increases to 5-dB penalty with 10-dB attenuation of the new data. This is probably due to noise from the amplifier in the wavelength converter. In this experiment, no BER measurements were made for the 10- and 40-Gb/s data, which have been reported elsewhere for packets [5] and continuous data [6].

III. CONCLUSIONS

From the measurements it is clear that this type of wavelength converter can be used to passively erase a 2.5-Gb/s NRZ header from a high-speed RZ payload. Compared to other approaches using time-domain header [1], [2], no timing control is required to erase the header. To insert a new header timing control would be necessary to align the new header to the wavelength converted payload. New 2.5-Gb/s data can then be rewritten in different ways. Here a separate transmitter was used for the new data, which showed no crosstalk penalty from the previously erased data. This makes the system more stable compared to the approach of premodulating and slightly detuning the local CW light in the wavelength converter as demonstrated in [5], but requires a high extinction ratio of the new header source when the payload is present. Otherwise, the local header source would cause the payload data to be degraded due to interferometric crosstalk. A third option which has not been experimentally investigated, is to encode the new header by frequency-modulating the local CW laser in the wavelength converter. With the present tuning speed of about 5 ns this would limit the bit rate to a maximum of 100 Mb/s, but with further advances in tunable laser technology this could be an interesting option.

REFERENCES

[1] P. Gambini, M. Renaud, C. Guillemot, F. Callegati, I. Andonovic, B. Bostica, D. Chiaroni, G. Corazza, S. L. Danielsen, P. Gravey, P. B. Hansen, M. Henry, C. Janz, A. Kloch, R. Krahenbuhl, C. Raffaelli, M. Schilling, A. Talneau, and L. Zucchelli, "Transparent optical packet switching: Network architecture and demonstrators in the KEOPS project," IEEE J. Select. Areas Commun., vol. 16, pp. 1245–1259, Sept. 1998.

[2] D. Chiaroni, C. Chauzat, D. de Bouard, F. Masetti, M. Sotom, M. Bachmann, P. Doussiere, and M. Schilling, "Novel all-optical multi-functional regenerative interface for WDM packet-switching systems," in Proc. ECOC'96, vol. 4, Olso, Norway, Sept. 1996, ThD 1.4, pp. 115–118.

[3] D. J. Blumenthal, A. Carena, L. Rau, V. Curri, and S. Humphries, "All-optical label swapping with wavelength conversion for WDM-IP networks with subcarrier multiplexed addressing," IEEE Photon. Technol. Lett., vol. 11, pp. 1497–1499, Nov. 1999.

[4] A. Viswanathan, N. Feldman, Z. Wang, and R. Callon, "Evolution of multiprotocol label switching," IEEE Commun. Mag., vol. 36, pp. 165–173, May 1998.

[5] B.-E. Olsson, P. Öhlén, L. Rau, G. Rossi, O. Jerphagnon, R. Doshi, D. S. Humphries, D. J. Blumenthal, V. Kaman, and J. E. Bowers, "Wavelength routing of 40 Gbit/s packets with 2.5 Gbit/s header erasure/rewriting using an all-fiber wavelength converter," presented at the ECOC'99, Nice, France, Postdeadline paper PD3-4.

[6] B.-E. Olsson, P. Öhlén, L. Rau, and D. J. Blumenthal, "A simple and robust high-speed wavelength converter using fiber cross-phase modulation and filtering," in Proc. Optical Fiber Communications Conf., OFC'2000, Baltimore, MD, 2000, paper WE1.

Optical SCM Data Extraction Using a Fiber-Loop Mirror for WDM Network Systems

Giammarco Rossi, *Member, IEEE*, Olivier Jerphagnon, *Student Member, IEEE*, Bengt-Erik Olsson, and
Daniel J. Blumenthal, *Senior Member, IEEE*

Abstract—We demonstrate the use of a polarization-independent dual-port filter to extract subcarrier multiplexed (SCM) data from a baseband/SCM channel while the baseband is passed through with minimal distortion. This architecture solves the fiber dispersion-induced fading problem for SCM channels and eliminates the complexity of single-sideband modulation techniques by suppressing the optical carrier at the tap port prior to photodetection. Bit-error-rate (BER) measurements were performed on the baseband channel showing that the SCM removal prior to photodetection reduces crosstalk with the subcarrier channel. The BER on the SCM data shows no effect of dispersion-induced fading. The periodic optical frequency characteristic of the filter can be matched to the ITU grid, making this tap applicable to multichannel WDM networks.

Index Terms—Fiber-loop mirrors, optical filtering, optical label switching, optical networks, optical RF filters, subcarrier multiplexing, wavelength division multiplexing, WDM networks.

I. INTRODUCTION

THE UTILIZATION of subcarrier multiplexed (SCM) data channels in optical networks has many potentially important roles including packet addressing [1], label removal for all-optical label swapping [2], performance monitoring using subcarriers [3], and network management and control [4]. These networks require an efficient method to monitor, extract, and potentially erase subcarrier information using inexpensive receivers and electronics [5]. Techniques to extract SCM data from an optical baseband channel should address critical issues such as power penalties due to fiber dispersion-induced subcarrier fading. Optical filtering techniques have been used to simplify SCM receiver design by prefiltering a subcarrier channel prior to photodetection [6] and can be used to recover a single sideband optical subcarrier channel and greatly reduce dispersion-induced performance degradation [7].

In this letter, we demonstrate a new application of the fiber-loop mirror [8] as a dual-output filter to extract optical
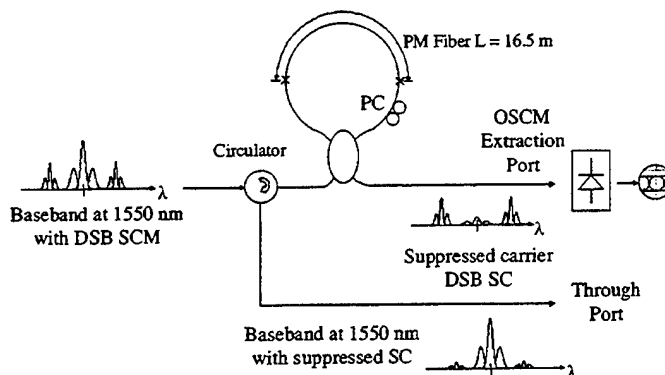
Fig. 1. Dual-output SCM channel extraction filter using an FLM. Data on suppressed carrier SCM channel are recovered using a photodetector.

SCM (OSCM) baseband channels from a combined baseband/SCM data channel. The optical baseband channel passes through the filter for further processing, routing, transmission, or reinsertion of new OSCM data. The OSCM extraction port produces a suppressed carrier SCM signal that is demodulated using a direct detection photodetector. The resulting receiver complexity is simpler than direct and coherent RF receivers combined with photodetectors and does not suffer the power penalty due to dispersion-induced SCM fading. Thus, the complexity of single sideband subcarrier transmitters is also avoided. Since the filter is periodic in frequency, it can be locked to the ITU grid, allowing multiple SCM channels to be extracted simultaneously from a WDM data stream while preserving the baseband data.

II. DESCRIPTION OF THE TAP

The tap is realized using a fiber-loop mirror (FLM) [8] with a PM fiber as shown in Fig. 1. The input signal consists of a combined optical baseband channel and SCM double-sideband (DSB) modulated channel. The FLM transfer function is set so that the OSCM extraction port notch is located at the optical carrier frequency. As shown in Fig. 1, the DSB SCM data is output to the drop port with its optical carrier suppressed while the baseband channel is reflected by the FLM and passed to the through port using an optical circulator. The SCM baseband data is recovered directly using a simple photodetector. The suppression of the optical carrier at the tap port eliminates the fiber-induced dispersion fading.

A. FLM Filter Architecture

The filter architecture is based on a polarization-independent linear FLM [9] that employs a section of birefringent fiber with

Fig. 2. The optical transfer functions for the two outputs illustrate WDM operation by setting the mode spacing at a submultiple of the ITU 100-GHz channel spacing.

Fig. 3. Schematic explanation of the effect of a narrow notch filter: The filter does not fully suppress the low-frequency tones of baseband long patterns, inducing crosstalk at the subcarrier detection port (left). The problem may be overcome by using a flattened notch (right).

a length–birefringence product chosen to support a given optical channel spacing and subcarrier frequency. The differential group delay (DGD) due to the birefringence translates into an amplitude variation through an interference condition between counterpropagating optical signals at the fiber coupler. This gives rise to a periodic transmission function between the input and the two output ports, as shown in Fig. 2. Due to the Sagnac configuration, the loop mirror is polarization-independent both for amplitude and phase response. The filter can potentially give a very high rejection ratio in the notch for a coupling ratio close to 0.5 [10]; in our case, we measured a notch depth of 30 dB.

B. Transmitter Section

The baseband data and SCM signal were encoded on the optical carrier by means of a dual-arm Mach–Zehnder LiNbO$_3$ electrooptical modulator with a 3-dB bandwidth of 18 GHz. The generation scheme of [11] was used: on one arm of the modulator, 10-Gb/s data were encoded, while the other arm was fed with a 100-Mb/s ASK modulated 16.7-GHz RF tone. This system is a compact way to multiplex subcarrier and data but results in a tradeoff of the extinction ratio for the baseband transmission and introduces several distortion mechanisms: in order to transmit the subcarrier, the baseband modulation depth must be decreased and the Mach–Zehnder transfer function nonlinearity introduces distortion between baseband and subcarrier data. This translates to a power penalty for baseband bit-error rate (BER) with respect to the pure baseband optimal transmission. These effects can be minimized with proper adjustment of the modulator bias, data amplitude, and subcarrier power but cannot be eliminated once the signal is generated.

C. Receiver Section

The use of optical prefiltering greatly reduces receiver complexity for OSCM signals. The elimination of the optical carrier with baseband data allows direct detection of the OSCM data without the need for electrical envelope detection of the RF signal. Once the optical carrier has been suppressed, the OSCM data is additive in power and therefore the dispersion-induced phase shift between the two sidebands is eliminated.
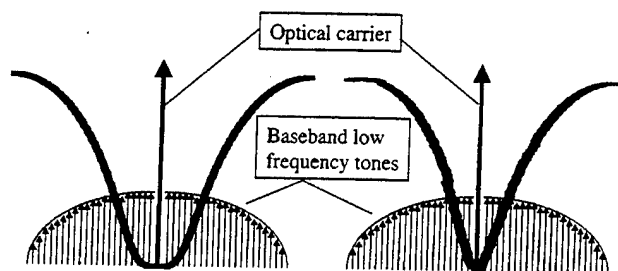
For the baseband, optical prefiltering suppresses the subcarrier prior to square law detection at the receiver, and greatly reduces crosstalk between the baseband and the subcarrier data. This degradation is additive to the distortion generated at the transmitter, as described above.

III. EXPERIMENTAL RESULTS

The loop was constructed with birefringent fiber with a measured polarization dispersion of 1.825 ps/m. A WDM system with 100-GHz channel spacing with 16.7-GHz SCM frequency requires a filter periodicity of 33.4 GHz which corresponds to a DGD of 29.9 ps. The necessary length of PM fiber is then 16.5 m. The filter 3-dB bandwidth is 16.7 GHz, suitable for transmitting baseband data up to 10 Gb/s. Higher bit rates are limited by the bandwidth of the filter, not by the polarization dispersion. In Fig. 2, we report the two complementary transfer functions of the filter we realized and used in the experiment. The pictures are taken with a resolution of 20 pm. The notch depth shown in the picture is limited by the power dynamic of the OSA. The difference in insertion loss is due to the fact that the through port signal passes twice in the isolators and in the experimental setup, also through an APC/FC adapter. The actual periodicity is slightly different from the nominal 100-GHz spacing, but it can prove the point of potential compatibility with a WDM ITU grid. The transmission performance was measured using a 10-Gb/s $2^7 - 1$ PRBS combined with a $2^{31} - 1$ PRBS 100-Mb/s ASK modulated 16.7-GHz subcarrier using the transmitter architecture described in [11]. The reason for having $2^7 - 1$ in the baseband is due to crosstalk between the modulated baseband and the subcarrier. The pattern length is critical since, for longer pattern lengths, the low-frequency components fall into the subcarrier data band. In our case, the notch is so narrow that it eliminates the carrier but cannot as effectively erase all the low-frequency components of the baseband. In the case of short word lengths, the leftover tones are more widely spaced and the disturbances can be effectively reduced with electrical filtering after the detector. The problem could be avoided by using a flattened notch [12] in order to have enough rejection on a wider bandwidth, as shown in Fig. 3.

A. Baseband Data

In Fig. 4, a back-to-back BER measurement for the 10-Gb/s channel without the SCM channel (denoted by ×) is compared to the direct detection of the 10 Gb/s channel in the presence of
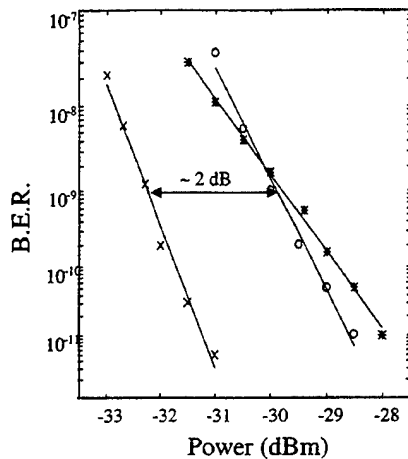
Fig. 4. Back-to-back BER for 10-Gb/s baseband. ×: baseline, optimal conditions for baseband transmission without SCM channel. *: baseband multiplexed with subcarrier channel before the LMF. o: BER after prefiltering with LMF.

Fig. 5. Calculated received RF power for a DSB 16.7 GHz signal with $D = 17$ ps/nm-km and $\alpha = 0.2$ dB/km (Solid Curve) with data point corresponding to the experimental conditions. Eye diagrams, measured using the LMF with various fiber lengths show elimination of fading, in particular the insets show that the eyes diagrams back to back and after 10 km (the null in the fading curve) are identical.

the SCM channel before and after the fiber loop mirror filter (LMF) (denoted by * and o, respectively). The SCM multiplexed signal (*) shows a degradation both in the BER slope and receiver sensitivity that can be explained by the way the mixed subcarrier/baseband signal is generated as previously explained in Section II-B and to the intermodulation crosstalk at the receiver (Section II-B). This last effect is significantly reduced by optical prefiltering, as it results from the improvement of the BER slope measured after the FLM (o). The remaining 2-dB power penalty, apart from the already mentioned distortion at the transmitter, is due to distortion by the LMF and other LMF instabilities as discussed in Section III-B.

B. Subcarrier Data

The receiver sensitivity (for a BER of 10^{-7}) of the suppressed carrier SCM detection was measured constant over more than 60 km of standard fiber, as reported in Fig. 5. We limited the measurement of the BER to 10^{-7} also because the filter was sensitive to mechanical and temperature disturbances; however, we are currently implementing active stabilization of the filter for improved performance. In the lower picture of Fig. 5, the fading curve calculated for our experimental conditions can be seen. A null is present at 12 km, but the inset in the upper picture clearly shows that, even in that case, the eye diagram is clearly open.

IV. CONCLUSION

We have proposed and demonstrated a subcarrier tap based on a dual-port polarization-independent LMF. This approach enables extraction of a double-sideband optical subcarrier data channel from a baseband channel with minimal distortion to the baseband. Suppression of the optical carrier at the drop port allows for double-sideband subcarrier transmission without dispersion-induced fading and allows data recovery using a simple photodetector. Distortion of the recovered baseband is reduced due to a decrease in the intermodulation distortion components at the photodetctor. In the future, the periodic nature of the LMF

transfer function may be utilized for simultaneous extraction of multiple SCM channels from a WDM stream at the input. Due to the ultrawide bandwidth of the transfer function, this filter can also be locked to the ITU grid.

REFERENCES

[1] A. Budman, E. Eichen, J. Schlafer, R. Olshansky, and F. McAleavey, "Multigigabit optical packet switch for self-routing networks with subcarrier addressing," in *Conf. Optical Fibers and Communications (OFC)*, San Jose, CA, February 2–7, 1992, Paper TuO4, pp. 90–91.

[2] D. J. Blumenthal, A. Carena, L. Rau, V. Curri, and S. Humphries, "All-optical label swapping with wavelength conversion for WDM-IP networks with subcarrier multiplexed addressing," *IEEE Photon. Technol. Lett.*, vol. 11, pp. 1497–1499, Nov. 1999.

[3] K.-P. Ho and J. M. Kahn, "Methods for crosstalk measurement and reduction in dense WDM systems," *J. Lightwave Technol.*, vol. 14, pp. 1127–35, June 1996.

[4] R. Gaudino, M. Len, G. Desa, M. Shell, and D. J. Blumenthal, "MOSAIC: A multiwavelength optical subcarrier multiplexed controlled network," *IEEE J. Select. Areas Commun.*, vol. 16, pp. 1270–1285, Sept. 1998.

[5] D. J. Blumenthal, J. Laskar, R. Gaudino, S. Han, M. D. Shell, and M. D. Vaughn, "Fiber optic links supporting baseband data and subcarrier-multiplexed control channels and the impact of MMIC photonic/microwave interfaces," *IEEE Trans. Microwave Theory Tech.*, vol. 45, pp. 1443–1452, Aug. 1997.

[6] P. A. Greenhalgh, R. D. Abel, and P. A. Davies, "Optical prefiltering in subcarrier systems," *Electron. Lett.*, vol. 28, no. 19, pp. 1850–1852, September 10, 1992.

[7] P. D. Sargis, R. E. Haigh, K. G. McCammon, and S. Young, "Subcarrier multiplexing with dispersion reduction," *Electron. Lett.*, vol. 31, no. 20, pp. 1769–1770, September 28, 1995.

[8] D. B. Mortimore, "Fiber loop reflectors," *J. Lightwave Technol.*, vol. 6, pp. 1217–1225, July 1988.

[9] M. Ibsen, M. K. Durkin, M. J. Cole, and R. I. Laming, "Sinc-sampled fiber Bragg gratings for identical multiple wavelength operation," *IEEE Photon. Technol. Lett.*, vol. 10, pp. 842–844, June 1998.

[10] B. E. Olsson and P. A. Andrekson, "A simple method for loss and coupling ratio determination in fused fiber couplers," *IEEE Photon. Technol. Lett.*, vol. 8, pp. 399–401, Mar. 1996.

[11] R. Gaudino and D. J. Blumenthal, "A novel transmitter architecture for combined baseband data and subcarrier-multiplexed control links using differential Mach–Zehnder external modulators," *IEEE Photon. Technol. Lett.*, vol. 9, pp. 1397–1399, Oct. 1997.

[12] Y. Han, Q. Li, X. Liu, and B. Zhou, "Architecture of high-order all-fiber birefringent filters by the use of the Sagnac interferometer," *IEEE Photon. Technol. Lett.*, vol. 11, pp. 90–92, Jan. 1999.

All-Optical Label Swapping Networks and Technologies

Daniel J. Blumenthal, *Senior Member, IEEE, Member, OSA*, Bengt-Erik Olsson, Giammarco Rossi,
Timothy E. Dimmick, Lavanya Rau, Milan Mašanović, Olga Lavrova, *Student Member, IEEE*, Roopesh Doshi,
Olivier Jerphagnon, John E. Bowers, *Fellow, IEEE*, Volkan Kaman, Larry A. Coldren, *Fellow, IEEE, Fellow, OSA*,
and John Barton

Invited Paper

Abstract—All-optical label swapping is a promising approach to ultra-high packet-rate routing and forwarding directly in the optical layer. In this paper, we review results of the DARPA Next Generation Internet program in all-optical label swapping at University of California at Santa Barbara (UCSB). We describe the overall network approach to encapsulate packets with optical labels and process forwarding and routing functions independent of packet bit rate and format. Various approaches to label coding using serial and subcarrier multiplexing addressing and the associated techniques for label erasure and rewriting, packet regeneration and packet-rate wavelength conversion are reviewed. These functions have been implemented using both fiber and semiconductor-based technologies and the ongoing effort at UCSB to integrate these functions is reported. We described experimental results for various components and label swapping functions and demonstration of 40 Gb/s optical label swapping. The advantages and disadvantages of using the various coding techniques and implementation technologies are discussed.

I. INTRODUCTION

INTERNET traffic is growing exponentially and is forcing next generation Internet Protocol (IP) networks to scale far beyond present speed, capacity, performance, and packet forwarding rates. In fiber-based optical networks, next generation optical IP routing will require technologies to support packet routing and forwarding operations at Terabit wire rates that are compatible with wavelength division multiplexed (WDM) transmission and routing. Up to 50% of IP traffic consists of packets smaller than 522 bytes and 50% of these packets are in the 40–44 byte range. New low-latency packet forwarding and routing technologies will be required that can handle wire-rate routing of the smallest packets at rates in excess of Gigapackets/s. These technologies should support new streamlined IP routing protocols such as Multiprotocol Label Swapping (MPLS) [1] that simplify route lookup and separate the routing and forwarding functions.

All-Optical Label Swapping (AOLS) [2]–[4] implements the packet-by-packet routing and forwarding functions of MPLS directly in the optical layer. This is in contrast to next generation commercial optical networks that will use MPLS to set up optical circuits over which flows of electronic packets are routed [5]. For future optical networks, it will be desirable to perform optical routing layer functions independent of the IP packet length and payload bit rate. AOLS approaches should interface seamlessly to both WDM and TDM systems. This leads to the concept of using optical labels to "encapsulate" the IP packet in the optical layer. The optical label format is chosen to best match the optical routing and forwarding technology and to satisfy other constraints in the optical layer (e.g., the current lack of flexible optical buffering technologies).

In this paper, we describe AOLS research at the University of California at Santa Barbara (UCSB) supported under the DARPA sponsored Next Generation Internet (NGI) program and the DARPA sponsored Center for Multidisciplinary Optical Switching Technology (MOST) and the NGI partner Cisco Systems and NGI industrial affiliates New Focus, Agilent Technologies, and Netcom Systems and performed in collaboration with the DARPA supported NGI program at Telecordia Technologies.

The paper is organized into seven sections. Section II describes the overall concept of AOLS, its application in optical networks and optical Internet protocol routers. The key building blocks used to implement AOLS are also described. In Section III we review two different label-coding techniques that

D. J. Blumenthal, B.-E. Olsson, L. Rau, M. Mašanović, O. Lavrova, R. Doshi, V. Kaman, L. A. Coldren, and J. Barton are with the Optical Communications and Photonic Networks Laboratory, Department of Electrical and Computer Engineering, University of California, Santa Barbara, CA 93106 USA.

G. Rossi was with the Optical Communications and Photonic Networks Laboratory, Department of Electrical and Computer Engineering, University of California, Santa Barbara, CA 93106 USA. He is now with Agilent Technologies, Turin Technology Center, 10148 Torino, Italy.

T. E. Dimmick was with the Optical Communications and Photonic Networks Laboratory, Department of Electrical and Computer Engineering, University of California, Santa Barbara, CA 93106 USA, while on a leave of absence from the Laboratory for Physical Sciences, College Park, MD 20740 USA.

O. Jerphagnon is with Calient Networks, San Jose, CA 95138 USA.

J. E. Bowers is with Calient Networks, San Jose, CA 95138 USA, on leave from the University of California, Santa Barbara, CA 93106 USA.

Publisher Item Identifier S 0733-8724(00)10706-6.
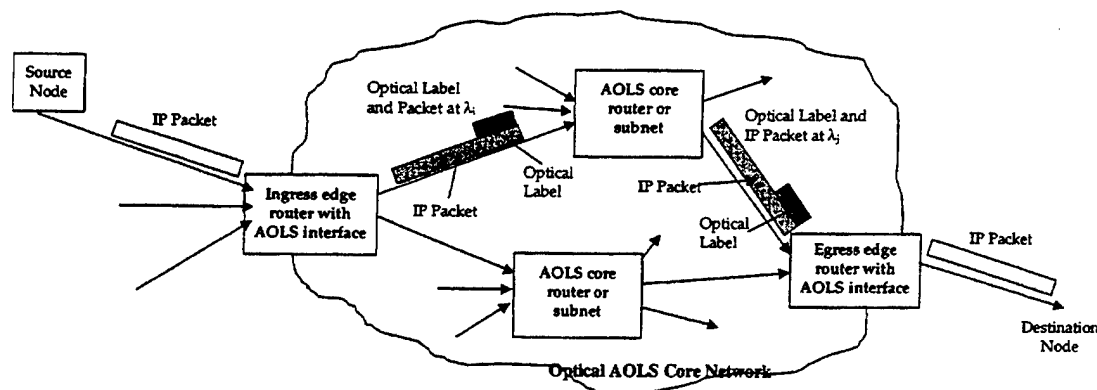
Fig. 1. Optical label swapping with wavelength conversion in an optical core network using edge and core WDM IP routers.
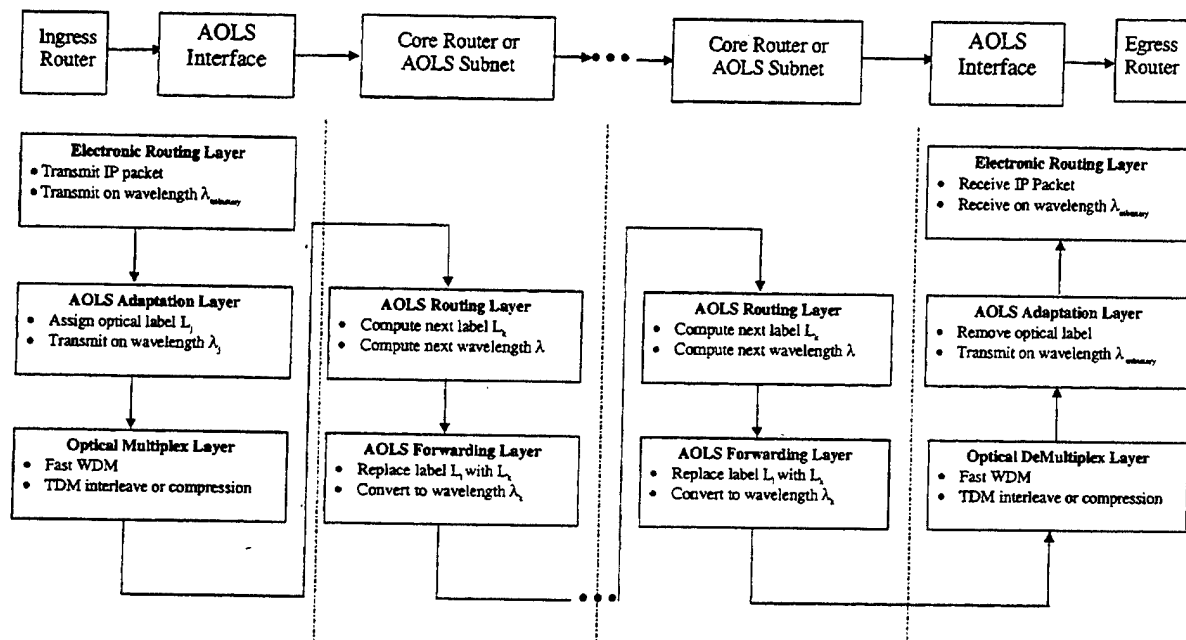
Fig. 2. Layered routing and forwarding hierarchy and associated network element connection diagram for an AOLS network.

have been used to date. Section IV introduces issues specific to building multihop AOLS networks. Several technologies that have been used to realize AOLS building blocks are covered in Section V and the AOLS subsystems are covered in Section VI. Systems experimentally demonstrated at UCSB are described in Section VII.

II. ALL-OPTICAL LABEL SWAPPING (AOLS)

An AOLS optical packet core network is illustrated in Fig. 1. IP packets enter the core network at an ingress router and travel multiple hops through the core, exiting at an egress router. Packets are handled within the network by core AOLS routers or AOLS subnets, as described in [2]. Fig. 2 depicts the physical network elements connected by fiber links and the packet routing and forwarding hierarchy. IP packets are generated at the electronic routing layer and processed in an adaptation layer that "encapsulates" IP packets with an optical label without modifying the original packet structure. The adaptation layer also shifts the packet and label to a new

wavelength specified by local routing tables. An optical multiplexing layer multiplexes labeled packets onto a shared fiber medium. Several optical multiplexing approaches may be used including insertion directly onto an available WDM channel, packet compression through optical time division multiplexing or time interleaving through optical time division multiplexing [6]. This technique is not limited to IP packets and other packet or cell structures like ATM may also be routed.

Once inside the core network, core routers or AOLS subnets [2] perform routing and forwarding functions. The routing function computes a new label and wavelength from an internal routing table given the current label, current wavelength, and fiber port. The routing tables (at egress and core routers) are generated by converting IP addresses into smaller pairs of labels and wavelengths and distributing them across the network much in the same way that multiprotocol label switching (MPLS) is used in today's IP networks [1]. The forwarding function involves swapping the original label with the new label and physically converting the labeled packet to the new wavelength. Other switching or buffering mechanisms (space, time, etc.) are also
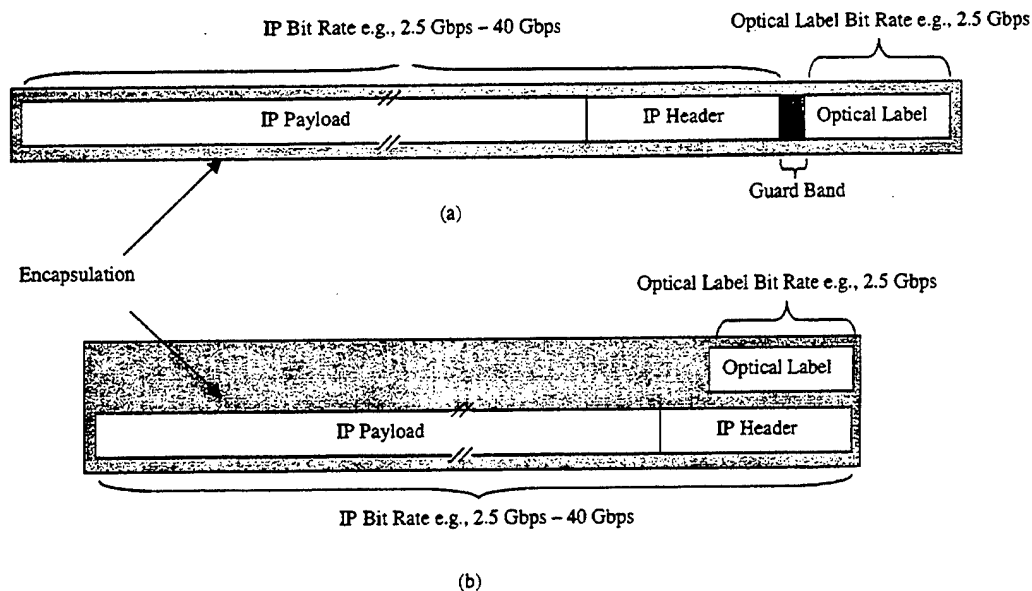
Fig. 3. Optical label coding techniques: (a) fixed rate serial label and (b) optical subcarrier multiplexed label.

configured in the forwarding process. The reverse process of optical demultiplexing, adaptation and electronic routing are performed at the egress node.

III. OPTICAL LABEL CODING TECHNIQUES

The method of coding the label onto a packet impacts the channel bandwidth efficiency, the transmission quality of the packet and label, and the best method to wavelength convert the packet and optically swap the label. Two approaches to optical label coding are the serial label [7], [8] and the optical subcarrier multiplexed label [3], [9]–[11], as illustrated in Fig. 3. With serial coding a fixed bit rate label is multiplexed at the head of the IP packet with the two separated by an optical guard-band (OGB) as shown in Fig. 3(a). The OGB is use to facilitate label removal and reinsertion without static packet buffering and to accommodate finite switching times of optical switching and wavelength conversion. The bit-serial label is encoded on the same optical wavelength as the IP packet and is encoded as a baseband signal. For optical subcarrier multiplexed labels a baseband label is modulated onto a RF subcarrier and then multiplexed with the IP packet on the same wavelength [see Fig. 3(b)]. This multiplexing may be performed electronically or optically as described in [2]–[4], [12]–[14]. An OGB is not necessary in the subcarrier case since the label is transmitted in parallel with the packet. It is only necessary that the label fit within the boundaries of the packet, however an OGB may be used if accumulated misalignment of the label and payload occurs during multiple hops.

Packet transparency is realized by setting a fixed label bit rate and modulation format independent of the packet bit rate. The choice of label bit rate is driven by a combination of factors including the speed of the burst-mode label recovery electronics and the duration of the label relative to the shortest packets at the fastest packet bit rates. Additionally, running the label at a lower bit rate allows the use of lower cost electronics to process the

label. The label and packet bits can be encoded using different data formats to facilitate data and clock recovery. For example, if the IP packet is compressed to 40 Gb/s using an RZ data format, the label can be encoded at 2.5 Gb/s using NRZ format. A 20-bit label transmitted at 2.5 Gb/s occupies the same duration as a 40-byte packet transmitted at 40 Gb/s.

Encapsulation of IP packets using optical labels has advantages in that the contents of the original IP packet are not modified and the label is coded at the same wavelength as the IP packet. In the serial case, erasure and rewriting of the label may be performed independently of the IP packet bit rate, however, timing of the label replacement and possibly erasure process is somewhat time critical. The subcarrier labels have the advantage that they can be removed and replaced more asynchronously with respect to the packet but potentially suffer from dispersion induced fading, a problem that can be remedied as described in a later section.

IV. AOLS FUNCTIONS AND BUILDING BLOCKS

Label recovery, label swapping and packet forwarding are the basic functions handled by the AOLS building blocks, shown in Fig. 4. In a core router or AOLS subnet [see Fig. 4(a)], a burst-mode label recovery module is used to recover label clock and data for processing in electronic routing circuitry without significantly perturbing the through-going optical packet data. The routing circuit maps the incoming label and wavelength to a new label and wavelength based on internal routing tables. The label erasure process may be built into this stage depending on the implementation technology. The second stage performs label erasure (if not performed in the first stage), wavelength conversion and label rewriting using a wavelength converter or combination of converter and optical filter. A fiber optic delay follows the label recovery stage to match the routing processing delay with the arrival of the packet at the second optical stage. An edge router [see Fig. 4(a)] utilizes a slightly modified first
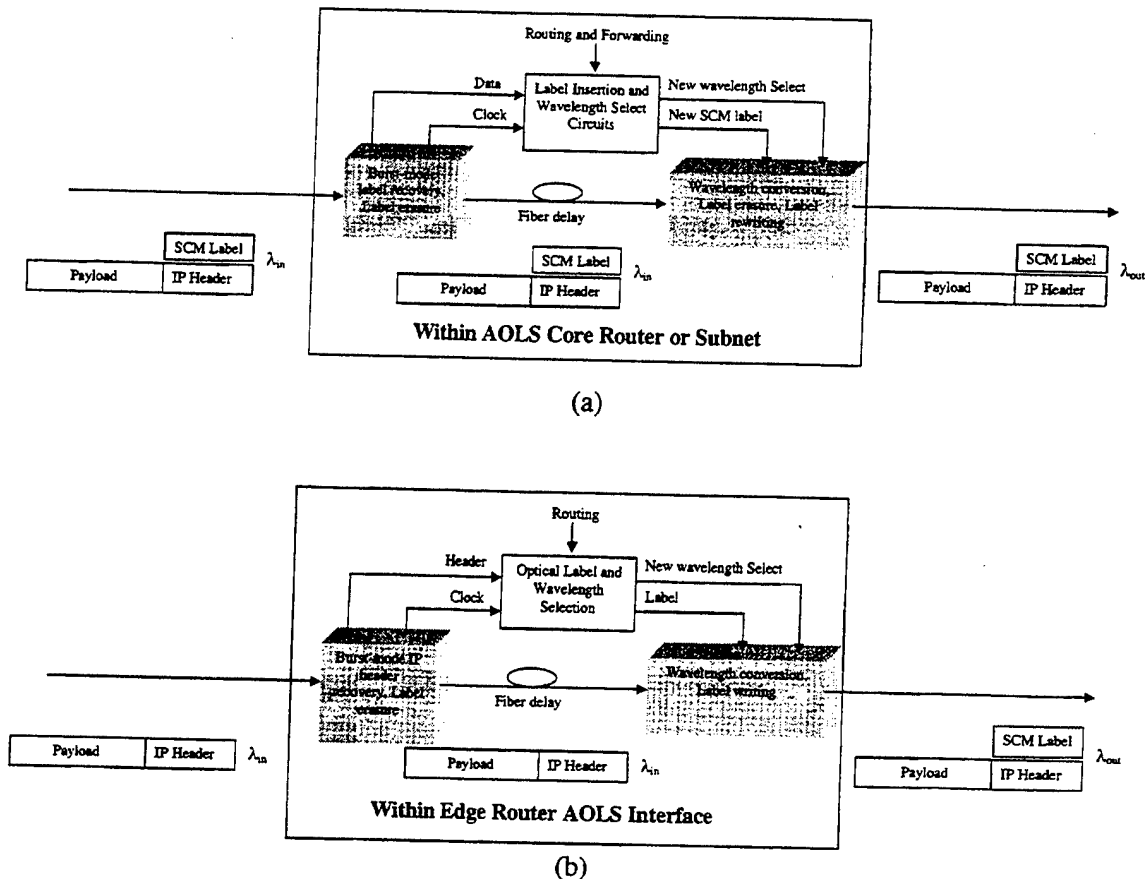
Fig. 4. Building blocks for AOLS (a) core router and (b) core optical routers or subnets.

stage to detect the IP packet header with minimal disturbance to the packet. The second stage performs the same wavelength conversion and label rewriting processes as in the core router, however, the wavelength conversion may be optoelectronic-optic (OEO) depending on the network architecture.

V. ISSUES IN MULTIHOP AOLS NETWORKS

Routing in multihop optical packet network brings to the table a complex set of issues that must take into account the integrity of data transmission and the bursty nature of the data. We briefly discuss the three issues of routing in a burst-mode environment, cascadability, and buffering. Each issue is complex enough to dedicate a paper on the topic and many papers on packet congestion and buffering have been written to date [11], [15].

A. Burst Mode Routing

The main issues in burst-mode routing are summarized in Fig. 5. Packets arrive at a routing node with unknown amplitude and phase relative to a local time reference. The inter-packet spacing is also unknown. For subcarrier coded labels, the data envelope must be recovered from a detected subcarrier with unknown RF phase. For any coding technique, data and clock recovery must be performed without *a priori* knowledge of the optimal threshold or clock phase. To efficiently use the label channel, the header should be extracted within the first few bits. These qualities are addressed in burst-mode receiver technology described in several publications [16], [17]. The optical packet

channel must also be able to accommodate burst-mode operation. The process of label erasure, wavelength conversion, label rewriting, and potential packet regeneration must operate under similar conditions as the label receiver, particularly with respect to amplitude dynamic range.

B. Congestion and Buffering

Optical packet collisions can occur at any core router node or at the edge egress points. Additionally, congestion within the packet handling hardware can occur if the label routing and packet forwarding functions are not pipelined properly. The cumulative interface delay, which is defined as the time involved to route a packet from the input port to the output port of a router, is on the order of tens of micrometers in today's state-of-the-art routers. However with an optimally designed label-processing and routing unit, the time required to process a header should be less than 100 ns. In a bursty network, inter-packet time intervals are not constant, therefore, the incoming packets may have to be buffered while a packet is being routed. The improvement in the packet processing time reduces the buffering time and thereby decreases latency. The routing function should incorporate packet forwarding, label erasure and rewriting the new label. The new label must be replaced with minimum knowledge of the payload contents. Wavelength conversion can facilitate all the above functions. The subject of packet buffering and contention is not a focus of this paper, and there have been multiple publications on this subject [11], [15].
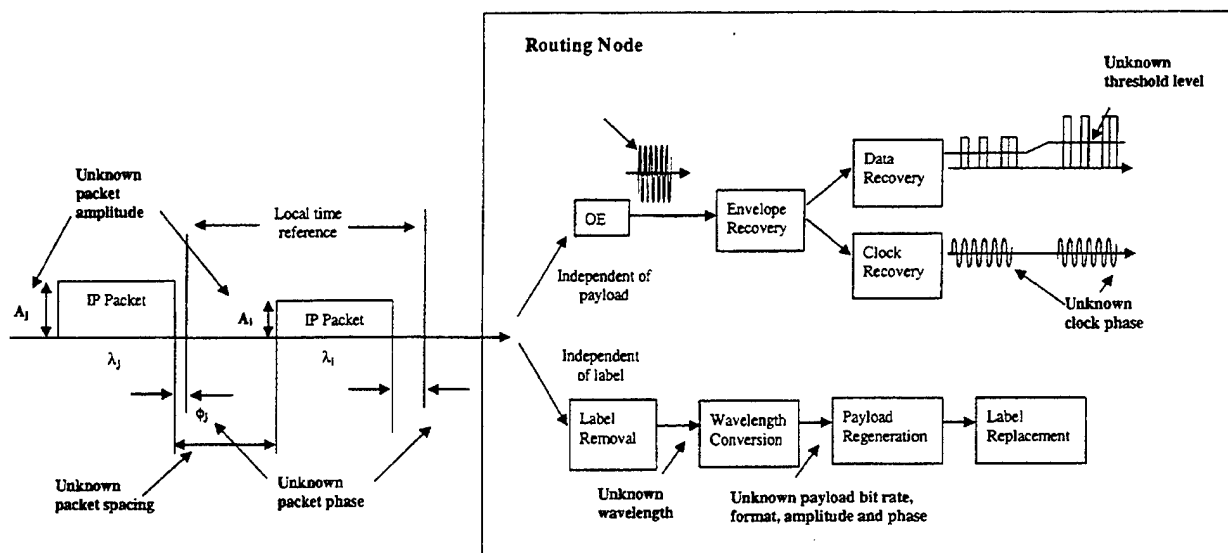
Fig. 5. At each router, label recovery/swapping and packet routing and forwarding must be performed on data that arrives on an unknown wavelength with unknown phase and amplitude.
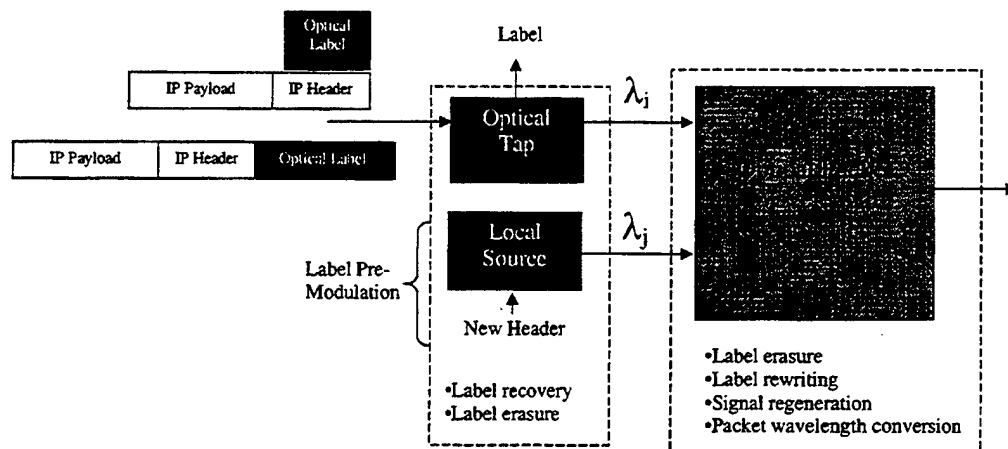
Fig. 6. General model of an AOLS wavelength converter subsystem.

VI. AOLS TECHNOLOGIES

In this section, we review various technologies that have been used to build AOLS subsystems and systems demonstrators. These technologies are classified into AOLS wavelength converters, fiber loop mirrors, wavelength agile sources, optical demultiplexers and packet transmitters.

A. AOLS Packet Wavelength Converters

In general, an AOLS packet wavelength converter performs the functions of label optical label erasure, packet rate wavelength conversion, packet regeneration and optical label rewriting. A general model of an AOLS wavelength converter subsystem including the label tap is shown in Fig. 6. Shown at the inputs of Fig. 6 are the two possible types of labeled packet inputs (serial or OSCM). Depending on the combination of label coding technique and wavelength converter technology, the label tap may or may not handle the label erasure function. A tap that handles the function of erasure and label recovery is described in the next section on fiber loop mirrors.

AOLS wavelength converters have the general capability to simultaneously erase and rewrite during the conversion process. If the label is placed in a properly designed region of the optical or electrical bandwidth or intensity, the packet data at (λ_i) is transferred over to the new wavelength (λ_j) and the label on the original wavelength is not transferred to (λ_j). At the same time, the new label may be pre-modulated onto the new wavelength source (λ_j) and will appear with the wavelength converted packet at (λ_j) and not be transferred to the original wavelength (λ_i). Certain wavelength converter geometries also allow the new header to be written into the wavelength converter module directly.

The packet wavelength converter is also used to perform signal regeneration of the packet to support multihop operation. This regeneration is at least 2R where the extinction ratio is enhanced and the "0" and "1" level noise reduced. 3R regeneration with retiming may also be performed [18].

1) Semiconductor Optical Amplifier (SOA) Based Converters: Cross-gain modulation (XGM) in SOAs is a well understood effect that allows an intensity-modulated signal to

SGDBR Laser

Input λ_i

Output λ_m, λ_i
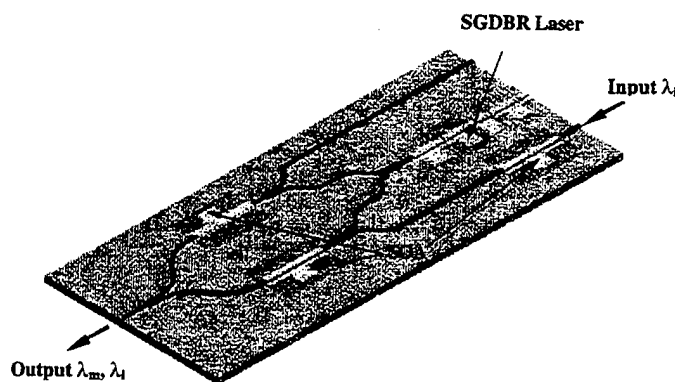
Fig. 7. SOA-based MZI-WC layout of UCSB device.

be transferred from wavelength to another wavelength [19], [20]. Operation at 10 Gb/s or more is possible using this technique and polarization insensitive conversion is possible using amplifiers with polarization insensitive gain [21]. XGM technique decreases the extinction ratio of the output signal (8 dB) and is asymmetric for frequency-up-conversion and frequency-down-conversion. XGM can also introduce chirping and amplitude distortion unless designed properly. This conversion technique is bit rate transparent out to a maximum designed frequency and works for amplitude modulation schemes only. The XGM-WC is also an inverting converter and must be used in conjunction with a secondary device to provide noninverting operation that is important for multihop applications.

The cross phase modulation effect is utilized in an interferometer configuration and can be realized using SOA-based waveguide structures. Fig. 7 shows a Mach–Zehnder interferometer wavelength converter (MZI-WC) under fabrication at UCSB under the NGI program. The input signal passes through one of the interferometer arms and optically modulates the phase of that arm. The interferometric effect converts this phase modulation to an amplitude modulation as the probe signal traverses both arms. XPM produces a high extinction ratio for the converted signal (better than 15 dB) due to its highly nonlinear transfer characteristic. The device may be operated in an inverting or noninverting mode, however, the threshold characteristic of the XPM-WC restricts the dynamic range of the input signal such that the average signal level rests at the proper transfer characteristic operating point. Due to its high quality output signal, this technique represents an attractive solution for AOLS systems. In a later section on AOLS implementations we describe how to combine XGM and XPM converters to gain the full functionality of and AOLS-WC. The signal integrity can be compromised by accumulated distortion of the payload and label due to fiber dispersion and nonlinearities and accumulated SNR degradation due optical amplifier noise and system nonlinearities [3], [4]. Dispersion induced bit broadening, and, in particular, PMD [22], is a very important factor in high-speed (40 Gb/s and higher bit rate) systems. In general, the SNR and bit shape of packets with bit rate of 10 Gb/s and greater will have to be managed or regenerated in multihop systems. Using 2R regeneration during the wavelength conversion process can address the dispersion-induced bit broadening and SNR degradation issues.

2) Fiber XPM Wavelength Converter: To allow operation at ultrahigh bit rates we have demonstrated a new wavelength converter based on nonlinearities in an optical fiber [23] that supports operation at 40 Gb/s and beyond (possibly up to several hundred gigabits per second). In this scheme, we utilize XPM in a dispersion shifted fiber imposed from the incoming data onto CW light, followed by conversion of the phase modulation to amplitude modulation using optical filtering, as shown in Fig. 8. The incoming data is combined with a CW light signal and sent through an optical fiber where the data imposes a phase modulation onto the CW light via fiber XPM. This phase modulation generates optical sidebands on the CW signal, which are converted to amplitude modulation by suppressing the original CW carrier using an optical notch filter. A conventional band-pass filter to select one of the two sidebands then follows the notch filter. However, in principle it is sufficient to use a single band pass filter, e.g., a fiber bragg-grating or fiber-loop mirror, provided that it can suppress the original CW carrier enough.

Fig. 9 shows the eye-pattern (a) before and (b) after wavelength conversion of 40 Gb/s data. The polarization dependence for XPM in a fiber is 5 dB and the polarization dependence as measured with a power meter for the wavelength converter could vary between 2 and 8 dB, depending on the position and bandwidth of the band-pass filter. However, the polarization dependence can be eliminated by utilizing polarization scrambling [24] or circularly polarized fiber [25]. Even though a long fiber was used, no stability problems were observed and the system was only mechanically polarization sensitive before combining the data and CW light. Since the filter arrangement was polarization insensitive environmental disturbances to the DSF did not affect the performance apart from a small timing shift, which can be compensated for by a clock recovery circuit.

Since this scheme relays on optical filtering the issue of wavelength tunability of the filters is critical. The wavelength converter must have the ability to be reconfigured to convert to an arbitrary wavelength within a few nanoseconds. Tunable lasers are today available that can be tuned to an arbitrary wavelength within less than a nanosecond [26] but tunable filters are usually not very fast. In a practical implementation, an important feature of a wavelength converter is to allow no conversion and conversion to wavelength channels near the input wavelength. Using this type of wavelength converter scheme, this can be achieved by simply switching the CW laser off and move the output filter to the actual wavelength and filter out a part of the due to self-phase modulation broadened spectrum [27]. Another important issue is cascadability of multiple wavelength converters. Due to the inherent nonlinear transmission and virtually instantaneous response of the wavelength converter it should be well suited for multi-hop operation. Simulations show that more than 100 hops can be passed without any significant degradation in SNR or timing jitter. This is, however, subject to further experimental investigations.

B. Suppressed Carrier SCM Taps Using Fiber Loop Mirrors (FLMs)

If double sideband SCM modulation is used to encode labels, periodic signal fading occurs due to fiber dispersion. The amount of fading will vary depending on the inter-node
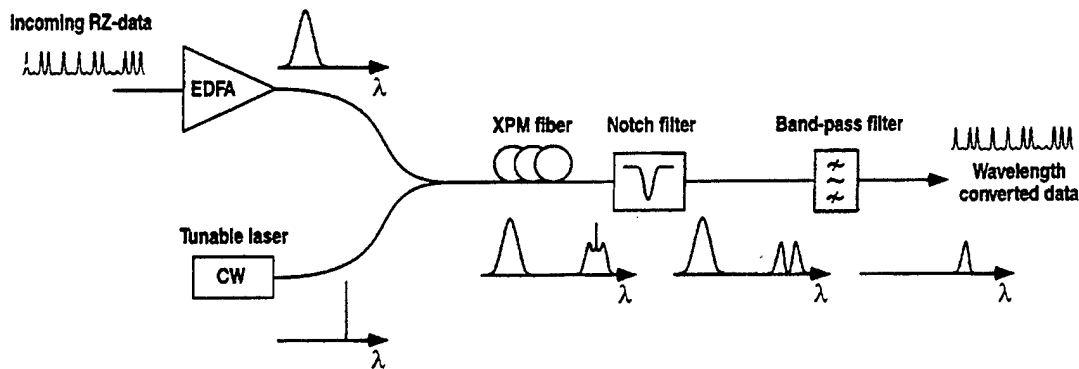
Fig. 8.   Principle of operation of high-speed XPM fiber-based wavelength converter.

(a)

(b)
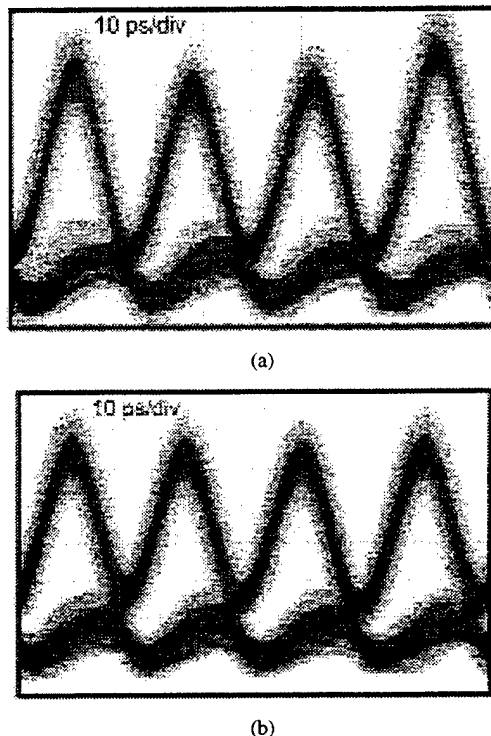
Fig. 9.   (a) Nonlinear transmission characteristic of fiber XPM-WC and (b) 40 Gb/s original and converted eye diagrams.

distance and will help determine the required dynamic range of the burst-mode subcarrier receiver. Therefore, either dispersion compensation or dispersion insensitive detection techniques must be employed.

When the subcarrier signal is detected at a square law photoreceiver the subcarrier amplitude depends upon the phase difference between the two sidebands. When this signal is propagated through a fiber, the dispersion induces a relative time delay between the subcarrier sidebands. Thus the received power P_S has a dependence on the distance traversed in the fiber. For certain values of fiber length L (or ω_s for a fixed fiber length) the received power P_S is null and the signal is cancelled out. In a multihop system where the length of fiber through which the light travels is unknown, this effect will cause label loss.

By suppressing the subcarrier, the sidebands are detected as individual wavelengths carrying the same information and the beat products between each sideband and the optical carrier is no longer detected. Therefore, only the information modulated

on the sidebands is recovered and dispersion induced fading is eliminated. We have successfully employed a fiber loop mirror (FLM) to solve the subcarrier fading problem while at the same time providing a means to simultaneously tap and erase SCM labels [14]. The fiber loop mirror, shown in Fig. 10(a), drops the suppressed carrier signals to the tap port for detection and label recovery. The pass-through port forward the baseband packet with erased label to a wavelength conversion stage. The filter peaks are designed with a period to match the ITU grid. The filter employs two birefringent elements of equal length oriented with principal axis at 45° to one another and a half wave plate with principal axes oriented at 45° with respect to the nearest birefringent element. The use of two birefringent elements of equal length in series produces a wide passband for transmission between the input port and the through port and a narrow passband for transmission between the input port and the OSCM extraction port. The filter can be implemented entirely in fiber using birefringent fiber and polarization controllers or it may be implemented using birefringent crystals. The transmission spectrum of an all-fiber version of the filter fabricated at UCSB is shown in Fig. 10(b) and was measured using a broadband light source and a high-resolution optical spectrum analyzer.

C. Wavelength Agile Sources

Packet wavelength conversion critically depends on the switching speed of a tunable laser used as the local source for the new wavelength. New multi-element widely tunable lasers with the capability of tuning over hundreds of channels represent the current state of the art in semiconductor laser development. There is a wide variety of tunable laser designs and they all have a number of common characteristics. They have active sections for gain integrated with passive waveguide elements that are used for wavelength control, they employ some form of grating architecture for wavelength discrimination, and all use carrier injection for tuning. In this paper we describe three of the most promising candidates to be used as wavelength agile sources—Sampled Grating DBR (SGDBR), Super Structure Grating DBR (SSGDBR) and Grating assisted co-directional Coupler with Sampled Reflector (GCSR). The second part of this section will describe recent advances in the fast switching of a GCSR laser.

1) Wavelength Agile Laser Structures: The Sampled Grating DBR (SGDBR) lasers were the first ones among the mentioned widely tunable laser structures [28]. The SGDBR
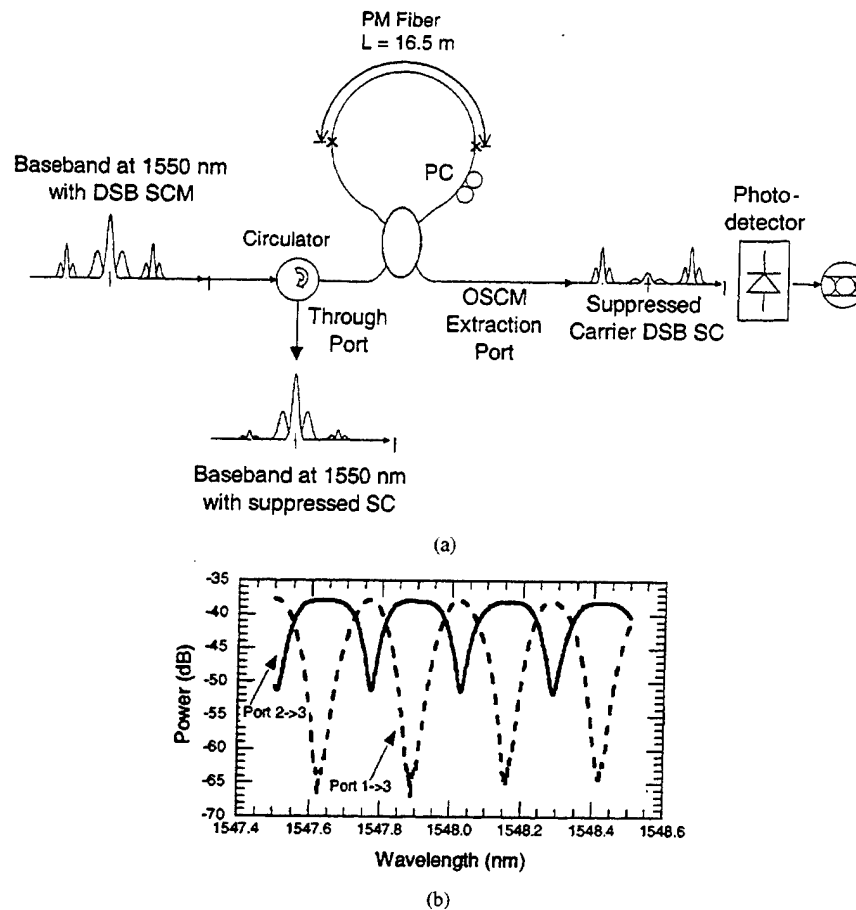
Fig. 10. (a) Schematic of an all-fiber birefringent loop mirror filet (LMF). (b) Transmission spectrum of an all-fiber version of the filter.

is similar in structure to a DBR laser except that it employs a Vernier tuning mechanism to increase its tuning range. The SGDBR uses a pair of grating mirrors at either end of the cavity [Fig. 11(a)]. The gratings in the mirrors are periodically sampled which results in a sequence of equally spaced short grating bursts. These give the mirrors a comb like reflection spectrum with multiple equally spaced peaks. Different sampling periods are used in the front and back mirror to give them different peak spacing. This allows only a single pair of peaks to be aligned concurrently. The laser operates at the wavelength where the peaks from the front and back mirrors are aligned [Fig. 11(b)].

The Super Structure Grating DBR (SSGDBR) is a modification of the SGDBR design and is only different by the design of the mirrors [29], [30]. In the SSGDBR, the grating in the mirrors are periodically chirped instead of sampled. The advantage of this approach is that the grating occupies the entire length of the mirror so that a much higher reflectivity can be achieved with a lower coupling constant in the grating. The other main advantage is that the reflectivity of the individual peaks can be tailored such that all of the reflection peaks have the same magnitude.

The Grating assisted co-directional Coupler with Sampled Reflector (GCSR) [31], [32] device as the name indicated uses a grating assisted co-directional coupler within the laser as a frequency discriminator [Fig. 11(c)]. The wavelength selection is illustrated in Fig. 11(d). The coupler filter is tuned such that one peak of the comb generated by the Sampled

Reflector coincides with the maximum transmission of the coupler. The resulting reflectivity is a main peal surrounded by lower side peaks. The coarse tuning is obtained when only the coupler current is changed. The lasing wavelength is tuned in large steps corresponding to the reflector peak separation. Depending on the device the tuning range extends between 50 and 114 nm. The medium tuning occurs when both coupler and reflector are tuned at the same rate such as the same peak is selected all the time. The medium tuning range is between 5 and 15 nm, similar to the tuning range of a DBR laser. The fine tuning occurs when the phase current is changed. The lasing wavelength is tuned continuously over a cavity mode spacing. By combining the three types of tuning it is possible to obtain a truly continuous tuning,where any wavelength can be achieved.

2) Fast Switching Wavelength Agile Transmitters: By using proper driving circuitry and conditions it is possible to obtain fast (on the order of several nanoseconds) switching between ITU grid lasing modes over a broad range of wavelengths. We have demonstrated fast switching of the GCSR laser under digital control. Two arrays of HBT-based laser drivers were used to obtain different levels of output current that were used to drive coupler and reflector tuning sections, thus making it possible to achieve different lasing wavelengths. Schematic of this setup is shown in Fig. 12(a). If n laser drivers are used for both coupler and reflector sections, 2×2^n different channels may be accessed. Fig. 12(b) shows measured switching time for 36 chan-
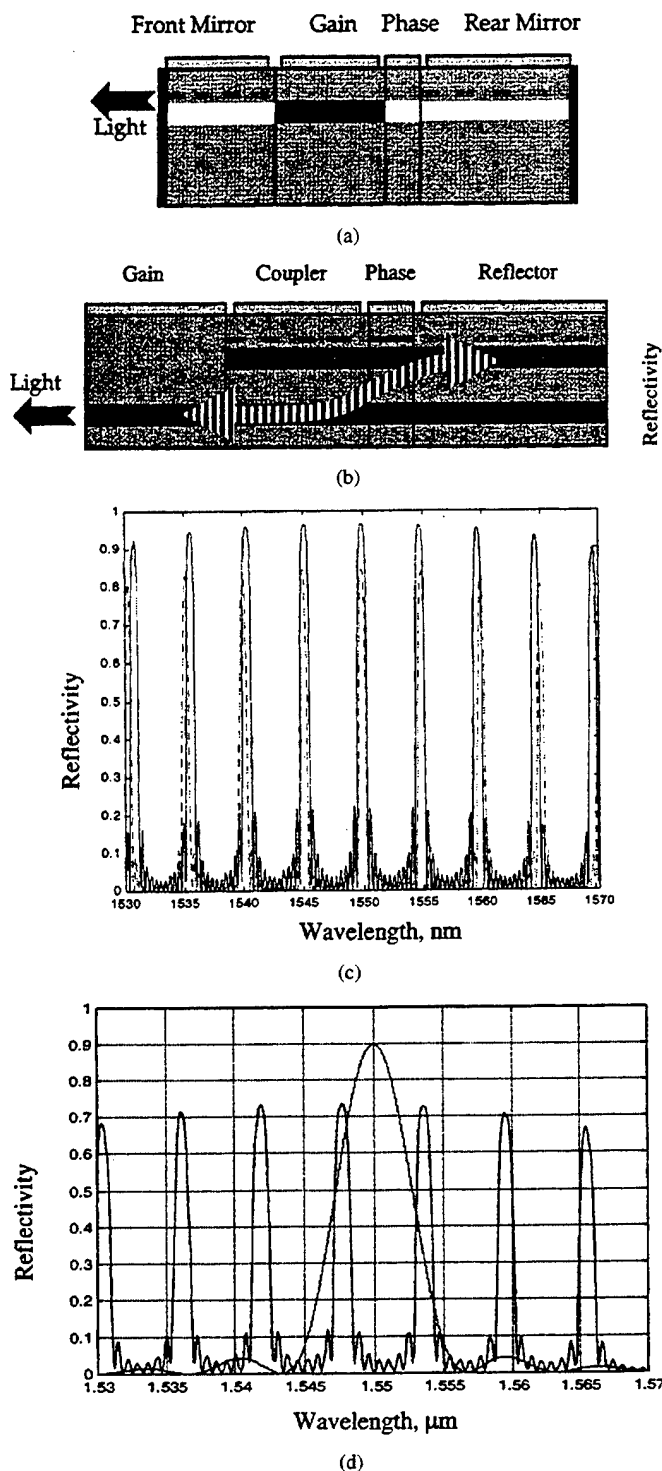
Fig. 11. SGDBR laser structure.

Fig. 12. (a) Schematic of fast switching using a GCSR laser and (b) measured switching times for 36 ITU frequency channels.

nels located on the ITU frequency grid. The longest switching time is less than 4.5 ns.

D. Electroabsorption Modulators for 40 Gb/s Packet Detection

High-speed demultiplexing is one of the key technology in high bit rate time-division-multiplexed transmission systems. Demultiplexing based on high-speed integrated circuit technology has been demonstrated at 60 Gb/s [33]; however, it has been limited to 40 Gb/s in fiber transmission experiments. On the other hand, optical demultiplexing using a sinusoidally driven electroabsorption modulator (EAM) has emerged as a simple alternative approach to electrical demultiplexing [34], with demonstrations at bit rates up to 160 Gb/s [35]. Due to its nonlinear attenuation characteristic, a highly reverse biased EA modulator is capable of producing a short switching window with high extinction ratio for selecting the desired channel from the incoming data stream.

Optical demultiplexing based on EAMs fabricated at UCSB was recently deployed in the 40 Gb/s wavelength routing experiment [8]. The 400-μm long EA modulator is based on a traveling-wave electrode structure with ten periods of strain-compensated InGaAsP quantum wells fabricated by MOCVD on semi-insulating InP substrate [36], as shown in Fig. 13. The device achieved a maximum extinction of 38 dB while its modulation bandwidth was 16 GHz. The 400-mm EA modulator was reverse biased at −4.8 V and driven by a 6 V_{PP} 10 GHz RF signal to generate a 14-ps switching window, which was synchronized to the desired 40 Gb/s optical channel by an electrical delay line. The demultiplexed optical channel was then optically amplified and detected by a 10-GHz receiver.
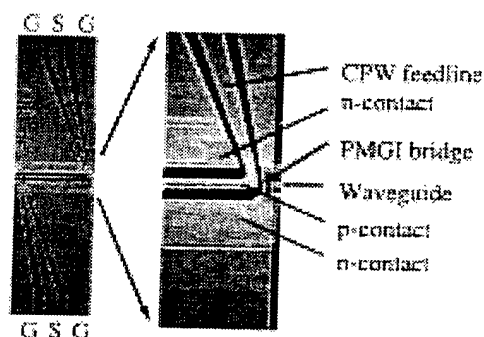
Fig. 13. High frequency EAM used for 40 Gb/s optical demultiplexing and (a) 40 Gb/s input and (b)–(e) demultiplexed outputs.
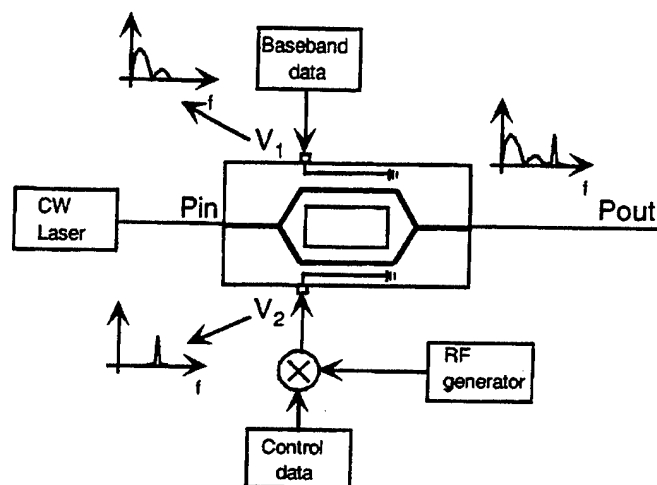
Fig. 14. Optical subcarrier multiplexed transmitter based on differential external modulator.

E. Packet Transmitters

Generation of packets requires compatible coding of the payload and label with the label swapping hardware within the network. In this section we describe transmitters that can generate packets with subcarrier or serial labels.

1) OSCM Transmitters: The ideal OSCM transmitter is one that is simple, robust, permits an arbitrary subcarrier to carrier modulation ratio, and does not introduce penalty into either the baseband data or the subcarrier signal. It is also desirable that the introduction of chirp in the baseband and subcarrier signals be avoided or controlled. In this section we describe two techniques for the generation of hybrid baseband and optically subcarrier multiplexed signals that have been employed at UCSB.

The first technique is the simplest to implement and most robust. In this technique a differential Mach–Zehnder external modulator is used to impress both the baseband data and the subcarrier signal onto the optical carrier simultaneously. Details of the tradeoffs for this type of transmitter are given in [11]. A schematic diagram of this transmitter is shown in Fig. 14. Only a single Mach–Zehnder modulator is employed to impress both the subcarrier signal as well as the baseband data onto the optical carrier. One port of the Mach–Zehnder is driven with the baseband signal and the other port receives the subcarrier signal. The second transmitter architecture that has been employed at

UCSB overcomes some of the disadvantages of the differentially driven Mach–Zehnder transmitter [14]. This design had, however, increased complexity and requires stability issues to be addressed. A schematic diagram of this transmitter is shown in Fig. 15(a). In this transmitter the baseband data and the subcarrier signal are impressed on the same optical carrier independently using two separate external modulators. The separate signals are then combined using an optical multiplexer. Because the signals are generated separately they can be optimized independently and their relative amplitudes controlled using optical attenuation prior to the multiplexer. In order to avoid coherent interference between the signals, filtering must be employed to remove the carrier from one of the signals. In addition, the subcarrier signal must be out-of-band relative to the baseband data signal or filtering of the baseband signal to remove spectral content of at the subcarrier frequency must be done. In our method both the multiplexing and the required filtering is achieved using a birefringent loop mirror filter shown in Fig. 15(b).

The principal advantage of this transmitter is that the strength of the subcarrier signal relative to the baseband signal may be easily controlled and that there is no subcarrier amplitude dependent penalty introduced in the baseband data. In addition, both the chirp of the subcarrier signal and the baseband data signal may be controlled independently. The primary disadvantage of this technique is that the filter spectral response must be stable relative to the laser wavelength necessitating tight temperature control of the birefringent elements in the filter or some type of closed loop locking arrangement.

2) Time Multiplexed Transmitters: For low bit rate transmitters, 10 Gb/s and below, the label and the payload will probably have the same data format and the whole packet can be encoded using conventional modulation techniques for either NRZ or RZ data format. For high bit rate transmitters, beyond 40 Gb/s, it will most likely be necessary to use OTDM transmitters where several low bit rate data streams are time multiplexed together. The label is attached to the packet, at a lower bit rate to allow lower cost label processing electronics to be used. Fig. 16 shows a possible implementation of such transmitter generating a 40 Gb/s IP-packet with a 2.5 Gb/s attached time domain label. The incoming low bit rate IP packet is demultiplexed and.stored in an electronic $4 \times N$ memory bank that effectively acts as a serial to parallel converter. This memory bank can be made of fast electronic memory arranged in a way that it is possible fill the memory at the incoming bit rate and to read the four memory banks in parallel. Once the whole packet is stored, the four rows are read in parallel at 10 Gb/s. Since in practice electronic memory can not be read at 10 GHz, multiple memory banks operating at the speed of the memory have to be multiplexed together constituting a memory read at 10 GHz. Each 10 Gb/s electrical channel subsequently drives an optical RZ transmitter the gives 10 Gb/s RZ data with about 10 ps pulses, e.g., an integrated transmitter consisting of a DFB laser with two integrated EAMs. The relative timing between the 10 Gb/s channels are adjusted to be 25 ps between each channel by using optical delays. Finally the four channels are interleaved in a fiber coupler to generate a 40 Gb/s data sequence. The label is generated simply by encoding the label data at 2.5 Gb/s NRZ on light with the same wavelength as the RZ sources and then attached to the

(a)

(a)
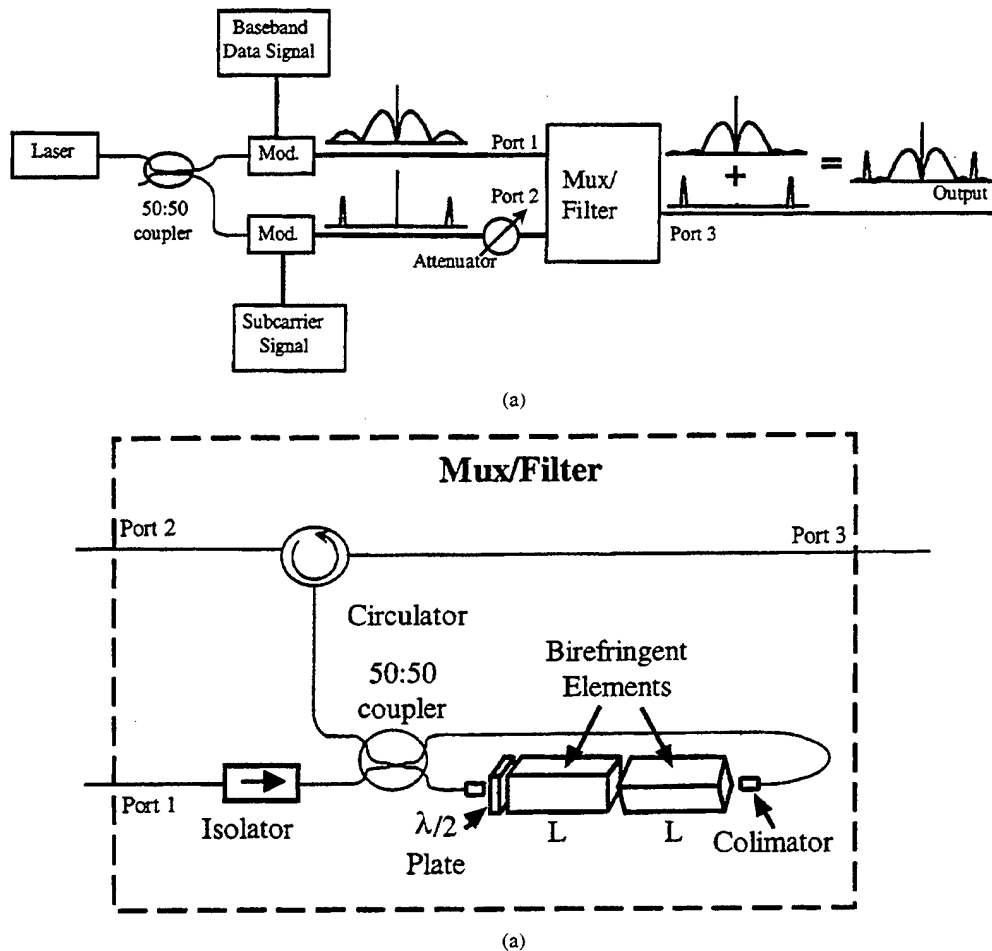
Fig. 15. Optically multiplexed SCM transmitter.
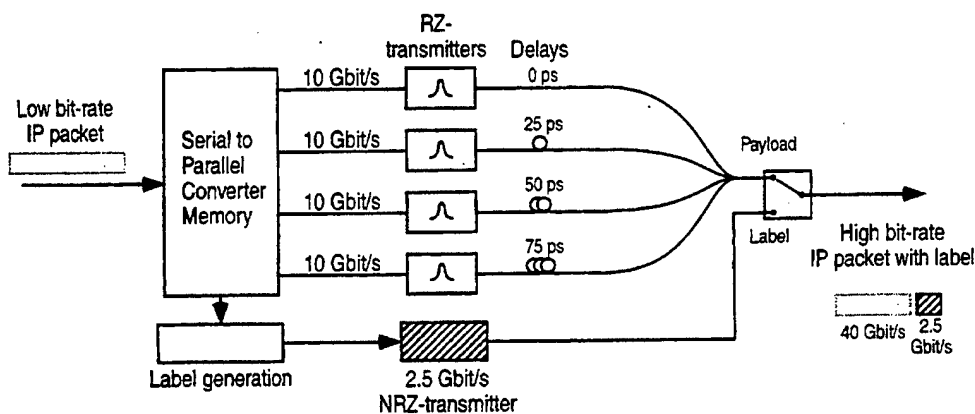
Fig. 16. Implementation of a high-speed packet serial label transmitter.

40 Gb/s packet after proper adjustment of the relative timing. Since all optical sources emit light at the same wavelength, it is in practice difficult to achieve the extinction ratio (ER) required from the sources when being in off-state. Therefore an optical switch is used at the output to avoid coherent crosstalk between the label source and the RZ data, This scheme can be extended to higher bit rates simply by increasing the number of rows in the serial to parallel converting memory and by decreasing the output pulse width from the RZ transmitters. The RZ transmitters can either be four individual transmitters constituted by DFB lasers with integrated electroabsorption modulators, or, if very short pulses are required, one common pulse source, e.g., a fiber ring laser, can be shared by four different data encoding modulators.

VII. AOLS SUBSYSTEM IMPLEMENTATIONS

In this section we review subsystems that realize the functions described in Fig. 4 using the technologies in the previous section.
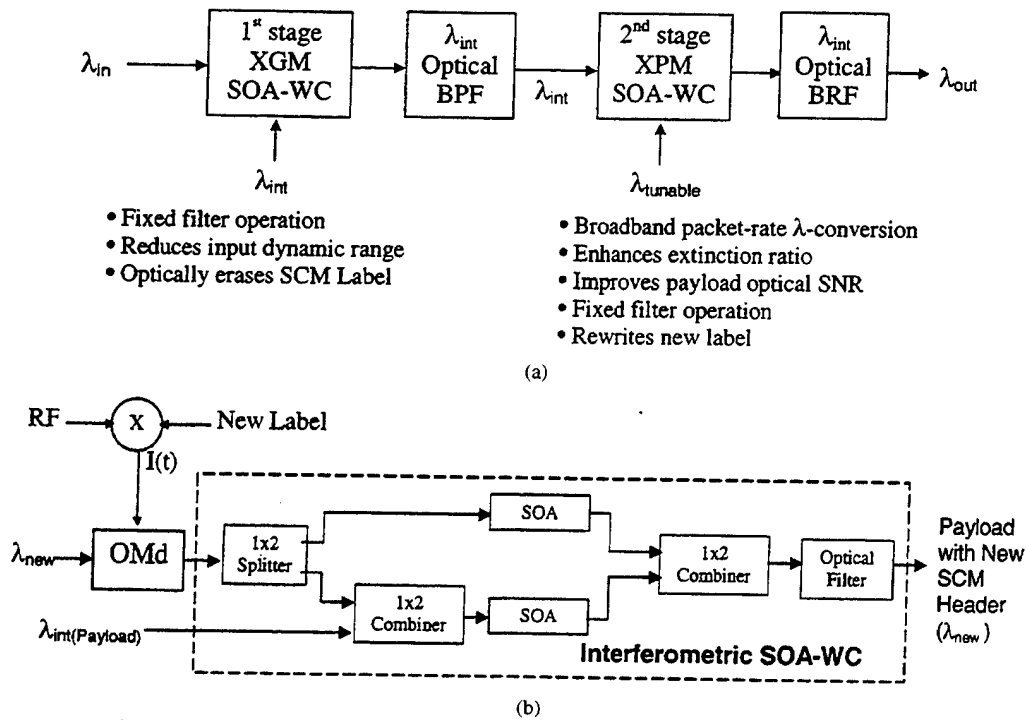
Fig. 17.   (a) Two-stage AOLS wavelength converter using cascaded SOA XGM and XPM modules and (b) second stage XPM-WC.

A. Two-Stage SOA Wavelength Converters with Subcarrier Labels

We have implemented and demonstrated an AOLS wavelength converter using a two-stage SOA wavelength converter module [37], [38] shown in Fig. 17(a). The two-stage geometry is designed to address key issues in wavelength conversion and optical label swapping. The XGM-WC stage erases the SCM header using the inherent low-pass filtering function of XGM wavelength conversion in SOAs, as described in [38]. It is also used to convert packets from an arbitrary network wavelength to a fixed internal wavelength allowing the use of fixed optical band pass filters (BPF) to pass only the internal wavelength and reject the original wavelength. Another key benefit of the two-stage geometry is that the first stage converts an arbitrary polarization at the input to a fixed polarization at the output for the second stage converter, making it easier to fabricate the XPM-WC technology. The first stage also reduces the packet optical power dynamic range and sets the packet average optical power level for the XPM-WC. The inverting operation of the XPM-WC is used in the.second stage, as shown in Fig. 17(b) to provide noninverting operation after both stages. The highly nonlinear transfer function of the interferometric wavelength converter in the second stage is used to enhance the optical extinction ratio (2R regeneration) and convert the packet to an outgoing wavelength with a fixed band reject filter (BRF) that passes only the new tunable wavelengths. A fast wavelength tunable laser is utilized to enable packet-rate wavelength conversion. The new label is pre-modulated onto the fast tunable laser. As part of our NGI program we are leveraging recent developments in the field of photonic integrated circuits (PICs) to realize two-stage AOLS technology through integration of fast widely tunable lasers with SOAs, waveguides and on-chip wavelength monitors.

B. Fiber Loop Mirrors with Subcarrier Labels and Two-Stage SOA-WC

The fiber loop mirror (FLM) module provides label removal and a tap for SCM labels that is immune to fiber dispersion and utilizes a simple detector for label recovery. The packet without label is passed to the through port and may be injected into a two-stage AOLS-WC based on SOA technology as shown in Fig. 18. This architecture combines very high suppression of the original label over the complete ITU grid with the wavelength conversion and label rewriting properties of the integrated two-stage wavelength converters.

C. Fiber Wavelength Converters and Serial Labels

Optical label swapping of an attached time domain label to a packet can be implemented using the inherent nonlinear transfer function and differentiating nature of fiber XPM wavelength converter. The transmission function of the wavelength converter is highly nonlinear, which also depends on the derivative of the input signal. By using different data formats, bit rates, and power levels for the label and the payload, while keeping the energy per bit constant, it is possible to remove the label upon wavelength conversion.

A particular scheme that has been investigated is where the payload is in RZ format and the header is in NRZ format. This allows efficient use of bandwidth for the payload while retaining simplicity in handling the labels. If, for example, 10 ps pulses are used for a 40 Gb/s payload and 2.5 Gb/s NRZ data and if equal energy per received bit is assumed, the peak power of the labels will be 16 dB lower than the peak power of the payload. Thus the transmission through the wavelength converter will be extremely low. In addition the transmission through the wavelength converter depends on the derivative of the input
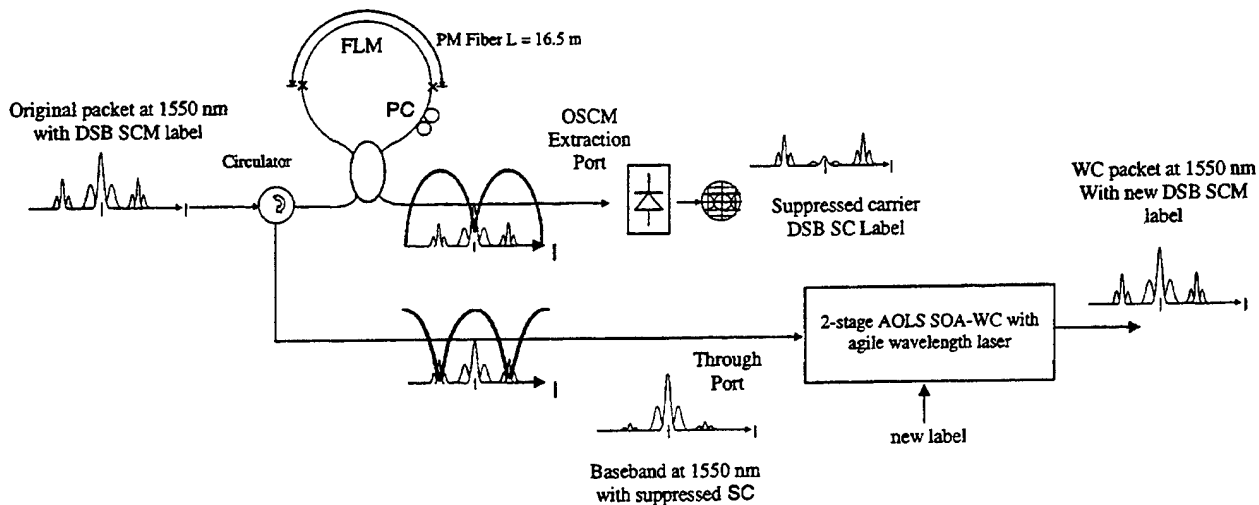
Fig. 18. AOLS module using FLM to remove SCM label and two-stage AOLS-WC to convert packet and rewrite label.
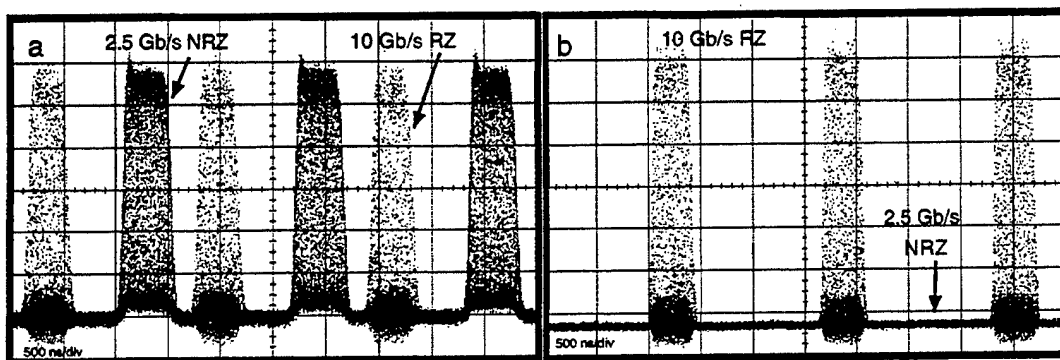
Fig. 19. Packets of 2.5 Gb/s NRZ data and 10 Gb/s RZ data (a) before and (b) after wavelength conversion.

signal, why only transitions in the NRZ data will experience some transmission. All energy in the input data with zero derivative will be blocked in the wavelength converter, i.e. most energy in NRZ data will not drive the wavelength converter. After removing the incoming label a new label can easily be inserted either by adding a new label from a separate source after the wavelength converter or simply by premodulating the new label on the CW light that determines the output wavelength.

To demonstrate the concept of label replacement, a system similar to that in Fig. 8 was used. Packets of 10 Gb/s RZ data was mixed with 2.5 Gb/s NRZ as shown in Fig. 19(a). The frequency deviation that generates the optical side bands of the CW light will depend on the derivative of the input pulse power, which is turned into amplitude modulation after filtering. Due to this differentiating nature, the rise and fall times determine the conversion efficiency, which means that the wavelength converter will block low frequencies. In Fig. 19(b) it can clearly be seen how the 10 Gb/s RZ data is converted and the 2.5 Gb/s NRZ data is suppressed. It should be noted that NRZ data can not be converted, as only the edges of a signal are converted. In a sequence of consecutive ONEs, only the first ONE would generate an output signal. However, there would still be some output that could cause crosstalk when a new header is inserted, even though the old header data has been corrupted. For RZ data, the pulse width, and not the bit rate will determine the conversion ef-

ficiency. In another experiment, the 10 Gb/s RZ data and the 2.5 Gb/s NRZ data were switched manually, to measure the optical spectra, and to measure the penalty for rewriting new 2.5 Gb/s data where the original data was erased. At the input to the wavelength converter, the average power of the NRZ and the RZ data were equal and after removal of the original NRZ data a new 2.5 Gb/s NRZ data was inserted. The bit-error rate was measured for the original and rewritten data using $2^{31} - 1$ pseudo-random data and no penalty was observed due to the original data in the rewritten 2.5 Gb/s NRZ data. From the measurements it is clear that this type of wavelength converter can be used to passively erase a 2.5 Gb/s NRZ header from a high-speed RZ payload. Compared to other approaches using time-domain header [8], [39], no timing control is required to erase the header. New 2.5 Gb/s data can then be rewritten in different ways. Here a separate transmitter was used for the new data, which showed now crosstalk penalty from the previously erased data. This makes the system more stable compared to the approach of premodulating and slightly detuning the local CW light in the wavelength converter, but requires a high extinction ratio of the new header source when the payload is present. A third option, which has not been experimentally investigated, is to encode the new header by frequency modulating the local CW laser in the wavelength converter. With the present tuning speed of about 5 ns this would limit the bit rate to a maximum of 100 Mbit/s, but with
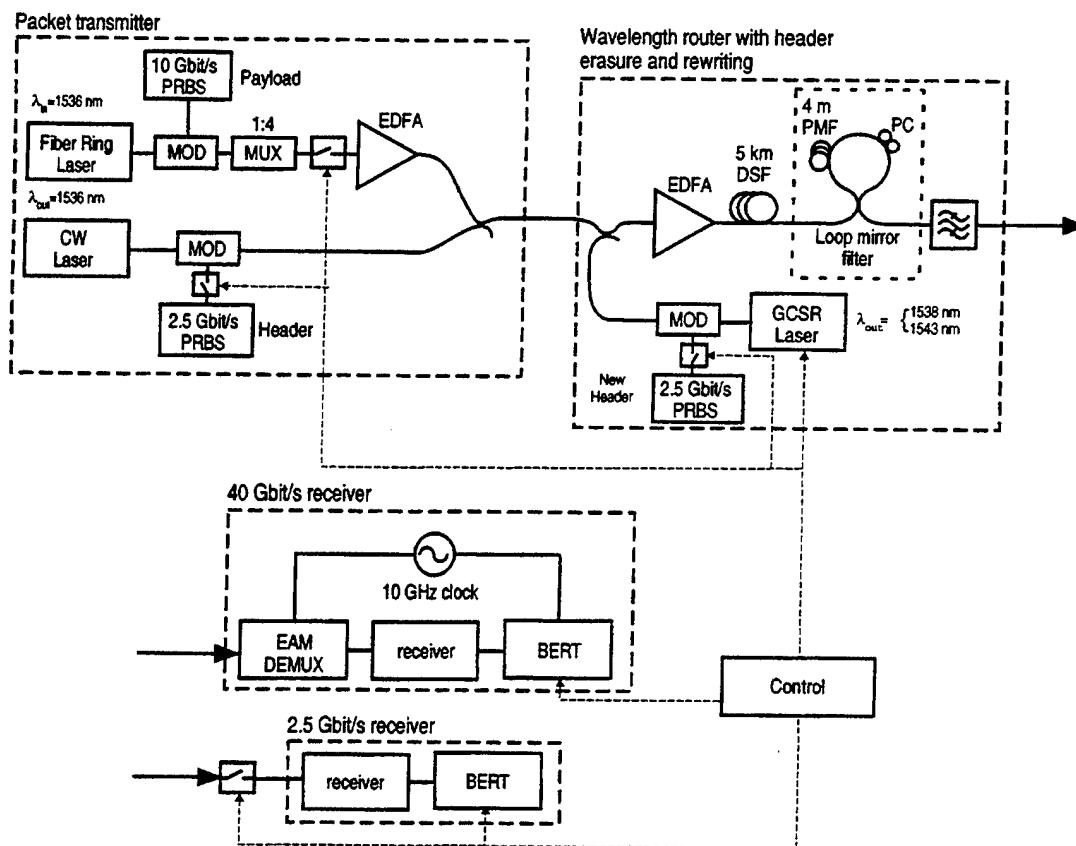
Fig. 20. Experimental setup of the packet routing experiment. MOD: LiNbO3 modulator; MUX: Passive 10–40 Gb/s multiplexer; EDFA: Erbium-doped fiber amplifier; DSF: Dispersion shifted fiber; PMF: Polarization-maintaining fiber; PC: Polarization controller; GCSR: Grating coupled sampled rear reflector laser; EAM DEMUX: Demultiplexer using an electro-absorption modulator; BERT: Bit-error-rate test set.

further advances in tunable laser technology this could be an interesting option.

VIII. EXPERIMENTAL DEMONSTRATIONS

A. *40 Gb/s AOLS Using Fiber XPM Wavelength Converter*

To demonstrate AOLS at high bit rates an experiment was performed where packets of 40 Gb/s data was routed to different wavelengths using a wavelength converter. The 40 Gb/s payload was in RZ format and an attached time domain label was encoded using NRZ at 2.5 Gb/s. By using a fast tunable laser each packet can be routed to different wavelengths. The attached label is also replaced upon wavelength conversion by using the technique described in Section VII-C above.

Fig. 20 shows the experimental set-up. The packet generator consisted of an actively mode-locked fiber ring laser generating 10 ps at 1536 nm followed by a LiNbO3 modulator encoding 10 Gb/s data. The 10 Gb/s data were injected into a passive 10 to 40 Gb/s multiplexer and an acousto-optical modulator (AOM) gated out a 2.5 μs payload that was combined with a 2.5 Gb/s 500 ns long label. The label was aligned in front of the payload with 100 ns guard band determined by the 100 ns rise time in the AOM. A 100 ns guard band was inserted between each packet, giving a total packet length of 3.2 μs. The packets were then injected into the wavelength converter which consisted of an erbium-doped fiber amplifier (EDFA) followed by 5 km dispersion-shifted fiber (DSF) with a zero-dispersion wavelength
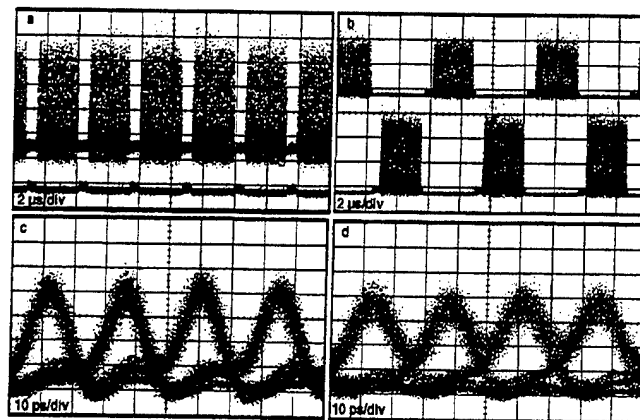
Fig. 21. (a) Packets and (c) 40 Gb/s eye-patterns before wavelength routing. (b) Packets routed to 1538 nm and 1543 nm and (d) eye pattern of routed packet at 1543 nm.

of 1542 nm. A fast tunable laser [31] that could be tuned to either 1538 or 1543 nm within 5 ns, determined the new wavelength. This laser was also used to encode the new 2.5 Gb/s label before entering the wavelength converter. After the DSF, a loop mirror filter was used to suppress the original CW light. A second filter was used to select one of the two sidebands and to suppress the original data. The use of only one sideband retained the pulse width and time bandwidth product (TBP) from the input pulse. The 40 Gb/s receiver consisted of a 40 Gb/s to 10 Gb/s demultiplexer followed by a 10 Gb/s preamplified
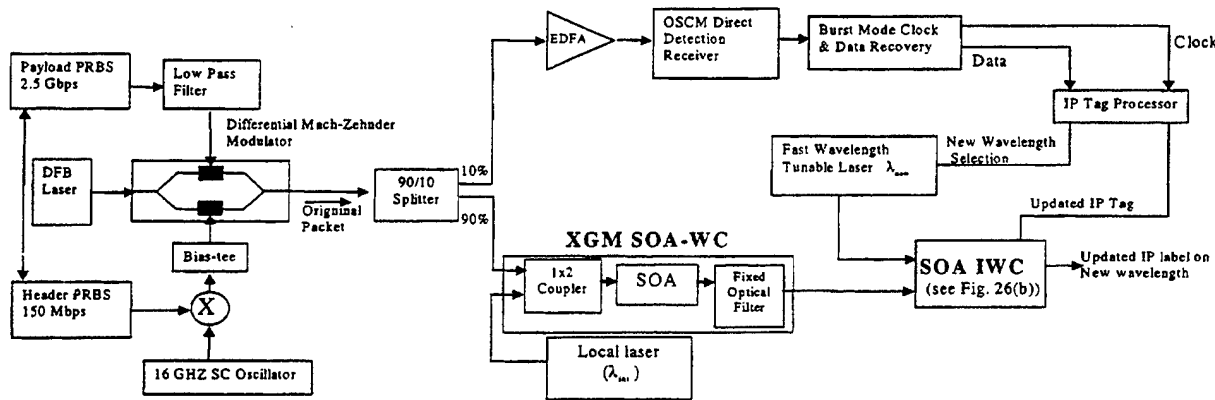
Fig. 22.   Subcarrier multiplexed AOL experiment with two-stage SOA-based label swapping and wavelength conversion.

receiver. The 2.5 Gb/s label receiver consisted of an AOM to remove the payload, which otherwise would dominate the measured optical average power, followed by an optically preamplified receiver. The BER measurements were made on both payload and label, and gated to select appropriate time interval. Fig. 21(a) shows the input packets consisting of the 40 Gb/s RZ payload and the 2.5 Gb/s NRZ label with about 10 dB less peak power. In the lower trace the labels without the payload is reported. Fig. 21(b) shows every other packet routed to 1538 nm and 1543 nm with new inserted labels. The eye patterns shown in Fig. 21(c) and (d) was taken by zooming into the payload, before (1536 nm) and after wavelength converter (1543 nm). BER measurements were performed on both label and payload on incoming and outgoing packets and less than 4 dB penalty at a $BER = 10^{-9}$ was observed for all routed packets. The power penalty at a $BER = 10^{-9}$ for the replaced labels was less than 2.5 dB. For wavelength routing at 10 Gb/s, the penalty was less than 1 dB for the payload, which indicates that a major part of the penalty is due to instabilities in the 40 Gb/s data.

B. 2.5 Gb/s AOLS Using Two-Stage SOA Wavelength Converters

The WDM AOLS experiment that utilized a two–stage wavelength converter is shown in Fig. 22 [3], [4]. An OSCM packet transmitter was used to generate a 150 Mbps label on an RZ coded, ASK modulated 16 GHz subcarrier. Labels consist of a 16-bit preamble, an 84-bit tag and a 4-bit framing sequence. The payload is an NRZ coded, 2.5 Gb/s PRBS and the 16 GHz subcarrier supports payload bit rates out to 10 Gb/s. The packet duration is 1 ms. Label clock and data are recovered on a packet-by-packet basis following a 10% fiber tap, an EDFA and an OSCM direct-detection receiver. The OSCM receiver utilizes a fast Schottky barrier diode for envelope detection. A SAW filter is used to recover the tag clock for each packet and a fixed digital delay is needed to realign data and clock. A tag switching processor is required to perform serial-to-parallel conversion, compute a new label, multiplex the new label onto a RF subcarrier and set a fast wavelength tunable laser to the new wavelength within 12 ns.

A two-stage modified XGM/IWC was used to perform wavelength routing, optical label erasure and label rewriting at the

IP packet rate. The OSCM label was removed during XGM due to the low pass frequency response of wavelength conversion in an SOA [38]. The XGM-WC converts incoming WDM packets to a fixed internal wavelength λ_{int} that is passed to the next stage using a fixed frequency optical filter. The XGM-WC is also used to set a stable operating point for the IWC. One arm of an InGaAsP IWC is injected with the optically filtered output of the XGM-WC. The output of a rapidly tunable 4-section GCSR laser transmitter is injected to both arms of the IWC. We measured the transmission BER for the label-switched payload with an observed maximum 4 dB power penalty for all four wavelengths. The power penalty is expected to decrease when optimally designed wavelength converters are used.

IX. SUMMARY

We have presented research results of the UCSB NGI project in AOLS. The AOLS approach to wire-rate packet encapsulation, routing and forwarding directly in the optical layer hold promise to support terabit-per-second fiber capacities independent of packet bit-rate and protocol. Two primary optical label coding techniques, serial- and subcarrier multiplexed-labels, were described and the functional blocks used to erase labels, rewrite labels, and convert packets to a new wavelength were reviewed. Issues involving burst-mode packet routing in an AOLS environment were discussed. Results were presented for both fiber and semiconductor-based technologies that have been used to perform AOLS functions. Key approaches to transmitting and processing subcarrier labels were described based on fiber loop mirrors used to realize supressed carrier, subcarrier label detectors that are immune to fiber dispersion induced signal fading. These taps can also be used to erase subcarrier labels in conjunction with semiconductor optical amplifer-based wavelength converters used to rewrite the labels and convert the packets to a new wavelength. Current work on highly integrated SOA-based AOLS modules was also described. For high bit-rates, new AOLS all-fiber wavelength converter subsystems were used to erase and rewrite 2.5 Gb/s serial encoded labels and wavelenth convert 40 Gb/s packets. We discussed how these technologies could be combined to realize AOLS subsystems. Key experimental system demonstration results were also presented.

REFERENCES

[1] A. Viswanathan, N. Feldman, Z. Wang, and R. Callon, "Evolution of multiprotocol label switching," *IEEE Commun. Mag.*, vol. 36, pp. 165–173, May 1998.

[2] A. Carena, M. D. Vaughn, R. Gaudino, M. Shell, and D. J. Blumenthal, "OPERA: An optical packet experimental routing architecture with label swapping capability," *J. Lightwave Technol.*, vol. 16, Dec. 1998. Special Issue on Photonic Packet Switching.

[3] D. J. Blumenthal, A. Carena, L. Rau, V. Curri, and S. Humphries, "All-optical label swapping with wavelength conversion for WDM-IP networks with subcarrier multiplexed addressing," *IEEE Photon. Technol. Lett.*, vol. 11, Nov. 1999.

[4] ——, "WDM optical IP tag switching with packet-rate wavelength conversion and subcarrier multiplexed addressing," presented at the Optical Fiber Communications/International Conference on Integrated Optics and Optical Fiber Communication'99, San Diego, CA, Feb. 21–26, 1999. Paper ThM1.

[5] D. Awduche, Y. Rekhter, J. Drake, and R. Coltun, "Multi-Protocol Lambda Switching: Combining MPLS Traffic Engineering Control with Optical Crossconnects,", 2001. Internet Draft, Work in Progress.

[6] P. Toliver, K.-L. Deng, I. Glesk, and P. R. Prucnal, "Simultaneous optical compression and decompression of 100-Gb/s OTDM packets using a single bidirectional optical delay line lattice," *IEEE Photon. Technol. Lett.*, vol. 11, pp. 1183–1185, Sept. 1999.

[7] C. Guillemot, M. Renaud, P. Gambini, C. Janz, I. Andonovic, R. Bauknecht, B. Bostica, M. Burzio, F. Callegati, M. Casoni, D. Chiaroni, F. Clerot, S. L. Danielsen, F. Dorgeuille, A. Dupas, A. Franzen, P. B. Hansen, D. K. Hunter, A. Kloch, R. Krahenbuhl, B. Lavigne, A. Le Corre, C. Raffaelli, M. Schilling, J.-C. Simon, and L. Zucchelli, "Transparent optical packet switching: The european ACTS KEOPS project approach," *J. Lightwave Technol.*, vol. 16, pp. 2117–2134, Dec. 1998.

[8] B. E. Olsson, P. Öhlén, L. Rau, G. Rossi, O. Jerphagnon, R. Doshi, D. S. Humphries, D. J. Blumenthal, V. Kaman, and J. E. Bowers, "Wavelength routing of 40 Gbit/s packets with 2.5 Gbit/s header erasure/rewriting sing all-fiber wavelength converter," *Electron. Lett.*, vol. 31, no. 4, pp. 345–347, Feb. 2000.

[9] P. Gambini, M. Renaud, C. Guillemot, F. Callegati, I. Andonovic, B. Bostica, D. Chiaroni, G. Corazza, S. L. Danielsen, P. Gravey, P. B. Hansen, M. Henry, C. Janz, A. Kloch, R. Krahenbuhl, C. Raffaelli, M. Schilling, A. Talneau, and L. Zucchelli, "Transparent optical packet switching: Network architecture and demonstrators in the KEOPS project," *IEEE J. Select. Areas Commun.*, vol. 16, pp. 1245–1259, Sept. 1998.

[10] A. Budman *et al.*, "Multigigabit optical packet switch for self-routing networks with subcarrier addressing," in *Optical Fiber Communications Conf. '92*, San Jose, CA, Feb. 4–7, 1992, pp. 90–91.

[11] D. J. Blumenthal, P. R. Prucnal, and J. R. Sauer, "Photonic packet switches: Architectures and experimental implementations," *Proc. IEEE*, vol. 82, no. 11, pp. 1650–1667, Nov. 1994. Invited Paper.

[12] R. Gaudino and D. J. Blumenthal, "A novel transmitter architecture for combined baseband data and subcarrier-multiplexed control links using differential Mach-Zehnder external modulators," *IEEE Photon. Technol. Lett.*, vol. 9, pp. 1397–1399, Oct. 1997.

[13] D. J. Blumenthal, J. Laskar, R. Gaudino, S. Han, M. Shell, and M. D. Vaughn, "Fiber optic links supporting baseband data and subcarrier-multiplexed control channels and the impact of MMIC photonic/microwave interfaces," *IEEE JLT/MTT Joint Special Issue on Microwave Photonics II, Trans. Microwave Theory Tech.*, vol. 45, pp. 1443–1452, Aug. 8, 1997.

[14] T. Dimmick, R. Doshi, R. Rajaduray, and D. Blumenthal, "Optically multiplexed transmitter for hybrid baseband and subcarrier multiplexed signals," presented at the Eur. Conf. Optical Communications'00, 2000.

[15] D. K. Hunter, M. C. Chia, and I. Andonovic, "Buffering in optical packet switches," *J. Lightwave Technol.*, vol. 16, pp. 2081–2094, Dec. 1998.

[16] Y. Ota and R. G. Swartz, "Burst mode compatible optical receiver with a large dynamic range," *J. Lightwave Technol.*, vol. 8, pp. 1897–1903, Dec. 1990.

[17] B. Sartorius, C. Bornholdt, O. Brox, H. J. Ehrke, D. Hoffmann, R. Ludwig, and M. Mohrle, "Bit-rate flexible all-optical clock recovery," presented at the Optical Fiber Communications Conference/International Conference on Integrated Optics and Optical Fiber Communication'99, San Diego, CA, Feb. 21–26, 1999. Paper FB1.

[18] D. Chiaroni, B. Lavigne, A. Jourdan, L. Hamon, C. Janz, and M. Renaud, "New 10 Gbit/s 3R NRZ optical regenerative interface based on semiconductor optical amplifiers for all-optical networks," in *Int. Conf. Integrated Optics and Optical Fiber Communication—Eur. Conf. Optical Communications'97*, vol. 5, Sept. 22–25, 1997, pp. 41–45.

[19] T. Durhuus, B. Mikkelsen, C. Joergensen, S. L. Danielsen, and K. E. Stubkjaer, "All-optical wavelength conversion by semiconductor optical amplifiers," *J. Lightwave Technol.*, vol. 14, pp. 942–954, June 1996.

[20] S. J. B. Yoo, "Wavelength conversion technologies for WDM network applications," *J. Lightwave Technol.*, vol. 14, pp. 955–966, June 1996.

[21] D. Wolfson and K. E. Stubkjaer, "Bit error rate assessment of 20 Gbit/s all-optical wavelength conversion for co- and counter-directional coupling scheme," *Electron. Lett.*, vol. 34, no. 23, pp. 2259–2261, Nov. 1998.

[22] C. D. Poole, R. W. Tkach, A. R. Chraplyvy, and D. A. Fishman, "Fading in lightwave systems due to polarization-mode dispersion," *IEEE Photon. Technol. Lett.*, vol. 3, pp. 68–70, Jan. 1991.

[23] B. E. Olsson, P. Öhlén, L. Rau, and D. J. Blumenthal, "A simple and robust 40 Gbit/s wavelength converter using fiber cross-phase modulation and optical filtering," *IEEE Photon. Technol. Lett.*, vol. 12, pp. 846–848, July 2000.

[24] B. E. Olsson and P. A. Andrekson, "Polarization independent all-optical AND-gate using randomly birefirngent fiber in a nonlinear optical loop mirror," in *Proc. Optical Fiber Comm. Conf.*, vol. 2, 1998, pp. 375–376.

[25] Y. Liang, J. W. Lou, J. K. Andersen, J. C. Stocker, O. Boyraz, M. N. Islam, and D. A. Nolan, "Polarization-insensitive nonlinear optical loop mirror demultiplexing with twisted fiber," *Opt. Lett.*, vol. 24, pp. 726–728, 1999.

[26] O. A. Lavrova, G. Rossi, and D. J. Blumenthal, "Rapid frequency tunable transmitter with large number of channels accessible in less than 5 ns," presented at the Eur. Conf. Optical Communications'00, 2000. Paper 6.3.5.

[27] P. V. Mamyshev, "All-optical data regeneration based on self-phase modulation effect," in *Eur. Conf. Optical Communications'98*, vol. 24, Madrid, Spain, 1998, pp. 475–476.

[28] B. Mason, S.-L. Lee, M. E. Heimbuch, and L. A. Coldren, "Directly modulated sampled grating DBR lasers for long-haul WDM communication systems," *IEEE Photon. Technol. Lett.*, vol. 9, pp. 377–379, Mar. 1997.

[29] H. Ishii, H. Tanobe, F. Kano, Y. Tohmori, Y. Kondo, and Y. Yoshikuni, "Broad-range wavelength coverage (62.4 nm) with superstructure-grating DBR laser," *Electron. Lett.*, vol. 32, no. 5, pp. 454–455, Feb. 1996.

[30] M. Öberg, P.-J. Rigole, S. Nilsson, T. Klinga, P. Backbom, K. Streubel, J. Wallin, and T. Kjellberg, "Complete single mode coverage over 40 nm with a super structure grating DBR laser," *J. Lightwave Technol.*, vol. 13, pp. 1892–1898, Oct. 1995.

[31] M. Öberg, S. Nilsson, K. Streubel, J. Wallin, L. Backbom, and T. Klinga, "74 nm wavelength tuning range of an InGaAsP/InP vertical grating assisted codirectional coupler laser with rear sampled grating reflector," *IEEE Photon. Technol. Lett.*, vol. 5, pp. 735–738, July 1993.

[32] P.-J. Rigole, S. Nilsson, L. Backbom, T. Klinga, J. Wallin, B. Stalnacke, E. Berglind, and B. Stoltz, "114-nm wavelength tuning range of a vertical grating assisted codirectional coupler laser with a super structure grating distributed bragg reflector," *IEEE Photon. Technol. Lett.*, vol. 7, pp. 697–699, July 1995.

[33] A. Felder, M. Moller, M. Wurzer, M. Rest, T. F. Meister, and H.-M. Rein, "60 Gbit/s regenerating demultiplexer in SiGe bipolar technology," *Electron. Lett.*, vol. 33, pp. 1984–1986, 1997.

[34] M. Suzuki, H. Tanaka, and Y. Matsushima, "10 Gbit/s optical demultiplexing and switching by sinusoidally driven InGaAsP electroabsorption modulators," *Electron. Lett.*, vol. 28, pp. 934–935, 1992.

[35] B. Mikkelsen, G. Raybon, R. J. Essiambre, K. Dreyer, Y. Su, L. E. Nelson, J. E. Johnson, G. Shtengel, A. Bond, D. G. Moodie, and A. D. Ellis, "160 Gbit/s single-channel transmission over 300 km nonzero-dispersion fiber with semiconductor based transmitter and demultiplexer," presented at the ECOC'99, vol. PD2-3, 1999.

[36] S. Z. Zhang, Y. J. Chiu, P. Abraham, and J. E. Bowers, "25 GHz polarization-insensitive electroabsorption modulators with traveling-wave electrodes," *IEEE Photon. Technol. Lett.*, vol. 11, pp. 191–193, 1999.

[37] B. Mason, G. Fish, and D. J. Blumenthal, Integrated wavelength tunable single and two-stage wavelength converter.

[38] M. D. Vaughn and D. J. Blumenthal, "All-optical updating of subcarrier encoded packet headers with simultaneous wavelength conversion of baseband payload in semiconductor optical amplifiers," *IEEE Photon. Technol. Lett.*, vol. 9, pp. 827–829, June 1997.

[39] P. Öhlén, B. E. Olsson, and D. J. Blumenthal, "All-optical header erasure and penalty-free rewriting in a fiber-based high-speed wavelength converter," *IEEE Photon. Technol. Lett.*, vol. 12, pp. 663–665, 2000.

Timothy E. Dimmick received the B.S. degree in electrical engineering from the University of Maryland, College Park, in 1983 and the Ph.D. degree (also from the University of Maryland) in 1990.

He is a visitor to the Optical Communications and Photonic Networks (OCPNs) from the Laboratory for Physical Sciences, College Park, MD. His research work includes the development of all fiber narrow-band acoustooptic tunable filters, fiber-optic sensors, optically preamplified receievers, ultrafast diode-pumped solid-state lasers, and coherent light detection and optical signal processing systems. He is currently working to develop optical network performance monitoring techniques using optical subcarrier multiplexed signals.

Daniel J. Blumenthal (S'91–M'93–SM'97) received the B.S.E.E. degree from the University of Rochester, NY, in 1981, the M.S.E.E. degree from Columbia University, NY, in 1988, and the Ph.D. degree from the University of Colorado, Boulder, in 1993.

From 1993 to 1997, he was Assistant Professor in the School of Electrical and Computer Engineering at the Georgia Institute of Technology. He is currently the Associate Director for the Center on Multidisciplinary Optical Switching Technology (MOST) and Associate Professor in the Department of Electrical and Computer Engineering at the University of California, Santa Barbara. He heads the Optical Communications and Photonic Networks (OCPNs) Research. His current research areas are in optical communications, wavelength division multiplexing, photonic packet switched and all-optical networks, all-optical wavelength conversion, optical subcarrier multiplexing, and multispectral optical information processing.

Dr. Blumenthal is recipient of a 1999 Presidential Early Career Award for Scientists and Engineers (PECASE) from the White House and the DoD, a 1994 NSF Young Investigator (NYI) Award and a 1997 Office of Naval Research Young Investigator Program (YIP) Award. He is a member of the Optical Society of America (OSA) and the IEEE Lasers and Electro-Optics Society (LEOS).

Lavanya Rau received the Masters degree in physics in August 1995 from the Indian Institute of Technology, Bombay. She is currently pursuing the Ph.D. degree in optical communication at the University of California, Santa Barbara.

She worked at the Lawrence Livermore National Laboratory in the summer of 1997, where she studied the effectiveness of AOTF in the NTONC Network. Her research interests include optical wavelength conversion, optical subcarrier multiplexing, and optical internet protocol routing.

Milan Mašanović was born in Pancevo, Yugoslavia, on August 7, 1974. He graduated from the School of Electrical Engineering, University of Belgrade, Yugoslavia, in 1998. He received the M.Sc. degree in electronics and photonics in 2000. and is currently working on the Ph.D. degree in Electrical and Computer Engineering Department, University of California at Santa Barbara.

His current research includes design of photonic integrated circuits and their applications in optical label swapping architectures.

Bengt-Erik Olsson received the Ph.D. degree in May 1998 from Chalmers University of Technology,Sweden, where he worked on applications of the nonlinear optical loop mirror as well as development of measurement technologies for polarization mode dispersion.

After receiving the Ph.D. degree, he worked within the European ACTS program MIDAS on two field experiments deploying solitons and midspan spectral inversion at 40 Gb/s and 80 Gb/s transmission. In January 1999, he joined Prof. Blumenthal's group at the University of California at Santa Barbara (UCSB) working on high-speed optical networking issues.He has authored or coauthored over 30 technical papers within these research activities.

Olga Lavrova (S'00) was born in St. Petersburg, Russia, in 1974. She received the B.S. degree in physics and the M.S. degree in electrical engineering from the St. Petersburg State Electrical Engineering University. In 1997, she joined the Electrical and Computer Engineering Department of the University of California at Santa Barbara and is currently pursuing the Ph.D. degree in the Optical Communications and Photonic Networks Laboratory.

Her current work includes experimental and analytical studies of widely tunable semiconductor lasers and their applications in optical network systems.

Giammarco Rossi received the "laurea" degree in electronic engineering with honors from the University of Pavia, Italy, in 1994 with a thesis on quantum effects in photodetection. As a Ph.D. student, he worked in the Optoelectronics device research unit of CSELT (Centro Studi E Laboratori Telecomunicazioni, Torino, Italy) and in the Optoelectronic research group of the University of Pavia. He received the Ph.D. degree in electronics in 1999 from the University of Pavia with a dissertation on high-speed semiconductor lasers for advanced optical communication systems.

Dr. Rossi is the recipient of the best thesis in optoelectronics of the year 1999 by the LEOS Italian chapter.

Roopesh Doshi received the B.S. degree in electrical engineering from the California Institute of Technology, Pasadena, in 1998. He is currently working towards the Ph.D. degree in the Electrical and Computer Engineering Department of the University of California at Santa Barbara.

He joined AstroTerra Corporation, San Diego, CA, where he worked on a wide area testbed for a free-space laser communications network, as well as a ship-to-shore free-space laser communications system. His research areas are performance monitoring, all-optical label swapping, and optical internet protocol routing.

Olivier Jerphagnon received the Masters degree in electrical and computer engineering from the Grenoble Institute of Technology (INPG), France, in July 1998. He then continued his academics at the University of California at Santa Barbara (UCSB) as a Teaching Assistant in the Electrical and Computer Engineering Department, and as part of the Optical Communication and Photonics Networks research group. He received the Master of Science degree in electronics and photonics from UCSB in December 1999.

His research interests include high-frequency electronics, fiber optics communication, and new generation of optical networks. He is now an Optical Engineer at Calient Networks.

John E. Bowers (S'78–M'81–SM'85–F'93) received the M.S. and Ph.D. degrees in applied physics from Stanford University, Stanford, CA.

He is CTO and cofounder of Calient Networks. He is on leave from University of California at Santa Barbara (UCSB), where he is director of the Multidisciplinary Optical Switching Technology Center (MOST), and a professor in the Department of Electrical Engineering at the University of California, Santa Barbara. He has worked for AT&T Bell Laboratories and Honeywell before joining UCSB. He has published five book chapters, over 300 journal papers, over 300 conference papers and has received 18 patents.

Dr. Bowers is a Fellow of the American Physical Society, a recipient of the IEEE LEOS William Streifer Award, Sigma Xi's Thomas F. Andrew prize, and the NSF Presidential Young Investigator Award.

Volkan Kaman received the B.S. degree in electrical engineering from Cornell University, Ithaca, NY, in 1995, the M.S. degree from the University of California at Santa Barbara (UCSB) in 1997, and the Ph.D. degree from UCSB

His research interests are in high-speed electrical and optical TDM systems and applications of electroabsorption modulators for optical processing.

Larry A. Coldren (S'67–M'72–SM'77–F'82) received the Ph.D. degree in electrical engineering from Stanford University, Stanford, CA, in 1972.

After 13 years in the research area at Bell Laboratories, he was appointed Professor of Electrical and Computer Engineering at the University of California at Santa Barbara (UCSB) in 1984. In 1986, he assumed a joint appointment with Materials and ECE. At UCSB, his efforts have included work on novel guided-wave and vertical-cavity modulators and lasers as well as the underlying materials growth and dry-etching technology. He is now investigating the integration of various optoelectronic devices, including optical amplifiers and switches, tunable lasers, receivers, and surface-emitting lasers. He is also heavily involved in new materials growth and fabrication technology essential to the fabrication of such integrated optoelectronic components. He has authored or coauthored over 300 papers, three book chapters, and one textbook, and has been issued 26 patents.

He is a Fellow of the Optical Society of America (OSA), a past Vice-President of IEEE-LEOS, and has been active in technical meetings. He is currently Director of the multicampus DARPA supported Heterogeneous Optoelectronic Technology Center.

John Barton, photograph and biography not available at the time of publication.

All-Optical Demultiplexing Using Fiber Cross-Phase Modulation (XPM) and Optical Filtering

Bengt-Erik Olsson and Daniel J. Blumenthal, *Senior Member, IEEE*

Abstract—All-optical demultiplexing of 80-Gb/s data to 10 Gb/s is demonstrated using spectral broadening-induced by cross-phase modulation (XPM) with subsequent optical band-pass filtering. Due to the time derivative effect of XPM, the control pulsewidth can be larger than the bit-slot of the incoming data, and still give a switch window suitable for demultiplexing. Operation at 10^{-12} bit-error rate is demonstrated. In principle, this approach will scale to extremely high bit rates due to the ultrafast fiber nonlinearities.

Index Terms—Cross-phase modulation, fiber nonlinearities, optical demultiplexing, optical filtering, optical networks, optical time-division multiplexing, optical-wavelength conversion.

I. INTRODUCTION

FUTURE ultrahigh bit-rate optical time division mul-
tiplexed (OTDM) systems may require all-optical demultiplexing to down convert the high bit-rate data to, e.g., 10 or 40 Gb/s where electronic circuits can be used. Many examples of such demultiplexers have been proposed over the years. The most common device is the nonlinear optical loop mirror (NOLM) that allows switching due to cross-phase modulation (XPM), in either a fiber [1] or a semiconductor optical amplifier (SOA) [2]. Another approach is to use four-wave-mixing (FWM) in either an SOA or a fiber [3]. In all these schemes, the switch window for the demultiplexed OTDM channel can usually not be shorter than the pulsewidth of the control pulse that initiates the XPM or FWM, and thus, a very short high-quality optical pulse is required [4].

In this letter, we demonstrate a new 1550-nm waveband demultiplexer based on XPM in a fiber that utilizes the time derivative effect of XPM-induced spectral broadening. Low bit-error-rate (BER) operation ($<10^{-12}$) is demonstrated with 80-Gb/s data optically demultiplexed to 10 Gb/s. In principle, this approach will scale to extremely high bit rates, in excess of 160 Gb/s, due to the ultrafast fiber nonlinearities. This approach is based on optically induced frequency shifting of the modu-
lated input signal with a control pulse. The leading edge of the control pulse, generates a red shift of the spectrum of the XPM modulated input signal, and the trailing edge generates a blue shift. Optically-induced frequency shifting has previously been
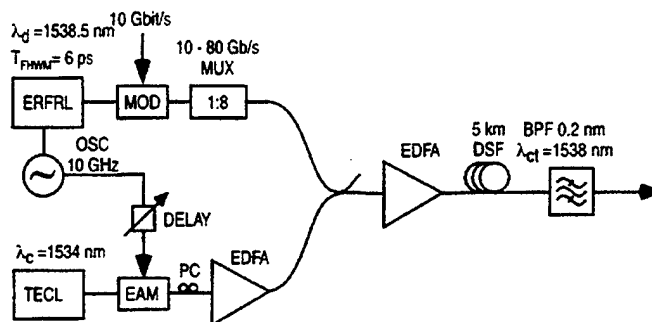
Fig. 1. Experimental setup. ERFRL: Erbium-doped fiber ring laser. MOD: LiNbO3 modulator. MUX: Passive 10–80 Gb/s multiplexer. TECL: Tunable external cavity laser. EAM: Electroabsorption modulator. PC: Polarization controller. EDFA. OSC: 10-GHz microwave oscillator. DELAY: Variable electrical delay. DSF: Dispersion-shifted fiber. BPF: Bandpass filter.

demonstrated for pulses at an 980-nm 82-MHz repetition rate using a resonantly-excited semiconductor nonlinear waveguide combined with an optical filter [5], however, demonstration at communications bit rates (10 Gb/s) and wavelength with real data, was not investigated and only single-pulse operation shown.

Previously, we have reported wavelength conversion using this technique, where the incoming data modulates the phase of a continuous wave (CW) signal with subsequent conversion to amplitude modulation [6]. In this letter, only one of the OTDM data channels in the high bit-rate data is spectrally broadened, and that channel is extracted using a narrow-band optical band-pass filter (BPF) at either side of the original spectrum. Thus, if dispersive walkoff is neglected, only one edge of the control pulse governs the width of the demultiplexing switch window. Therefore, a control pulse broader than the actual bit slot can be used for demultiplexing. Another important feature of this demultiplexer compared to the interferometric techniques like the NOLM, is its insensitivity to environmental disturbances.

II. EXPERIMENTS

The experimental setup is shown in Fig. 1. An actively mode-locked fiber ring laser generated 6-ps pulses at a 1538.5-nm wavelength with a 10-GHz repetition rate. 10-Gb/s PRBS $2^{31} - 1$ data was encoded onto the fiber ring laser output using an external modulator. A passive optical interleaver multiplexer was used to generate an 80-Gb/s data stream. The control pulses were generated using an electroabsorption modulator that output 14-ps pulses at a wavelength of 1534
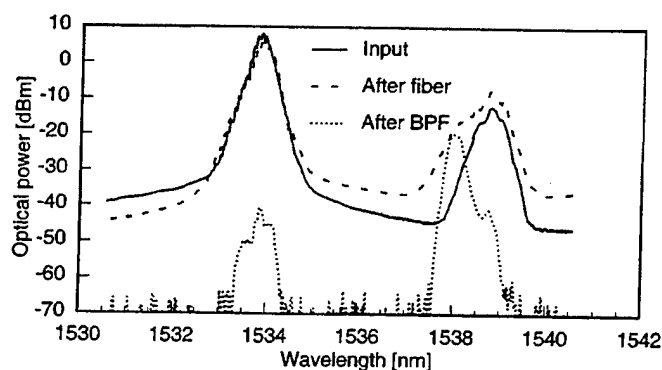
Fig. 2. Optical spectrum at the input of the DSF, after the DSF, and after the 0.2-nm BPF.

Fig. 4. Measured switch window of the demultiplexer.

Fig. 3. 80-Gb/s eye pattern. (a) Demultiplexed 10-Gb/s channels (b)–(i). The extinction ratios of the output pulses were estimated to be better than 15 dB.

nm. The 80-Gb/s data and the control pulses were combined in a 50 : 50 coupler and amplified in an erbium-doped fiber amplifier (EDFA) to +18 dBm average output power. A 5-km dispersion shifted fiber (DSF) with a zero dispersion wavelength of 1543 nm, was used to induce XPM from the control pulses on to one of the 10-Gb/s data channels in the 80-Gb/s data stream.

The optical spectrum was broadened only during the time slot of one 10-Gb/s channel, and that channel was extracted by using a narrow 0.2-nm optical BPF positioned at a center wavelength of 1538 nm. The output from the BPF was then sent to an optically preamplified receiver for inspection on a sampling oscilloscope, as well as for BER measurements. Fig. 2 shows the optical spectra in various points of the system. The solid trace shows the spectrum after the 50 : 50 combiner. The power ratio between the control pulse and the 80-Gb/s data was about 20 dB, to avoid saturation of the EDFA in front of the DSF from the incoming data. The dashed trace shows the spectrum after the DSF, where the spectrum of the 80-Gb/s data is broadened due to XPM from the control pulse. The dotted trace in Fig. 2 shows the filtered XPM broadened spectrum, i.e., the demultiplexed channel at the output. Since the BPF is only 0.2 nm, the output pulsewidth of the demultiplexed data is 17 ps. Fig. 3(a) shows the input 80-Gb/s data eye pattern as measured with a 40-GHz detector on a 50-GHz sam-

pling oscilloscope. Fig. 3(b)–(i) shows the eight demultiplexed 10-Gb/s channels. No crosstalk was present even though the control pulsewidth was 14 ps and the bit-slot at 80-Gb/s is 12.5 ps. The extinction ratios of the output pulses were estimated to be better than 15 dB.

To estimate the actual switch window in the device, the cross correlation between a 6-ps data pulse and a 14-ps control pulse was measured. Fig. 4 shows the measured cross correlation between the two pulses in the demultiplexer. The measurement was made by sliding the 14-ps control pulses across the 6-ps data pulses, while recording the demultiplexer output power with a power meter. The width of the switch window was 11 ps, even though a 14-ps control pulse was used, which is suitable to demultiplex 80 Gb/s. We also noticed a somewhat rectangular shape of the switch window, which is due to dispersive walkoff between control and data pulse, and this effect is useful to absorb timing jitter in the incoming data. The net polarization dependence of the demultiplexer was about 3 dB, even though the polarization dependence of XPM in standard DSF is 5 dB. The reason for this, is that for orthogonal relative polarization of data and control pulses, the spectral broadening is at its minimum, and for decreased orthogonality, the spectrum gets broader, but still leaving energy within the filter band width. However, the polarization dependence depends heavily on the available pump power, as well as the position of the BPF.

BER measurements of the demultiplexed data are shown in Fig. 5. The back-to-back receiver sensitivity was measured from 10 Gb/s to −36.8 dBm, after the data modulator. Full BER plots are shown for channel one to four, and BER measurements around 10^{-9} are shown for channel five to eight. All channels performed almost the same, giving a penalty of about 2 dB. This penalty is believed to arise primarily due to nonoptimal filtering of the narrow bandwidth demultiplexed 10-Gb/s data in the receiver. The optically preamplified receiver included a 0.6-nm optical BPF that is close to optimum for 6-ps pulses, and thus gives a low receiver sensitivity for the original 10-Gb/s data. After demultiplexing, the pulsewidth is 17 ps with a spectral width of 0.2 nm, which is far from optimum for this particular receiver. In fact, sending the original 10-Gb/s data with 6-ps pulses through the 0.2-nm filter, before entering the receiver gave also about 2-dB penalty, but with a slightly better slope of the BER.
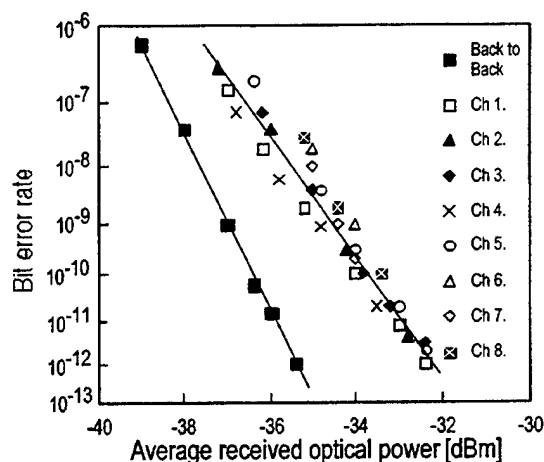
Fig. 5. BER measurements for 80–10-Gb/s demultiplexing.

III. CONCLUSION

A new all-optical demultiplexer based on XPM in a fiber followed by a narrow optical BPF is described and demonstrated. An 80-Gb/s data channel was successfully demultiplexed to 10 Gb/s with <2 dB receiver penalty using a control pulse of 14 ps. Due to the derivative effect of XPM, a control pulse that is wider than the bit-slot of the high bit-rate data can be utilized. The demultiplexer is insensitive to environmental disturbances, and can be made polarization independent by using a diversity scheme [7], circular birefringent fiber [8], or possibly by managing the input power condition. The demultiplexer scheme, is also well suited for simultaneous demultiplexing by using both slopes of the control pulse, and control pulses at multiple wavelengths, which is subject to further investigation.

REFERENCES

[1] K. J. Blow, N. J. Doran, and P. B. Nelson, "Demonstration of the nonlinear fiber loop mirror as an ultrafast all-optical demultiplexer," *Electron. Lett.*, vol. 26, pp. 962–964, 1990.

[2] J. P. Sokoloff, P. R. Prucnal, I. Glesk, and M. Kane, "A terahertz optical asymmetric demultiplexer (TOAD)," *IEEE Photon. Technol. Lett.*, vol. 5, pp. 787–790, July 1993.

[3] P. A. Andrekson, N. A. Olsson, and J. R. Simpson, "16 Gbit/s all-optical demultiplexing using four-wave mixing," *Electron. Lett.*, vol. 27, pp. 922–924, 1991.

[4] M. Jinno, "Effects of crosstalk and timing jitter on all-optical time division demultiplexing using a nonlinear fiber Sagnac interferometer switch," *J. Lightwave Technol.*, vol. 30, pp. 2842–2853, Dec. 1994.

[5] S. Nakamura, Y. Ueno, and K. Tajima, "Ultrafast (200-fs switching, 1.5-Tb/s demultiplexing) and high-repetition (10 GHz) operations of a polarization-discriminating symmetric Mach–Zehnder all-optical switch," *IEEE Photon. Technol. Lett.*, vol. 10, pp. 1575–1577, Nov. 1998.

[6] B. E. Olsson, P. Öhlén, L. Rau, and D. J. Blumenthal, "A simple and robust 40 Gbit/s wavelength converter using fiber cross-phase modulation and optical filtering," *Photon. Technol. Lett.*, pp. 846–848, July 2000.

[7] B. E. Olsson and P. A. Andrekson, "Polarization independent Kerr-switch using a polarization diversity loop," in *Proc. Eur. Conf. Opt. Comm. (ECOC)*, Madrid, Spain, 1998, pp. 185–186.

[8] Y. Liang, J. W. Lou, J. K. Andersen, J. C. Stocker, O. Boyraz, and M. N. Islam, "Polarization-insensitive nonlinear optical loop mirror demultiplexing with twisted fiber," *Opt. Lett.*, vol. 24, pp. 726–728, 1999.

WDM to OTDM Multiplexing Using an Ultrafast All-Optical Wavelength Converter

Bengt-Erik Olsson, Lavanya Rau, and Daniel J. Blumenthal, *Senior Member, IEEE*

Abstract—A robust and scalable all-optical multiplexer combining four 10-Gb/s WDM channels into one 40-Gb/s OTDM channel is presented. The multiplexer generates a coherent output data stream, which does not suffer from channel interference as passively generated OTDM data do.

Index Terms—Fiber optics, optical multiplexing, optical networks.

I. INTRODUCTION

THE RAPID increase in the demand for more optical transmission bandwidth has led to a great interest in increasing the bit rate of individual data channels in wavelength–division-multiplexed (WDM) networks. The highest bit rate of single channel transmitters in deployed networks today is 10 Gb/s, even though 40-Gb/s transmitters are expected in the near future. An alternative way to accomplish higher bit rates is to optically time-division-multiplex (OTDM) multiple 10-Gb/s return-to-zero (RZ) data streams together using passive-time interleaving multiplexers. The traditional method of doing this is by having a 10-GHz clock source, usually a mode-locked or gain-switched laser, generates short pulses and splits the clock signal into the desired number of channels, and subsequently encode data on each of them. All channels are then time interleaved in optical combiners with appropriate time delays between each channel. The main problem with this method is that very high quality clock pulses are necessary to avoid interference problems between adjacent channels [1], leading to a variation in pulse amplitude and, if the pulses are not perfectly coherent, a time varying drift in amplitude. In practice, very short pulses, typically less than one quarter of a bit slot with high extinction ratio (>30 dB) are required to achieve a noiseless OTDM data sequence. Here, we demonstrate a multiplexer that takes four channels from a WDM transmitter with nonreturn-to-zero (NRZ) format and convert them to NRZ format, and subsequently wavelength convert all four WDM channels to one wavelength to obtain one OTDM channel. The advantage of this scheme is that existing WDM transmitter technology can be used, while increasing the single channel transmission bit rate, as well as eliminating some problems with passive OTDM multiplexing. For example, the long coherence length of the local laser determines the coherence length of the output optical data. WDM to time-division-multiplexing (TDM) conversion has previously been demonstrated using semiconductor optical amplifier (SOA) technology [2], as well as using the nonlinear optical loop mirror (NOLM) [3]. However, the SOA technology has a limited frequency response and even at 40 Gb/s, it is difficult to obtain short enough pulses at the output to constitute a RZ signal. The NOLM is in general, not suitable for wavelength conversion, since the pulses that induce cross-phase modulation (XPM) have to be very short compared to the bit slot to avoid crosstalk due to unwanted XPM from the high average power [4].

In this experiment, we use an ultrafast wavelength converter based on XPM in an optical fiber [5], which in principle can allow operation at several hundred gigabits [6]. An advantage with this scheme is that the requirements on the RZ pulses are lower due to the nonlinear transfer function of the wavelength converter, which allows pulses with moderate extinction ratio to be used. The output of the wavelength converter is given by the derivative of the input signal, which also allows broader pulses to be used at the input.

II. EXPERIMENTAL RESULTS AND DISCUSSION

The basic idea is to demonstrate conversion of 4·10 Gb/s WDM channels to one 40-Gb/s OTDM channel. Fig. 1 shows the experimental setup used for the multiplexer demonstration. Four tunable lasers generated continuous-wave (CW) light at 1544.0, 1545.6, 1547.2, and 1548.8 nm. 10-Gb/s pseudorandom bit stream (PRBS) NRZ data with a word length of $2^{31} - 1$ was encoded on all wavelengths, and adjacent wavelength channels were encoded with different data. The four WDM channels were then converted to RZ data by injecting the synchronized WDM channels into an electroabsorption modulator (EAM) followed by a 200-m dispersion compensating fiber (DCF) ($D = -67$ ps/nm · km). With this arrangement, pulses with a pulsewidth between 8–9 ps were obtained for all four WDM channels. Care was taken to equalize the output pulsewidth between the channels by adjusting the dc-bias point of the EAM without leading to a significant crosstalk in the EAM. The total loss in the EAM was 25 dB at the chosen operating point, and it was a tradeoff between maximum allowed input power to avoid crosstalk in the EAM, and signal-to-noise ratio (SNR) at the output of the following erbium-doped fiber amplifier (EDFA). Here the total average power into the EAM was +9 dBm, which

Fig. 1. Experimental setup. TECL: Tunable external cavity laser. PC: Polarization controller; MOD: LiNbO₃ external modulator. EDFA; EAM; FBG; DCF; DSF: Dispersion shifted fiber. BPF: 0.4-nm optical bandpass filter.

gave rise to a moderate crosstalk between the WDM channels. The DCF after the EAM served as a pulse compressor, since the pulses from the EAM had some positive chirp, but also to align the four RZ data channels to be delayed 25 ps between each channel. By looking at the four wavelength channels in the time domain, e.g., with a high-speed oscilloscope, the signal looked like a 40-Gb/s OTDM data stream, even though each channel resides on a different wavelength. Since the EDFA after the EAM added noise, a fiber Bragg grating (FBG) was used to remove amplified spontaneous emission (ASE) noise at the wavelength of the output of the wavelength converter. The WDM RZ signals were then combined with CW light at 1554.5 nm and amplified in an EDFA to an average power of 350 mW. An 850-m dispersion shifted fiber (DSF) with a zero dispersion wavelength of 1550 nm was used to impose a phase modulation onto the CW light by XPM in the fiber. This phase modulation was then converted to amplitude modulation by a filter arrangement, which consisted of a FBG to remove the intense original data channels signals, as well as an optical bandpass filter to select one of the generated side bands of the CW light [5]. The output 40-Gb/s OTDM data were investigated using a 40-GHz photo detector on a 50-GHz sampling oscilloscope. An EAM driven at 10 GHz was used to demultiplex the 40-Gb/s data to 10 Gb/s, where bit-error-rate (BER) measurements were performed.

Fig. 2 shows the optical spectrum at various points of the system. The solid line shows the spectrum into the wavelength converter with the four 10-Gb/s RZ signals and the CW light, the dashed line shows the spectrum after the DSF in the wavelength converter, and the dotted line shows the output signal from the wavelength converter. Fig. 3(a) shows the eye pattern of the 4×10 Gb/s WDM channels after the EAM and the DCF. Although each channel is on its own wavelength, they now look like a 40-Gb/s OTDM data stream. Fig. 3(b) shows the output 40-Gb/s OTDM data after the wavelength converter, which is a clearly open 40-Gb/s eye pattern. BER measurements were performed on the output 40-Gb/s data by demultiplexing the data into four 10-Gb/s data channels and the BER of all four channels were measured and are presented in Fig. 4. Fig. 4 also shows the back-to-back measurements for one of the original 10-Gb/s channels after conversion from NRZ to RZ without the presence of the other WDM channels in the EAM. A 3-dB receiver penalty at a BER of 10^{-9} was observed for all channels in the
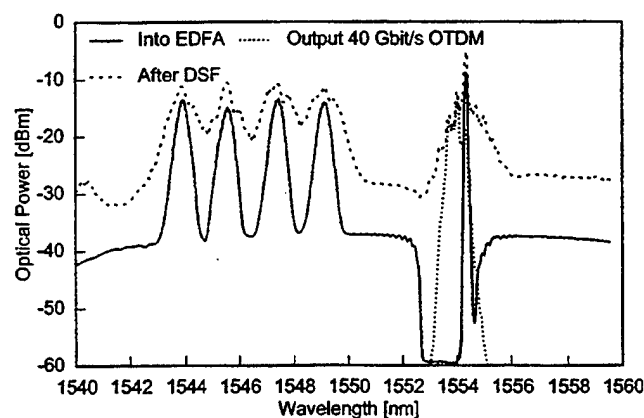
Fig. 2. Spectrum of the input signal to the EDFA in the wavelength converter (solid line), spectrum after the DSF (dashed line), and spectrum of the output 40-Gb/s OTDM data (dotted line). The output extinction ratio is >20 dBm.
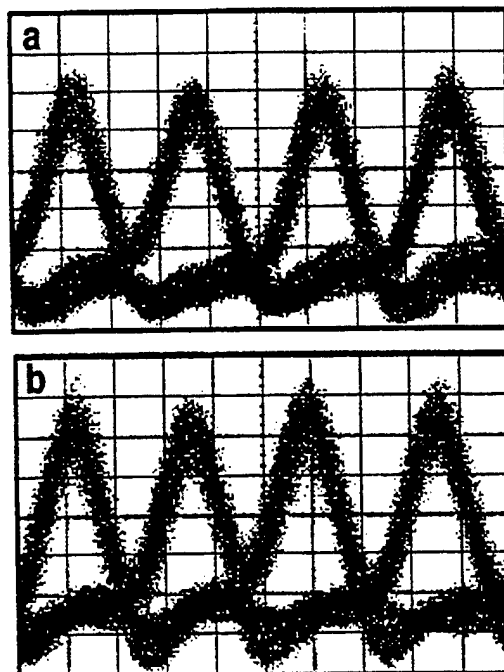
Fig. 3. (a) Eye patterns of the 4·10-Gb/s WDM channels before wavelength conversion. (b) The output 40-Gb/s OTDM data after wavelength conversion.
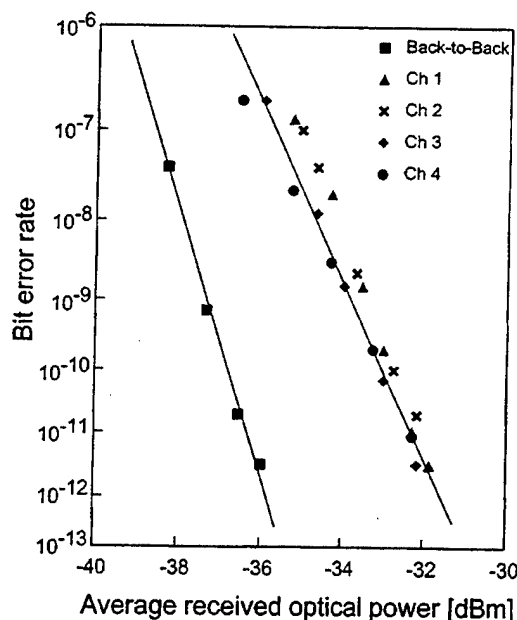
Fig. 4. BER measurements of one input 10-Gb/s channel, back-to-back (■), and the four channels of the output 40-Gb/s OTDM data stream.
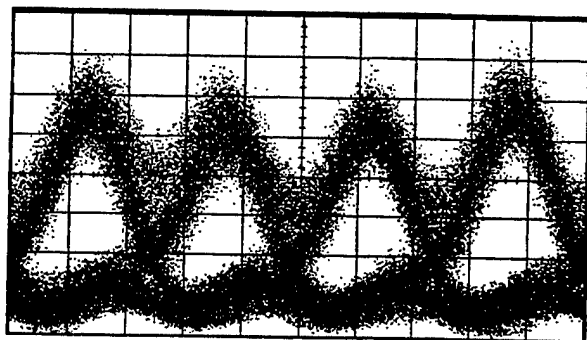
Fig. 5. 10-Gb/s RZ data sent through a passive 10–40-Gb/s OTDM multiplexer. The extinction ratio of the pulses in approximately 20 dB (10 ps/div).

output 40-Gb/s OTDM data. This penalty is primarily due to crosstalk between the WDM channels in the first EAM in the NRZ to RZ conversion process, and also partly due to the high loss in the EAM, which decreases the signal-to-noise ratio (SNR) after the following EDFA. We believe that an EAM with less total insertion loss would eliminate this penalty since a higher SNR would then be maintained and the input power into the EAM can be lower to reduce the crosstalk.

An advantage with this wavelength converter scheme is that only moderate requirements on the input RZ-data channels are required, since the transmission through the wavelength converter is nonlinear and conversion is only intensity dependent. This means that the extinction ratio of the RZ pulses is

not critical. The output data is now perfectly coherent and no interference effects occur between adjacent channels in the OTDM pulse train, which can be present in classic passive OTDM multiplexers. To demonstrate the difference between the presented multiplexer and a passive OTDM multiplexer, the 10-Gb/s RZ-data of channel 1 was sent into a passive split-and-interleave 10–40-Gb/s multiplexer. Fig. 5 shows the output 40-Gb/s eye pattern of that OTDM multiplexer and the eyes are heavily distorted and unstable due to interference between adjacent pulses, which occurs due to a limited ER from the pulse source (ER 20 dB).

III. CONCLUSION

A novel WDM to OTDM multiplexer using an ultrafast wavelength converter is presented. The multiplexer allows high quality conversion from four NRZ WDM channels at 10-Gb/s to one 40-Gb/s OTDM channel. The 3-dB power penalty observed in the output 40-Gb/s data stream can be eliminated if an EAM with lower loss or higher saturation power is obtained. The system is scalable both in terms of the number of input channels, only limited by the bandwidth of the wavelength converter [6], as well as to higher input bit rates in the incoming WDM channels.

REFERENCES

[1] M. Lønstrup-Nielsen, B. E. Olsson, and D. J. Blumenthal, "Pulse extinction ratio improvement using SPM in an SOA for OTDM systems applications," in *Eur. Conf. Optical Communications*, Munich, Germany, 2000.

[2] K. A. Williams, M. F. C. Stephens, D. Nesset, A. E. Kelly, R. V. Penty, and M. J. Fice, "WDM-TDM transmultiplexing at 40 Gb/s using an integrated DFB laser amplifier," in *Eur. Conf. Optical Communications*, vol. 2, Nice, France, 1999, pp. 168–169.

[3] M. R. H. Daza, H. F. Liu, M. Tsuchiya, Y. Ogawa, and T. Kamiya, "All-optical WDM-to-TDM conversion with total capacity of 33 Gb/s for WDM networks links," *IEEE J. Select. Topics Quantum Electron.*, vol. 2, pp. 1287–1294, Oct. 1997.

[4] B. E. Olsson, A. Boyle, and P. A. Andrekson, "Control pulse-induced crosstalk in propagation diversity and conventional nonlinear optical loop mirrors," *IEEE Photon. Technol. Lett.*, vol. 10, pp. 1632–1634, Nov. 1998.

[5] B. E. Olsson, P. Öhlén, L. Rau, and D. J. Blumenthal, "A simple and robust 40-Gb/s wavelength converter using fiber cross-phase modulation and optical filtering," *IEEE Photon. Technol. Lett.*, vol. 12, pp. 846–848, July 2000.

[6] P. Öhlén, B. E. Olsson, and D. J. Blumenthal, "Wavelength dependence and power requirements of a wavelength converter based on XPM in a dispersion shifted optical fiber," *Photon. Technol. Lett.*, vol. 12, pp. 522–524, May 2000.

LP01 mode to the cladding modes supported by the glass-air interface. The thick line is the transmission taken while the fibre was in index-matching fluid. As can be seen, the coupling peaks for the cladding modes in the index matching fluid case are reduced due to a decrease in guidance and the peak wavelengths move towards longer wavelength due to an increase of the modal effective refractive index. Meanwhile, the peak for coupling into the LP11 mode is not affected by the changing environment of the fibre, giving strong evidence that this mode is a core mode which has virtually no power distribution at the glass-air interface of the fibre. Coupling into the leaky LP11 mode is also very much stronger than the strongest peak for the cladding mode coupling, ~5 dB in this case. Coupling into the leaky LP11 mode can be further improved by having a grating with strong non-circular symmetry and appropriate fibre design.
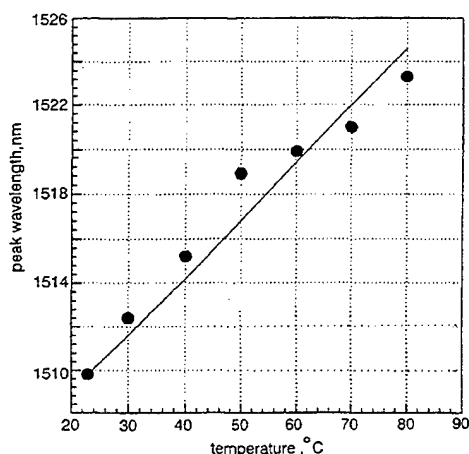
Fig. 4 *Temperature sensitivity of long period grating in depressed cladding fibre*

● data
——— linear fit, 0.26nm/°C

A long period grating was written into the fibre used above to demonstrate this method. The fibre was H_2-loaded before a ~2cm grating was written by a 193nm ArF excimer laser using an amplitude mask. The transmission of the fibre was monitored and then translated into absorption. This is plotted in Fig. 3. The temperature sensitivity of the grating is also measured and plotted in Fig. 4. The sensitivity was measured as 0.26nm/°C for this grating. This is typical for long period gratings.

To summarise, we have demonstrated a new method for use in long period gratings, which has enhanced coupling strength and is insensitive to the fibre glass-air interface.

References

1   VENGSAKAR. A.M., PEDRAZZANI. J.R., JUDKINS. J.B., and LEMAIRE. P.J.: 'Long-period fibre gratings based gain equaliser', *Opt. Lett.*, 1996, 21, pp. 336–338

2   HEWLETT, S.J., LOVE. J.D., MELTZ. G., BAILEY. T.J., and MOREY. W.W.: 'Cladding-mode coupling characteristics of Bragg gratings in depressed cladding fibre', *Electron. Lett.*, 1995, 31, pp. 820–822

3   DONG. L., REEKIE. L., CRUZ. J.L., CAPLEN. J.E., DE SANDRO. J.P., and PAYNE. D.N.: 'Optical fibres with depressed claddings for suppression of coupling into cladding modes in fibre Bragg gratings', *IEEE Photonics Technol. Lett.*, 1997, 9, pp. 64–66

Compact InGaAsP/InP 1 × 2 optical switch based on carrier induced supression of modal interference

G.A. Fish, L.A. Coldren and S.P. DenBaars

Indexing terms: Optical switches, Photonic switching

A novel, compact optical switch designed for use with integrated amplifiers to create more scalable photonic crossconnects is reported. The basic operation of the switch is described and experimentally verified. On/off ratios of 16.2dB (7.5dB) in the bar (cross) state are demonstrated with currents < 30mA and a very low bar state excess loss of 0.5dB.

Introduction: InGaAsP/InP based photonic integrated cross connects are rapidly maturing and will be very attractive components for future optical networks. Current research in this area can be loosely devided into three catagories: purely passive switches such as the digital optical switch (DOS) [1] and Mach-Zender interferometer (MZI) [2] or directional coupler based switches [3], completely active switches involving amplifier gates [4], and combination passive switches and amplifiying gates, such as the S^3 or COSTA [5]. The last of these categories shows the most promise for large $N×N$ crossconnects, since it has achieved very low insertion loss and crosstalk levels, which would be difficult to obtain with purely passive switches, while maintaining a scalability which is not possible in a gate array.

The switching elements used in the COSTA are based on carrier induced total internal reflection (TIR) [6] and exhibit high switching currents and/or large excess losses typical of these devices [5, 7, 8] which may impose limitations on scalability. In this Letter, we present a novel method for optical switching and its application towards fabricating compact switches suitable for integration with amplifiers in a expandable crossconnect.
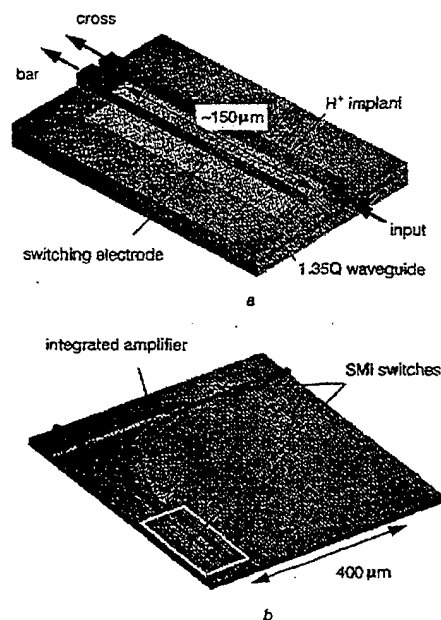
Fig. 1 *Schematic diagrams of SMI switch*

a Input waveguide coupled off-centre to TMI region whose output is altered when current is applied
b Integration with amplifier and additional switch to form single element of crossconnect

Switch design and fabrication: Switches for use in conjunction with amplifiers in nonbroadcasting architectures (e.g. the S^3) have slightly different criteria than stand alone switching elements. Namely, the bar state excess loss of the switch should be made as low as possible, as most of the switches encountered in a non-broadcasting crossconnect will be in the bar state. The cross state loss is less important and it is only neccessary that the integrated amplifier can easily overcome it. The switching current should also

be as small as possible to avoid heating and to simplify driver circuits, as multiple switch/amplifier pairs will be operated simultaneously.

To achieve these requirements at the same time in an amplified switch, we have developed the structure shown in Fig. 1a, which we refer to as a supressed modal interference (SMI) switch. The basic principle is novel and involves injecting current into a multimode inteference section in such a way as to change its imaging properties to achieve a different output. To create a 1×2 switch, a singlemode input waveguide was coupled off centre to a two-mode interference (TMI) section which is precisely one beat length long.
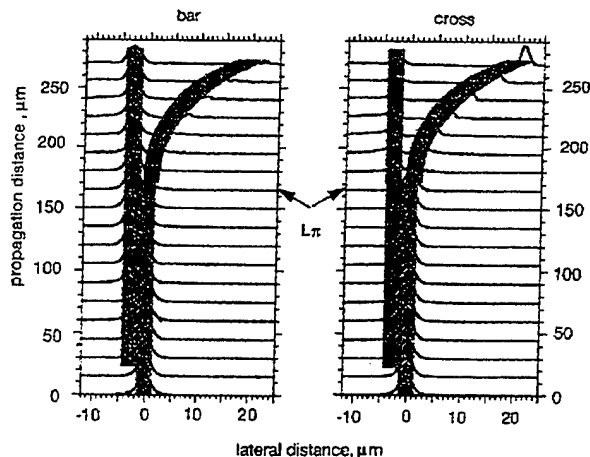
Fig. 2 *Beam propagation method (BPM) simulations of SMI switch in operation*

a Modal interference causes optical field to bypass curve in bar state
b Suppression of interference with current injection directs field into curve in cross state

Similar to 2×2 TIR switches [7] of the past, in the absence of current, the input mode excites the modes of the TMI section and its image appears on the opposite half of the TMI section after travelling one beat length, as shown in Fig. 2a. By injecting current on the unimplanted half of the TMI section, its mode spectrum is changed until only a singlemode exists, supressing modal interference, and the light is guided straight into the curved amplifier section, Fig. 2b. Beam propagation method (BPM) simulations predict that as much as 70% of the light can be coupled into the curved section while maintaining only 0.3dB of excess loss in the bar state.

Combining the SMI switches with a small radius amplifier to create a very compact crossconnect element, shown in Fig. 1b, is complicated by the different lateral index contrast required by the two elements. Switches must have small index contrasts to be effective, while small radius bends require large index contrasts to reduce bending loss. The solution of this problem is to etch additional cladding material from the outside of the curve, as illustrated in Fig. 1b.

Fabrication of the amplified SMI switch requires only two MOCVD growth steps whereby a base structure with an MQW active region is grown on top of 0.35µm thick 1.35Q waveguides selected to give high index change against absorption loss when injecting carriers [9]. The active region is removed in the passive sections of the device and the p-cladding and contact layers are regrown including a stop etch layer to define the lateral index contrast of the switch region. Ridge waveguides are dry-etched using CH₄/H₂/Ar followed by a wet H₃PO₄/HCl clean up etch to the stop etch layer. This gives a well controlled, uniform waveguide width and lateral index constrast required for these type of devices [10]. Further etching on the outside of the curve section follows using Br/H₃PO₄/H2O. Finally, the devices are covered with SiN_x, metallised, and proton implanted to isolate the various sections and define the unbiased half of the SMI switch.

Switch characteristics: To verify the BPM analysis, the near field pattern at the end of various length SMI switches was imaged using an IR camera and light from an on-chip LED in front of the switch. This proved to be very useful, allowing the beat length of 130 µm to be measured directly and the evolution of the switching

to be observed, as shown in Fig. 3b. To separately characterise the SMI switch without amplification, the curved amplifier was pumped as an LED (λ = 1540nm) and light was coupled out of the switch input using a lensed (R = 9µm) optical fibre. The bar state was similarly characterised using an additional on-chip LED contained in this path. The on/off ratios of the switch in the cross and bar states were measured as 7.5 and 16.2dB, respectively, with < 30mA of injected current, as illustrated in Fig. 3a. The intial dip in the contrast ratio of the cross state is due to the SMI switch being slightly longer than one beat length. The light output of the bar state was compared to that of several straight waveguides with no switches to give an estimate of 0.5dB for the bar state excess loss.
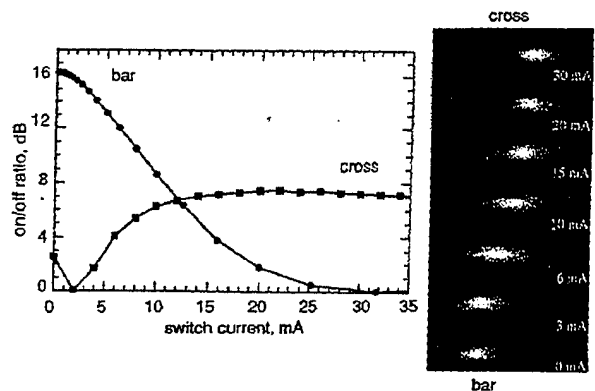
Fig. 3 *Contrast ratios and near field image of SMI switch*

a Contrast ratios of bar and cross states with applied current showing 16.2dB and 7.5dB contrasts, respectively, with < 30mA
b Near field image of end of SMI switch of length L_π as current is applied, showing supression of modal interference

Conclusion: We have presented a novel method for optical switching by modifying the imaging properties of modal interference sections through current injection (supressed modal interference) and have applied this method to fabricate 1×2 switches that can be used in conjunction with amplifiers to form lossless, scalable, optical crossconnects. The switches exhibited a very low excess bar state loss of 0.5dB and on/off ratios of 16dB (bar) and 7.5dB (cross) with switching currents < 30mA.

G.A. Fish, L.A. Coldren and S.P. DenBaars (*Electrical and Computer Engineering, University of California, Santa Barbara, CA 93106, USA*)

References

1   VINCHANT, J.F., RENAUD, M., ERMAN, M., PEYRE, J.L., JARRY, P., and PAGNOD-ROSSIAUX, P.: 'InP digital optical switch: key element for guided-wave photonic switching', *IEE Proc. J. Optoelectron.*, 1993, **140**, (5), pp. 301–307

2   KRAHENBUHL, R., KYBURZ, R., VOGT, W., BACHMANN, M., BRENNER, T., GINI, E., and MELCHIOR, H.: 'Low-loss polarisation-insensitive InP-InGaAsP optical space switches for fibre optical communication', *IEEE Photonics Technol. Lett.*, 1996, **8**, (5), pp. 632–634

3   WENGER, G., SCHIENLE, M., BELLERMANN, J., HEINBACH, M., EICHINGER, S., MULLER, J., ACKLIN, B., STOLL, L., and MULLER, G.: 'A completely packaged strictly nonblocking 8×8 optical matrix switch on InP/InGaAsP', *J. Lightwave Technol.*, 1996, **14**, (10), pp. 2332–2337

4   VAN BERLO, W., JANSON, M., LUNDGREN, L., MORNER, A.C., TERLECKI, J., GUSTAVSSON, M., GRANESTRAND, P., and SVENSSON, P.: 'Polarisation-insensitive, monolithic 4×4 InGaAsP-InP laser amplifier gate switch matrix', *IEEE Photonics Technol. Lett.*, 1995, **7**, (11), pp. 1291–1293

5   KIRIHARA, T., OGAWA, M., INOUE, H., KODERA, H., and ISHIDA, K.: 'Lossless and low-crosstalk characteristics in an InP-based 4×4 optical switch with integrated single-stage optical amplifiers', *IEEE Photonics Technol. Lett.*, 1994, **6**, (2), pp. 218–221

6   INOUE, H., KIRIHARA, T., SASAKI, Y., and ISHIDA, K.: 'Carrier-injection type optical S³ switch with travelling-wave amplifier', *IEEE Photonics Technol. Lett.*, 1990, **2**, (3), pp. 214–215

7   VAN ROIJEN, R., VAN DER HEIJDEN, J.M.M., TIEMEIJER, L.F., THIJS, P.J.A., VAN DONGEN, T., BINSMA, J.J.M., and VERBEEK, B.H.: 'Over 15dB gain from a monolithically integrated optical switch with an amplifier', *IEEE Photonics Technol. Lett.*, 1993, **5**, (5), pp. 529–531

8   KWANG-RYONG, O., KI-SUNG, P., DAE-KON, O., HONG-MAN, K., HYUNG MOO, P., and KWYRO, L.: 'A very low operation current InGaAsP/InP total internal reflection optical switch using p/n/p/n current blocking layers', *IEEE Photonics Technology Lett.*, 1994, **6**, (1), pp. 65–67

9   VINCHANT, J.F., CAVAILLES, J.A., ERMAN, M., JARRY, P., and RENAUD, M.: 'InP/GaInAsP guided-wave phase modulators based on carrier-induced effects: theory and experiment', *J. Lightwave Technol.*, 1992, **10**, (1), pp. 63–70

10   PEYRE, J.L., GOUTELLE, A., PAGNOD-ROSSIAUX, P., and VINCHANT, J.F.: 'Improved fabrication of 4×4 polarisation insensitive switch matrices on InP by introduction of an etch stop layer'. Conf. Proc. 5th Int. Conf. Indium Phosphide and Related Materials, Paris, France, 1993

Performance of behaviour of scattering mechanisms in time-scale domain against random noise for centimetre wave radar

T. Le-Tien and D.T. Nguyen

Indexing terms: Radar, Wavelet transforms, Scattering, Random noise

The behaviour of scattering mechanisms in the time-scale domain against random noise is presented for stepped frequency radar. The down range profile is obtained from the continuous wavelet transform (CWT) of the backscattered data. Local maxima detected corresponding to different noise levels confirm the invariant location and number of scattering centres in the range profile. They provide crucial information for automatic target recognition.

Introduction: Radar is a technique for detecting and measuring the location and characteristics of objects which reflect electromagnetic energy coming from an antenna system. The scattering mechanisms which describe the behaviour of objects to the incident waves can be separated into two major categories: namely dispersive and nondispersive scattering mechanisms. For nondispersive scattering such as corners, edges, or specular reflections, the local scattering features can be extracted from the local maxima of the target response in the time domain. The local maxima are located in the early time portion of the backscattered data and represent the highest energy concentration. Their appearances are commonly sharp in the time domain but spread out in the frequency domain, whereas for frequency dispersive scattering such as from some radar absorbing materials, ducts or inlets [1, 6], the corresponding impulse response will be spread in the time domain. The response of the frequency dispersive scattering gives information about the global features in the frequency domain rather than the local features in the time domain.

The inverse scattering problem of identifying objects in the far field using backscattered data has been of interest only on nondispersive scattering mechanisms which reflect most energy of the incident wave. It is well-known that at sufficiently high frequencies, the target can be approximated as a set of points on the object, namely isolated nondispersive scattering centres [2, 4]. The response of the object is assumed to be a sum of individual responses of scattering centres. The range profile for colocated transmit/receive antennae represents the scattering distribution of the object along the radial distance. It is obtained from the conversion of the backscattered data (frequency domain) into the range domain [5]. It provides information about the strength, location, and number of individual scattering centres. The crucial information about the object can be estimated from the local maxima of the response in the range profile. Some salient features extracted from this information can then be used as feature vectors for automatic target recognition.

In this Letter, the continuous wavelet transform is applied to backscattered data with various noise levels in the frequency domain. The wavelet transformed signal at a specific scale according to the number of frequency samples of the data is converted into the range domain to obtain the down range profile. The local maxima corresponding to scattering information are then detected against different random noise levels. They demonstrate how the scattering centres are sensitive to random noise.

Noisy range profile based on the CWT: The CWT of a signal $f(t)$ corresponding to $F(\omega)$ in frequency domain is defined [3] as

$$CWT(a, b) = (\sqrt{a}/2\pi) \int F(\omega)\Phi^*(a\omega)\exp(j\omega b)d\omega \quad (1)$$

where $\Phi(\omega)$ is the Fourier transform of the mother wavelet $\phi(t)$, a is the scale and b is the translating factor. Eqn. 1 is equivalent to filtering the signal $f(t)$ with the bandpass filter $\Phi(a\omega)$ whose bandwidth changes according to the scale a.

The signal $f(t)$ can be recovered from its CWT as follows:

$$f(t) = (1/C) \iint_\infty CWT(a, b)\phi_{a,b}(t)(1/a^2)dadb \quad (2)$$

where

$$C = \int_\infty (|\Phi(\omega)|^2/|\omega|)d\omega < \infty \quad (3)$$

is the admissibility condition of the CWT.

Let the incident electric field with the wave number $k = \omega/c$, where c is the speed of light, be

$$\vec{E}_{inc}(\vec{r}) = \vec{E}_o \exp(-jk\hat{z}.\vec{r}) \quad (4)$$

The backscattered field as measured by a linearly polarised receiving antenna can be expressed as [2, 4]

$$\vec{E}(k, z) \simeq \{\vec{E}_o(\exp(jkz)/z)\} \sum_{n=1}^{N} A_n(k) \exp(-j2k\hat{z}.\vec{r}_n) \quad (5)$$

where $\vec{r}_n$ is the location of nth scattering centre, $\hat{z}$ is the unit vector in z direction and $A_n(k)$ is a weighting coefficient determined by the scattering process. By normalising electric field for a given polarisation [4], eqn. 5 can be rewritten as

$$E(k) = \sum_{n=1}^{N} A_n(k) \exp(-j2kr_n) \quad (6)$$

In noisy environments, the backscattered data can be expressed as

$$E_n(k) = \sum_{n=1}^{N} A_n(k) \exp(-j2kr_n) + N(k) \quad (7)$$

where $N(k)$ is Gaussian noise corresponding to the kth sample.

The Morlet Wavelet in the normalised-frequency domain (wave number domain) is given by

$$\phi(k) = (\sqrt{\pi/\alpha}) \exp(-(k - k_o)^2/4\alpha) \quad (8)$$

where α and k_o are constants, $k = \omega/c$ is the normalised frequency in the continuous wavelet transform.

Then the CWT of eqn. 7 can be obtained as follows:

$$CWT(a, b) = \left(\sqrt{\frac{a}{4\alpha\pi}}\right) \int_\infty \sum_{n=1}^{N} A_n(k) \exp(-(ak - k_o)^2/4\alpha)$$
$$\times \exp(-jk(2r_n - b))dk + CWT_n(a, b) \quad (9)$$

where $CWT_n(a, b)$ is the CWT of $N(k)$. It can be seen from eqn. 9 that the amplitude of scattering centres vary according to the weighting coefficients, the value of a, and $CWT_n(a, b)$.

Simulation results: The backscattered data is obtained from 128 stepped frequency samples reflected from an aircraft model observed using a centimetre wave radar. The starting frequency and frequency step are chosen to be 10GHz and 20MHz, respectively. The Morlet mother wavelet has values of α and k_o equal to 0.5 and 2, respectively. The signal-to-noise ratio (SNR) is chosen to range from 6 to 30dB in the simulation. This is taken into account for every stepped frequency sample of the backscattered data.

Figs. 1 and 2 show the frequency responses of the model and their CWT-based range profile with the SNR of 6 and 12dB,

Suppressed Modal Interference Switches with Integrated Curved Amplifiers for Scaleable Photonic Crossconnects

Gregory A. Fish, Larry A. Coldren, *Fellow, IEEE,* and Stephen P. DenBaars

Abstract— A novel, compact optical switch that incorporates two 1 × 2 suppressed modal interference (SMI) switches with an integrated curved amplifier is demonstrated as a basic component for scaleable, lossless photonic crossconnects. The basic operation of the switch is described and measured on/off ratios of 22 dB (16 dB) are reported for the cross (bar) state with switching currents of less than 25 mA per section. Lossless switching was attained in the amplified cross state, while only 0.5 dB of excess loss was measured in the unamplified bar state. Cascading of these elements should lead to $N \times N$ lossless, optical crossconnects with crosstalk levels near 40 dB.

Index Terms—Integrated optoeletronics, optical switches.

I. INTRODUCTION

PHOTONIC space switches are very attractive components for future optical networks. Considerable effort and a variety of methods have been applied to meet their principle requirements, namely, low insertion, low crosstalk, wide optical bandwidth, polarization insensitivity, fast switching speed, scalability, and small size. Both passive and active semiconductor space switches in InGaAsP–InP have achieved very promising results and have nearly fulfilled all of the above requirements at a size of 4 × 4 [1]–[4]. An important remaining issue involves maintaining these levels of performance as the devices are scaled to larger and larger arrays. For example, in laser amplifier gate arrays the insertion loss and crosstalk scales with the array size. Clearly, large arrays will have difficulty maintaining 0-dB insertion loss and begin to suffer crosstalk penalties. While in passive switches, although the insertion loss and crosstalk does not increase as severely per additional channel, the physical size becomes such that larger arrays are not as tractable. Combining several smaller arrays into larger ones, while more feasible, is not as attractive as one monolithic device from a packaging perspective and has been predicted to have degraded performance in simulations [5].

To address these issues we report a novel compact optical switch with a scaleable architecture that still provides zero insertion loss and high contrast. As in the single-slip-structure (S^3) [6], we utilize a combination of switching elements and a

traveling-wave optical amplifier which has been shown to be very effective in providing lossless, low-crosstalk switching while maintaining scaleability [3].

The switching elements used in our design are novel and based on carrier injection induced changes in a modal interference coupler, called suppressed modal interference (SMI) switching, the details of which are previously published [8] and summarized below. To give a very compact basic element for a crossconnect, two SMI switching elements are integrated with a small radius (250 μm) curved amplifier to form a complete optically amplified suppressed modal interference switch (OASIS) illustrated in Fig. 1(a). As shown, the input and output waveguides are orthogonal for increased compactness and reduced crosstalk between crossing guides, a problem appearing in lower angle switch architectures [3], [4]. By combining 16 OASIS elements as shown in Fig. 1(b), a 4 × 4 crossconnect that occupies only a few square millimeters is achievable. This represents a significant reduction in size over existing crossconnects, and allows cascading of 4 × 4 or bigger blocks on chip with additional amplifiers to achieve even larger arrays while maintaining zero insertion loss.

II. SWITCH DESIGN AND FABRICATION

To gain an improvement over an amplifier gate array that simply uses splitters, the SMI switches used in the OASIS have very little excess loss in the bar state, yet switch enough power into the amplified path that the cross state loss can be zero. The principle by which the SMI switch operates is injecting carriers to modify the lateral index profile of a multimode interference (MMI) section to produce a different output at the end of the MMI section. In detail, a 3-μm-wide input ridge waveguide is coupled off center to a 6-μm-wide multimode interference section, as shown in Fig. 1(a). The interference section has two modes and is exactly one beat length long (150 μm, in this case) such that the input field, starting on the left-hand side of the MMI section is inverted at the output and appears on the right-hand side of the MMI where it couples into the 3-μm-wide bar state output waveguide. To switch to the cross state, current is injected on the left half of the MMI section modifiying the lateral index profile such that the higher order modes are cut off, suppressing the modal interference and the light is guided down the right half of the MMI section and into the curved cross state output waveguide. Some important aspects in the design of the switch involve tailoring the lateral index profile of the waveguides to have

(a)

(b)
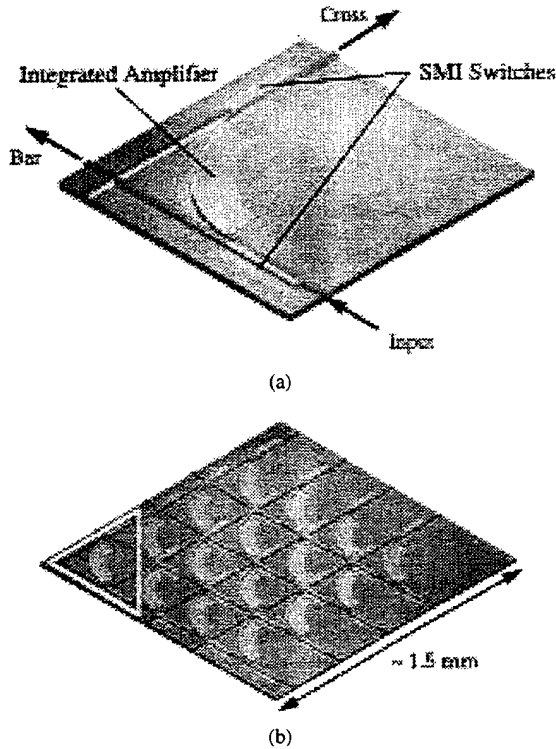
Fig. 1. (a) Schematic diagram of an OASIS element showing the integration of two SMI switches with a small radius curved amplifier. (b) By cascading 16 OASIS elements very compact 4 × 4 (<4 mm²) crossconnects can be achieved.

Fig. 2. Schematic diagram of the testing setup illustrating the monitored LED sources and lensed fiber used to test the switching response of an OASIS element consisting of two switches (S_1 and S_2) and a curved amplifier (A_1).

(a)

(b)
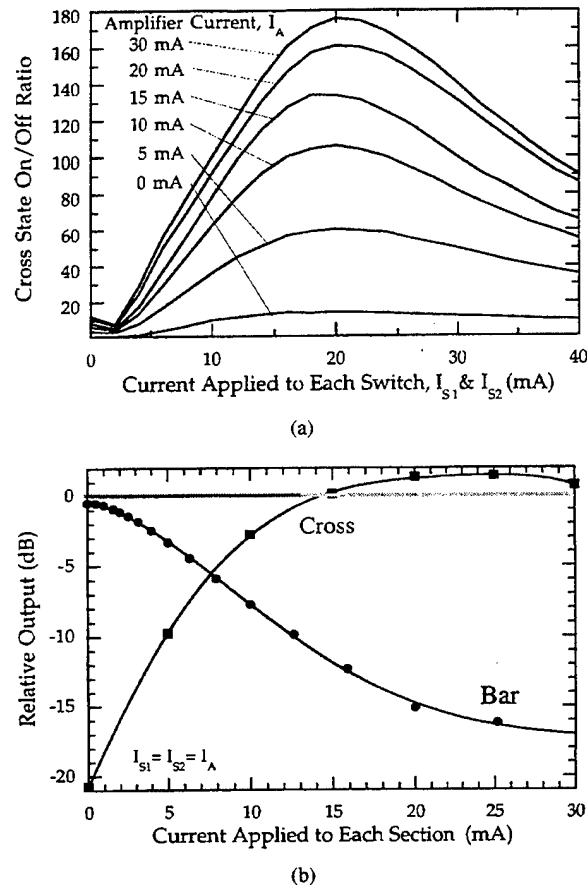
Fig. 3. (a) Cross-state output relative to that at zero bias as the current to both switches is increased at a given amplifier current level. (b) Cross and bar outputs relative to straight reference guides as current is applied simultaneously to each switch and the amplifier section.

high confinement of the mode, yet still be weakly guided enough to allow for switching with modest injection levels. We chose a lateral index contrast of 0.02 to satisfy this criteria. It is also important to confine the injected carriers to the left half of the MMI section when switching, so a series of H+ implants are performed to prevent conduction from the right to the left half of the MMI ridge.

Combining the SMI switches with a 250-μm radius curved amplifier is complicated by the different lateral index contrast required by the two elements. Switches must have small index contrasts to be effective (less than 0.03) while small radius bends require large index contrasts (greater than 0.06) to reduce bending loss. To solve this problem, we etched additional cladding material from the outside of the curve, as shown in Fig. 1(a).

Fabrication of the OASIS involves only two MOCVD growth steps in which a base structure with an offset MQW (four 1% compressive InGaAsP wells) active region grown on top of 0.35 μm, InGaAsP ($\lambda_g = 1.35$ μm, i.e., 1.35 Q) waveguides. The active region is removed in the passive sections of the device and the p-cladding and contact layers are regrown including a 1.1-Q stop etch layer (located 0.14 μm above the waveguide) to define the lateral index contrast (chosen to be about 0.02) of the passive waveguides. 3-μm-wide ridge waveguides are dry etched using CH$_4$–H$_2$–Ar followed by a wet H$_3$PO$_4$–HCl clean up etch to the stop etch layer, this gives a well-controlled uniform lateral waveguide contrast required for these type of devices [7]. Further etching on the outside of the curve section follows using Br–H$_3$PO$_4$–H$_2$O.

Finally, the devices are covered with SiN$_x$, metallized and proton implanted to isolate the various sections and define the unbiased half of the SMI switches.

III. DEVICE CHARACTERISTICS

On-chip MQW LED's ($\lambda = 1540$ nm) having the same layer structure as the curved amplifier were used as sources to test the switching characteristics of the OASIS. While monitoring the back side power, light from the front side of a LED was

sent through an OASIS element and collected at either the bar or cross state output with a lensed (radius 9 μm) single-mode optical fiber and a lock-in amplifier, as illustrated in Fig. 2. To evaluate the excess loss in the switch, several straight waveguides without switches were used to provide a reference level. Fig. 3(a) shows the performance of an OASIS at various levels of amplifier current as the current to injected into each SMI switches is increased. On–off ratios of nearly 23 dB are achieved with less than 25 mA of current injected into each of the sections. The reversal of the on–off ratio at switch currents higher than 20 mA is attributed to mode mismatch between the input guide and the modified modal interference region which was observed in near field images taken of the end of the SMI switch [8]. In Fig. 3(b) the bar- and cross-state powers are compared to reference waveguides showing that the OASIS has an excess loss of around 0.5 dB in the bar state and can achieve an "excess gain" of nearly 2 dB in the cross state with contrast ratios of 16 and 22 dB, respectively. When multiple OASIS elements are combined in a $N \times N$ crossconnect as shown in Fig. 1(a), output is taken only from the cross state, so these measured on–off ratios could be combined to give expected crosstalk levels near 40 dB for most nonbroadcasting switch configurations.

IV. CONCLUSION

We have presented the results of a novel 1×2 amplified switch (OASIS) where a contrast of over 22 dB has been achieved without loss in the cross state and only 0.5 dB of excess bar state loss. Orthogonal inputs and outputs should allow very compact, easily expandable crossconnects with reduced crosstalk to be created from multiple OASIS elements.

REFERENCES

[1] M. Renaud, J. F. Vinchant, A. Goutelle, B. Martin, G. Ripoche, M. Bachmann, P. Pagnod, and F. Gaborit, "Compact digital optical switches for low insertion loss large switch arrays on InP," in *Proc. 21st Eur. Conf. Optical Communications, Symp. Broadband Networks for Video and Multimedia Services,*, 1995, pp. 99–102.
[2] G. Wenger, M. Schienle, J. Bellermann, M. Heinbach, S. Eichinger, J. Muller, B. Acklin, L. Stoll, and G. Muller, "A completely packaged strictly nonblocking 8·8 optical matrix switch on InP/InPGaAsP," *J. Lightwave Technol.*, vol. 14, pp. 2332–2337, 1996.
[3] T. Kirihara, M. Ogawa, H. Inoue, H. Kodera, and K. Ishida, "Lossless and low-crosstalk characteristics in an InP-based 4*4 optical switch with integrated single-stage optical amplifiers," *IEEE Photon. Technol. Lett.*, vol. 6, pp. 218–221, 1994.
[4] W. van Berlo, M. Janson, L. Lundgren, A. C. Morner, J. Terlecki, M. Gustavsson, P. Granestrand, and P. Svensson, "Polarization-insensitive, monolithic 4*4 InGaAsP-InP laser amplifier gate switch matrix," *IEEE Photon. Technol. Lett.*, vol. 7, pp. 1291–1293, 1995.
[5] L. Gilner, "Analysis of input power dynamic ranges in two types of expanded semiconductor optical amplifier gate switch arrays," *IEEE Photon. Technol. Lett.*, vol. 8, pp. 536–538, 1996.
[6] H. Inoue, T. Kirihara, Y. Sasaki, and K. Ishida, "Carrier-injection type optical S/sup 3/switch with traveling-wave amplifier," *IEEE Photon. Technol. Lett.*, vol. 2, pp. 214–215, 1990.
[7] J. L. Peyre, A. Goutelle, P. Pagnod-Rossiaux, and J. F. Vinchant, "Improved fabrication of 4*4 polarization insensitive switch matrices on InP by introduction of an etch stop layer," in *Proc. 5th Int. Conf. Indium Phosphide and Related Materials*, 1993, pp. 84–87.
[8] G. A. Fish, S. P. DenBaars, L. A. Coldren, "Compact, InGaAsP/InP 1×2 optical switch based on carrier induced supression of modal interference" *Electron. Lett.*, vol. 33, pp. 1298–1299, 1997.

Compact, 4 × 4 InGaAsP–InP Optical Crossconnect with a Scaleable Architecture

Gregory A. Fish, Beck Mason, Larry A. Coldren, *Fellow, IEEE,* and Steven P. DenBaars

Abstract— An InP–InGaAsP 4 × 4 optical crossconnect occupying only 2 × 2 mm^2 was demonstrated by combining 16 1 × 2 optically amplified suppressed interference switches (OASIS) in a square array architecture. On/off ratios of 33 ± 4 dB were measured for a majority of these elements and fiber-to-fiber insertion loss of 3 dB was obtained using additional on-chip amplification stages.

Index Terms—Integrated optoelectronics, optical switches.

I. INTRODUCTION

INCREASINGLY, optical crossconnects are being proposed as the basis for various photonic packet switching nodes [1], [2]. Many of these strategies involve using the crossconnects to provide simultaneous packet routing and buffering of multiple input channels through the use of optical fiber delay lines. In addition to the typical optical switching requirements, (e.g., low crosstalk, low insertion loss, and high switching speed) these applications demand crossconnects with a large number of channels, as several buffering channels are usually needed to provide lossless packet routing for relatively few data channels [1].

Crossconnects based upon semiconductor optical amplifiers (SOA) gates are well suited for these applications, as they are compact and have demonstrated lossless, low crosstalk (−50 dB) switching, with speeds sufficient for cell routing (2 ns) [3]. Unfortunately, most SOA gate arrays to date use tree architectures where the loss per channel increases as N^2 (N being the number of channels), so it is unlikely these strategies can be scaled to significantly larger sizes. Combining optical switches with SOA's has been shown to be a very effective method in creating a more scaleable crossconnect which can have lower loss and crosstalk than a simple gate array [4]. Building upon this concept, we demonstrate a very compact 4 × 4 (2 × 2 mm^2) optical crossconnect using sixteen 1 × 2 optically amplified suppressed interference switches (OASIS) [5] elements as shown in Fig. 1(a). By arranging the sixteen elements in the square array architecture shown in Fig. 1(b), the average insertion loss reduces to roughly N times the excess loss of the optical switches [called the suppressed modal interference (SMI) switch] within an OASIS element, which can be made small (∼0.5 dB) [6].
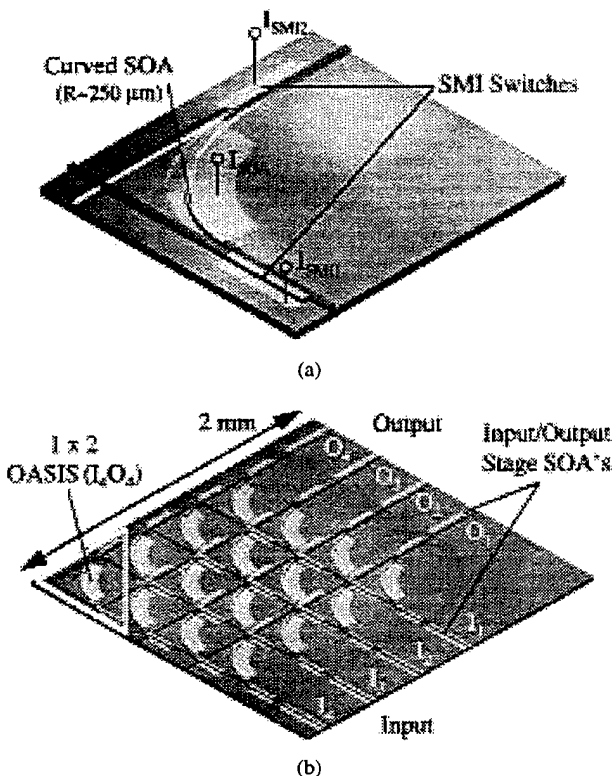
Fig. 1. (a) Schematic diagram of a 1 × 2 OASIS element illustrating the integration of a curved SOA with two SMI switches. (b) Sixteen 1 × 2 OASIS have been combined to form a very compact (2 × 2 mm^2) 4 × 4 optical crossconnect with orthogonal input and output waveguides. Input/output stage SOA's were integrated to help overcome fiber coupling losses.

II. SWITCH DESIGN AND FABRICATION

The details of the design of the SMI switches and their integration with a SOA to form the OASIS have been previously reported [5], [6]. The operation of the SMI switch can be summarized as follows. The input waveguide of the SMI switch is coupled to a modal interference region which is designed to image the input onto the straight bar state output waveguide, as shown in Fig. 1(a). By injecting current into the switching electrode, the width of modal interference section is effectively reduced, creating a singlemode waveguide which guides the light into the curved SOA located in the cross state output waveguide. The published measurements of the SMI switches have shown they can provide 16 dB (8 dB) contrast ratios for the bar (cross) state with an excess loss of 0.5 dB for the bar state and 3–4 dB (estimated) for the cross state. Adding the amplifier to the cross state improved its contrast to 22 dB with a net gain of 2 dB.
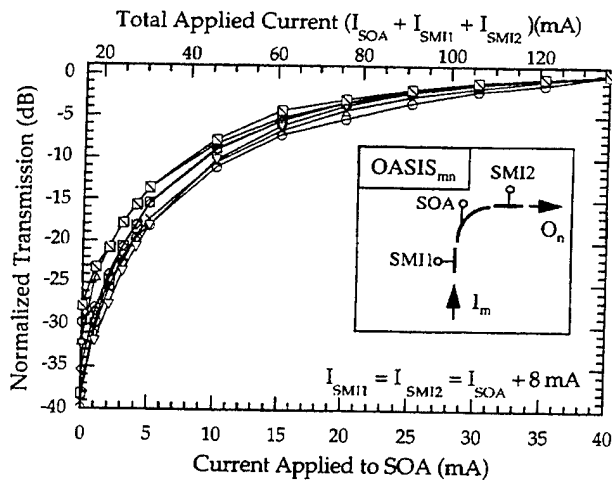
Fig. 2. On-chip measurements of the on/off ratios of a number of OASIS elements of the 4 × 4 crossconnect. The current to the SOA and two SMI switches is swept simultaneously from the off state to the on state. The off state of the SOA and the SMI switches was at 0 and 8 mA, respectively.

Fig. 3. Fiber-to-fiber transmission of I_2O_2 (input channel 2 to output channel 2) illustrating a -3-dB insertion loss, 39-dB on/off ratio, and -38-dB crosstalk contributions to the other channels. The input/output stage SOA's are biased at constant 60 mA for each channel.

Fabrication of the OASIS involves only two MOCVD growth steps in which a base structure with a MQW (four 1% compressive InGaAsP wells) active region grown on top of 0.35-μm-thick InGaAsP ($\lambda_g = 1.35$ μm, i.e., 1.35-Q) waveguides. The active region is removed in the passive sections of the device and the p-cladding and contact layers are regrown including a 1.1-Q stop etch layer (located 0.14 μm above the waveguide) to define the lateral index contrast (chosen to be about 0.02) of the passive waveguides and SMI switches. 3-μm-wide ridge waveguides are dry etched using $CH_4/H_2/Ar$ followed by a wet H_3PO_4/HCl clean up etch to the stop etch layer. This gives a well controlled uniform lateral waveguide contrast required for these type of devices. Further dry etching on the outside of the curved section increases the waveguide's lateral index contrast to reduce the bending losses that occur at this small radius (250 μm). Finally, the devices are covered with SiN_x, metallized and proton implanted to isolate the various sections and define the unbiased half of the SMI switches.

Fig. 4. Fiber to fiber transmission of I_4O_1 illustrating operation over a 45-nm wavelength span with an insertion loss within 3 dB of the minimum while maintaining at least a 39-dB on/off ratio throughout.

III. DEVICE CHARACTERISTICS

Prior to testing, a quarter-wavelength-thick SiO_x antire-flection coating was applied to the input and output facets of a 4 × 4 OASIS crossconnect. To initially test the on-chip performance of the device, the input optical amplifier of a particular channel is pumped as an LED and its emission is collected (using a 9-μm radius lensed optical fiber and a lock-in amplifier) from an orthogonal output channel after traversing through an OASIS element. Fig. 2 shows the mea-sured on/off ratio of several of the OASIS elements as the current to the SOA and the two SMI switches are increased simultaneously from the off state to the on state. The off state of the SMI switches in this array was at 8 mA, due to the narrowing of the waveguides during processing. Future processing adjustments will create SMI switches with zero bias off states, as originally designed. Measurements on eleven of the sixteen functioning OASIS (some were damaged during

testing) yielded an average on/off ratio of 33 ± 4 dB. On chip measurements of the crosstalk contributions of an input channel to undesired output channels were very similar to the off state of the given OASIS element indicating that the 90° crossing angle of input and output waveguides is effective at eliminating crosstalk at these junctions.

Fiber-to-fiber measurements were conducted using lensed fibers ($R \sim 9$ μm) and an external cavity tunable laser emitting at 1550 nm with a optical power of -20 dBm as the source. To help overcome fiber coupling losses (5–6 dB/facet) both input and output amplifiers of the measured channel were biased at a constant 60 mA throughout the measurements. Fig. 3 shows the fiber-to-fiber transmission of I_2O_2 (input channel 2 to output channel 2) indicating an insertion loss of 3 dB, a 39-dB on/off ratio, and -38-dB crosstalk contributions to the other output channels. The fiber-to-fiber transmission and on/off ratios were measured versus wavelength using these same conditions (input/output SOA biased at 60 mA) for channel I_4O_1, and are illustrated in Fig. 4. The insertion loss remains within 3 dB of the nominal minimum over a 45-nm range with an on/off ratio better than 38 dB.
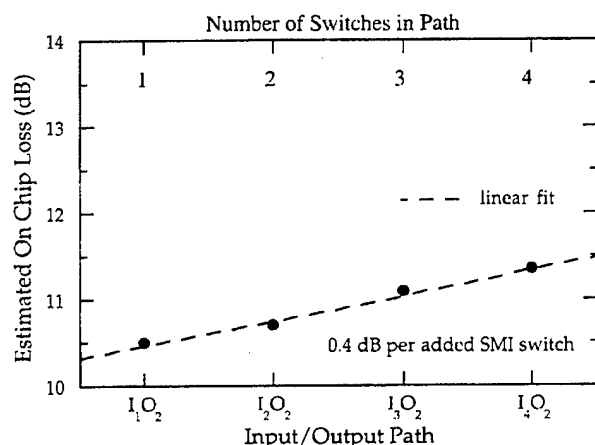
Fig. 5. Estimated on-chip loss of channels I_1O_2, I_2O_2, I_3O_2, and I_4O_2. The high value of loss was attributed to excess roughness in the curved SOA waveguide. The small increase in loss as additional SMI switches are encountered demonstrates the enhanced scalability of this design.

All the above measurements were carried out using the best case polarization (lowest insertion loss). The worst-case polarization at 1540 nm for channel I_4O_1 has an additional 14 dB of insertion loss, but maintains a 35 dB on off ratio. The origin of this polarization sensitivity is due (almost entirely) to the compressively strained MQW active regions, as BPM simulations of the SMI switches predict negligible polarization sensitivity. By incorporating polarization insensitive MQW active regions [7], [8], this problem can be eliminated.

Although good on/off ratio performance was obtained, the on-chip losses (estimated to be 10–15 dB) were much higher than expected based on past measurements of single 1×2 OASIS elements [5]. This loss was attributed to excess roughness in the curved waveguides that was not present in past 1×2 devices. Fig. 5 shows the estimated on-chip losses of various paths through the array without the use of the input/output amplifier stages. The loss is estimated by comparing the light emitted from the back of the input SOA (which is used as a source) to the light level at the output of the switch and subtracting the gain of the output SOA. Despite the large total loss of around 10 dB, the loss increases by only 0.4 dB for each

SMI switch in the path, confirming the enhanced scalability of this architecture.

IV. CONCLUSION

A very compact 4×4 optical crossconnect (2×2 mm^2) with a more scaleable architecture was demonstrated. On/off ratios of 33 ± 4 dB were measured for a majority of the channels. A fiber-to-fiber insertion loss of 3 dB was obtained with the use of additional input and output stage SOA's. Present high on-chip losses of 10 to 15 dB should be reduced with future improvements to the fabrication process; thus 0-dB insertion loss should also be obtainable. Despite this high total loss, paths including additional switches had only 0.4 dB per switch more loss, confirming the scaleable nature of this design.

REFERENCES

[1] L. E. Moser and P. M. Melliar-Smith, "Lossless packet switching with small buffers," *Proc. Inst. Elect. Eng.-Commun*, vol. 143, pp. 335–40, 1996.
[2] D. A. C. C. Jayasinghe, S. J. Madden, W. L. R. Perera, and P. L. Chu, "Cross-talk effects in fiber feedback buffer memories with single-substrate space switches," in *Proc. LEOS'96 9th Annu. Meet.*, 1996, pp. 320–321.
[3] R. Krahenbuhl, R. Kyburz, W. Vogt, M. Bachmann, T. Brenner, E. Gini, and H. Melchior, "Low-loss polarization-insensitive InP–InGaAsP optical space switches for fiber optical communication," *IEEE Photon. Technol. Lett.*, vol. 8, pp. 632–634, 1996.
[4] T. Kirihara, M. Ogawa, H. Inoue, H. Kodera, and K. Ishida, "Lossless and low-crosstalk characteristics in an InP-based 4×4 optical switch with integrated single-stage optical amplifiers," *IEEE Photon. Technol. Lett.*, vol. 6, pp. 218–21, 1994.
[5] G. A. Fish, L. A. Coldren, and S. P. DenBaars, "Suppressed modal interference switches with integrated curved amplifiers for scaleable photonic crossconnects," *IEEE Photon. Technol. Lett.*, vol. 10, pp. 230–232, 1998.
[6] _____, "Compact InGaAsP/InP 1*2 optical switch based on carrier induced suppression of modal interference," *Electron. Lett.*, vol. 33, pp. 1898–1900, 1997.
[7] A. E. Kelly, I. F. Lealman, L. J. Rivers, S. D. Perrin, and M. Silver, "Polarization insensitive, 25 dB gain semiconductor laser amplifier without antireflection coatings," *Electron. Lett.*, vol. 32, pp. 1835–1836, 1996.
[8] D. Sigogne, A. Ougazzaden, D. Meichenin, B. Mersali, A. Carenco, J. C. Simon, I. Valiente, C. Vassallo, and L. Billes, "1.55 μm polarization insensitive InGaAsP strained MQW optical amplifier integrated with short spot-size converters," *Electron. Lett.*, vol. 32, pp. 1403–1405, 1996.

Low-Loss Substrate-Removed (SURE) Optical Waveguides in GaAs–AlGaAs Epitaxial Layers Embedded in Organic Polymers

Steven R. Sakamoto, *Member, IEEE*, Cem Ozturk, Young Tae Byun, Jack Ko, and Nadir Dagli, *Member, IEEE*

Abstract— Low-loss single-mode semiconductor rib optical waveguides fabricated in GaAs–AlGaAs epitaxial layers are removed from GaAs substrates and bonded to transfer substrates using a benzocyclobutene organic polymer. Optical quality facets were obtained by cleaving through the transfer substrate. An average propagation loss of 0.39 and 0.48 dB/cm at 1.55 μm wavelength for TE and TM polarizations, respectively, were measured. This was on average 0.05 dB/cm greater than control guides fabricated in GaAs–AlGaAs epilayers on GaAs substrates with air as the top cladding. This demonstrates the feasibility of a process enabling semiconductor polymer integration and processing both sides of an epitaxial layer.

Index Terms—GaAs–AlGaAs materials/devices, optical device fabrication, optical waveguides, optoelectronic devices, organic polymer materials/devices.

I. INTRODUCTION

FOR ALL integrated optoelectronic devices functionality is provided by the epitaxial layer. In most cases a substrate is not desirable but has to be present for epitaxial growth and handling during processing. There are significant disadvantages associated with the presence of the substrate. All compound semiconductor substrates have high relative dielectric constants resulting in excessive capacitance. Combined with the high sheet resistance at microwave frequencies, substrates hinder the performance of high-speed devices such as modulators [1] and photodetectors [2]. Compound semiconductor substrates also have high thermal resistances resulting in inefficient removal of heat and thermal crosstalk. Therefore, removing the substrate eliminates these difficulties while introducing further advantages. After removing the substrate, the remaining epilayers can be bonded to transfer substrates using organic polymers resulting in semiconductor polymer integration. Hence, low propagation loss, low cost, and easier fiber pigtailing of polymer waveguides can be combined with the superior electrooptic properties of semi-conductor waveguides. Furthermore the ability to pattern and process both sides of an epilayer enables new and novel high performance devices. In this letter, we investigate the feasibility of removing high performance optical waveguides from their substrates and bonding them to transfer substrates using organic polymers. We also characterize these waveguides to see how they perform with the addition of new processing steps and materials. Such waveguides could be the basic building blocks of future high-performance optoelectronic devices.

II. WAVEGUIDE FABRICATION

Cross-sectional profiles of the two types of waveguides fabricated in this letter are shown in Fig. 1. Fig. 1(a) shows the substrate-removed (SURE) waveguides fabricated in gallium arsenide/aluminum gallium arsenide (GaAs–AlGaAs) epilayers and embedded in an organic polymer called benzocyclobutene (BCB). This polymer is known to produce easily fiber pigtailed high quality optical waveguides [3]. Fig. 1(b) shows a conventional waveguide fabricated using the same material structure. These types are used as control waveguides.

First, an appropriate unintentionally doped epitaxial layer was designed and grown by molecular beam epitaxy (MBE). The epitaxial layer shown in Fig. 1 is the same for both types of waveguides and is designed for optical waveguiding at 1.55 μm. It consists of a 2.05-μm-thick $Al_{0.3}Ga_{0.7}As$ bottom cladding to prevent the leakage of the guided mode of the conventional waveguide into the substrate, a 0.73-μm GaAs core layer, and a 0.8-μm $Al_{0.3}Ga_{0.7}As$ top cladding layer. There is also a 0.1-μm-thick AlAs layer between the bottom cladding and the substrate. This layer is used as an etch stop layer during substrate removal. Two separate samples were cleaved from this wafer. The first sample was used for the novel SURE waveguides and the other for the control waveguides.

On both epitaxial layers, straight 4-μm-wide waveguides were patterned with photoresist using standard lithography. The single-mode guides were then wet etched 5000 Å using a 10:1 1M citric acid:H_2O_2 solution. At this point the fabrication of the control sample was complete and it was cleaved, mounted and measured.

To continue with the fabrication of the SURE waveguides a mechanical grade semi-insulating GaAs transfer substrate was solvent cleaned, spin coated first with AP-8000 adhesion

(a)

(b)

Fig. 1. (a) Schematic cross-sectional profile of the SURE waveguide. (b) Conventional rib waveguide.

Fig. 2. SEM photograph of a cleaved facet of a waveguide in a substrate removed GaAs–AlGaAs epitaxial layer embedded in BCB.

promoter and then with 9-μm of Cyclotene 3022-57 BCB [4]. The rib waveguides fabricated earlier were spin coated with the same adhesion promoter and were placed epi side down on the BCB coated GaAs transfer substrate. Following this a full cure of BCB at 250 °C for one hour was performed in a nitrogen purged oven. When fully cured the BCB thin film acts as a glue that keeps the transfer substrate bonded to the substrate containing the epilayer and the fabricated waveguides. In the curing process there are no volatile by-products.[1] The entire stack was mounted on a glass microscope slide, GaAs transfer substrate down, using wax. This exposed the growth substrate only. To remove the growth substrate from the epi layer, a wet spray etch was performed. This consisted of a 30:1 mixture of H_2O_2:NH_4OH sprayed as a fine mist onto the substrate. This etch stops on the AlAs etch stop layer after the entire substrate is removed. After removing the substrate, the AlAs etch stop layer was removed in a 1:1 HF:H_2O solution. This left the thin epi layer with optical waveguides on it bonded to the GaAs transfer substrate via the BCB layer. At this stage the waveguides are as shown in Fig. 1(a). The remaining exposed epi layer was very smooth and uniform in spite of being on top

of the BCB. No cracks, waviness or bubbles were observed on epilayers as large as 2.5 cm by 2.5 cm. The planarity of the epi was good enough for another lithography. We were able to fabricate patterns as small as 2 μm and as long as 2 cm on such epilayers using conventional optical lithography. Part of the reason for this uniformity was the lack of volatile by-products during the curing of BCB and the very smooth and planar BCB surface obtained after spinning and curing.

Optical quality facets are needed to characterize the SURE waveguides. This is achieved by cleaving the GaAs transfer substrate together with the epilayer bonded to it. This requires the alignment of the crystal planes of the transfer substrate and the substrate containing the epilayer during bonding. We observed that BCB becomes less viscous at high temperatures during curing, causing the samples to move around on top of the transfer substrate coated with BCB. We took advantage of this by placing the samples on a 10° angled block after a rough alignment of the cleaved edges of both substrates. The substrate containing the epilayer was free to move during the cure so as to allow the cleaved edge of the substrate containing the epi layer to align to the cleaved edge of the BCB coated transfer substrate. For such low angles, the liquid tension near the edge prevented the sample from falling off of the BCB coated transfer substrate. This aligned the cleavage planes of the epilayer and the transfer substrate to a high enough precision. Finally, optical quality facets were made by cleaving. This was done by nicking the corner of the transfer substrate with a sharp blade, then by applying pressure to allow the cleave to propagate both laterally and vertically through the BCB and the epi layer. Despite cleaving through a ~500-μm-thick transfer substrate, 9 μm of BCB polymer, and the epi layer, good quality facets shown in Fig. 2 were obtained. It should be pointed out that this is not the only way to obtain optical quality facets. This approach is used to obtain high-quality facets easily in order to be able to carefully study the feasibility of the substrate removal process. Dry etching is another very viable possibility. This would allow any other substrate with good adhesion to BCB and resistance to substrate etching to be used. For cleaving, one can use other

(a)

(b)
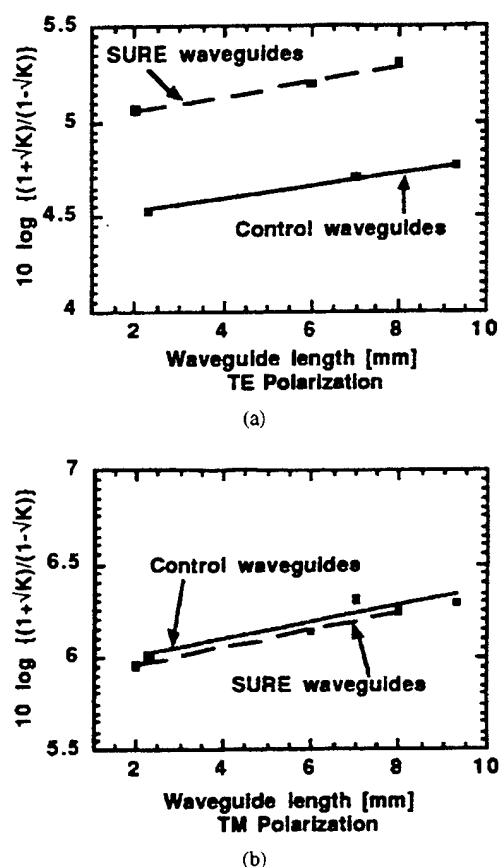
Fig. 3. $10 \log \{(1 + \sqrt{K})/(1 - \sqrt{K})\}$ as a function of different sample lengths for control and SURE waveguides for TE and TM polarizations. K is the ratio of the minima and maxima of the transmission through the waveguides when the input wavelength is changed slightly.

substrates that can be cleaved, even noncrystalline substrates that can be broken along a straight edges.

III. EXPERIMENTAL RESULTS

Both waveguide samples were mounted and characterized on an optical bench. The output of a fiber pigtailed 1.55-μm distributed-feedback (DFB) laser was coupled into the waveguides using cleaved fiber. The near-field pattern at the output was imaged on a vidicon camera using a microscope objective and a collimating lens. The image was displayed on a monitor. We observed the near-field mode patterns and measured the propagation loss of the waveguides. Both types of waveguides were single mode. The Fabry–Perot resonance technique and sequential cleaving were used to measure the propagation loss and facet reflectivity of the waveguides [4], [5]. The output power was detected using a Ge photodetector connected to an optical power meter. We varied the temperature of the DFB laser through an external thermoelectric temperature controller. This results in slight changes in the operating wavelength of the laser which in turn modifies the transmission through the Fabry–Perot cavity formed by the cleaved facets of the optical waveguides. Noting the ratio of the minima and maxima of this transmission,

K, and plotting $10 \log \{1 + \sqrt{K})/(1 - \sqrt{K})\}$ as function of different sample lengths, one can determine the propagation loss and facet reflectivity of the waveguide. Specifically, the slope of this plot is propagation loss in dB/length and the intercept is $10 \log(R^2)$, where R^2 is the facet power reflectivity. The experimental results are shown in Fig. 3.

Twenty waveguides with an initial length of 9 mm, cutback to 7 and 2 mm, were measured on the control sample. A linear fit to the measured data produced an average waveguide loss of 0.34 and 0.45 dB/cm for TE and TM polarized inputs, respectively. The initial length of the SURE waveguides was 8 mm, which were then cutback to 6 and 2 mm. The average TE and TM propagation loss for ten such waveguides was 0.39 and 0.48 dB/cm, respectively. On average, the loss of the SURE waveguides was 0.05 dB/cm higher than the control waveguides, which was well within the experimental error of the measured values. This shows that the propagation loss increase due to this novel process was marginal. The extrapolated facet reflectivity of the control waveguides were 0.36 and 0.25 for TE and TM polarizations, respectively. Corresponding values for SURE waveguides were 0.32 and 0.26. The slight variation again indicates overall good quality facets. No measurable variation was observed between the mode shapes of the two types of waveguides.

IV. CONCLUSION

We have successfully demonstrated the feasibility of substrate removal and bonding the remaining epilayer on transfer substrates using BCB in the fabrication of optoelectronic devices in the GaAs–AlGaAs material system. In particular, optical waveguides fabricated in epilayers removed from substrates and embedded in BCB had an average propagation loss of 0.39 dB/cm and 0.48 dB/cm at 1.55 μm for TE and TM polarizations respectively. This was only on average 0.05 dB/cm greater than control guides fabricated on GaAs substrates with air as the top cladding. The substrate removal process produced a smooth epi layer on which fine-line lithography was possible. This demonstrates the feasibility of processing both sides of an epilayer. Optical quality cleaved facets were also produced by aligning the crystal axis of the growth and transfer substrates during bonding. Presently, we are utilizing this novel process to fabricate low-voltage high-speed electrooptic modulators.

REFERENCES

[1] R. Spickermann, S. R. Sakamoto, M. G. Peters, and N. Dagli, "GaAs/AlGaAs traveling wave electro-optic modulator with an electrical bandwidth >40 GHz," Electron. Lett., vol. 32, no. 12, pp. 1095–1096, June 1996.
[2] A. R. Hawkins, T. E. Reynolds, D. R. England, D. I. Babic, M. J. Mondry, K. Struebel, and J. E. Bowers, "Silicon heterointerface photodetector," Appl. Phys. Lett., vol. 68, no. 26, pp. 26–28, June 1996.
[3] C. F. Kane and R. R. Krchnavek, "Benzocyclobutene optical waveguides," IEEE Photon. Technol. Lett., vol. 7, pp. 535–537, May 1995.
[4] R. G. Walker, H. E. Shephard, and R. R. Bradley, "Simple and accurate loss measurement technique for semiconductor optical waveguides," Electron. Lett., vol. 21, no. 50, pp. 581–583, 1985.
[5] Y. T. Byun, K. H. Park, S. H. Kim, S. S. Choi, and T. K. Lim, "Single-mode GaAs/AlGaAs W waveguides with a low propagation loss," Appl. Opt., vol. 35, no. 6, pp. 928–933, Feb. 20, 1996.

Femtosecond-rate space-to-time conversion

Dan Marom,* Dmitriy Panasenko, Pang-Chen Sun, and Yeshaiahu Fainman

*Department of Electrical and Computer Engineering, University of California, San Diego, 9500 Gilman Drive,
La Jolla, California 92093-0407*

A real-time spatial–temporal processor based on cascaded nonlinearities converts space-domain images to time-domain waveforms by the interaction of spectrally decomposed ultrashort pulses and spatially Fourier-transformed images carried by quasi-monochromatic light waves. We use four-wave mixing, achieved by cascaded second-order nonlinearities with type II noncollinear phase matching, for femtosecond-rate processing. We present a detailed analysis of the nonlinear mixing process with waves containing wide temporal and angular bandwidths. The wide bandwidths give rise to phase-mismatch terms in each process of the cascade. We define a complex spatial–temporal filter to characterize the effects of the phase-mismatch terms, modeling the deviations from the ideal system response. New experimental results that support our findings are presented. © 2000 Optical Society of America [S0740-3224(00)01410-7]

OCIS codes: 070.1170, 320.5540, 190.7110, 190.4380.

1. INTRODUCTION

Methods for ultrafast optical waveform synthesis (also referred to as pulse shaping) have been investigated for diverse applications in the natural sciences and engineering. Reviews of various pulse-shaping techniques can be found in Refs. 1 and 2. Based on linear-system theory, filtering the temporal-frequency components of an ultrashort optical pulse results in high-resolution waveform synthesis. The filtering can be achieved by spatially dispersing the frequency components in a spectral processing device (SPD), a free-space optical setup consisting of diffraction gratings and lenses, and inserting a spatial mask with the encoded amplitude and phase information. After the spectral decomposition wave[3] (SDW) has been filtered by the spatial mask, the frequency components are recomposed in the SPD to generate the synthesized temporal waveform. Early pulse-shaping experiments used prefabricated masks to filter the SDW,[4] which later were replaced by active-filtering devices such as spatial light modulators[5] and acousto-optic modulators.[6] This approach may not yield an adequate time response for adaptive control of the synthesized waveform needed for some applications, as it is limited by computation time, signal propagation delay, and modulator response time. Additionally, most modulators operate with either phase or amplitude modulation, requiring a complicated cascade of two devices for complete complex-amplitude filtering.[7] An alternative approach for generating the spectral filter uses *in situ* optical holographic recording of the interference of the spatial Fourier transform (FT) of a spatial image and a reference point source.[8,9] The recorded spatial-frequency information serves as a spectral filter for the SDW of an incident ultrashort reference pulse. The synthesized waveform is correlated to the spatial image used in the recording, resulting in a space-to-time converted image. This approach can be interpreted as a four-wave mixing process between two waves carrying spatial FT information and two SDW's with the temporal FT information, resulting in the exchange of information between the

spatial and temporal channels. The holographic recording medium's characteristics determine the performance of the information exchange between the four interacting waves. For example, using holographic film will require a long recording and processing time. Thick holograms formed in bulk photorefractive crystals yield high diffraction efficiency but also require a long recording time owing to slow electron mobility essential in buildup of a space-charge field[9] (from tens of microseconds to several minutes). Multiple-quantum-well (MQW) semiconductor photorefractives can perform holographic recording with a microsecond response time yet result in low diffraction efficiency owing to the short interaction length.[10,11]

For compatibility with the requirements of ultrafast applications such as high-speed optical communication with ultrashort pulses and quantum control of atomic and molecular vibrational states, the synthesized waveform must be updated, or modulated, at high rates with both amplitude and phase information. Such a femtosecond-rate response time can be provided only by parametric processes that involve bound-electron nonlinearities. Our space-to-time conversion scheme, first reported in Ref. 12, exchanges the information from a spatial image to a temporal waveform by a four-wave mixing process in a $\chi^{(2)}$ nonlinear crystal. The cascaded second-order nonlinearity (CSN) arrangement we are utilizing consists of a frequency-sum generation process followed by a frequency-difference generation process that satisfies the type II noncollinear phase-matching condition.[13] The nonlinear wave mixing occurs in the Fourier domain of the temporal and spatial channels (see Fig. 1). The frequency-sum process mixes the SDW of the input ultrashort pulse and the spatial FT of the spatial-image information illuminated with a quasi-monochromatic plane wave. The resultant intermediate wave is determined by the product of the complex amplitudes of the temporal and spatial FT fields. The cascaded frequency-difference process mixes the intermediate wave with the spatial FT of a point source illuminated by the same quasi-
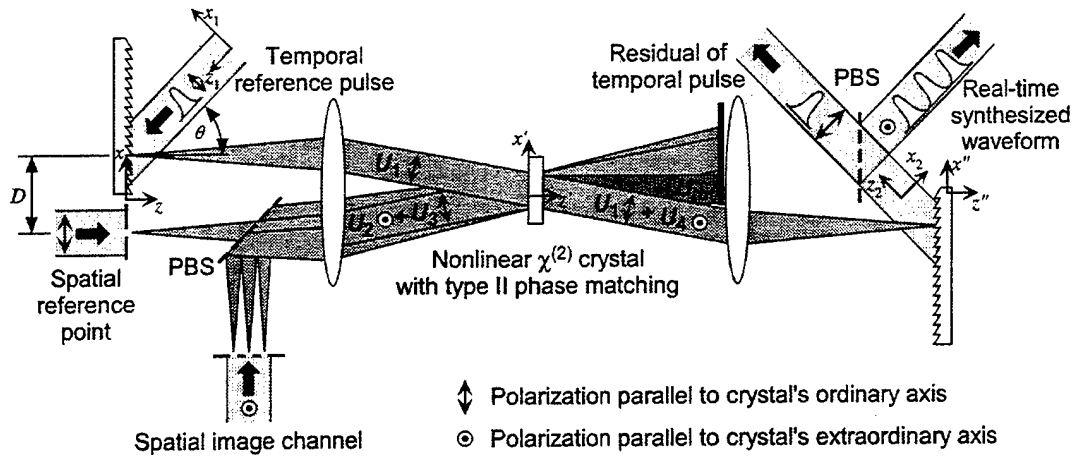
Fig. 1. Femtosecond-rate space-to-time conversion setup based on nonlinear wave mixing with noncollinear type II cascaded second-order nonlinearities in the Fourier-domain plane of the temporal and spatial channels. A frequency-sum process between waves U_1 and U_2 gives rise to the wave U_{int}. A frequency-difference process between the waves U_{int} and U_3 generates the desired output wave U_4.

monochromatic plane wave. The second spatial wave contains no information, in either the space or the time domain, and its function is to downconvert the carrier frequency of the intermediate wave generated by the first nonlinear process. The resultant field in the CSN process is the filtered SDW, which is recomposed to yield the synthesized output temporal waveform.

In this paper we describe and analyze in depth the space-to-time conversion process employing CSN, achieving a femtosecond response time and high conversion efficiency. In contrast to our initial analysis in the time domain,[12] a temporal-frequency-domain analysis is presented in Section 2, in which we develop the expression for the synthesized temporal waveform under the assumption of an ideal CSN process with perfect phase matching. In Section 3 we investigate the effects of the phase-mismatch terms in the cascaded processes and characterize them with a complex spatial–temporal transfer function. The derivation of the phase-mismatch terms' dependence on the temporal- and spatial-frequency bandwidths is deferred to the appendix. Experimental results verifying the findings of our analysis are presented in Section 4, illustrating the ability to convert both amplitude and phase information with this technique. We conclude with a summary and discussion in Section 5.

2. ANALYSIS OF THE SPACE-TO-TIME CONVERTER

The nonlinear interaction between the SDW of the input ultrashort pulse and the quasi-monochromatic waves at the Fourier plane of the optical setup is analyzed in this section under the following assumptions: (i) The nonlinear wave-mixing process is weak, such that the amplitude of the generated wave is proportional to the product of the complex amplitudes of the mixed waves. (ii) The interacting waves are phase matched for all temporal frequencies contained in the bandwidth of the short pulse and spatial frequencies of the spatial image. We defer the justification and discussion on the validity of this last assumption to Section 3, in which a complex filtering response function is introduced to characterize the effect of

phase mismatch on the conversion process. Since the space-to-time conversion occurs for one-dimensional spatial signals, the y-axis information is omitted. In the following, we first analyze the input temporal- and spatial-information channels, followed by an analysis of the CSN wave-mixing process giving rise to the synthesized temporal waveform.

A. Input Optical Channels

An ultrashort optical pulse, with a temporal envelope waveform of $p(t)$, is utilized at the input temporal channel of the SPD. The pulse is propagating in free space toward a diffraction grating, at an angle θ relative to the grating normal (see Fig. 1). The input ultrashort pulse is characterized in the propagating pulse's coordinate system (x_1, z_1) as

$$E_{pulse}(x_1, z_1; t) = w_1(x_1)p\left(t - t_0 - \frac{z_1}{c}\right)$$
$$\times \exp\left[j\left(\frac{\omega_0}{c}z_1 - \omega_0 t\right)\right], \quad (1)$$

where $w_1(\ )$ defines the transversal field distribution or the spatial mode of the pulse, c is the speed of light in vacuum, ω_0 is the center optical frequency, and t_0 is an arbitrary time reference. The pulse is propagating in the z_1 direction at a group velocity and a phase velocity of the speed of light. We assume the spatial mode size of the pulse is sufficiently large to ignore diffraction effects in the region of interest near the grating for the representation of Eq. (1) to be valid.

Since we are assuming that the nonlinear wave mixing of the space-to-time converter operates in the linear regime, the signal analysis may be performed in the temporal-frequency domain. We Fourier transform (FT) Eq. (1) to perform a temporal-frequency decomposition of the short pulse, yielding

$$\tilde{E}_{pulse}(x_1, z_1; \omega) = w_1(x_1)\exp\left(j\frac{\omega}{c}z_1\right)\tilde{p}(\omega - \omega_0)$$
$$\times \exp[j(\omega - \omega_0)t_0], \quad (2)$$

where the tilde overscript denotes a FT, e.g., $\tilde{p}(\omega)$ $= \int p(t)\exp(j\omega t)\mathrm{d}t$. We perform a rotation of the coordinate system from (x_1, z_1) to (x, z) for compatibility with the coordinate system of the SPD, yielding

$$\tilde{E}_{\text{pulse}}(x, z; \omega) = w_1(-z \sin\theta + x \cos\theta)$$
$$\times \exp\left[j\frac{\omega}{c}(-z \cos\theta - x \sin\theta)\right]$$
$$\times \tilde{p}(\omega - \omega_0)\exp[j(\omega - \omega_0)t_0]. \quad (3)$$

To find the incident field on the input grating of the SPD, the field of Eq. (3) is evaluated at $z = 0$. The effect of the grating diffraction can be modeled by adding the grating momentum, k_g, in the x direction to the k vector that characterizes the propagation direction of the wave, resulting in

$$\tilde{E}_{\text{input}}(x, 0; \omega) = w_1(x \cos\theta)\exp\left[-j\left(\frac{\omega}{c}\sin\theta - k_g\right)x\right]$$
$$\times \tilde{p}(\omega - \omega_0)\exp[j(\omega - \omega_0)t_0]. \quad (4)$$

The grating momentum, k_g, and the incidence angle, θ, are chosen such that the center frequency ω_0 will diffract in the direction of the optical axis of the system. Setting $\omega_0 \sin\theta/c = k_g$ and substituting the grating's k vector, $k_g = 2\pi/\Lambda$, where Λ is the grating period, yields $\sin\theta = \lambda_0/\Lambda \equiv \alpha$, where λ_0 is the center wavelength. To further simplify the notation, we define a new spatial-aperture function such that $w(x) = w_1(x \cos\theta)$. Without loss of generality we also shift the input aperture of the beam from the optical axis of the system by $D/2$. This is done to satisfy the noncollinear beam-propagation requirement in the Fourier plane of the SPD for phase matching in the CSN process. The input temporal-channel field to the optical processor, u_{tc1}, is therefore characterized by

$$\tilde{u}_{\text{tc1}}(x; \omega) = w\left(x - \frac{D}{2}\right)\exp\left[-j(\omega - \omega_0)\frac{\alpha x}{c}\right]$$
$$\times \tilde{p}(\omega - \omega_0)\exp[j(\omega - \omega_0)t_0]. \quad (5)$$

We may inverse FT Eq. (5) to generate the input signal in the time domain, yielding

$$u_{\text{tc1}}(x; t) = w\left(x - \frac{D}{2}\right)p\left(t - t_0 + \frac{\alpha x}{c}\right)\exp(-j\omega_0 t).$$
$$(6)$$

Equation (6) describes the short pulse scanning across the fixed aperture at a velocity of $-c/\alpha$ in the x direction. For convenience we may wish to set the time-delay parameter such that the traveling pulse is at the center of the aperture at $t = 0$. This is achieved by setting $t_0 = \alpha D/2c$.

The temporal-channel field of Eq. (5) is spatially Fourier transformed by a lens of focal length f, yielding the SDW U_1 of the short pulse,

$$U_1(x'; \omega) = \tilde{p}(\omega - \omega_0)\exp[j(\omega - \omega_0)t_0]$$
$$\times \int_{-\infty}^{\infty} w\left(x - \frac{D}{2}\right)\exp\left[-j(\omega - \omega_0)\frac{\alpha x}{c}\right]$$
$$\times \exp\left(-j2\pi\frac{xx'}{\lambda f}\right)\mathrm{d}x, \quad (7)$$

where we defer solving this Fourier integral to the nonlinear wave-mixing analysis of Section 3. The two spatial channels, one containing the encoding information and the second a point source, are modeled next.

A mask containing spatial-domain information is placed in the input plane of the processor, alongside the diffraction grating used for the input temporal channel. The mask is shifted from the optical axis by $-D/2$ to satisfy the requirement of noncollinear beam propagation in the Fourier plane of the SPD. The information mask of the spatial channel is illuminated with a quasi-monochromatic light source at center frequency ω_1. The first input spatial channel of the processor, u_{sc1}, can be expressed as

$$u_{\text{sc1}}(x, z = 0; t) = m\left(x + \frac{D}{2}\right)\exp(-j\omega_1 t), \quad (8)$$

where $m(x)$ is the spatial-information mask. The first input spatial-channel field is spatially Fourier transformed by the lens, yielding the field U_2, which we express in the temporal-frequency domain by taking the temporal FT, generating

$$U_2(x'; \omega) = \delta(\omega - \omega_1)\int_{-\infty}^{\infty} m\left(x + \frac{D}{2}\right)$$
$$\times \exp\left(-j2\pi\frac{xx'}{\lambda_1 f}\right)\mathrm{d}x, \quad (9)$$

where $\delta(\ )$ is the Dirac delta function. The spatial wave contains no temporal-frequency bandwidth owing to our illumination with a quasi-monochromatic light source.

The second spatial channel consists of a point source at the input plane that is illuminated by the same quasi-monochromatic light source as the first spatial channel. The point source is shifted from the optical axis by $-D/2$, as the first spatial channel has been. A polarization-selective beam splitter (see PBS in Fig. 1) is used for efficient superposition of the two spatial channels necessary for the wave-mixing process. The second input spatial-channel field to the processor, u_{sc2}, can be expressed as

$$u_{\text{sc2}}(x; t) = \delta\left(x + \frac{D}{2}\right)\exp(-j\omega_1 t). \quad (10)$$

The second input spatial-channel field is also spatially Fourier transformed by the lens, yielding the field in the Fourier plane U_3, expressed in the temporal-frequency domain as

$$U_3(x';\ \omega) = \delta(\omega - \omega_1)\int_{-\infty}^{\infty}\delta\left(x + \frac{D}{2}\right)$$

$$\times \exp\left(-j2\pi\frac{xx'}{\lambda_1 f}\right)\mathrm{d}x. \qquad (11)$$

We next examine the space–time conversion process by nonlinear wave mixing the three waves defined in Eqs. (7), (9), and (11).

B. Four-Wave Mixing by the Cascaded Second-Order Nonlinearity Process

A nonlinear crystal exhibiting a large nonlinear susceptibility $\chi^{(2)}$ is placed at the Fourier plane of the SPD (see Fig. 1). The two optical waves, U_1 and U_2, from the input temporal channel and the first spatial channel interact within the crystal, giving rise to an intermediate wave U_{int} in a frequency-sum process. The type II noncollinear phase-matching condition is satisfied by (i) adjusting the polarization directions of the temporal and spatial channels to coincide with the crystal's ordinary and extraordinary directions, respectively, and (ii) setting the interacting input waves to propagate noncollinearly. The second condition is satisfied by the spatial separation of the input channels, resulting in a propagation-direction-difference angle of D/f between U_1 and U_2. The complex amplitude of the generated intermediate wave is proportional to the nonlinear polarization arising from the two fundamental waves, yielding

$$U_{\mathrm{int}}(x';\ \omega) \propto \chi_{\mathrm{eff}}^{(2)}\int_{-\infty}^{\infty}U_1(x';\ \omega - \Omega)U_2(x';\ \Omega)\mathrm{d}\Omega$$

$$= \chi_{\mathrm{eff}}^{(2)}U_1(x';\ \omega - \omega_1)U_2(x';\ \omega_1), \qquad (12)$$

where $\chi_{\mathrm{eff}}^{(2)}$ is the effective nonlinear-susceptibility coefficient at the propagation directions of the interacting waves, and we assume it to be independent of ω in the temporal-frequency bandwidth of interest. The convolution integral describing the nonlinear polarization is trivial to solve since U_2 has no temporal-frequency bandwidth. The intermediate wave is therefore shifted up in frequency by ω_1, such that U_{int} is oscillating at a center frequency of $\omega_0 + \omega_1$ and is polarized in the extraordinary direction owing to the type II interaction.

Next, we consider the interaction of the third wave U_3 with the other waves in the nonlinear crystal. Since the crystal exhibits type II phase matching, there is no interaction between the wave from the temporal channel U_1 and the wave from the second spatial channel U_3, as they are both polarized in the ordinary-axis direction of the crystal. The collinear waves from the two spatial channels produce a second-harmonic wave, but it is of no interest for our study of the spatial–temporal processor. The signal of interest is generated from the interaction of the wave from the second spatial channel U_3 and the intermediate wave U_{int} generated in the frequency-sum process. These two waves are orthogonally polarized and satisfy the noncollinear phase-matching condition for a frequency-difference generation process. The noncollinear phase-matching condition is automatically satisfied because U_2 and U_3 have the same optical frequency and

copropagate. The interaction of U_3 and U_{int} gives rise to a fourth wave U_4 at the output of the nonlinear crystal, which is our signal of interest, given by

$$U_4(x';\ \omega) \propto \chi_{\mathrm{eff}}^{(2)}\int_{-\infty}^{\infty}U_{\mathrm{int}}(x';\ \omega + \Omega)U_3^*(x';\ \Omega)\mathrm{d}\Omega$$

$$= \chi_{\mathrm{eff}}^{(2)}U_{\mathrm{int}}(x';\ \omega + \omega_1)U_3^*(x';\ \omega_1)$$

$$= (\chi_{\mathrm{eff}}^{(2)})^2 U_1(x';\ \omega)U_2(x';\ \omega_1)U_3^*(x';\ \omega_1). \qquad (13)$$

The nonlinear polarization has the form of a correlation integral in the frequency-difference process. This integral is again trivial to solve, as the second spatial channel is also quasimonochromatic. The output wave is equivalent to a four-wave mixing process achieved by cascaded second-order nonlinearities. The resultant wave, U_4, is the SDW of the synthesized waveform with center frequency ω_0, generated by filtering the input SDW U_1 by a spatially modulated wave. It is copropagating with U_1 and polarized in the extraordinary direction (as U_{int} is extraordinary and U_3 is ordinary). Polarization optics may be used to separate the copropagating waves U_1 and U_4 (see Fig. 1).

The generated field U_4 is spatially Fourier transformed by a lens of focal length f, yielding the optical field on the output diffraction grating, given by

$$u_{tc2}(x'';\ \omega)$$

$$= \int_{x'} U_4(x';\ \omega)\exp\left(-j\frac{x'x''}{\lambda f}\right)\mathrm{d}x'$$

$$\propto \bar{p}(\omega - \omega_0)\exp[j(\omega - \omega_0)t_0]$$

$$\times \int_{x_1} w\left(x_1 - \frac{D}{2}\right)\exp\left[-j(\omega - \omega_0)\frac{\alpha x_1}{c}\right]$$

$$\times \int_{x_2} m\left(x_2 + \frac{D}{2}\right)\int_{x_3}\delta\left(x_3 + \frac{D}{2}\right)$$

$$\times \int_{x'}\exp\left[-j2\pi x'\left(\frac{x''}{\lambda f} + \frac{x_1}{\lambda f} + \frac{x_2}{\lambda_1 f} - \frac{x_3}{\lambda_1 f}\right)\right]$$

$$\times \mathrm{d}x'\mathrm{d}x_1\mathrm{d}x_2\mathrm{d}x_3. \qquad (14)$$

Integrating over the variables x', x_2, and x_3 yields

$$u_{tc2}(x'';\ \omega) = \bar{p}(\omega - \omega_0)\exp[j(\omega - \omega_0)t_0]$$

$$\times \int_{x_1} w\left(x_1 - \frac{D}{2}\right)m\left[-\frac{\lambda_1}{\lambda}(x'' + x_1)\right]$$

$$\times \exp\left[-j(\omega - \omega_0)\frac{\alpha x_1}{c}\right]\mathrm{d}x_1. \qquad (15)$$

Assuming $\Delta\lambda \ll \lambda_0$ for typical ultrashort pulses, we can also eliminate the wavelength dependence in the encoding mask by replacing λ with λ_0. It is possible to conduct the analysis without this assumption, resulting in weakly chirped output signals.[14] We next perform a change of variable by defining a new integration variable, τ, such that $x'' + x_1 = -c\tau/\alpha$. The resultant field on the grating is given by

$$u_{tc2}(x''; \omega) = \tilde{p}(\omega - \omega_0)\exp[j(\omega - \omega_0)t_0]$$

$$\times \exp\left[j(\omega - \omega_0)\frac{\alpha x''}{c}\right]$$

$$\times \int_{\tau} w\left(-\frac{c}{\alpha}\tau - x'' - \frac{D}{2}\right)m\left(\frac{\lambda_1}{\lambda_0}\frac{c}{\alpha}\tau\right)$$

$$\times \exp[j(\omega - \omega_0)\tau]\mathrm{d}\tau. \qquad (16)$$

The effect of diffraction from the output grating of the SPD is introduced into Eq. (16), yielding

$$u_{\text{out1}}(x''; \omega) = \tilde{p}(\omega - \omega_0)\exp[j(\omega - \omega_0)t_0]$$

$$\times \exp\left\{j\left[(\omega - \omega_0)\frac{\alpha}{c} + k_g\right]x''\right\}$$

$$\times \int_{\tau} w\left(-\frac{c}{\alpha}\tau - x'' - \frac{D}{2}\right)m\left(\frac{\lambda_1}{\lambda_0}\frac{c}{\alpha}\tau\right)$$

$$\times \exp[j(\omega - \omega_0)\tau]\mathrm{d}\tau. \qquad (17)$$

The momentum of the diffraction grating, $k_g = \alpha\omega_0/c$, cancels the angular-dispersion term of the output field, such that all the frequency components of the short pulse copropagate at an angle θ relative to the optical axis. To propagate away from the grating plane, we reintroduce the longitudinal dependence as appears in Eq. (3) [using the local z'' coordinate (see Fig. 1) and neglecting a constant phase factor from the shift from z to z'']. We also replace the aperture function $w(\ )$ by the original spatial-mode function of the input waveform, $w_1(\ )$ [see Eq. (4)]. Additionally, we eliminate the $D/2$ shift in the pupil function, which was introduced to satisfy the phase-matching condition in the Fourier plane of the processor, yielding

$$u_{\text{out1}}(x'', z'', \omega) = \tilde{p}(\omega - \omega_0)\exp[j(\omega - \omega_0)t_0]$$

$$\times \exp\left[j\frac{\omega}{c}(x''\sin\theta - z''\cos\theta)\right]$$

$$\times \int_{\tau} w_1\left(-x''\cos\theta - z''\sin\theta\right.$$

$$\left. - \frac{c}{\alpha}\tau\cos\theta\right)m\left(\frac{\lambda_1}{\lambda_0}\frac{c}{\alpha}\tau\right)$$

$$\times \exp[j(\omega - \omega_0)\tau]\mathrm{d}\tau. \qquad (18)$$

We perform a rotation of coordinate systems from the optical system's (x'', z'') to that of the output pulse (x_2, z_2) (see Fig. 1) and take the inverse temporal FT to get the output in space–time coordinates,

$$E_{\text{out}}(x_2, z_2; t) = \exp\left[j\left(\frac{\omega_0}{c}z_2 - \omega_0 t\right)\right]$$

$$\times \int_{\tau} w_1\left(-x_2 - \frac{c}{\alpha}\tau\cos\theta\right)m\left(\frac{\lambda_1}{\lambda_0}\frac{c}{\alpha}\tau\right)$$

$$\times p\left(t - t_0 - \frac{z_2}{c} - \tau\right)\mathrm{d}\tau. \qquad (19)$$

Equation (19) describes the output temporal pulse as an integral that mixes the information from the input temporal-pulse structure, the spatially encoded mask, and the spatial-aperture function. This type of association between the spatial and temporal characteristics has been shown for other cases of ultrafast-waveform processing.[4,15,16] When the beam size of the input short-pulse signal is very narrow, the desired functionality will not be achieved. Therefore in most practical cases of interest we operate the SPD in the high-resolution limit. In this case, the spatial-mode extent (or, more precisely, time-of-flight duration) $w_1(c\tau\cos\theta/\alpha)$ is much longer than the duration of the ultrashort pulse $p(\tau)$. Thus the integral can be approximated by simply evaluating the input pupil at $\tau = t - t_0 - z_2/c$, which is the center coordinate of the short pulse $p(t)$, and taking it out of the integral, yielding

$$E_{\text{out}}(x_2, z_2; t) \cong \exp\left[j\left(\frac{\omega_0}{c}z_2 - \omega_0 t\right)\right]$$

$$\times w_1\left[-x_2 - \frac{c}{\alpha}\cos\theta\left(t - t_0 - \frac{z_2}{c}\right)\right]$$

$$\times y\left(t - t_0 - \frac{z_2}{c}\right), \qquad (20)$$

where $y(t)$ is defined by the convolution of the input pulse and a time-scaled encoding mask, such that

$$y(t) \equiv \int_{\tau} m\left(\frac{\lambda_1}{\lambda_0}\frac{c}{\alpha}\tau\right)p(t - \tau)\mathrm{d}\tau = m\left(\frac{\lambda_1}{\lambda_0}\frac{c}{\alpha}t\right) \otimes p(t). \qquad (21)$$

Equation (20) describes an ultrafast waveform propagating in free space in the z_2 direction. The temporal characteristic of the output waveform, $y(t)$, is determined by the convolution operation of Eq. (21). The spatial mode of the output waveform is now space–time dependent, as is characteristic in filtering experiments of spatially dispersed temporal-frequency components.[17,18] This dependence travels along with the output waveform and represents a linear skew of the spatial mode relative to the time position of the output waveform $y(t)$. Thus there may be variations of the observed waveform at different spatial locations, a phenomenon that may influence point processes such as detection, spatial filtering, and coupling of the output signal into a single-mode fiber. We next analyze the conversion process in the nonlinear crystal, taking into account the effect of the phase-mismatch terms of the CSN.

3. CASCADED SPATIAL–TEMPORAL WAVE MIXING

The real-time spatial–temporal wave mixing is performed by cascaded femtosecond-rate parametric interactions in a crystal exhibiting a strong $\chi^{(2)}$ coefficient. The CSN process uses a combination of frequency upconversions and frequency downconversions and has to satisfy the conditions of energy and momentum conservation for effective energy transfer. Owing to the broad temporal bandwidth of ultrashort pulses and the broad angular

bandwidth of the spatial-information channel, it will be practically impossible to satisfy the phase-matching requirement necessary to achieve high conversion efficiency. Therefore nonuniform signal conversion across the temporal and spatial bandwidths will be observed, as phase matching cannot be supported in every situation. In this section we focus on the analysis of the nonlinear conversion process in the crystal.

To simplify the analysis, we assume that the generated waves in the three-wave mixing processes of the cascade are operating in the linear-conversion regime (i.e., weak interaction leading to nondepleting fundamental waves). The linear interaction allows us to decompose the waves to their temporal- and spatial-frequency domains, to treat each frequency component individually, and to integrate over the temporal and spatial bandwidths to get the output waveform. By decomposing the waves, we may use the monochromatic plane-wave solution of the wave-mixing process. The plane-wave solution will be valid as long as the nonlinear crystal is within the confocal parameter of the SDW. Since we are interested in high-resolution processing, which has a short confocal parameter, the allowable crystal length will be limited, thereby reducing the conversion efficiency. In general, there will be a trade-off between the resolution and the conversion efficiency, which is not within the scope of this study. We express the spatially and temporally decomposed input fields inside the nonlinear crystal, followed by a solution to the coupled-wave equations under the nondepleting-pump approximation. We calculate the phase-mismatch terms in the appendix.

A. Decomposed Temporal and Spatial Fields Inside the Nonlinear Birefringent Crystal

The spectrally decomposed field from the input temporal channel is found by evaluating the Fourier integral of Eq. (7), yielding

$$U_1(x';\ \omega) = \bar{p}(\omega - \omega_0)\bar{w}\left\{\frac{\alpha}{2\pi c}\left[\frac{\omega x'}{\alpha f} + (\omega - \omega_0)\right]\right\}$$
$$\times \exp\left(-j\frac{2\pi}{\lambda}\frac{D}{2f}x'\right)$$
$$\times \exp\left[-j(\omega - \omega_0)\frac{\alpha D}{2c}\right], \qquad (22)$$

where the spatial FT of the input-pupil function, $\bar{w}(\ )$, has mixed space- and temporal-frequency variables, characterizing the spatial dispersion, and we use $t_0 = \alpha D/2c$. The spatial width of $\bar{w}$ also defines the confocal parameter, which limits our crystal length. The spatial linear phase term in Eq. (22) determines the propagation direction, owing to the spatial shift of the input pupil by $D/2$. We denote the angle between the z axis and the k vector of the propagating wave as $\theta_1 = -D/2f$, using the paraxial approximation. The SDW is incident upon the nonlinear crystal in the FT plane of the lens. At the crystal interface, located at $z' = 0$ (see Fig. 1), the wave is refracted into the crystal in accordance to Snell's law. The SDW in the crystal, when ne-

glecting the Fresnel reflection at the boundary and accounting for field attenuation in a higher-index material, can be expressed as

$$\hat{U}_1(x';\ \omega) = \frac{\bar{p}(\omega - \omega_0)}{\sqrt{n_o^{(\omega)}}}\bar{w}\left\{\frac{\alpha}{2\pi c}\left[\frac{\omega x'}{\alpha f} + (\omega - \omega_0)\right]\right\}$$
$$\times \exp\left(-j\frac{2\pi}{\hat{\lambda}}\frac{D}{2n_o^{(\omega)}f}x'\right)$$
$$\times \exp\left[-j(\omega - \omega_0)\frac{\alpha D}{2c}\right], \qquad (23)$$

where $n_o^{(\omega)}$ is the refractive index for ordinary-polarized light at frequency ω, and the hat overscript denotes variables inside the crystal (e.g., $\hat{\lambda} = \lambda/n_o^{(\omega)}$). Note that the linear phase terms of Eqs. (22) and (23) are equal in magnitude, owing to the conservation of momentum in the x' direction (i.e., kinematic condition). The propagation direction inside the crystal is frequency dependent, owing to the dispersive nature of the refractive index of the crystal.

The mask containing the spatial-domain information generates the field U_2 in the FT plane, found by evaluating the Fourier integral of Eq. (9). For the purpose of this analysis we model the spatial-information channel by $\delta(x - \xi)$, a Dirac delta function shifted from the center of the information mask by the parameter ξ. The synthesized waveform from an arbitrary mask $m(x)$ is calculated by multiplying the delta-function response by $m(\xi)$ and integrating over the parameter ξ (yielding the convolution integral). By use of the delta-function model the first input spatial channel generates an extraordinary-polarized plane wave with a single spatial frequency,

$$U_2(x',\ \xi;\ \omega_1) = \exp\left[j\frac{2\pi}{\lambda_1}\left(\frac{D}{2f} - \frac{\xi}{f}\right)x'\right]. \qquad (24)$$

The angle between the z' axis and the propagation direction of this wave is denoted by $\theta_2(\xi) = (D/2 - \xi)/f$. The refracted field in the crystal, $\hat{U}_2$, preserves the momentum in the x' direction and attenuates the field by the extraordinary refractive index. Evaluating the propagation angle and k vector is complicated by the refractive-index dependence on the propagation direction and is performed in the appendix.

The second spatial channel, consisting of the delta function at $x = -D/2$, generates an ordinary-polarized plane wave in the Fourier plane of the processor. Evaluating Eq. (11) and accounting for the refraction into the crystal yields

$$\hat{U}_3(x';\ \omega_1) = \frac{1}{\sqrt{n_o^{(\omega_1)}}}\exp\left(j\frac{2\pi}{\hat{\lambda}_1}\frac{D}{2n_o^{(\omega_1)}f}x'\right), \qquad (25)$$

where $n_o^{(\omega_1)}$ is the ordinary refractive index at frequency ω_1. The angle between the z' axis and the propagation direction of the field before refraction is denoted by $\theta_3 = D/2f$. The nonlinear interaction of the input fields $\hat{U}_1$, $\hat{U}_2$, and $\hat{U}_3$ is analyzed next.

B. Solution of Coupled-Wave Equations Characterizing Cascaded Processes

The general solution to the coupled-mode equations governing noncollinear three-wave processes can be very complex.[19] When we limit the analysis to weak interactions with nondepleting input waves and slowly varying functions in space and time (which holds for the SDW), an analytic solution to the process is possible. Owing to the nondepleting-wave approximation, only two differential equations remain, which describe the evolution of the intermediate wave, $\hat{U}_{\text{int}}$, generated by a frequency-sum process, and the resultant output wave, $\hat{U}_4$, generated by a frequency-difference process. Geometrical factors are introduced to the coupled equations owing to the noncollinear arrangement (where we ignore the effect of the walk-off angle between the k vector and the Poynting vector in the propagation of extraordinary-polarized fields in an anisotropic crystal). We denote the angle between the z axis and the k vector of the intermediate wave as $\hat{\theta}_{\text{int}}$ and the angle between the z axis and the k vector of the output field as $\hat{\theta}_4$ (both defined inside the crystal). Both these angles vary as a function of ω and ξ (the dependence is evaluated in the appendix). Neglecting absorption in the crystal, the differential equations governing wave mixing of monochromatic plane waves are given by[20]

$$\frac{\mathrm{d}\hat{U}_{\text{int}}(x', \xi, z; \omega)}{\mathrm{d}z}$$

$$= j \frac{\omega_0 + \omega_1}{2 \cos(\bar{\hat{\theta}}_{\text{int}})} \sqrt{\frac{\mu}{\varepsilon_{\text{int}}}} d$$

$$\times \{\hat{U}_1(x', z; \omega - \omega_1)\hat{U}_2(x', \xi, z; \omega_1)$$

$$\times \exp[j\Delta k^{(1)}(\omega, \xi)z] + \hat{U}_3(x', z; \omega_1)$$

$$\times \hat{U}_4(x', \xi, z; \omega - \omega_1)\exp[j\Delta k^{(2)}(\omega, \xi)z]\}, \quad (26a)$$

$$\frac{\mathrm{d}\hat{U}_4(x', \xi, z; \omega)}{\mathrm{d}z}$$

$$= j \frac{\omega_0}{2 \cos(\bar{\hat{\theta}}_4)} \sqrt{\frac{\mu}{\varepsilon_4}} d\hat{U}_{\text{int}}(x', \xi, z; \omega + \omega_1)$$

$$\times \hat{U}_3^*(x', z; \omega_1)\exp[-j\Delta k^{(2)}(\omega, \xi)z], \quad (26b)$$

where d is the second-order nonlinear optical coefficient. The right-hand side of the equations have been simplified by substituting the center-frequency value for the propagation-direction angles, $\bar{\hat{\theta}}_{\text{int}}$ and $\bar{\hat{\theta}}_4$, the electric permittivity and magnetic permeability, ε and μ, and the optical carrier in the term preceding the nonlinear polarization. The phase-mismatch terms for the frequency-sum and frequency-difference processes, $\Delta k^{(1)}(\omega, \xi)$ and $\Delta k^{(2)}(\omega, \xi)$, respectively, are given by

$$\Delta k^{(1)}(\omega, \xi) = \hat{k}_1(\omega) + \hat{k}_2(\xi) - \hat{k}_{\text{int}}(\omega, \xi), \quad (27a)$$

$$\Delta k^{(2)}(\omega, \xi) = \hat{k}_3 - \hat{k}_{\text{int}}(\omega, \xi) + \hat{k}_4(\omega, \xi). \quad (27b)$$

Figure 2 illustrates a graphical representation of the phase-mismatch terms of Eqs. (27a) and (27b). The

equations describing the phase mismatch in the wave-mixing processes are nonlinear. To simplify the phase-mismatch representation, we perform a small-signal analysis about $\omega = \omega_0$ and $\xi = 0$ and linearize the relationship. The details of the linearization process and evaluation of the two phase-mismatch terms are presented in the appendix.

A simple analytic solution to the coupled differential equations can be obtained by arguing that since the generated wave $\hat{U}_4$ is weaker than the input waves, we can neglect the second nonlinear polarization term in Eq. (26a) (i.e., $\hat{U}_1\hat{U}_2 \gg \hat{U}_3\hat{U}_4$). This assumption decouples the differential equations, implying that the rate at which the intermediate wave is depleted by the second process of the cascade is much smaller than the rate at which it is being generated. Therefore Eq. (26a) of the intermediate field is dependent on the two known input fields and can be solved directly. This solution is inserted into Eq. (26b) describing the evolution of the output wave, which can also be solved directly now, as the driving waves are completely characterized. The solution yields

Polarization parallel to crystal's ordinary axis

Polarization parallel to crystal's extraordinary axis
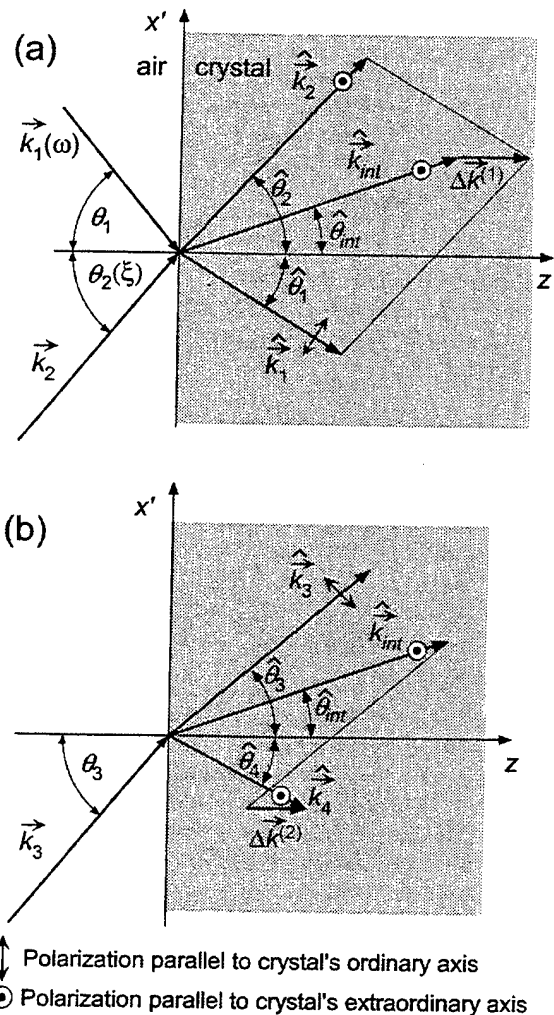
Fig. 2. Graphical representation of the phase mismatch in noncollinear mixing in an anisotropic crystal for (a) the upconversion process and (b) the downconversion process.

$$\hat{U}_4(x', \xi, z; \omega)$$

$$\propto \hat{U}_1(x'; \omega)\hat{U}_2(x', \xi; \omega_1)\hat{U}_3^*(x'; \omega_1)H_{\mathrm{NL}}(\omega, \xi, z), \quad (28)$$

where the complex transfer function, $H_{\mathrm{NL}}(\omega, \xi, z)$, characterizes the response of the cascaded wave-mixing process and is given by

$$H_{\mathrm{NL}}(\omega, \xi, z) = \frac{\exp\{j[\Delta k^{(1)}(\omega, \xi) - \Delta k^{(2)}(\omega, \xi)]z\} - 1}{[\Delta k^{(1)}(\omega, \xi) - \Delta k^{(2)}(\omega, \xi)]\Delta k^{(1)}(\omega, \xi)}$$

$$- \frac{\exp[-j\Delta k^{(2)}(\omega, \xi)z] - 1}{\Delta k^{(1)}(\omega, \xi)\Delta k^{(2)}(\omega, \xi)}. \quad (29)$$

The complex transfer function of Eq. (29) depends on the temporal-frequency component of the input pulse, on the spatial frequency arising from the amount of shift ξ of the delta function in the encoding mask, and on the length of the nonlinear crystal. Since the complex transfer function is temporal-frequency dependent, the output waveform will not be transform limited. However, any predominant quadratic-phase term can be eliminated by longitudinal adjustment of the output grating. Reintroducing the encoding-mask information, the SDW of the synthesized waveform at the edge of the crystal is defined by

$$\hat{U}_4(x', L_c; \omega) \propto \hat{U}_1(x'; \omega)\hat{U}_3^*(x'; \omega_1)$$

$$\times \int_{\xi} m(\xi)\hat{U}_2(x', \xi; \omega_1)H_{\mathrm{NL}}(\omega, \xi, L_c)\mathrm{d}\xi,$$

$$(30)$$

where we replaced the interaction distance z by the thickness of the crystal, L_c. To find the output temporal waveform, Eq. (30) needs to be spatially Fourier transformed to the output plane, diffracted from the output grating, and inverse temporally Fourier transformed. Equation (30) cannot be solved analytically except for the most trivial cases, thus requiring a computation program to calculate the precise space-to-time converted waveform. Such a program could also compute the conversion efficiency, which will be information dependent.

For practical reasons it is desirable for the space-to-time processor to operate efficiently. The conversion efficiency of the wave-mixing process with CSN can be calculated with Parseval's theorem, as the total power in the spectral representation is equal to the total power in the time domain. Since Eq. (30) defines the SDW of the synthesized waveform, the power spectrum is equal to the spatial intensity distribution at the output face of the crystal. The power spectrum, or output intensity, can be evaluated analytically for a simple mask such as $m(x) = \delta(x)$, yielding

$$I_4(x'; \omega) \propto P_1 P_2 P_3 |\bar{p}(\omega - \omega_0)|^2$$

$$\times \left| \tilde{w}\left\{ \frac{\alpha}{2\pi c}\left[\frac{\omega x'}{\alpha f} + (\omega - \omega_0) \right] \right\} \right|^2$$

$$\times |H_{\mathrm{NL}}(\omega, 0, L_c)|^2, \quad (31)$$

where we introduce the optical powers P_1, P_2, and P_3 of the input temporal channel, the spatial-information channel, and the spatial reference channel, respectively, and

$$|H_{\mathrm{NL}}(\omega, 0, L_c)|^2$$

$$= \left(\frac{L_c}{\Delta k^{(1)}} \right)^2 \left(\mathrm{sinc}^2\left\{ [\Delta k^{(1)}(\omega, 0) - \Delta k^{(2)}(\omega, 0)]\frac{L_c}{2} \right\} \right.$$

$$+ \mathrm{sinc}^2\left[\Delta k^{(2)}(\omega, 0)\frac{L_c}{2} \right]$$

$$- 2\,\mathrm{sinc}\left\{ [\Delta k^{(1)}(\omega, 0) - \Delta k^{(2)}(\omega, 0)]\frac{L_c}{2} \right\}$$

$$\left. \times \mathrm{sinc}\left[\Delta k^{(2)}(\omega, 0)\frac{L_c}{2} \right]\cos\left[\frac{\Delta k^{(1)}(\omega, 0)L_c}{2} \right] \right). \quad (32)$$

The transfer function will perform spectral filtering, as is evident from Eq. (31). The conversion efficiency, defined as the ratio of the powers of the output synthesized waveform to the input temporal channel, depends linearly on the power level of each spatial pump channel. Our findings were experimentally validated and are presented in the following section.

4. EXPERIMENTAL RESULTS OF SPACE-TO-TIME CONVERSIONS

The operation of the spatial–temporal processor of Fig. 1 was verified by synthesizing various ultrafast temporal waveforms. In the experiments we used a commercial laser system consisting of a Ti:sapphire ultrashort pulse oscillator and a regenerative amplifier. The system generates ultrashort laser pulses of 100-fs duration at a center wavelength of 800 nm with an energy level of 1 mJ per pulse. For the intense quasi-monochromatic light source required by the spatial channels we used 90% of the emitted output-pulse power and stretched the pulse to a several-picosecond duration by a grating pair. The stretched pulse was split into two beams for implementing the two quasi-monochromatic spatial channels. Since the CSN process occurs with a femtosecond-scale time response, the slow temporal-frequency variation in the stretched pulses does not affect the wave-mixing process, as long as the temporal frequencies of the two spatial channels are instantaneously equal. The remaining 10% of the short-pulse laser output power was used as the reference ultrashort pulse in the input temporal channel. The SDW U_1 is generated by a 600-lines/mm blazed grating that provides an angular-dispersion parameter of $\alpha = 0.48$ and a lens of $f = 375$ mm focal length. The spatial–temporal wave mixing by the $\chi^{(2)}$ media was performed in a 2-mm-thick type II β-barium borate crystal. Several experiments were conducted to illustrate this real-time processing technique, demonstrating its ability to control amplitude and phase in the output temporal waveform by a complex-amplitude spatial-information channel.

All the synthesized waveforms were observed with a real-time pulse-imaging setup.[21] The pulse-imaging technique generates a spatial signal at the output plane that is proportional to the temporal convolution of the synthesized waveform and a reference ultrashort pulse. The reference-pulse source used in the pulse imager was the residual input pulse of the spatial–temporal processor, after separating it from the synthesized output wave-

form with a polarizing beam splitter. We viewed the output signal's intensity with a charge-coupled device and extracted the temporal information from the image.

A. Conversion Efficiency and Spectral Response

For initial characterization of the spatial–temporal wave-mixing process by CSN, the two monochromatic waves were focused by cylindrical lenses to form line sources at the input spatial channels. The resulting spatial plane waves U_2 and U_3 interact with the SDW, U_1, of an input transform-limited short pulse. Since the plane waves contain no information, in either the space or the time domain, their function is to upconvert, then downconvert, the carrier frequency of the SDW, generating by the CSN process the new SDW U_4. The downconverted SDW U_4 was generated only in the presence of the waves from the two spatial channels, verifying that the output SDW is produced by a CSN process.

The dependence of the synthesized waveform's output power to the optical power in each of the spatial channels was characterized by placing variable neutral-density filters in the spatial channels (see Fig. 3). The linear dependence of the output power to each spatial channel is verified by the excellent fit to the 10-dB/dec line. When both spatial channels' powers are varied simultaneously, the output power variation fits the 20-dB/dec line. The linear dependence confirms our assumption of the nondepleting pump approximation in Section 3. However, we observed that the dependence is sublinear when the spatial channels' powers were weak. This effect is more pronounced when only one of the spatial channels is attenuated. We believe this is due to depletion of the attenuated pump wave, as our analysis of Section 3 did not take into account strong interaction that may lead to such fundamental-wave depletion. The maximum conversion efficiency of the space-to-time processor, measured as the ratio of the input-pulse optical power to the output-pulse optical power, was 16%, illustrating the ad-

Fig. 4. (a) Measured power spectrum of the input pulse (solid curve) and the generated output pulse (dashed curve) exhibiting spectral filtering owing to a spectrally dependent phase mismatch in the processor. Also shown is the theoretical output power spectrum (dot-dash curve) calculated by applying the spectral filter to the measured input power spectrum. (b) Pulse images of the input pulse (solid curve) and the generated output pulse (dashed curve), demonstrating the increased duration of the output pulse owing to spectral filtering.

vantage of the CSN approach as opposed to conventional $\chi^{(3)}$ nonlinearity for four-wave mixing.[22]

The power spectrum of the output pulse was compared with that of the input pulse (see Fig. 4a). The observed spectral narrowing is due to an increasing phase mismatch as the frequencies deviate from the center frequency. A theoretical curve of the expected output-pulse power spectrum [based on Eq. (31)] shows a close correspondence to the actual observed spectrum. The theoretical curve was generated by evaluating the phase mismatch for the two processes in the cascade with published β-barium borate parameters[23] for type II noncollinear interaction with a 4° internal angle between the fundamental waves (assuming both processes are phase matched at $\omega = \omega_0$ and $\xi = 0$). We adjusted the center frequency of the theoretical curve to match the measured data. Owing to the reduction of the available bandwidth from spectral filtering, we observed an accompanying increase in the temporal duration of the output pulse (see Fig. 4b). The measured full width at half-maximum of the detected image in the time-to-space converter increased from 182 to 288 fs.

Fig. 3. Output power measurements as a function of spatial pump-beam powers. Varying one spatial channel while keeping the second constant illustrates the linear dependence of the output temporal power on each spatial channel. Varying the power of the spatial channels simultaneously displays a quadratic dependence, as expected.

B. Packet of Ultrafast Pulses

Novel uses for bursts of ultrashort pulses, such as terahertz-rate excitation and optical communication with ultrashort data packets, have increased the interest in developing techniques for generation of such ultrashort-pulse sequences. With the femtosecond-rate space-to-time converter, such a pulse sequence can be generated by a one-dimensional mask containing an array of point sources. The mask information can be expressed by

$$m(x) = \sum_{n=-N/2}^{N/2} A_n \delta(x - n\Delta x), \qquad (33)$$

where Δx is the fixed pitch between adjacent point sources, and A_n is a scalar weight term that may be a binary bit (value of 1 or 0), a real number, or a complex number. By use of this information mask in Eq. (21), the temporal output signal takes the form

$$
\begin{aligned}
y(t) &= \sum_{n=-N/2}^{N/2} A_n \delta\left(t - \frac{\omega_1}{\omega_0}\frac{\alpha}{c} n\Delta x\right) \otimes p(t) \\
&= \sum_{n=-N/2}^{N/2} A_n p\left(t - \frac{\omega_1}{\omega_0}\frac{\alpha}{c} n\Delta x\right). \qquad (34)
\end{aligned}
$$

In the space-to-time mapping, the spatial pitch Δx in the mask has been converted to a temporal separation of $\Delta t = \omega_1 \alpha \Delta x/\omega_0 c$.

Various masks containing narrow slits have been used in the space-to-time setup to generate ultrafast pulse packets. Previously, we reported results using a mask with a 0.8-mm pitch.[12] A finer mask with a 0.4-mm pitch was used to generate a denser ultrafast pulse packet (see Fig. 5). A cylindrical lenslet array was used to focus the spatial beam into the mask for increased light throughput. The spatial beam mode shape resulted in nonuniform power on each spatial slit. This power distribution has been transferred to the ultrafast pulse packet. The space-to-time mapping coefficient transforms the 0.4-mm spatial pitch to a time-domain separation of $\Delta t = 0.64$ ps (with $\omega_1 = \omega_0$ and $\alpha = 0.48$). The
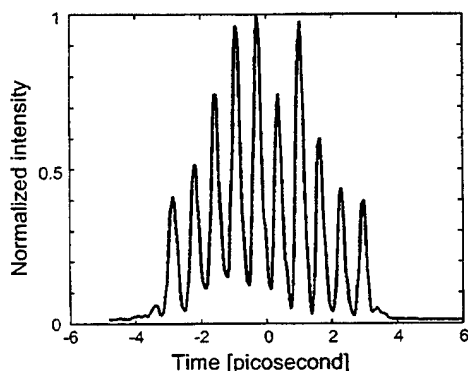
Fig. 5. 1.56-THz-rate ultrashort-pulse packet generated by a spatial-information mask consisting of a sequence of point sources separated by 0.4 mm.

measured temporal separation was 0.645 ps with a resolution of 33 fs, resulting in a 1.56-THz-rate pulse packet.

C. Square Pulse

Generation of synthesized square pulses by spectral filtering is not a simple task. The mask should contain amplitude information over a wide dynamic range as well as phase information for implementing negative values. Space-to-time mapping techniques simplify the task of complex mask preparation, while the requirement for a wide dynamic range in the recording medium remains. In photorefractives, where the recorded space-charge field is dependent on the modulation function, the recording process exhibits a nonlinear dependence on the recording beams. While this enables nonlinear processing,[24] for generation of high-fidelity square pulses a weak information beam must be used, giving rise to shallow modulation depths and low diffraction efficiency.

In our wave-mixing approach with CSN the amplitude of the synthesized wave is dependent on the amplitudes of the three input waves (as long as wave depletion and phase mismatch are negligible). This linear relationship gives rise to high-fidelity conversion from space to time. In the case of a square pulse the synthesized signal may be expressed as

$$y(t) = \text{rect}\left(\frac{t}{T}\right) \otimes p(t), \qquad (35)$$

where $T = \omega_1 \alpha X/\omega_0 c$ is the duration of the rect function and X is the width of the slit.

An adjustable slit was placed in the spatial-information channel to experiment with several synthesized square-pulse durations. The generated waveforms (see Fig. 6) were modified in real time by changing the slit width, and the square pulses were immediately observed with the pulse imager on a monitor. At wide slit widths, nonuniformity across the top of the square pulse has been observed. We have verified that the reason is due to nonuniformity in the illumination of the spatial channel. An image of the spatial-information channel in the space-to-time processor matched well with the observed image of the synthesized waveform in the time-to-space converter. There are two limitations to the maximum slit width that can be used: the resolution of the SPD [see Eq. (19)], and the optical power from the tight focus of the spatial channel in the Fourier plane may exceed the damage threshold of the nonlinear crystal.

D. Spherical Wave Front

To demonstrate the ability to encode phase information, a point source, generated by focusing the spatial beam with a cylindrical lens, was used as the spatial-information channel. Translating the lens longitudinally away from the input plane formed a spherical wave front with variable quadratic phase on the input plane of the spatial-information channel. As the translation of the line source from the input plane is increased (in either the positive or the negative direction), the output SDW acquires a larger positive or negative quadratic phase and after recomposing on the output grating, emerges as a

chirped pulse (either a positive or negative chirp). The measured synthesized chirped pulses exhibited, as expected, broader pulses along with a reduction of the peak intensity.[12]

The effect of a longitudinal translation of the point source away from the input plane of the processor is expressible as a convolution with a quadratic-phase function[25] (free space propagation), resulting in the field distribution in the spatial-information channel,

$$m(x) = \frac{\exp(jk\zeta)}{j\lambda_1\zeta}\exp\left(\frac{j\omega_1}{c}\frac{x^2}{2\zeta}\right), \quad (36)$$

where ζ is the displacement of the focus plane of the cylindrical lens from the input plane of the processor. The phase information described in Eq. (36) gives rise to the synthesized waveform

$$y(t) = \frac{\exp(jk\zeta)}{j\lambda_1\zeta}\exp\left[\frac{j\omega_1}{c}\frac{\left(\frac{\omega_0 ct}{\omega_1\alpha}\right)^2}{2\zeta}\right] \otimes p(t), \quad (37)$$

which describes a chirp function (quadratic temporal-frequency variation) imposed on the input pulse. A Fourier-domain representation of the output synthesized signal is easier to interpret in this case, yielding

$$\tilde{y}(\omega) \propto \exp\left[-j\left(\frac{\omega-\omega_0}{\omega_0}\right)^2\frac{\omega_1\zeta\alpha^2}{c}\right]\tilde{p}(\omega-\omega_0). \quad (38)$$

From Eq. (38) it is clear that the amount of chirp is linearly dependent on the displacement ζ.

To measure the amount of chirp that is present in the synthesized waveform, we utilize a unique property of the pulse imager. Since the pulse imager generates the complex-amplitude information of the temporal convolution operation in spatial coordinates, the resulting spatial quadratic phase in the image of a chirped pulse can be used to gauge the amount of chirp. By longitudinally translating the output plane, a location can be found where the wave focuses to its tightest spot size, eliminating the spatial quadratic phase.[21] Therefore as the pulse chirp is increased (either positively or negatively), the lo-
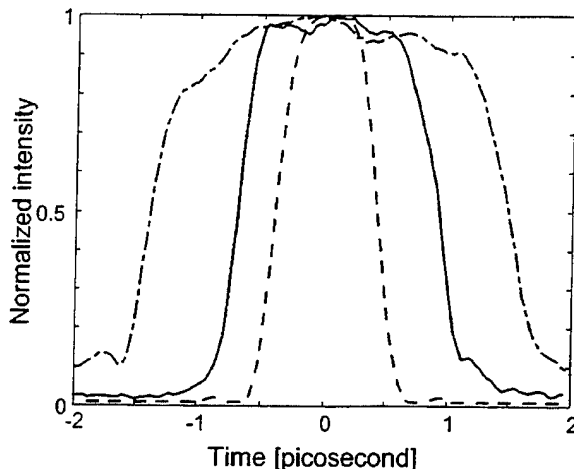
Fig. 6. Superimposed images of square pulses generated by varying the width of a square aperture in the spatial channel.
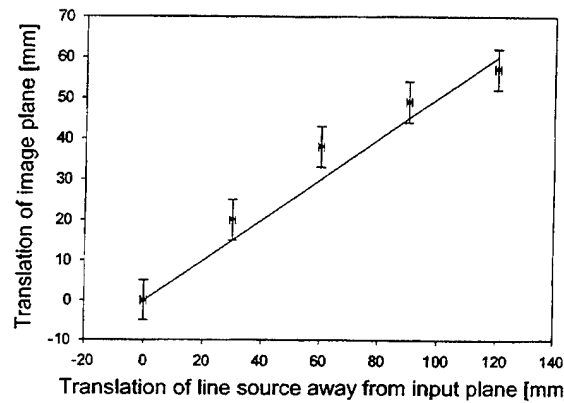
Fig. 7. Linear correspondence between translation of the point source away from the input plane of space-to-time converter and translation of the image-formation plane in the pulse imager. The solid line corresponds to a theoretical curve of slope 1/2.

cation of the plane at which the wave focuses changes (either farther or closer). The spatial output signal of the pulse imager can be expressed as[21]

$$b(x'') = p\left(\frac{2\alpha}{c}x''\right) \otimes y\left(-\frac{2\alpha}{c}x''\right)$$

$$= p\left(\frac{2\alpha}{c}x''\right) \otimes p\left(-\frac{2\alpha}{c}x''\right)$$

$$\otimes \exp\left[\frac{j\omega_1}{c}\frac{\left(\frac{\omega_0}{\omega_1}2x''\right)^2}{2\zeta}\right], \quad (39)$$

which corresponds to the convolution of the ultrashort pulses with a quadratic-phase function. Using the kernel of free-space propagation at frequency $2\omega_0$, $\exp[j(2\omega_0/c)(x''^2/2Z)]$, where Z is the displacement from the image plane, we seek the value of Z that will cancel the quadratic-phase terms in Eq. (39). This value of Z corresponds to the location where the signal focuses to its tightest spot size. The value of Z is given by

$$Z = -\frac{\omega_1}{\omega_0}\frac{\zeta}{2}. \quad (40)$$

This scaling rule is dependent on the ratio of the frequencies used in the spatial and temporal channels of the space-to-time converter and a factor of 2 owing to the doubled-frequency output of the pulse imager.

We have verified experimentally the relation in Eq. (40) by finding the location where the output of the pulse imager focuses, for each translated location used in the spatial channel of the space-to-time converter (see Fig. 7). In our experiment the scaling rule reduces to 1/2 since $\omega_1 = \omega_0$. Thus we have a correspondence between the longitudinal translation of the line source in the input spatial channel of the spatial–temporal processor and the longitudinal translation of the focus plane of the pulse imager.

5. CONCLUSION AND DISCUSSION

We have introduced and experimentally demonstrated femtosecond-rate space-to-time conversion of amplitude and phase information from a quasi-monochromatic spatial-image channel to an ultrafast temporal waveform. Relative to other spatial–temporal processing techniques, the CSN four-wave mixing approach provides femtosecond-rate processing owing to the fast bound-electron nonlinearity and high efficiency on account of a relatively large $\chi^{(2)}$ coefficient. Such capabilities are required for quantum control experiments or ultrafast data modulation in optical communications, where rapid, high-fidelity waveform manipulations are required.

To model limitations imposed by phase-matching considerations in the nonlinear wave-mixing process, we have introduced a complex transfer function to characterize the system response. The phase mismatch in the wave-mixing process arises from the broad temporal- and spatial-frequency content of the input temporal-pulse and spatial-image information, respectively. The transfer function can be used to compute the precise space-to-time converted waveform and assist in optimal selection of a nonlinear crystal for real-time pulse shaping. The conversion efficiency from the input reference pulse to the output synthesized waveform was found to depend on the power levels of the two spatial channels.

Several experiments were conducted to illustrate the ability to convert amplitude and phase information from the space domain to the time domain with high efficiency. The spectrum reduction in the synthesized waveform owing to the complex transfer function was observed and was in good agreement with the predicted spectrum. All the experiments were conducted on a single-shot basis, highlighting the benefit of processing with a fast nonlinear effect.

The space-to-time conversion process that we have demonstrated uses an identical quasi-monochromatic light source in the two spatial channels. This requirement is typical for holographic processing, where the two waves need to be mutually coherent during the long recording phase. Since our processor is based on a real-time four-wave mixing process, this requirement can be alleviated. The necessary condition for a faithful signal conversion by nonlinear wave mixing is that each of the spatial channels be implemented with a monochromatic light source, with no temporal bandwidth. With this condition the nonlinear polarization term can be trivially calculated [as we have done in Eqs. (12) and (13)]. It is therefore feasible to perform wavelength tuning of the synthesized temporal waveform by use of different optical frequencies in the two spatial channels. The center frequency of the synthesized temporal waveform is shifted by the frequency difference of the two sources used in the spatial channels. Since quasi-monochromatic light sources are used in reality, we require that the coherence time of the light sources be much longer than the time window of the SPD (which is a very simple requirement to satisfy). The propagation directions of the fields from the two spatial channels may require adjustment, such that the phase-matching condition is satisfied for the two processes of the cascade. The hypothesized wavelength-tuning property of the real-time four-wave mixing processor is unique to our space-to-time technique and cannot be accomplished by holographic recording means.

APPENDIX A: EVALUATION OF PHASE-MISMATCH TERMS

The output signal of the CSN process was shown in Subsection 3.B to depend on the phase-mismatch terms in the coupled-wave equations characterizing the generation of the new fields. The phase mismatch occurs since the phase-matching requirement for efficient energy transfer cannot be supported for the temporal bandwidth of the SDW and the angular bandwidth of the spatial-information channel. In this appendix we derive the phase-mismatch terms for the two processes of the cascade, using the information-channel model of a delta function shifted by an amount ξ. The phase-mismatch terms obtained in this appendix are inserted into Eq. (29), describing the complex transfer function of the processor.

The first nonlinear interaction of the cascade, the frequency-sum process, generates the intermediate wave, $\hat{U}_{\text{int}}$. (Note that all properties of the waves inside the crystal are with the hat overscript.) The phase mismatch of the first process of the cascade is defined by the vector equation, Eq. (27a), where the phase mismatch must lie in the z direction owing to the kinematic condition (conservation of momentum in the x' direction). Since the interacting waves are propagating at very small angles relative to the z axis, we can use the paraxial approximation (note that Fig. 2 shows greatly exaggerated angles), simplifying the phase-mismatch expression to the sum of the k-vector magnitudes, i.e., $\Delta k^{(1)}(\omega, \xi) \cong \hat{k}_1(\omega) + \hat{k}_2(\xi) - \hat{k}_{\text{int}}(\omega, \xi)$. We next find these k-vector magnitudes for evaluation of the first phase-mismatch term.

The first input wave, $\hat{U}_1$, from the input temporal channel, is polarized parallel to the crystal's ordinary axis. Therefore the wave-vector magnitude is independent of its propagation direction and is given by $\hat{k}_1(\omega) \approx k(\omega_0) + (\partial k/\partial \omega)(\omega - \omega_0)$. To find the wave-vector magnitude of the intermediate wave, $\hat{U}_{\text{int}}$, and its propagation direction, we apply the kinematic condition using the paraxial approximation, yielding

$$\hat{k}_{\text{int}}(\omega, \xi)\hat{\theta}_{\text{int}}(\omega, \xi) = \hat{k}_1(\omega)\hat{\theta}_1(\omega) + \hat{k}_2(\xi)\hat{\theta}_2(\xi)$$

$$= k_1(\omega)\theta_1 + k_2\theta_2(\xi), \qquad (A1)$$

where the second equality results from invoking the kinematic condition on the input fields across the crystal interface. (Before refraction into the crystal, θ_1 is not frequency dependent, as all the components propagate in the same direction [see Eq. (22)], and the magnitude of k_2 does not vary with the shift of in ξ, as it is a quasi-monochromatic wave.) To analyze the effect of varying the parameters $\Delta\omega = \omega - \omega_0$ and ξ, we perform a small-signal perturbation about $\omega = \omega_0$ and $\xi = 0$ by defining the following:

$$\hat{k}_{\text{int}}(\omega, \xi) = \overline{\hat{k}}_{\text{int}} + \Delta\hat{k}_{\text{int}},$$

$$\hat{\theta}_{\text{int}}(\omega, \xi) = \overline{\hat{\theta}}_{\text{int}} + \Delta\hat{\theta}_{\text{int}},$$

$$k_1(\omega) = \frac{\omega_0}{c} + \frac{\Delta\omega_0}{c},$$

$$\theta_2(\xi) = \frac{D}{2f} - \frac{\xi}{f}, \qquad (A2)$$

where $\overline{\hat{k}}_{int}$ and $\overline{\hat{\theta}}_{int}$ are the k-vector magnitude and angle of propagation, respectively, for the intermediate wave evaluated at $\omega = \omega_0$ and $\xi = 0$. Inserting the perturbed expressions into Eq. (A1), neglecting second-order terms of the form $\Delta\hat{k}_{int}\Delta\hat{\theta}_{int}$, and simplifying the expression by removing the constant terms that satisfy the equality on both sides of the equation yields

$$\Delta\hat{k}_{int}\overline{\hat{\theta}}_{int} + \overline{\hat{k}}_{int}\Delta\hat{\theta}_{int} = -\frac{D}{2f}\frac{\Delta\omega}{c} - \frac{\omega_1}{c}\frac{\xi}{f}, \qquad (A3)$$

where we used $\theta_1 = -D/2f$ and $k_2 = \omega_1/c$. We can further simplify the expression by setting $\Delta\hat{k}_{int} = (\partial\hat{k}_{int}/\partial\omega)\Delta\omega + (\partial\hat{k}_{int}/\partial\theta)\Delta\hat{\theta}_{int}$, resulting in

$$\Delta\hat{\theta}_{int} = -\frac{\dfrac{D}{2fc} + v_{g\_int}^{-1}\overline{\hat{\theta}}_{int}}{\dfrac{\partial\hat{k}_{int}}{\partial\theta}\overline{\hat{\theta}}_{int} + \overline{\hat{k}}_{int}}\Delta\omega - \frac{\dfrac{\omega_1}{cf}}{\dfrac{\partial\hat{k}_{int}}{\partial\theta}\overline{\hat{\theta}}_{int} + \overline{\hat{k}}_{int}}\xi, \qquad (A4)$$

where we used the definition of the group velocity, $v_{g\_int} = (\partial\hat{k}_{int}/\partial\omega)^{-1}$. Using this result, we can express the k vector of the intermediate wave as

$$\hat{k}_{int}(\omega, \xi) = \overline{\hat{k}}_{int} + \left(v_{g\_int}^{-1} - \frac{\partial\hat{k}_{int}}{\partial\theta}\frac{\dfrac{D}{2fc} + v_{g\_int}^{-1}\overline{\hat{\theta}}_{int}}{\dfrac{\partial\hat{k}_{int}}{\partial\theta}\overline{\hat{\theta}}_{int} + \overline{\hat{k}}_{int}}\right)$$

$$\times (\omega - \omega_0) - \frac{\dfrac{\partial\hat{k}_{int}}{\partial\theta}\dfrac{\omega_1}{c}}{\dfrac{\partial\hat{k}_{int}}{\partial\theta}\overline{\hat{\theta}}_{int} + \overline{\hat{k}}_{int}}\frac{\xi}{f}. \qquad (A5)$$

The term $\partial\hat{k}_{int}/\partial\theta$ is evaluated by $[(\omega_0 + \omega_1)/c] \times (\partial n_e^{(\omega_0+\omega_1)}/\partial\theta)$, where the rate of change of the extraordinary refractive index at angle $\overline{\hat{\theta}}_{int}$ can be found by differentiating the equation governing the refractive-index dependence on angle θ of an anisotropic crystal.[26]

Next, we find the k-vector properties of the wave from the spatial-information channel, $\hat{U}_2$, which is also polarized in the direction of the extraordinary axis. Since this wave is quasimonochromatic, the propagation direction inside the crystal determines the wave-vector magnitude. We find the propagation direction by using the kinematic condition across the crystal interface together with a small-signal perturbation, yielding

$$\hat{k}_2(\hat{\theta}_2)\hat{\theta}_2 = \frac{\omega_1}{c}n_e^{(\omega_1)}[\hat{\theta}_2(\xi)]\hat{\theta}_2(\xi)$$

$$\cong \frac{\omega_1}{c}(n_2 + \Delta n_2)(\overline{\hat{\theta}}_2 + \Delta\hat{\theta}_2)$$

$$= \frac{\omega_1}{c}\left(\frac{D}{2f} - \frac{\xi}{f}\right), \qquad (A6)$$

where $\overline{\hat{\theta}}_2$ is the angle between the propagation direction and the z axis for no spatial shift of the delta function. By neglecting second-order terms of the form $\Delta n_2\Delta\hat{\theta}_2$, and expressing the index change as $\Delta n_2 = (dn_e^{(\omega_1)}/d\theta)\Delta\hat{\theta}_2$, we find

$$\Delta\hat{\theta}_2 = \frac{-\dfrac{\xi}{f}}{n_2 + \overline{\hat{\theta}}_2\left.\dfrac{dn_e^{(\omega_1)}}{d\theta}\right|_{\theta=\overline{\hat{\theta}}_2}}, \qquad (A7)$$

where the derivative of the refractive index can again be calculated.[26] The k vector of the field is given by $\omega_1(n_2 + \Delta n_2)/c$, yielding

$$k_2(\xi) \cong \frac{\omega_1}{c}n_e^{(\omega_1)}(\overline{\hat{\theta}}_2) + \frac{\omega_1}{c}\left.\frac{dn_e^{(\omega_1)}}{d\theta}\right|_{\theta=\overline{\hat{\theta}}_2}$$

$$\times \frac{-\dfrac{\xi}{f}}{n_e^{(\omega_1)}(\overline{\hat{\theta}}_2) + \overline{\hat{\theta}}_2\left.\dfrac{dn_e^{(\omega_1)}}{d\theta}\right|_{\theta=\overline{\hat{\theta}}_2}}. \qquad (A8)$$
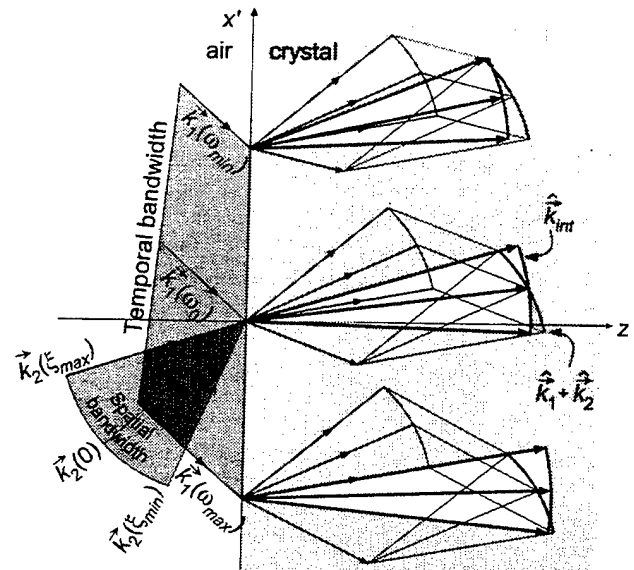
Fig. 8. Illustration of phase mismatch owing to broad temporal bandwidth (spatially dispersed along x') and angular bandwidth. The vector sum of the two fundamental waves generates a k-vector front that is compared with the available k-vector front of the frequency-sum wave. Exact phase matching is possible at each temporal frequency with different components of the spatial angular bandwidth.

The phase mismatch of the first process of the cascade is therefore found by combining the expressions for the wave-vector magnitudes, resulting in

$$
\Delta k^{(1)}(\omega, \xi)
$$

$$
= \hat{k}_1(\omega) + \hat{k}_2(\xi) - \hat{k}_{\mathrm{int}}(\omega, \xi)
$$

$$
= \left[\frac{\omega_0}{c} n_o^{(\omega_0)} + \frac{\omega_1}{c} n_e^{(\omega_1)}(\bar{\theta}_2) - \frac{\omega_0 + \omega_1}{c} n_e^{(\omega_0 + \omega_1)}(\bar{\theta}_{\mathrm{int}}) \right]
$$

$$
+ \left(v_{g\_1}^{-1} - v_{g\_\mathrm{int}}^{-1} + \frac{\partial \hat{k}_{\mathrm{int}}}{\partial \theta} \frac{\dfrac{D}{2fc} + v_{g\_\mathrm{int}}^{-1}\bar{\theta}_{\mathrm{int}}}{\dfrac{\partial \hat{k}_{\mathrm{int}}}{\partial \theta} \bar{\theta}_{\mathrm{int}} + \bar{k}_{\mathrm{int}}} \right)
$$

$$
\times (\omega - \omega_0) + \left[\frac{-\dfrac{\omega_1}{c} \dfrac{\mathrm{d}n_e^{(\omega_1)}}{\mathrm{d}\theta}\Big|_{\theta=\bar{\theta}_2}}{n_e^{(\omega_1)}(\bar{\theta}_2) + \bar{\theta}_2 \dfrac{\mathrm{d}n_e^{(\omega_1)}}{\mathrm{d}\theta}\Big|_{\theta=\bar{\theta}_2}} \right.
$$

$$
\left. + \frac{\dfrac{\partial \hat{k}_{\mathrm{int}}}{\partial \theta} \dfrac{\omega_1}{c}}{\dfrac{\partial \hat{k}_{\mathrm{int}}}{\partial \theta} \bar{\theta}_{\mathrm{int}} + \bar{k}_{\mathrm{int}}} \right] \frac{\xi}{f}
$$

$$
\equiv \Delta k^{(1)}(\omega_0, 0) + \frac{\partial \Delta k^{(1)}}{\partial \omega}(\omega - \omega_0) + \frac{\partial \Delta k^{(1)}}{\partial \xi} \xi. \quad (A9)
$$

The constant term of the phase mismatch is set to zero by proper crystal selection, cut, and orientation set to satisfy the phase-matching condition for the center frequency ω_0 and without spatial offset ξ. Figure 8 graphically illustrates the difference between the vector sum of $\hat{k}_1(\omega)$ (spatially dispersed in the x' direction) and $\hat{k}_2(\xi)$ (broad spatial bandwidth at every location) and $\hat{k}_{\mathrm{int}}(\omega, \xi)$ (available wave vectors that the crystal supports).

The calculation of the phase-mismatch term is repeated for the second interaction of the cascade, the frequency-difference process, which generates the output wave, $\hat{U}_4$. By reasoning of the paraxial approximation the phase mismatch of the second process of the cascade is again an equation with wave-vector magnitudes, i.e., $\Delta k^{(2)}(\omega, \xi) = \hat{k}_3 + \hat{k}_4(\omega, \xi) - \hat{k}_{\mathrm{int}}(\omega, \xi)$. The magnitude of the wave vector from the second spatial channel is $\omega_1 n_o^{(\omega_1)}/c$, as the quasi-monochromatic wave is polarized in the direction of the crystal's ordinary axis. The wave-vector properties of the output wave are calculated with the kinematic condition, yielding

$$
\hat{k}_4(\omega, \xi)\hat{\theta}_4(\omega, \xi) = \hat{k}_{\mathrm{int}}(\omega, \xi)\hat{\theta}_{\mathrm{int}}(\omega, \xi) - \hat{k}_3\hat{\theta}_3
$$

$$
= k_1(\omega)\theta_1 + k_2\theta_2(\xi) - k_3\theta_3, \quad (A10)
$$

where Eq. (A1) was used to simplify the expression. A small-signal perturbation about $\omega = \omega_0$ and $\xi = 0$ is performed on Eq. (A10) to analyze the effect of the temporal and angular bandwidths. Using $\Delta\hat{k}_4 = (\partial\hat{k}_4/\partial\omega)\Delta\omega$

$+ (\partial\hat{k}_4/\partial\theta)\Delta\hat{\theta}_4$, neglecting second-order terms of the form $\Delta\hat{k}_4\Delta\hat{\theta}_4$, and simplifying the resulting expression, we obtain

$$
\Delta\hat{\theta}_4 = -\frac{\dfrac{D}{2fc} + v_{g\_4}^{-1}\bar{\theta}_4}{\dfrac{\partial\hat{k}_4}{\partial\theta}\bar{\theta}_4 + \bar{k}_4}\Delta\omega - \frac{\dfrac{\omega_1}{c}}{\dfrac{\partial\hat{k}_4}{\partial\theta}\bar{\theta}_4 + \bar{k}_4}\frac{\xi}{f}. \quad (A11)
$$

The similarity between the expressions describing the perturbation angles $\Delta\hat{\theta}_{\mathrm{int}}$ and $\Delta\hat{\theta}_4$ [Eqs. (A4) and (A11)] arises from the identical dependence on the variational parameters on the right-hand sides of Eqs. (A1) and (A10). The wave-vector magnitude of the output field is expressed by

$$
\hat{k}_4(\omega, \xi) = \bar{k}_4 + \left(v_{g\_4}^{-1} - \frac{\partial\hat{k}_4}{\partial\theta}\frac{\dfrac{D}{2fc} + v_{g\_4}^{-1}\bar{\theta}_4}{\dfrac{\partial\hat{k}_4}{\partial\theta}\bar{\theta}_4 + \bar{k}_4} \right)(\omega - \omega_0)
$$

$$
- \frac{\dfrac{\partial\hat{k}_4}{\partial\theta}\dfrac{\omega_1}{c}}{\dfrac{\partial\hat{k}_4}{\partial\theta}\bar{\theta}_4 + \bar{k}_4}\frac{\xi}{f}. \quad (A12)
$$

The phase mismatch of the second process of the cascade is therefore given by

$$
\Delta k^{(2)}(\omega, \xi)
$$

$$
= \hat{k}_3 + \hat{k}_4(\omega, \xi) - \hat{k}_{\mathrm{int}}(\omega, \xi)
$$

$$
= \left[\frac{\omega_1}{c} n_0^{(\omega_1)} + \frac{\omega_0}{c} n_e^{(\omega_0)}(\bar{\theta}_4) - \frac{\omega_0 + \omega_1}{c} n_e^{(\omega_0 + \omega_1)}(\bar{\theta}_{\mathrm{int}}) \right]
$$

$$
+ \left(v_{g\_4}^{-1} - v_{g\_\mathrm{int}}^{-1} + \frac{\partial\hat{k}_{\mathrm{int}}}{\partial\theta}\frac{\dfrac{D}{2fc} + v_{g\_\mathrm{int}}^{-1}\bar{\theta}_{\mathrm{int}}}{\dfrac{\partial\hat{k}_{\mathrm{int}}}{\partial\theta}\bar{\theta}_{\mathrm{int}} + \bar{k}_{\mathrm{int}}} \right.
$$

$$
\left. - \frac{\partial\hat{k}_4}{\partial\theta}\frac{\dfrac{D}{2fc} + v_{g\_4}^{-1}\bar{\theta}_4}{\dfrac{\partial\hat{k}_4}{\partial\theta}\bar{\theta}_4 + \bar{k}_4} \right)(\omega - \omega_0)
$$

$$
+ \left(\frac{\dfrac{\partial\hat{k}_{\mathrm{int}}}{\partial\theta}\dfrac{\omega_1}{c}}{\dfrac{\partial\hat{k}_{\mathrm{int}}}{\partial\theta}\bar{\theta}_{\mathrm{int}} + \bar{k}_{\mathrm{int}}} - \frac{\dfrac{\partial\hat{k}_4}{\partial\theta}\dfrac{\omega_1}{c}}{\dfrac{\partial\hat{k}_4}{\partial\theta}\bar{\theta}_4 + \bar{k}_4} \right)\frac{\xi}{f}
$$

$$
\equiv \Delta k^{(2)}(\omega_0, 0) + \frac{\partial\Delta k^{(2)}}{\partial\omega}(\omega - \omega_0) + \frac{\partial\Delta k^{(2)}}{\partial\xi}\xi.
$$

$$
(A13)
$$

The constant term of the phase mismatch in the second process can be shown to be nonzero by use of the phase-

matching condition from the first process of the cascade. The resulting constant phase mismatch is given by

$$\Delta k^{(2)}(\omega_0, 0) = \frac{\omega_0}{c}[n_e^{(\omega_0)}(\bar{\theta}_4) - n_o^{(\omega_0)}]$$

$$- \frac{\omega_1}{c}[n_e^{(\omega_1)}(\bar{\theta}_2) - n_o^{(\omega_1)}]. \quad (A14)$$

The phase mismatch is caused by the crystal's birefringence. The two quasi-monochromatic spatial waves, which copropagate in free space, have different propagation directions inside the crystal since each wave experiences a different refractive index. Therefore the second process cannot be phase matched for the center temporal- and spatial-frequency components. However, the location of the point source in the second spatial input channel [see Eq. (10)] can be slightly shifted in experiment from $-D/2$, such that the second process is also phase matched and high conversion efficiency is achieved. This results in a small propagation-angle offset between the residual wave U_1 and the output wave U_4, which is expected owing to the kinematic condition and was observed in our experiments.

Evaluation of the various propagation angles inside the crystal and the crystal properties at these angles are required for determining $\Delta k^{(1)}$ and $\Delta k^{(2)}$, which are used in conjunction with the nonlinear conversion analysis of Section 3.

ACKNOWLEDGMENTS

*Curent address: Lucent Technologies, Room 4B-411, 101 Crawfords Corner Road, Holmdel, New Jersey 07733.

REFERENCES

1. C. Froehly, B. Colombeau, and M. Vampouille, "Shaping and analysis of picosecond light pulses," in *Progress in Optics XX*, E. Wolf, ed. (North-Holland, Amsterdam, 1983), pp. 65–153.
2. A. M. Weiner, "Femtosecond optical pulse shaping and processing," Prog. Quantum Electron. **19**, 161–237 (1995).
3. Y. T. Mazurenko, "Holography of wave packets," Appl. Phys. B **50**, 101–114 (1990).
4. A. M. Weiner, J. P. Heritage, and E. M. Kirschner, "High-resolution femtosecond pulse shaping," J. Opt. Soc. Am. B **5**, 1563–1572 (1988).
5. A. M. Weiner, D. E. Leaird, J. S. Patel, and J. R. Wullert, "Programmable femtosecond pulse shaping by use of a multielement liquid-crystal phase modulator," Opt. Lett. **15**, 326–328 (1990).
6. M. E. Fermann, V. di Silva, D. A. Smith, Y. Silberberg, and A. M. Weiner, "Shaping of ultrashort optical pulses by using an integrated acousto-optic tunable filter," Opt. Lett. **18**, 1505–1507 (1993).
7. M. M. Wefers and K. A. Nelson, "Programmable phase and amplitude femtosecond pulse shaping," Opt. Lett. **18**, 2032–2034 (1993).
8. M. C. Nuss and R. L. Morrison, "Time-domain images," Opt. Lett. **20**, 740–742 (1995).
9. P. C. Sun, Y. Mazurenko, W. S. C. Chang, P. K. L. Yu, and Y. Fainman, "All-optical parallel-to-serial conversion by holographic spatial-to-temporal frequency encoding," Opt. Lett. **20**, 1728–1730 (1995).
10. M. C. Nuss, M. Li, T. H. Chiu, A. M. Weiner, and A. Partovi, "Time-to-space mapping of femtosecond pulses," Opt. Lett. **19**, 664–666 (1994).
11. Y. Ding, R. M. Brubaker, D. D. Nolte, M. R. Melloch, and A. M. Weiner, "Femtosecond pulse shaping by dynamic holograms in photorefractive multiple quantum wells," Opt. Lett. **22**, 718–720 (1997).
12. D. M. Marom, D. Panasenko, P.-C. Sun, and Y. Fainman, "Spatial-temporal wave mixing for space-to-time conversion," Opt. Lett. **24**, 563–565 (1999).
13. M. A. Krumbügel, J. N. Sweetser, D. N. Fittinghoff, K. W. DeLong, and R. Trebino, Opt. Lett. **22**, 245–247 (1997).
14. D. M. Marom, P. C. Sun, and Y. Fainman, "Analysis of spatial-temporal converters for all-optical communication links," Appl. Opt. **37**, 2858–2868 (1998).
15. O. E. Martinez, "Grating and prism compressors in the case of finite beam size," J. Opt. Soc. Am. B **3**, 929–934 (1986).
16. M. M. Wefers and K. A. Nelson, "Analysis of programmable ultrashort waveform generation using liquid-crystal spatial light modulators," J. Opt. Soc. Am. B **12**, 1343–1362 (1995).
17. J. Paye and A. Migus, "Space–time Wigner functions and their applications to the analysis of a pulse shaper," J. Opt. Soc. Am. B **12**, 1480–1490 (1995).
18. M. M. Wefers and K. A. Nelson, "Space–time profiles of shaped ultrafast optical waveforms," IEEE J. Quantum Electron. **32**, 161–172 (1996).
19. Y. R. Shen, *The Principles of Nonlinear Optics* (Wiley, New York, 1984), Chap. 6.
20. M. Schubert and B. Wilhelmi, *Nonlinear Optics and Quantum Electronics* (Wiley, New York, 1986), Chap. 1.
21. P. C. Sun, Y. T. Mazurenko, and Y. Fainman, "Femtosecond pulse imaging: ultrafast optical oscilloscope," J. Opt. Soc. Am. A **14**, 1159–1170 (1997).
22. J. B. Khurgin, A. Obeidat, S. J. Lee, and Y. J. Ding, "Cascaded optical nonlinearities: microscopic understanding as a collective effect," J. Opt. Soc. Am. B **14**, 1977–1983 (1997).
23. V. G. Dmitriev, G. G. Gurzadyan, and D. N. Nikogosyan, *Handbook of Nonlinear Optical Crystals*, 2nd ed. (Springer-Verlag, Berlin, 1997).
24. Y. Ding, D. D. Nolte, M. R. Melloch, and A. M. Weiner, "Time-domain image processing using dynamic holography," IEEE J. Sel. Top. Quantum Electron. **4**, 332–341 (1998).
25. J. W. Goodman, *Introduction to Fourier Optics*, 2nd ed. (McGraw-Hill, New York, 1996), Chap. 4.
26. A. Yariv and P. Yeh, *Optical Waves in Crystals* (Wiley, New York, 1984), Chap. 12.

Linear and nonlinear operation
of a time-to-space processor

Dan M. Marom,* **Dmitriy Panasenko, Pang-Chen Sun, and Yeshaiahu Fainman**

*Department of Electrical and Computer Engineering, University of California, San Diego, 9500 Gilman Drive,
La Jolla, California 92093-0407*

The operational characteristics of a time-to-space processor based on three-wave mixing for instantaneous imaging of ultrafast waveforms are investigated. We assess the effects of various system parameters on the processor's important attributes: time window of operation and signal conversion efficiency. Both linear and nonlinear operation regimes are considered, with use of a Gaussian pulse profile and a Gaussian spatial mode model. This model enables us to define a resolution measure for the processor, which is found to be an important characteristic. When the processor is operated in the linear interaction regime, we find that the conversion efficiency of a temporal signal to a spatial image is inversely proportional to the resolution measure. In the nonlinear interaction regime, nonuniform signal conversion due to fundamental wave depletion gives rise to a phenomenon that can be used to enhanced the imaging operation. We experimentally verify this nonlinear operation. © 2001 Optical Society of America

OCIS codes: 320.7100, 070.4340, 320.7110, 190.4380, 190.4420, 190.1900.

1. INTRODUCTION

Ultrafast temporal signals are difficult to acquire, as direct detection of the temporal information is impossible owing to the limited response time of existing solid-state optoelectronic photodetectors. Spatial imaging of ultrafast waveforms offers an invaluable ability, because the complex-amplitude temporal information is converted to a spatial distribution for subsequent detection by slower, parallel optoelectronic devices. Information about the temporal waveform envelope can be inferred from the detected one-dimensional spatial image. Recently, a single-shot technique for time-to-space conversion based on wave mixing spectrally decomposed waves (SDW's) has been introduced and experimentally demonstrated.[1] The time-to-space conversion is generated by three-wave mixing with the SDW of an information-carrying ultrashort temporal waveform and an inverted SDW of a reference ultrashort pulse in the Fourier plane of a spectral processing device (SPD) (see Fig. 1). The two SDW's in the Fourier plane are mixed in a $\chi^{(2)}$ crystal, generating a quasi-monochromatic wave at a doubled frequency. A spatial Fourier transform of the generated second-harmonic field to the output plane produces a spatial image, thereby performing a linear mapping of the information from the time-to-space domain. The novelty of this technique is that the usual relationship between the time window of observation and the physical aperture of the nonlinear crystal[2,3] is decoupled by spectral processing. Additionally, the spatially dispersed frequency components automatically compensate for group velocity mismatch, permitting high conversion efficiency.[4] Moreover quadratic phase compensation is achieved by displacing the output observation plane, permitting chirp cancellation in optical fiber transmissions.[5]

These desirable features make this time-to-space converter suited for future ultrafast optical communication systems.[6]

In this paper, we study in detail the operation trade-offs of the time-to-space converter. More specifically, we investigate the relationship between the conversion efficiency and the observation time window. This information is important in the design of an optical time-division multiplexing system based on ultrafast pulse packets. We find that the processor can be set to operate in the linear regime, under weak three-wave interaction, or in the nonlinear regime, where fundamental wave depletion is exhibited. For the linear regime we derive expressions for the output spatial signal and for the conversion efficiency, finding that the efficiency-resolution product of the processor is an invariant property; improving one parameter degrades the other. When the reference pulse power exceeds certain power levels, the spatial frequency bandwidth of the second harmonic broadens owing to nonuniform signal conversion. The nonlinear operation generates a spatial image with a narrower spot size than in the linear regime, resulting in an enhanced resolution output image due to the nonlinear signal processing.[7] We perform numerical simulations for this nonlinear conversion case based on a Gaussian pulse model and find the required reference pulse power levels for best temporal resolution and maximal conversion efficiency.

The paper is organized as follows: In Section 2 we establish the Gaussian beam profile and Gaussian pulse envelope model that is used throughout this paper, where we find the relationship between the size of the beam and the pulse duration to the resolution of the SPD. The linear and the nonlinear operating regimes of the time-to-space conversion processor are investigated in Sections 3
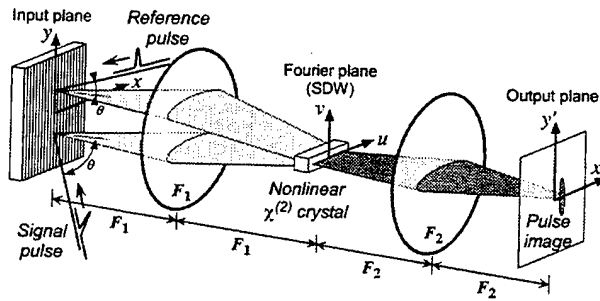
Fig. 1. Time-to-space conversion by using wave mixing of inverted spectrally decomposed waves from a signal and a reference pulse: F_1, F_2, focal length.

and 4, respectively. Experimental results verifying our analysis in terms of enhanced-resolution imaging are presented in Section 5, followed by a conclusion in Section 6.

2. GAUSSIAN MODEL OF INPUT WAVES

The signal and reference pulses that are used in the time-to-space conversion are introduced to the SPD from two opposite sides (see Fig. 1), such that the directions of their spatial dispersions will be mutually inverted. The beams carrying the signal and reference pulses are incident on the input grating of the SPD at angles of $+\theta$ and $-\theta$ relative to the input grating normal, respectively. The angle θ depends on the grating frequency and is chosen such that the diffracted wave at the center frequency of the ultrashort pulse is propagating along the optical axis of the SPD. The diffracted field immediately behind the grating for the signal pulse can be expressed as

$$U_{in}(x, y; t) = E_s w\left(\frac{x}{L_x}\right) w\left(\frac{y}{L_y}\right) p\left(\frac{t - t_0 - \alpha x/c}{\tau}\right)$$
$$\times \exp(j\omega_0 t), \quad (1)$$

where $p(t)$ is the normalized temporal envelope of the ultrashort pulse and $w(x)$ and $w(y)$ are the normalized transversal beam profiles in the x and y directions (assuming that a separable function characteristic is applicable), defining the input pupil function. The parameters τ, L_x, and L_y characterize the pulse duration and the size of the input pupil function on the grating in the x and the y directions, respectively. In general, $L_x = L_y/\cos(\theta)$ if the input beam is circular, owing to the projection on the grating at angle θ. However, the beam can be anamorphically imaged on the grating to achieve independent control over L_x and L_y. The constants E_s, α, c, t_0, and ω_0 are the field strength, grating angular dispersion parameter [$\alpha = \sin(\theta)$], speed of light in vacuum, arbitrary time shift, and center angular frequency of the ultrashort pulse, respectively. Equation (1) describes a short pulse scanning across the fixed aperture at a velocity of c/α in the x direction. This velocity is greater than the speed of light in vacuum owing to the projection of the pulse front on a tilted plane.

We invoke the following two customary assumptions[8,9] in our study: temporal Gaussian pulse envelope and spatial Gaussian beam profile. The Gaussian beam profile is commonly used for spatial confinement of propagating waves and is a known solution to the paraxial Helmholtz

equation.[10] The Gaussian pulse envelope is also found to be a good descriptor of ultrashort pulses. We define the pulse envelope and its corresponding temporal Fourier transform (TFT) by

$$p(t) = \exp\left(-\frac{t^2}{2}\right) \overset{\text{TFT}}{\Leftrightarrow} P(\omega) = \sqrt{2\pi} \exp\left(-\frac{\omega^2}{2}\right), \quad (2)$$

where ω is the angular frequency. Similarly, we define the Gaussian spatial beam profile and its corresponding spatial Fourier transform (SFT) by

$$w(x) = \exp(-x^2) \overset{\text{SFT}}{\Leftrightarrow} W(f_x) = \sqrt{\pi} \exp(-\pi^2 f_x^2), \quad (3)$$

where f_x is the spatial frequency. The difference between the TFT and SFT is due to the inclusion of 2π in the angular frequency term of the TFT, consistent with standard notation. Using the Gaussian model for the spatial modes and temporal profile, we rewrite Eq. (1) as

$$U_{in}(x, y; t) = E_s \exp\left(-\frac{x^2}{L_x^2}\right) \exp\left(-\frac{y^2}{L_y^2}\right)$$
$$\times \exp\left[-\frac{1}{2\tau^2}\left(t - t_0 - \frac{\alpha x}{c}\right)^2\right] \exp(j\omega_0 t).$$
$$(4)$$

Let us make the following observation (see Fig. 2): The width of the spatial beam profile in the x direction is proportional to L_x. The instantaneous spatial width of the pulse scanning across the grating is proportional to $\sqrt{2}\tau c/\alpha$. The ratio of these two widths, $N \equiv \alpha L_x/\sqrt{2}\tau c$, is a measure of the resolution of the SPD and describes the number of pulses that fit into the input pupil function. Its significance is similar to the space–bandwidth product in a traditional spatial-domain optical processing system as will be illustrated next. (Note that N is identical to Weiner's resolution measure,[9] expressed using the parameters of our model.)

The input field of Eq. (4) undergoes a SFT by the first lens of the SPD, with focal length F_1, generating the field in the Fourier plane. The expression is simplified by using the resolution parameter N, yielding the temporal field in local spatial coordinates u and v:
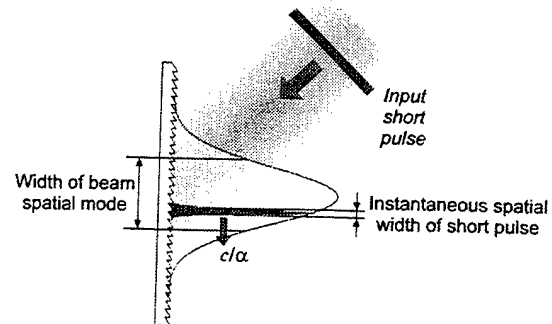
Fig. 2. Gaussian beam mode and Gaussian pulse envelope incident on the diffraction grating. The ratio of their spatial widths determines the resolution of the system.

$$U_{\text{SDW}}(u, v; t) = \frac{E_s L_x L_y \pi}{\lambda_0 F_1 \sqrt{1 + N^2}} \exp\left[-\frac{(t - t_0)^2}{2\tau^2(1 + N^2)} \right]$$

$$\times \exp\left[-\left(\frac{L_x \omega_0 u}{2cF_1}\right)^2 \frac{1}{1 + N^2} \right]$$

$$\times \exp\left[-\left(\frac{L_y \omega_0 v}{2cF_1}\right)^2 \right]$$

$$\times \exp\left[-j \frac{2\pi}{\lambda_0} \frac{cu}{\alpha F_1} \frac{N^2}{1 + N^2}(t - t_0) \right]$$

$$\times \exp(j\omega_0 t). \tag{5}$$

A TFT can be applied to Eq. (5), revealing the spatial dispersion of the field, given by

$$\tilde{U}_{\text{SDW}}(u, v; \omega) = \frac{E_s L_x L_y \pi \tau \sqrt{2\pi}}{\lambda_0 F_1} \exp\left[-\frac{\tau^2}{2}(1 + N^2) \right.$$

$$\times \left. \left(\omega - \omega_0 + \frac{u\omega_0}{\alpha F_1} \frac{N^2}{1 + N^2} \right)^2 \right]$$

$$\times \exp\left[-\left(\frac{L\omega_0 u}{2cF_1}\right)^2 \frac{1}{1 + N^2} \right]$$

$$\times \exp\left[-\left(\frac{L\omega_0 v}{2cF_1}\right)^2 \right] \exp[-j(\omega - \omega_0)t_0]. \tag{6}$$

Note that optical fields in the temporal frequency domain are denoted with a tilde overscript, $\tilde{U}$. Equations (5) and (6) are the time domain and frequency domain representations of the spectrally decomposed wave[11] (SDW) at the Fourier plane. Some important observations can be made on the properties of the SDW from inspecting Eqs. (5) and (6): (i) From Eq. (5) we learn that the duration of the SDW is increased by a factor of $\sqrt{1 + N^2}$. This time corresponds to the time of flight of the pulse through the aperture in the input plane (see Fig. 2). (ii) The spatial dispersion of the temporal frequency components are observed in the first Gaussian function of Eq. (6), yielding $d\omega/du = -(\omega_0/\alpha F_1)N^2/(1 + N^2)$. The spatial dispersion is manifest in Eq. (5) as a Doppler shift of the temporal frequency as a function of the spatial coordinate u. The Doppler frequency shift arises from the movement of the input pulse (or light source) across the diffraction grating. This movement also leads to (iii) The phase fronts of the SDW field [Eq. (5)] vary as a function of time, and the instantaneous angle between the wave vector and the optical axis of the SPD in the paraxial approximation is $(c/\alpha F_1)(N^2/1 + N^2)(t - t_0)$. (iv) The temporal bandwidth at any location u is determined by the first Gaussian function of Eq. (6) and is a $(1 + N^2)^{1/2}$ fraction of the total bandwidth. The frequency resolution can be calculated by dividing the total width of the field [given by the second Gaussian function of Eq. (6)] by the width for a single temporal-frequency component (given by the first Gaussian function when substituting $\omega = \omega_0$, for example). This ratio is again found to be $(1 + N^2)^{1/2}$. In the limit of high-resolution operation (i.e., $N \gg 1$), we will

observe that the SDW duration is $N\tau$, the bandwidth at any point has decreased by a factor of N, and the spatial resolution of frequency components is N. In contrast, if we operate at the low-resolution limit (i.e., $N \ll 1$), the SDW duration will be the same as that of the incident pulse (i.e., τ), and there will be no spatially varying Doppler shift term and no spatial resolution of the frequency components. In this low-resolution case, monochromatic diffraction effects are more pronounced than the bandwidth of the optical source.[10]

As a last step, we calculate the confocal length of the SDW, required as an approximate limit to the possible interaction length in the wave-mixing process under Gaussian beam focusing. The confocal length is calculated from the spatial width (or waist) of the SDW [from Eq. (5)]. The field distribution obeys an independent Gaussian mode for the u and v directions or an elliptical cross section. We find that the two independent confocal lengths for the u and the v directions are $2Z_{0u} = 2n_{\omega_0}F_1^2\lambda_0(1 + N^2)/\pi L_x^2$ and $2Z_{0v} = 2n_{\omega_0}F_1^2\lambda_0/\pi L_y^2$, respectively, where n_{ω_0} is the refractive index of the crystal at frequency ω_0. If one of the confocal lengths is significantly smaller than the other, then it serves as the limit to the interaction length. Usually $L_x \approx L_y$ and $N \gg 1$, resulting in $2Z_{0v}$ as the limiting interaction length. As the size of the input pupil is increased, the confocal length is decreased.

The characteristics of the spectrally decomposed waves are required in our analysis of the time-to-space conversion, which is evaluated in Sections 3 and 4 in the linear and the nonlinear regimes.

3. LINEAR TIME-TO-SPACE CONVERSION

In this section we analyze the wave-mixing process and the dependence of the spatial output signal on the parameters of the SPD in the linear regime, where the fundamental input waves are nondepleting. When this assumption is used, the SDW of the signal and reference pulses are completely characterized and we may find the nonlinear polarization term that arises in the nonlinear crystal. Armed with the nonlinear polarization, we solve the wave equation for the generated quasi-monochromatic third wave, whose spatial frequency modulation carries the temporal-frequency information of the signal pulse. This resultant wave undergoes a SFT to the output plane of the SPD, giving rise to a spatial signal that contains the desired temporal location information t_0 (see Fig. 1). Finally, we calculate the total energy that has been converted to the spatial domain, from which we can find the conversion efficiency from the input temporal pulse to the output spatial signal. This approach differs from Weiner's conversion efficiency estimation, which is based on the SDW's averaged power density[4] (averaged in duration and distribution). We believe that our approach is justified since the conversion is produced by a fast parametric point process, and therefore one should take into account the temporal dynamics and field distribution of the SDW's, as evaluated in Section 2.

A. Nonlinear Polarization

The two mutually inverted SDW's of the signal pulse and the reference pulse interact by using a three-wave-mixing process in a crystal exhibiting a second-order nonlinearity. Since we are operating in the linear interaction regime, the analysis can be performed in the temporal frequency domain. Therefore the nonlinear polarization can be expressed as a convolution of the two input waves in the temporal frequency domain. The SDW of the signal pulse in the temporal frequency domain is given by Eq. (6). The reference pulse generates a similar SDW with an inverted spatial dispersion sign. Consequently, we can express the nonlinear polarization term as[12]

$$P^{NL}(u, v, z; \omega)$$

$$= 2\epsilon_0 d_{\text{eff}} \int_{-\infty}^{\infty} \tilde{U}_{SDW}^S(u, v; \varpi) \tilde{U}_{SDW}^R(u, v; \omega - \varpi)$$

$$\times \exp[j[k_S(\varpi) + k_R(\omega - \varpi)]z] d\varpi, \qquad (7)$$

where d_{eff} is the nonlinear optical coefficient, which is assumed to be constant across the interaction bandwidth as a nonresonant nonlinearity is used, S and R denote the signal and the reference SDW waves, $k_S(\cdot)$ and $k_R(\cdot)$ are the wave-vector magnitudes as a function of the temporal frequency, and the integration variable ϖ has units of temporal frequency. We express the wave-vector dependence on a temporal frequency variable Ω by using a Taylor series expansion about $\Omega = \omega_0$, yielding

$$k_S(\varpi) = k(\omega_0) + (\varpi - \omega_0) \frac{\partial k(\Omega)}{\partial \Omega}\bigg|_{\Omega=\omega_0} + \dots,$$

$$k_R(\omega - \varpi) = k(\omega_0) + (\omega - \varpi - \omega_0) \frac{\partial k(\Omega)}{\partial \Omega}\bigg|_{\Omega=\omega_0} + \dots .$$

(Note: we assume a type I interaction where the two fundamental waves are polarized parallel to the crystal's ordinary axis. Therefore the Taylor coefficients for the two expansions are identical.) When we express the sum of the two k vectors by using only the first two terms of the series expansion, the resultant can be shown to be independent of ϖ and can therefore be taken out of the integral. The nonlinear polarization can therefore be approximated by

$$P^{NL}(u, v, z; \omega)$$

$$= 2\epsilon_0 d_{\text{eff}} \exp\left\{ j\left[2k(\omega_0) \right.\right.$$

$$\left.\left. + k(\omega - 2\omega_0) \frac{\partial k(\Omega)}{\partial \Omega}\bigg|_{\Omega=\omega_0} \right] z \right\} G(u, v; \omega), \quad (8)$$

where

$$G(u, v; \omega) = \int_{-\infty}^{\infty} \tilde{U}_{SDW}^S(u, v; \varpi) \tilde{U}_{SDW}^R(u, v; \omega - \varpi) d\varpi$$

is the convolution operation in the temporal frequency domain.

B. Generated Wave

The nonlinear polarization of Eq. (8) serves as the driving force for the wave equation of the generated third wave, governed by[12]

$$\frac{\partial}{\partial z} \tilde{U}_{\text{sum}}(u, v, z; \omega) = \frac{j}{2} \frac{\omega^2 \mu_0}{k(\omega)} P^{NL}(u, v, z; \omega)$$

$$\times \exp[-jk_{\text{sum}}(\omega)z], \qquad (9)$$

which is the differential equation obtained from the monochromatic plane-wave solution, when the slowly varying envelope and nondepleting pump approximations are used. We next expand $k_{\text{sum}}(\omega)$ in a Taylor series about $\Omega = 2\omega_0$, keeping only the first two terms of the expansion. This procedure is carried out for the phase term only, because it will oscillate rapidly with propagation along z. Using the Taylor approximation and inserting the nonlinear polarization of Eq. (8) into Eq. (9) yields

$$\frac{\partial}{\partial z} \tilde{U}_{\text{sum}}(u, v, z; \omega)$$

$$= j \frac{2\omega_0}{c n_{2\omega_0}} d_{\text{eff}} G(u, v; \omega)$$

$$\times \exp[-j[k(2\omega_0) - 2k(\omega_0)]z] \exp\{-j(\omega - 2\omega_0)$$

$$\times [(\partial k/\partial \Omega)|_{\Omega=2\omega_0} - (\partial k/\partial \Omega)|_{\Omega=\omega_0}]z\}. \qquad (10)$$

We assume that the phase-matching condition, $k(2\omega_0) = 2k(\omega_0)$, can be satisfied by proper crystal selection and orientation. Equation (10) can be integrated from 0 to L_c, the length of the crystal, assuming a zero initial state [i.e., $\tilde{U}_{\text{sum}}(u, v, 0; \omega) = 0$]. The field outside the output face of the crystal is given by

$$\bar{U}_{\text{sum}}(u, v, L_c; \omega)$$

$$= j \frac{2\omega_0}{c n_{2\omega_0}} E_s E_r \sqrt{n_{2\omega_0}} \left(\frac{L_x L_y \pi \tau \sqrt{2\pi}}{\sqrt{n_{\omega_0}} \lambda_0 F_1} \right)^2$$

$$\times \frac{\sqrt{\pi}}{\tau \sqrt{1 + N^2}} d_{\text{eff}} L_c \exp\left[-2\left(\frac{L_y \omega_0 v}{2cF_1} \right)^2 \right]$$

$$\times \exp\left[-\frac{2}{1 + N^2} \left(\frac{L_x \omega_0 u}{2cF_1} \right)^2 \right] \exp\left[-\frac{t_0^2}{4\tau^2(1 + N^2)} \right]$$

$$\times \exp\left[j\omega_0 t_0 \frac{u}{\alpha F_1} \frac{N^2}{1 + N^2} \right] A(\omega) \qquad (11)$$

with $A(\omega)$ defined by

$$A(\omega) = \exp\left[-\frac{(\omega - 2\omega_0)^2 \tau^2}{2} \frac{1 + N^2}{2} \right]$$

$$\times \text{sinc}\left[(\omega - 2\omega_0) \frac{\beta L_c}{2} \right]$$

$$\times \exp\left[-j(\omega - 2\omega_0) \frac{\beta L_c + t_0}{2} \right], \qquad (12)$$

where $\beta = (\partial k/\partial \Omega)|_{\Omega=2\omega_0} - (\partial k/\partial \Omega)|_{\Omega=\omega_0}$ is the inverse group velocity mismatch and we used the explicit solution

of the convolution $G(u, v; \omega)$ in deriving Eq. (11). We observe that the spatial dependence of the output signal has been decoupled from the temporal-frequency variable. This is a fundamental property of wave mixing two mutually inverted SDW's. The spatial dependence in Eq. (11) contains the following components: (i) a confined spatial extent prescribed by the spatial Gaussian functions, (ii) an attenuation factor with Gaussian dependence on the time delay t_0 between the signal and the reference pulses, and (iii) a spatial linear phase term that carries the timing information t_0. The temporal-frequency dependence of $A(\omega)$ consists of the generated Gaussian bandwidth multiplied by a spectral filter in the form of the sinc function. The generated sum wave can also be expressed in the time domain when an inverse TFT is performed, which would result in the replacement of $A(\omega)$ in Eq. (11) by $a(t)$, given by

$$a(t) = \frac{\exp(j2\omega_0 t)}{\sqrt{\pi}\tau\beta L_c\sqrt{1 + N^2}} \exp\left[-\frac{(t - t_0/2)^2}{\tau^2(1 + N^2)} \right]$$

$$\otimes \; \mathrm{rect}\left(\frac{t}{\beta L_c} - \frac{1}{2} \right). \tag{13}$$

Since the TFT of a product is a convolution, $a(t)$ is defined by a convolution between Gaussian and rectangular temporal envelopes with a center frequency of $2\omega_0$. In the case that $\beta L_c \ll \tau N$, spectral filtering due to group velocity mismatch will be negligible and the spectrum $A(\omega)$ and the temporal profile $a(t)$ will be Gaussian. In contrast, when $\beta L_c \gg \tau N$, the spectrum will have a sinc dependence due to phase-matching considerations and the temporal profile will be rectangular.

C. Output Spatial Signal

The field at the output plane of the SPD is evaluated by the SFT of the generated field from the three-wave-mixing process. We express this output field in the time domain, yielding

$$U_{\mathrm{out}}(x', y'; t)$$

$$= j\frac{d_{\mathrm{eff}}}{\sqrt{n_{2\omega_0}n_{\omega_0}}} 2^3\pi^{7/2}E_s E_r \frac{L_x L_y \tau}{\lambda_0{}^2 F_2} L_c a(t)$$

$$\times \exp\left[-\frac{t_0{}^2}{4\tau^2(1 + N^2)} \right] \exp\left[-2\left(\frac{F_1}{F_2}\frac{y'}{L_y}\right)^2 \right]$$

$$\times \exp\left[-2\left(\frac{F_1}{F_2}\right)^2\frac{1 + N^2}{L_x{}^2}\left(x' - \frac{ct_0}{2\alpha}\frac{F_2}{F_1}\frac{N^2}{1 + N^2} \right)^2 \right]. \tag{14}$$

The last two Gaussian terms in Eq. (14) characterize the spot size of the output spatial signal. The location of this Gaussian signal is determined by the temporal information t_0, weighted by the SPD parameters. This term represents the time-to-space converted signal. The amplitude of the output signal is weighted by the Gaussian time window of the SPD, limiting the possible values of t_0. The resolution of the time-to-space converter is determined by these two parameters. It can be shown that the ratio of the spatial widths of the observed range of

output values to the spot size reduces exactly to N, the resolution of the SPD. This result is consistent with our linear conversion regime, illustrating that the space–bandwidth product is preserved. We next analyze the conversion efficiency of the processor.

D. Conversion Efficiency

The time-to-space processor functions in real time, generating the time-varying output spatial field. However, all detection devices respond to the optical intensity. The time-dependent intensity is calculated from Eq. (14), where the amplitudes of the signal and reference pulses have been expressed by their relationship to the signal and the reference pulse energies $\mathcal{E}_s$ and $\mathcal{E}_r$, respectively (see Appendix A) along with the definitions relating the refractive index, the electric permeability, and the speed of light in vacuum, yielding

$$I_{\mathrm{out}}(x', y'; t) = \frac{1}{2}\sqrt{\frac{\epsilon_0}{\mu}}|U_{\mathrm{out}}(x', y'; t)|^2$$

$$= \frac{d_{\mathrm{eff}}^2}{n_{2\omega_0}n_{\omega_0}^2}\frac{1}{\epsilon_0 c}\frac{2^9\pi^4}{\lambda_0{}^4 F_2{}^2}\mathcal{E}_s\mathcal{E}_r L_c{}^2|a(t)|^2$$

$$\times \exp\left[-\frac{t_0{}^2}{2\tau^2(1 + N^2)} \right]$$

$$\times \exp\left[-4\left(\frac{F_1}{F_2}\frac{y'}{L_y}\right)^2 \right]$$

$$\times \exp\left[-4\left(\frac{F_1}{F_2}\right)^2\frac{1 + N^2}{L^2} \right.$$

$$\left. \times \left(x' - \frac{ct_0}{2\alpha}\frac{F_2}{F_1}\frac{N^2}{1 + N^2} \right)^2 \right]. \tag{15}$$

Using the expression for the intensity distribution, we find the total energy at the output, yielding

$$\mathcal{E}_{\mathrm{out}} = \int_{-\infty}^{\infty}\int_{-\infty}^{\infty}\int_{-\infty}^{\infty} I_{\mathrm{out}}(x', y'; t)\mathrm{d}x\mathrm{d}y\mathrm{d}t$$

$$= \frac{d_{\mathrm{eff}}^2}{n_{2\omega_0}n_{\omega_0}^2}2^7\pi^5\mathcal{E}_s\mathcal{E}_r\frac{1}{\epsilon_0 c}\frac{L_x L_y L_c{}^2}{\lambda_0{}^4 F_1{}^2\sqrt{1 + N^2}}$$

$$\times \exp\left[-\frac{t_0{}^2}{2\tau^2(1 + N^2)} \right]\int_{-\infty}^{\infty}|a(t)|^2\mathrm{d}t, \tag{16}$$

which can be simplified with Parseval's relationship,

$$\int_{-\infty}^{\infty}|a(t)|^2\mathrm{d}t = \frac{1}{2\pi}\int_{-\infty}^{\infty}|A(\omega)|^2\mathrm{d}\omega$$

$$= \frac{1}{2\pi}\int_{-\infty}^{\infty}\exp\left[-\frac{\Omega^2\tau^2}{2}(1 + N^2) \right]$$

$$\times \mathrm{sinc}^2\left(\Omega\frac{\beta L_c}{2} \right)\mathrm{d}\Omega, \tag{17}$$

with a change of integration variable $\Omega = \omega - 2\omega_0$. The output energy can be expressed in analytic form for

two limiting cases, when the spectral filtering is negligible ($\beta L_c \ll \tau N$) or dominant ($\beta L_c \gg \tau N$).

In the limit of a high-resolution SPD (i.e., a large pupil mode size, leading to $N \gg 1$), which is usually the case of interest, the Gaussian spectrum will be much narrower than the sinc function. We find that the output energy is given by

$$\mathcal{E}_{\text{out}} = \frac{d_{\text{eff}}^2}{n_{2\omega_0} n_{\omega_0}^2} 2^{13/2} \pi^{9/2} \mathcal{E}_s \mathcal{E}_r \frac{1}{\epsilon_0 c} \frac{L_c^2}{\lambda_0^4 F_1^2} \frac{L_x L_y}{\tau N^2}$$

$$\times \exp\left(-\frac{t_0^2}{2\tau^2 N^2}\right). \qquad (18)$$

The actual interaction length in the crystal L_c, is determined by the minimum of either one of the two confocal lengths of the SDW or the actual length of the crystal.

The output energy can also be evaluated for the case of a very small pupil mode size. In this case, spectral filtering due to the group velocity mismatch will be predominant in Eq. (17). This extreme case is of no interest to us because there is no time-to-space conversion.

E. Efficiency-Resolution Product

Let the conversion efficiency be defined as $\eta = \mathcal{E}_{\text{out}}/\mathcal{E}_s$, the total energy converted from the time-to-space domains. We can manipulate Eq. (18) to express the product of the conversion efficiency and N, the resolution of the SPD. After simplifying we find that

$$\eta N = \frac{d_{\text{eff}}^2}{n_{2\omega_0} n_{\omega_0}^2} 2^7 \pi^{9/2} \mathcal{E}_r \frac{L_c^2}{\lambda_0^4 F_1^2} \frac{L_y}{\epsilon_0 \alpha} \exp\left(-\frac{t_0^2}{2\tau^2 N^2}\right). \quad (19)$$

Thus the efficiency-resolution product is invariant to L_x. One parameter can be improved at the expense of the other, under the assumption that L_c is less than the confocal distance. The implication of this result is that the performance can be improved by increasing L_y and/or decreasing F_1, resulting in tighter focusing of the SDW. However, this leads to a reduction in the confocal length.

In the limiting case of confocal focusing, where we choose the interaction length to equal the confocal length in the vertical direction as defined in Section 2 (because it is shorter than the confocal length in the horizontal direction when $L_x \approx L_y$), we find that

$$\eta N = \frac{d_{\text{eff}}^2}{n_{2\omega_0}} 2^9 \pi^{5/2} \frac{\mathcal{E}_r}{\epsilon_0} \frac{F_1^2}{\alpha L_y^3 \lambda_0^2} \exp\left(-\frac{t_0^2}{2\tau^2 N^2}\right). \quad (20)$$

It is possible to define $f\# = F_1/L_y$, and conclude that the performance of the time-to-space converter improves as $f\#$ increases. Since $L_y \approx L_x$ and $N \propto L_x$, for a large time window to be converted to a space-domain image with a confocal crystal length, a severe conversion efficiency penalty must be paid.

The invariance of the efficiency-resolution product to L_x could be intuitively explained by the following reasoning: The duration of the input field to the SPD is proportional to L_x (input spatial mode), while the field amplitude is proportional to $1/\sqrt{L_x}$ (see Appendix A). The corresponding SDW has the same dependence on L_x for both amplitude and duration parameters. The amplitude of the generated second-harmonic field under the lin-

ear conversion regime is therefore proportional to $1/L_x$, while the duration is still proportional to L_x. The power of the generated field is proportional to $1/L_x^2$ with no change in the duration. Consequently, the energy of the spatial signal is proportional to $1/L_x$, as is the conversion efficiency. Since the resolution N is proportional to L_x, the efficiency-resolution product is invariant to L_x.

The expressions derived in this subsection are valid for weak interaction leading to the linear conversion behavior. However, in many practical cases of interest, the analyzed ultrafast signal is much weaker than the reference pulse. While this arrangement can lead to a high conversion efficiency, it may violate our basic assumption of linear interaction with nondepleting fundamental waves. Therefore a complete analysis should allow fundamental wave depletion, and it is conducted in Section 4.

4. NONLINEAR TIME-TO-SPACE CONVERSION

The three-wave-mixing process of the time-to-space converter is reexamined in this section under the assumption of a strong reference pulse interacting with a weak signal pulse. The reference pulse's SDW is considered to be nondepleting, while the SDW of the signal pulse and the generated quasi-monochromatic second-harmonic wave will experience periodic power exchanges. Owing to the temporal dynamics of the interacting waves, the analysis needs to be performed in the time domain (as opposed to the temporal frequency domain of Section 3), requiring the introduction of a time derivative to the coupled-wave equations. We resolve this complication by restricting our solution to the high-resolution case, where the temporal bandwidth of the waves at any spatial location decreases and approaches a quasi-monochromatic wave. Thus we can use the quasi-static solution to solve the wave-mixing process, ignoring the effect of group velocity mismatch (more thorough justification provided in Appendix B).

A. High-Resolution Spectrally Decomposed Waves

A general expression for the signal pulse's SDW in the high-resolution limit can be evaluated by the SFT of Eq. (1), yielding

$$U_{\text{SDW}}^S(u, v; t)$$

$$= \frac{E_s L_y c \tau}{\alpha \lambda_0 F_1} W\left(\frac{\omega_0 L_y v}{2\pi c F_1}\right) w\left[\frac{c(t - t_0)}{\alpha L_x}\right]$$

$$\times P\left(-\frac{u\tau\omega_0}{\alpha F_1}\right) \exp\left[-j\frac{\omega_0 u}{\alpha F}(t - t_0)\right] \exp(j\omega_0 t), \quad (21)$$

where $W(\cdot)$ and $P(\cdot)$ are the SFT and the TFT of $w(\cdot)$ and $p(\cdot)$, respectively. In our limiting case of high-resolution SDW, the spatial extent in the x direction of the moving ultrashort pulse in Eq. (1) is much smaller than the size of the beam. Thus, in deriving Eq. (21), we simplified the Fourier integral by sampling the spatial mode at the location of the short pulse and taking the aperture effect out of the integral. The temporal frequency dependence of the SDW, evaluated by the TFT of Eq. (21), is given by

$U_{\mathrm{SDW}}^{S}(u, v; \omega)$

$$= \frac{E_s L_x L_y \tau}{\lambda_0 F_1} W\!\left(\frac{\omega_0 L_y v}{2\pi c F}\right) W\!\left[\frac{\alpha L_x \omega_0}{c}\left(\frac{\omega}{\omega_0} - 1 + \frac{u}{\alpha F_1}\right)\right]$$

$$\times P\!\left(-\frac{u\tau\omega_0}{\alpha F_1}\right)\exp[-j(\omega - \omega_0)t_0]. \tag{22}$$

The term mixing the temporal frequency components with the spatial coordinate u in the SFT of the input aperture characterizes the spatial dispersion. Since the beam aperture L_x is large in the high-resolution case, its SFT is a very narrow function. Its width determines the temporal frequency overlap or bandwidth $\Delta\omega$ at any point on the spatial coordinate u. The center temporal frequency component at the spatial coordinate u for the signal SDW is given by

$$\omega_{\mathrm{sig}} = \omega_0 - \frac{u\omega_0}{\alpha F}. \tag{23a}$$

The reference pulse SDW can be described by expressions similar to Eqs. (21) and (22), yet with an opposite spatial dispersion direction. Its temporal frequency to spatial coordinate relationship is therefore given by

$$\omega_{\mathrm{ref}} = \omega_0 + \frac{u\omega_0}{\alpha F}. \tag{23b}$$

We next calculate the phase mismatch of the wave-mixing process at an arbitrary spatial location u due to the temporal frequency bandwidth.

B. Phase Mismatch in Wave-Mixing High-Resolution Spectrally Decomposed Waves

The phase mismatch between the generated spatial wave and the two fundamental SDW's at any spatial location is a function of the wave-vector dependence on temporal frequency. We express this dependence by a Taylor expansion about ω_0 for the fundamental SDW and about $2\omega_0$ for the generated second-harmonic wave, as has been done in the linear analysis case. When the Taylor expansions are used, the phase mismatch is given by

$$\Delta k = k_{\mathrm{sum}}(\omega_{\mathrm{sig}} + \delta\omega_s + \omega_{\mathrm{ref}} + \delta\omega_r) - k_S(\omega_{\mathrm{sig}} + \delta\omega_s)$$

$$- k_R(\omega_{\mathrm{ref}} + \delta\omega_r)$$

$$= \left[k(2\omega_0) + \left.\frac{dk}{d\omega}\right|_{2\omega_0}(\omega_{\mathrm{sig}} + \omega_{\mathrm{ref}} - 2\omega_0 + \delta\omega_s\right.$$

$$\left. + \delta\omega_r)\right] - \left[k(\omega_0) + \left.\frac{dk}{d\omega}\right|_{\omega_0}(\omega_{\mathrm{sig}} - \omega_0 + \delta\omega_s)\right]$$

$$- \left[k(\omega_0) + \left.\frac{dk}{d\omega}\right|_{\omega_0}(\omega_{\mathrm{ref}} - \omega_0 + \delta\omega_r)\right]$$

$$= [k(2\omega_0) - 2k(\omega_0)]$$

$$+ \beta \cdot (\omega_{\mathrm{sig}} + \omega_{\mathrm{ref}} - 2\omega_0 + \delta\omega_s + \delta\omega_r)$$

$$= \beta \cdot (\delta\omega_s + \delta\omega_r) \leqslant \beta \cdot |\Delta\omega|, \tag{24}$$

where $\delta\omega_s$ and $\delta\omega_r$ are frequency terms that are contained in the bandwidth $\Delta\omega$ at each spatial location for the signal and reference SDW. Equation (24) states that the phase mismatch is bound by the product of the inverse group velocity mismatch β (defined in Subsection 3.B) and the bandwidth $\Delta\omega$ at any point on the spatial coordinate u. Since the bandwidth is inversely proportional to L_x, the phase mismatch can be reduced by increasing L_x until the effect of this phase mismatch can be ignored (see Appendix B). In deriving the phase mismatch bound of Eq. (24), we assume that the constant term of the phase mismatch is eliminated by proper crystal orientation, set to satisfy the phase-matching condition. Additionally, owing to the opposite spatial dispersion directions, $\omega_{\mathrm{sig}} + \omega_{\mathrm{ref}} = 2\omega_0$ [see Eqs. (23a) and (23b)]. Finally, $\delta\omega_s$ and $\delta\omega_r$ are bound on $(-\Delta\omega/2, \Delta\omega/2)$ such that their sum is always less than or equal to $|\Delta\omega|$.

C. Solution of Nonlinear Wave-Mixing Spectrally Decomposed Waves

By increasing the SDW resolution, both the bandwidth and phase mismatch at each location are reduced, such that we can assume that in the high-resolution limit the waves are essentially quasi-monochromatic and the three interacting waves are phase matched. Thus the nonlinear wave-mixing problem can be treated with the quasi-static approximation, with the differential equations characterizing the three wave mixing defined by[12]

$$\frac{\partial}{\partial z} U_{\mathrm{SDW}}^{S}(u, v, z; t)$$

$$= j\frac{\omega_0}{cn_{\omega_0}}d_{\mathrm{eff}}U_{\mathrm{sum}}(u, v, z; t)U_{\mathrm{SDW}}^{R*}(u, v; t),$$

$$\frac{\partial}{\partial z} U_{\mathrm{sum}}(u, v, z; t)$$

$$= j\frac{2\omega_0}{cn_{2\omega_0}}d_{\mathrm{eff}}U_{\mathrm{SDW}}^{S}(u, v, z; t)U_{\mathrm{SDW}}^{R}(u, v; t), \tag{25}$$

where we assume that the SDW arising from the reference pulse $U_{\mathrm{SDW}}^{R}(u, v; t)$ is nondepleting. This set of coupled equations resemble those of the frequency-sum process with monochromatic plane waves, and their solution is known to be oscillatory with respect to z. We apply the oscillatory solution with zero initial condition for the generated sum wave, yielding

$$U_{\mathrm{sum}}(u, v, z; t)$$

$$= j\sqrt{\frac{2n_{\omega_0}}{n_{2\omega_0}}}\frac{U_{\mathrm{SDW}}^{R}(u, v; t)}{|U_{\mathrm{SDW}}^{R}(u, v; t)|}U_{\mathrm{SDW}}^{S}(u, v, z = 0; t)$$

$$\times \sin\!\left(\sqrt{\frac{2\omega_0^2}{c^2 n_{\omega_0} n_{2\omega_0}}}d_{\mathrm{eff}}|U_{\mathrm{SDW}}^{R}(u, v; t)|z\right). \tag{26}$$

One can make a small-signal approximation (i.e., $\sin(x) = x$], yielding the results for the linear time-to-space conversion process in the case of negligible spectral filtering (or high resolution). A general form of the SDW, see Eq. (21), or a Gaussian pulse and Gaussian spatial mode

model, see Eq. (5) with $N \gg 1$, can be used in Eq. (26) to characterize the generated wave. However, the nonlinear relationship on the amplitude of the reference SDW prohibits continuing the analysis to the output plane of the processor. Moreover, the reference SDW amplitude is time varying according to the spatial mode of the input beam. A computation program can calculate the SFT of the field at the output of a crystal of length L_c at all times t to generate the field at the observation plane. With the time-varying field, the detected instantaneous intensity can be computed as well as the total energy conversion from the input signal pulse energy to the output spatial wave energy.

However, we can calculate the conversion efficiency from Eq. (26). Using the relationship relating field and intensity, we find that

$$I_{\text{sum}}(u, v, L_c; t)$$

$$= 2I_{\text{SDW}}^S(u, v, 0; t)\sin^2\left\{2\pi \frac{d_{\text{eff}}L_c}{\lambda_0}\left[\frac{4I_{\text{SDW}}^R(u, v; t)}{\epsilon_0 c n_{2\omega_0}n_{\omega_0}^2}\right]^{1/2}\right\}$$

$$(27)$$

For total conversion efficiency, Eq. (27) needs to be integrated over the spatial and the temporal extent. The factor of 2 arises from an equal energy contribution from the reference SDW for every converted photon from the signal SDW.

D. Modeling and Numerical Solution

To characterize the nonlinear time-to-space conversion, a program for calculating the output spatial signal and its accompanying properties was employed, by using a Gaussian pulse envelope and a rectangular beam profile. The rectangular window eliminates the temporal variations of the reference pulse amplitude, simplifying the calculations. Since we are interested in qualitative insight into the nonlinear conversion effect, we computed the output spatial signal from a generated signal of the form $\exp(-x^2)\sin[K\exp(-x^2)]$. The parameter K accounts for the amplitude of u_{ref}, the nonlinear optical coefficient d_{eff}, and the other constants such as the crystal length and refractive indices in Eq. (26). The magnitude squared of the Fourier transform of the output field represents the output intensity distribution observed in the time-to-space conversion.

The results of the simulation (see Fig. 3) illustrate the following: For small values of K the sine function behaves linearly and the generated wave is weak. Its shape is of a smooth Gaussian envelope, both in the Fourier transform plane and at the output plane. As the value of K increases, the generated wave in the Fourier plane exhibits a nonlinear amplitude increase across its spatial distribution. The increase rate is reduced near the center of the Gaussian mode and approaches its maximal value, in accordance with a sine function behavior. Consequently, owing to the Fourier transform relationship, the corresponding pulse image at the output becomes narrower. This image-narrowing feature signifies an improvement in the resolution capability of the time-to-space converter, as the total time window did not change. For greater values of K a dip in the generated wave is developed due to a downconversion process of

photons that have been initially generated in a frequency-sum process. For large values of K, complete modulation of the Gaussian spatial mode occurs, resulting in two separate Gaussian diffraction spots. The phenomenon of a nonuniform signal depletion across the transverse spatial profile is also observed when focusing beams for second-harmonic generation and optical parametric amplification experiments.[13–15] Figure 4 shows a comparison of the output image's spatial distribution by superimposing the normalized traces for small K (linear conversion) and $K = 2.5$ (nonlinear conversion). The image-narrowing feature, resulting in enhanced resolution, is clearly evident.

Two criteria were used to compare the output images: A FWHM measure and a normalized second moment of the profile, i.e.,

$$\int_{-\infty}^{\infty} x^2 I_{\text{out}}(x)\mathrm{d}x \bigg/ \int_{-\infty}^{\infty} I_{\text{out}}(x)\mathrm{d}x.$$

A plot of the two width criteria as a function of K relative to the linear conversion case shows that an optimal value exists for achieving the best resolution (see Fig. 5). K values exceeding the optimal value result in sidelobes in
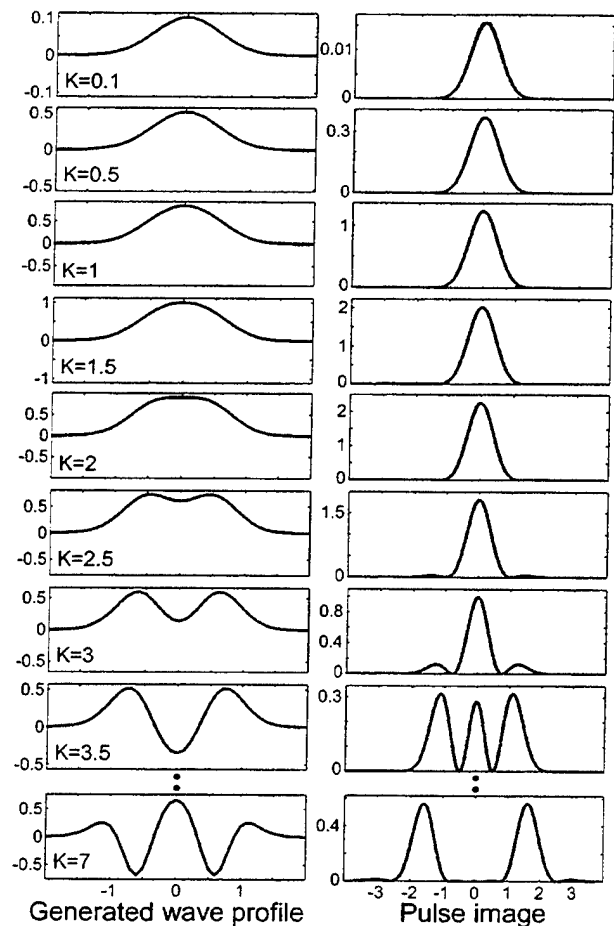
Fig. 3. Field distribution of the converted wave in the Fourier plane (left column) and the intensity distribution in the output plane after a spatial Fourier transform (right column) as a function of the reference pulse power (parameterized by K).
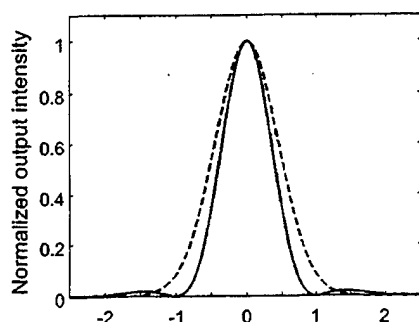
Fig. 4. Enhanced-resolution imaging: comparison of the output image for linear (dashed curve) and nonlinear (solid curve for $K = 2.5$) conversions.
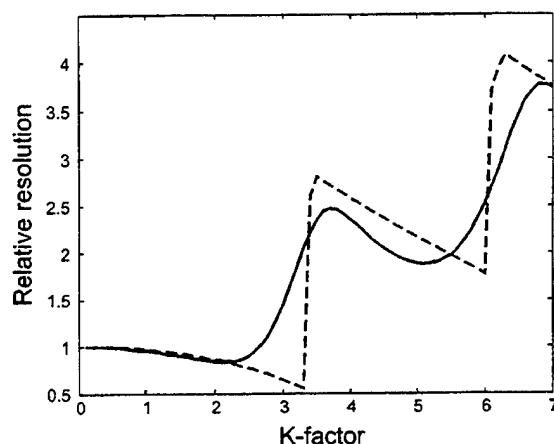
Fig. 5. Resolution improvement of the output signal as a function of reference pulse power K. Dashed curve, FWHM criteria; solid curve, standard deviation measure.
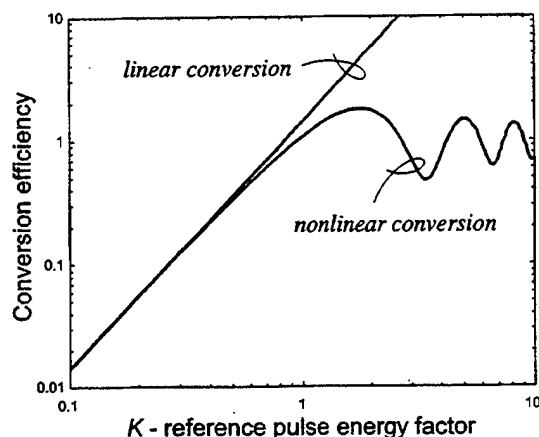
Fig. 6. Conversion efficiency as a function of reference pulse power K. The linear conversion is shown to provide acceptable results for $K < 0.5$.

the output image due to modulation in the Fourier plane, thereby reducing the resolution. The FWHM measure exhibits an abrupt increase when the intensity of the slidelobes exceeds the half-maximum value, whereas the second moment varies smoothly.

The conversion efficiency was calculated with Eq. (27) and $t_0 = 0$ as a function of K (see Fig. 6). The efficiency in the linear case [when $\sin(x) = x$ is used] is plotted as well and follows a 20-dB/dec slope. We can conclude that

the linear case is applicable for $K < 0.5$. The maximum conversion efficiency is approximately 1.80, or 90% of the photons in the input signal pulse. For large values of K the conversion efficiency oscillates about 1; yet the corresponding pulse images consist of two diffracted signals and are of no interest for time-to-space conversion.

The new result predicting enhanced-resolution time-to-space mapping was observed experimentally and is described next.

5. ENHANCED-RESOLUTION EXPERIMENT

To demonstrate the enhanced-resolution time-to-space conversion, we operated the pulse imager in the nonlinear regime. We used a high-power ultrashort pulse laser producing 1-mJ pulses of 100-fs duration at an 800-nm center wavelength. The pulses were divided by a beam splitter to create a signal and a reference pulse (5% and 95% of the power, respectively). The SDW's of the pulses, generated by 600-line/mm gratings and a 375-mm lens, were mixed in a 2-mm-long β barium borate (BBO) crystal in a type I phase-matching configuration. The reference pulse power was adjusted by a neutral-density (ND) filter wheel for experimentation with different values of the parameter K. (Large ND values correspond to small values of K.) The intensity distribution of the generated wave in the Fourier plane (as opposed to the amplitude in the theoretical plots) and their corresponding output image intensity profile were detected as a function of the ND setting (see Fig. 7). As predicted in the com-
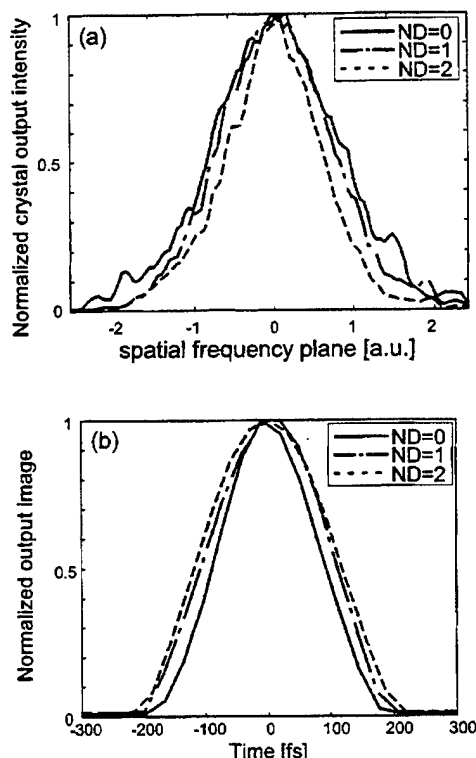
Fig. 7. Experimental results: (a) intensity distribution in the Fourier plane, (b) output pulse image, as functions of the reference pulse attenuation. A high ND setting corresponds to a small K value. Broadening in the Fourier plane and narrowing in the corresponding pulse images are exhibited.
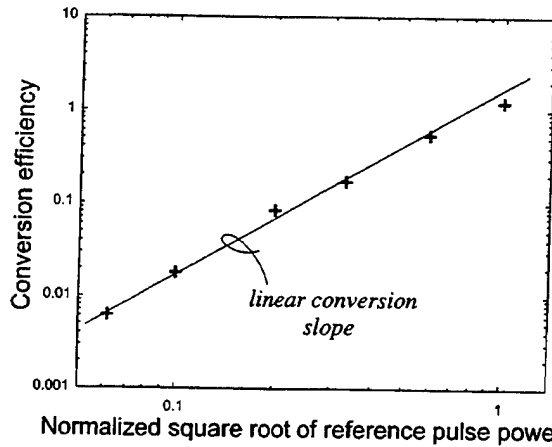
Fig. 8. Measured conversion efficiency as a function of the square root of the reference pulse power. Conversion follows the linear slope of 20 dB/dec.

puter simulation program, at a low ND setting the generated wave in the Fourier plane is broader and its corresponding output image is narrower. A plot of the conversion efficiency versus the square root of the reference pulse power shows that we are still operating in the vicinity of the linear conversion zone (see Fig. 8), as no saturation effects are observed. This can be attributed to using a Gaussian spatial mode, which varies in time, causing the nonlinear conversion to be less pronounced than in the rectangular window used in the nonlinear conversion analysis.

6. CONCLUSION

The operational characteristics of a time-to-space processor based on three wave mixing for instantaneous imaging of ultrafast waveforms has been analyzed. A model based on a Gaussian pulse envelope and a Gaussian spatial mode has been developed. This model closely describes most cases of interest, where ultrashort pulse packets from a possible optical data communication system are to be detected. Using the properties of the Gaussian model and the SPD, we define the resolution parameter of the processor. The resolution parameter dictates the observation time window for our processor and also plays a vital role in the wave-mixing process.

Both the linear and the nonlinear conversion regimes were investigated, yielding the output spatial signal form and conversion efficiency. In the linear conversion regime we find that we can define an efficiency-resolution product, which is an invariant measure depending on the system parameters. Thus efficiency can be traded for resolution and vice versa. In the nonlinear regime we show that, by using a strong reference pulse, we can enhance the spatial bandwidth of the signal, thereby achieving enhanced temporal-resolution imaging. Numerical simulation results are used to demonstrate this effect. The maximum possible power conversion efficiency was found to approach 180%. The numerical data also illustrate the operation transition point between the linear and the nonlinear regimes, which is important in the design of this processor. The nonlinear operation was also

realized experimentally, demonstrating the expected enhanced-resolution performance.

The three-wave-mixing process was analyzed with the assumption of a bulk nonlinear crystal. However, it should be possible to achieve other functionalities, such as further increasing the resolution enhancement, by lateral patterning of the nonlinear crystal. This has been demonstrated in quasi-phased-matched periodically poled LiNbO$_3$, for generation of a flat-top field.[16] The same principle can be applied to the time-to-space processor, which may achieve an even finer spot size after a SFT.

APPENDIX A: PULSE AMPLITUDE AND ENERGY RELATIONSHIP

The SPD resolution was shown to depend on the input pupil size on the diffraction grating with the increasing resolution and time window at a larger pupil. For the purpose of the time-to-space converter, the nonlinear wave-mixing efficiency depends on the instantaneous input powers. When the mode on the grating is increased by use of two lenses in a telescope configuration, a larger spatial mode can be supported, but the peak power is reduced as the pulse carries finite energy. In this Appendix we find the relationship between the pulse energy and peak power by using our Gaussian pulse and Gaussian spatial mode model.

Using the expression for the input field on the diffraction grating of the SPD, Eq. (4), we find the instantaneous intensity distribution, given by

$$
\begin{aligned}
I_{\text{in}}(x, y; t) &= \frac{1}{2} \sqrt{\frac{\epsilon_0}{\mu}} |U_{\text{in}}(x, y; t)|^2 \\
&= \frac{1}{2} \sqrt{\frac{\epsilon_0}{\mu}} E_s{}^2 \exp\left(-\frac{2x^2}{L_x{}^2}\right) \\
&\quad \times \exp\left(-\frac{2y^2}{L_y{}^2}\right) \exp\left[-\frac{1}{\tau^2}\left(t - t_0 - \frac{\alpha x}{c}\right)^2\right].
\end{aligned}
$$
(A1)

Using the expression for the instantaneous intensity distribution, we find the total energy on the grating, i.e.,

$$
\int_{-\infty}^{\infty}\int_{-\infty}^{\infty}\int_{-\infty}^{\infty} I_{\text{in}}(x, y; t)\,dx\,dy\,dt \equiv \mathcal{E}_s,
$$

and by setting the expression equal to the energy of the short pulse $\mathcal{E}_s$, we may express the field amplitude as a function of the pulse energy and pupil size, yielding

$$
E_s = \left(\frac{\mathcal{E}_s}{L_x L_y \tau} \frac{4}{\pi^{3/2}} \sqrt{\frac{\mu}{\epsilon_0}}\right)^{1/2}.
$$
(A2)

As expected, when the spatial extent increases or the pulse duration increases for fixed pulse energy, the instantaneous field amplitude decreases.

APPENDIX B: VALIDITY OF THE QUASI-STATIC APPROXIMATION FOR WAVE MIXING WITH HIGH-RESOLUTION SPECTRALLY DECOMPOSED WAVES

The effect of group velocity mismatch gives rise to temporal walk-off when we are wave mixing ultrashort pulses. Since the time-to-space processor performs the wave-mixing operation on the SDW's of the pulses, the walk-off effect is greatly reduced since the bandwidth at every point $\Delta\omega$ is smaller than the total bandwidth and the duration is extended [see Eqs. (21) and (22)]. When the Gaussian approximations for the pulse envelope and spatial mode (Section 2) are used, the bandwidths is $1/N$ of the total bandwidth.

Since in our assumptions the signal and the reference beams have the same spatial mode size L_x, they will also have the same bandwidth at any point. The phase mismatch at any location u is caused by the group velocity mismatch and is bound by $\beta\Delta\omega$ [see Eq. (24)], where β is the inverse group velocity mismatch and $\Delta\omega$ can be reduced by increasing L_x. It is possible to define a quasi-static interaction length, $L_{qs} = 1/(\beta\Delta\omega)$, which characterizes an effective length from which the effect of group velocity mismatch is perceptible. If the interaction length in the nonlinear crystal is less than the quasi-static interaction length, i.e., $L_c < L_{qs}$, then we can neglect the effect of group velocity mismatch. Thus the nonlinear wave-mixing problem can be treated in the quasi-static approximation without a partial derivative with respect to time in the differential equations characterizing the wave-propagation phenomena.

With the assumption of a high-resolution SDW, L_{qs} can be made very large, and we can use the known quasi-static solutions obtained for the case of monochromatic waves.

ACKNOWLEDGMENTS

*Current address, Lucent Technologies, Room 4B-411, 101 Crawfords Corner Road, Holmdel, New Jersey 07733.

REFERENCES

1. P. C. Sun, Y. T. Mazurenko, and Y. Fainman, "Femtosecond pulse imaging: ultrafast optical oscilloscope," J. Opt. Soc. Am. A **14**, 1159–1170 (1997).
2. J. Janszky, G. Corradi, and R. N. Gyuzalian, "On a possibility of analysing the temporal characteristics of short light pulses," Opt. Commun. **23**, 293–298 (1977).
3. F. Salin, P. Georges, G. Roger, and A. Brun, "Single-shot measurement of a 52-fs pulse," Appl. Opt. **26**, 4528–4531 (1987).
4. A. M. Kan'an and A. M. Weiner, "Efficient time-to-space conversion of femtosecond optical pulses," J. Opt. Soc. Am. B **15**, 1242–1245 (1998).
5. P. C. Sun, Y. T. Mazurenko, and Y. Fainman, "Real-time one-dimensional coherent imaging through single-mode fibers by space–time conversion processors," Opt. Lett. **22**, 1861–1863 (1997).
6. D. M. Marom, P.-C. Sun, and Y. Fainman, "Analysis of spatial–temporal converters for all-optical communication links," Appl. Opt. **37**, 2858–2868 (1998).
7. B. Javidi and D. Painchaud, "Distortion-invariant pattern recognition with Fourier-plane nonlinear filters," Appl. Opt. **35**, 318–331 (1996).
8. R. N. Thurston, J. P. Heritage, A. M. Weiner, and W. J. Tomlinson, "Analysis of picosecond pulse shape synthesis by spectral masking in a grating pulse compressor," IEEE J. Quantum Electron. **QE-22**, 682–696 (1986).
9. A. M. Weiner, J. P. Heritage, and E. M. Kirschner, "High-resolution femtosecond pulse shaping," J. Opt. Soc. Am. B **5**, 1563–1572 (1988).
10. J. W. Goodman, *Introduction to Fourier Optics*, 2nd ed. (McGraw-Hill, New York, 1996).
11. Y. T. Mazurenko, "Holography of wave packets," Appl. Phys. B **50**, 101–114 (1990).
12. P. N. Butcher and D. Cotter, *The Elements of Nonlinear Optics* (Cambridge U. Press, New York, 1990).
13. D. Eimerl, "High average power harmonic generation," IEEE J. Quantum Electron. **QE-23**, 575–592 (1987).
14. C. Sang-Kyung, L. Ruo-Ding, K. Chonghoon, and K. Prem, "Traveling-wave optical parametric amplifier: investigation of its phase-sensitive and phase-insensitive gain response," J. Opt. Soc. Am. B **14**, 1564–1575 (1997).
15. K. Chonghoon, L. Ruo-Ding, and K. Prem, "Deamplification response of a traveling-wave phase-sensitive optical parametric amplifier," Opt. Lett. **19**, 132–134 (1994).
16. G. Imeshev, M. Proctor, and M. M. Fejer, "Lateral patterning of nonlinear frequency conversion with transversely varying quasi-phase-matching gratings," Opt. Lett. **23**, 673–675 (1998).

Real-Time Spatial–Temporal Signal Processing With Optical Nonlinearities

Dan M. Marom, *Member, IEEE*, Dmitriy Panasenko, Pang-Chen Sun, Yuri T. Mazurenko, and Yeshaiahu Fainman, *Senior Member, IEEE*

Abstract—The instantaneous response time of parametric optical nonlinearities enable real-time processing of, and interaction between, spatial and temporal optical waveforms. We review the various signal-processing alternatives based on three- and four-wave-mixing arrangements among spatial and temporal information carrying waveforms. The fast response time of the interaction permits information exchange between the time and space domains, providing the ability to correlate and convolve signals from the two domains. We demonstrate the usefulness of real-time signal processing with optical nonlinearities with the following experiments: converting waveforms from the time to space domain as well as from the space to time domain, spectral phase conjugation and spectral inversion of ultrafast waveforms, transmission of the spatial correlation function on an ultrafast waveform, and a suggestion for a single-shot triple autocorrelation measurement.

Index Terms—Femtosecond pulse shaping, optical information processing, optical signal processing, space-to-time conversion, time reversal, time-to-space conversion, ultrafast processes.

I. INTRODUCTION

HARNESSING ultrashort laser pulse technology for future high-capacity optical communication systems may result in new paradigms for information transmission. Ultrashort pulses can be used as a basis for time-division multiplexing in a fiber communication application, with the potential to carry ultra-high-speed data [1], [2]. The broad spectrum of ultrashort pulses can be utilized as a low-noise multiple-channel optical source for distribution of data using wavelength-division multiplexing by implementing spectral slicing techniques in either the time [3] or the space [4] domain. Data networking applications may benefit from the asynchronous property of code-division multiple access (CDMA), which can be performed by spectrally encoding and decoding ultrashort pulses with unique codes assigned to all users of the network [5], [6]. More sophisticated data modulation formats, such as ultrafast pulse packet transmission on designated time slots [7] and hybrid pulse position modulation with CDMA encoding [8], can result in perfor-

mance gains due to efficient utilization of the ultrashort pulse bandwidth. The ultrafast modulation and detection processes that these techniques require cannot be accomplished by conventional electronic means, due to the limited response time of electronic components, and require novel real-time optical processors based on instantaneous nonlinear phenomena.

During the last few years, we have developed real-time optical processors utilizing nonlinear wave mixing of two or three input waves originating from spatial or temporal channels for synthesizing, processing, and detecting ultrafast waveforms. These devices perform real-time optical signal processing that can be applied to data conversion between slow parallel channels and an ultrafast serial signal. For the data modulation application, we demonstrated a space-to-time mapping processor that converts spatial frequency information from an input spatial channel to the temporal frequency content of an input ultrashort pulse [9], [10]. Using a four-wave-mixing arrangement utilizing cascaded second-order nonlinearities, the output channel yields an ultrafast waveform that is a time-scaled replica of the input spatial image. For detection of ultrafast waveforms, we built a time-to-space mapping processor, which mixes two spatially inverted temporal frequency information waves in a three-wave-mixing arrangement, generating a spatial signal carrying the temporal image for detection by slower electronic means [11], [12]. The two input temporal channels, the first carrying the desired ultrafast information and the second a reference ultrashort pulse, yield a quasi-monochromatic wave due to the mixing process at every point in space between two spectral components that result in a constant carrier frequency (due to the mutually inverted spectra arrangement in the space domain). By introducing only temporal information channels to our processor, we have demonstrated real-time optical processing of temporal waveforms. We performed time-reversal experiments using a four-wave-mixing arrangement with information carrying ultrafast waveform and two reference ultrashort pulses [13]. The time-reversal experiments were based on performing spectral phase conjugation and spectral inversion operations, achieving time reversal of the electrical field and of the complex amplitude waveform, respectively. Spectral phase conjugation is an important feature for compensation of chromatic dispersion and some nonlinear effects of an optical fiber communication link [14].

In this paper, we explore the different real-time signal-processing capabilities that are possible with three- and four-wave-mixing arrangements of spatial and temporal input waveforms. We adopt the methodology for invention introduced by Lohmann [15] to unravel all wave-mixing
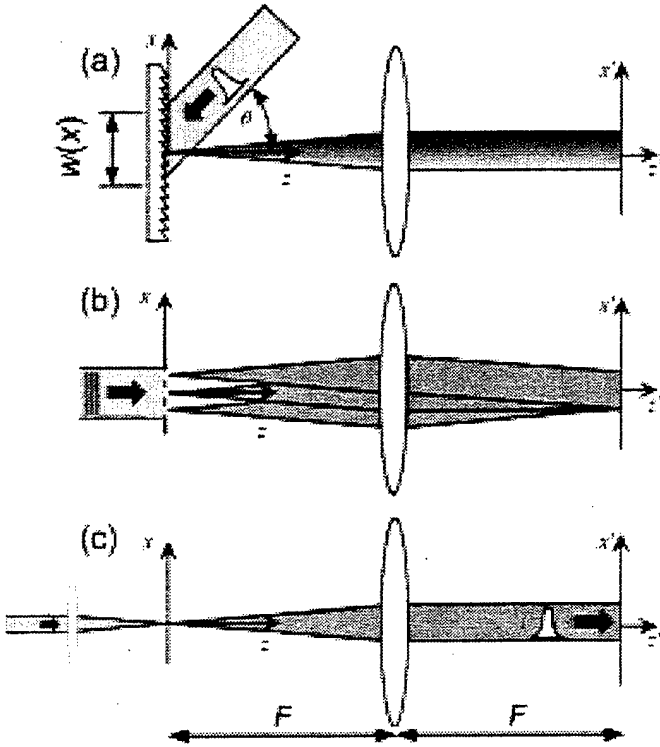
Fig. 1. Input optical waves for consideration in Fourier plane processing. (a) Spectrally decomposed wave, (b) spatial frequency information, and (c) ultrashort pulse.

combinations of the input optical signals. A table is constructed for each interaction type, with columns for the various input waveforms, leading to a unique output signal at each row. We find that this generalized approach describes not only the experiments we have reported but also experiments conducted by others in the past and some new results that are described herein. We demonstrate the transmission of the correlation function of spatial images on an ultrafast waveform and describe a measurement technique of ultrashort pulses that provides the triple correlation values, from which the precise pulse intensity could be extracted.

This paper is organized as follows. Section II defines the input spatial and temporal waves that we consider for interaction via the optical nonlinearities. We limit the scope of this study to interaction at the Fourier plane of a 4-F system, where spatial and temporal frequency information appears. The resulting output waveform combinations in the cases of three- and four-wave mixing are analyzed in Sections III and IV, respectively. New results are described in Sections V and VI, followed by concluding remarks.

II. SPATIAL AND TEMPORAL INPUT WAVES

The spatial and temporal input waves interact by the nonlinear mixing process at the Fourier plane of a 4-F processor. The 4-F arrangement has traditionally been used for coherent processing of spatial images [16] and modified for processing of ultrafast waveforms by introducing diffraction gratings at the input and output planes [17]. The input waves that are to be considered in the wave-mixing processing are (see Fig. 1): 1) spectrally decomposed wave (SDW), i.e., spatially dispersed temporal frequency information; 2) monochromatic wave carrying spatial frequency information; and 3) ultrashort pulse with no spatial information. We assume that all input waves have the same center angular frequency ω_0. Furthermore, the information contained in the y-axis is omitted, as we consider one-dimensional (1-D) spatial images only and the temporal information is inherently 1-D. We configure the input optical signals with a lateral displacement, for convenience as well as for satisfaction of the noncollinear phase matching requirement. This lateral shift introduces a constant linear phase component in the Fourier plane, which is omitted here for brevity.

The SDW is generated by diffracting the ultrafast waveform signal $p(t)$ from the input plane grating, at an incidence angle θ relative to the grating normal, such that the diffracted wave at the center frequency of the ultrashort pulse is propagating parallel to the optical axis. The field at the back focal plane of the lens, or the Fourier plane, is described by [12]

$$U_{\text{SDW}}(x'; t) = w\left(-\frac{ct}{\alpha}\right) P\left(\frac{x'\omega_0}{\alpha F}\right) \exp\left(j\frac{\omega_0 x'}{\alpha F}t\right)$$
$$\times \exp(-j\omega_0 t) \qquad (1a)$$

where

$P(\omega)$ temporal Fourier transform of $p(t)$;

$w(\bullet)$ beam projection profile on the input diffraction grating (or pupil function);

α grating's angular dispersion parameter ($\alpha = \sin(\theta)$);

F lens focal length;

c speed of light in vacuum.

Equation (1a) describes a wave of finite duration (limited by the pupil function), whose transverse profile (along x') carries the temporal spectrum information, with a rotating wave-vector in time. It represents the limiting case of a high-resolution SDW, applicable when the duration of the ultrafast waveform is much shorter than the travel time across the pupil function. In certain signal-processing applications, it is desirable to disperse the spectra in the opposite direction. For this case, we introduce the ultrafast waveform from the opposite size (at angle $-\theta$), utilizing the opposite diffraction order, resulting in the SDW field

$$U_{\text{SDW}}(x'; t) = w\left(\frac{ct}{\alpha}\right) P\left(-\frac{x'\omega_0}{\alpha F}\right) \exp\left(-j\frac{\omega_0 x'}{\alpha F}t\right)$$
$$\times \exp(-j\omega_0 t). \qquad (1b)$$

We assume that the pupil functions of the SDWs of (1a) and (1b) are equal and even functions, resulting in an identical duration and temporal variation for the two functions. Further inspection shows that the temporal frequency information is reversed, as is the wave-vector rotation direction.

The spatial information wave is generated by a 1-D mask $m(x)$ placed at the input plane of the lens and illuminated by a monochromatic light source. At the back focal plane of the lens, we observe the spatial frequency information, given by [16]

$$U_{\text{Spatial}}(x'; t) = M\left(\frac{x'}{\lambda_0 F}\right) \exp(-j\omega_0 t) \qquad (2)$$

where $M(f_x)$ is the spatial Fourier transform of the image and λ_0 is the wavelength.

TABLE I
ULTRAFAST SIGNAL-PROCESSING ALTERNATIVES WITH THREE-WAVE MIXING

Input U_1	Input U_2	Resultant U_3	Output signal	Comments
SDW	SDW	SDW with doubled spatial dispersion	Ultrafast waveform: convolution of input waveforms	Output at doubled carrier center frequency
SDW	Inverted SDW	Quasi-monochromatic wave	Spatial signal: correlation of input waveforms	When one input wave is transform limited → time-to-space conversion
Spatial frequency wave	Spatial frequency wave	Spatial frequency wave	Spatial signal: convolution of input images	
SDW	Spatial frequency wave	SDW	Ultrafast waveform: correlation of input waveform and spatial image	Output at doubled carrier center frequency
Ultrashort pulse	Ultrashort pulse	Ultrashort pulse	Image of output wave: correlation of input waveforms	Standard intensity cross-correlation measurement
Spatial frequency wave	Ultrashort pulse	Ultrashort pulse	N.A.	Can be used for frequency up-conversion
SDW	Ultrashort pulse	Ultrashort pulse	Image of output wave: convolution of input ultrafast waveforms	Can be used for time-to-space conversion

Finally, we also consider a wave that carries the temporal information directly (as opposed to the temporal frequency information) with no spatial dependence, defined by

$$U_{\text{Temp}}(x';t) = p(t)\exp(-j\omega_0 t). \qquad (3)$$

When this signal is utilized with a real-time nonlinearity, it performs a time gating functionality.

The waves defined in (1)–(3) interact using the parametric processes of a nonlinear crystal. We seek to identify the signal-processing capabilities that are enabled by the ability to generate the product of the waves. For this purpose, the wave-mixing crystal is thin, such that phase mismatch and walkoff effects are not considered. Depending on the combination of input waves, the output signal will be in either the time domain or the space domain. It is further assumed that all waveforms arrive at the processor at the same time (i.e., no time delay between waveforms), unless otherwise noted. In a three-wave-mixing arrangement, the product of the two waves is produced by a noncollinear frequency-sum process. The output wave will be at a doubled carrier frequency. In the four-wave-mixing arrangement, the output is at the same carrier frequency due to the degenerate configuration. We implemented the four-wave mixing by a cascade of three-wave processes; frequency-sum followed by frequency-difference in a noncollinear type-II phase-matching arrangement [18]. In this arrangement, the output signal is copropagating with one of the input signals, but at an orthogonal polarization state. The output signal can be extracted with a polarization beam splitter.

The three-wave-processing capabilities are developed next.

III. ULTRAFAST PROCESSING WITH THREE-WAVE MIXING

In a three-wave-mixing process, two input waves generate a third output wave that is proportional to the product of the two waves, i.e., $U_3 \propto \chi^{(2)} U_1 U_2$. Each of the input fundamental waves U_1 and U_2 can have the form of any one of the three

waves of (1)–(3). Table I summarizes all the fundamental wave combinations and the resulting processing achieved at the output signal.

A. SDW–SDW Mixing

The wave produced by the product of two input fundamental waves of the form of (1a) is given by

$$U_3(x';t) = w^2\left(-\frac{ct}{\alpha}\right) P_1\left(\frac{x'\omega_0}{\alpha F}\right) P_2\left(\frac{x'\omega_0}{\alpha F}\right)$$
$$\times \exp\left(j\frac{2\omega_0 x'}{\alpha F}t\right)\exp(-j2\omega_0 t). \qquad (4)$$

Applying a spatial Fourier transform to the output plane, with the Fourier kernel adjusted for the new carrier frequency, yields

$$U_{\text{out}}(x'';t) \propto y\left(2\left(t-\frac{\alpha x''}{c}\right)\right) w^2\left(-\frac{ct}{\alpha}\right)\exp(-j2\omega_0 t) \qquad (5)$$

where $y(t) = p_1(t) \otimes p_2(t)$ and $\otimes$ denotes the convolution operator. The new ultrafast waveform $y(\bullet)$ scans along the output plane at a velocity of c/α. If the signal of (5) is diffracted from a grating with a spatial frequency that is double that of the grating in the input plane of the processor, then the waveform will propagate in free space. The doubled spatial frequency is required since the center wavelength has been halved. The new waveform is proportional to the convolution of the two input waveforms, resulting from the information exchange among the temporal frequency components of $p_1(t)$, $p_2(t)$, and $y(t)$.

B. SDW–Inverted SDW Mixing

The wave produced by the product of two mutually inverted SDW is given by

$$U_3(x';t) = w\left(-\frac{ct}{\alpha}\right) w\left(\frac{ct}{\alpha}\right) P_1\left(\frac{x'\omega_0}{\alpha F}\right) P_2\left(-\frac{x'\omega_0}{\alpha F}\right)$$
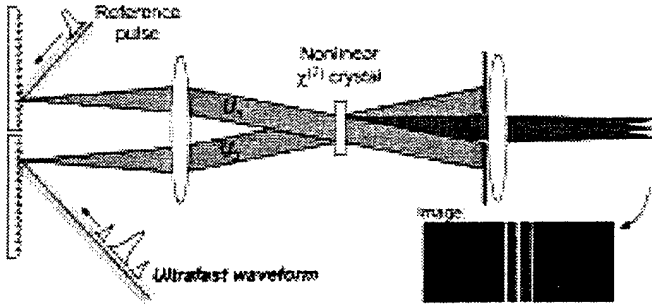$$\times \exp(-j2\omega_0 t). \qquad (6)$$

Fig. 2. Experimental setup for time-to-space conversion using mutually inverted spectrally decomposed waves with three-wave mixing. Inset: experimental result showing converted image from an ultrafast pulse sequence. Temporal information can be inferred from image with knowledge of scaling factor.

Applying a spatial Fourier transform, with the Fourier kernel adjusted for the new carrier frequency, yields

$$U_{out}(x''; t) \propto y\left(-\frac{2\alpha x''}{c}\right) w\left(-\frac{ct}{\alpha}\right) w\left(\frac{ct}{\alpha}\right) \exp(-j2\omega_0 t) \tag{7}$$

where $y(t) = p_1(t) \otimes p_2(-t)$. The stationary spatial signal, $y(\bullet)$, is proportional to the convolution of the two input waveforms, where one of them is reversed in time. This mixing process was developed for time-to-space conversion by using a reference transform-limited pulse for the reversed waveform [11], as illustrated in Fig. 2. We have performed such time-to-space conversions with ultrashort pulses varying in energy levels from subnanojoules (for compatibility with optical communication applications [19]) to millijoules with both LBO and β-barium borate (BBO) crystals, with information conversion efficiencies as high as 120% [12] (the conversion efficiency can exceed 100% due to an equal energy contribution from the reference pulse). The high conversion efficiency is possible due to the favorable phase matching that the mutually inverted SDWs support [20].

C. Mixing Spatial Information Channels

The wave produced by the product of two spatial frequency information channels is given by

$$U_3(x'; t) = M_1\left(\frac{x'}{\lambda_0 F}\right) M_2\left(\frac{x'}{\lambda_0 F}\right) \exp(-j2\omega_0 t). \tag{8}$$

Applying a spatial Fourier transform yields

$$U_{out}(x''; t) = y(-2x'') \exp(-j2\omega_0 t) \tag{9}$$

where $y(x) = m_1(x) \otimes m_2(x)$. The output spatial signal is a convolution of the input images and is a typical output signal in Fourier optics [16] apart from the scaling factor of two, caused by the frequency doubling. The same signal-processing functionality can be achieved with photorefractive recording media, as the fast response time of the parametric processes is not required here.

D. SDW–Spatial Wave Mixing

The wave produced by the product of a SDW of the form of (1a) and a spatial frequency information wave of the form of (2) is given by

$$U_3(x'; t) = w\left(-\frac{ct}{\alpha}\right) P_1\left(\frac{x'\omega_0}{\alpha F}\right) M_2\left(\frac{x'}{\lambda_0 F}\right)$$
$$\times \exp\left(j\frac{\omega_0 x'}{\alpha F} t\right) \exp(-j2\omega_0 t). \tag{10}$$

Applying a spatial Fourier transform to the output plane, with the Fourier kernel adjusted for the new carrier frequency, yields

$$U_{out}(x''; t) \propto y\left(t - \frac{2\alpha x''}{c}\right) w\left(\frac{ct}{\alpha}\right) \exp(-j2\omega_0 t) \tag{11}$$

where $y(t) = p_1(t) \otimes m_2(ct/\alpha)$. The new ultrafast waveform $y(\bullet)$ scans along the output plane at a velocity of $c/2\alpha$. Since both the scanning velocity at the output and the center wavelength have been halved, it is necessary to place a grating with a spatial frequency that is quadruple that of the grating in the input plane of the processor for the waveform to propagate in free space. The new waveform is proportional to the convolution of the input ultrafast waveform and the spatial image, when scaled by c/α to a time-domain variable. Mixing the temporal frequency content of an ultrashort pulse $p_1(t)$ with the spatial frequency information of an image $m_2(x)$ can therefore be used to perform pulse shaping for the output waveform $y(t)$, albeit at a converted wavelength.

E. Mixing Ultrashort Pulses

The wave produced by the product of two ultrashort pulses of the form of (3), while allowing for a timing difference τ between the pulses, is given by

$$U_3(x'; t) = p_1(t)p_2(t + \tau) \exp(-j2\omega_0 t). \tag{12}$$

Suppose next that we place a slow detector at the output of the crystal to measure the intensity of the generated second harmonic light. The instantaneous intensity that is incident on the detector is

$$I_3(x'; t) = |U_3(x'; t)|^2 = |p_1(t)p_2(t + \tau)|^2 = I_1(t)I_2(t + \tau). \tag{13}$$

However, due to the slow response time of detector, the measurement registers the accumulated signal, given by

$$I_3(\tau) = \int I_1(t)I_2(t + \tau)\, dt. \tag{14}$$

The output signal is the well-known intensity cross-correlation of the ultrafast waveforms, the most fundamental short pulse characterization technique [21], [22]. Note that the intensity cross-correlation signal is observable in space in a noncollinear arrangement (by imaging the output light), but our simplified

TABLE II
ULTRAFAST SIGNAL-PROCESSING ALTERNATIVES WITH FOUR-WAVE MIXING

Input U_1	Input U_2	Input U_3	Resultant U_4	Output signal	Comments
SDW	SDW	SDW	SDW	Ultrafast waveform: convolution and correlation among input waveforms.	Spectral phase conjugation for dispersion compensation
SDW	Inverted SDW	Inverted SDW	SDW	Ultrafast waveform: convolutions among waveform, inverted waveform, and conjugated waveform	True time-inversion for complex amplitude waveforms.
SDW	Spatial frequency wave	Spatial frequency wave	SDW	Ultrafast waveform: convolution and correlation among input waveform and spatial images	Space-to-time conversion when one spatial channel is delta function
Spatial frequency wave	SDW	SDW	Spatial frequency wave	Spatial wave: correlation of temporal waveforms convolved to spatial wave	Time-to-space conversion with dispersion compensation
SDW	Inverted SDW	Spatial frequency wave	Spatial frequency wave	Spatial wave: convolution of temporal waveforms correlated to spatial wave	
Spatial frequency wave	Spatial frequency wave	Spatial frequency wave	Spatial frequency wave	Spatial wave: convolution and correlation among spatial images	
SDW	Ultrashort pulse	Ultrashort pulse	Ultrashort pulse	Spatial image: Intensity triple cross-correlation	Exact waveform can be extracted from triple correlation

representation of (3) does not take into account the space–time dependence of the propagating waveform.

F. Mixing Spatial Waves With Ultrashort Pulses

The wave produced by the product of a spatial frequency information wave and an ultrashort pulse is given by

$$U_3(x';t) = M_1\left(\frac{x'}{\lambda_0 F}\right) p_2(t) \exp(-j2\omega_0 t). \quad (15)$$

This signal has no significant signal-processing application that comes to mind.

G. SDW–Ultrashort Pulse Mixing

Mixing an SDW with an ultrashort pulse introduces a time gating on the wave, resulting in the output second harmonic wave

$$U_3(x';t) = w\left(-\frac{ct}{\alpha}\right) P_1\left(\frac{x'\omega_0}{\alpha F}\right) \exp\left(j\frac{\omega_0 x'}{\alpha F}t\right) p_2(t) \times \exp(-j2\omega_0 t). \quad (16)$$

Applying a spatial Fourier transform to the output plane, with the Fourier kernel adjusted for the new carrier frequency, yields

$$U_{out}(x'';t) \propto p_1\left(t - \frac{2\alpha x''}{c}\right) p_2(t) w\left(-\frac{ct}{\alpha}\right) \exp(-j2\omega_0 t). \quad (17)$$

We wish to record the output spatial signal by placing a sensing device that integrates the output intensity, such as a charge-coupled device (CCD) camera. The observed image is given by

$$I_{out}(x'') = \int |U_{out}(x'';t)|^2 dt \approx \int I_1\left(t - \frac{2\alpha x''}{c}\right) I_2(t) dt \quad (18)$$

where we assumed that the long aperture duration is negligible due to the short duration of the ultrafast waveforms (consistent with our assumption of a high-resolution SDW). The image corresponds to the intensity cross-correlation of the two ultrafast waveforms, converted to the space domain and permitting single-shot measurement. This approach was used for one of the earliest experiments demonstrating time-to-space conversion, albeit with a slower excitonic nonlinear process in a ZnSe film [23]. It is also possible to perform the time-to-space conversion by placing the nonlinear crystal at the image plane of the grating instead of at the Fourier plane, as recently demonstrated [24].

IV. ULTRAFAST PROCESSING WITH FOUR-WAVE MIXING

In a degenerate four-wave-mixing process, three input waves at the same carrier frequency generate a fourth output wave that is proportional to $U_4 \propto \chi^{(3)} U_1 U_2 U_3^*$. The output wave is also at the same carrier frequency as the input waves. Each of the input fundamental waves U_1, U_2, and U_3 can have the form of any one of the three waves defined by (1)–(3). Table II summarizes the input wave combinations of interest and the resulting processing achieved at the output signal.

A. SDW Mixing

The wave produced by the three input fundamental waves of the form of (1a) is given by

$$U_4(x';t) = w^3\left(-\frac{ct}{\alpha}\right) P_1\left(\frac{x'\omega_0}{\alpha F}\right) P_2\left(\frac{x'\omega_0}{\alpha F}\right) P_3^*\left(\frac{x'\omega_0}{\alpha F}\right) \times \exp\left(j\frac{\omega_0 x'}{\alpha F}t\right) \exp(-j\omega_0 t). \quad (19)$$
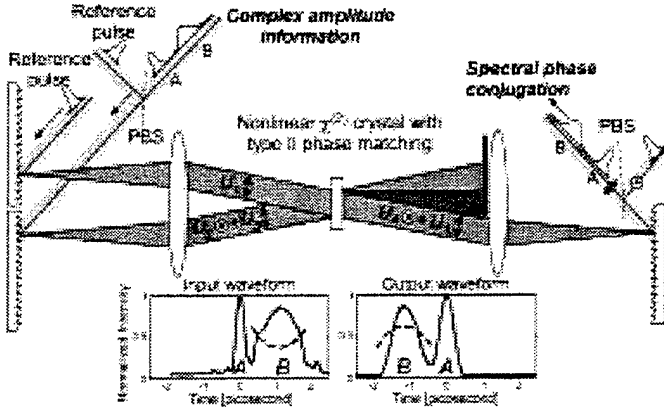
Fig. 3. Experimental setup for time reversal using spectral phase conjugation with four-wave mixing. Inset: experimental result showing time reversal of pulses A and B and chirp flipping (dashed line corresponds to simulated phase function).

Fig. 4. Experimental setup for time reversal using spectral inversion with four-wave mixing. Inset: experimental result showing time reversal of pulses A and B and preservation of chirp sign (dashed line corresponds to simulated phase function).

Applying a spatial Fourier transform yields

$$U_{\text{out}}(x''; t) \propto y\left(t - \frac{\alpha x''}{c}\right) w^3\left(\frac{ct}{\alpha}\right) \exp(-j\omega_0 t) \quad (20)$$

where $y(t) = p_1(t) \otimes p_2(t) \otimes p_3^*(-t) = p_1(t) \otimes p_2(t) \star p_3(t)$ and $\star$ denotes the correlation operation. The new ultrafast waveform $y(\bullet)$ scans along the output plane at a velocity of $-c/\alpha$ and can be coupled to free-space propagation by diffraction from a grating identical to the grating at the input plane of the processor. The new waveform is proportional to the convolution of the first and second input waveforms with the third waveform, which is time-reversed and conjugated. A convolution with the time-reversed and conjugated signal is equivalent to a correlation operation. Thus, the output waveform is a combination of a convolution and correlation among the input waveforms. If $p_1(t)$ and $p_2(t)$ are both transform-limited pulses, the output spectra is a phase conjugate of the spectra of $p_3(t)$, which is an important application for dispersion compensation in optical fiber communication links. We have performed the spectral phase conjugation experiment (see Fig. 3) with a signal wave consisting of a pulse pair: a chirped pulse followed by a transform limited pulse [13]. As expected, the two pulses exchanged location, while the chirped pulse also reversed its chirp sign. All pulses were obtained from a millijoule source pulse and processed in a BBO crystal with cascaded second-order nonlinearities.

B. SDW and Inverted SDW Mixing

There are several options for choosing which channels to introduce to the processor from the opposite side, such that their corresponding SDW will be inverted. When the SDWs of waves U_2 and U_3 are inverted, the wave produced by the three input fundamental waves is given by

$$U_4(x'; t) = w\left(-\frac{ct}{\alpha}\right) w^2\left(\frac{ct}{\alpha}\right) P_1\left(\frac{x'\omega_0}{\alpha F}\right) P_2\left(-\frac{x'\omega_0}{\alpha F}\right)$$
$$\times P_3^*\left(-\frac{x'\omega_0}{\alpha F}\right) \exp\left(j\frac{\omega_0 x'}{\alpha F} t\right) \exp(-j\omega_0 t). \quad (21)$$

Applying a spatial Fourier transform yields

$$U_{\text{out}}(x''; t) \propto y\left(t - \frac{\alpha x''}{c}\right) w\left(-\frac{ct}{\alpha}\right) w^2\left(\frac{ct}{\alpha}\right) \exp(-j\omega_0 t) \quad (22)$$

where $y(t) = p_1(t) \otimes p_2(-t) \otimes p_3^*(t) = p_1(t) \otimes p_2(-t) \star p_3(-t)$. The unique feature of this arrangement is that the output waveform is proportional to the time-reversed complex amplitude waveform of the second channel. We have demonstrated this property for the first time [13], to the best of our knowledge, by using transform-limited pulses for $p_1(t)$ and $p_2(t)$. The signal wave consisted of a pulse pair: a chirped pulse followed by a transform-limited pulse. As expected, the two pulses exchanged location, while the chirped pulse preserved its chirp sign (see Fig. 4).

C. SDW and Spatial Wave Mixing I

The wave produced by the interaction of an SDW with two spatial frequency information waves is given by

$$U_4(x'; t) = w\left(-\frac{ct}{\alpha}\right) P_1\left(\frac{x'\omega_0}{\alpha F}\right) M_2\left(\frac{x'}{\lambda_0 F}\right) M_3^*\left(\frac{x'}{\lambda_0 F}\right)$$
$$\times \exp\left(j\frac{\omega_0 x'}{\alpha F} t\right) \exp(-j\omega_0 t). \quad (23)$$

Applying a spatial Fourier transform yields

$$U_{\text{out}}(x''; t) \propto y\left(t - \frac{\alpha x''}{c}\right) w\left(-\frac{ct}{\alpha}\right) \exp(-j\omega_0 t) \quad (24)$$

where $y(t) = p_1(t) \otimes m_2(ct/\alpha) \otimes m_3^*(-ct/\alpha) = p_1(t) \otimes m_2(ct/\alpha) \star m_3(ct/\alpha)$. The output ultrafast waveform carries the correlation information of the two spatial channels. Such a configuration can be useful for performing a spatial correlation function and transmitting the correlation information to a remote site on a temporal channel. The spatial correlation feature was demonstrated and is discussed in Section V. When one of the spatial channels is a delta function, the result is a space-to-time conversion [9], [10] (see Fig. 5). All the input optical signals were generated from a single millijoule source

pulse; the pulse was stretched with a grating pair for implementing the two monochromatic spatial channels.

D. SDW and Spatial Wave Mixing II

A different arrangement of the input interacting waves produces the equivalent of real-time time-to-space conversion, similar to that achieved with spectral holography [25]. The wave produced by the interaction of a spatial wave with two SDWs is given by

$$U_4(x';t) = w^2 \left(-\frac{ct}{\alpha}\right) M_1 \left(\frac{x'}{\lambda_0 F}\right) P_2 \left(\frac{x'\omega_0}{\alpha F}\right) P_3^* \left(\frac{x'\omega_0}{\alpha F}\right)$$
$$\times \exp(-j\omega_0 t). \tag{25}$$

Applying a spatial Fourier transform yields

$$U_{\text{out}}(x'';t) \propto y(-x'')w^2 \left(-\frac{ct}{\alpha}\right) \exp(-j\omega_0 t) \tag{26}$$

where $y(x) = m_1(x) \otimes p_2(\alpha x/c) \star p_3(\alpha x/c)$. The stationary output signal carries the information of the correlation of the two waveforms, scaled to a spatial dependence, convolved with the spatial signal. Such a configuration can be useful for dispersion cancellation when two waveforms are transmitted along the same path [7]. When the input spatial signal carries no information (delta function), the output signal results in a time-to-space conversion by four-wave mixing, achieving the same result as holographic four-wave mixing, albeit in real-time.

E. SDW, Inverted SDW, and Spatial Wave Mixing

It is possible to mix SDW and get a spatial output by wave mixing an SDW, an inverted SDW, and a spatial frequency information wave. The resulting wave is given by

$$U_4(x';t) = w \left(-\frac{ct}{\alpha}\right) w \left(\frac{ct}{\alpha}\right) P_1 \left(\frac{x'\omega_0}{\alpha F}\right) P_2 \left(-\frac{x'\omega_0}{\alpha F}\right)$$
$$\times M_3^* \left(\frac{x'}{\lambda_0 F}\right) \exp(-j\omega_0 t). \tag{27}$$

Applying a spatial Fourier transform yields

$$U_{\text{out}}(x'';t) \propto y \left(-\frac{\alpha x''}{c}\right) w \left(-\frac{ct}{\alpha}\right) w \left(\frac{ct}{\alpha}\right) \exp(-j\omega_0 t) \tag{28}$$

where $y(t) = p_1(t) \otimes p_2(-t) \otimes m_3^*(-ct/\alpha) = p_1(t) \otimes p_2(-t) \star m_3(ct/\alpha)$. The stationary output signal carries the information of the convolution of the two waveforms (where one is reversed in time) and a correlation with the spatial signal. Such a configuration can be useful to correlate an incoming waveform $p_1(t)$ with a spatial image and requiring a spatial output for subsequent detection (by using a featureless reference pulse for the second temporal channel).

F. Spatial Wave Mixing

Three spatial frequency information waves interacting via degenerate four-wave mixing generate an output wave given by

$$U_4(x';t) = M_1 \left(\frac{x'}{\lambda_0 F}\right) M_2 \left(\frac{x'}{\lambda_0 F}\right) M_3^* \left(\frac{x'}{\lambda_0 F}\right)$$
$$\times \exp(-j\omega_0 t). \tag{29}$$
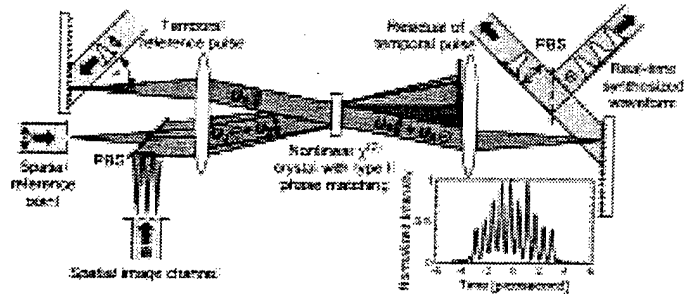
Fig. 5. Experimental setup for space-to-time conversion with four-wave mixing. Inset: experimental result showing conversion of spatial information (regularly placed slits) to an ultrafast waveform consisting of a pulse sequence at 1.56-THz repetition rate.

Applying a spatial Fourier transform yields

$$U_{\text{out}}(x'';t) = y(-x'') \exp(-j\omega_0 t) \tag{30}$$

where $y(x) = m_1(x) \otimes m_2(x) \otimes m_3^*(x) = m_1(x) \otimes m_2(x) \star m_3(x)$. The convolution and correlation relationship among the input spatial images is typical in holographic signal processing. Utilizing nonlinear wave mixing yields the same results in real time.

G. SDW and Ultrashort Pulse Mixing

A time-delay parameter is added to one of the ultrashort pulses for describing the interaction of an SDW with two ultrashort pulses. The output wave is therefore given by

$$U_4(x';t) = w \left(-\frac{ct}{\alpha}\right) P_1 \left(\frac{x'\omega_0}{\alpha F}\right) \exp \left(j \frac{\omega_0 x'}{\alpha F} t\right)$$
$$\times p_2(t)p_3^*(t-t_0) \exp(-j\omega_0 t). \tag{31}$$

Applying a spatial Fourier transform yields

$$U_{out}(x'';t) = w \left(-\frac{ct}{\alpha}\right) p_1 \left(t - \frac{\alpha x''}{c}\right) p_2(t)p_3^*(t-t_0)$$
$$\times \exp(-j\omega_0 t). \tag{32}$$

The observed image on a slow detection device such as a film or camera is described by

$$S_{\text{out}}(x'';t_0)$$
$$= \int_{-\infty}^{\infty} |U_{out}(x'';t)|^2 \, dt$$
$$\approx w^2(0) \int_{-\infty}^{\infty} I_1 \left(t - \frac{\alpha x''}{c}\right) I_2(t)I_3(t-t_0) \, dt \tag{33}$$

where we used the approximation that the field strength variation due to the spatial beam mode does not change for the short duration of the sampling pulse. The image contains the triple cross-correlation information of the three input ultrashort waveform intensities. The triple correlation requires two time-lag parameters. In the result of (33), one time-lag parameter is mapped to the spatial domain, while the other is set by the relative time delay between the second and third ultrafast waveforms. If all the input waveforms to the processor are identical, then the triple autocorrelation data can be used to extract the exact intensity profile of the input short pulse. To reconstruct the input waveform intensity profile, the complete two-dimensional (2-D) cor-

Fig. 6. Experimental setup for the information exchange among two input spatial channels and an input ultrafast waveform. The output ultrafast waveform contains the correlation information of the two spatial channels.

Fig. 7. Ultrafast waveforms containing the correlation information of two rectangular apertures in the spatial domain. Solid curve: ultrafast waveform from two narrow rectangular spatial signals of identical width. Dashed curve: wider, unequal rectangular spatial signals, resulting in a trapezoid correlation function.
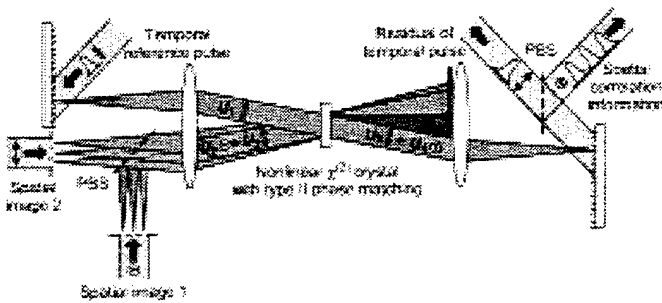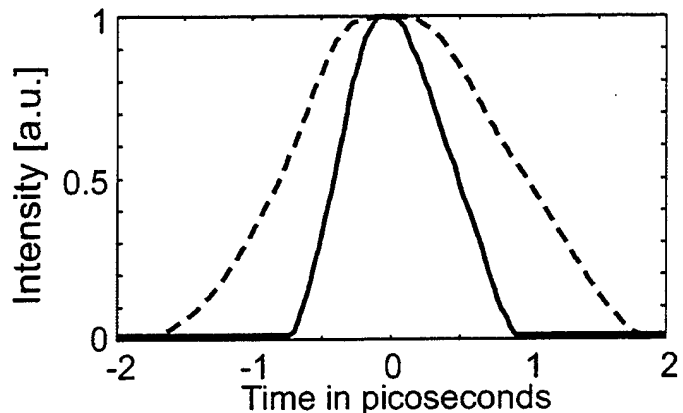
relation matrix is required [26]. Using this arrangement would require a sequence of measurements, varying the parameter t_0 for each measurement. A single-shot variant of this technique is described in Section VI.

V. SPATIAL CORRELATION FUNCTION CARRIED ON AN ULTRAFAST WAVEFORM

Mixing spectrally decomposed waves and spatially Fourier transformed images results in an information exchange between the temporal spectra of the ultrashort pulse and the spatial spectra of the image. The information exchange results in waveform synthesis by a space-to-time conversion. A three-wave-mixing arrangement for the information exchange results in a temporal signal with a doubled center frequency. When the synthesized waveform is required to have an identical center frequency, a degenerate four-wave-mixing arrangement is utilized, with a second spatial signal consisting of a (featureless) point source. In this section, the information exchange between the two spatial images and the ultrafast waveform is demonstrated (see Fig. 6).

Mixing an SDW and two spatially Fourier transformed images using a degenerate four-wave-mixing process results in an output temporal waveform that is a convolution of the input temporal waveform with the correlation of the two spatial images, properly scaled to a time-domain representation, i.e., $y(t) = p_1(t) \otimes m_2(ct/\alpha) \star m_3(ct/\alpha)$. In the experiments, a commercial laser system consisting of a Ti : Sapphire ultrashort pulse oscillator and a regenerative amplifier was used. The system generates ultrashort laser pulses of 100 fs duration at a center wavelength of 800 nm with an energy level of 1 mJ per pulse. Ninety percent of the emitted output pulse power was utilized for the intense quasi-monochromatic light source required by the spatial channels and stretched to a duration of several picoseconds by a grating pair. The stretched pulse was split into two beams for implementing the two quasi-monochromatic spatial channels. The remaining 10% of the short pulse laser output power was used as the reference ultrashort pulse in the input temporal channel. The SDW U_1 is generated by a 600-lines/mm blazed grating that provides an angular dispersion parameter of $\alpha = 0.48$ and a lens of $F = 375$ mm focal length. The four-wave mixing is performed by cascaded second-order nonlinearities in a 2-mm-long type-II BBO crystal. Several experiments were conducted to illustrate this real-time spatial–temporal processing technique. All the output waveforms were observed with a time-to-space

converter based on three-wave mixing with mutually inverted SDW. The reference pulse source required for the pulse imager was the residual input pulse of the spatial–temporal processor, after separating it from the output waveform with a polarizing beam splitter. The output signal's intensity was viewed with a CCD camera, and the temporal information was extracted from the image.

The first experiment consisted of placing two variable slits in the spatial channels, implementing a rectangular spatial distribution. The correlation function of two rectangular signals has a trapezoidal shape; the plateau is observed for correlation delays smaller than the width of the narrower rectangle. When the two rectangles are of identical width, the correlation function is triangular. If the width of one of the rectangles is very small (approaching a point source), then the output signal will result in a space-to-time conversion and resemble a square pulse (generation of square pulses using this technique reported in [10]). The ultrafast output waveform will contain smoothed features due to the convolution operation with the input ultrashort pulse. Additional smoothing is performed in the waveform imaging operation. The experimental results of Fig. 7 precisely illustrate the correlation function of rectangular signals described above. A triangular pulse shape was observed for equal rectangular widths (solid curve), while a trapezoidal pulse shape was observed for unequal rectangular widths (dashed curve).

A second experiment was performed with spatial channels that are coded with pseudorandom masks. The phase mask (for implementing values of ± 1) was prepared by wet-etching the spatial information into a quartz substrate. The spatial information consisted of contiguous equal-width rectangular sections (each 75 μm) encoded with transmission values of ± 1 according to a 127 maximal length sequence [see Fig. 8(a)]. The maximal length sequence was chosen for the low correlation values it exhibits for any delay other than zero. When the mask was placed in one spatial channel and the second consisted of a point source, a space-to-time conversion was performed and the resulting waveform appeared random [see Fig. 8(b)]. When both spatial channels had an identical mask, a correlation peak at the zero delay location appeared [see Fig. 8(c)]. At other
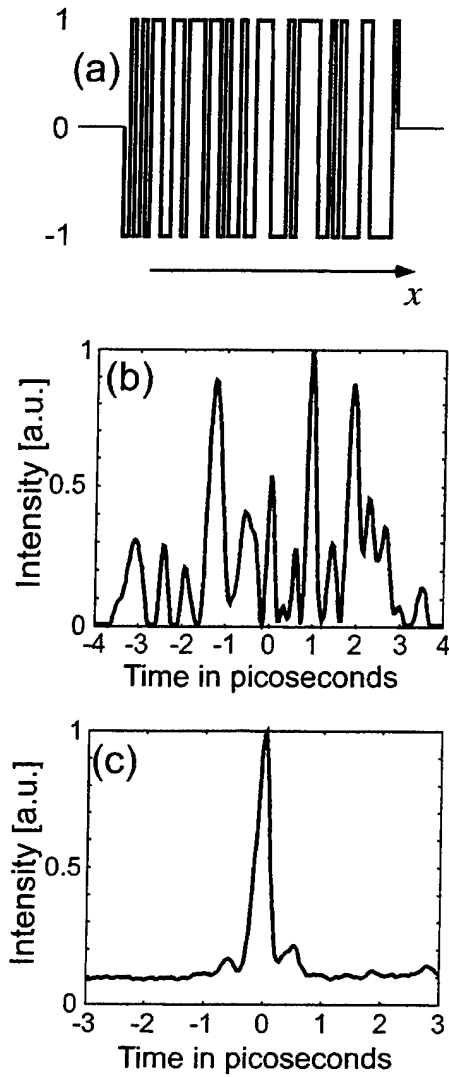
Fig. 8. Ultrafast spatial-temporal processing with pseudorandom information. (a) Maximal length sequence used for spatial mask information. (b) Synthesized space-to-time conversion signal from mask using a point source for second channel. (c) Correlation function of two identical masks carried on a temporal waveform.

Fig. 9. Ultrashort pulse trains with different periods to generate a single-shot triple correlation measurement.

delay times, the ultrafast waveform had a small signal from the nonzero correlation values.

This type of processor can be used for transmitting spatial correlation information via a temporal channel. Such capability may be important for transmission of information from a hostile environment for detection at a safer location.

VI. SINGLE-SHOT IMPLEMENTATION OF THE TRIPLE AUTOCORRELATION

Wave mixing an SDW and two ultrashort pulses resulted in an output plane image that contained some of the triple correlation values, as developed in Section IV. For reconstruction of the original intensity profile of the ultrashort pulse, the entire correlation matrix is required. Therefore, a sequence of measurements is necessary to fully characterize the ultrashort pulse intensity. The parameter that is changed between subsequent measurements is the relative time delay between the two ultrashort

pulses. In this section, a single-shot technique based on ultrashort pulse trains for sampling the SDW is described.

We modify the technique described above by using two ultrashort pulse trains instead of the two ultrashort pulses. Generating a pulse train of identical ultrashort pulses is possible with waveform synthesis techniques. Additionally, all pulses are assumed to have an identical waveform. The period between consecutive pulses is different for the two pulse trains. Let one pulse train have pulse separation of Δ_1 and the other Δ_2, and let $\Delta_1 \approx \Delta_2$ (see Fig. 9). The resulting output field is given by [see (32)]

$$U_{\text{out}}(x'';t) = w\left(-\frac{ct}{\alpha}\right) p\left(t - \frac{\alpha x''}{c}\right) \left(\sum_n p(t - n\Delta_1)\right)$$

$$\times \left(\sum_m p^*(t - m\Delta_2)\right) \exp(-j\omega_0 t). \quad (34)$$

Since the pulse separations Δ_1 and Δ_2 are nearly equal, U_{out} will be zero if $n \neq m$. Therefore, we can rewrite (34) as

$$U_{\text{out}}(x'';t) = \sum_n w\left(-\frac{ct}{\alpha}\right) p\left(t - \frac{\alpha x''}{c}\right) p(t - n\Delta_1)$$

$$\times p^*(t - n\Delta_2) \exp(-j\omega_0 t). \quad (35)$$

The observed image on a slow detection device such as a film or camera is then described by

$$S_{\text{out}}(x'') = \int_{-\infty}^{\infty} |U_{\text{out}}(x'';t)|^2 \, dt$$

$$= \int_{-\infty}^{\infty} \left(\sum_n w\left(-\frac{ct}{\alpha}\right) p\left(t - \frac{\alpha x''}{c}\right)\right.$$

$$\times p(t - n\Delta_1)p^*(t - n\Delta_2)\right)$$

$$\times \left(\sum_k w\left(-\frac{ct}{\alpha}\right) p^*\left(t - \frac{\alpha x''}{c}\right)\right.$$

$$\times p^*(t - k\Delta_1)p(t - k\Delta_2)\right) dt. \quad (36)$$

Again, since the pulse separations Δ_1 and Δ_2 are nearly equal, S_{out} will be zero if $n \neq k$. Therefore

$$
S_{out}(x'') = \sum_n \int_{-\infty}^{\infty} w^2 \left(-\frac{ct}{\alpha} \right) I \left(t - \frac{\alpha x''}{c} \right) I(t - n\Delta_1)
$$
$$
\times I(t - n\Delta_2) \, dt
$$
$$
\approx \sum_n w^2 \left(-\frac{cn\Delta_1}{\alpha} \right) \int_{-\infty}^{\infty} I \left(t - \frac{\alpha x''}{c} \right)
$$
$$
\times I(t - n\Delta_1) I(t - n\Delta_2) \, dt \tag{37}
$$

where we used the approximation that the field strength variation due to the spatial beam mode does not change for the short duration of each sampling pulse at time $t = n\Delta_1$. Let us assume that $\Delta_2 = \Delta_1 + \varepsilon$. Additionally, with a change of integration variable, (37) can be rewritten as

$$
S_{out}(x'') \approx \sum_n w^2 \left(-\frac{cn\Delta_1}{\alpha} \right) \int_{-\infty}^{\infty} I \left(\xi + n\Delta_1 - \frac{\alpha x''}{c} \right)
$$
$$
\times I(\xi) I(\xi - n\varepsilon) \, dt. \tag{38}
$$

The integral in (38) is now identifiable as the triple autocorrelation integral, where one lag parameter is mapped to the spatial domain while the second lag parameter is $n\varepsilon$. Each order of n is mapped to a different location on the spatial output (centered at $x'' = cn\Delta_1/\alpha$) and is associated with the lag $n\varepsilon$. Therefore, the triple correlation matrix values are raster scanned on the 1-D output space. Each order n is also scaled by the input pupil function. This effect can be accounted for by measuring the profile and normalizing the measurement or by ensuring that the mode is uniform. After collecting the 1-D correlation values and assembling the matrix, an algorithm can be applied to find the exact intensity profile of the ultrashort pulse. The sampling method described here can be associated with bandwidth adaptation techniques [27], where a 2-D distribution is converted to a 1-D distribution. Such bandwidth adaptation techniques have also been applied to time-to-2-D space and 2-D space-to-time conversions [28].

VII. DISCUSSION AND CONCLUSION

We have examined the different signal-processing capabilities that are enabled when spatial and temporal information bearing waves interact via fast parametric processes. The methodical process of investigating all the input wave combinations describes the experiments we have conducted in the past and reveals new options for processing of ultrafast data. These techniques can be used for synthesis, processing, and detection of ultrafast waveforms. Such capabilities may be utilized in future high-capacity communication systems, ultrafast optical computation, and scientific uses in investigation of ultrafast phenomena and quantum control.

As our analysis showed, there are many methods one may choose for conversion of data from the time-to-space domain: time-domain noncollinear arrangement, mixing the time domain with the SDW (or at the image plane of the grating), and mixing two mutually inverted SDWs. All methods generate the intensity cross-correlation signal with a reference transform limited pulse [compare (18) and the intensity of (7), for example]. The different arrangements offer functional trade-offs among time window of apparatus, phase matching, and walkoff effects; crystal (or interaction) length; and conversion efficiency. However, it was not within the scope of this paper to analyze which technique offers the best performance for a given set of constraints.

The instantaneous nature of wave-mixing processes for information conversion from the spatial domain to the temporal domain is best utilized when the spatial information channel is rapidly changing. In our analysis, we have assumed that the spatial information is stationary with respect to the temporal channel time window. This could be accomplished by a 1-D fiber array, which supplies synchronized parallel data streams (for such telecom-oriented applications, the wave-mixing process has to be optimized for the expected low power levels). If the spatial channel information changes during the time window of the spectral processor, the output signal will exhibit different temporal information across its transverse extent. It should be noted that when the spatial information is varying at slow rates, alternative Fourier plane processing elements such as photorefractives may be employed (spectral holography [29]).

Ultrafast waveform synthesis by space-to-time conversion can be performed by three- and four-wave-mixing arrangements. The degenerate four-wave-mixing arrangement is the more useful option, as it is usually desirable to modify an input ultrashort pulse to a prescribed waveform without a center frequency shift. However, since all the processing is performed by real-time parametric interaction, it is possible to add a wavelength-tuning feature. When utilizing the four-wave-mixing process with tunable lasers for implementation of the spatial channels, the center frequency of the synthesized waveform will be shifted by the frequency difference of the two spatial lasers, in accordance with the energy conservation principle.

REFERENCES

[1] V. W. S. Chan, K. L. Hall, E. Modiano, and K. A. Rauschenbach, "Architectures and technologies for high-speed optical data networks," *J. Lightwave Technol.*, vol. 16, pp. 2146–68, 1998.

[2] M. Nakazawa, E. Yoshida, T. Yamamoto, E. Yamada, and A. Sahara, "TDM single channel 640 Gbit/s transmission experiment over 60 km using 400 fs pulse train and walk-off free, dispersion flattened nonlinear optical loop mirror," *Electron. Lett.*, vol. 34, pp. 907–908, 1998.

[3] M. C. Nuss, W. H. Knox, and U. Koren, "Scalable 32 channel chirped-pulse WDM source," *Electron. Lett.*, vol. 32, pp. 1311–12, 1996.

[4] E. A. De Souza, M. C. Nuss, W. H. Knox, and D. A. B. Miller, "Wavelength division multiplexing with femtosecond pulses," *Opt. Lett.*, vol. 20, pp. 1166–1168, 1995.

[5] A. M. Weiner, J. P. Heritage, and J. A. Salehi, "Encoding and decoding of femtosecond pulses," *Opt. Lett.*, vol. 13, pp. 300–302, 1988.

[6] J. A. Salehi, A. M. Weiner, and J. P. Heritage, "Coherent ultrashort light pulse code-division multiple access communication systems," *J. Lightwave Technol.*, vol. 8, pp. 478–491, 1990.

[7] D. M. Marom, P.-C. Sun, and Y. Fainman, "Analysis of spatial–temporal converters for all-optical communication links," *Appl. Opt.*, vol. 37, pp. 2858–2868, 1998.

[8] K.-S. Kim, D. M. Marom, L. B. Milstein, and Y. Fainman, "Hybrid pulse position modulation/ultrashort light pulse code division multiple access," *IEEE Trans. Commun.*, submitted for publication.

[9] D. M. Marom, D. Panasenko, P.-C. Sun, and Y. Fainman, "Spatial–temporal wave mixing for space–time conversion," *Opt. Lett.*, vol. 24, pp. 563–565, 1999.

[10] D. Marom, D. Panasenko, P.-C. Sun, and Y. Fainman, "Femtosecond-rate space-to-time conversion," *J. Opt. Soc. Amer. B*, vol. 17, pp. 1759–1773, 2000.

[11] P. C. Sun, Y. T. Mazurenko, and Y. Fainman, "Femtosecond pulse imaging: Ultrafast optical oscilloscope," *J. Opt. Soc. Amer. A*, vol. 14, pp. 1159–1170, 1997.

[12] D. M. Marom, D. M. Panasenko, P.-C. Sun, and Y. Fainman, "Linear and nonlinear operation of a time-to-space processor," *J. Opt. Soc. Amer. A*, vol. 18, pp. 448–458, 2001.

[13] D. Marom, D. Panasenko, R. Rokitski, S. Pang-Chen, and Y. Fainman, "Time reversal of ultrafast waveforms by wave mixing of spectrally decomposed waves," *Opt. Lett.*, vol. 25, pp. 132–134, 2000.

[14] A. Yariv, D. Fekete, and D. M. Pepper, "Compensation for channel dispersion by nonlinear optical phase conjugation," *Opt. Lett.*, vol. 4, pp. 52–54, 1979.

[15] A. W. Lohmann, "Teaching how to invent—Is it possible?," *Israel J. Technol.*, vol. 18, pp. 214–217, 1980.

[16] J. W. Goodman, *Introduction to Fourier Optics*, 2nd ed. New York: McGraw-Hill, 1996.

[17] C. Froehly, B. Colombeau, and M. Vampouille, "Shaping and analysis of picosecond light pulses," in *Progress in Optics XX*, E. Wolf, Ed. Amsterdam, The Netherlands: North-Holland, 1983, pp. 65–153.

[18] J. B. Khurgin, A. Obeidat, S. J. Lee, and Y. J. Ding, "Cascaded optical nonlinearities: Microscopic understanding as a collective effect," *J. Opt. Soc. Amer. B*, vol. 14, pp. 1977–1983, 1997.

[19] P. C. Sun, Y. T. Mazurenko, and Y. Fainman, "Real-time one-dimensional coherent imaging through single-mode fibers by space-time conversion processors," *Opt. Lett.*, vol. 22, pp. 1861–1863, 1997.

[20] A. M. Kan'an and A. M. Weiner, "Efficient time-to-space conversion of femtosecond optical pulses," *J. Opt. Soc. Amer. B*, vol. 15, pp. 1242–1245, 1998.

[21] J. Janszky, G. Corradi, and R. N. Gyuzalian, "On a possibility of analysing the temporal characteristics of short light pulses," *Opt. Commun.*, vol. 23, pp. 293–298, 1977.

[22] F. Salin, P. Georges, G. Roger, and A. Brun, "Single-shot measurement of a 52-fs pulse," *Appl. Opt.*, vol. 26, pp. 4528–4531, 1987.

[23] K. Ema, M. Kuwata-Gonokami, and F. Shimizu, "All-optical sub-Tbits/s serial-to-parallel conversion using excitonic giant nonlinearity," *Appl. Phys. Lett.*, vol. 59, pp. 2799–2801, 1991.

[24] K. Oba, P.-C. Sun, Y. T. Mazurenko, and Y. Fainman, "Femtosecond single-shot correlation system: A time-domain approach," *Appl. Opt.*, vol. 38, pp. 3810–3817, 1999.

[25] M. C. Nuss, M. Li, T. H. Chiu, A. M. Weiner, and A. Partovi, "Time-to-space mapping of femtosecond pulses," *Opt. Lett.*, vol. 19, pp. 664–666, 1994.

[26] T. Feurer, S. Niedermeier, and R. Sauerbrey, "Measuring the temporal intensity of ultrashort laser pulses by the triple correlation," *Appl. Phys. B*, vol. 66, pp. 163–168, 1998.

[27] D. Mendlovic and A. W. Lohmann, "Space-bandwidth product adaptation and its application to superresolution: Fundamentals," *J. Opt. Soc. Amer. A*, vol. 14, pp. 558–562, 1997.

[28] T. Konishi and Y. Ichioka, "Ultrafast image transmission by optical time-to-two-dimensional-space-to-time-to-two dimensional space conversion," *J. Opt. Soc. Amer. A*, vol. 16, pp. 1076–1088, 1999.

[29] A. M. Weiner, D. E. Leaird, D. H. Reitze, and E. G. Paek, "Femtosecond spectral holography," *IEEE J. Quantum Electron.*, vol. 28, pp. 2251–2261, 1992.

Dmitriy Panasenko was born in Moscow, Russia, in 1972. He received the M.Sc. degree from Moscow Institute of Physics and Technology, Russia, in 1995. He is currently pursuing the Ph.D. degree at the University of California, San Diego (UCSD).

He is a Fannie and John Hertz Foundation Graduate Fellow at UCSD. His research interests include ultrashort laser pulse processing and detection techniques and their application to optical communication.

Pang-Chen Sun, photograph and biography not available at the time of publication.

Yuri T. Mazurenko, photograph and biography not available at the time of publication.

Yeshaiahu Fainman (M'93–SM'01) received the Ph.D. degree from Technion—Israel Institute of Technology, Haifa, in 1983.

He is a Professor of Electrical and Computer Engineering at the University of California, San Diego. His current research interests are in nonlinear space–time processes using femtosecond laser pulses for optical communications, near-field phenomena in optical nanostructures, quantum cryptography and communication, 3-D quantitative imaging, and programmable and multifunctional diffractive and nonlinear optics. He has contributed more than 100 manuscripts to referred journals and more than 170 conference presentations and conference proceedings. He has served on several conference program committees, organized symposiums, and workshops. Currently, he is a Topical Editor of the *Journal of the Optical Society of America A: Optical Signal Processing and Imaging Science.*

Prof. Fainman is a Fellow of the Optical Society of America and SPIE. He received the Miriam and Aharon Gutvirt Prize.

Dan M. Marom (S'98–M'01) was born in Detroit, MI, in 1967. He received the B.Sc. and M.Sc. degrees from Tel-Aviv University, Israel, in 1989 and 1995, respectively, and the Ph.D. degree from the University of California, San Diego (UCSD), in 2000.

His doctoral dissertation dealt with femtosecond-rate optical signal processing with applications in ultrafast communications. From 1996 through 2000, he was a Fannie and John Hertz Foundation Graduate Fellow at UCSD. In 2000, he joined Bell Laboratories, Holmdel, NJ, to pursue his interests in optical communications.

Dr. Marom received the IEEE Lasers and Electro-Optics Society Best Student Paper Award in 1999 for his work describing instantaneous time reversal of complex amplitude ultrafast waveforms.

Design and Evaluation of the Fibonacci Optical ATM Switch

Allen Shum, P.M. Melliar-Smith, and Louise E. Moser

Abstract—An ATM switch architecture that uses optical delay fibers as buffers is presented. Based on the remarkable properties of the Fibonacci numbers, the architecture requires few fibers and yields low cell loss rates and latencies across diverse time-correlated and heavily loaded traffic profiles. Moreover, the control algorithm of the architecture is computationally efficient and can be executed in real time. Simulation studies indicate that the cell loss rate decreases exponentially as the number of fibers increases and that the probability mass function for the cell latency decays rapidly as the latency increases.

Index Terms—Asynchronous transfer mode, optical ATM switch.

◆

1 INTRODUCTION

TODAY's electronic ATM switches are the bottleneck of an ATM network: ATM cells are not switched fast enough to match the transmission speed of the optical channels. It is expected that the gap between the electronic switching and optical transmission speeds will continue to increase as optical transmission technology matures. A solution to this problem is to implement ATM switches using optical technology.

The major functions of an ATM switch are to route incoming cells to the appropriate output channels and to provide buffering for them, if necessary. The construction of a single monolithic fabric to interconnect large numbers of input and output channels may not be feasible due to physical and cost contraints. Consequently, the switching fabric of a high-performance ATM switch typically consists of a network of smaller switching elements, as shown in Fig. 1, with each small switching element having its own buffers, optical crossbar switch, and control unit, as shown in Fig. 2. Such an organization lends itself naturally to parallel processing of cells and parallel routing decisions.

In optical switches, static buffering is not feasible and buffers are constructed by switching ATM cells into optical fibers that act as delay lines. The longer the fiber, the longer the delay and the greater the number of cells buffered in the fiber. By switching an ATM cell through a sequence of fiber delay lines, any required delay can be achieved. The difficulty of building an optical crossbar switch increases rapidly with the number of fibers. Consequently, it is important to minimize the number of fiber delay lines while still achieving efficient operation of the switch. Although packet switch architectures using optical delay fibers as buffers have been proposed in the literature [4], [5], [7], [10],

[12], as far as we can determine, studies on how to design an optical switch that addresses ATM-specific requirements while requiring few fibers and low processing complexity do not exist.

In this paper, we present the design of a novel optical ATM switch architecture. The Fibonacci buffer organization of the switch uses fewer fibers to achieve lower cell loss rates under diverse time-correlated and heavily loaded traffic profiles than existing buffer organizations. Moreover, the control algorithm is computationally efficient and can be executed in real time. The architecture guarantees that the cell sequence integrity of each input-output channel pair is maintained and that the maximum latency is below a specified threshold.

This paper is organized as follows: In Section 2, we identify the issues and challenges in designing an optical ATM buffer architecture. In Section 3, we present our optical ATM switch architecture, followed by an analysis of the time and space complexity of the design. In Section 4, we present the performance results of the architecture, as indicated by simulation studies, and also a heuristic that can determine an empirically lossless optical ATM switch. In Section 5, we provide a discussion of related work and, in Section 6, we summarize the results of our work.

2 PROBLEM STATEMENT

In an optical ATM switch, the buffering of a cell for k time slots is accomplished by causing the cell to traverse a sequence of optical fibers such that the propagation delay over the fibers is exactly k time slots. A fiber is of length i if the time required to propagate a cell through the fiber is exactly i time slots.

The three components of an ATM buffer organization are the buffer set, the switching fabric, and the control algorithm. The *buffer set* refers to the set of optical delay fibers used for buffering. The *switching fabric* is the structure that physically routes cells from the input to the output, e.g., a crossbar. The *control algorithm* is the procedure that determines how cells are stored or propagated through the switching fabric.

- A. Shum is with SPAWAR Systems Center, 53560 Hull St., San Diego, CA 92152. E-mail: shum@spawar.navy.mil.
- P.M. Melliar-Smith and L.E. Moser are with the Department of Electrical and Computer Engineering, University of California, Santa Barbara, CA 93106. E-mail: {pmms, moser}@ece.ucsb.edu.
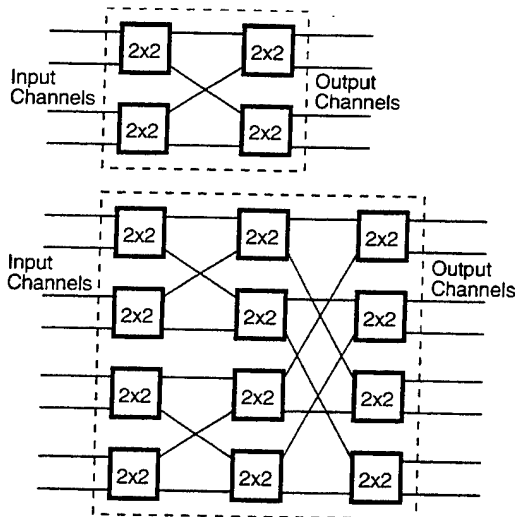
Fig. 1. A 4-input and 4-output switch fabric with two stages of 2×2 switching elements and an 8-input and 8-output switch fabric with three stages of 2×2 switching elements.

Fig. 2. A 2×2 optical switching element.

Cell loss refers to the discarding of a cell when a sequence of fibers to buffer the cell cannot be found. *Latency*, in our context, refers to the queuing delay that cells may experience at the switch. An *arrival process* or *traffic profile* describes the arrivals of cells at the input channels and at their destination output channels.

Because the function of a buffer is to prevent cell loss during periods of traffic overloads, the most important performance metric of an ATM buffer architecture is the cell loss rate. Unlike other packet-switched networks, which are designed to support data applications that do not have stringent delay requirements, an ATM network must also transport real-time applications; consequently, low predictable latency is a typical requirement of an ATM switch. In an ATM network, the order in which cells are transmitted over a virtual connection, i.e., the *cell sequence integrity*, must be maintained. In other words, the goal of an ATM buffer organization design is to find a switching fabric, a buffer set, and a control algorithm so that the cell loss, latency, and cell sequence integrity requirements are satisfied while requiring low processing complexity and a small number of fibers.

The design of an optical ATM buffer organization poses several challenges:

1. *Minimizing cell loss and latency.* A low cell loss rate can be achieved by providing a large buffer, but this would entail large latencies at the switch; conversely, a small buffer can keep cell latency low but may result in excessive cell loss. Maintaining low latency and minimizing cell loss are, therefore, conflicting objectives. In the design of an optical ATM buffer organization, using long fibers tends to reduce cell loss without increasing the number of fibers since longer fibers can accommodate more cells, e.g., a length-k fiber can store up to k cells at any particular time; however, longer fibers introduce or result in greater delays as the transit delay through a length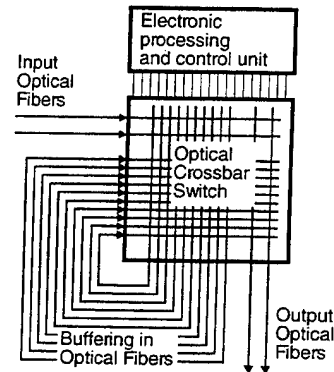-k fiber is k time slots. Simultaneously satisfying cell loss and latency requirements with few fibers is difficult.

2. *Preserving cell sequence integrity.* Maintaining the order in which cells arrive and depart on each input-output channel pair severely constrains how an ATM switch can be organized. The switching fabric of a high-performance switch typically consists of a network of smaller elements, with each switching element having its own buffer organization and processing unit. To preserve the cell sequence integrity, either all cells on each input-output channel pair traverse the same sequence of switching elements or a reordering mechanism at the edge of the switching fabric must be employed to resequence out-of-order cells. The traversing of a unique path requires that sufficient buffering capacity be available at each switching element.

For time-correlated and heavily loaded traffic, a large buffer must be provided at each switching element to prevent excessive cell loss. A large buffer introduces higher latency and results in higher cost. Much of the deleterious effect of time-correlated traffic over an input-output channel pair can be mitigated by distributing the traffic over several routes, but this results in out-of-order cells. The mechanism that resequences out-of-order cells typically requires timestamps, extra buffer capacity at the edge of the switching fabric, and delaying of cells.

3. *Limiting factors.* The limiting factors to implementing an ATM buffer organization are that the number of fibers must be small and that the processing requirement must be low. These are conflicting factors since the use of fewer fibers requires the use of a sophisticated control algorithm so that the few fibers are used efficiently. Sophisticated control algorithms tend to have higher time and space complexity. Designing a low-complexity control algorithm that can efficiently utilize few fibers is not easy.

4. *Performance evaluation.* Performance evaluation of an ATM switch poses another challenge. Mathematical analysis of the behavior of an ATM switch is typically intractable. Simulation, the usual alternative to evaluating mathematically intractable de-
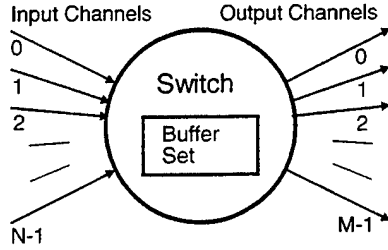
Fig. 3. An N-input and M-output ATM switch with an optical buffer set.

Fig. 4. Transition diagram of a 2-state MMBP.

signs, also faces significant difficulty since the primary performance measure of interest for an ATM switch involves the sampling of statistically rare events, i.e., cell loss. For example, the usual cell loss requirement of an ATM switch is on the order of 10^{-8}. To ascertain whether an ATM architecture would satisfy such a criterion requires the generation of at least 10^{10} ATM cells in a simulation run. The computational cost of such runs is prohibitive.

3 THE OPTICAL ATM BUFFER ORGANIZATION

We address the design of a small switching element, as shown in Fig. 2. Our analysis focuses on the buffer organization and cell loss rate as a function of the number of fibers. This allows us to determine the minimum number of fibers necessary to achieve acceptable performance from the switch.

3.1 The Optical ATM Switch Model

The ATM switch model that we use to evaluate our design has N input and M output channels, which are labeled 0 through $N - 1$ and 0 through $M - 1$, respectively, as shown in Fig. 3. The channels are synchronized to a common time line, which is divided into infinitely many consecutive time slots of unit duration corresponding to the transmission time of a single ATM cell. Cell arrivals to the input channels occur only at the beginning of a time slot. A cell arriving on input channel i is routed instantaneously to output channel j with probability q_{ij}, where $0 \leq i \leq N - 1$, $0 \leq j \leq M - 1$, $q_{ij} \geq 0.0$, and $\sum_{j=0}^{M-1} q_{ij} = 1$ for $0 \leq i \leq N - 1$. A cell is transmitted on an output channel only at the beginning of a time slot and departs the switch at the end of the same time slot. An arriving cell to an output channel is transmitted on the channel if the channel is idle; otherwise, it traverses the switching fabric and remains there until the output channel becomes available, i.e., all prior arriving cells from the same input channel have been transmitted.

Cells arrive on input channel i according to an independent 2-state Markov-modulated Bernoulli process, $MMBP_i$, for $0 \leq i \leq N - 1$. An $MMBP_i$ input stream transitions among the two states s_1^i and s_2^i. At the beginning of each time slot, input stream i moves from state s_j^i to s_k^i with probability $\alpha_{jk}^i > 0$, where $1 \leq j, k \leq 2$ and $\alpha_{j1}^i + \alpha_{j2}^i = 1$ for $j = 1$ and 2. In state s_1^i, the input stream i generates a cell at the beginning of a time slot and, in state s_2^i, the input stream generates nothing. A state transition diagram of a two-state $MMBP$ input stream is shown in Fig. 4.

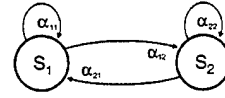A phenomenon common to all discrete-time, finite-buffer ATM switches with multiple input and output channels is

that many cells can arrive *simultaneously* at the switch and it is possible that not all of the cells can be accommodated in the buffer. There must be a protocol, referred to as an *arbitration scheme*, to determine how the arriving cells are to be discarded. The arbitration scheme is such that a cell from input channel i is admitted into the buffer before a cell from input channel j if $i < j$. We evaluate the performance of our design using this ATM multiplexer model. The simulation results are given in Section 4.

3.2 The Architecture

We now present our optical ATM buffer organization and the rationale behind its design. Because the efficacy of our optical ATM switch is due to the remarkable properties of the Fibonacci numbers, it is referred to as the *Fibonacci Optical ATM Switch*. To facilitate the presentation, we introduce the following variables:

- m, the number of distinct fiber types,
- L_i, the length of a type-i fiber, where $1 \leq i \leq m$,
- $\underline{n} = (n_1, \ldots, n_m)$, where n_i is the number of fibers of length L_i,
- $n_{fibers} = \sum_{j=1}^{m} n_i$ the total number of optical delay fibers,
- D_{max}, the maximum latency of the switch.

The buffer set, the switching fabric, and the control algorithm of the architecture are as follows:

1. *Buffer Set*

    a. *The number m of fiber types. m is set to*

    $$\left\lfloor \frac{log_{10}(\sqrt{5}(D_{max} + \frac{1}{2}))}{log_{10}\phi} \right\rfloor - 1,$$

    where $\phi = \frac{1+\sqrt{5}}{2}$ and D_{max} is the latency requirement of the switch. The justification for setting this value to m can be found in Appendix A.

    b. *The type-i fiber length L_i, where $1 \leq i \leq m$. L_i is set to F_{i+1}, where F_{i+1} is the (i + 1)st term of the Fibonacci sequence defined by $F_{i+1} = F_i + F_{i-1}$, $F_0 = 0$, and $F_1 = 1$. This buffer set is referred to as the Fibonacci buffer set.

    c. *The number n_i of type-i fibers, where $1 \leq i \leq m$. n_i is set to an integer that is greater than or equal to 1. While m and L_i are uniquely determined by the latency requirement D_{max}, the proper choice of n_i depends on the cell loss requirement of the switch and can be determined through simulation studies.

The selection of m and L_i is based on the following observations:

    a. *The fiber lengths should be exponentially increasing. This corresponds to requiring that L_i is on the

order of γ^i, where $\gamma > \sqrt{2}$. This requirement is due to the fact that longer fibers can retain more cells. As a result of using exponentially increasing fiber lengths, the addition of one fiber can significantly increase the capacity of the optical buffer.

b. *The fiber lengths should be such that there exists a binary representation (of these fiber lengths) for each integer between 1 and D_{max}, inclusive.* This offers a means of finding a length-n fiber sequence efficiently. To minimize cell latencies, a control algorithm must try to find a length-n fiber sequence to buffer a cell that must be delayed for at least n time slots; however, the number of possible length-n fiber sequences is typically an exponential function of $L_1, \ldots, L_m, m$, and n (see Appendix B). This suggests that we cannot consider all possible combinations of fiber sequences of length n. An alternative is to permit a fiber of each length to be included in the sequence at most once, i.e., by representing n as $n = \sum_{j=1}^{m} \sigma_j L_j$, where $\sigma_j \in \{0,1\}$, and including a fiber of length L_j in the fiber sequence only when $\sigma_j = 1$. We say that $\underline{\sigma} = \sigma_m \sigma_{m-1} \cdots \sigma_1$ is a *binary* representation of n on $L_1, \ldots, L_m$. A buffer set consisting of fibers of lengths $L_1, L_2, \ldots, L_m$ is referred to as a *flexible* buffer set if, for every integer n, $1 \le i \le D_{max}$, there exists an m-digit binary representation or sequence $\sigma_m \sigma_{m-1} \cdots \sigma_1$ for n.

While several binary representations of an integer on a Fibonacci buffer set may be possible, one particular binary representation—the "greedy" Fibonacci representation—is used by the control algorithm of our architecture. The greedy representation $\sigma_m \sigma_{m-1} \cdots \sigma_1$ of $n \in [1, D_{max}]$ on $L_m, L_{m-1}, \ldots, L_1$ is determined recursively as follows: If $F_{k+1} \le n$ and $F_{k+2} > n$, then set $\sigma_m, \sigma_{m-1}, \ldots, \sigma_{k+1}$ to 0 and σ_k to 1. The greedy representation of $n - F_{k+1}$ on $L_{k-1}, L_{k-2}, \ldots, L_1$ determines $\sigma_{k-1}, \sigma_{k-2}, \ldots, \sigma_1$. For example, the greedy Fibonacci representation of the integer 10 on fiber lengths 1, 2, 3, 5, 8, 13 is 010010. We prove (see Appendix C) that the greedy representation always exists and that no adjacent 1s are possible in the representation. Consequently, a greedy Fibonacci representation consists of at most $\lceil \frac{m}{2} \rceil$ 1s and, typically, very few 1s for a wide range of integers.

Although the 2-exponential buffer set, i.e., with fiber lengths $1, 2, 4, 8, \ldots, 2^{m-1}$, also has exponentially increasing fiber lengths and is flexible, the property of requiring very few fibers to construct a fiber sequence makes the Fibonacci buffer set preferable to the 2-exponential buffer set in the context of our architecture. A comparison of the two flexible buffer sets can be found in Section 4.4.

2. *Control Algorithm.* The control algorithm consists of a set of data structures, a fiber sequence selection algorithm, and an update procedure, as follows:

a. *Data Structures*

i. $D_{min}[i,j]$, where $0 \le i \le N-1$ and $0 \le j \le M-1$. $D_{min}[i,j]$ at time n is the minimium delay that a cell arriving at input i and departing at output j must stay within the buffer. This preserves the cell sequence integrity over input i and output j.

ii. $T[i,j]$, where $0 \le i \le D_{max} - 1$ and $1 \le j \le n_{fibers}$. T at time n is referred to as the *insertion table* at time n. $T[i,j]$ may take on one of two values: OCCUPIED and EMPTY. $T[i,j] = OCCUPIED$ indicates that a cell will be inserted into the fiber j at time $n+i$.

iii. $Transmission[i,j]$, where $0 \le i \le D_{max}$ and $0 \le j \le M-1$. $Transmission[i,j]$ takes on a value of either YES or NO. $Transmission[i,j] = YES$ at time n indicates that a cell will be transmitted on output channel j at time $n+i$ and $Transmission[i,j] = NO$ otherwise.

b. *Fiber Sequence Selection Algorithm*

i. *Tuning Parameters.* The fiber sequence selection algorithm, which is described in Fig. 5, requires the following tunable parameters:

A. $k_{MaxPerm}$. Let $\underline{\sigma} = \sigma_m \cdots \sigma_1$ be the binary representation of the integer k, i.e., $k = \sum_{j=1}^{m} \sigma_j F_{j+1}$ and $\sigma_j \in \{0,1\}$, and $\sigma_{k_1}, \sigma_{k_2}, \ldots, \sigma_{k_j}$ be the nonzero elements of $\underline{\sigma}$. There are $j!$ permutations of length-k fiber sequences. This suggests that the algorithm, in spite of considering only the binary representation on the fiber lengths, needs to examine up to $j!$ permutations to determine whether a cell can be admitted to the buffer. $k_{MaxPerm}$, where $1 \le k_{MaxPerm} \le \lceil \frac{m}{2} \rceil !$, restricts the maximum number of possible length-k fiber sequences that the algorithm examines before making a decision on whether an unused length-k fiber sequence exists.

B. $k_{MaxBackOff}$. Suppose that a cell destined to output j arrives on input channel i at time n and that it needs to be delayed for at least k time slots. The algorithm first finds an integer m' such that $m' \ge k$ and there is no scheduled transmission on the output j at time $n+m'$. It then determines whether there exists a fiber sequence of length m'. If so, the cell is admitted; otherwise, the algorithm attempts to find an integer $l > m'$

```
FindFiberSequence ($d_{min}$, $j$)
Begin
$NumberBackOff$ — 0;
$FoundFiberSequence$ — $NO$;
If $k_{algorithm} = Always$ then
    Begin
    Set $k$ to be the smallest integer such that
            $d_{min} \leq k$
            $Transmission[k, j] = NO$ and
            The greedy Fibonacci representation of $k$ consists of at most $k_{MaxFibers}$ 1's;
    End
Else
    Begin
    Set $k$ to be the smallest integer such that
            $d_{min} \leq k$ and
            $Transmission[k, j] = NO$;
    End;

While (($FoundFiberSequence = NO$) and ($k < D_{max}$) and ($NumberBackOff \leq k_{MaxBackOff}$))
    Begin
    Let $\underline{\sigma} = \sigma_m \ldots \sigma_1$ be the greedy Fibonacci representation of $k$
    Let $\sigma_{k_1}, \sigma_{k_2}, \ldots, \sigma_{k_n}$ be the nonzero elements of $\underline{\sigma}$
    $NumPermExamined$ — 0;
    $FoundPermutation$ — $NO$;
    While (($NumPermExamined \leq min(k_{MaxPerm}, n!)$) and ($FoundPermutation = NO$))
            Begin
            $NumPermExamined$ — $NumPerExamined + 1$;
            Select a permutation on $L_{k_n}, L_{k_{n-1}}, \ldots, L_{k_1}$, say, $L_{k_n} L_{k_{n-1}} \ldots L_{k_1}$;
            Determine whether there exists $\underline{l} = \{l_{k_n}, l_{k_{n-1}}, \ldots, l_{k_1}\}$, where $l_{k_i}$ is a fiber of length $L_{k_i}$,
            such that each of $T[0, l_{k_n}], T[L_{k_n}, l_{k_{n-1}}], \ldots, T[\sum_{i=2}^{n} L_{k_i}, l_{k_1}]$ is equal to $EMPTY$;
            If $\underline{l}$ exists then
                Begin
                Schedule the cell to traverse the fiber sequence $l_{k_n} l_{k_{n-1}} \cdots l_{k_1}$;
                $D_{min}[i, j]$ — $k$;
                $Transmission[k, j]$ — $YES$;
                Set each of $T[0, l_{k_n}], T[L_{k_n}, l_{k_{n-1}}], \ldots, T[\sum_{i=2}^{n} L_{k_i}, l_{k_1}]$ to $OCCUPIED$;
                $FoundPermutation$ — $YES$;
                $FoundFiberSequence$ — $YES$;
                End;
            End;
            If ($FoundFiberSequence = NO$) then
                Begin
                $NumberBackOff$ — $NumberBackOff + 1$;
                Set $k$ — $NextValue(k, j)$, where $NextValue(k, j)$ is the smallest integer $l$ such that
                        $k < l$
                        $Transmission[l, j] = NO$ and
                        The greedy Fibonacci representation of $l$ requires no more than $k_{MaxFibers}$ 1's;
                End;
    End;
End.
```

Fig. 5. Fiber sequence selection.

such that there is no output collision at time $n + l$ and there exists a fiber sequence of length l to accommodate the cell. This is refered to as *backoff*. Although backing off can accommodate a cell that is otherwise discarded, it has a serious deleterious effect: The subsequent arriving cells of the (i, j) input-output channel pair at time $n + 1$ must be delayed by l, rather than m', time slots. Since a cell requiring a larger delay typically needs to use more fibers, the performance of the architecture suffers as the number of

backoffs increases. $k_{MaxBackOff}$, which can take on any value between 1 and $D_{max} - 1$, restricts the number of times that the control algorithm backs off to accommodate an arriving cell.

C. $k_{MaxFibers}$. Although the maximum number k of fibers required to represent an integer between 1 and D_{max} is $\lceil \frac{m}{2} \rceil$, k becomes large as m increases. $k_{MaxFibers}$ limits the maximum number of fibers that can be used to accommodate a cell. The effect of $k_{MaxFibers}$ is as follows: Suppose that a cell needs to be delayed for at least k_1 time slots, but the greedy Fibonacci representation of k_1 requires n 1s, where $n > k_{MaxFibers}$. The algorithm must find the smallest integer k_2 such that $k_2 > k_1$ and that its binary representation consists of no more than $k_{MaxFibers}$ 1s. A consequence of using $k_{MaxFibers}$ is an increase in the delay of the cell. Because of the cell sequence integrity requirement, the delays of subsequently arriving cells also increase. $k_{MaxFibers}$ can be used in two contexts, depending on whether the parameter $k_{algorithm}$ is set to Always or BackOffOnly. If $k_{algorithm} = BackOffOnly$, the parameter $k_{MaxFibers}$ is used only when the algorithm is performing a backoff. If $k_{algorithm} = Always$, each buffered cell must always traverse no more than $k_{MaxFibers}$ fibers. $k_{MaxFibers}$ may take on any value between 1 and $\lceil \frac{m}{2} \rceil$, inclusive.

D. $k_{algorithm}$. $k_{algorithm}$ takes on one of two values: Always and BackOffOnly. This parameter specifies whether the restriction of using $k_{MaxFibers}$ fibers in a fiber sequence is always used or is used only during a backoff.

ii. The Algorithm. Upon receiving a cell that has arrived on input i and is destined to output j, the algorithm examines $D_{min}[i,j]$ and $Transmission[0,j]$ to determine whether the cell needs to be buffered. If $Transmission[0,j] = YES$ or $D_{min}[i,j] > 0$, the cell must be buffered. The minimum time d_{min} that the cell needs to be buffered is $max\{1, D_{min}[i,j]\}$. The FindFiberSequence procedure with input parameters d_{min} and j is invoked to find a length-k fiber sequence such that $d_{min} \leq k$ and $Transmission[k,j] = NO$; that is, the procedure finds a fiber sequence of length k such that $d_{min} \leq k$ so as to maintain cell sequence integrity and such that no other cell has

been scheduled to be transmitted on output channel j at time k. The procedure is shown in Fig. 5.

iii. The Update Algorithm. At the beginning of each time slot, the data structures D_{min}, T, and Transmission are updated as follows:

$D_{min}[i,j] \leftarrow max(0, D_{min}[i,j] - 1)$

for each (i,j)-pair such that

$0 \leq i \leq N - 1$ and $0 \leq j \leq M - 1$

$T[i,j] \leftarrow T[i+1,j]$ for $0 \leq i < D_{max} - 1$

and $T[D_{max} - 1, j] \leftarrow EMPTY$,

where $1 \leq j \leq n_{fibers}$

$Transmission[i,j] \leftarrow Transmission[i+1,j]$,

for $0 \leq i \leq D_{max} - 1$

and $Transmission[D_{max}, j] \leftarrow NO$,

where $0 \leq j \leq M - 1$.

3. Switching Fabric. The switching fabric of the ATM switch transfers a cell arriving on an input channel or exiting a delay fiber to an output channel or another delay fiber. Any nonblocking $(N + n_{fibers}) \times (M + n_{fibers})$ switch, such as a crossbar, as shown in Fig. 1 for $M = N = 2$ or a Benes network [11], can be used as the switching fabric.

3.3 Example of Operation

We now illustrate the basic operation of the control algorithm and, in particular, of the FindFiberSequence procedure. Let $N = M = 2$, $k_{MaxFibers} = 3$, and $D_{max} = 10$. Then, $m = 5$, $L_1 = 1$, $L_2 = 2$, $L_3 = 3$, $L_4 = 5$, and $L_5 = 8$. Let $n_1 = 1$, $n_2 = 1$, $n_3 = 1$, $n_4 = 1$, and $n_5 = 1$. Suppose that, at time n, the states of the data structures D_{min}, T, and Transmission are as shown in Fig. 6 and that a cell that is destined for output 0 arrives at input 1. Because $D_{min}[1,0] = 3$, the cell must be buffered for at least three time slots. Time $n + 3$ would be the earliest time that the cell may be transmitted at output 0, but $Transmission[3,0] = X$ indicates that a cell has already been scheduled to use the output at time $n + 3$. $Transmission[4,0] = EMPTY$ indicates that the output is idle at time $n + 4$ and the cell may be transmitted at that time. This implies that the cell must be buffered for four time slots.

Because the greedy Fibonacci representation of four on fiber lengths 1, 2, 3, 5, and 8 is 00101, the cell must traverse a fiber sequence consisting of fibers of lengths 1 and 3. There are two such fiber sequences, $l_1 l_3$ and $l_3 l_1$. If the cell were to traverse the sequence $l_1 l_3$, $T[0,1]$ and $T[1,3]$ would have to be empty in order for the cell to be inserted into fiber 1 at time n and into fiber 3 at time $n + 1$. $T[1,3] = X$ and $T[0,3] = X$ indicate that neither of the two sequences $l_1 l_3$ nor $l_3 l_1$ can be used. The control algorithm must back off to another integer larger than 4. $Transmission[5,0] = EMPTY$ indicates that the cell may be transmitted on output 0 at time $n + 5$ and that it should be delayed for five time slots. The greedy Fibonacci representation of 5 is 01000. The representation has only one nonzero element and, because $k_{MaxFibers} \geq 1$, 5 is an eligible backoff

Fig. 6. State of T, D_{min}, and $Transmission$.

candidate. Because $T[0,5]$ is unoccupied, the cell may be inserted into fiber 5 at time n. The algorithm schedules the cell to traverse fiber 5 at time n and updates the data structures D_{min}, T, and $Transmission$ accordingly.

3.4 Salient Characteristics of the Architecture

The architecture regards the $D_{max}n_{fibers}$ entries of the insertion table T as "resources"; hence, the time dimension as well as the fibers can be exploited to store cells. A cell needing to be buffered is considered to be a "consumer" of the resources. The efficacy of the architecture depends on its ability 1) to limit the number of entries used by each cell, 2) to reduce the probability of time-correlated cells contending for the same set of resources at about the same time, and 3) to make the product $D_{max}n_{fibers}$ large while keeping n_{fibers} small. All of these goals must be achieved without incurring prohibitively large delays.

The Fibonacci buffer set, in conjunction with the control algorithm, can satisfy 1), 2), and 3) without relaxing the latency or cell sequence integrity requirements. The maximum number of nonzero elements in the greedy Fibonacci representation of an integer between 1 and D_{max}, inclusive, is no larger than $\lceil \frac{m}{2} \rceil$ and, therefore, a cell may consume at most $\lceil \frac{m}{2} \rceil$ entries. Although $\lceil \frac{m}{2} \rceil$ is already a rather small number, in practice, the number of fibers required by a cell is much smaller than this theoretical maximum. The contention of the same table entries at about the same time is alleviated by permuting the fiber sequences to be traversed and by backing off. For example, the two permutations $l_{k_n}l_{k_{n-1}}\cdots l_{k_1}$ and $l_{k_1}l_{k_2}\cdots l_{k_n}$ of a fiber sequence on $L_{k_1}, L_{k_2}, \ldots, L_{k_n}$ correspond to two completely different sets of entries in the insertion table. As the number n of fibers in a fiber sequence increases, the number of permutations increases exponentially, i.e., $n!$. This offers massive redundancy when finding a corresponding set of n unused entries is difficult. The backoff algorithm alters the set of resources required by an arriving cell.

The Fibonacci buffer set has the remarkable property that the greedy representations of adjacent integers k and $k+1$ look very different for a wide range of ks. For example, the greedy representations of 1 to 10 on fiber lengths 1, 2, 3, 5, and 8 are 00001, 00010, 00100, 00101, 01000, 01001, 01010, 10000, 10001, and 10010, respectively. By backing off a delay of k to $k+1$, for example, the resources required by a cell

can be altered dramatically. Since D_{max} grows linearly with F_m and F_m is an exponentially increasing function of m, increasing m by 1 would result in an exponential increase in D_{max}. Therefore, the size of the insertion table $D_{max}n_{fibers}$ can grow exponentially with n_{fibers}. It should be noted that making $D_{max}n_{fibers}$ large constitutes only part of the solution. The other part is to ensure that most of the $D_{max}n_{fibers}$ entries can be utilized. This requires the proper selection of $\underline{n}$. Because the Fibonacci buffer set is flexible, a cell needing to be delayed for k time slots has the opportunity to be delayed for exactly k time slots unless it is backed off to a larger integer. In cases where backoffs are rare, most cells are delayed for an amount that is close to their theoretical minimum.

3.5 Time and Space Complexity

The actual time complexity of the control algorithm depends on the tuning parameters. We found that the architecture is most robust when

$$k_{MaxFibers} = \left\lceil \frac{m}{2} \right\rceil,$$

$$k_{algorithm} = BackOffOnly,$$

$$k_{MaxPerm} = 2,$$

and

$$k_{MaxBackOff} = D_{max} - 1.$$

The complexity of the control algorithm, measured in terms of the switch parameters D_{max}, N, M, and n_{fibers}, corresponding to this set of tuning parameters is as follows:

1. *Space Complexity.* The space complexity of the control algorithm refers to the memory requirement for the data structures D_{min}, T, and $Transmission$. Because T requires the most memory, the space complexity of the algorithm is $O(D_{max}n_{fibers})$ bits.

2. *Time Complexity.* Because a fiber sequence may contain up to $\lceil \frac{m}{2} \rceil$ fibers and $m = O(log_{\phi}D_{max})$, the control algorithm requires $O(log_{\phi}D_{max})$ steps to determine whether there exists a fiber sequence of length k. Since there are up to D_{max} ks to consider, the time complexity of the algorithm per cell is $O(D_{max}log_{\phi}D_{max})$. In a lossless architecture, however, the expected time complexity is approximately $O(log_{\phi}D_{max})$, as the expected number of backoffs is small. The parameter D_{max} (the maximum latency that a cell may be buffered in the switch) is, in practice, a small constant because an ATM switch typically has a very stringent latency requirement. Therefore, the control algorithm has low expected time complexity in such an architecture and can be executed in real time.

4 PERFORMANCE OF THE ARCHITECTURE

We evaluated the performance of the architecture under a diverse set of time-correlated and heavily loaded traffic profiles through simulation studies. For each traffic profile, we obtained the buffer set $(n_1, n_2, \ldots, n_m)$ that resulted in an empirically lossless architecture. An ATM switch is

empirically lossless if no cell loss can be detected during a simulation run of $O(10^7)$ time slots. The model for the performance evaluation is described in Section 3.1. To simplify the evaluation, we set $N = M = 2$, as our goal is to design a buffer organization for a small-dimension ATM switching element, with symmetric traffic profiles, i.e., the input process of each input channel is the same and destinations of arriving cells are uniformly distributed among the M output channels. This corresponds to setting $q_{ij} = \frac{1}{M}$ for $0 \le i, j \le 1$ and $\alpha_{ij}^k = \alpha_{ij}$ for $k = 0, 1$ and $1 \le i, j \le 2$.

We define X and $X_{Bernoulli}$ to be the number of consecutive time slots in which the 2-state MMBP of an input channel and a Bernoulli process, respectively, would generate a cell in each time slot. The *time correlation index* τ of the 2-state MMBP is defined as $\tau = \frac{E(X)}{E(X_{Bernoulli})}$; therefore, the Bernoulli process in which cells are generated independently of each other has a time correlation index of 1. An input process in which cell arrivals are positively time-correlated has $\tau > 1$, where a larger value of τ indicates more time correlation. Because we assume that, for symmetry, destinations of cells are uniformly distributed among the output channels, the correlation of the destinations of cells is not considered. The offered load ρ and the time correlation index τ of a 2-state MMBP uniquely determine the MMBP's state transition probabilities α_{ij} for $1 \le i, j \le 2$ as follows:

$$\alpha_{11} = \frac{\tau - (1 - \rho)}{\tau}; \quad \alpha_{12} = 1 - \alpha_{11} \qquad (1)$$

$$\alpha_{22} = \frac{\tau - \rho}{\tau}; \quad \alpha_{21} = 1 - \alpha_{22}. \qquad (2)$$

We evaluated the performance of the switch under traffic profiles with $\rho = 0.6, 0.7$, and 0.8, and $\tau = 1, 2, 4, 8, 16$, and 32 through simulation studies. The duration of each simulation run was 10^7 time slots. We anticipated that the sampling error of the simulation studies would be considerable at the region where the cell loss rate is extremely small, e.g., less than 10^{-5}. Because the number of cells generated for each run is on the order of 10^7, a cell loss value that is less than 10^{-6} should be construed as simulation noise. Although such a cell loss value cannot be regarded as statistically valid, it provides the valuable indication that cell loss is rare in the switch architecture.

The sample distribution of d_{min}, which is the minimum time that an arriving cell needs to be delayed, was also collected. We used the sample distribution to estimate the latency experienced by each arriving cell. For various buffer sets, latencies D_{max} and traffic profiles, the cell loss rates are shown in Figs. 7, 8, 9, 10, 11, and 12. Because a cell loss rate of 0 corresponds to $-\infty$ on the y-axis, we substituted 10^{-7} as the value for 0 in Figs. 7, 8, 9, 10, 11, and 12. The sample distributions of d_{min} for cases where $\rho = 0.8$ and $\tau = 1, 2, 4, 8, 16, 32$ are shown in Figs. 13, 14, 15, 16, 17, and 18. In each case, the corresponding empirically lossless buffer set tabulated in Table 1 in Section 4 is used. The relative frequency at latency k is the percentage of arriving cells that find $d_{min} = k$. Because a relative frequency of 0 corresponds to
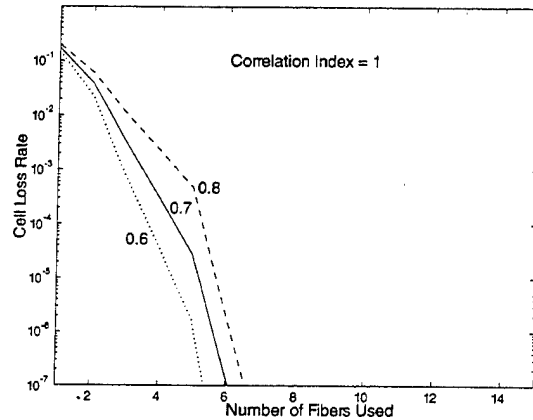

Fig. 7. Cell loss rates for $\rho = 0.6, 0.7, 0.8$ and $\tau = 1$.

$-\infty$ on the y-axis, we substituted 10^{-8} for a relative frequency of 0 in the figures. Note the exponential decay of the relative frequencies in all of the figures. For example, in Fig. 13, the relative frequency for $d_{min} = 2$ is on the order of 10^{-1}, but the relative frequency for $d_{min} = 5$ is on the order of 10^{-3}, which is a decrease in the relative frequency by two orders of magnitude as d_{min} increases from 2 to 5. The fact that all of the sample distributions of d_{min} exhibit this behavior indicates that the latency mass function of the Fibonacci switch decreases very rapidly as the latency increases.

4.1 Tunable Parameters

After examining the impact of the tuning parameters on the architecture through several simulation studies, we found that the backoff mechanism, due to the cell sequence integrity constraint, can have a deleterious effect on the performance of the switch. Consequently, slowing the backoff, i.e., backing off to a small integer rather than to a large integer, is crucial. This corresponds to setting $k_{MaxFibers} = \lceil \frac{m}{2} \rceil$. We also found that, as long as each backoff is slow, allowing a large number of backoffs is preferable, i.e., setting $k_{MaxBackOff} = D_{max} - 1$. We also conducted studies to examine whether the performance of the switch would improve by searching all possible permutations of a fiber sequence and found that, in many cases, searching for more permutations does not significantly improve the cell loss performance of the architecture (see Appendix F).
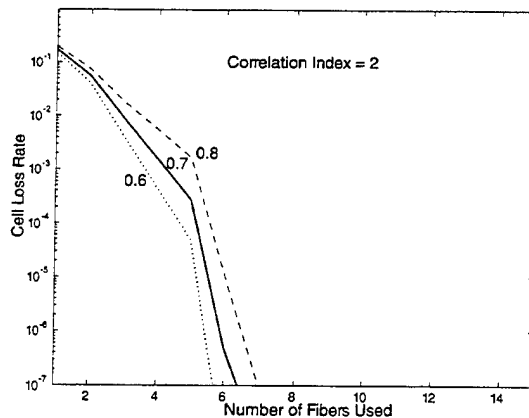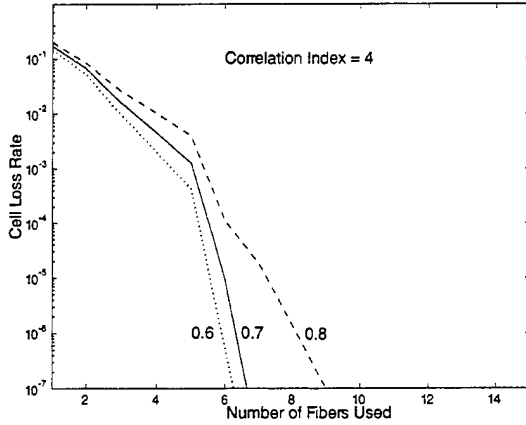

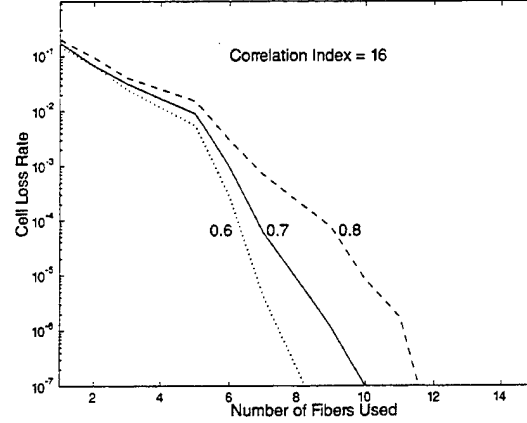Fig. 8. Cell loss rates for $\rho = 0.6, 0.7, 0.8$ and $\tau = 2$.

Fig. 9. Cell loss rates for $\rho = 0.6, 0.7, 0.8$ and $\tau = 4$.

Fig. 11. Cell loss rates for $\rho = 0.6, 0.7, 0.8$ and $\tau = 16$.

Empirically, searching for only two permutations of a fiber sequence on $L_{k_1}, L_{k_2}, \ldots, L_{k_n}$ suffices to achieve good performance. In particular, assuming that $k_n > k_{n-1} > \cdots > k_1$, the control algorithm examines only the two permutations $l_{k_n} l_{k_{n-1}} \cdots l_{k_1}$ and $l_{k_1} l_{k_2} \cdots l_{k_n}$.

## 4.2 Heuristic for an Empirically Lossless Switch Architecture

A buffer set that results in an empirically lossless switch architecture is referred to as an *empirically lossless buffer set*. Because a small value of D_{max} would require a large value of n_{fibers} to keep $D_{max} n_{fibers}$ large, we vary D_{max} as if it were a design parameter to determine its effect on the architecture. Our goal is to search for the largest acceptable D_{max} so that the number of fibers used in an empirically lossless buffer set is as small as possible. A buffer set $\underline{n} = (n_1, n_2, \ldots, n_m)$ can be augmented by one fiber in two ways: $\underline{n}$ becomes $(n_1, n_2, \ldots, n_m, 1)$ or $\underline{n}$ becomes $(n_1, n_2, \ldots, n_m) + \delta_{jm}$, where $1 \leq j \leq m$ and δ_{jm} is an m-vector with 1 in the jth entry and zero otherwise. That is, a buffer set can be augmented by adding a fiber of a new fiber type or a fiber of an existing fiber type. Adding a fiber type of length F_{m+2} requires D_{max} to be modified so that $F_{m+2} \leq D_{max}$.

The heuristic that we used to obtain the empirically lossless buffer sets under various traffic scenarios is as follows: Initially, we set $D_{max} = 1$, $m = 1$, and $\underline{n} = (1)$. We

then conducted a simulation study to determine whether $\underline{n} = (1)$ is an empirically lossless buffer set. If not, we set $D_{max} \leftarrow 2D_{max}$ and $m \leftarrow i$ such that F_{i+1} is the largest Fibonacci number that is no larger than the new D_{max}. The number of fibers for each new fiber type introduced is 1. For example, the design parameters $D_{max} = 1$, $m = 1$, and $\underline{n} = (1)$ become $D_{max} = 2$, $m = 2$, and $\underline{n} = (1, 1)$. We then conducted another simulation run to see whether the augmented buffer set $(1, 1)$ results in an empirically lossless architecture. The process of extending the buffer set by adding a new fiber type continues until a new buffer set yields a higher cell loss rate than the previous buffer set. We then regress to the previous buffer set (assuming that it consists of m' fiber types) and augment it by adding a fiber of length 1. Then, we add a fiber of length 2 if the new buffer set is not empirically lossless and so on until $n_i = n_j$ for all i, j between 1 and m'. The buffer set, if needed to be extended, is augmented by adding a new fiber type of length $F_{m'+1}$ and the process repeats.

The empirically lossless buffer sets obtained by the heuristic for the cases where $\rho = 0.8$ and $\tau = 1, 2, 4, 8, 16, 32$ are shown in Table 1. The corresponding D_{max} and the total number n_{fibers} of fibers in each buffer set are also tabulated. For example, for the case where $\tau = 32$, the empirically lossless buffer set, the maximum latency D_{max}, and the total number of fibers used are $\underline{n} = (2, 2, 2, 2, 2, 2, 1, 1, 1)$, 64, and 15, respectively. $\underline{n} =$
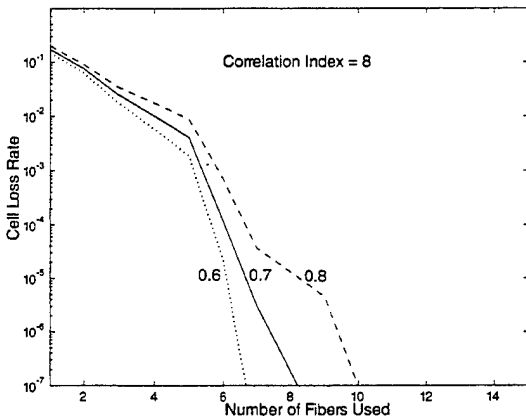
Fig. 10. Cell loss rates for $\rho = 0.6, 0.7, 0.8$ and $\tau = 8$.
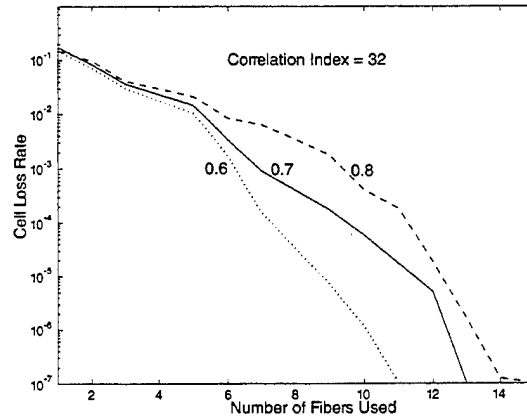
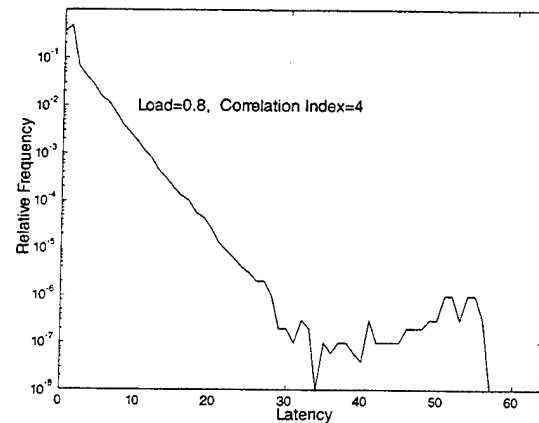Fig. 12. Cell loss rates for $\rho = 0.6, 0.7, 0.8$ and $\tau = 32$.

Fig. 13. Sample distribution of d_{min} for $\rho = 0.8$ and $\tau = 1$.
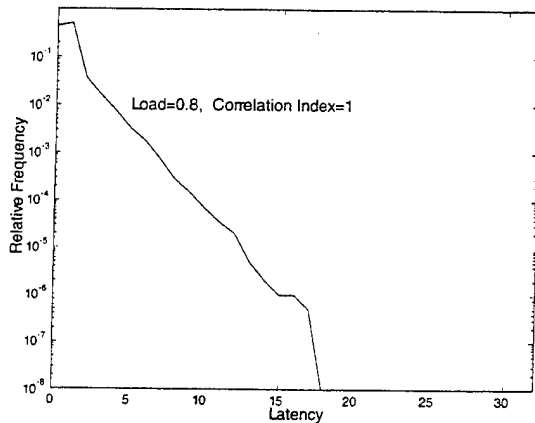
Fig. 15. Sample distribution of d_{min} for $\rho = 0.8$ and $\tau = 4$.

$(2, 2, 2, 2, 2, 2, 1, 1, 1)$ indicates that there are two fibers of each fiber type of lengths 1, 2, 3, 5, 8, and 13 and one fiber of each fiber type of lengths 21, 34, and 55.

4.3 Feasibility of an Empirically Lossless Switch Architecture

We now discuss the feasibility of implementing an empirically lossless switch architecture under the most bursty traffic profile, i.e., $\tau = 32$ and $\rho = 0.8$, that we have examined. The expected number of consecutive cell arrivals on an input channel is 160. Although the expected burst length on an input to an ATM switch can be arbitrarily large, we assume that ATM traffic management mechanisms, such as call admission control, routing, and policing, of the network would regulate traffic so that the expected burst length on an input channel exceeding a threshold as large as 160 is unlikely. The empirically lossless buffer set for the traffic profile consists of 15 fibers. This suggests that the corresponding switching fabric must be of dimensions 17×17.

Of the possible optical switching fabrics, the classical crossbar is perhaps the most desirable because of its control and design simplicity, but, since the number of crosspoints required grows quadratically with the numbers of inputs and outputs, a concern is that it may be impossible or impractical to implement a 17×17 optical crossbar. It has been found that optical crossbars as large as 32×32 are
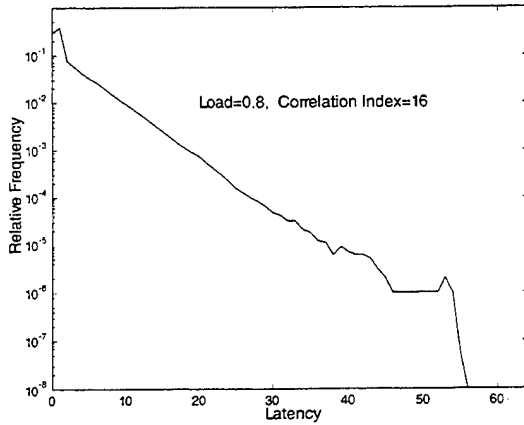
feasible [1]; therefore, implementing the empirically lossless buffer set using an optical crossbar is well within the limits achievable by today's technology. It is difficult to build a large optical crossbar so that all of its crosspoints function properly; consequently, the fabrication yield of large optical crossbars with perfect crosspoints is typically low. Because of the greedy Fibonacci representation, a cell cannot traverse fibers of length F_i and F_{i+1} for any i where $2 \leq i \leq m + 1$ and, therefore, a fiber of length F_i need not be connected to a fiber of length F_{i+1} and vice versa. This means that an imperfect optical crossbar can be used as the switching fabric of our architecture and that the yield of constructing the fabric would be high. The ability of our architecture to function with imperfect switching fabrics significantly enhances its viability.

4.4 Comparison of Fibonacci and 2-Exponential Buffer Sets

We now show why the Fibonacci buffer set performs better than the 2-exponential buffer set, even though both are flexible and have exponentially increasing fiber lengths. The key observation is that the more effective buffer set should, on average, require fewer fibers to store an ATM cell and should have fewer 1s in the cell's binary representation.

We show that the Fibonacci buffer set requires fewer 1s to represent a set of integers between 1 and n, where n is very large, thereby demonstrating that it is more efficient.
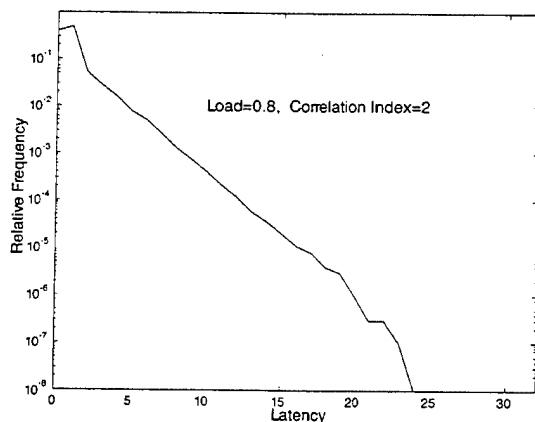
Fig. 14. Sample distribution of d_{min} for $\rho = 0.8$ and $\tau = 2$.
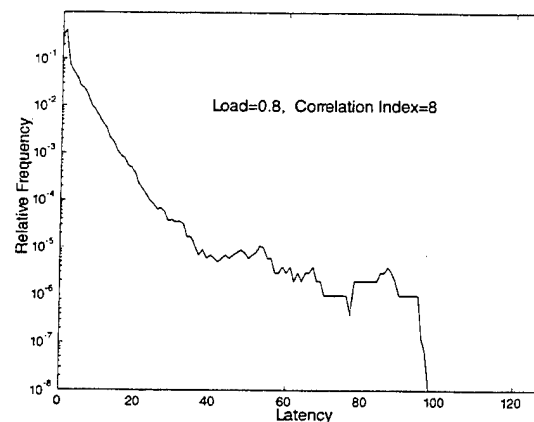
Fig. 16. Sample distribution of d_{min} for $\rho = 0.8$ and $\tau = 8$.

Fig. 17. Sample distribution of d_{min} for $\rho = 0.8$ and $\tau = 16$.

TABLE 1
Empirically Lossless Buffer Sets for Cases
where $\rho = 0.8$ and $\tau = 1, 2, 4, 8, 16, 32$

τ	Empirically Lossless Buffer Set $\underline{n}$	D_{max}	n_{fibers}
1	(1,1,1,1,1,1,1)	32	7
2	(1,1,1,1,1,1,1)	32	7
4	(1,1,1,1,1,1,1,1,1)	64	9
8	(1,1,1,1,1,1,1,1,1,1)	128	10
16	(2,2,2,1,1,1,1,1,1)	64	12
32	(2,2,2,2,2,2,1,1,1)	64	15

Let k_1 and k_2 be the largest integers such that $2^{k_1} \le n$ and $F_{k_2+1} \le n$, respectively. Any integer x between 1 and n can be represented as $x = \sum_{j=0}^{k_1} \psi_j 2^j$ and $x = \sum_{j=1}^{k_2} \theta_j F_{j+1}$, where $\psi_j, \theta_j \in \{0, 1\}$. We wish to determine whether there exists an asymptotic relationship between k_1 and k_2, as n becomes very large. Since $n \le 2^{k_1} - 1$, $k_1 = \lceil log_2(n+1) \rceil$. As n becomes large, $k_1 \approx log_2 n$; similarly, since $\frac{1}{\sqrt{5}} \phi^{k_2+1} \le n$, $k_2 \approx log_\phi(\sqrt{5}n)$. From

$$\frac{k_1}{k_2} \approx \frac{log_2 n}{log_\phi(\sqrt{5}n)} \approx \frac{\frac{log_{10} n}{log_{10} 2}}{\frac{log_{10}(\sqrt{5}n)}{log_{10} \phi}},$$

it follows that:

$$\frac{k_1}{k_2} \approx \frac{log_{10} \phi}{log_{10} 2} \approx \frac{0.2089785}{0.301029995} \approx 0.694211607.$$

This implies that $k_2 \approx 1.44 k_1$, as n becomes large. If $1, 2, 4, 8, \ldots, 2^{k_1}$, i.e., the 2-exponential buffer set, were used to represent a fiber sequence of length x, where x is uniformly distributed between 1 and n, then the expected number of 1s in the binary representation of x is $0.5 k_1$. If $1, 2, 3, 5, 8, \ldots, F_{k_2+1}$, i.e., the Fibonacci buffer set, were used to represent x, the expected number of 1s in the binary representation of x is $0.2763 k_2$, as 0.2763 is the expected number of 1s in a digit of a greedy Fibonacci representation. Although $k_2 \approx 1.44 k_1$, $(0.2763)(1.44)k_1 \approx 0.4 k_1$; hence, the
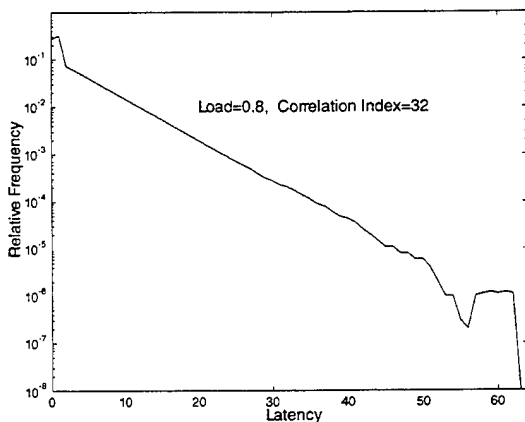
Fibonacci representation requires only $0.4 k_1$ 1s to represent an integer, whereas the 2-exponential representation requires $0.5 k_1$.

We performed two simulation studies to compare the efficacy of the two buffer sets; the results validated the conclusion of the mathematical comparison. In one study, the Fibonacci buffer set was used; in the other, the 2-exponential buffer set was used. The switch parameters for both studies were $M = N = 2$, $\tau = 8$, and $\rho = 0.8$. The results of the two studies, which demonstrate the superiority of the Fibonacci buffer set, are shown in Fig. 19. In the figure, the performance of the two buffer sets is comparable when the number of fibers is five or fewer. When the number of fibers is increased from five to six and from six to seven, the performance of the 2-exponential buffer set worsens, while the performance of the Fibonacci buffer set continues to improve. In particular, when the number of fibers is seven, the cell loss rate effected by the 2-exponential buffer set is 10^{-1}, three orders of magnitude larger than that achieved by the Fibonacci buffer set.

Fig. 18. Sample distribution of d_{min} for $\rho = 0.8$ and $\tau = 32$.
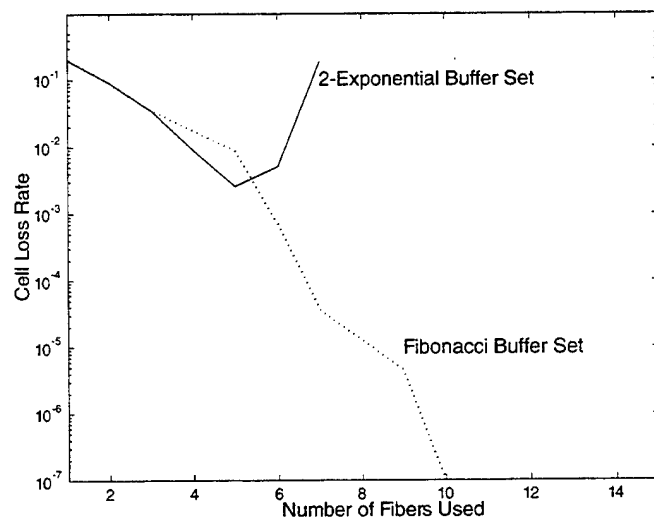
Fig. 19. Cell loss rates achieved by the Fibonacci and the 2-exponential buffer sets for the case where $\rho = 0.8$ and $\tau = 8$.
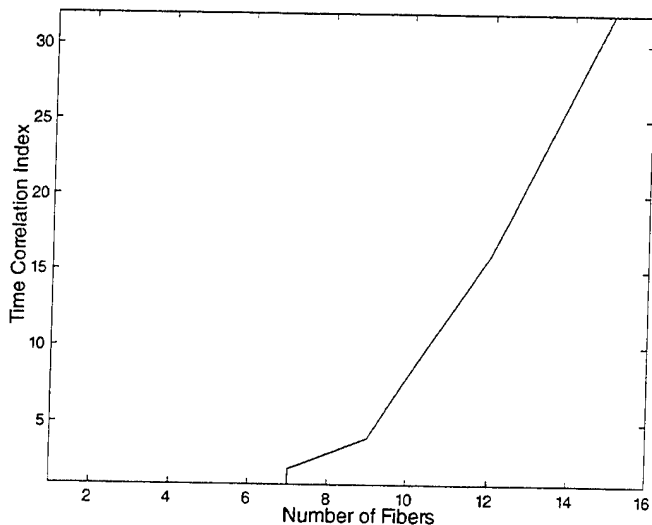
Fig. 20. The number of fibers required in the empirically lossless buffer set for $\rho = 0.8$ and for various values of the time correlation index τ.

4.5 Performance Characteristics

The architecture exhibits the following performance characteristics:

1. *The cell loss rate decreases exponentially as the number of fibers increases.* The cell loss performance curves in Figs. 7, 8, 9, 10, 11, and 12 indicate that an increase of one fiber results in approximately an order of magnitude decrease in the cell loss rate of the architecture. For example, for the case where $\rho = 0.8$ and $\tau = 32$, the cell loss rate corresponding to the buffer set $\underline{n} = (2, 2, 2, 2, 1, 1, 1, 1, 1)$ is on the order of 10^{-5}, but, when the buffer set is augmented to $(2, 2, 2, 2, 2, 1, 1, 1, 1)$, the cell loss rate decreases to the order of 10^{-6}.

2. *The latency mass function decays rapidly as the latency increases.* The mode of d_{min} is between 0 and 1, and the relative frequencies decay rapidly as the delay increases, e.g., the percentage of cells experiencing a minimum delay of k time slots is approximately an order of magnitude larger than the percentage of cells that are delayed for $k + 1$ time slots. This pattern, which is present in all of the simulation studies, indicates that most cells are not artificially delayed by the architecture for the purpose of reducing cell loss.

3. *The deleterious effect of an exponential increase in time correlation can be mitigated by a linear increase in the number of fibers.* The simulation results indicate that the effect of an exponential increase in τ can be offset by the addition of a few fibers, as shown in Fig. 20. For example, for the case where $\rho = 0.8$ and $\tau = 1$, the empirically lossless buffer set consists of seven fibers. For the case where $\rho = 0.8$ and $\tau = 32$, the buffer set corresponding to a lossless architecture requires 15 fibers. The effect of a 2^5-fold increase in time correlation is negated by the addition of only eight fibers.

5 RELATED WORK

There are two general approaches to designing a packet switch using optical delay fibers as buffers: *deflection* and *nondeflection*. The driving principle behind the deflection approach, which is used in [2], [3], [4], is to distribute the packets so that the traffic arriving at each switching element is sufficiently smooth or noncorrelated. The result is that a small number of buffers within a switching element, coupled with the deflection of packets to noncongested outputs, suffices to achieve a low packet loss rate. A significant drawback of this approach, which limits its applicability to ATM networks, is that packets may be delivered out of order and that latency may be high.

The approaches proposed by Varvarigos in [14] can alleviate many of the deleterious effects, e.g., out-of-order packet delivery and high latency, of the deflection approach. Although those approaches can guarantee lossless communication and use only a few fibers, they require the flow control strategy of [6], which ensures that the traffic satisfies a certain smoothness constraint. The effectiveness of the flow control strategy depends on the selection of an appropriate frame size F. A large value of F may result in high latency and may require the use of a large number of fibers to achieve lossless communication. On the other hand, the burstiness of traffic that can be sent over a connection is proportional to F. To accommodate traffic with a high degree of burstiness or time correlation, i.e., traffic typically found in today's ATM networks, a large value of F must be used, but this results in high latency and low throughput. The approaches proposed by Varvarigos, therefore, inherit some of the disadvantages of the flow control strategy.

In the nondeflection approach, which is the focus of this paper, the emphasis is on providing sufficient buffering at each switching element so that cell loss is kept below an acceptable threshold. Among the research studies that use the nondeflection approach, the closest in spirit to this paper are [5], [7].

In [5], Cruz and Tsai propose a 2×2 optical packet switch. The "baseline" switch consists of n stages of 2-state switching elements, with each switching element having an optical delay fiber of equal length Δ to buffer excess packets. Cruz and Tsai show that, with a sufficiently large Δ and noncorrelated traffic at the inputs, the baseline switch can achieve a low cell loss rate while using only a few stages or fibers. When the traffic on the input channels is correlated, the analysis is no longer applicable and the performance of the baseline switch is essentially unknown. An "augmented" switch is obtained by inserting additional optical delay fibers between adjacent stages in the baseline switch. Those fibers must be large and of relatively prime lengths; however, only a few fibers suffices to achieve a low cell loss rate.

While Cruz and Tsai focus on the design of a 2×2 switch, Haas considers the construction of an arbitrary dimension packet switch in [7]. The switching fabric of the architecture consists of k optical delay fibers of unequal lengths. An arriving packet is inserted into one of the fibers such that there is no transmission collision at any of the output channels and the packet sequence integrity is

maintained. Packets that cannot be accommodated are discarded.

There are important differences between our switch and the switches considered in [5], [7]. While the baseline switch of [5] can achieve a good cell loss performance with only a few fibers, the latency is $n\Delta$, which may be excessive for an ATM switch. Furthermore, good performance can be achieved only if the input traffic is noncorrelated. While the noncorrelated traffic class may be an adequate approximation for the traffic in a very high-speed future ATM network, in today's environment, ATM traffic tends to be heavily correlated. If the augmented switch of [5] were used to accommodate time-correlated traffic, the packet sequence integrity would not be maintained and the latency would be prohibitively high, e.g., on the order of thousands of time slots; consequently, neither the baseline switch nor the augmented switch is suitable for ATM applications. In comparison, our design yields a low cell loss rate even under highly time-correlated traffic and results in a much lower latency. While our control algorithm is more complex, its expected time complexity is $O(logD_{max})$, which is suitable for high-speed operation.

The pioneering design of [7] provides a framework for building an optical packet switch, but the issue of how to resolve the trade-off between using few fibers and achieving a low loss rate has not been adequately addressed. Indeed, it appears that the design would require a large number of fibers to achieve a sufficiently low loss rate acceptable to ATM applications. For example, consider the case where the number of input and output channels is 4, the fiber lengths are 5, 10, 15, and 20, the offered load on each input is 0.8, and the expected burst length is 10, which roughly corresponds to $\tau = 2$. With four fibers, the corresponding loss rate is on the order of 10^{-1} for the architecture of [7]. In contrast, for the similar case where $\rho = 0.8$ and $\tau = 2$, and where the expected burst length is also 10, our design requires only seven fibers to achieve an empirically lossless architecture. Because each simulation run generates on the order of 10^7 cells, an empirical zero cell rate suggests that the actual cell loss rate effected by the Fibonacci switch is smaller than $O(10^{-5})$. Hence, the use of three additional fibers by the Fibonacci switch has resulted in a reduction of at least four orders of magnitude in the cell loss rate.

6 CONCLUSION

An ATM switch architecture using optical delay fibers as buffers has been presented. Because of the remarkable properties of the Fibonacci numbers, the architecture is computationally efficient, requires few fibers, and yields low latency and cell loss rate across diverse time-correlated and heavily loaded traffic profiles. The buffer sets corresponding to an empirically lossless 2×2 ATM switch architecture under diverse traffic scenarios have been presented. The architecture exhibits the desirable characteristics that the cell loss rate decreases exponentially as the number of fibers increases, that the probability mass function for the sample latency decays rapidly, and that an exponential increase in the time correlation of traffic can be offset by a small increase in the number of fibers.

Because of these salient characteristics, this architecture may play an integral role in future optical ATM networks.

APPENDIX A

INDEX OF LARGEST FIBONACCI NUMBER $\leq D_{max}$

We wish to determine the number m of fiber types required by a Fibonacci buffer set to represent any integer between 1 and D_{max}, inclusive. Since $m + 1$ is the index of the largest Fibonacci number less than or equal to D_{max}, i.e., $F_{m+1} \leq D_{max}$ and $F_{m+2} > D_{max}$, the index $m + 1$ of the largest Fibonacci number $F_{m+1} \leq D_{max}$ may be computed as follows: From [13], $F_n = \frac{1}{\sqrt{5}}\phi^n - \frac{1}{\sqrt{5}}\hat{\phi}^n$, where $\phi = \frac{1}{2}(1 + \sqrt{5})$ and $\hat{\phi} = \frac{1}{2}(1 - \sqrt{5})$. Since $|\frac{1}{\sqrt{5}}(\frac{1-\sqrt{5}}{2})^n| \leq \frac{1}{2}$,

$$F_n = \left\lfloor \frac{1}{\sqrt{5}}\phi^n + \frac{1}{2} \right\rfloor.$$

Then, $F_{m+1} = \lfloor \frac{1}{\sqrt{5}}\phi^{m+1} + \frac{1}{2} \rfloor$. Since $\lfloor \frac{1}{\sqrt{5}}\phi^{m+1} + \frac{1}{2} \rfloor \leq D_{max}$,

$$\frac{1}{\sqrt{5}}\phi^{m+1} + \frac{1}{2} \leq D_{max} + 1$$

$$\phi^{m+1} \leq \sqrt{5}\left(D_{max} + \frac{1}{2}\right)$$

$$m + 1 \leq log_\phi\left(\sqrt{5}\left(D_{max} + \frac{1}{2}\right)\right)$$

$$m + 1 = \left\lfloor log_\phi\left(\sqrt{5}\left(D_{max} + \frac{1}{2}\right)\right) \right\rfloor.$$

Since $log_\phi x = \frac{log_{10}x}{log_{10}\phi}$, the number of distinct fiber types m required to represent an integer in $[1, D_{max}]$ is

$$\left\lfloor \frac{log_{10}(\sqrt{5}(D_{max} + \frac{1}{2}))}{log_{10}\phi} \right\rfloor - 1.$$

APPENDIX B

NUMBER OF LENGTH-n NUMBER SEQUENCES ON k FIBER TYPES

We wish to determine the number of ways to construct a fiber sequence of length n using fibers of lengths L_1, $L_2, \ldots, L_k$, without considering the ordering of the fibers within a sequence. Let $T_{L_i}(z)$ be the generating function of the number of ways to construct a sequence of length n using only lengths $L_1, L_2, \ldots, L_i$. Then,

$$T_{L_1}(z) = 1 + z^{L_1} + z^{2L_1} + \ldots$$
$$T_{L_{i-1}}(z) = (1 + z^{L_{i-1}} + z^{2L_{i-1}} + \ldots)T_{L_i}(z).$$

This implies that:

$$T_{L_k}(z) = \frac{1}{\prod_{j=1}^{k}(1 - z^{L_j})}.$$

The number of length-n fiber sequences on $L_1, L_2, \ldots, L_k$ is the coefficient of the z^n term of $T_{L_k}(z)$. Although we could not obtain a closed-form expression of this coefficient, the form of $T_{L_k}(z)$ suggests that it is an exponential function of

n, k, and $L_1, L_2, \ldots, L_k$ and that it is impractical to examine all possible length-n fiber sequences.

APPENDIX C

GREEDY FIBONACCI REPRESENTATION OF AN INTEGER n

We prove by induction that a greedy Fibonacci representation of any positive integer n exists. If $n = 1$, then $n = F_2$; therefore, the basis of the induction holds. Suppose that there exists a greedy representation for any integer $\hat{n}$ such that $\hat{n} < n$. Let $n > 2$ and F_k be the largest Fibonacci number less than or equal to n, i.e., $F_k \leq n$ and $F_{k+1} > n$. Thus, $n - F_k < F_{k-1}$ since, otherwise, $F_{k-1} + F_k = F_{k+1} < n$. This proves that F_{k-1} cannot be included and that no adjacent 1s are possible in the greedy representation. Finally, $n = F_k + (n - F_k)$. By the induction hypothesis, there exists a greedy Fibonacci representation of $n - F_k$; thus, there exists a greedy Fibonacci representation of n which is the concatenation of F_k and the greedy representation of $n - F_k$.

APPENDIX D

SELF-CONVOLUTION OF THE FIBONACCI SEQUENCE

Our goal is to determine $\sum_{k=0}^{n} F_{n-k} F_k$, which is required for the derivation of the salient properties of the Fibonacci numbers given in Appendix E. $\sum_{k=0}^{n} F_{n-k} F_k$ is the coefficient of the nth term of $F^2(z)$, where $F(z)$ is the generating function of the Fibonacci sequence and, from [13], $F(z) = \frac{z}{1-z-z^2}$. Performing a partial fraction expansion on $F(z) = \frac{z}{1-z-z^2}$, we determine that $F(z) = \frac{1}{\sqrt{5}} \left(\frac{1}{1-\phi z} - \frac{1}{1-\hat{\phi} z} \right)$. Then,

$$F^2(z) = \frac{1}{5} \left(\frac{1}{1-\phi z} - \frac{1}{1-\hat{\phi} z} \right)^2$$

$$F^2(z) = \frac{1}{5} \left(\frac{1}{(1-\phi z)^2} - \frac{2}{(1-\phi z)(1-\hat{\phi} z)} + \frac{1}{(1-\hat{\phi} z)^2} \right).$$

Since $\frac{1}{(1-\phi z)^2} = \sum_{j=0}^{\infty} (j+1)\phi^j z^j$, $\frac{2}{(1-\phi z)(1-\hat{\phi} z)} = 2\sum_{j=0}^{\infty} F_{j+1} z^j$, and $\frac{1}{(1-\hat{\phi} z)^2} = \sum_{j=0}^{\infty} (j+1)\hat{\phi}^j z^j$,

$$F^2(z) = \frac{1}{5} \left(\sum_{j=0}^{\infty} (j+1)\phi^j z^j - 2\sum_{j=0}^{\infty} F_{j+1} z^j + \sum_{j=0}^{\infty} (j+1)\hat{\phi}^j z^j \right).$$

Since $\frac{1}{(1-\phi z)} = 1 + \phi z + \phi^2 z^2 + \cdots + \phi^n z^n + \cdots$, the coefficient of the z^n term of $\frac{1}{(1-\phi z)}$ is ϕ^n. Similarly, the nth coefficient of $\frac{1}{(1-\hat{\phi} z)}$ is $\hat{\phi}^n$. This implies that $\phi^n + \hat{\phi}^n$ is equal to the coefficient of the z^n term of $\frac{1}{(1-\phi z)} + \frac{1}{(1-\hat{\phi} z)}$. Thus, since $\phi + \hat{\phi} = 1$ and $\phi\hat{\phi} = -1$,

$$\frac{1}{(1-\phi z)} + \frac{1}{(1-\hat{\phi} z)} = \frac{2-(\phi+\hat{\phi})z}{(1-\phi z)(1-\hat{\phi} z)} = \frac{2-z}{1-z-z^2}$$

$$\frac{2-z}{1-z-z^2} = \frac{2}{1-z-z^2} - \frac{z}{1-z-z^2}.$$

The coefficient of the z^n term of $\frac{2}{1-z-z^2}$ can be determined as follows:

$$\frac{1}{(1-\phi z)(1-\hat{\phi} z)} = \frac{F(z)}{z}.$$

Since

$$\frac{F(z)}{z} = F_0 z^{-1} + F_1 z^0 + F_2 z^1 + \cdots + F_n z^{n-1} + F_{n+1} z^n + \cdots,$$

the coefficient of the z^n term of $\frac{2}{(1-\phi z)(1-\hat{\phi} z)}$ is $2F_{n+1}$. The generating function of the Fibonacci sequence is $\frac{z}{1-z-z^2}$ and F_n is the coefficient of the z^n term. Thus, the coefficient of the z^n term of $\frac{2-z}{1-z-z^2}$ is

$$2F_{n+1} - F_n.$$

This implies that $\phi^n + \hat{\phi}^n = 2F_{n+1} - F_n$. Since $\frac{1}{(1-\phi z)^2} = \sum_{j=0}^{\infty} (j+1)\phi^j z^j$ and $\frac{1}{(1-\hat{\phi} z)^2} = \sum_{j=0}^{\infty} (j+1)\hat{\phi}^j z^j$,

$$\frac{1}{(1-\phi z)^2} + \frac{1}{(1-\hat{\phi} z)^2} = \sum_{j=0}^{\infty} (j+1)(\phi^j + \hat{\phi}^j) z^j$$

$$= \sum_{j=0}^{\infty} (j+1)(2F_{j+1} - F_j) z^j$$

$$F^2(z) = \frac{1}{5} \sum_{j=0}^{\infty} (j+1)(2F_{j+1} - F_j) z^j - \frac{2}{5} \sum_{j=0}^{\infty} F_{j+1} z^j$$

$$F^2(z) = \frac{1}{5} \sum_{j=0}^{\infty} \left((j+1)(2F_{j+1} - F_j) - 2F_{j+1} \right) z^j.$$

The coefficient of the z^n term of $F^2(z)$ is:

$$\frac{2nF_{n+1} - (n+1)F_n}{5}.$$

The self-convolution of the Fibonacci sequence is:

$$\sum_{k=0}^{n} F_k F_{n-k} = \frac{2nF_{n+1} - (n+1)F_n}{5}.$$

APPENDIX E

PROPERTIES OF THE GREEDY FIBONACCI REPRESENTATION

We now demonstrate several salient properties of the greedy Fibonacci representation. If $D = \sum_{j=1}^{n} \sigma_j F_{j+1}$, where $\sigma_j \in \{0, 1\}$, we express D as $\underline{\sigma} = \sigma_n \sigma_{n-1} \cdots \sigma_1$. The n-digit greedy representation $\underline{\sigma} = \sigma_n \cdots \sigma_1$ is referred to as an n-string.

Property A. $T_{kn} = F_{(n+1)-k} F_k$ for $1 \leq k \leq n$, where T_{kn} refers to the number of n-strings in which the kth digit is 1.

Proof. Let $1 < k < n$. The fact that $\sigma_k = 1$ implies that $\sigma_{k+1} = 0$ and $\sigma_{k-1} = 0$ since no consecutive 1s are possible in a greedy Fibonacci representation. Then, $\underline{\sigma} = \underline{\alpha} 010 \underline{\beta}$, where $\underline{\alpha}$ and $\underline{\beta}$ are an $(n-k-1)$-string and a $(k-2)$-string, respectively. This suggests that $T_{kn} = N_{n-k-1} N_{k-2}$, where N_j is the number of possible j-strings. Since all numbers from 0 to $F_{j+2} - 1$ can be represented by a j-string, $N_j = F_{j+2}$; therefore, $T_{kn} = F_{n-k+1} F_k$ for $1 < k < n$. When $k = 1$, $\underline{\sigma} = \gamma 01$, where γ is an $(n-2)$-string. This implies that $T_{1n} = N_{n-2} = F_n$. Similarly, $T_{nn} = N_{n-2} = F_n$. Since $F_n = F_{n-n+1} F_n$ and $F_n = F_{n-1+1} F_1$, $T_{kn} = F_{n-k+1} F_k$ for all k such that $1 \leq k \leq n$. □
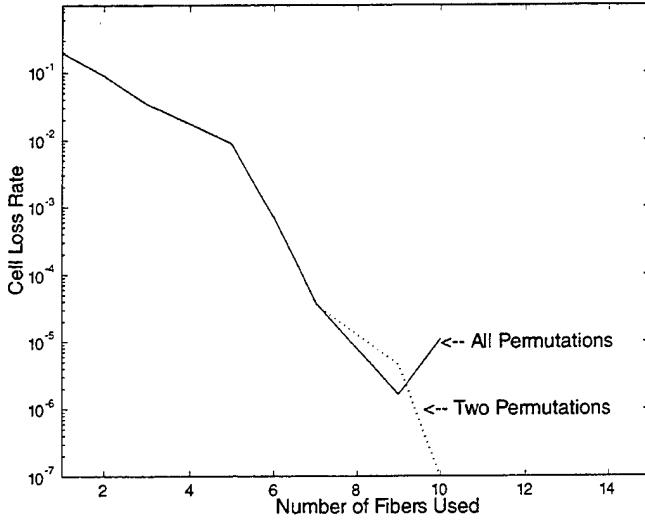
Fig. 21. Cell loss rates for the cases where all permutations and two permutations, respectively, of a fiber sequence are examined and where $\rho = 0.8$ and $\tau = 8$.

Property B. $T_n = \frac{2(n+1)F_{n-2} - (n+2)F_{n-1}}{5}$, where T_n is the total number of 1s in all n-strings.

Proof.

$$T_n = \sum_{k=1}^{n} T_{kn} = \sum_{k=1}^{n} F_{(n+1)-k} F_k.$$

Since $F_{n+1-k} = F_0 = 0$ when $k = n+1$ and $F_k = 0$ when $k = 0$, $T_n = \sum_{k=0}^{n+1} F_{n+1-k} F_k$. From Appendix E, $\sum_{k=0}^{n} F_{n-k} F_k = \frac{2nF_{n-1} - (n+1)F_n}{5}$. This implies that

$$T_n = \sum_{j=0}^{n+1} F_{(n+1)-k} F_k = \frac{2(n+1)F_{n+2} - (n+2)F_{n+1}}{5}.$$

$\square$

Property C. $\bar{X}_n = \frac{2(n+1)F_{n-2} - (n+2)F_{n-1}}{5} \frac{1}{F_{n-2}-1}$, where $\bar{X}_n$ is the average number of 1s in a nonzero n-string.

Proof. $\bar{X}_n$ is the ratio of the sum of the total number of 1s in all n-strings and the number of nonzero n-strings, i.e., $\bar{X}_n = \frac{T_n}{F_{n-2}-1}$. The assertion follows from Property B. $\square$

Property D. $E_n = \frac{1}{n\bar{X}_n} = \frac{1}{n} \frac{2(n+1)F_{n-2} - (n+2)F_{n-1}}{5} \frac{1}{F_{n-2}-1}$, where E_n is the probability that a digit in an n-string contains a 1.

Proof. Implied in Property D is that the n-string is chosen uniformly among all possible nonzero n-strings. E_n is the ratio of the average number of 1s in a nonzero n-string and the number of digits in an n-string, i.e., $\frac{\bar{X}_n}{n}$, which is the assertion. $\square$

Property E.

$$\lim_{n \to \infty} E_n = \frac{2}{5} - \frac{1}{5}\frac{1}{\phi}.$$

Proof. Since $E_n = \frac{2(n+1)F_{n-2}}{5n(F_{n-2}-1)} - \frac{(n+2)F_{n-1}}{5n(F_{n-2}-1)}$, as $n \to \infty$, $F_{n+2} - 1 \approx F_{n+2}$. Since $F_n = \lfloor \frac{1}{\sqrt{5}}\phi^n + \frac{1}{2} \rfloor$, $\lim_{n\to\infty} F_n = \frac{1}{\sqrt{5}}\phi^n$ and $\lim_{n\to\infty} \frac{F_{n-1}}{F_{n-2}} = \frac{1}{\phi}$. This implies that

$$\lim_{n \to \infty} E_n = \frac{2}{5} - \frac{1}{5}\frac{1}{\phi} \approx 0.2763932.$$

$\square$

APPENDIX F
EFFECT OF SEARCHING ALL PERMUTATIONS

We now demonstrate that searching for all permutations of a fiber sequence, in general, does not appreciably decrease the cell loss rate of the architecture. As an example, consider the following two simulation studies with $\tau = 8$ and $\rho = 0.8$. In one of the simulation studies, the algorithm searched only the two permutations of a fiber sequence, as described in Section 4.1; in the other simulation study, the algorithm examined all possible permutations. As indicated in Fig. 21, the performance of the two studies is nearly identical. Searching for only two permutations suffices to achieve nearly the same level of performance as that of exhaustive searching and, therefore, is preferable as it results in significantly lower computational complexity.

REFERENCES

[1] J Bowers et al., "Multidisciplinary Optical Switching Technology Center Annual Report," AFOSR F49620-96-1-0349, Dept. of Electrical and Computer Eng., Univ. of California, Santa Barbara, 1997.
[2] D. Blumenthal, K. Chen, J. Ma, R. Feuerstein, and J. Sauer, "Demonstration of a Deflection Routing 2 × 2 Photonic Switch for Computer Interconnects," IEEE Photonics Technology Letters, vol. 4, no. 2, pp. 169-173, Feb. 1992.
[3] A. Bononi, F. Forghieri, and P. Prucnal, "Design and Channel Constraint Analysis of Ultrafast Multihop All-Optical Networks with Deflection Routing Employing Solitons," J. Lightwave Technology, vol. 11, no. 12, pp. 2166-2176, Dec. 1993.
[4] I. Chlamtac and A. Fumagalli, "An Optical Switch Architecture for Manhattan Networks," IEEE J. Selected Areas in Comm., vol. 11, no. 4, pp. 550-559, May 1993.
[5] R. Cruz and J. Tsai, "COD: Alternative Architectures for High Speed Packet Switching," IEEE/ACM Trans. Networking, vol. 4, no. 1, pp. 11-21, Feb. 1996.
[6] S. Golestani, "Congestion-Free Communication in High-Speed Packet Networks," IEEE J. Selected Areas in Comm., vol. 39, no. 12, pp. 1802-1812, Dec. 1991.
[7] Z. Haas, "The 'Staggering Switch': An Electronically Controlled Optical Packet Switch," IEEE J. Lightwave Technology, vol. 11, nos. 5/6, pp. 925-936, May/June 1993.
[8] M. Hluchyj and M. Karol, "Queueing in High-Performance Packet Switching," IEEE J. Selected Areas in Comm., vol. 6, no. 9, pp. 1587-1597, Dec. 1988.
[9] M. Karol, M. Hluchyj, and S. Morgan, "Input vs. Output Queueing on a Space-Division Packet Switch," IEEE Trans. Comm., vol. 35, no. 12, pp. 1347-1356, Dec. 1987.
[10] F. Masetti, P. Gavignet-Morin, D. Chiaroni, and G. Da Loura, "Fiber Delay Lines Optical Buffer for ATM Photonic Switching Applications," Proc. IEEE INFOCOM, vol. 3, pp. 935-942, Mar. 1993.
[11] M. Schwartz, Broadband Integrated Networks. Englewood Cliffs, N.J.: Prentice Hall, 1996.
[12] Y. Shimazu and M. Tsukada, "Ultrafast Photonic ATM Switch Optical Output Buffers," J. Lightwave Technology, vol. 10, no. 2, pp. 265-272, Feb. 1992.

[13] A. Shum, "Design and Evaluation of Optical ATM Switches," PhD dissertation, Dept. of Electrical and Computer Eng., Univ. of California, Santa Barbara, Jan. 1998.
[14] E. Varvarigos, "The 'Packing' and the 'Scheduling' Packet Switch Architectures for Almost-All Optical Lossless Networks," submitted for publication.
[15] E. Varvarigos and J. Lang, "A Virtual Circuit Deflection Protocol for Multigigabit Networks and Its Performance for the Manhattan Street Topology," submitted for publication.

Allen Shum received the BA degree in applied mathematics from the University of California, Berkeley, in 1984, and the MS and PhD degrees in electrical and computer engineering from the University of California, Santa Barbara, in 1987 and 1998, respectively. He has been with the SPAWAR Systems Center, San Diego, as a computer scientist and an electrical engineer since 1988. His research interests are in the design and evaluation of communication networks.

P.M. Melliar-Smith received a PhD degree in computer science from the University of Cambridge, England. He is a professor in the Department of Electrical and Computer Engineering at the University of California, Santa Barbara. His research interests include high-speed communication networks and protocols, distributed systems, and fault tolerance.

Louise E. Moser received a PhD degree in mathematics from the University of Wisconsin, Madison. She is a professor in the Department of Electrical and Computer Engineering at the University of California, Santa Barbara. She has served as an associate editor for the *IEEE Transactions on Computers* and an area editor for *Computer* magazine in the area of networks. Her research interests span the areas of distributed systems, computer networks, and software engineering.

▷ **IEEE Computer Society publications cited in this article can be found in our Digital Library at** http://computer.org/publications/dlib.